



GNSS Array-based Acquisition: Theory and Implementation

Ph.D. Dissertation

Javier Arribas Lázaro

Centre Tecnològic de Telecomunicacions de Catalunya (CTTC)
Parc Mediterrani de la Tecnologia
Av. Carl Friedrich Gauss 7 B4
08860 Castelldefels, Barcelona (SPAIN)
e-mail: javier.arribas@cttc.es

Ph.D. Thesis Advisor: Dr. Carles Fernández-Prades
Centre Tecnològic de Telecomunicacions de Catalunya (CTTC)
Av. Carl Friedrich Gauss 7 B4
08860 Castelldefels, Barcelona (SPAIN)
e-mail: carles.fernandez@cttc.es

Ph.D. Thesis Tutor: Dra. Ana Isabel Pérez-Neira
Full Professor
Universitat Politècnica de Catalunya (UPC)
Campus Nord UPC, Edifici D5
c/ Jordi Girona, 1-3
08034 Barcelona (SPAIN)
e-mail: ana.isabel.perez@upc.edu

July 5, 2012

A mis abuelas Silvina y Salomé.

Abstract

This Dissertation addresses the signal acquisition problem using antenna arrays in the general framework of Global Navigation Satellite Systems (GNSS) receivers. The term GNSS classifies those navigation systems based on a constellation of satellites, which emit ranging signals useful for positioning. Although the American GPS is already available, which coexists with the renewed Russian Glonass, the forthcoming European contribution (Galileo) along with the Chinese Compass will be operative soon. Therefore, a variety of satellite constellations and signals will be available in the next years. GNSSs provide the necessary infrastructures for a myriad of applications and services that demand a robust and accurate positioning service. The positioning availability must be guaranteed all the time, specially in safety-critical and mission-critical services.

Examining the threats against the service availability, it is important to take into account that all the present and the forthcoming GNSSs make use of Code Division Multiple Access (CDMA) techniques. The ranging signals are received with very low pre-correlation signal-to-noise ratio (in the order of -22 dB for a receiver operating at the Earth surface). Despite that the GNSS CDMA processing gain offers limited protection against Radio Frequency Interferences (RFI), an interference with a interference-to-signal power ratio that exceeds the processing gain can easily degrade receivers' performance or even deny completely the GNSS service, specially conventional receivers equipped with minimal or basic level of protection towards RFIs. As a consequence, RFIs (either intentional or unintentional) remain as the most important cause of performance degradation. A growing concern of this problem has appeared in recent times.

Focusing our attention on the GNSS receiver, it is known that signal acquisition has the lowest sensitivity of the whole receiver operation, and, consequently, it becomes the performance bottleneck in the presence of interfering signals. A single-antenna receiver can make use of time and frequency diversity to mitigate interferences, even though the performance of these techniques is compromised in low SNR scenarios or in the presence of wideband interferences. On the other hand, antenna arrays receivers can benefit from spatial-domain processing, and thus mitigate the effects of interfering signals. Spatial diversity has been traditionally applied to the signal tracking operation of GNSS receivers. However, initial tracking conditions depend on signal acquisition, and there are a number of scenarios in which the acquisition process can fail as stated before. Surprisingly, to the best of our knowledge, the application of antenna arrays to GNSS signal acquisition has not received much attention.

This Thesis pursues a twofold objective: on the one hand, it proposes novel array-based acquisition algorithms using a well-established statistical detection theory framework, and on the other hand, it demonstrates both their real-time implementation feasibility and their performance in realistic scenarios.

The Dissertation starts with a brief introduction to GNSS receivers fundamentals, providing some details about the navigation signals structure and the receiver's architecture of both GPS and Galileo systems. It follows with an analysis of GNSS signal acquisition as a detection problem, using the Neyman-Pearson (NP) detection theory framework and the single-antenna acquisition signal model. The NP approach is used here to derive both the optimum detector (known as *clairvoyant detector*) and the so-called Generalized Likelihood Ratio Test (GLRT) detector, which is the basis of almost all of the current state-of-the-art acquisition algorithms. Going further, a novel detector test statistic intended to jointly acquire a set of GNSS satellites

is obtained, thus reducing both the acquisition time and the required computational resources. The effects of the front-end bandwidth in the acquisition are also taken into account.

Then, the GLRT is extended to the array signal model to obtain a new detector which is able to mitigate temporally uncorrelated interferences even if the array is unstructured and moderately uncalibrated, thus becoming one of the main contributions of this Dissertation. The key statistical feature is the assumption of an arbitrary and unknown covariance noise matrix, which attempts to capture the statistical behavior of the interferences and other non-desirable signals, while exploiting the spatial dimension provided by antenna arrays. Closed form expressions for the detection and false alarm probabilities are provided. Performance and interference rejection capability are modeled and compared both to their theoretical bound. The proposed array-based acquisition algorithm is also compared to conventional acquisition techniques performed after blind null-steering beamformer approaches, such as the power minimization algorithm. Furthermore, the detector is analyzed under realistic conditions, accounting for the presence of errors in the covariance matrix estimation, residual Doppler and delay errors, and signal quantization effects. Theoretical results are supported by Monte Carlo simulations.

As another contribution of this Dissertation, the second part of the work deals with the design and the implementation of a novel Field Programmable Gate Array (FPGA)-based GNSS real-time antenna-array receiver platform. The platform is intended to be used as a research tool tightly coupled with software defined GNSS receivers. A complete signal reception chain including the antenna array and the multichannel phase-coherent RF front-end for the GPS L1/Galileo E1 was designed, implemented and tested. The details of the digital processing section of the platform, such as the array signal statistics extraction modules, are also provided. The design trade-offs and the implementation complexities were carefully analyzed and taken into account. As a proof-of-concept, the problem of GNSS vulnerability to interferences was addressed using the presented platform. The array-based acquisition algorithms introduced in this Dissertation were implemented and tested under realistic conditions. The performance of the algorithms were compared to single antenna acquisition techniques, measured under strong in-band interference scenarios, including narrow/wide band interferers and communication signals.

The platform was designed to demonstrate the implementation feasibility of array-based acquisition algorithms, leaving the rest of the receiver operations (mainly, tracking, navigation message decoding, code and phase observables, and basic Position, Velocity and Time (PVT) solution) to a Software Defined Radio (SDR) receiver running in a personal computer, processing in real-time the spatially-filtered signal sample stream coming from the platform using a Gigabit Ethernet bus data link. In the last part of this Dissertation, we close the loop by designing and implementing such software receiver.

The proposed receiver targets multi-constellation/multi-frequency architectures, pursuing the goals of efficiency, modularity, interoperability, and flexibility demanded by user domains that require non-standard features, such as intermediate signals or data extraction and algorithms interchangeability. In this context, we introduce an open-source, real-time GNSS software defined receiver (so-named GNSS-SDR) that contributes with several novel features such as the use of software design patterns and shared memory techniques to manage efficiently the data flow between receiver blocks, the use of hardware-accelerated instructions for time-consuming vector operations like carrier wipe-off and code correlation, and the availability to compile and run on multiple software platforms and hardware architectures. At this time of writing (April 2012), the receiver enjoys of a 2-dimensional Distance Root Mean Square (DRMS) error lower than 2 meters in a GPS L1 C/A scenario with 8 satellites in lock and a Horizontal Dilution Of Precision (HDOP) of 1.2.

Resumen

Esta tesis aborda el problema de la adquisición de la señal usando arrays de antenas en el marco general de los receptores de Sistemas Globales de Navegación por Satélite (GNSS). El término GNSS engloba aquellos sistemas de navegación basados en una constelación de satélites que emiten señales útiles para el posicionamiento. Aunque el GPS americano ya está disponible, coexistiendo con el renovado sistema ruso GLONASS, actualmente se está realizando un gran esfuerzo para que la contribución europea (Galileo), junto con el nuevo sistema chino Compass, estén operativos en breve. Por lo tanto, una gran variedad de constelaciones de satélites y señales estarán disponibles en los próximos años. Estos sistemas proporcionan las infraestructuras necesarias para una multitud de aplicaciones y servicios que demandan un servicio de posicionamiento confiable y preciso. La disponibilidad de posicionamiento se debe garantizar en todo momento, especialmente en los servicios críticos para la seguridad de las personas y los bienes.

Cuando examinamos las amenazas de la disponibilidad del servicio que ofrecen los GNSSs, es importante tener en cuenta que todos los sistemas presentes y los sistemas futuros ya planificados hacen uso de técnicas de multiplexación por división de código (CDMA). Las señales transmitidas por los satélites son recibidas con una relación señal-ruido (SNR) muy baja, medida antes de la correlación (del orden de -22 dB para un receptor ubicado en la superficie de la tierra). A pesar de que la ganancia de procesado CDMA ofrece una protección inherente contra las interferencias de radiofrecuencia (RFI), esta protección es limitada. Una interferencia con una relación de potencia de interferencia a potencia de la señal que excede la ganancia de procesado puede degradar el rendimiento de los receptores o incluso negar por completo el servicio GNSS. Este riesgo es especialmente importante en receptores convencionales equipados con un nivel mínimo o básico de protección frente las RFIs. Como consecuencia, las RFIs (ya sean intencionadas o no intencionadas), se identifican como la causa más importante de la degradación del rendimiento en GNSS. El problema está causando una preocupación creciente en los últimos tiempos, ya que cada vez hay más servicios que dependen de los GNSSs.

Si centramos la atención en el receptor GNSS, es conocido que la adquisición de la señal tiene la menor sensibilidad de todas las operaciones del receptor, y, en consecuencia, se convierte en el factor limitador en la presencia de señales interferentes. Un receptor de una sola antena puede hacer uso de la diversidad en tiempo y frecuencia para mitigar las interferencias, aunque el rendimiento de estas técnicas se ve comprometido en escenarios con baja SNR o en presencia de interferencias de banda ancha. Por otro lado, los receptores basados en múltiples antenas se pueden beneficiar del procesado espacial, y por lo tanto mitigar los efectos de las señales interferentes. La diversidad espacial se ha aplicado tradicionalmente a la operación de tracking de la señal en receptores GNSS. Sin embargo, las condiciones iniciales del tracking dependen del resultado de la adquisición de la señal, y como hemos visto antes, hay un número de situaciones en las que el proceso de adquisición pueden fallar. En base a nuestro grado de conocimiento, la aplicación de los arrays de antenas a la adquisición de la señal GNSS no ha recibido mucha atención, sorprendentemente.

El objetivo de esta tesis doctoral es doble: por un lado, proponer nuevos algoritmos para la adquisición basados en arrays de antenas, usando como marco la teoría de la detección de señal estadística, y por otro lado, demostrar la viabilidad de su implementación y ejecución en tiempo real, así como su medir su rendimiento en escenarios realistas.

La tesis comienza con una breve introducción a los fundamentos de los receptores GNSS, proporcionando algunos detalles sobre la estructura de las señales de navegación y la arquitectura del receptor aplicada a los sistemas GPS y Galileo. Continua con el análisis de la adquisición GNSS como un problema de detección, aplicando la teoría del detector Neyman-Pearson (NP) y el modelo de señal de una única antena. El marco teórico del detector NP se utiliza aquí para derivar tanto el detector óptimo (conocido como detector clarividente) como la denominada Prueba Generalizada de la Razón de Verosimilitud (en inglés, Generalized Likelihood Ratio Test (GLRT)), que forma la base de prácticamente todos los algoritmos de adquisición del estado del arte actual. Yendo más lejos, proponemos un nuevo detector diseñado para adquirir simultáneamente un conjunto de satélites, por lo tanto, obtiene una reducción del tiempo de adquisición y de los recursos computacionales necesarios en el proceso, respecto a las técnicas convencionales. El efecto del ancho de banda del receptor también se ha tenido en cuenta en los análisis.

A continuación, el detector GLRT se extiende al modelo de señal de array de antenas para obtener un detector nuevo que es capaz de mitigar interferencias no correladas temporalmente, incluso utilizando arrays no estructurados y moderadamente descalibrados, convirtiéndose así en una de las principales aportaciones de esta tesis. La clave del detector es asumir una matriz de covarianza de ruido arbitraria y desconocida en el modelo de señal, que trata de captar el comportamiento estadístico de las interferencias y otras señales no deseadas, mientras que utiliza la dimensión espacial proporcionada por los arrays de antenas. Se han derivado las expresiones que modelan la probabilidades teóricas de detección y falsa alarma. El rendimiento del detector y su capacidad de rechazo a interferencias se han modelado y comparado con su límite teórico.

El algoritmo propuesto también ha sido comparado con técnicas de adquisición convencionales, ejecutadas utilizando la salida de conformadores de haz que utilizan algoritmos de filtrado de interferencias, como el algoritmo de minimización de la potencia. Además, el detector se ha analizado bajo condiciones realistas, representadas con la presencia de errores en la estimación de covarianzas, errores residuales en la estimación del Doppler y el retardo de señal, y los efectos de la cuantificación. Los resultados teóricos se apoyan en simulaciones de Monte Carlo.

Como otra contribución principal de esta tesis, la segunda parte del trabajo trata sobre el diseño y la implementación de una nueva plataforma para receptores GNSS en tiempo real basados en array de antenas que utiliza la tecnología de matriz programable de puertas lógicas (en inglés Field Programmable Gate Array (FPGA)). La plataforma está destinada a ser utilizada como una herramienta de investigación estrechamente acoplada con receptores GNSS definidos por software.

Se ha diseñado, implementado y verificado la cadena completa de recepción, incluyendo el array de antenas y el front-end multi-canal para las señales GPS L1 y Galileo E1. El documento explica en detalle el procesado de señal que se realiza, como por ejemplo, la implementación del módulo de extracción de estadísticas de la señal. Los compromisos de diseño y las complejidades derivadas han sido cuidadosamente analizadas y tenidas en cuenta.

La plataforma ha sido utilizada como prueba de concepto para solucionar el problema presentado de la vulnerabilidad del GNSS a las interferencias. Los algoritmos de adquisición introducidos en esta tesis se implementaron y probaron en condiciones realistas. El rendimiento de los algoritmos se comparó con las técnicas de adquisición basadas en una sola antena. Se han realizado pruebas en escenarios que contienen interferencias dentro de la banda GNSS, incluyendo interferencias de banda estrecha y banda ancha y señales de comunicación.

La plataforma fue diseñada para demostrar la viabilidad de la implementación de nuevos algoritmos de adquisición basados en array de antenas, dejando el resto de las operaciones del receptor (principalmente, los módulos de tracking, decodificación del mensaje de navegación, los observables de código y fase, y la solución básica de Posición, Velocidad y Tiempo (PVT)) a un receptor basado en el concepto de Radio Definida por Software (SDR), el cual se ejecuta en un ordenador personal. El receptor procesa en tiempo real las muestras de la señal filtradas espacialmente, transmitidas usando el bus de datos Gigabit Ethernet.

En la última parte de esta Tesis, cerramos ciclo diseñando e implementando completamente

este receptor basado en software. El receptor propuesto está dirigido a las arquitecturas de multi-constalación GNSS y multi-frecuencia, persiguiendo los objetivos de eficiencia, modularidad, interoperabilidad y flexibilidad demandada por los usuarios que requieren características no estándar, tales como la extracción de señales intermedias o de datos y intercambio de algoritmos. En este contexto, se presenta un receptor de código abierto que puede trabajar en tiempo real, llamado GNSS-SDR, que contribuye con varias características nuevas. Entre ellas destacan el uso de patrones de diseño de software y técnicas de memoria compartida para administrar de manera eficiente el flujo de datos entre los bloques del receptor, el uso de la aceleración por hardware para las operaciones vectoriales más costosas, como la eliminación de la frecuencia Doppler y la correlación de código, y la disponibilidad para compilar y ejecutar el receptor en múltiples plataformas de software y arquitecturas de hardware. A fecha de la escritura de esta Tesis (abril de 2012), el receptor obtiene un rendimiento basado en la medida de la raíz cuadrada del error cuadrático medio en la distancia bidimensional (en inglés, 2-dimensional Distance Root Mean Square (DRMS) error) menor de 2 metros para un escenario GPS L1 C/A con 8 satélites visibles y una dilución de la precisión horizontal (en inglés, Horizontal Dilution Of Precision (HDOP)) de 1.2.

Resum

Aquesta tesi aborda el problema de l'adquisició del senyal utilitzant arrays d'antenes en el marc general dels receptors de Sistemes Globals de Navegació per Satèl·lit (GNSS). El terme GNSS engloba aquells sistemes de navegació basats en una constel·lació de satèl·lits que emeten senyals útils per al posicionament. Encara que el GPS americà ja està disponible, coexistint amb el renovat sistema rus GLONASS, la contribució europea (Galileu), juntament amb el nou sistema xinès Compass, estaran operatius en breu. Per tant, una gran varietat de constel·lacions de satèl·lits i senyals estaran disponibles els propers anys. Aquests sistemes proporcionen les infraestructures necessàries per a una multitud d'aplicacions i serveis que requereixen un servei de posicionament fiable i precís. La disponibilitat de posicionament s'ha de garantir en tot moment, especialment als serveis crítics per a la seguretat de les persones i els béns.

Quan analitzem les amenaces de la disponibilitat del servei que ofereixen els GNSSs, és important tenir en compte que, tots els sistemes presents i els sistemes futurs ja planificats fan ús de tècniques de multiplexació per divisió de codi (CDMA). Els senyals transmesos pels satèl·lits són rebudes amb una relació senyal-soroll (SNR) molt baixa, mesurada abans de la correlació (de l'ordre de -22 dB per a un receptor situat a la superfície de la Terra). Tot i que el guany de processat CDMA ofereix una protecció limitada contra les interferències de radiofreqüència (RFI), una interferència amb una relació de potència d'interferència a potència del senyal que excedeix el guany de processament pot degradar el rendiment dels receptors o fins i tot negar per complet el servei GNSS. Aquest risc és especialment important en receptors convencionals equipats amb un nivell mínim o bàsic de protecció cap a les RFI. Com a conseqüència, les RFI (ja siguin intencionades o no intencionades), es mantenen com la causa més important de la degradació del rendiment en GNSS. El problema està causant una creixent preocupació als últims temps, ja que cada vegada hi ha més serveis que depenen dels GNSSs.

Si centrem l'atenció en el receptor GNSS, és conegut que l'adquisició del senyal té la menor sensibilitat de totes les operacions del receptor, i, en conseqüència, esdevé el factor limitant en presència de senyals interferents. Un receptor d'una sola antena pot fer ús de la diversitat en temps i freqüència per mitigar les interferències, encara que el rendiment d'aquestes tècniques es veu compromès en escenaris amb baixa SNR o en presència d'interferències de banda ampla. D'altra banda, els receptors basats en múltiples antenes es poden beneficiar del processat espacial, i per tant mitigar els efectes dels senyals interferents. La diversitat espacial s'ha aplicat tradicionalment a l'operació de tracking del senyal en receptors GNSS. No obstant això, les condicions inicials del tracking depenen del resultat de l'adquisició del senyal, i com hem vist abans, hi ha un nombre de situacions en què el procés d'adquisició poden fallar. Sorprenentment, donat el nostre grau de coneixement, l'aplicació dels arrays d'antenes per a l'adquisició del senyal GNSS no ha rebut molta atenció.

L'objectiu d'aquesta tesi doctoral és doble: d'una banda, proposar nous algorismes per a l'adquisició basats en arrays d'antenes, usant com a marc la teoria de la detecció de senyal estadística, i d'altra banda, demostrar la viabilitat de la seva implementació i execució en temps real, així com mesurar el seu rendiment en escenaris realistes.

La tesi comença amb una breu introducció als fonaments dels receptors GNSS, proporcionant alguns detalls sobre l'estructura dels senyals de navegació i l'arquitectura del receptor aplicada als sistemes GPS i Galileu. Continua amb l'anàlisi de l'adquisició GNSS com un problema de detecció, aplicant la teoria del detector Neyman-Pearson (NP) i el model de senyal d'una única

antena. El marc teòric del detector NP s'utilitza aquí per derivar tant el detector òptim (coneugut com a detector clarivident) i l'anomenada Prova Generalitzada de la Raó de Versemblança (en anglès, Generalized Likelihood Ràtio Test (GLRT)), que forma la base de gairebé tots els algorismes d'adquisició de l'estat de l'art actual. Anant més lluny, proposem un nou detector dissenyat per adquirir simultàniament un conjunt de satèl·lits. Per tant, obté una reducció del temps d'adquisició i dels recursos computacionals necessaris en el procés. L'efecte de l'ample de banda del receptor també s'ha tingut en compte.

Com a solució proposada al problema, el detector GLRT s'ha estés al model de senyal d'array d'antenes per obtenir un detector nou que és capaç de mitigar interferències no correlades temporalment, fins i tot utilitzant arrays no estructurats i moderadament no calibrats, convertint-se així en una de les principals aportacions d'aquesta tesi. La clau del detector és assumir una matriu de covariància de soroll arbitrària i desconeguda en el model de senyal, que tracta de captar el comportament estadístic de les interferències i altres senyals no desitjades, mentre que utilitza la dimensió espacial proporcionada pels arrays d'antenes. S'han derivat les expressions que modelen la probabilitats teòriques de detecció i falsa alarma. El rendiment del detector i la seva capacitat de rebuig a interferències s'han modelat i comparat amb el seu límit teòric.

L'algorisme proposat també s'ha comparat amb tècniques d'adquisició convencionals, executades utilitzant la sortida de conformadors de feix que utilitzen algoritmes de filtrat d'interferències, com l'algorisme de minimització de la potència. A més a més, el detector s'ha analitzat sota condicions realistes, representades amb la presència d'errors en l'estimació de covariàncies, errors residuals en l'estimació del Doppler i el retard de senyal, i els efectes de la quantificació. Els resultats teòrics es recolzen en simulacions de Montecarlo.

Com una altra contribució principal d'aquesta tesi, la segona part del treball tracta sobre el disseny i la implementació d'una nova plataforma per a receptors GNSS en temps real basats en array d'antenes. La plataforma utilitza la tecnologia de matriu programable de portes lògiques (en anglès Field Programmable Gate Array (FPGA)) i està destinada a ser utilitzada com una eina d'investigació estretament acoblada amb receptors GNSS definits per software.

S'ha dissenyat, implementat i verificat la totalitat de la cadena de recepció, incloent l'array d'antenes i el front-end multicanal per als senyals GPS L1 i Galileu E1. El document explica en detall el processat de senyal que es realitza, com ara, la implementació del mòdul d'extracció d'estadístiques del senyal. Els compromisos de disseny i les complexitats derivades han estat acuradament analitzades i tingudes en compte.

La plataforma ha estat utilitzada com a prova de concepte per solucionar el problema presentat de la vulnerabilitat del GNSS a les interferències. Els algorismes d'adquisició introduïts en aquesta tesi s'han implementat i provat en condicions realistes. El rendiment dels algorismes es va comparar amb les tècniques d'adquisició basades en una sola antena. S'han realitzat proves en escenaris que contenen interferències dins de la banda GNSS, incloent interferències de banda estreta i banda ampla i senyals de comunicació.

La plataforma ha sigut dissenyada per demostrar la viabilitat de la implementació de nous algorismes d'adquisició basats en array d'antenes, deixant la resta de les operacions del receptor (principalment, els mòduls de tracking, decodificació del missatge de navegació, els observables de codi i fase, i la solució bàsica de Posició, Velocitat i Temps (PVT)) a un receptor basat en el concepte de Ràdio Definida per Software (SDR), que s'executa en un ordinador personal. El receptor processa en temps real les mostres del senyal filtrades espacialment i transmeses usant el bus de dades Gigabit Ethernet.

L'última part d'aquesta Tesi tanca el cicle, dissenyant i implementant completament aquest receptor per software. El receptor proposat està dirigit a les arquitectures de multi-constel·lació GNSS i multi-freqüència, perseguint els objectius d'eficiència, modularitat, interoperabilitat i flexibilitat demandada per usuaris que requereixen característiques no estàndard, com ara l'extracció de senyals intermèdies o de dades i intercanvi d'algorismes. En aquest context, es presenta un receptor de codi obert que pot treballar en temps real, anomenat GNSS-SDR. El receptor contribueix amb diverses característiques noves. Destaquen l'ús de patrons de disseny de software i tècniques de memòria compartida per administrar de manera eficient el flux de dades entre els blocs del receptor, l'ús de l'acceleració per maquinari per a les operacions vectorials més costoses, com

l'eliminació de la freqüència Doppler i la correlació de codi, i la disponibilitat per compilar i executar el receptor en múltiples plataformes de software i arquitectures de hardware. A data de l'escriptura d'aquesta Tesi (abril del 2012), el receptor obté un rendiment basat en la mesura de l'arrel quadrada de l'error quadràtic mitjà en la distància bidimensional (en anglès, 2-dimensional Distance Root Mean Square (DRMs) error) menor de 2 metres per a un esce-
nari GPS L1 C/A amb 8 satèl·lits visibles i una dilució de la precisió horitzontal (en anglès, Horizontal Dilution Of Precision (HDOP)) de 1.2.

Preface

Después de estos maravillosos 4 años dedicados a realizar mi doctorado, estoy seguro de que el recuerdo que voy a conservar es la excepcional calidad, tanto humana como profesional, de la gente con la que me he cruzado durante el viaje.

Quiero agradecer en primer lugar a Carles (oficialmente, Dr. Carles Fernández-Prades) su infinita paciencia, que finalmente logró vencer a mi cabezonería. De él he aprendido lo que es ser un científico, es un ejemplo a seguir en todos los aspectos. Además de compartir su pasión por la ciencia, la cual ha dado pie a infinidad de buenos momentos discutiendo proyectos futuros y aplicaciones inverosímiles, su cercanía y su calidad humana es digna de remarcar. Cómo no agradecer también la dedicación que me ha brindado Pau (oficialmente, Dr. Pau Closas). Las horas que le he robado discutiendo ideas y buscando soluciones han sido incontables, y en todas las ocasiones, su paciencia y capacidad de análisis han sido simplemente excepcionales. Un hueco en este homenaje está reservado para Luis Esteve y sus críticas constructivas y aportaciones, que por cierto, aún tenemos pendiente las birras del GNSS-SDR!. ¡Ha sido una suerte compartir trabajo y amistad con vosotros durante estos años!

También es imprescindible nombrar a mis compañeros del CTTC que siempre han estado allí para hacerme más llevadero el día a día. Sin un orden en particular, Dani, Anica, Iñaki, Tatjana, Biljana, Luis, Jordi, Jorge, Miguel Ángel, María, Laia, Ana María y David entre otros. Un agradecimiento especial va para la dirección del CTTC, por haberme acogido en su programa de doctorado y que espero que siga muchos años formando excelentes investigadores.

Hablar de pasión por la ciencia es hablar de mi socio y amigo Enric Fraile. Quizá es él uno de los grandes culpables de la culminación del doctorado. Desde que nos conocimos en la universidad ha intentado transmitirme el valor del trabajo bien hecho, la dedicación y la disciplina. ¡Creo que al fin lo ha conseguido!. Espero seguir colaborando con él muchos años más en el Radio Club de La Salle junto a grandes personas como Eduard, Antonio, Luis del Molino, Alvar, Jaume Ruiz, David Badía, Joan Ramón y Joan Lluís Pijoan entre otras.

Mis amigos de toda la vida también han tenido un papel importante en esta aventura. Va a ser difícil nombrarlos a todos!. El llamado “GulaGrupo” formado por Marc, Hugo, Txus (oficialmente, Dr. Jesús Alonso Zárate, o también el vocalista y bajista de “Cebra de paso”), Maribel, Cristina, Guillem, Alicia, Albert, Mónica, Javi “Pala” son los compañeros de viaje ideales. A ellos les debo una fuente inagotable de buenos momentos que hacen recargar las pilas para volver al trabajo cada lunes. Ariadna Grau me ha enseñado el doctorado de la vida, y por ello siempre tendrá un lugar especial. Mis compañeros de carrera representados entre otros por Germán, Suso, Xavi Grau, Xavi Guerrero (y Marta), Dani R., Gonzalvo han aportado su parte con las interminables noches en Barcelona, y, a 600 km de distancia también se encuentran otras personas imprescindibles en esta ecuación, entre ellas Agustín “Palanka”, Arturo, Baltasar, Javi T., José Luís, Alaitz, Cristina y todos mis amigos de Mozoncillo (Segovia) y Fuentelmonge (Soria). Es un placer compartir mi tiempo con vosotros!.

Finalmente, y con todo mi cariño, quiero dedicarles este trabajo a mi familia. A mis padres Luis y Esther por su incondicional apoyo, generosidad y paciencia, igual que a mi tía María. Me gustaría que vivierais también este éxito como vuestro, ya que rinde homenaje a los valores y la educación que me habéis ofrecido durante toda mi vida.

Contents

Abstract	v
Resumen	vii
Resum	xi
Preface	xv
Notation	xxix
Acronyms	xxxi
1 Introduction	1
1.1 Motivation and Objectives	1
1.2 Thesis Outline and Reading Directions	3
1.3 Research Contributions	4
1.3.1 Book chapters	4
1.3.2 Journal papers	4
1.3.3 International conferences	4
1.3.4 National conferences	5
2 Global Navigation Satellite Systems (GNSS) basics	7
2.1 GNSS civil signals	7
2.1.1 GNSS transmitter signal structure	8
2.1.2 GPS signals	11
2.1.3 Galileo signals	13
2.1.4 Other systems	15
2.2 Signal propagation	17
2.2.1 Carrier Doppler effect	17
2.2.2 Attenuation	18
2.2.3 Interferences	19
2.3 GNSS Receivers	21
2.3.1 Simplified receiver signal model	21
2.3.2 Receiver block diagram	21
2.3.3 Baseband signal model	23
2.3.4 Satellite synchronization and PVT solution	23
2.3.4.1 Acquisition	23
2.3.4.2 Tracking	25
2.3.4.3 Navigation data demodulation and decoding	27
2.3.4.4 Position, Velocity, and Time (PVT) solution	28
2.4 Summary	29
3 Signal acquisition techniques	31
3.1 Acquisition signal model	32
3.2 Detection theory	32
3.2.1 Neyman-Pearson detector	33

3.2.2	Uniformly Most Powerful test	33
3.2.3	Performance Metrics	34
3.3	Single-antenna GNSS signal acquisition	35
3.3.1	Optimum detector	35
3.3.2	GLRT approach	37
3.3.2.1	Maximum Likelihood Estimators	37
3.3.2.2	Acquisition test function	38
3.3.2.3	Performance analysis	38
3.4	Joint Acquisition Strategy	41
3.4.1	Augmented local satellite signal replica	41
3.4.2	Computational cost	42
3.4.3	Performance analysis	43
3.4.4	Simulation results	47
3.5	The effect of the receiver bandwidth	51
3.5.1	Simulation results	52
3.6	Acquisition schemes	56
3.7	Performance degradation sources	59
3.8	Summary	62
4	Antenna Array-Based GNSS Signal Acquisition for Interference Mitigation	63
4.1	Array signal model	64
4.2	Antenna array optimum detector	65
4.2.1	Sensitivity analysis	67
4.3	GLRT approach	68
4.3.1	Maximum Likelihood Estimators	69
4.3.2	Acquisition test function	69
4.4	White noise assumption	70
4.4.1	Performance analysis	70
4.5	Colored noise assumption	72
4.5.1	Performance analysis	73
4.5.1.1	Uniformly Most Powerful test condition	74
4.5.1.2	Sensitivity analysis	74
4.5.1.3	Interference rejection capability	75
4.6	Acquisition after beamforming	79
4.6.1	Performance of the GLRT detector after beamforming	79
4.6.2	Power minimization beamformer	81
4.7	Performance in realistic conditions	85
4.7.1	A Metric to measure the presence of errors in $\hat{\mathbf{R}}_{xx}$	86
4.7.2	Acquisition time effect in $\hat{\mathbf{R}}_{xx}$	86
4.7.3	Signal quantization effects in $\hat{\mathbf{R}}_{xx}$	87
4.7.4	Signal quantization effects in $\hat{\mathbf{r}}_{xd}$	89
4.7.5	Satellite signal synchronization errors	89
4.8	Simulation results	90
4.8.1	Ideal conditions	91
4.8.2	Realistic conditions	96
4.9	Summary	99
5	Design and implementation of a real-time array-based GNSS receiver platform	101
5.1	Multichannel coherent front-end: design fundamentals	102
5.1.1	Radio Frequency antenna array signal model	103
5.1.2	System block diagram	104
5.1.3	Antenna elements	105
5.1.4	Low Noise Amplifier	107
5.1.4.1	Noise Figure	108
5.1.4.2	Linearity parameters	111
5.1.5	Frequency mixer	113

5.1.6	Reference and local signal oscillators	114
5.1.7	RF and IF filters	114
5.1.8	Intermediate Frequency amplifier	115
5.1.9	Analog-to-Digital conversion	116
5.2	Front-end requirements and specifications	117
5.2.1	Passband and stopband bandwidths	119
5.2.2	Gain	119
5.2.3	Noise figure and linearity parameters	120
5.2.4	Specifications summary and detailed block diagram	121
5.3	Simulations and design validation	124
5.4	Part selection and implementation measurements	127
5.4.1	Antenna array elements	127
5.4.2	RF low noise amplifier and RF bandpass filter	129
5.4.2.1	Prototype design and implementation	129
5.4.2.2	Measurements	131
5.4.3	RF mixer and IF bandpass filter	136
5.4.3.1	Prototype design and implementation	136
5.4.3.2	Measurements	136
5.4.4	IF variable gain amplifier	140
5.4.4.1	Prototype design and implementation	141
5.4.4.2	Measurements	142
5.5	Local oscillator	145
5.5.1	Frequency synthesizer	145
5.5.2	Distribution network	145
5.5.3	Measurements results	147
5.6	Single-channel prototype validation	147
5.6.1	S Parameters	148
5.6.1.1	Linearity	156
5.6.2	Noise Figure	156
5.6.3	Phase noise	158
5.6.4	Output spectrum	158
5.6.5	Analog-to-Digital conversion	159
5.6.6	Prototype performance summary	160
5.7	Multichannel extension	161
5.7.1	PCB design	162
5.7.2	Array implementation	163
5.8	FPGA Processing	168
5.8.1	FPGA interface with multichannel ADC	168
5.8.2	GNSS array platform block diagram	169
5.8.3	Real-time GNSS signal acquisition	171
5.8.3.1	Autocovariance matrix estimation	171
5.8.3.2	Cross-correlation vector estimation	174
5.8.3.3	High-level operations	175
5.9	FPGA interface with GNSS software receivers	177
5.10	Platform validation	180
5.10.1	Antenna array and RF front-end calibration	180
5.10.2	Acquisition hardware accelerators	182
5.11	Anechoic chamber measurement set-up and results	185
5.12	Summary	190
6	Real-time GNSS Software Defined Receiver	191
6.1	Introduction to GNSS software receivers	192
6.2	Software development methodology	193
6.2.1	Software design notation	193
6.2.1.1	UML notation for class diagrams	193
6.2.1.2	UML notation for finite state machines	194
6.2.2	Design Patterns for GNSS Software Receivers	195

6.2.3	Computer Programming Style	197
6.2.3.1	C++ as a suitable programming language for GNSS SDR receivers	198
6.2.3.2	Development ecosystem	198
6.3	GNSS-SDR design	199
6.3.1	GNU Radio architecture	200
6.3.2	GNSS-SDR architecture	202
6.3.2.1	Signal sources	202
6.3.2.2	Core components	203
6.3.2.3	Data outputs	205
6.4	GNSS-SDR Implementation	205
6.4.1	Control plane	206
6.4.2	Signal processing plane	208
6.4.2.1	Signal source	208
6.4.2.2	Signal conditioner	211
6.4.2.3	Channel	211
6.4.2.4	Acquisition	212
6.4.2.5	Signal synchronization information exchange	213
6.4.2.6	Tracking	216
6.4.2.7	Telemetry decoder	218
6.4.2.8	Observables	221
6.4.2.9	PVT	222
6.5	GNSS-SDR Performance	223
6.5.1	Receiver configuration	224
6.5.2	Simulated scenarios	225
6.5.2.1	Agilent E4438C GPS personality	225
6.5.2.2	Spirent GSS6700	228
6.5.3	Real-life signals	231
6.6	Summary	235
6.A	Tracking pull-in algorithm	236
7	Conclusions and Directions for Future Research	239
Bibliography		243
Index		261

List of Figures

2.1	Single channel GNSS modulation.	9
2.2	Composite signal modulation.	10
2.3	Spectrum allocation of Galileo and GPS RF links [Und10].	10
2.4	Simplified GNSS receiver high-level block diagram.	22
2.5	Correlation output versus time-delay and Doppler-shift of a noise-free Galileo E1 satellite signal and the same signal corrupted with white noise ($CN0 = 44$ dB-Hz).	23
2.6	Autocorrelation function of a full-bandwidth Galileo-like E1 and GPS-like L1 C/A signals.	26
2.7	Classical GNSS tracking diagram.	27
3.1	A binary hypothesis detector regions.	35
3.2	$T_{GL}(\mathbf{x})$ normalized histogram and theoretical PDF in both \mathcal{H}_1 and \mathcal{H}_0 acquisition hypotheses for Galileo E1 signal acquisition simulation.	40
3.3	Simulated acquisition search grid for GPS L1 C/A signal with $M = 12$ visible satellites and equal $CN0 = 45$ dB-Hz, and different number of satellites present in local replica.	43
3.4	Proposed joint-acquisition algorithm flow chart.	44
3.5	Number of correlations needed in single-dwell acquisition vs. the number of satellites present in local code replica for GPS L1 C/A.	45
3.6	False alarm and detection probabilities for GPS L1 C/A signal with $M_s = 12$ visible satellites and a receiving signal to noise density ratio of $CN0 = 44$ dB-Hz, and different number of satellites (A) present in local replica.	47
3.7	Histogram of $T_r(\mathbf{x} \mathcal{H}_1)$ and $T_r(\mathbf{x} \mathcal{H}_0)$ test statistics for GPS L1 C/A signal with $M_s = 12$ visible satellites and a receiving signal to noise density ratio of $CN0 = 44$ dB-Hz, and different number of satellites (A) present in local replica.	48
3.8	GPS L1 C/A $CN0 = 44$ dB-Hz. Simulated and theoretical (dashed) acquisition ROC curves for different number of satellites present in the local signal replica.	50
3.9	Galileo E1 $CN0 = 38$ dB-Hz. Simulated and theoretical (dashed) acquisition ROC curves for different number of satellites present in the local signal replica.	50
3.10	Theoretical and simulated Galileo E1 MBOC(6,1,1/11) SNR versus the baseband bandwidth.	52
3.11	Autocorrelation of Galileo E1 MBOC(6,1,1/11) signal with the local replica versus τ for different baseband bandwidths.	53
3.12	Theoretical and simulated P_{fa} (blue) and P_d (red) for single-antenna GLRT acquisition over different baseband bandwidths.	54
3.13	Theoretical and simulated ROC for single-antenna GLRT acquisition over different baseband bandwidths.	55
3.14	CMF detector block diagram.	56
3.15	NCMF detector block diagram.	57
3.16	GLRT detector block diagram.	57
3.17	PCND detector block diagram.	58
3.18	PCDD detector block diagram.	58
3.19	PDD detector block diagram.	59

4.1	$T_{NP}(\mathbf{X})$ histogram and theoretical PDF in both \mathcal{H}_1 and \mathcal{H}_0 acquisition hypotheses for Galileo E1 signal acquisition simulation.	67
4.2	$T_{Wh}(\mathbf{X})$ normalized histogram and theoretical PDF in both \mathcal{H}_1 and \mathcal{H}_0 acquisition hypotheses for Galileo E1 signal acquisition simulation.	72
4.3	$T_{GL}(\mathbf{X})$ normalized histogram and theoretical PDF in both \mathcal{H}_1 and \mathcal{H}_0 acquisition hypotheses for Galileo E1 signal acquisition simulation.	74
4.4	Evolution of $\delta_{T_{GL}}(\rho, N, \bar{\mathbf{h}}, \bar{\mathbf{h}}_i)$ in the presence of an uncorrelated interference impinging into the array from $Az = 45^\circ$ and $El = 45^\circ$, with $\rho = 1$	78
4.5	Acquisition after generic beamforming.	80
4.6	$T_{PWR}(\mathbf{X})$ normalized histogram and theoretical PDF in both \mathcal{H}_1 and \mathcal{H}_0 acquisition hypotheses for Galileo E1 signal acquisition simulation.	82
4.7	Galileo E1 acquisition P_d vs. satellite CN0 in the presence of wideband interference for different algorithms and no DOA estimation error in the MVDR beamformer ($T_{MVDR}(\mathbf{X})$).	83
4.8	Galileo E1 acquisition P_d vs. satellite CN0 in the presence of wideband interference for different algorithms and 15° DOA estimation mean pointing error in the MVDR beamformer ($T_{MVDR}(\mathbf{X})$).	84
4.9	Galileo E1 acquisition P_d vs. satellite CN0 in the presence of wideband interference for different algorithms and 20° DOA estimation mean pointing error in the MVDR beamformer ($T_{MVDR}(\mathbf{X})$).	84
4.10	GNSS receiver block diagram, as simulated.	85
4.11	$dist_g(\mathbf{R}_{xx}, \hat{\mathbf{R}}_{xx})$ vs. T_{acq} with a CW interference impinging into the array with $IN0 = 85$ dB-Hz. $\hat{\mathbf{R}}_{xx}$ was computed using 64-bits double floating-point resolution and the conditions of Table 4.4.	87
4.12	$dist_g(\mathbf{R}_{xx}, \hat{\mathbf{R}}_{x_q x_q})$ vs. different quantization bits and a CW interference impinging into the array with different $IN0$	88
4.13	$T_{GL}(\mathbf{X})$ histogram in ideal conditions, in an scenario with a CWI impinging into the array with $IN0 = 80$ dB-Hz.	93
4.14	$T_{NP}(\mathbf{X})$, $T_{GL}(\mathbf{X})$, and $T_{Wh}(\mathbf{X})$ ROCs performance in ideal conditions, in an scenario with an in-band CW interference impinging into the array with different $IN0 = \{45, 55, 65, 75, 85\}$ dB-Hz. For clarity reasons some theoretical and simulated curves are omitted.	93
4.15	$T_{NP}(\mathbf{X})$, $T_{GL}(\mathbf{X})$, and $T_{Wh}(\mathbf{X})$ ROCs performance in ideal conditions, in an scenario with an uncorrelated wideband interference impinging into the array with different $IN0 = \{45, 55, 65, 75, 85\}$ dB-Hz. For clarity reasons some theoretical and simulated curves are omitted.	94
4.16	Acquisition performance of $T_{GL}(\mathbf{X})$ for $N = 1 - 12$ antenna elements, with a wideband interference impinging into the array with $IN0 = 85$ dB-Hz. The $T_{GL}(\mathbf{X})$ theoretical ROC curves are plotted in dashed lines.	95
4.17	Evolution of the P_d for a fixed $P_{fa} = 0.001$ in the presence of an increasing number of wideband interferences. Each of the points contains 4000 independent realizations.	95
4.18	Effect of the $dist_g(\mathbf{R}_{xx}, \hat{\mathbf{R}}_{xx})$ in the acquisition performance of $T_{GL}(\mathbf{X})$, with a CWI impinging into the array with $IN0 = 85$ dB-Hz.	97
4.19	Acquisition performance of $T_{GL}(\mathbf{X}_q)$ for 1-8 bits uniform quantization and 1-8 bits PQN model, with a CW interference impinging into the array with $IN0 = 85$ dB-Hz. .	98
4.20	P_d in an scenario with satellite CN0 = 44 dB-Hz, and single CW interference impinging into the array with $IN0 = 70 - 136$ dB-Hz, for $P_{fa} = 0.001$ and different quantization bits $N_b = 2 - 8$ bits.	98
5.1	Definition of Directions of Arrival angles.	104
5.2	Simplified system block diagram.	105
5.3	Detailed front-end block diagram for one antenna element.	106
5.4	Arrangement of antenna array elements.	107
5.5	Low Noise Amplifier symbol.	108
5.6	Graphical representation of intermodulation products [Gil03a].	109

5.7 GPS C/A Root Mean Square (RMS) code tracking error Cramér-Rao bound (CRB) vs. input CN0, observation time $T = 1$ s and baseband bandwidth $B_{bb} = 1 - 12$ MHz.	110
5.8 GPS C/A RMS code tracking error vs. front-end F_{dB} , observation time $T = 1$ s, input $CN_0 = 49$ dB, and baseband bandwidth $B_{bb} = 1 - 12$ MHz.	111
5.9 Compression point and Interception Points definitions [Gil03b].	112
5.10 Frequency mixer symbol.	113
5.11 Required input power (P_{bit-i}) vs. ADC active bits for $V_{FSR} = 2$, $Z_{ADC} = 50 \Omega$, and $N_b = 12$	120
5.12 Front-end gain (G_{FE}) vs. ADC active bits for $V_{FSR} = 2$, $Z_{ADC} = 50 \Omega$, and $N_b = 12$	121
5.13 Proposed front-end architecture and performance parameters.	122
5.14 S-parameters incident and reflected waves representation.	125
5.15 Generic GNSS front-end diagram.	126
5.16 Simulated front-end gain and noise figure.	127
5.17 Simulated front-end phase noise.	127
5.18 Simulated front-end GNSS link gain and image frequency rejection.	129
5.19 Garmin GA27c active antenna.	129
5.20 Antenna array prototype.	130
5.21 Differences between radiation patterns of some antenna elements in elevation.	130
5.22 RF LNA prototype schematic.	132
5.23 RF LNA prototype PCB.	133
5.24 RF LNA prototype picture.	134
5.25 RF LNA input-output matching measurements.	134
5.26 RF LNA amplification magnitude and phase measurements.	135
5.27 RF LNA prototype compression measurements.	135
5.28 RF LNA prototype noise figure measurements.	135
5.29 Mixer and IF filter prototype schematic.	137
5.30 Mixer and IF filter prototype PCB.	138
5.31 Mixer and IF filter prototype picture.	139
5.32 Mixer prototype gain measurement for $f_{LO} = 1505.42$ MHz and $P_{LO} = -5$ dBm.	140
5.33 Mixer prototype gain measurement for $f_{LO} = 1645.42$ MHz and $P_{LO} = -5$ dBm.	140
5.34 Mixer prototype compression point measurement.	141
5.35 Mixer prototype noise figure analyzer configuration.	141
5.36 Mixer prototype noise figure measurement.	142
5.37 AD8369 functional block diagram.	142
5.38 IF VGA prototype schematic.	143
5.39 IF VGA prototype PCB.	144
5.40 IF VGA prototype picture.	145
5.41 IF VGA prototype measured S-parameters.	146
5.42 IF VGA prototype measured compression point.	147
5.43 IF VGA prototype measured noise figure.	148
5.44 PLL generic block diagram.	148
5.45 LMX2531 block diagram.	149
5.46 LMX2531 Evaluation Module PCB.	149
5.47 PLL control software and register settings for LMX2531EVM.	150
5.48 Two ports Wilkinson divider theoretical schematic.	150
5.49 Two ports Wilkinson divider schematic and electromagnetic simulation model.	151
5.50 Eight ports Wilkinson divider electromagnetic simulation model.	151
5.51 Eight ports Wilkinson PCB layout and prototype.	152
5.52 Simulated(blue) and measured(red) eight ports Wilkinson Input to output attenuation.	152
5.53 Eight ports Wilkinson measured output signal power differences.	152
5.54 Eight ports Wilkinson measured output signal phase differences.	153
5.55 Measured phase PLL phase noise after the Wilkinson power divider for $f_{OL} = 1505.42$ MHz.	153
5.56 Single-channel front-end and local oscillator network prototype picture.	154

5.57 Single-channel front-end prototype S parameters measurement set-up.	154
5.58 Single-channel front-end prototype gain and bandwidth.	155
5.59 Single-channel front-end prototype measured compression point.	156
5.60 Single-channel front-end prototype noise figure measurement set-up.	157
5.61 Single-channel front-end prototype measured noise figure.	157
5.62 Single-channel front-end prototype measured gain (using N8975A).	157
5.63 Single-channel front-end prototype measured phase noise.	158
5.64 Measured output spectrum.	158
5.65 ADC custom adapter board for FPGA digital interface.	160
5.66 ADC board and FPGA platform rack.	160
5.67 ADC active bits vs. input power at IF.	161
5.68 Front-end and ADC verification test.	161
5.69 Multichannel front-end top-level schematic.	164
5.70 Multichannel front-end PCB design.	165
5.71 RF LNA SMD footprint and soldering detail.	165
5.72 RF SAW filter SMD footprint and soldering detail.	165
5.73 Multichannel front-end PCB picture.	166
5.74 Multichannel front-end board mounted in the antenna array frame.	166
5.75 LO synthesizer and Wilkinson divider.	167
5.76 ADC FPGA interface block diagram.	169
5.77 Digital beamforming platform detailed block diagram.	170
5.78 Conceptual schematic of $\hat{\mathbf{R}}_{\mathbf{xx}}$ computation.	172
5.79 Schematic of the real-time logic for $\hat{\mathbf{R}}_{\mathbf{xx}}$	173
5.80 Conceptual schematic of $\hat{\mathbf{R}}_{\mathbf{xd}}$ computation.	174
5.81 Schematic of the real-time logic for $\hat{\mathbf{r}}_{\mathbf{xd}}$	175
5.82 Embedded processor acquisition software flowchart.	176
5.83 $T_{\text{GL}}(\mathbf{X})$ acquisition software flowchart.	178
5.84 GNSS array platform custom Ethernet frame.	179
5.85 Antenna array and front-end calibration setup in an anechoic chamber.	181
5.86 Uncalibrated and calibrated snapshots plots for $f_{\text{ref}} = 10$ kHz.	182
5.87 Calibration validation using MUSIC DOA estimation.	183
5.88 DOA elevation estimation pointing error for $\theta = 0^\circ$ and $\theta = 180^\circ$	184
5.89 VHDL components testing methodology.	184
5.90 Picture of the interference scenario setup.	185
5.91 Doppler and delay grid search plot for in-band CW interference scenario.	186
5.92 Doppler and delay grid search plot for in-band 4G/LTE interference scenario.	187
5.93 Deflection coefficient evolution in CW interference scenario.	188
5.94 Deflection coefficient evolution in LTE interference scenario.	189
6.1 Class relations in UML diagram.	194
6.2 Sample FSM statechart UML diagram.	195
6.3 GNU Radio scheduler illustrative flow graph.	202
6.4 Diagram of the modules that form the GNSS software receiver. Each module accepts multiple implementations, which can be selected by the user.	203
6.5 GNSS-SDR user interoperability diagram.	206
6.6 GNU Radio class hierarchy for the signal processing blocks.	209
6.7 GNSS-SDR generic interface for signal processing blocks.	210
6.8 Receiver's class hierarchy.	210
6.9 Internal view of signal conditioner block.	211
6.10 Simplified version of the channel states [Cha01].	212
6.11 UML diagram of the Gnss_Satellite and Gnss_Signal classes.	214
6.12 UML diagram of the gnss_synchro class.	215
6.13 GNSS-SDR tracking module internal block diagram.	216
6.14 GPS C/A navigation message structure [Bor07].	218
6.15 GNSS-SDR telemetry decoder module internal block diagram.	219
6.16 GNSS-SDR GPS C/A telemetry word to navigation message subframe decoder FSM UML diagram.	220

6.17 GNSS-SDR pseudorange estimation using common transmission time.	221
6.18 GNSS-SDR precision in the Agilent New York GPS simulated scenario.	226
6.19 GNSS-SDR ENU position error in the Agilent New York GPS scenario.	227
6.20 Google Earth KML 3D position evolution in the Agilent New York GPS scenario.	227
6.21 GNSS-SDR precision in the Spirent simulated scenario.	229
6.22 GNSS-SDR accuracy in the Spirent GPS simulated scenario.	230
6.23 GNSS-SDR precision obtained in a real-life scenario using 100 ms of Position-Velocity-Time (PVT) averaging.	232
6.24 GNSS-SDR precision obtained in a real-life scenario using 1000 ms of PVT averaging.	233
6.25 Google Earth KML 3D position evolution in a real-life scenario.	234
6.26 Code delay estimation error term in ΔK_{chips} due to acquisition Doppler estimation error.	238
6.27 Code delay estimation error term in ΔK_{chips} due to acquisition Doppler estimation error.	238
7.1 The Claus Hypothesis.	242

List of Tables

2.1	List of civil GPS links, codes and modulations.	11
2.2	List of Galileo links, codes and modulations.	13
2.3	Other Global Navigation Satellite System (GNSS) links.	16
2.4	Sources and Services of Interference vs. Harmonics [Buc97].	20
2.5	Sources and Services of image Interference for single-conversion GPS L1 / Galileo E1 front-end [Wil02].	21
2.6	Acquisition and tracking sensitivity values for some commercial GPS IC, extracted from [Gol07, Cam10, Wei11].	24
3.1	GPS L1 C/A code Maximum cross-correlation power (zero Doppler Differences).	46
3.2	Simulation parameters.	49
3.3	Comparative of detectors	59
4.1	Sensitivity of the clairvoyant detector for different P_{fa} and P_{fa} , with $N = 8$ elements circular antenna array, $f_s = 6$ MSPS, $T_{acq} = 4$ ms, and $\hat{R}_{dd} = 1$.	69
4.2	GLRT detector's sensitivity for selected P_{fa} and P_{fa} , with $N = 8$ elements circular array, $f_s = 6$ MSPS, $T_{acq} = 4$ ms, and $\hat{R}_{dd} = 1$.	75
4.3	Grid search signal synchronization errors and their equivalent SNR loss.	90
4.4	Simulation parameters	91
4.5	Performance expressions for the detectors in ideal conditions.	92
5.1	GPS L1 C/A SNR degradation vs. ADC resolution assuming Gaussian noise [Par96].	117
5.2	Commonly used intermediate frequencies.	118
5.3	f_s candidates for different k values and $f_{IF} = 70$ MHz.	118
5.4	Front-end frequency plan.	119
5.5	Front-end channel design specifications summary.	122
5.6	RG174 cable losses for IF and RF frequencies.	122
5.7	RF SAW bandpass filter parameter values.	123
5.8	IF SAW bandpass filter parameter values.	123
5.9	Proposed gain/loss distribution and noise figure values.	124
5.10	Compression point design specifications.	124
5.11	Simulated local oscillator phase noise.	125
5.12	Simulated front-end performance values compared to design specifications.	128
5.13	GA27c active antenna specifications summary.	128
5.14	MAX2659 1st RF LNA specifications summary.	131
5.15	SAFSE1G57KA0T90 SAW filter specifications summary.	131
5.16	MAX2650 2nd RF LNA specifications summary.	133
5.17	RF LNA and RF filtering measured specifications summary.	134
5.18	MAX2681 mixer specifications summary.	136
5.19	Sawtek 854669 70 MHz SAW filter specifications summary.	138
5.20	RF mixer and IF bandpass filter measured specifications summary.	139
5.21	AD8369 IF VGA specifications summary.	142
5.22	IF amplification measured performance values summary.	144
5.23	National Instruments LMX2531 PLL specifications.	149

5.24	Wilkinson 1:8 prototype specifications.	149
5.25	ADS5273 features, extracted from [Tex05a].	159
5.26	Simulated and measured front-end performance compared the design specifications summary.	162
5.27	Acquisition operations time performance for $T_{GL}(\mathbf{X})$	177
6.1	Position accuracy measurements [Nov03].	223
6.2	GNSS-SDR post-processing configuration.	224
6.3	GNSS-SDR real-time configuration.	224
6.4	Agilent E4438C GPS Personality simulated scenario parameters.	225
6.5	Spirent GSS6560 simulated scenario parameters.	228
6.6	CTTC roof-top antenna USRP + DBSRX2 scenario.	231
6.7	Satellites' CN0s reported by GNSS-SDR in a real-life scenario.	231

Notation

Boldface upper-case letters denote matrices and boldface lower-case letters denote vectors.

\mathbb{R}, \mathbb{C} The set of real and complex numbers, respectively.

$\mathbb{R}^{N \times M}, \mathbb{C}^{N \times M}$ The set of $N \times M$ matrices with real- and complex-valued entries, respectively.

\hat{x} Estimation and true value of parameter x .

$f(x)|_{x=a}$ Function $f(x)$ evaluated at $x = a$.

$|x|$ Absolute value (modulus) of scalar x .

$\|\mathbf{x}\|$ l^2 -norm of vector \mathbf{x} , defined as $(x = \mathbf{x}^H \mathbf{x})^{\frac{1}{2}}$.

$\dim\{\mathbf{x}\}$ Dimension of vector \mathbf{x} .

$[\mathbf{x}]_r$ The r-th vector element.

$[\mathbf{X}]_{r,c}$ The matrix element located in row r and column c.

$[\mathbf{X}]_{:,r}$ The r-th row of matrix \mathbf{X} .

$[\mathbf{X}]_{:,c}$ The c-th column of matrix \mathbf{X} .

$\text{Tr}\{\mathbf{X}\}$ Trace of matrix \mathbf{X} . $\text{Tr}\{\mathbf{X}\} = \sum_{n=1}^N [\mathbf{X}]_{n,n}$.

$\det(\mathbf{X})$ Determinant of matrix \mathbf{X} .

$\text{diag}(\mathbf{x})$ A diagonal matrix whose diagonal entries are given by \mathbf{x} .

\mathbf{I} Identity matrix. A subscript can be used to indicate the dimension.

\mathbf{X}^* Complex conjugate of matrix \mathbf{X} (also applied to scalars).

\mathbf{X}^T	Transpose of matrix \mathbf{X} .
\mathbf{X}^H	Complex conjugate and transpose (Hermitian) of matrix \mathbf{X} .
$\mathbf{P}_\mathbf{X}$	Orthogonal projector onto the subspace spanned by the columns of \mathbf{X} . $\mathbf{P}_\mathbf{X} = \mathbf{X}(\mathbf{X}^H \mathbf{X})^{-1} \mathbf{X}^H$.
$\mathbf{P}_{\mathbf{X}}^\perp$	Orthogonal projector onto the orthogonal complement to the columns of \mathbf{X} . $\mathbf{P}_{\mathbf{X}}^\perp = \mathbf{P}_\mathbf{X} - \mathbf{I}$.
$\mathcal{N}(\boldsymbol{\mu}, \boldsymbol{\Sigma})$	Multivariate Gaussian distribution with mean $\boldsymbol{\mu}$ and covariance matrix $\boldsymbol{\Sigma}$.
$\mathcal{CN}(\boldsymbol{\mu}, \boldsymbol{\Sigma})$	Multivariate Complex Gaussian distribution with mean $\boldsymbol{\mu}$ and covariance matrix $\boldsymbol{\Sigma}$.
$\mathbb{E}\{\cdot\}$	Statistical expectation.
$\text{var}\{\cdot\}$	Statistical variance.
$f(t) * g(t)$	Convolution between $f(t)$ and $g(t)$.
$\arg \max_x f(x)$	Value of x that maximizes $f(x)$.
$\arg \min_x f(x)$	Value of x that minimizes $f(x)$.
$\max_x f(x)$	$f(x)$ maximum value.
$\min_x f(x)$	$f(x)$ minimum value.
$\Re\{\cdot\}, \Im\{\cdot\}$	Real and imaginary parts, respectively.
$p(\mathbf{x}; \boldsymbol{\theta})$	Conditional probability density function of the random vector \mathbf{x} subject to the parameter vector $\boldsymbol{\theta}$.
<i>i.i.d.</i>	Independent identically distributed.
<i>r.v.</i>	Independent identically distributed.

Acronyms

ADC	Analog-to-Digital Converter
AGC	Automatic Gain Control
A-GPS	Assisted-GPS
ANSI	American National Standards Institute
API	Application Programming Interface
ASIC	Application Specific Integrated Circuit
AWGN	Additive White Gaussian Noise
BASS	Block Adjustment of Synchronizing Signal
BB	Baseband
BER	Bit Error Rate
BOC	Binary Offset Carrier
BPF	Band-Pass Filter
BPSK	Binary Phase-Shift Keying
CAF	Cross-Ambiguity Function
CBOC	Composite Binary Offset Carrier
CDF	Cumulative Distribution Function
CDMA	Code Division Multiple Access
CEP	Circular Error Probability
CFAR	Constant False Alarm Rate
CF	Characteristic Function
CMF	Coherent Matched Filter
CN0	Carrier-to-Noise density ratio
COTS	Commercial Off-The-Shelf
CP	Compression Point
CPLD	Complex Programmable Logic Device
CPU	Central Processing Unit
CRB	Cramér-Rao bound
CRPA	Controlled Reception Pattern Antennas
CUT	Component Under Test
CWGN	Complex White Gaussian Noise
CWI	Continuous Wave Interference

DBF	Digital Beamforming
DCM	Digital Clock Manager
DDR	Double Data Rate
DDS	Direct Digital Synthesizer
DFT	Discrete Fourier Transform
DGNSS	Differential GNSS
DLL	Delay Locked Loop
DME	Distance Measuring Equipment
DOA	Direction Of Arrival
DOP	Dilution Of Precision
DPE	Direct Position Estimation
DRMS	Distance Root Mean Square
DS-CDMA	Direct-Sequence Code Division Multiple Access
DSP	Digital Signal Processor
DTFT	Discrete-Time Fourier Transform
DVB-T	Digital Video Broadcasting – Terrestrial
EDA	Electronic Design Automation
EGNOS	European Geostationary Navigation Overlay System
EIRP	Effective Isotropic Radiated Power
ENOB	Effective Number Of Bits
ENU	East North Up
ETSI	European Telecommunications Standards Institute
FCC	Federal Communications Commision
FDMA	Frequency Division Multiple Access
FEC	Forward Error Correction
FFT	Fast Fourier Transform
FH-CDMA	Frequency-Hopping Code Division Multiple Access
FIFO	First-In First-Out
FIR	Finite Impulse Response
FLL	Frequency Locked Loop
FMC	FPGA Mezzanine Card
FPGA	Field Programmable Gate Array
FSM	Finite State Machine
FSR	Full-Scale Range
GAGAN	GPS and GEO Augmented Navigation
GBAS	Ground-Based Augmentation Systems
GIS	Geographic Information System
GLONASS	GLObalnaya Navigasionnay Sputnikovaya Sistema
GLRT	Generalized Likelihood Ratio Test

GNSS	Global Navigation Satellite System
GPS	Global Positioning System
GSM	Global System for Mobile Communications
HDOP	Horizontal Dilution Of Precision
HOW	Hand Over Word
HS-GNSS	High Sensitivity GNSS
IC	Integrated Circuit
IEEE	Institute of Electrical and Electronics Engineers
IF	Intermediate Frequency
IIR	Infinite Impulse Response
IMU	Inertial Measurement Unit
IN0	Interference-to-Noise density ratio
IP3	third-order Interception Point
ITU	International Telecommunications Union
KML	Keyhole Markup Language
LAAS	Local Area Augmentation System
LHCP	Left Hand Circular Polarization
LMS	Least Mean Squares
LNA	Low Noise Amplifier
LO	Local Oscillator
LOS	Line-of-Sight
LOSS	Line-of-Sight Signal
LPF	Low-Pass Filter
LPP	LTE Positioning Protocol
LRT	Likelihood Ratio Test
LSB	Least Significant Bit
LS	Least Squares
LVDS	Low Voltage Differential Signaling
MA	Moving Average
MBOC	Multiplexed Binary Offset Carrier
MC	Monte Carlo
MEO	Medium Earth Orbit
MF	Matched Filter
MLE	Maximum Likelihood Estimator
ML	Maximum Likelihood
MLR	Monotone Likelihood Ratio
MMSE	Minimum Mean Square Error
MSAS	Multi-functional Satellite Augmentation System
MSB	Most Significant Bit

MVDR	Minimum Variance Distortionless Response
NATO	North Atlantic Treaty Organization
NCO	Numerically Controlled Oscillator
NF	Noise Figure
NMEA	National Marine Electronics Association
NP	Neyman-Pearson
PCB	Printed Circuit Board
PCI	Peripheral Component Interconnect
PC	Personal Computer
PDF	Probability Density Function
PLL	Phase Locked Loop
PPM	Parts Per Million
PPS	Precision Positioning Service
PQN	Pseudo Quantization Noise
PRN	Pseudo Random Noise
PRS	Public Regulated Service
PSD	Power Spectral Density
PVT	Position-Velocity-Time
QPSK	Quadrature Phase-Shift Keying
QRD	QR Decomposition
RAM	Random Access Memory
RFI	Radio Frequency Interference
RF	Radio Frequency
RHCP	Right Hand Circular Polarization
RINEX	Receiver Independent Exchange Format
RMS	Root Mean Square
ROC	Receiver Operating Characteristic
ROM	Read Only Memory
RRLP	Radio Resource Location Services Protocol
RTK	Real-Time Kinematic
SAR	Search And Rescue
SAW	Surface Acoustic Wave
SBAS	Space-Based Augmentation System
SCM	Sample Covariance Matrix
SCORE	Spectral Self-Coherence Restoral
SDCM	System of Differential Correction and Monitoring
SDR	Software Defined Radio
SIMD	Single Instruction, Multiple Data
SMA	Sub-Miniature version A

SNAS	Satellite Navigation Augmentation System
SNIR	Signal-to-Noise-and-Interference Ratio
SNR	Signal-to-Noise Ratio
SoC	System on Chip
SoL	Safety of Live
SPS	Standard Positioning Service
SSC	Spectral Separation Coefficient
SSE	Streaming SIMD Extensions
SS	Spread Spectrum
STAP	Space-Time Adaptive Processing
TACAN	TACtical Air Navigation
THD	Total Harmonic Distortion
ToA	Time of Arrival
TOW	Time Of Week
TTFF	Time To First Fix
UHD	Universal Hardware Driver
UHF	Ultra High Frequency
UML	Unified Modeling Language
UMP	Uniformly Most Powerful
UMTS	Universal Mobile Telecommunications System
UPC	Universitat Politècnica de Catalunya
USB	Universal Serial Bus
USRP	Universal Software Radio Peripheral
UWB	Ultra Wide Band
VCO	Voltage Controlled Oscillator
VDOP	Vertical Dilution Of Precision
VGA	Variable Gain Amplifier
VHDL	Very High Speed Integrated Circuit Hardware Description Language
VHF	Very High Frequency
VOLK	Vector-Optimized Library of Kernels
WAAS	Wide-Area Augmentation System
WGS	World Geodetic System
WSSUS	Wide Sense Stationary with Uncorrelated Scattering

Chapter 1

Introduction

It's not that I'm so smart, it's just that I stay with problems longer.

Albert Einstein.

SATELLITE-based navigation and positioning service has swiftly become a crucial dependency of a myriad of services and applications. Its current civil applications include among others ground, air, and sea transportation of passengers and goods, surveying and mapping, precise time reference and clock dissemination, and emergency response coordination.

The ability to obtain a three-dimensional location using a Global Navigation Satellite System (GNSS) receiver everywhere in the Earth surface, or in its near space, is one of the major contributions of GNSS to the transport safety of persons and goods achieved in the 20th century. Moreover, in recent times, its capability of providing a reliable time reference source is used also in the synchronization of global electronic transactions, such as inter-bank exchanges, telecommunications networks, and the smart management of the power grid. Its popularity spread dramatically, becoming an embedded feature on portable devices such as mobile phones, digital cameras, and portable gaming consoles.

It is important to stress that the positioning and timing availability must be guaranteed all the time, specially in safety-critical or mission-critical services. In that sense, examining the threats against the service availability we found that the Radio Frequency Interferences (RFIs) is one of the main causes of GNSS performance degradation or even the complete denial of service.

In this Dissertation, we address this problem proposing novel algorithms that exploit the spatial diversity provided by antenna arrays to mitigate the interference effects, and we demonstrate both their real-time implementation feasibility and their performance in realistic scenarios.

1.1 Motivation and Objectives

The Radio Frequency (RF) signals transmitted by all the present and the forthcoming GNSSs make use of Code Division Multiple Access (CDMA) techniques. The ranging signals are received with very low pre-correlation signal-to-noise ratio (in the order of -22 dB for a receiver operating at the Earth surface). Despite that the GNSS CDMA processing gain can be high (in the order of 43 dB for the American Global Positioning System (GPS) Standard Positioning Service (SPS)), which offers limited protection against RFI, an interference with a interference-to-signal ratio that exceeds the processing gain can easily degrade receivers' performance or even deny completely the GNSS service, specially in conventional receivers equipped with minimal or basic level of protection towards RFIs. As a consequence, RFIs (either intentional or unintentional) remain the most important cause of performance degradation. A growing concern of this problem has appeared in recent times, highlighting among others the interference threat caused by the

deployment of 4G communication services in RF frequency bands adjacent to those allocated to GNSS.

A GNSS receiver, after signal downconversion and sampling, executes several sequential signal processing operations: signal acquisition, signal tracking, telemetry demodulation, navigation message decoding, pseudoranges computation, and finally estimates its position and time. Each process depends on its predecessor, either using its outputs to initialize the algorithms or processing the data outputs. However, the signal acquisition process is the starting point of the entire receiver operations and thus its performance plays a critical role. The acquisition process is in charge of detecting the presence of a specific signal that belongs to a particular GNSS satellite, and, in case of positive detection, it should provide a coarse estimation of its current synchronization parameters. In case of a cold acquisition (i.e., without any prior information), this detection process should be performed for every satellite available in the GNSS constellation.

It is known that signal acquisition has the lowest sensitivity of the whole receiver operation, and, consequently, it becomes the performance bottleneck in the presence of interfering signals. A single-antenna receiver can make use of time and frequency diversity to mitigate them, even though the performance of these techniques is compromised in low Signal-to-Noise Ratio (SNR) situations or in the presence of wideband interferences. On the other hand, antenna-array receivers can incorporate the spatial information to the time and frequency information in order to improve its performance. From an information theory point of view, this spatial ability provides another source of diversity, which can be employed to separate the desired signal from noise, understood as any unwanted signal, including interferences. Spatial diversity has been mainly applied to the signal tracking operation of GNSS receivers. Surprisingly, to the best of our knowledge, the application of antenna arrays to GNSS signal acquisition has not received much attention. Therefore, there are challenging open fields for further research in this direction.

This Thesis pursues a twofold objective: on one hand proposes novel array-based acquisition algorithms using a well-established statistical detection theory framework, and on the other hand demonstrates both their real-time implementation feasibility and their performance in realistic scenarios.

The journey starts with an analysis of the GNSS acquisition problem as a detection problem, using the Neyman-Pearson (NP) detection theory framework. The NP performance criterion maximizes the probability of detection subject to a given false alarm rate. The NP approach is very convenient for the problem at hand, and it is the basis of almost all of the current state-of-the-art single-antenna acquisition algorithms. This Dissertation reviews the derivation of both the NP optimum detector and the Generalized Likelihood Ratio Test (GLRT) detector algorithms, and derives their theoretical performance considering the effects of the limited front-end bandwidth. Furthermore, we propose a novel test statistic detector intended to jointly acquire a set of GNSS satellites, thus reducing both the acquisition time and the required computational resources.

Then, the GLRT is extended to the array signal model to obtain a novel detector that is able to mitigate temporally uncorrelated interferences, even if the array is unstructured and moderately uncalibrated, thus becoming one of the main contributions of this Dissertation. The key statistical feature is the assumption of an arbitrary and unknown covariance noise matrix, which attempts to capture the statistical behavior of the interferences and other non-desirable signals, while exploiting the spatial dimension provided by antenna arrays. Heading towards a possible implementation of the proposed algorithm, the detector is analyzed under realistic conditions, accounting for the presence of errors in the covariance matrix estimation, residual carrier Doppler and code delay errors, and signal quantization effects.

Along the Dissertation, the focus will move from a theoretical approach towards a practical case study. The second part of the work deals with the design and the implementation of a novel Field Programmable Gate Array (FPGA)-based antenna-array GNSS receiver platform that demonstrates the implementation feasibility, in real-time, and the performance with real-life scenarios of the proposed acquisition algorithms.

In the last part of this Dissertation we complete the receiver chain by designing and imple-

menting a GNSS software receiver pursuing the goals of efficiency, modularity, interoperability, and flexibility demanded by user domains that require non-standard features, such as intermediate signals extraction and receiver algorithms reconfiguration and interchangeability. In this context, we introduce an open-source, real-time GNSS software defined receiver (so-named GNSS-SDR) that contributes with several novel features, among them, the use of software design patterns and shared memory techniques to manage efficiently the data flow between receiver blocks, the use of Single Instruction, Multiple Data (SIMD) hardware-accelerated instructions for time-consuming vector operations like carrier wipe-off and code correlation, and the availability to compile and run on multiple software platforms and hardware architectures (cross-platform portability).

1.2 Thesis Outline and Reading Directions

The Dissertation consists of seven chapters, where review material and novel contributions are presented. Even though the presented document is mainly addressed to signal-processing researchers, it covers several additional aspects such as the design and testing of RF front-ends and digital signal processing implementation in both Field Programmable Gate Array (FPGA) and Personal Computer (PC). The mathematical notation and the acronyms used along the Dissertation can be consulted at the beginning of the document.

The Dissertation is organized as follows. **Chapter 2** starts with a brief introduction to GNSS receivers basics, providing some details about the navigation signals structure of both the American GPS and the European Galileo systems. The signal propagation channel is modeled stressing the interference problem, and several potential interfering sources are listed. The chapter concludes with an overview of a navigation receiver architecture. Nevertheless, the aim of the chapter is not to perform an exhaustive exposition of those systems, and the reader is referred to the references therein for further details.

Chapter 3 follows with an analysis of GNSS signal acquisition as a detection problem, using the NP detection theory framework and the single-antenna acquisition signal model. The NP approach is used here to derive both the optimum detector (known as *clairvoyant detector*) and the GLRT detector. The GLRT detector assumes no prior knowledge of the satellite signal synchronization parameters. Going further, a novel detector test statistic intended to jointly acquire a set of GNSS satellites is obtained, thus reducing both the acquisition time and the required computational resources. The effects of the front-end bandwidth are also taken into account.

Then, **Chapter 4** extends the GLRT to the array signal model to obtain an original detector which is able to mitigate temporally uncorrelated interferences even if the array is unstructured and moderately uncalibrated, thus becoming one of the main contributions of this Dissertation. Closed form expressions for the detection and false alarm probabilities are provided. Performance and interference rejection capability are modeled and compared both to their theoretical bound. The proposed array-based acquisition algorithm performance is compared to conventional acquisition techniques performed after blind null-steering beamformer approaches, such as the power minimization algorithm. Furthermore, the detector is analyzed under realistic conditions, accounting for the presence of errors in the covariance matrix estimation, residual carrier Doppler and code delay errors, and signal quantization effects. Theoretical results are supported by Monte Carlo simulations.

In order to validate the proposed algorithm with real-life satellite signals, **Chapter 5** delves into the design and the implementation of a novel FPGA-based GNSS real-time antenna-array receiver platform, intended to be used as a research tool tightly coupled with software defined GNSS receivers. A complete signal reception chain including the antenna array and the multi-channel phase-coherent RF front-end for the GPS L1/ Galileo E1 was designed, implemented and tested. The details of the digital processing section of the platform such as the array auto-correlation matrix and cross-correlation vector estimation modules are also provided. The design trade-offs and the implementation complexities were carefully analyzed and taken into account. As a proof-of-concept, the problem of GNSS vulnerability to interferences was addressed using

the presented platform. The array-based acquisition algorithms introduced in the Dissertation were implemented and tested under realistic conditions. The performance of the algorithms were compared to single antenna acquisition techniques, measured under strong in-band interference scenarios, including narrow/wide band interferers and communication signals.

The platform was designed to demonstrate the implementation feasibility of novel array-based acquisition algorithms, leaving the rest of the receiver operations (mainly, tracking, navigation message decoding, code and phase observables estimation, and basic PVT solution) to a Software Defined Radio (SDR) receiver running in a PC, which process the real-time spatially-filtered signal sample stream. In **Chapter 6** we close the loop by designing and implementing such software receiver. The Chapter introduces an open-source, real-time GNSS software defined receiver (so-named GNSS-SDR) that contributes with several novel features, among them, the use of software design patterns and shared memory techniques to manage efficiently the data flow between receiver blocks, the use of Single Instruction, Multiple Data (SIMD) hardware-accelerated instructions for time-consuming vector operations like carrier wipe-off and code correlation, and the availability to compile and run on multiple software platforms and hardware architectures. We focus the efforts in provide the reader with a balanced content between the receiver design and the software implementation details. At this time of writing (April 2012), the receiver enjoys of a 2-dimensional Distance Root Mean Square (DRMS) error lower than 2 meters for a GPS L1 C/A 8 satellites in lock scenario with a Horizontal Dilution Of Precision (HDOP) of 1.2.

Finally, conclusions, and some guidelines for future research arising from this work can be found in **Chapter 7**.

1.3 Research Contributions

The research contributions of this Dissertation are pointed out in the summary available at the end of each chapter. In addition, during the PhD. period we also published some work not directly related to the main topic of this Dissertation collaborating in the Network of Excellence in Wireless COMmunications (NEWCOM++) European project within the indoor positioning measurement campaign among others. The full list of publications is provided hereafter.

1.3.1 Book chapters

- [Arr12a] J. Arribas, P. Closas, C. Fernández-Prades, M. Cuntz, M. Meurer, and A. Konovaltsev, “Advances in the theory and implementation of GNSS antenna array receivers”, *Microwave and Millimeter Wave Circuits and Systems*, Chap. 9, John Wiley & Sons Limited, 2012, in press.

1.3.2 Journal papers

- [Arr12b] J. Arribas, C. Fernández-Prades, and P. Closas, “Antenna Array Based GNSS Signal Acquisition for Interference Mitigation”, accepted in IEEE Transactions on Aerospace and Electronic Systems, 2012.

1.3.3 International conferences

- [FP11b] C. Fernández-Prades, P. Closas, and J. Arribas, “Eigenbeamforming for Interference Mitigation in GNSS Receivers”, *Proceedings of the International Conference on Localization and GNSS (ICL-GNSS)*, Tampere (Finland), June 2011.
- [FP11a] C. Fernández-Prades, J. Arribas, and P. Closas, “GNSS-SDR: an open source tool for researchers and developers”, in *Proceedings of the ION GNSS 2011, Portland, Oregon (USA)*, September 2011.

- [Arr11a] J. Arribas, C. Fernández-Prades, and P. Closas, “Antenna Array Based GNSS Signal Acquisition: Real-time Implementation and Results”, *Proceedings of the ION GNSS 2011, Portland, Oregon (USA)*, September 2011.
- [Arr11b] J. Arribas, C. Fernández-Prades, and P. Closas, “Array-Based GNSS Acquisition In The Presence Of Colored Noise”, *Proceedings of the 36th IEEE International Conference on Acoustics, Speech, and Signal Processing, ICASSP’11*, Prague, Czech Republic, May 2011.
- [FP10a] C. Fernández-Prades, C. Avilés, L. Esteve, J. Arribas, and P. Closas, “Design patterns for GNSS software receivers”, in *Proceedings of the 5th ESA Workshop on Satellite Navigation Technologies, NAVITEC’2010*, Noordwijk, The Netherlands, December 2010.
- [Arr10a] J. Arribas, P. Closas, and C. Fernández-Prades, “Joint acquisition strategy of GNSS satellites for computational cost reduction”, *Proceedings of the 5th ESA Workshop on Satellite Navigation Technologies, NAVITEC’2010*, Noordwijk, The Netherlands, December 2010.
- [Sot10] F. Sottile, M. A. Spirito, P. Closas, J. Arribas, C. Fernández-Prades, M. Kieffer, M. Nájar, A. Mallat, P. Gérard, L. Vandendorpe, D. Dardari, N. Decarli, and A. Conti, “Evaluation of tracking algorithms using heterogeneous technologies”, *Demo at the IEEE Global Communications Conference, (IEEE GLOBECOM 2010)*, Miami, Florida (USA), December 2010.
- [Arr10b] J. Arribas, C. Fernández-Prades, and P. Closas, “Receiver Operating Characteristic For Array-Based GNSS Acquisition”, *Proceedings of XVIII European Signal Processing Conference, EUSIPCO*, pp. 1082–1086, Aalborg, Denmark, August 2010.
- [Dhi10] A. Dhital, P. Closas, C. Fernández-Prades, J. Arribas, F. Sottile, M. A. Spirito, Z. Xiong, M. Kieffer, E. Lagunas, and M. Nájar, “Evaluation of tracking algorithms using the NEWCOM++ WPRB database measurements”, *Demo at the Future Networks & Mobile Summit (FUNEMS)*, Florence (Italy), June 2010.
- [Clo10a] P. Closas, J. Arribas, and C. Fernández-Prades, “Testing for normality of UWB-based distance measurements by the Anderson-Darling statistic”, *Proceedings of Future Networks & Mobile Summit (FUNEMS)*, Florence (Italy), June 2010.
- [FP09c] C. Fernández-Prades, P. Closas, and J. Arribas, “Implementation of digital beamforming in GNSS receivers”, *Proceedings of the 4th European Workshop on GNSS Signals and Signal Processing*, Oberpfaffenhofen, München (Germany), December 2009.
- [Arr09a] J. Arribas, D. Bernal C., Fernández-Prades, P. Closas, and J. A. Fernández-Rubio, “A novel real-time platform for digital beamforming with GNSS software defined receivers”, *Proceedings of the ION GNSS 2009, Savannah, GA (USA)*, September 2009.
- [FP09a] C. Fernández-Prades, J. Arribas, and P. Closas, “The decoupling of DOA/Synchronization parameters in colored noise environments”, *Proceedings of NEWCOM++ ACoRN Joint Workshop*, Barcelona (Spain), April 2009.

1.3.4 National conferences

- [Arr09b] J. Arribas, C. Fernández-Prades, D. Bernal, and J. A. Fernández-Rubio, “Plataforma de conformación de haz digital para receptores GNSS en tiempo real”, *Proceedings XXIV Simposium Nacional de la Unión Científica Internacional de Radio (URSI 2009)*, Santander (Spain), September 2009.
- [Sol09] M. Solé, J. Arribas, C. Fernández-Prades, D. Bernal, and J. A. Fernández-Rubio, “Correlador doble delta para GPS en tiempo real”, in *Proceedings XXIV Simposium Nacional de la Unión Científica Internacional de Radio (URSI 2009)*, Santander (Spain), September 2009.

Chapter 2

Global Navigation Satellite Systems (GNSS) basics

God not only plays dice, He also sometimes throws the dice where they cannot be seen.

Stephen Hawking.

WHEN we talk about satellite-based positioning we refer to the determination of position of observing sites, located anywhere, in land, sea or air, by means of artificial satellites. A historical review of satellite-based positioning can be found in [Ash06]. Currently Global Navigation Satellite System (GNSS) is the general concept used to identify those satellite-based positioning systems that enable the determination of the user position by means of measured distances between the receiver and a set of visible satellites. These distances are calculated estimating the propagation time of the transmitted signals, traveling from each satellite to the receiver. Finally, the receiver computes the position using a trilateration procedure with the estimated distances and the predicted satellite positions. The aim of this Chapter is to provide a brief introduction of the GNSS basics focusing on the European Galileo and the American Global Positioning System (GPS), identifying sources of performance degradation, and establishing the working definitions and context for the contributions presented in this Dissertation.

Further information can be found in classical reference textbooks where the GPS is explained from a receivers system point of view, see e.g. [Par96, Kap05] among others. For the new trends of Software Defined Radio (SDR) receiver, the reader is referred to [Tsu00, Bor07]. A recent reference that deals with the latest GNSS is [HW08].

The Chapter is organized as follows: Section 2.1 presents the available GNSS civil signals and their structure, focused on the details of the American GPS and the European Galileo systems. Section 2.2 deals with the GNSS propagation channel effects and its particularities, stressing the interference problem and listing the possible interference sources. Finally, Section 2.3 presents a basic GNSS receiver architecture, detailing each of the composing modules.

2.1 GNSS civil signals

All current GNSSs have in common the transmission of a ranging Spread Spectrum (SS) signal by a constellation of Medium Earth Orbit (MEO) satellites¹. The first true GNSS was the American GPS, originally developed for military applications. The purpose of the transmitted

¹The MEO is the region of space around the Earth above low Earth orbit (altitude of 2,000 km) and below geostationary orbit (altitude of 35,786 km). The existing GNSS constellations are in the altitude range of 19,100 km to 23,222 km.

signal was to provide all the necessary information for the military forces to accurately determine their position, velocity, and time in a common reference system, anywhere on or near the earth, on a continuous basis and all-weather conditions [Woo85].

A GNSS receiver estimates the distances to a set of satellites with known positions, by means of measuring the propagation time, and obtains its coordinates using trilateration techniques, estimating the distance between each of the visible satellites and the receiver. Nowadays, with the evolution of GNSS, the applications of global positioning technology have been exploited in practically all the human activities. GNSS positioning technology is no longer used exclusively for military purposes, but has become the core service of a myriad of civil applications, including among others:

- navigation: ground, air, and sea transportation of passengers and goods,
- surveying and mapping,
- precise time reference and clock dissemination, and
- emergency response coordination and Search And Rescue (SAR) services

The modernized GNSS signal needs to carry enough information to provide a variety of services, including indoor positioning, Safety of Live (SoL) services, integrity-related information, and even broadcast of customer messages [HW08].

We can split the GNSS signal contents in two categories:

- ranging signal: enables the receiver to measure the signal propagation time differences between satellites, and consequently, to estimate their apparent distances, and
- navigation message: informs the receiver of the satellite orbits model parameters, GNSS clock model parameters and other service-related data, which enables the receiver to estimate the satellite positions and time. It is important to mention that the navigation message is modulated as a telemetry signal, which is also synchronized with the ranging signal. The receiver uses this feature to eliminate the ambiguities of the ranging signal.

In this work we focus the research on the civil navigation signals of the most evolved GNSSs: The American modernized GPS and the forthcoming European Galileo. Hereafter it can be found an overview of their characteristics.

2.1.1 GNSS transmitter signal structure

The GNSS signal structure can be expressed as a generic Direct-Sequence Code Division Multiple Access (DS-CDMA) signal [HW08], transmitted synchronously by all the satellites of the constellation. The baseband model of the transmitted signal by the i -th satellite is defined as:

$$s_{T,i}(t) = e_{I,i}(t) + j e_{Q,i}(t), \quad (2.1)$$

where the subindex I and Q denote in-phase and quadrature component respectively, and are defined as:

$$e_{I,i}(t) = \sqrt{2P_{I,i}} \sum_{m_I=-\infty}^{\infty} b_{I,i}(m_I) \sum_{u_I=1}^{N_{c_I}} \sum_{k_I=1}^{L_{c_I}} c_{I,i}(k_I) g_I(t - m_I T_{b_I} - u_I T_{PRN_I} - k_I T_{c_I}) \quad (2.2)$$

$$e_{Q,i}(t) = \sqrt{2P_{Q,i}} \sum_{m_Q=-\infty}^{\infty} b_{Q,i}(m_Q) \sum_{u_Q=1}^{N_{c_Q}} \sum_{k_Q=1}^{L_{c_Q}} c_{Q,i}(k_Q) g_Q(t - m_Q T_{b_Q} - u_Q T_{PRN_Q} - k_Q T_{c_Q}), \quad (2.3)$$

with the following definitions for the I component - analogous for the Q component:

- $P_{I,i}$ is the transmitted signal power, equal for all the satellites in the constellation.
- $b_{I,i}(m) \in \{-1, 1\}$ is the sequence of telemetry bits, with T_{b_I} being the bit period.

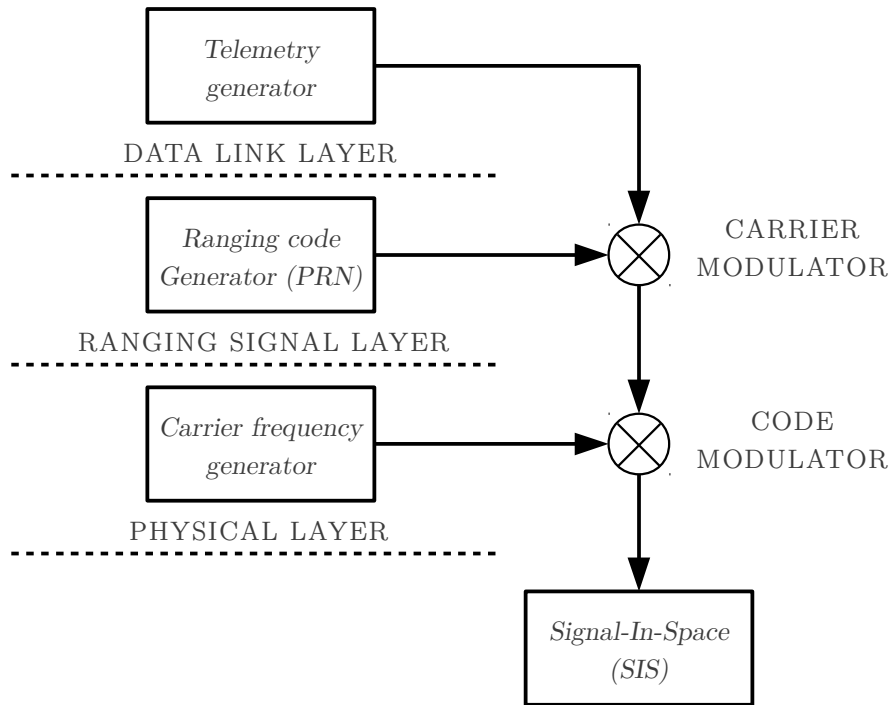


Figure 2.1: Single channel GNSS modulation.

- **composite signals**: the evolved GNSS signals provide improved accuracy and robustness against the propagation channel effects and higher telemetry data rates. The transmission of telemetry over the ranging signal limits the coherent integration time due to the telemetry bit transitions. The most harmful effect of the telemetry bits transitions in the receiver is a sensitivity degradation up to 6 dB in terms of signal tracking threshold due to the use of a Costas loop in the Phase Locked Loop (PLL) discriminator [Kap05].

A composite signal is created to solve this issue. The pilot channel contains the ranging signal and the data channel broadcasts the telemetry information. The separation between the pilot and data channel could be made using different spreading codes or adding a phase difference, usually 90° . The pilot channels usually use long PRN sequences, referred to as tiered codes, which are composed by a short primary code, that allows fast acquisition, and a secondary code to increase the code gain. The receiver can track the ranging signal using a coherent PLL discriminator without losing sensitivity [Kap05].

In addition, the data and pilot PRN sequences are synchronous with respect to each other, which allows a simpler synchronization process [Und10, Win08]. Fig. 2.2 shows a conceptual composite signal modulation scheme.

The transmitted passband Radio Frequency (RF) signal can be expressed as:

$$s_{RF,i}(t) = \Re\{s_{T,i}(t)e^{j2\pi f_c t}\}, \quad (2.4)$$

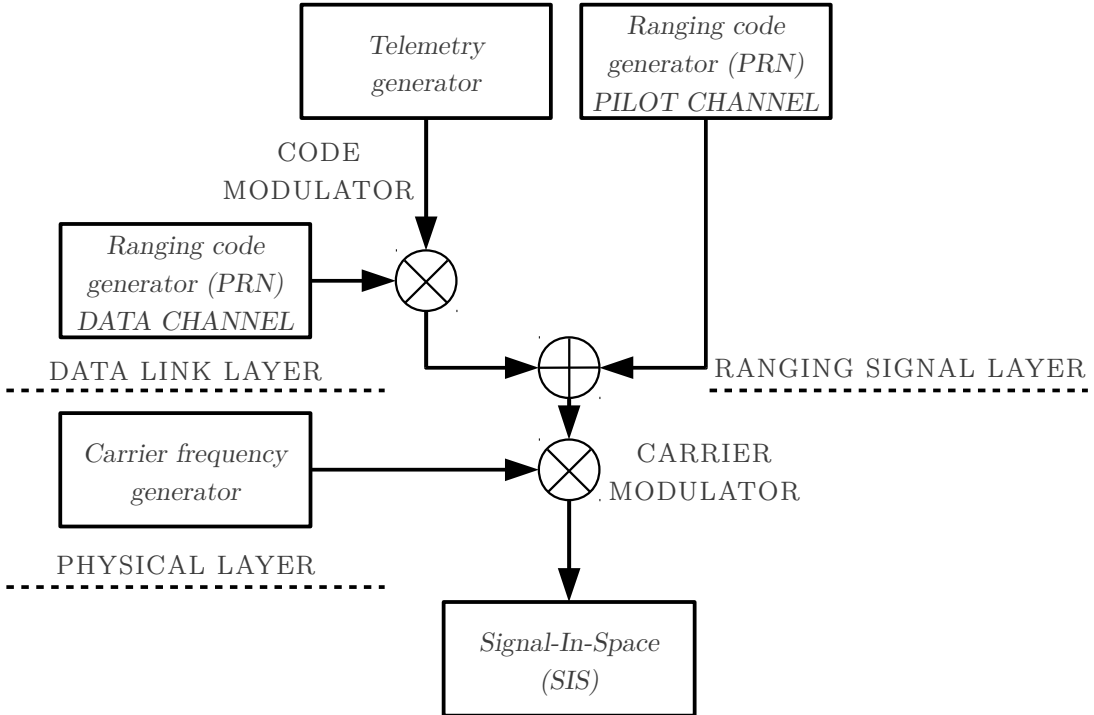


Figure 2.2: Composite signal modulation.

where \Re denotes the real part of the complex-valued quantity in the brackets and f_c is the carrier frequency, which depends on the GNSS link.

Currently, all GPS and Galileo links are located in the L-Band² band. Figure 2.3, extracted from [Und10], shows the spectrum allocation for both systems. The use of C-Band³ frequencies for navigation purposes is being considered for the future generation of GNSSs [Irs04]. The smaller wavelength reduces the size of the antennas and allows the use of smaller antenna arrays.

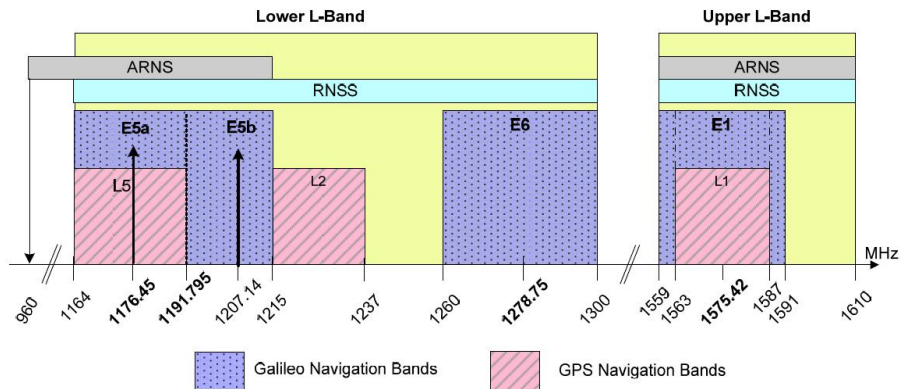


Figure 2.3: Spectrum allocation of Galileo and GPS RF links [Und10].

²This is the Institute of Electrical and Electronics Engineers (IEEE) radar band nomenclature, covering from 0.3 – 3 GHz. The International Telecommunications Union (ITU) nomenclature for L-BAND band is Ultra High Frequency (UHF).

³Covering from 4 – 8 GHz.

2.1.2 GPS signals

The American GPS started the fully operational service in 1993 and its civil positioning signal is now widely used by mass-market commercial receivers. The satellite constellation include 24 operational MEO satellites deployed in 6 planes with an inclination of 55° . The constellation distribution is designed to provide global coverage, specially in the most populated regions. The satellites have an orbital period of approximately half a sidereal day⁴ with an altitude of about 20200 km above the Earth [HW08]. Two positioning services are provided, referred to as the Precision Positioning Service (PPS) and Standard Positioning Service (SPS). The PPS service is available primarily to the military forces of the United States and its allies, and the SPS service is open to the civilian users.

The modernized GPS signals include three different links: L1, L2 and L5. The carrier frequency for each link is obtained from a fundamental frequency of $f_0 = 10.23$ MHz. Table 2.1 shows the most significant parameters of the current and forthcoming civil links, codes and modulations⁵. The reader is referred to [Win10, Win08, Win05] for the details and particularities of the signal structures and services.

Link	f_c [MHz]	PRN code	BW [MHz]	Pwr [dBW]	L_c [chips]	Code rate (1/ T_c)	Mod.	Ch.	Serv.
L1	$f_0 \cdot 154$ 1575.42	C/A ¹	20.46	-158.5	1023	$f_0/10$	BPSK(1)	single	SPS ²
		P ⁴	20.46	-161.5	$6.1871 \cdot 10^{12}$	f_0	BPSK(10)	single	PPS ³
		L1CD ⁵	30.69	-158.25	10230	$f_0/10$	BOC(1,1)	data	Civil
		L1CP ⁵	30.69	-163	$10230 \cdot 1800$	$f_0/10$	BOC(1,1)	pilot	Civil
L2	$f_0 \cdot 120$ 1227.60	P ⁴	20.46	-158.5	$6.1871 \cdot 10^{12}$	f_0	BPSK(10)	single	PPS ³
		L2CM ⁴	24	-158.5	10230	$f_0/10$	BPSK(1)	single	Civil
		L2CL ⁴	24	-158.5	$10230 \cdot 75$	$f_0/10$	BPSK(1)	pilot	Civil
L5	$f_c \cdot 115$ 1176.45	L5I ⁶	24	-157.9	$10230 \cdot 10$	f_0	BPSK(10)	data	SoL
		L5Q ⁶	24	-157.9	$10230 \cdot 20$	f_0	BPSK(10)	pilot	SoL

¹ Coarse Acquisition [Win10].

² Standard Positioning Service.

³ Precise Positioning Service.

⁴ [Win10].

⁵ [Win08].

⁶ [Win05].

Table 2.1: List of civil GPS links, codes and modulations.

It is possible to particularize the baseband signal model of (2.1) for the different GPS links, as described in [FP11c]

- **GPS L1:** is available in all the satellites in the constellation. The baseband signal can be written as

$$s_T^{(\text{GPS L1})}(t) = e_{L1I}(t) + j e_{L1Q}, \quad (2.5)$$

⁴A sidereal day is approximately 23 hours, 56 minutes, 4.091 seconds, corresponding to the time it takes for the Earth to complete one rotation relative to the vernal equinox.

⁵The modulation index is referred to $\frac{f_0}{10}$.

with

$$e_{L1I}(t) = \sum_{l=-\infty}^{\infty} D_{NAV} [[l]_{204600}] \oplus C_{P(Y)} [|l|_{L_{P(Y)}}] g(t - lT_{c,P(Y)}), \quad (2.6)$$

$$e_{L1Q}(t) = \sum_{l=-\infty}^{\infty} D_{NAV} [[l]_{20460}] \oplus C_{C/A} [|l|_{L_{1023}}] g(t - lT_{c,C/A}), \quad (2.7)$$

where \oplus is the exclusive-or operator (modulo-2 addition) that can be interpreted as a Binary Phase-Shift Keying (BPSK) modulator, $|l|_L$ means l modulo L , $[l]_L$ means the integer part of $\frac{l}{L}$, D_{NAV} is the GPS navigation message telemetry bit sequence, transmitted at 50 bps, $T_{c,P(Y)} = \frac{1}{f_0}$ s, $T_{c,C/A} = \frac{10}{f_0}$ s, $L_{P(Y)} = 6.1871 \cdot 10^{12}$, and $g(t)$ is a rectangular pulse of a chip-period duration centered at $t = 0$ and filtered at the transmitter.

Notice that the GPS L1 signal is composed of two independent single channel positioning signals. Both the SPS C/A and PPS signals contain a ranging signal modulated by the telemetry bitstream. The PPS spreading codes, referred as P codes are sequences of seven days in length that can be used also by the civilian users, however, the GPS mission control center can turn on the anti-spoofing mode, encrypting the P codes⁶, and thus denying non-US military users the PPS service. The satellites that have activated the P code encryption inform the user with the corresponding anti-spoof flag in the navigation message.

With the modernization of the GPS satellite constellation, a new civil positioning signal named L1C will be available with the first Block III satellite vehicles, currently scheduled for 2013, which will also provide the legacy C/A signal to ensure backward compatibility with the existing receivers.

- **GPS L2C:** is only available for Block IIR-M and subsequent satellite vehicles. The in-phase component is the same as in the GPS L1 signal, which carries the PPS signal, but with an optional presence of the navigation message. The baseband signal can be written as

$$s_T^{(\text{GPS L2C})}(t) = e_{L2I}(t) + j e_{L2CQ}, \quad (2.8)$$

with

$$e_{L2I}(t) = e_{L1I}(t), \quad (2.9)$$

$$e_{L2CQ}(t) = \sum_{l=-\infty}^{\infty} D_{CNAV} [[l]_{10230}] \oplus C_{CL} [|l|_{L_{CL}}] g_{1/2}(t - lT_{c,L2C}) + \quad (2.10)$$

$$+ C_{CM} [|l|_{L_{CM}}] g_{1/2} \left(t - \left(l + \frac{3}{4} \right) T_{c,L2C} \right), \quad (2.11)$$

where $T_{c,L2C} = \frac{2}{f_0}$ s and $g_{1/2}(t)$ is a rectangular pulse of half chip-period duration, thus time multiplexing both codes. The civilian long code C_{CL} is $L_{CL} = 10230 \cdot 75$ chips long, repeating every 1.5 s, while the civilian moderate code C_{CM} is $L_{CM} = 10230$ chips long with a period of 20 ms. The CNAV navigation message is an upgraded version of the NAV data, containing higher precision representation and nominally more accurate data than the NAV data. It is transmitted at 25 bps with Forward Error Correction (FEC) encoding, resulting in 50 sps. This redundancy allows the demodulation of the telemetry signal under challenging environments (e.g. indoor scenarios or under heavy foliage [Kap05]). According to the latest interface specifications document [Win10], the e_{L2CQ} component of GPS L2C signal can be switched to a conventional GPS C/A signal component, whose navigation data can be also switched off.

- **GPS L5:** is only available in Block IIF and subsequent satellite blocks. The baseband signal can be written as

$$s_T^{(\text{GPS L5})}(t) = e_{L5I}(t) + j e_{L5Q}, \quad (2.12)$$

⁶The encrypted P code is referred to as Y code.

with

$$e_{L5I}(t) = \sum_{m=-\infty}^{\infty} C_{nh_{10}} [|m|_{10}] \oplus D_{CNAV} [|m|_{10}] \oplus \quad (2.13)$$

$$\oplus \sum_{l=1}^{102300} C_{L5I} [|l|_{10230}] g(t - mT_{c,nh} - lT_{c,L5}), \quad (2.14)$$

$$e_{L5Q}(t) = \sum_{m=-\infty}^{\infty} C_{e,h_{20}} [|m|_{20}] \oplus \sum_{l=1}^{102300} C_{L5Q} [|l|_{10230}] g(t - mT_{c,nh} - lT_{c,L5}), \quad (2.15)$$

where $T_{c,nh} = 1 \cdot 10^{-3}$ s and $T_{c,L5} = \frac{1}{f_0}$ s. Notice that the E5Q signal component is a pure ranging signal (pilot signal) and does not contain telemetry modulation.

2.1.3 Galileo signals

The forthcoming civil European Galileo system is designed to have a constellation of 27 operational + 3 spare satellites in three MEOs planes, inclined 56° with respect to the equatorial plane [HW08]. The constellation is designed to provide a minimum of 6 visible satellites worldwide, with an elevation mask of 10°. Two experimental satellites named GIOVE-A and GIOVE-B, were launched in 2005 and 2008, respectively. These satellites emit Galileo-like signals aiming at testing several aspects of the project such as environmental effects, expected orbit perturbations and validation of signal structure. As of 2011, the first two fully operational Galileo satellites were launched by a Soyuz vehicle from Europe's Spaceport in French Guiana on October, 21st. On December 2011 Galileo transmitted its state-of-the-art modulated signals across three spectral bands, known as E1, E5 and E6, simultaneously for the first time. The initial service is expected around 2014, with an initial constellation of 18 satellites, and the fully operational service with a minimum of 30 satellites is scheduled by the end of the decade, according to the European GNSS Supervisory Authority (GSA). Galileo and GPS will share the UHF band and even some carrier frequencies. Five Galileo RF links are defined: E1, E6, E5, E5a and E5b [Und10]. Again, the carrier frequencies are obtained from the fundamental frequency $f_0 = 10.23$ MHz. Table 2.2 shows the most significant parameters of Galileo links, codes and modulations⁷.

Link	f_c [MHz]	PRN code	BW [MHz]	Pwr [dBW]	L_c [chips]	Code rate (1/ T_c)	Mod.	Ch.	Serv.
E1	$f_0 \cdot 154$	E1-B	24.552	-160	4092	$f_0/10$	CBOC (6,1,1/11)	data	SoL
		E1-C	24.552	-160	$4092 \cdot 25$	$f_0/10$	CBOC (6,1,1/11)		
E6	$f_0 \cdot 125$	E6-B	40.92	-158	5115	$f_0/2$	BPSK(5)	data	CS ¹
		E6-C	40.92	-158	$5115 \cdot 100$	$f_0/2$	BPSK(5)		
E5a	$f_0 \cdot 115$	E5a-I	20.46	-158	$10230 \cdot 20$	f_0	BPSK(10)	data	OS ²
		E5a-Q	20.46	-158	$10230 \cdot 100$	f_0	BPSK(10)		
E5b	$f_0 \cdot 118$	E5b-I	20.46	-158	$10230 \cdot 4$	f_0	BPSK(10)	data	SoL ³
		E5b-Q	20.46	-158	$10230 \cdot 100$	f_0	BPSK(10)		

¹ Commercial Service.

² Open Service.

³ Includes both OS and CS.

Table 2.2: List of Galileo links, codes and modulations.

⁷The modulation index is referred to $\frac{f_0}{10}$.

- **Galileo E1:** is a two-channel composite navigation signal that contains a Composite Binary Offset Carrier (CBOC) modulation with two subcarriers. The baseband signal can be written as

$$s_T^{(\text{Gal E1})}(t) = \frac{1}{\sqrt{2}} (e_{E1B}(t)(\alpha sc_A(t) + \beta sc_B(t)) - e_{E1C}(t)(\alpha sc_A(t) - \beta sc_B(t))), \quad (2.16)$$

where the square wave subcarriers are defined as

$$sc_A(t) = \text{sgn}(\sin(2\pi f_{s,E1A} t)), \quad (2.17)$$

$$sc_B(t) = \text{sgn}(\sin(2\pi f_{s,E1B} t)), \quad (2.18)$$

and $\text{sgn}(\cdot)$ stands for the sign function, $f_{s,E1A} = \frac{f_0}{10}$ Hz, $f_{s,E1B} = 6\frac{f_0}{10}$ MHz are the subcarriers rate, $\alpha = \sqrt{\frac{10}{11}}$, and $\beta = \sqrt{\frac{1}{11}}$ are the amplitude relation factors, respectively. Channel B contains the I/NAV navigation message $D_{I/NAV}$, while Channel C is a pilot channel. Hereafter can be found both expressions:

$$e_{E1B}(t) = \sum_{l=-\infty}^{\infty} D_{I/NAV} [[l]_{4092}] \oplus C_{E1B} [[l]_{4092}] g(t - lT_{c,E1B}), \quad (2.19)$$

$$e_{E1C}(t) = \sum_{l=-\infty}^{\infty} C_{E1Cs} [|m|_{25}] \oplus \sum_{l=1}^{4092} C_{E1Cp} [l] g(t - mT_{c,E1Cs} - lT_{c,E1Cp}), \quad (2.20)$$

with $T_{c,E1B} = T_{c,E1Cp} = \frac{1}{f_0}$ Hz and $T_{c,E1Cs} = 4 \cdot 10^{-3}$ s. Both C_{E1B} and C_{E1Cp} primary codes are pseudorandom memory code sequences defined in [Und10], Annex C.7 and C.8. The secondary code C_{E1Cs} is also a memory code defined in the Galileo interface control document [Und10]. The E1 link also contains another channel, named Galileo E1A, intended for the so called Public Regulated Service (PRS), however the PRS signal structure and the spreading codes have not been made public at this time of writing (February 2012), to the author's knowledge.

- **Galileo E6:** it is also a two-channel navigation signal intended for the Commercial Service. The baseband expression can be written as

$$s_T^{(\text{Gal E6})}(t) = \frac{1}{\sqrt{2}} (e_{E6B}(t) - e_{E6C}(t)), \quad (2.21)$$

with

$$e_{E6B}(t) = \sum_{l=-\infty}^{\infty} D_{I/NAV} [[l]_{5115}] \oplus C_{E6B} [[l]_{L_{E6B}}] g(t - lT_{c,E6}), \quad (2.22)$$

$$e_{E6C}(t) = \sum_{l=-\infty}^{\infty} C_{E6Cs} [|m|_{100}] \oplus \sum_{l=1}^{L_{E6C}} C_{E6Cp} [l] g(t - mT_{c,E6s} - lT_{c,E6p}), \quad (2.23)$$

where $D_{C/NAV}$ is the C/NAV navigation telemetry stream, which is modulated with the encrypted ranging code C_{E6B} with a chip period $T_{c,E6} = \frac{2}{f_0}$. Codes C_{E6B} , C_{E6Cs} , and their respective lengths L_{E6B} and L_{E6C} have not been published at this time of writing . This link is also planned to transmit a Galileo E6A PRS channel.

- **Galileo E5** it is a four-channel navigation signal intended both for the Commercial and for the SoL services. It contains an AltBOC modulation, specially designed to make it envelope-constant, and thus, suitable to drive non-linear power amplifiers, as is described in [FP11c]. The baseband expression can be written as

$$s_T^{(\text{Gal E5})} = e_{E5a}(t)ssc_s^*(t) + e_{E5b}(t)ssc_s(t) + \quad (2.24)$$

$$+ \bar{e}_{E5a}(t)ssc_p^*(t) + \bar{e}_{E5b}(t)ssc_p(t), \quad (2.25)$$

where the single and product side-band carriers are

$$ssc_s(t) = sc_s(t) + jsc_s \left(t - \frac{T_s}{4} \right), \quad (2.26)$$

$$ssc_p(t) = sc_p(t) + jsc_p \left(t - \frac{T_s}{4} \right), \quad (2.27)$$

and

$$e_{E5a}(t) = e_{E5aI}(t) + je_{E5aQ}(t), \quad (2.28)$$

$$e_{E5b}(t) = e_{E5bI}(t) + je_{E5bQ}(t), \quad (2.29)$$

$$\bar{e}_{E5a}(t) = \bar{e}_{E5aI}(t) + j\bar{e}_{E5aQ}(t), \quad (2.30)$$

$$\bar{e}_{E5b}(t) = \bar{e}_{E5bI}(t) + j\bar{e}_{E5bQ}(t), \quad (2.31)$$

$$\bar{e}_{E5aI}(t) = e_{E5aQ}(t)e_{E5bI}(t)e_{E5bQ}(t), \quad (2.32)$$

$$\bar{e}_{E5aQ}(t) = e_{E5aI}(t)e_{E5bI}(t)e_{E5bQ}(t), \quad (2.33)$$

$$\bar{e}_{E5bI}(t) = e_{E5bQ}(t)e_{E5aI}(t)e_{E5aQ}(t), \quad (2.34)$$

$$\bar{e}_{E5bQ}(t) = e_{E5bI}(t)e_{E5aI}(t)e_{E5aQ}(t). \quad (2.35)$$

The signal components are defined as

$$e_{E5aI}(t) = \sum_{m=-\infty}^{+\infty} C_{E5aIs} [|m|_{20}] \oplus \sum_{l=1}^{10230} C_{E5aIp}[l] \oplus D_{F/NAV} [|l|_{204600}] g(t - mT_{c,E5s} - lT_{c,E5p}), \quad (2.36)$$

$$e_{E5aQ}(t) = \sum_{m=-\infty}^{+\infty} C_{E5aQs} [|m|_{100}] \oplus \sum_{l=1}^{10230} C_{E5aQp}[l] \cdot g(t - mT_{c,E5s} - lT_{c,E5p}), \quad (2.37)$$

$$e_{E5bI}(t) = \sum_{m=-\infty}^{+\infty} C_{E5bIs} [|m|_4] \oplus \sum_{l=1}^{10230} C_{E5bIp}[l] \oplus D_{I/NAV} [|l|_{40920}] g(t - mT_{c,E5s} - lT_{c,E5p}), \quad (2.38)$$

$$e_{E5bQ}(t) = \sum_{m=-\infty}^{+\infty} C_{E5bQs} [|m|_{100}] \oplus \sum_{l=1}^{10230} C_{E5bQp}[l] \cdot g(t - mT_{c,E5s} - lT_{c,E5p}), \quad (2.39)$$

where $T_{c,E5s} = 1 \cdot 10^{-3}$ s and $T_{c,E5p} = \frac{1}{f_0}$ s. Channel A contains the F/NAV navigation message $D_{F/NAV}$ in the in-phase component intended for the Open Service, while the quadrature component is a pilot channel. Channel B contains the I/NAV message also in the in-phase component, which contains the same page layout, but the page sequencing is different to allow a fast reception of data by a dual frequency receiver. Channel B quadrature component is a pilot channel. The single subcarrier $sc_s(t)$ and the product subcarrier $sc_p(t)$ of expressions 2.26 and 2.27 are

$$sc_s(t) = \frac{\sqrt{2}}{4} \operatorname{sgn} \left(\cos(2\pi f_s t - \frac{\pi}{4}) \right) + \frac{1}{2} \operatorname{sgn} (\cos(2\pi f_s t)) + \frac{\sqrt{2}}{4} \operatorname{sgn} \left(\cos(2\pi f_s t + \frac{\pi}{4}) \right), \quad (2.40)$$

$$sc_p(t) = \frac{\sqrt{2}}{4} \operatorname{sgn} \left(\cos(2\pi f_s t - \frac{\pi}{4}) \right) + \frac{1}{2} \operatorname{sgn} (\cos(2\pi f_s t)) - \frac{\sqrt{2}}{4} \operatorname{sgn} \left(\cos(2\pi f_s t + \frac{\pi}{4}) \right), \quad (2.41)$$

with a subcarrier frequency of $f_s = 15 \frac{f_s}{10}$ Hz, thus defining an AltBOC(15,10) modulation.

2.1.4 Other systems

In addition to Galileo and GPS, there exists the Russian satellite navigation system, referred as GLObalnaya Navigasjonnay Sputnikovaya Sistema (GLONASS) and the forthcoming Chinese

counterpart Compass system. Both are military systems which include civil signals in their links.

GLONASS have a constellation of 21+3 satellites with an altitude on the order of 19100 km and distributed in 3 orbital planes, inclined 64.8° with respect to the Earth equator. GLONASS uses Frequency Division Multiple Access (FDMA) to differentiate the transmitted signals from satellites in addition to the DS-CDMA modulation, to reduce the cross-correlation [Cen02]. Glonass civil signal structure is defined in [GLO08]. Two carrier frequencies are defined, covering two bands, $f_{GLOL1}^{(k)} = 1602 + k \cdot 0.5625$ MHz and $f_{GLOL2}^{(k)} = 1246 + k \cdot 0.4375$ MHz, where $k \in \{-7, 6, \dots, 5, 6\}$ is the channel number. Satellites in opposite points of an orbit plane transmit signals on equal frequencies, as these satellites will never be in view simultaneously by a ground-based user. The Glonass L1 baseband signal can be expressed as:

$$S_T^{GLOL1} = e_{L1I}(t) + j e_{L1Q}(t), \quad (2.42)$$

with BPSK(5) and BPSK(0.5) modulations

$$e_{L1I}(t) = \sum_{l=-\infty}^{\infty} D_{GNAV}[|l|_{102200}] \oplus C_{HP}[|l|_{L_{HP}}] g(t - lT_{c,HP}), \quad (2.43)$$

$$e_{L1Q}(t) = \sum_{l=-\infty}^{\infty} D_{GNAV}[|l|_{10220}] \oplus C_{SP}[|l|_{511}] g(t - lT_{c,SP}), \quad (2.44)$$

where $T_{c,HP} = (1/5.11) \mu s$, $T_{c,SP} = (1/0.511) \mu s$, and $L_{HP} = 3.3554 \cdot 10^7$. The navigation message D_{GNAV} is transmitted at 50 bps. The high precision ranging signal T_{HP} should be used with a Russian Federation Defense Ministry agreement.

Compass is the forthcoming evolution of the regional positioning system named Beidou, which is based on a constellation of four geostationary satellites. The Beidou-2 or Compass will consist of 24+3 MEO, 5 geostationary and 3 geosynchronous satellites [BEI06]. The MEO satellites are distributed in 3 orbits, inclined 55° . On December 2011, China released a “test version” interface control document (ICD) for its Compass GNSS [Bei11]. The publication partially covers its open B1 civil signal structure and PRN codes, but there is no information about the telemetry frame structure.

Table 2.3 shows the most relevant information of the GLONASS and Compass systems.

System	Link	f_c [MHz]	BW [MHz]	Service
Glonass	G1f	1602.00	7.875	SP ¹
	G1	1602.00	undisclosed	HP ²
	G2	1246.00	7.875	SP ¹
	G2	1246.00	undisclosed	HP ²
Compass	B1	1561.10	4.092	OS/M ³
	B1-2	1589.74	4.092	OS/M ³
	B2	1207.14	24	OS/M ³

¹ Standard Precision.

² High Precision.

³ Open Service / Military.

Table 2.3: Other GNSS links.

The performance of GNSS receivers can be improved using Differential GNSS (DGPS) techniques, based on differential corrections broadcasted by reference stations, and using augmentation systems to enhance also the system integrity. Augmentation systems can be divided

into Space-Based Augmentation System (SBAS) and Ground-Based Augmentation Systems (GBAS). Current SBAS systems are the American Wide-Area Augmentation System (WAAS) [WAA08], European Geostationary Navigation Overlay System (EGNOS) [Ene09], Japanese Multi-functional Satellite Augmentation System (MSAS), the Indian GPS and GEO Augmented Navigation (GAGAN) and the forthcoming Chinese and Russian's System of Differential Correction and Monitoring (SDCM). In GBAS category we found the pseudolite-based augmentation system or the Local-Area Augmentation System (LAAS).

2.2 Signal propagation

GNSS transmitted signal travels from MEO satellites to the receiver through the Earth atmosphere forming a radio-propagation channel which modifies its amplitude, phase and delay. The relative movement of both the satellite and the receiver and the surrounding objects also contribute to the distortion of the satellite signal. The German Aerospace Center (DLR) carried out a high resolution measurement campaign to investigate the land mobile satellite navigation channel. The aim was to characterize the GNSS propagation and obtain a mathematical model [Ste05]. Considering a direct propagation path and $M_p - 1$ secondary paths (multipath propagation), the channel for the i -th satellite could be modeled using a linear time-varying baseband-equivalent impulse response [Rap96]:

$$h_i(t) = \sum_{m=0}^{M_{p_i}-1} \alpha_{i,m}(t) e^{j\phi_{i,m}(t)} \delta(t - \tau_{i,m}(t)), \quad (2.45)$$

where $\alpha_{i,m}(t)$, $\phi_{i,m}(t)$ and $\tau_{i,m}(t)$ are the time-varying amplitude, phase and delay for the m -th propagation path for the i -satellite. The subindex $m = 0$ denotes Line-of-Sight Signal (LOSS). The statistical models of these parameters are known in the literature. The classical assumptions are that amplitudes are considered Rician-distributed for LOSS or Rayleigh-distributed when multipath exists [Rap96, Pro00]. The received phase is considered uniformly-distributed [Yak74], and time-delay is considered constant for an observation period on the order of tens of milliseconds [Nee94].

It is possible to apply the channel model to the RF satellite signal model (2.4), considering M_s satellites, the received signal $x(t)$ is the superposition of the transmitted satellite signals propagated through the atmosphere, modeled as the corresponding channel, plus an additive noise term, $n(t)$.

$$x_{RF}(t) = \sum_{i=1}^{M_s} s_{R,i} + n(t) = \Re \left\{ \sum_{i=1}^{M_s-1} (s_{T,i}(t) e^{j2\pi f_c t}) * h_i(t) \right\} + n(t) = \quad (2.46)$$

$$= \Re \left\{ \sum_{i=1}^{M_s} \sum_{m=0}^{M_p-1} \alpha_{i,m} e^{j\phi_{i,m}(t)} s_{T,i}(t - \tau_{i,m}(t)) e^{j2\pi f_c(t - \tau_{i,m}(t))} \right\} + n(t). \quad (2.47)$$

Hereafter are briefly explained the most relevant signal propagation effects.

2.2.1 Carrier Doppler effect

Since GNSS satellites do not have a geosynchronous orbit, there exists a relative movement between the receiver and the satellite. That movement, causes a Doppler effect on the carrier signal, which is the change in frequency of the carrier signal for an observer moving relative to the source of the signal. The general receiver signal model (2.47) contains this information implicitly as a linear component of the phase.

Considering only the LOSS contribution of a single satellite ($M_p = 1$ and $M_s = 1$) and neglecting the noise term, it is possible to write

$$x_{RF}(t) = \Re \left\{ \alpha(t) s_T(t - \tau_0(t)) e^{j2\pi f_c(t - \tau_0(t))} \right\} = \Re \left\{ s_R(t) e^{j2\pi f_c t} \right\}, \quad (2.48)$$

where $s_R(t) = \alpha(t) s_T(t - \tau_0(t)) e^{-j2\pi f_c \tau_0(t)}$ is the received complex baseband signal. Notice that we omit the channel phase term $e^{j\phi(t)}$ because we are interested in the effects caused by the time-varying $\tau_0(t)$.

The link between $\tau_0(t)$ and the carrier frequency deviation (Doppler effect) can be found in Closas' Ph.D. Thesis [Clo09a] among other sources. For the sake of completeness, hereafter we recall briefly the most relevant results.

If we approximate the last term of $s_R(t)$ using the first-order Taylor expansion in the neighborhood of an arbitrary instant t_0 as

$$e^{j2\pi f_c(t - \tau_0(t))} \approx e^{-j2\pi f_c \tau_0(t_0)} e^{-j2\pi f_c \left(\frac{\delta \tau_0(t)}{\delta t} \Big|_{t=t_0} \right) t} e^{j2\pi f_c \left(\frac{\delta \tau_0(t)}{\delta t} \Big|_{t=t_0} \right) t_0}, \quad (2.49)$$

then it is possible to write

$$f_d = -f_c \left(\frac{\delta \tau_0(t)}{\delta t} \Big|_{t=t_0} \right), \quad (2.50)$$

$$\phi_0 = -2\pi f_c \left(\tau_0(t_0) - \frac{\delta \tau_0(t)}{\delta t} \Big|_{t=t_0} \right), \quad (2.51)$$

which are the Doppler-deviation and phase shift of the received signal due to the travel time, respectively. Using (2.50) and the well-known equation of motion $\tau_0(t) = \frac{r_0(t)}{c}$, where $r_0(t)$ is the time-varying distance between the satellite and the receiver and c is the speed of light, it is possible to relate the Doppler deviation to the radial velocity v_{r0}

$$f_d = -f_c \left(\frac{\delta r_0(t)c}{c^2 \delta t} \Big|_{t=t_0} \right) = -f_c \frac{v_{r0}}{c}, \quad (2.52)$$

where $\frac{\delta r_0(t)}{\delta t} = v_{r0}$, assuming constant radial velocity. If the path includes scatterer elements, the resulting Doppler is the sum of the Doppler shift due to the radial velocity between the satellite and the first scatterer, the Doppler shift due to the radial velocity between scatterers, and the Doppler shift due to the radial velocity between the last scatterer and the receiver [Fon98]. The different paths are assumed to be independent, and the model for this assumption is usually referred as Wide Sense Stationary with Uncorrelated Scattering (WSSUS), which also includes the wide sense stationarity assumption [Bel63]. The Carrier signal is frequency-shifted according to a Doppler frequency f_d . For low speed receiver dynamics it is known [Tsu00], that $f_d \in \{-5, +5\}$ kHz. Taking into account a limited observation time, the carrier phase evolution will be considered linear in time, yielding $\phi_{i,m} = 2\pi f_{d,i,m} t + \phi_{i,m}$ in (2.45).

2.2.2 Attenuation

Considering the LOSS, the amplitude is affected by the free space path loss and the atmospheric attenuation. The signal propagation attenuation can be expressed as:

$$L_{PATH}(t) = 20 \log \left(\frac{\lambda}{4\pi r(t)} \right) + L_{ATM}(t, f_c), \quad (2.53)$$

where $\lambda = \frac{c}{f_c}$ is the carrier wavelength, $\mathbb{E}[r(t)] \simeq 2 \times 10^7$ m is the satellite-receiver expected distance, and $L_{ATM}(t, f_c)$ [dB] is the atmospheric attenuation due to the water vapor and other atmospheric particles and effects. In [Hei07] can be found a comparative table of sources of attenuation and its values for the L-band and C-band.

The received signal could suffer from a fluctuation in the amplitude due to changes in the transmission medium; this phenomena is named *signal fading* and it is a scenario-dependent

phenomena. The fading is usually caused by a Line-of-Sight (LOS) signal blocking by the surrounding obstacles, typically in urban or indoor scenarios. A fading model for the urban scenario can be found in [Klu03] and the effects of the building materials for the indoor scenario are modeled in [Klu04].

2.2.3 Interferences

Besides the multipath, an important source of GNSS signal degradation are the interferences, defined as disturbances that affects an electrical circuit due to either electromagnetic conduction or electromagnetic radiation emitted from an external source. In GNSSs, the most common source of interference is the presence of extra electromagnetic signals in the radio link frequencies or in the adjacent spectrum [Lan97], referred to as RFI.

The ranging signal is received with very low pre-correlation Signal-to-Noise Ratio (SNR), typically in the order of -29 to -20 dB for a receiver operated in open sky scenario at the Earth surface [Tsu00]. Despite that the GNSS DS-CDMA processing gain can be high (in the order of 43 dB⁸), which offers protection against low power RFIs, moderate and strong interferences (either intentional or unintentional) remain as the most important causes of performance degradation as reported in [VOL01]. In that sense, an interference with a Signal-to-Noise-and-Interference Ratio (SNIR) that exceeds the processing gain can easily degrade receivers' performance or even block completely the GNSS service, specially conventional receivers equipped with minimal or basic level of protection towards RFIs [War94, Gim98, Kap05]. A growing concern of this problem has appeared in recent times, see, e.g., [IAL08, HS08] among others. Furthermore, the forthcoming deployment of Lightsquared's 4G communication network could create a new interference situation specially when using the 1552.7 MHz band, as notified for first time by the U.S. National Telecommunications and Information Administration (NTIA) to U.S. Federal Communications Commission (FCC) in January 2011. The harmful effects on the GNSS receivers performance was recently deeply analyzed and reported by the FCC Light-Squared Technical Working Group in [FCC11]. Several other papers report the same problem, e.g. [Bou11].

A useful interference level metric is the ratio of interference power to white-noise spectral density ($IN0$), defined as:

$$IN0 = \frac{P_{int}}{kT_0}, \quad (2.54)$$

where P_{int} [W] is the interference power, $k = 1.38 \cdot 10^{-23}$ J/K is the Boltzmann's constant, and $T_0 = 290$ K is the ambient temperature reference value. The DS-CDMA signal design can mitigate a great number of interference signals, but in GNSS systems, the received signal weakness and the required accuracy for measuring the distance to the satellites, makes GNSS receivers specially sensitive to interferences. A number of works exists on the impact of GNSSs interferences and their mitigation. In [Lan97] can be found a classification of GNSS interference sources. Other works devoted to the effects of partial-band and narrow-band interferences, specifically on GPS, are [Bet00] and [Bet01]. The impact of interferences on the acquisition in a single-antenna receiver can be found in [Bor08]. Considering the spectral characteristics, the interferences can be classified in:

- narrowband interferences, which contain energy on a limited fraction of the radio link bandwidth. The impact on GPS receiver tracking operation is addressed in [Bet00]. Examples of potential narrowband interferences are the spurious emissions and out-of-band emissions of many broadcast and communications services.
 - Spurious emissions are defined as emissions on a frequency or frequencies which are outside the necessary bandwidth and the level of which may be reduced without affecting the corresponding transmission of information. Spurious emissions include harmonic emissions, parasitic emissions, intermodulation products and frequency conversion products but exclude out of band emissions [ETS04]. Harmonics is a component frequency of the signal that is an integer multiple of the fundamental frequency.

⁸Processing gain for GPS L1 C/A signal considering 20 ms of coherent acquisition [Tsu00].

- Out-of-band emissions are defined as emissions on a frequency or frequencies immediately outside the necessary bandwidth which results from the modulation process, but excludes spurious emissions [ETSO4].

Considering GPS L1 and Galileo E1 band, Table 2.4, shows a list of potential harmonics from Very High Frequency (VHF) and UHF band TV transmissions and other services. In [Buc97] an analysis of the impact of TV signals on the GPS service was investigated. Regarding the expected interference level of these services, the European Telecommunications Standards Institute (ETSI) defines a normative of spurious emissions for Digital Video Broadcasting – Terrestrial (DVB-T) [ETSO4] and for Global System for Mobile Communications (GSM) [ETSO0] service.

Other navigation systems such as Distance Measuring Equipment (DME) and TACTical Air Navigation (TACAN) can interfere with GNSSs, as is shown in [Bes04].

Order	Band [MHz]	Max. power [dBm]	Usage
L1	1571.42 – 1579.42	–	C/A-GPS, Galileo E1
2th	785.71 – 788.71	-30	UHF TV
3th	523.807 – 526.473	-30	UHF TV
4th	392.855 – 394.855	-36	Mobile/Station
5th	314.284 – 315.884	-36	Mobile/Station
6th	261.903 – 263.237	-36	Mobile/Station
7th	224.488 – 225.631	-36	Broadcasting
8th	196.427 – 197.428	-30	VHF TV
9th	174.602 – 175.491	-30	VHF TV
10h	157.142 – 157.942	-36	VHF Maritime
11th	142.856 – 143.584	-36	VHF Military
12th	130.952 – 131.618	-36	VHF COMs
13th	120.878 – 121.494	-36	VHF COMs
14th	112.244 – 112.816	-36	VOR/ILS
15th	104.761 – 105.295	-36	FM
16th	98.214 – 98.714	-36	FM

Table 2.4: Sources and Services of Interference vs. Harmonics [Buc97].

- wideband interferences, which contain energy on the whole radio link bandwidth. Potential sources include Ultra Wide Band (UWB) transmissions, see e.g. [Cum01, Giu05, Ham02]. The inter-system interferences for GPS and Galileo are studied in [CP03] and [Bet04] among others.

Regarding the possible interferences located on the frequency images of the receiver front end, for a single-conversion GPS L1 / Galileo E1 front-end, the possible interference sources are listed in Table 2.5.

When the interference signal is designed to degrade the GNSS performance it is called intentional interference. According to the American Volpe National Transportation System Center (2001) [VOL01], the intentional GNSS interferences can be classified in:

- jamming: when the GNSS signal is buried into a high-power interference signal, causing the receiver to not be able to detect the navigation signal. An analysis of the signal characteristics and the effective range of several civil GPS jammers is available in [Mit11, Kra11],
- spoofing: when the interference is a legitimate-appearing false signal, designed to shift the computed position solution of a user, and
- meaconing: when the interference signal is a re-broadcast of a received and delayed GNSS signal.

Band [MHz]	Usage
1435-1530	Mobile (aeronautical telemetry)
1530-1545	Mobile-satellite (space-to-Earth) Maritime mobile-satellite (space-to-Earth)
1545-1549.5	Aeronautical mobile-satellite (space-to-Earth) Mobile-satellite (space-to-Earth)
1549.5-1558.5	Aeronautical mobile-satellite (space-to-Earth) Mobile-satellite (space-to-Earth)
1613.8-1626.5	Mobile-satellite (Earth-to-space)
1626.5-1645.5	Mobile-satellite (Earth-to-space)
1646.5-1651	Aeronautical mobile-satellite (Earth-to-space)
1651-1660	Mobile-satellite (Earth-to-space)
1668-1675	Meteorological aids (radiosonde)
1700-1710	Meteorological-satellite (space-to-Earth)
1710-1755	Mobile communications

Table 2.5: Sources and Services of image Interference for single-conversion GPS L1 / Galileo E1 front-end [Wil02].

2.3 GNSS Receivers

This Section is devoted to give a brief introduction to GNSS receivers operation. To complement the information, the reader is referred to textbook references. Classical system analysis of a hardware-based GPS receiver can be found in [Par96] and [Kap05], while the software-based approach for GPS is detailed in [Tsu00] and [Bor07]. The last includes an introduction to Galileo receivers. A general textbook on GNSS which includes details on Glonass and Compass is [HW08]. For specific topics on the front-end design and the Position-Velocity-Time (PVT) solution, competent references are [Men09] and [HP08] respectively. Assisted-GPS (A-GPS) techniques and inertial sensors integration are covered in [Dig09] and [Far99].

Moreover, Chapter 5 in this dissertation is devoted to the design and implementation of real-time array-based GNSS receiver platform, which includes a multichannel coherent RF front-end design and their associated Digital Signal Processor (DSP) hardware. A complete software defined GNSS receiver is described in Chapter 6, which complements the platform and give specific details on the programming methodology and the implementation.

2.3.1 Simplified receiver signal model

In order to illustrate the GNSS receiver's operations, a simplified RF signal model is defined considering only the LOSS contribution coming from M_s satellites and the predominant propagation effects. $x_{RF}(t)$ is recalled here as

$$x_{RF}(t) = \Re \left\{ \sum_{i=1}^{M_s} \alpha_i(t) s_{T,i}(t - \tau_i(t)) e^{j2\pi(f_c + f_{d,i}(t))t} \right\} + n(t), \quad (2.55)$$

where f_c is the carrier frequency, $\{\alpha_i(t), f_{d,i}(t), \tau_i(t)\}$ are the complex amplitude, the explicit Doppler frequency defined in (2.52), and the time delay, respectively, which are the signal synchronization parameters for the i -th satellite signal, $n(t)$ is additive white Gaussian noise plus other undesired terms (such as multipath or interferences), and $s_{T,i}$ is the satellite baseband signal defined in (2.1).

2.3.2 Receiver block diagram

Figure 2.4 presents a generic architecture of a GNSS receiver. The first element is the antenna, which usually is Right Hand Circular Polarization (RHCP), because the satellite LOSS is RHCP

and the reflected signals, such as multipath replicas, often have the opposite polarization (Left Hand Circular Polarization (LHCP)) and this technique offer basic multipath protection [Par96]. The antenna gain radiation pattern has an hemispherical shape, suitable to cover all the sky directions. In this introductory section a single-antenna receiver is considered, leaving the analysis for multiple-antenna architectures to Chapter 4 and Chapter 5.

Next to the antenna, an RF front-end performs the analog signal amplification, bandwidth-limit filtering, and downconversion from the RF GNSS link center frequency to Intermediate Frequency (IF) or Baseband (BB). The front-end signal is digitized using an Analog-to-Digital Converter (ADC) with a suitable sampling frequency and resolution. In order to maximize the signal resolution, the receiver should implement an Automatic Gain Control (AGC) to take advantage of the full dynamic range of the ADC.

In a software-based GNSS receiver, a digital signal processor uses the ADC signal samples to obtain the PVT solution. It contains a channelized structure to acquire and track the GNSS signals, running in parallel and replicated once per satellite.

Inside each satellite channel, the acquisition module searches for the presence of a satellite signal. It obtains a coarse estimation for a specific time instant t_0 of the synchronization parameters $\hat{f}_{d,i}(t_0)$ and $\hat{\tau}_i(t_0)$, which are the Doppler frequency and the code delay, defined in (2.55).

Once the signal is acquired, the tracking blocks start to refine the estimated values given by the acquisition, making corrections every integration interval. Tracking can be considered as a double closed loop composed by the carrier tracking loop and the code tracking loop. The results of the tracking block are the code delay estimation and the telemetry symbols. These symbols are fed to the corresponding telemetry demodulator in charge of decoding the navigation message. The outputs of each satellite channel are feed to the PVT block, which uses the telemetry bits to obtain information of the satellite position and time, and the code delay estimation. This information is used to compute the distances between the receiver and

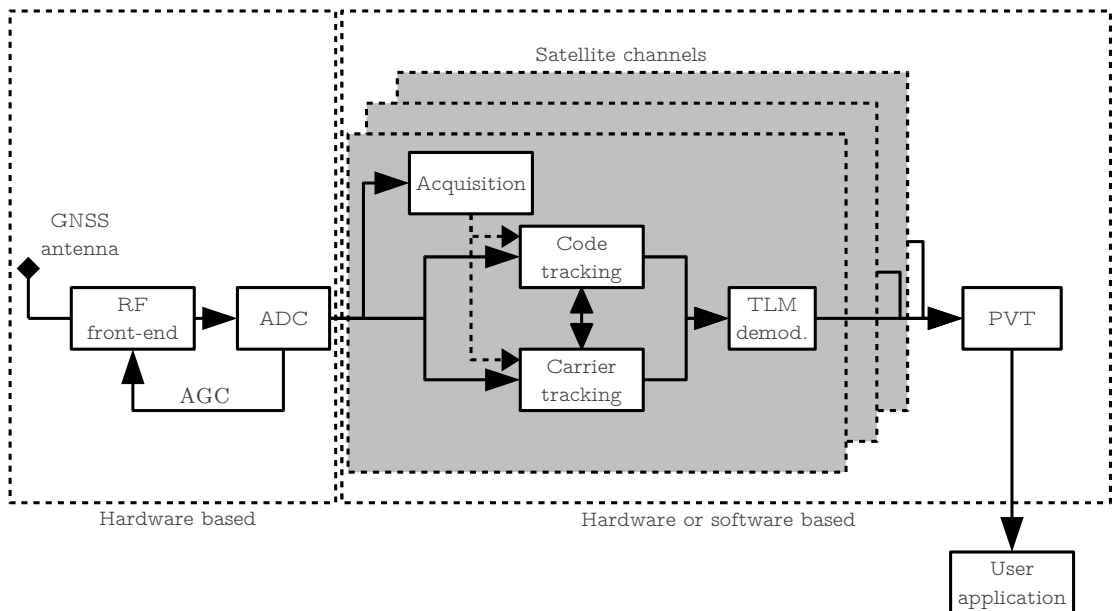


Figure 2.4: Simplified GNSS receiver high-level block diagram.

2.3.3 Baseband signal model

The BB signal model, derived from (2.55), considering the downconversion as an ideal process, can be expressed as:

$$x_{BB}(t) = \sum_{i=0}^{M_s-1} \alpha_i(t) s_{T,i}(t - \tau_i(t)) e^{j2\pi f_{d,i}(t)t} + n(t). \quad (2.56)$$

The BB signal, after the sampling process, neglecting the quantization impact and the interferences, can be expressed as:

$$x_{BB}(kT_s) = \sum_{i=0}^{M_s-1} \alpha_i(kT_s) s_{T,i}(kT_s - \tau_i(kT_s)) e^{j2\pi f_{d,i}(kT_s)t} + n(kT_s), \quad (2.57)$$

where k is the sample index and T_s is the sampling period. $n(t) \sim \mathcal{CN}(0, \sigma^2)$ is a complex, Gaussian process with zero-mean and variance σ^2 .

2.3.4 Satellite synchronization and PVT solution

The core functionality of a GNSS receiver is the synchronism recovering of the received satellite signals. Each of the synchronization parameters described in (2.55) should be estimated and tracked with the maximum available precision. These parameters provide information regarding the relative distance between the receiver and the corresponding satellite, which is used in the computation of the PVT solution. Hereafter are briefly described each of the operations involved in both the synchronism recovering and the PVT solution.

2.3.4.1 Acquisition

The digitized signal coming from the ADC is tested against the presence of useful satellite signals. The target is to detect if there is an specific satellite signal present, and, in case of positive detection, to provide a coarse estimation of the synchronization parameters for each of them. This operation is referred to as the acquisition process.

In a classical hardware-based GNSS receiver, acquisition performs the correlation of a block of received signal with a locally generated PRN code [Par96]. In order to cover all the possible values of the synchronization parameters, the process yields an exhaustive Doppler-shift and Code delay two-dimensional search grid, applied to each satellite PRN sequence. The correlation maximum is compared to a detection threshold and a decision is made. Fig. 2.5 shows the correlation output versus time-delay and Doppler-shift of a clear and noisy Galileo-like signal. The acquisition process is a critical stage in every GNSS receiver because it is in charge of

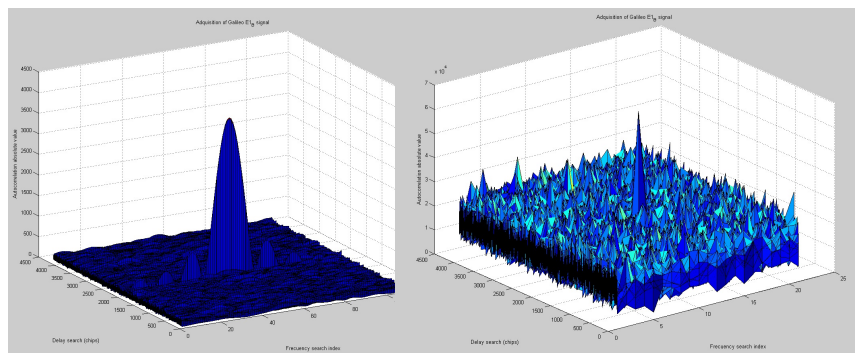


Figure 2.5: Correlation output versus time-delay and Doppler-shift of a noise-free Galileo E1 satellite signal and the same signal corrupted with white noise ($C/N_0 = 44$ dB-Hz).

GPS receiver IC	Acquisition sensitivity	Tracking sensitivity
Sirf SIRFStarIIe/LT	-140 dBm	-142 dBm
Atmel ATR0635	-142 dBm	-158.5 dBm
Sirf SIRFStarIII	-142 dBm	-159 dBm
CSR SIRFAtlasIV	-148 dBm	-161 dBm
uBlox Max 6	-148 dBm	-162 dBm
MediaTek MT3329	-148 dBm	-165 dBm

Table 2.6: Acquisition and tracking sensitivity values for some commercial GPS IC, extracted from [Gol07, Cam10, Wei11].

initializing the tracking process for each visible satellite and thus, it activates the rest of the receiver operations.

In GNSS, the power of the satellite signals received by the antenna is extremely weak compared with the receiver noise power. The thermal noise present at the antenna terminals can be approximated as:

$$P_n = kT_0B_p, \quad (2.58)$$

where B_p is the receiver passband bandwidth, k is the Boltzmann's constant, T_0 is the ambient temperature reference value, both already defined in the *IN0* equation (2.54). It is possible to define a ratio between the signal power and the noise power using the SNR and the *CN0*, as follows:

$$\rho = \frac{P_s}{P_n} \quad (2.59)$$

$$CN0 = \rho B_p, \quad (2.60)$$

where ρ is the SNR, P_s is the received signal power, and P_n is the noise power. Considering the GPS L1 C/A nominal signal power and bandwidth of Table 2.1, it is possible to compute the available SNR and Carrier-to-Noise density ratio (*CN0*) for a GPS receiver operating at the Earth surface in clear sky condition, obtaining $\rho = -30.8$ dB and $CN0 = 43$ dB-Hz. The satellite signal is clearly below the noise level. The acquisition process is in charge of raising the signal above the noise floor by means of the SS code gain to be able to detect its presence.

One of the most important performance indicators of a receiver is the sensitivity, defined as the lowest signal power detectable by a GNSS receiver under test in a interference-free environment [Mit08]. Two signal sensitivities can be defined:

- Acquisition sensitivity, is the minimum signal power at which a receiver can correctly identify the presence of a particular satellite signal in the incoming RF signal within a given time-out interval.
- Tracking sensitivity is the minimum signal power at which the receiver can perform the tracking process.

Since in a conventional receiver there is no prior information of the synchronization parameters, acquisition usually has the highest sensitivity of the whole receiver operations, see, e.g. [Sud01, Mit08, Wei11]. The acquisition sensitivity signal power can be in the order of 10 to 20 dB higher than the tracking sensitivity. Table 2.6 show a comparative of acquisition and tracking sensitivities for some Commercial Off-The-Shelf (COTS) GNSS receivers chipsets. At the time of writing (February 2012), typical values of achievable signal acquisition sensitivity for GPS L1 C/A can be set to around -157 dBm or 17 dB-Hz, assuming a -174 dBm-Hz noise power density, as reported in [Pan10].

This issue can cause a performance bottleneck, limiting the operation capabilities under adverse conditions, as is shown in Chapter 3, Section 3.7 of this dissertation.

Other useful receiver performance is the Time To First Fix (TTFF), defined as the elapsed time from the receiver startup to the first position estimation output. In GNSS applications

related to SoL and emergency call location (E-911) [FCC99] a limited TTFF is required. Depending on the status of the GNSS receiver, the startup process and the contributions to TTFF could be [Hei10]:

- Cold start: When the receiver does not have any prior useful information. The acquisition must be performed for all the satellites in the constellation, searching for all the possible Doppler-shifts and code delays.

$$TTFF_{cold} = T_{warm-up} + T_{acq} + T_{track} + T_{CED+GST} + T_{PVT}, \quad (2.61)$$

where

- $T_{warm-up}$ is the receiver warm-up time.
- T_{acq} is the acquisition time.
- T_{track} is the settling time for code and tracking process.
- $T_{CED+GST}$ is the navigation data read time (CED) plus the time to retrieve the system time reference (GST).
- T_{PVT} is the time to compute the navigation solution.
- Warm start: When the receiver has in memory a valid satellite almanac, which is an approximation of the orbital parameters for all satellites and a prior user position and time estimation. The acquisition search is reduced to the visible satellites according to the almanac and the last user position.

$$TTFF_{warm} = T_{warm-up} + T_{acq} + T_{track} + T_{GST} + T_{PVT}. \quad (2.62)$$

- Hot start: When the receiver relies not only on almanac but also on a valid satellite ephemeris data. The acquisition can use the precise orbital model using ephemeris data.

$$TTFF_{hot} = T_{acq} + T_{track}. \quad (2.63)$$

- Reacquisition: When the satellite signals have just been lost and the receiver can use the last Doppler shift and time estimation.

$$TTFF_{reacq} = T_{track}. \quad (2.64)$$

- Assisted acquisition: When the acquisition is assisted by additional information external to the satellite transmission, for instance, obtaining the satellite almanac using a cellular communications network. The TTFF depends on the level of assistance. The reader is referred to [Dig09] for more about the assisted GPS (A-GPS) techniques and its performance.

The acquisition process and its related algorithms are a major research topic in this dissertation. In that sense, the reader is referred to Chapter 3 for a complete theoretical analysis of the GNSS signal acquisition from a detection theory framework. It includes also the definition of performance metrics, an analysis of major sources of performance degradation, and an overview of the current state-of-the-art algorithms. The study of the applications of antenna arrays to signal acquisition is addressed in Chapter 4, where a novel statistical approach for interference mitigation is addressed.

2.3.4.2 Tracking

Once the acquisition process has detected and estimated the basic synchronization parameters, the tracking process takes their rough values given by acquisition and starts to refine them. The classical GNSS receiver implementation approach uses a PLL or a Frequency Locked Loop (FLL) to track the Doppler frequency and phase, forming the carrier loop discriminator. Basic code

delay tracking is performed using a Delay Locked Loop (DLL), which is a practical implementation of the Maximum Likelihood Estimator (MLE) of time-delay of a given satellite, assuming no multipath propagation [FP06].

The objective is to locate and track the maximum of the correlation function between the received signal and the local code. In a classical DLL implementation, the correlation peak is tracked using a minimum of three correlators: The *Early* correlator uses a half-chip advanced PRN replica, the *Prompt* correlator uses the reference PRN replica and the *Late* replica uses a half-chip delayed PRN replica. A discrimination function takes the correlator outputs and computes the code delay correction to be applied in the next iteration. Typically the correlation length is equal to the PRN sequence period. Fig. 2.6 shows a plot of the autocorrelation function of a Galileo-like E1 and GPS-like L1 C/A signals. The circles indicate the values of the Early (E), Prompt (P) and Late (L) correlators at the classical half-chip PRN delay with respect to the prompt replica. One of the improvements of the new GNSS signals is the sharpness of the autocorrelation peak, which enables the reduction of the correlators distance and thus, improve the code delay estimation precision. An inherent drawback, considering for instance the Galileo E1 signal, is the presence of secondary autocorrelation peaks. The receiver has to take into account this effect to avoid local maxima.

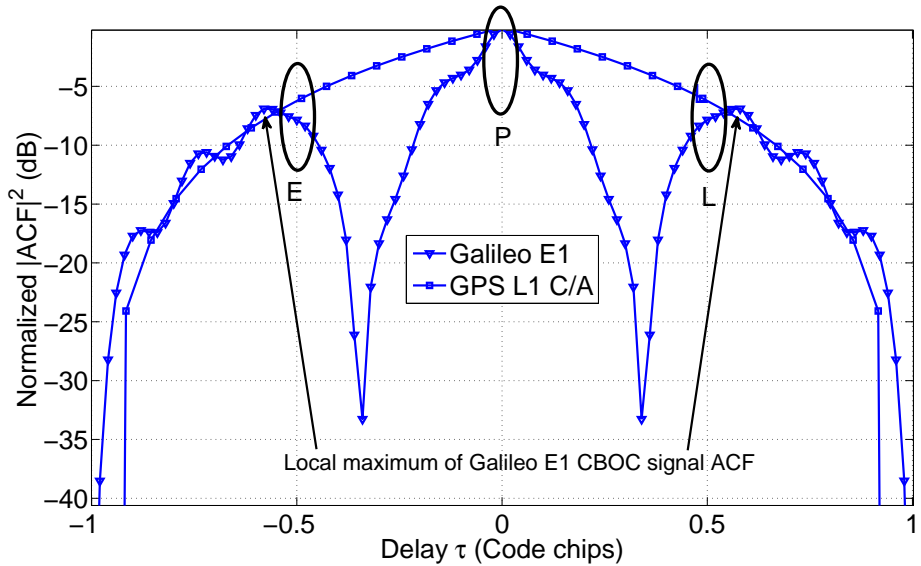


Figure 2.6: Autocorrelation function of a full-bandwidth Galileo-like E1 and GPS-like L1 C/A signals.

Fig. 2.7 shows a generic tracking operation; from left to right, the received baseband signal is first multiplied by a local carrier replica to eliminate the Doppler-shift, also referred to as carrier wipe-off process. Next, the Doppler-free signal is multiplied by a minimum of three local code replicas in order to eliminate the DS-CDMA modulation, named despreading or code wipe-off process. The despreaded signals of each of the local code replicas are integrated typically over an entire PRN epoch, obtaining the correlation information. These correlation values are feed to the carrier-loop and code loop discriminators, which are in charge of computing Doppler frequency and code delay corrections. The corrections are filtered and sent to the local carrier generator and the local code generator respectively and the process starts again for the next PRN epoch.

Finally, the output of the prompt code correlation is fed into a demodulator, which recovers the telemetry bits from the modulation symbols and decodes the navigation message [Tsu00, Bor07]. Due to historical reasons, the current software-based GNSS receivers still use this architecture, which is a replica of the hardware-based receivers. The tracking block feeds the navigation processor with both the code delay information and the navigation message. Each satellite signal is tracked independently forming a satellite tracking channel. High performance receivers also use the estimated carrier phase information to improve the PVT solution.

More advanced architectures can be applied to DLL operation, such as the double delta

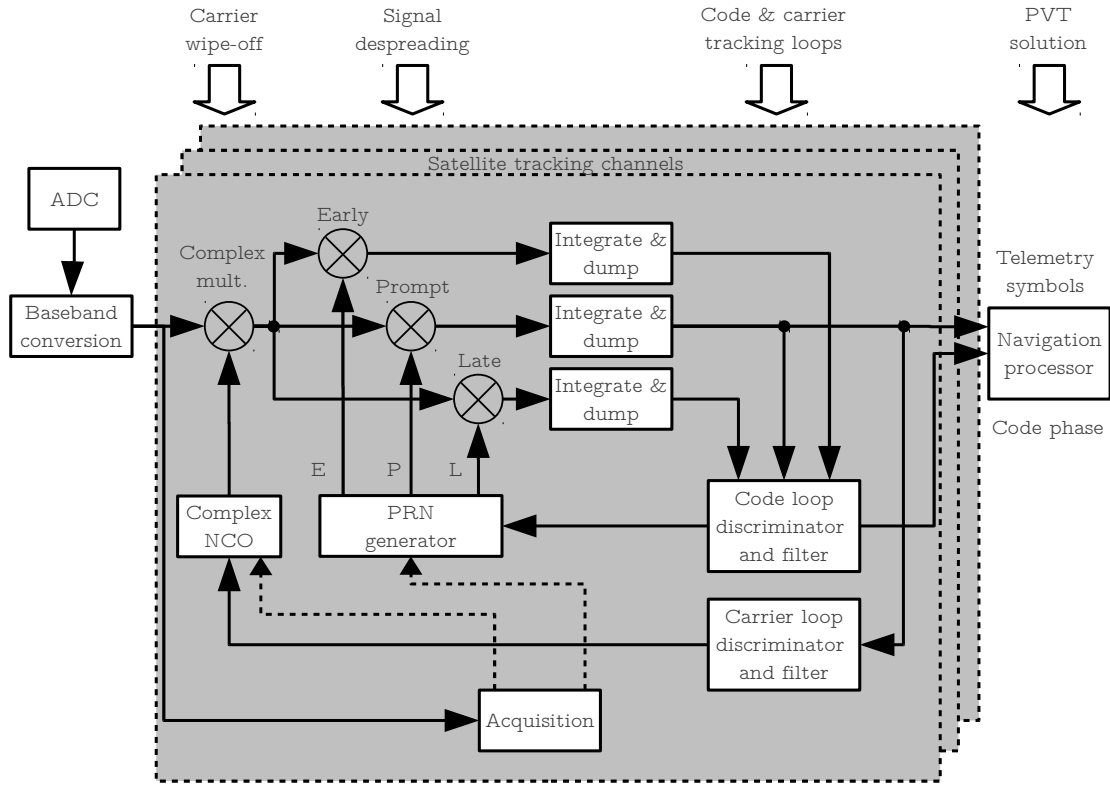


Figure 2.7: Classical GNSS tracking diagram.

correlator, which duplicates the early and late local signal replicas to mitigate the effects of the autocorrelation function distortion caused by multipath [Jon04].

Other approaches are recently proposed for the tracking operation, e.g., the so called Vector Tracking Loop. In contrast to traditional receivers, vector tracking algorithms exploit the inherent coupling between signal tracking and navigation solution computation, and combines them into a single step [Pet09a]. Vector tracking has many advantages over scalar tracking loops, including an increased immunity to interference and jamming signals. The tracking sensitivity is lowered by processing the signals in aggregate instead of separately.

A similar technique is introduced in Closas' Ph.D. Thesis [Clo09a], referred to as Direct Position Estimation (DPE); the tracking process is substituted by a joint estimation of the synchronization parameters for all the visible satellites and the receiver position. In DPE, the idea is to merge synchronization and position computation operations into a single estimation step. This new philosophy has important consequences in the receiver, including multiple access interference rejection and multipath mitigation [Clo09b].

2.3.4.3 Navigation data demodulation and decoding

The navigation data demodulation and decoding involves three operations, particularized for the specific GNSS link and channel modulation:

- **Telemetry symbol synchronization:** A conventional BPSK or Quadrature Phase-Shift Keying (QPSK) demodulator is used to track the phase transitions in the prompt correlator signal output. If the tracking is locked to a satellite signal, after both the carrier and code wipe-off processes, the remaining information is the telemetry data. Each of the telemetry bits is composed of several modulation symbols, thus, both symbol integration and bit synchronization operations are performed in this step,
- **Telemetry frame synchronization:** The navigation message is composed of several numbered telemetry frames. The frame synchronization is accomplished using a known

telemetry bit sequence named *preamble*, which is defined in the corresponding Interface Specifications document. The preamble is periodically transmitted usually at the start of every new frame. The receiver additionally checks the frame length, the parity, and the checksum. New GNSS signals are also coded using forward error correction codes and/or interleaving, in order to improve the reliability of data transmission and reduce the bit error rate, and

- **Navigation message decoding:** The received frame is processed and the bit sequence is split into fields and converted to satellite ephemeris data, clock data, and several GNSS messages and flags. The information regarding the frame structure, which includes the field positions and lengths, is available also in the corresponding interface control document.

The navigation data transmission is scheduled to give high priority (i.e., higher repetition frequency) to basic ephemeris and clock data, reducing the receiver's TTFF since the parameters required by the PVT computation are transmitted more often than the others. The complete satellite's almanac, extended clock model, and ionospheric correction model is available only when all the frames are received. For instance, the GPS L1 C/A signal carries basic ephemeris and clock data every 30 seconds, and the full telemetry dataset is available after 12.5 minutes [Win10].

2.3.4.4 Position, Velocity, and Time (PVT) solution

The computation of the PVT solution implies obtaining both the satellite observables and the satellite's positions, and executing the corresponding positioning algorithm. The GPS observables are a set of ranges measured from the receiver unknown position to the visible satellites. Since the ranges are affected by satellite and receiver clock errors, clock offsets, and other non-desirable effects, the range is typically referred to as *pseudorange*.

The basic pseudorange set is computed using two different timing informations:

- telemetry timing information: the ToA differences between satellite's telemetry frame pREAMbles are used to compute a coarse differential Time of Arrival (ToA) estimation between satellite signals. The ToA uncertainty is within one PRN code epoch period, and
- code delay estimation: it is used to refine the satellite's ToA obtaining a chip-level precision.

Using the existing civil GNSS signals, the code delay information is not enough to compute the ToA differences because it includes an ambiguity due to the fact that the PRN code epoch duration is shorter than the maximum differential ToA [Tsu00]. The telemetry timing information is used to solve this ambiguity. The differential ToA information is converted to a pseudorange set using the light speed constant.

The basic pseudorange observation equation can be defined as:

$$\rho_i = r_i + c(dt - dt_i) + \vartheta_i + e_i, \quad (2.65)$$

where ρ_i is the pseudorange, r_i is the geometrical range, c is the speed of light constant, dt and dt_i are the receiver and the satellite clock offsets, respectively, ϑ_i is the atmospheric delay, and e_i is the observational pseudorange error, for the i -th satellite.

Additionally, the observables may include carrier phases and Doppler-shifts measurements. A suitable GNSS receiver format for interchange observables data is the Receiver Independent Exchange Format (RINEX) [Gur09]. The navigation messages provides the receiver with the satellite orbital model, the satellite clock model, and other important parameters such as the propagation time correction and the satellite health. The receiver uses the ephemeris data to solve the Kepler's equations and obtain a prediction of the satellite positions associated to the pseudoranges set.

Finally, a trilateration algorithm computes the user's position, velocity and time. The geometrical non-lineal relation between the receiver position and the satellite positions can be defined as:

$$r_i = \sqrt{(X_i - X)^2 + (Y_i - Y)^2 + (Z_i - Z)^2}, \quad (2.66)$$

where $\{X, Y, Z\}$ and $\{X_i, Y_i, Z_i\}$ are the unknown geocentric coordinates of the observer and the i -th satellite, respectively. By inserting (2.66) in (2.65), using the orbital parameters broadcasted by the telemetry, the observer position can be computed with four or more pseudoranges, forming a determined (four visible satellites) or overdetermined (five or more visible satellites) non-linear equation system:

$$\rho_i = \sqrt{(X_i - X)^2 + (Y_i - Y)^2 + (Z_i - Z)^2} + c(dt - dt_i) + e_i. \quad (2.67)$$

The Least Squares (LS) method is a possible solver method to obtain the user position in GNSS. The system is linearized with a first order Taylor approximation, and the user position is initialized using the Bancroft algorithm [Ban85]. A MATLAB implementation of the LS solution can be found in [Bor07]. A highly efficient C++ implementation is available in Chapter 6 of this Dissertation.

If the PVT solution is obtained using the pseudoranges it is called *code navigation*, while if the solution uses also the carrier phase it is called *carrier navigation*. The second option is used in high-precision GNSS receivers due to the fact that the carrier wavelength is in the order of tens of centimeters, while the chip rate is in the order of tens of MHz, which is equivalent to a wavelength of hundred of meters. Thus, carrier tracking allows a more accurate estimation of the pseudorange and enables the application of highly sophisticated positioning algorithms.

Additionally, it is possible to use a GNSS reference station to provide real-time corrections of both the code and carrier phase for the receivers operated in the neighborhood. In this technique, referred to as DGNSS, the reference station, located in a known position, calculates pseudorange corrections and range rate corrections, which are transmitted to the mobile station, see [HW08, p.169].

If the transmitted DGNSS carrier phase correction has neglectable latency, then it is usually denoted as Real-Time Kinematic (RTK) technique. The Research Group of Astronomy and Geomatics (GAGE) from the Universitat Politècnica de Catalunya (UPC) has done an extensive work on code and carrier navigation and RTK [HP08]. In this sense, it is worth mentioning the wide-area RTK method and new ionospheric tomography and traveling ionospheric disturbance models published by the aforementioned group that dramatically increase the RTK service area, with permanent stations separated by up to 500 - 900 kilometers – requiring 100 to 1000 times fewer receivers covering a given region [HP10a].

Additionally, if the GNSS receiver is helped with an Inertial Measurement Unit (IMU), then the system is referred as *GNSS inertial navigation system*. The reader is referred to textbooks for more on this topic, for instance, [Far99].

2.4 Summary

This Chapter briefly presented the civil GNSS receiver basics following a logic signal path, starting with the satellite transmitted signals characteristics and ending with the details of a basic GNSS receiver operations, focused on the European Galileo and the American GPS GNSS.

The structures and particularities of both single channel legacy signals, such as GPS L1 C/A and modernized composite signals, such as the Galileo E1, are described in Section 2.1, covering the state-of-the-art of the present and near future GNSS. The signal propagation channel effects are presented in Section 2.2, emphasizing the extreme weakness of GNSS signals and their inherent interference sensibility. Common interference sources and its classification are described there.

Finally, the architecture of a GNSS receiver was shown in Section 2.3. A GNSS receiver computes its position from the estimation of synchronization parameters of the available satellite signals, which are obtained by several chained processes. Among them, signal acquisition is known to have the highest sensitivity of the whole receiver operations, thus becoming a performance bottleneck that limits the receiver operation capabilities under adverse conditions.

In the following Chapter, the signal acquisition process is analyzed in detail, providing the basics of the detection theory framework that is used to solve the GNSS acquisition problem from a single-antenna receiver point of view, providing the necessary background for our proposed improvements.

Chapter 3

Signal acquisition techniques

All truths are easy to understand once they are discovered; the point is to discover them.

Galileo Galilei.

FROM the Latin word *acquisitionem*, which means *the act of obtaining*, in GNSS terminology the acquisition process is in charge of obtaining the set of visible satellites, which involves two steps for each of them:

1. detecting the presence of a specific signal that belongs to a particular GNSS satellite, and
2. providing a coarse estimation of their current synchronization parameters.

From the signal processing point of view, GNSS acquisition should be posed as a detection problem, and in that sense, there exists an extensive literature on this topic such as generic detection textbooks, e.g. [Cas01, Sch91, Kay98], or specific Code Division Multiple Access (CDMA) communication systems signal detection references as [Ver98].

In detection theory, a well-known detection criterion is the so called Neyman-Pearson (NP) approach, which consist of the maximization of the probability of detection given a limited false alarm probability. This criterion is highly desirable for the problem at hand, and in the sequel its applicability to the detection of GNSS signals is analyzed.

This Chapter starts with a brief introduction to the NP detection theory framework. Section 3.1 presents the acquisition signal model and Section 3.2 highlights some important concepts including the *sufficient statistics*, the Uniformly Most Powerful (UMP) detector conditions, or the Likelihood Ratio Test (LRT) among others. In Section 3.3 the NP approach is used to derive both the optimum detector (known as *clairvoyant detector*) and the so called Generalized Likelihood Ratio Test (GLRT) detector, which is the basis of almost all of the current state-of-the-art acquisition algorithms. Moreover, Section 3.4 introduces a novel detector test statistics intended to jointly acquire a set of GNSS satellites, thus, reducing both the acquisition time and the required computational resources. Closed form performance expressions are obtained for all the detectors. The effects of the front-end bandwidth are also taken into account in Section 3.5.

The second part of the Chapter, starting in Section 3.6, is devoted to introduce a set of acquisition schemes that are used to increase the acquisition sensitivity or overcome the navigation data uncertainties. Finally, the acquisition perturbations are discussed in Section 3.7, focusing the analysis in the effects of interferences as well as defining a performance metric. The existing single-antenna mitigation techniques and their limitations are also briefly introduced in this Section.

3.1 Acquisition signal model

Consider that the RF signals coming from M_s GNSS satellites are received with a single-antenna receiver, amplified, filtered, and downconverted to an IF. The IF signal is then sampled, quantized, downconverted again to baseband in the digital domain, and arranged in a vector. The discrete baseband signal model can be defined as:

$$\mathbf{x}(t) \Big|_{t=kT_s} = \sum_{i=1}^{M_s} \alpha_i \mathbf{d}_i(t, f_{d,i}, \tau_i) + \mathbf{n}(t), \quad (3.1)$$

where

- $\mathbf{x}(t) = [x(t - (K - 1)T_s), \dots, x(t)] \in \mathbb{C}^{1 \times K}$ is the received signal vector containing K samples. The acquisition time can be defined as $T_{acq} = KT_s$ where $f_s = 1/T_s$ is the sampling frequency.
- $\alpha_i \in \mathbb{C}$ is the complex amplitude of the received i -th satellite signal, assumed constant during T_{acq} . The i -th satellite's power can be defined as $P_i = |\alpha_i|^2$.
- $\mathbf{d}_i(t, f_{d,i}, \tau_i) = [s_i(t - (K - 1)T_s - \tau_i) e^{j2\pi f_{d,i}(t-(K-1)T_s)}, \dots, s_i(t - \tau_i) e^{j2\pi f_{d,i}t}] \in \mathbb{C}^{1 \times K}$ is the discrete version of the satellite baseband signal at the front-end output after the digital downconversion, with normalized power and known structure $s_i(t)$, defined in Chapter 2, received with a propagation delay τ_i and a Doppler frequency $f_{d,i}$, which are also considered constant during T_{acq} . In our analysis, without losing generality, a telemetry-free signal is considered.
- $\mathbf{n}(t) = [n(t - (K - 1)T_s), \dots, n(t)] \in \mathbb{C}^{1 \times K}$ is a complex, circularly symmetric Additive White Gaussian Noise (AWGN) process $n(t) \sim \mathcal{CN}(0, \sigma^2)$, temporally uncorrelated, with zero-mean, and variance σ^2 . The noise term models both the thermal noise and other non desirable terms such as multipath, interferences, and the front-end spurious responses. It is considered that the noise have double-sided spectral density $\sigma^2 = \frac{N_0}{2}$ W/Hz.

For notation convenience, in the rest of this Chapter we group the received satellite signal parameters in a vector $\boldsymbol{\theta}_i = [\alpha_i, f_{d,i}, \tau_i]^T$. This signal model is used in the detection theory framework introduced in hereafter.

3.2 Detection theory

The GNSS signal acquisition process introduced in Section 2.3.4.1 determines the presence or the absence of a satellite signal. Two possible hypotheses exist, referred to as \mathcal{H}_0 or the *null hypothesis*, when there is no signal present, and \mathcal{H}_1 or the *alternative hypothesis*, when the desired signal is present. This type of detection problem is referred to in the literature as *binary hypothesis testing*. Additionally, the acquisition process should provide a coarse estimate of synchronization parameters in order to initialize the tracking process.

The analysis is focused on a single satellite's signal, thus neglecting the contribution of the rest of satellites. This assumption is realistic, considering that GNSS use pseudorandom noise codes with high processing gain and relatively small cross-correlation among them. Therefore, the influence of other satellites can be included in the noise term since those signals are well below the noise floor [Tsu00]. The signal model for both hypotheses is defined as follows¹:

$$\mathcal{H}_1 : \mathbf{x}(t) = \alpha \mathbf{d}(t, f_d, \tau) + \mathbf{n}(t), \quad (3.2)$$

$$\mathcal{H}_0 : \mathbf{x}(t) = \mathbf{n}(t), \quad (3.3)$$

where the terms are already defined in (3.1).

In a detection problem, the goal is to use the received data as efficiently as possible in making a decision, with the highest rate of *success*. From a statistical point of view, the detection process consists of:

¹The satellite subindex is dropped for the sake of the notation's simplicity.

1. Computation of the *sufficient statistics* in the received data, which consists of the separation of the useful information from what is irrelevant. The condition of sufficient statistics can be expressed as:

$$p(\mathbf{x}; T(\mathbf{x}), \boldsymbol{\theta}) = p(\mathbf{x}; T(\mathbf{x})), \quad (3.4)$$

where $p(\cdot)$ stands for the conditional Probability Density Function (PDF) of the received signal \mathbf{x} , $\boldsymbol{\theta}$ is the signal parameters vector defined in Section 3.1, and $T(\mathbf{x})$ is a function of \mathbf{x} . All the relevant information about $\boldsymbol{\theta}$ should be contained in $T(\mathbf{x})$.

2. Usage of the *sufficient statistics* to make a statistical inference from data \mathbf{x} . This condition implies the definition of a *test function* $T(\mathbf{x})$ and its comparison to a threshold γ .

If $T(\mathbf{x})$ is a sufficient statistic for $\boldsymbol{\theta}$, then the PDF of the received data can be expressed as (see e.g. [Kay93, p.104])

$$p(\mathbf{x}; \boldsymbol{\theta}) = u(T(\mathbf{x}); \boldsymbol{\theta})v(\mathbf{x}), \quad (3.5)$$

where $u(T(\mathbf{x}); \boldsymbol{\theta})$ is a function that relates $T(\mathbf{x})$ with $\boldsymbol{\theta}$, and $v(\mathbf{x})$ is the contribution of the noise and the nuisance parameters to the PDF. This decomposition of the PDF is referred to as Neyman-Fisher factorization theorem [Kay93].

In GNSS acquisition, the idea of sufficient statistics is to find a function $T(\mathbf{x})$ for $\boldsymbol{\theta}$, which extracts all the information needed for inference from the data \mathbf{x} about the parameter $\boldsymbol{\theta}$. All the relevant information is contained in the statistic $T(\mathbf{x})$. By applying the sufficient statistics a dimension-reduction is made because all the superfluous information is filtered out [Ben99].

3.2.1 Neyman-Pearson detector

A criterion commonly used for a detection problem is the maximization of the *detection probability* (P_d) subject to a given *false alarm probability* (P_{fa}). It is well known in the literature, see e.g., [Kay98], that the optimum detector for the case of known deterministic signals in AWGN is the NP detector, briefly defined hereafter and particularized for the GNSS signal model.

The NP test function is based on the LRT:

$$L(\mathbf{x}) = \frac{p(\mathbf{x}; \sigma^2, \boldsymbol{\theta}, \mathcal{H}_1)}{p(\mathbf{x}; \sigma^2, \mathcal{H}_0)} > \gamma, \quad (3.6)$$

where γ is the detection threshold, $p(\mathbf{x}; \sigma^2, \boldsymbol{\theta}, \mathcal{H}_1)$ and $p(\mathbf{x}; \sigma^2, \mathcal{H}_0)$ stand for the conditional PDF of \mathbf{x} for \mathcal{H}_1 and \mathcal{H}_0 hypotheses, respectively. The PDF for \mathcal{H}_1 is parameterized by the signal parameter vector $\boldsymbol{\theta}$ and by the noise variance σ^2 , and the PDF for \mathcal{H}_0 is parametrized only by σ^2 . In the literature, a problem which has unknown parameters in the PDF of \mathbf{x} , is referred to as *composite hypothesis* problem [Kay98]. The detection threshold γ is found from

$$P_{fa} = \int_{t:L(\mathbf{x})>\gamma}^{\infty} p(t; \mathcal{H}_0) dt, \quad (3.7)$$

and

$$P_d = \int_{t:L(\mathbf{x})>\gamma}^{\infty} p(t; \mathcal{H}_1) dt. \quad (3.8)$$

A class of detectors whose P_{fa} does not depend on any unknown input parameters, or equivalently, the PDF of the detector test statistic is completely known on the \mathcal{H}_0 hypothesis, is referred to as Constant False Alarm Rate (CFAR) detectors [Sch91]. The CFAR condition is highly convenient for the acquisition design in a GNSS receiver, since usually there is no information about signal parameters, which makes difficult to set a detection threshold.

3.2.2 Uniformly Most Powerful test

The best possible NP detector for a given problem is referred to as the UMP test [Cas01], which is a detector that has the highest possible P_d restricted to a given P_{fa} . If the data set \mathbf{x} has only one probability distribution for each hypothesis, that is, under a *simple hypothesis* problem, the UMP conditions are defined by the Neyman-Pearson Lemma:

Theorem 1 (Neyman-Pearson Lemma) Consider testing $\mathcal{H}_0 : \boldsymbol{\theta} = \boldsymbol{\theta}_0$ versus $\mathcal{H}_1 : \boldsymbol{\theta} = \boldsymbol{\theta}_1$, with the detection region \mathcal{R} and the complementary region \mathcal{R}^c defined as

$$\mathbf{x} \in \mathcal{R} \text{ if } p(\mathbf{x}; \boldsymbol{\theta}_1) > kp(\mathbf{x}; \boldsymbol{\theta}_0), \quad (3.9)$$

$$\mathbf{x} \in \mathcal{R}^c \text{ if } p(\mathbf{x}; \boldsymbol{\theta}_1) < kp(\mathbf{x}; \boldsymbol{\theta}_0), \quad (3.10)$$

for some $k \geq 0$, and

$$\beta = P_d(\mathbf{x} \in \mathcal{R}), \quad (3.11)$$

then (sufficiency condition), any test that satisfies (3.9) and (3.10) is a UMP level β test, that is, $P_d \geq \beta$.

The proof can be found in [Cas01, p.388].

If a NP detector assumes that the parameters of PDFs in both hypotheses are completely known, then the optimum detector is obtained, referred to as the *clairvoyant detector*, which is by definition a UMP test. The clairvoyant detector provides the performance upper bound for any NP detector.

As stated in this section, a composite hypotheses testing problem has a family of PDFs parameterized by one or more parameters $p(\mathbf{x}; \boldsymbol{\theta}) : \boldsymbol{\theta} \in \Theta$, where Θ is the parameter subspace. The NP Lemma holds for each individual $\boldsymbol{\theta} \in \Theta$. An extension of NP Lemma, which is valid only for *one-sided hypotheses* testing problems where $\theta_1 > \theta_0$ ², is the Karlin-Rubin Theorem.

Theorem 2 (Karlin-Rubin) Consider testing $\mathcal{H}_0 : \theta \leq \theta_0$ versus $\mathcal{H}_1 : \theta > \theta_0$. Suppose that $T(\mathbf{x})$ is a sufficient statistic for θ and the family of PDFs $u(T(\mathbf{x}); \theta)$ has a Monotone Likelihood Ratio (MLR). Then, for any γ , the test that accept \mathcal{H}_1 if and only if $T(\mathbf{x}) > \gamma$, is a UMP level β test.

The proof can be found in [Cas01, p.391].

The family of PDFs $u(T(\mathbf{x}); \theta)$ has MLR condition if, for every $\theta_2 > \theta_1$, the ratio $u(T(\mathbf{x}); \theta_2)/u(T(\mathbf{x}); \theta_1)$ is a monotone (non-increasing or non-decreasing) function of $T(\mathbf{x})$.

3.2.3 Performance Metrics

A binary hypothesis detector decides either \mathcal{H}_0 or \mathcal{H}_1 based on an observed set of data. To illustrate the detector's behavior, Fig. 3.1 plots the test statistic PDF of a simple detector for both $T(\mathbf{x}; \mathcal{H}_0) \sim \mathcal{N}(0, 1)$ and $T(\mathbf{x}; \mathcal{H}_1) \sim \mathcal{N}(1, 1)$. The threshold γ divides the data space into *decision regions*.

$$\mathcal{R} = \{\mathbf{x} : \text{reject } \mathcal{H}_0\} \quad (3.12)$$

$$\mathcal{R}^c = \{\mathbf{x} : \text{accept } \mathcal{H}_0\} \quad (3.13)$$

Depending on the true hypothesis value and the detected hypothesis it is possible to define the following probabilities:

- *Probability of detection*: (or Power of test) reject \mathcal{H}_0 when is \mathcal{H}_1 ($p(\mathcal{H}_1; \mathcal{H}_1)$), $P_d = p(T(\mathbf{x}) > \gamma; \boldsymbol{\theta}, \mathcal{H}_1)$
- *Probability of false alarm*: (or Type I error) reject \mathcal{H}_0 when is \mathcal{H}_0 ($p(\mathcal{H}_1; \mathcal{H}_0)$), $P_{fa} = p(T(\mathbf{x}) > \gamma; \mathcal{H}_0)$
- *Probability of miss*: (or Type II error) accept \mathcal{H}_0 when is \mathcal{H}_1 ($p(\mathcal{H}_0; \mathcal{H}_1)$), $P_m = 1 - P_d$

In a GNSS receiver, these values should be used to compute the system false alarm rate, which depends on the grid search strategy among other factors [Bor06]. It can be found a number of criteria in the literature; as an example, Borio defines $P_{fa} = 0.001$ as a suitable system false alarm rate [Bor08], while Tsui defines a suitable system false alarm rate for the acquisition of weak signals as $P_{fa} = 0.01$ [Tsu00].

²Notice that here we have a *univariate* parameter θ , in contrast to the multivariate parameter $\boldsymbol{\theta}$.

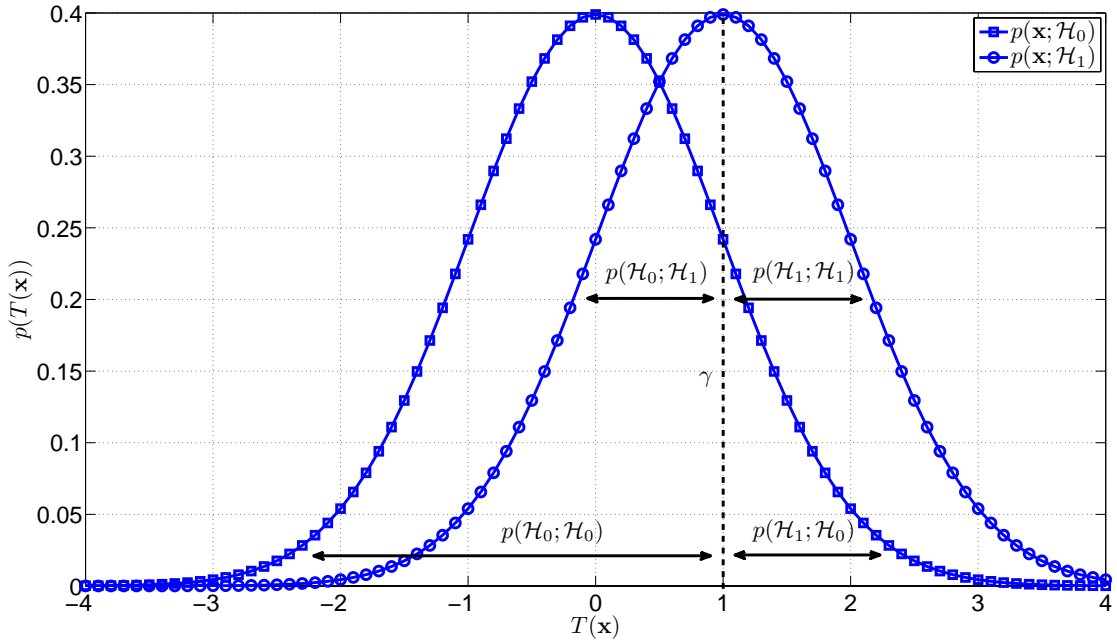


Figure 3.1: A binary hypothesis detector regions.

The performance of a given detector can be measured also in terms of P_d vs. P_{fa} , referred to as the Receiver Operating Characteristic (ROC) [Kay98]. The ROC curve is threshold-independent and thus represents the performance of the detector in the entire range of P_{fa} and P_d .

A useful parameter that gives an idea of the overlap between $p(T(\mathbf{x}); \mathcal{H}_0)$ and $p(T(\mathbf{x}); \mathcal{H}_1)$ is the so called *generalized signal-to-noise ratio* or *deflection coefficient* to measure the detector's performance [Kay98, Bar92]. The deflection coefficient is defined as

$$d^2 = \frac{(\mathbb{E}\{T(\mathbf{x}; \mathcal{H}_1)\} - \mathbb{E}\{T(\mathbf{x}; \mathcal{H}_0)\})^2}{\text{var}\{T(\mathbf{x}; \mathcal{H}_0)\}}, \quad (3.14)$$

where $\mathbb{E}\{T(\mathbf{x}; \mathcal{H}_1)\}$ and $\mathbb{E}\{T(\mathbf{x}; \mathcal{H}_0)\}$ stands for the test statistic expectation in \mathcal{H}_1 and \mathcal{H}_0 respectively, and $\text{var}\{T(\mathbf{x}; \mathcal{H}_0)\}$ stands for the variance of the test statistic in \mathcal{H}_0 .

This quantity measures the effectiveness of the quadratic statistic in separating the two hypotheses, although is not directly related to detection or false alarm probabilities.

3.3 Single-antenna GNSS signal acquisition

This Section is devoted to the development of GNSS acquisition algorithms using the detection theory framework introduced in the last Section. Closed form expressions for the detection and false alarm probabilities are given.

The sequel starts with the derivation of the NP optimum detector, which gives the performance upper bound for the single-antenna acquisition. However, this detector is not feasible in a real receiver due to the presence of unknown parameter values in the received satellite signal. To solve this situation, the natural extension of the NP detector is presented using the GLRT detector.

3.3.1 Optimum detector

If it is assumed that all the parameters of the LRT are known in the signal model (3.1) and using the PDF of a complex Gaussian variable for K observations in both $p(\mathbf{x}; \mathcal{H}_1)$ and $p(\mathbf{x}; \mathcal{H}_0)$, the

optimum detector arises:

$$L(\mathbf{x}) = \frac{p(\mathbf{x}; \sigma^2, \boldsymbol{\theta}, \mathcal{H}_1)}{p(\mathbf{x}; \sigma^2, \mathcal{H}_0)} = \frac{\frac{1}{\pi^K \sigma^{2K}} \exp \left\{ -\sigma^{-2} (\mathbf{x} - \mathbf{s}_{\boldsymbol{\theta}})(\mathbf{x} - \mathbf{s}_{\boldsymbol{\theta}})^H \right\}}{\frac{1}{\pi^K \sigma^{2K}} \exp \left\{ -\sigma^{-2} \mathbf{x} \mathbf{x}^H \right\}} > \gamma, \quad (3.15)$$

where $(\cdot)^H$ denotes conjugate transpose and $\mathbf{s}_{\boldsymbol{\theta}} = \alpha \mathbf{d}(f_d, \tau)$. The satellite signal parameters in $\boldsymbol{\theta}$ and the noise statistics are assumed completely known by the receiver, consequently, it holds the performance upper bound for the NP detector's family. This kind of detector is also referred to as the *clairvoyant detector*. By a straightforward manipulation of (3.15), it can be shown (see e.g., [Kay98, p.474]) that the NP detector test function becomes:

$$T_{\text{MF}}(\mathbf{x}) = \Re \left\{ \mathbf{x} \mathbf{s}_{\boldsymbol{\theta}}^H \right\} > \gamma'. \quad (3.16)$$

This detector is also named *replica-correlator*. An alternative interpretation of $T_{\text{MF}}(\mathbf{x})$ relating the correlation process to a Finite Impulse Response (FIR) is referred to Matched Filter (MF). The received signal is processed by a FIR filter with an impulse response equal to a time-reversed and conjugate version of the satellite signal. Both operations are equivalent. The detector is able to concentrate all the signal energy in the real part of the correlator output, since it is a coherent detector. Considering $z = \mathbf{x} \mathbf{s}_{\boldsymbol{\theta}}^H$, the first two statistical moments of $T_{\text{MF}}(\mathbf{x})$ are:

$$\begin{aligned} \mathbb{E}\{z; \mathcal{H}_1\} &= \sum_{t=t_0}^{t_K-1} \mathbb{E}\{x(t)s_{\boldsymbol{\theta}}^*(t)\} = \|\mathbf{s}_{\boldsymbol{\theta}}\|^2 = \varepsilon, \\ \mathbb{E}\{z; \mathcal{H}_0\} &= \sum_{t=t_0}^{t_K-1} \mathbb{E}\{x(t)s_{\boldsymbol{\theta}}^*(t)\} = 0, \\ \text{var}\{z; \mathcal{H}_0\} &= \sigma^2 \|\mathbf{s}_{\boldsymbol{\theta}}\|^2 = \sigma^2 \varepsilon, \end{aligned} \quad (3.17)$$

where $\|\cdot\|$ is defined as the Euclidian norm $\|\mathbf{u}\mathbf{u}^H\| = \sqrt{\mathbf{u}\mathbf{u}^H}$, $(\cdot)^*$ denotes complex conjugate and $\varepsilon = \|\mathbf{s}_{\boldsymbol{\theta}}\|^2$ is the signal energy. Considering now $\Re(z)$, the complex Gaussian noise is composed by a real and imaginary Gaussian variables, with half the total power on each. The distribution of $T_{\text{MF}}(\mathbf{x}) = \Re(z)$ can be written as:

$$T_{\text{MF}}(\mathbf{x}; \mathcal{H}_1) \sim \mathcal{N}\left(\varepsilon, \frac{\sigma^2 \varepsilon}{2}\right) \quad (3.18)$$

$$T_{\text{MF}}(\mathbf{x}; \mathcal{H}_0) \sim \mathcal{N}\left(0, \frac{\sigma^2 \varepsilon}{2}\right). \quad (3.19)$$

Using (3.14), the deflection coefficient is:

$$d^2 = \frac{2\varepsilon}{\sigma^2}. \quad (3.20)$$

The replica-correlator detector is optimum according to NP criterion, as a consequence, also have the performance bound for any detector. The theoretical performance indicators are:

$$P_{fa} = Q\left(\frac{\gamma'}{\sqrt{\sigma^2 \frac{\varepsilon}{2}}}\right) \quad (3.21)$$

$$P_d = Q\left(\frac{\gamma' - \varepsilon}{\sqrt{\sigma^2 \frac{\varepsilon}{2}}}\right), \quad (3.22)$$

where $Q(x) = 1 - \Phi(x)$ is the complementary Cumulative Distribution Function (CDF), with $\Phi(x)$ standing as the Gaussian CDF. The ROC can be computed using $P_d = Q\left(Q^{-1}(P_{fa}) - \sqrt{d^2}\right)$.

3.3.2 GLRT approach

In contrast to the detector derived in Section 3.3.1, here it is assumed that the GNSS receiver does not have *a priori* knowledge of the values of the synchronization parameters $\boldsymbol{\theta}$ at the acquisition stage, which is a realistic condition. Applying the NP criterion, it is possible to use the Generalized Likelihood Ratio Test (GLRT) statistic for the problem at hand, where the unknown parameters in the PDFs are replaced by their respective Maximum Likelihood (ML) estimators. The GLRT is expressed as [Kay98]:

$$L_{\text{GL}}(\mathbf{x}) = \frac{p(\mathbf{x}; \hat{\sigma}_{\mathcal{H}_1}^2, \hat{\boldsymbol{\theta}}, \mathcal{H}_1)}{p(\mathbf{x}; \hat{\sigma}_{\mathcal{H}_0}^2, \mathcal{H}_0)} > \gamma, \quad (3.23)$$

where $\hat{\boldsymbol{\theta}}$ is the MLE of $\boldsymbol{\theta}$ assuming that \mathcal{H}_1 is true. Since the noise variance is also unknown, $\hat{\sigma}_{\mathcal{H}_1}^2$ and $\hat{\sigma}_{\mathcal{H}_0}^2$ should be also estimated. Hereafter we re-visit the derivations for both the MLE of $\boldsymbol{\theta}$ and the acquisition test function.

3.3.2.1 Maximum Likelihood Estimators

The MLE derivation of both $\hat{\boldsymbol{\theta}}$ and $\hat{\sigma}_{\mathcal{H}_1}^2$ implies the maximization of $p(\mathbf{x}; \sigma_{\mathcal{H}_1}^2, \boldsymbol{\theta}, \mathcal{H}_1)$, and considering the signal model, the negative log-likelihood function of a complex Gaussian variable x for K observations, neglecting the irrelevant constants, can be defined as:

$$\Lambda_1(\sigma_{\mathcal{H}_1}^2, \alpha, f_d, \tau) = \ln(\sigma_{\mathcal{H}_1}^2) + \frac{C(\alpha, f_d, \tau)}{\sigma_{\mathcal{H}_1}^2}, \quad (3.24)$$

where it is defined the scalar value $C(\alpha, f_d, \tau) \in \mathbb{C}$ as³:

$$C = \hat{R}_{\mathbf{xx}} - \hat{R}_{\mathbf{xd}}\alpha^* - \alpha\hat{R}_{\mathbf{xd}}^* + |\alpha|^2\hat{R}_{\mathbf{dd}}, \quad (3.25)$$

and the autocorrelation and cross-correlation scalar values are:

- $\hat{R}_{\mathbf{xx}} = \frac{1}{K}\mathbf{xx}^H$ is the estimation of the received signal autocorrelation, which is also the input signal power estimation.
- $\hat{R}_{\mathbf{xd}} = \frac{1}{K}\mathbf{xd}^H$ is the estimation of the cross-correlation between the received signal and the GNSS reference signal.
- $\hat{R}_{\mathbf{dd}} = \frac{1}{K}\mathbf{dd}^H$ is the estimation of the GNSS reference signal autocorrelation. Considering normalized power, it is possible to assume $\hat{R}_{\mathbf{dd}} \simeq 1$. Notice that $\hat{R}_{\mathbf{dd}}$ does not depend on the synchronization parameters.

The next step is to find the ML estimator for each parameter, which is equivalent to minimize Λ_1 :

$$\hat{\sigma}_{\mathcal{H}_1}^2, \hat{\alpha}, \hat{f}_d, \hat{\tau}|_{ML} = \arg \min_{\sigma_{\mathcal{H}_1}^2, \alpha, f_d, \tau} \left\{ \Lambda_1(\sigma_{\mathcal{H}_1}^2, \alpha, f_d, \tau) \right\}, \quad (3.26)$$

by applying the gradient with respect to $\sigma_{\mathcal{H}_1}^2$, setting it to zero, and neglecting the constants, it is possible to find

$$\hat{\sigma}_{\mathcal{H}_1}^2 = C|_{\alpha=\hat{\alpha}, f_d=\hat{f}_d, \tau=\hat{\tau}}, \quad (3.27)$$

using the same procedure, we find $\hat{\alpha}$:

$$\hat{\alpha} = \hat{R}_{\mathbf{xd}}\hat{R}_{\mathbf{dd}}^{-1}|_{\sigma^2=\hat{\sigma}_{\mathcal{H}_1}^2, f_d=\hat{f}_d, \tau=\hat{\tau}}, \quad (3.28)$$

and finally, we obtain \hat{f}_d and $\hat{\tau}$ inserting (3.28) and (3.27) in (3.24). Discarding the constant terms:

$$\hat{f}_d, \hat{\tau} = \arg \max_{f_d, \tau} \left\{ |\hat{R}_{\mathbf{xd}}(f_d, \tau)|^2 \right\}, \quad (3.29)$$

³For the sake of simplicity of the notation, in this Section we omit the $\mathbf{d}(f_d, \tau)$ dependency on f_d and τ .

which is equal to the maximization of the power of the cross-correlation between the received signal and the GNSS signal. This expression is also known as the non-coherent MF estimator [Kay93]. Since it is not possible to obtain a closed expression for \hat{f}_d and $\hat{\tau}$, a grid based search can be used to find the function's maximum.

On the other hand, the MLE of $\sigma_{\mathcal{H}_0}^2$ is known to be directly the sample covariance estimator [Kay93]:

$$\hat{\sigma}_{\mathcal{H}_0}^2 = \hat{R}_{\mathbf{xx}}. \quad (3.30)$$

3.3.2.2 Acquisition test function

By applying the PDF of a complex Gaussian variable for K observations in both $p(\mathbf{x}; \mathcal{H}_1)$ and $p(\mathbf{x}; \mathcal{H}_0)$, according to the signal model (3.1), the GLRT expression of (3.23) can be expanded as:

$$L_{\text{GL}}(\mathbf{x}) = \frac{\frac{1}{\pi^K (\hat{\sigma}_{\mathcal{H}_1}^2)^K} \exp \left\{ -(\hat{\sigma}_{\mathcal{H}_1}^{-2}) C \right\}}{\frac{1}{\pi^K (\hat{\sigma}_{\mathcal{H}_0}^2)^K} \exp \left\{ -(\hat{\sigma}_{\mathcal{H}_0}^{-2}) \hat{R}_{\mathbf{xx}} \right\}} > \gamma, \quad (3.31)$$

and inserting the expressions for the ML estimators (3.28) and (3.27) on (3.31), using (3.25), the test statistic function can be written as:

$$T_{\text{GL}}(\mathbf{x}) = \max_{f_d, \tau} \left\{ \frac{\hat{R}_{\mathbf{xx}}}{\hat{R}_{\mathbf{xx}} - |\hat{R}_{\mathbf{xd}}(f_d, \tau)|^2 \hat{R}_{\mathbf{dd}}^{-1}} \right\} > \gamma, \quad (3.32)$$

where we can find an equivalent expression, dividing both the numerator and the denominator of the fraction by $\hat{R}_{\mathbf{xx}}$ and taking into account that $\hat{R}_{\mathbf{dd}}$ neither depends on the received data nor the synchronization parameters:

$$T_{\text{GL}}(\mathbf{x}) = \max_{f_d, \tau} \left\{ \frac{1}{1 - \frac{|\hat{R}_{\mathbf{xd}}(f_d, \tau)|^2 \hat{R}_{\mathbf{dd}}^{-1}}{\hat{R}_{\mathbf{xx}}}} \right\} \simeq \max_{f_d, \tau} \left\{ \frac{|\hat{R}_{\mathbf{xd}}(f_d, \tau)|^2}{\hat{R}_{\mathbf{xx}}} \right\} > \gamma. \quad (3.33)$$

The resulting test function is the generalized non-coherent MF detector [Kay98]. The detector involves again a maximization of a function depending on f_d and τ . A grid based search can be used to find the maximum and compare the resulting value against the threshold. Performing the grid search implies the generation of a local satellite signal, in our case, denoted by $\mathbf{d}(\check{f}_d, \check{\tau}) = \mathbf{s}_i(\check{f}_d, \check{\tau})$, where each pair of $(\check{f}_d, \check{\tau})$ forms a grid bin. Starting from this well-known result, a number of grid search strategies can be applied, see e.g. [Bor06]. On the other hand, the GNSS navigation message or the secondary spreading codes could degrade the performance on the detector, limiting the size acquisition signal block. In the literature can be found a number of techniques to overcome this effect, see e.g. [Pre09, Bor09b, Bor09a].

3.3.2.3 Performance analysis

In the performance analysis of the detector, it is assumed that the maximization of the test statistic over the acquisition search space of $(\check{f}_d, \check{\tau})$ is able to obtain the absolute maximum of the test function, and thus, perfect alignment $f_d = \check{f}_d$ and $\tau = \check{\tau}$ is achievable. This restrictive condition isolates the detector's performance from the effects caused by the misalignment of the local satellite signal replica (for instance, due to the quantization of the search grid).

In the aforementioned ideal situation, the PDF of $T_{\text{GL}}(\mathbf{x})$ can be found considering that the cross-correlation term is distributed as $\hat{R}_{\mathbf{xd}; \mathcal{H}_1} \sim \mathcal{CN}(\mu_{\hat{R}_{\mathbf{xd}}}, \sigma_{\hat{R}_{\mathbf{xd}}}^2)$. Hereafter can be found the

derivation of the first two moments:

$$\mu_{\hat{R}_{\mathbf{x}\mathbf{d}}} = \mathbb{E}\{\hat{R}_{\mathbf{x}\mathbf{d}}\} = \mathbb{E}\left\{\frac{1}{K}(\alpha\mathbf{d} + \mathbf{n})\mathbf{d}^H\right\} = \frac{1}{K}\left(\mathbb{E}\{\alpha\mathbf{d}\mathbf{d}^H\} + \mathbb{E}\{\mathbf{n}\mathbf{d}^H\}\right) = \alpha R_{\mathbf{d}\mathbf{d}} \simeq \alpha, \quad (3.34)$$

$$\sigma_{\hat{R}_{\mathbf{x}\mathbf{d}}}^2 = \mathbb{E}\{(\hat{R}_{\mathbf{x}\mathbf{d}} - \mu)(\hat{R}_{\mathbf{x}\mathbf{d}} - \mu)^H\} = \frac{1}{K^2}\mathbb{E}\{\underbrace{(\mathbf{n}\mathbf{d}^H)}_{\text{scalar}}\underbrace{(\mathbf{d}\mathbf{n}^H)}_{\text{scalar}}\} =$$

$$= \frac{1}{K^2}\mathbb{E}\{(\mathbf{d}\mathbf{n}^H)(\mathbf{n}\mathbf{d}^H)\} = \frac{1}{K^2}\mathbf{d}\mathbb{E}\{\mathbf{n}^H\mathbf{n}\}\mathbf{d}^H = \frac{R_{\mathbf{d}\mathbf{d}}R_{\mathbf{n}\mathbf{n}}}{K} \simeq \frac{\hat{R}_{\mathbf{x}\mathbf{x}}}{K}, \quad (3.36)$$

where $\mathbb{E}\{\cdot\}$ stands for the expectation operator and the variance formula for complex-valued random variables is used as $\sigma^2 = \mathbb{E}\{(x - \mu)(x - \mu)^H\}$, with $x \in \mathbb{C}$ and $\mu \in \mathbb{C}$. It is considered that the signal is uncorrelated with the noise ($\mathbb{E}\{\mathbf{n}\mathbf{d}^H\} = 0$) and $\mathbb{E}\{\mathbf{n}^H\mathbf{n}\} \simeq \mathbf{I}\sigma^2 = \mathbf{I}R_{\mathbf{n}\mathbf{n}}$, where \mathbf{I} stands for the identity matrix. Additionally, for the sake of simplicity of the analysis, it is assumed that the noise has a dominant contribution in $R_{\mathbf{x}\mathbf{x}}$ so that it can be approximated as $R_{\mathbf{x}\mathbf{x}} \simeq R_{\mathbf{n}\mathbf{n}}$, which is a realistic assumption due the extremely low power of the satellite signals as introduced in Chapter 2. On the other hand, in our analysis it is also assumed that the estimation of the input signal variance is performed with a large number of samples, that is $K \gg N$, which leads to consider $\hat{R}_{xx} \simeq R_{xx}$.

The test statistic have a quadratic form of a complex Gaussian variable. In order to identify the resulting distribution, it is useful to express $R_{\mathbf{x}\mathbf{x}} = QQ^*$ and if we define $V = Q^{-1}\hat{R}_{\mathbf{x}\mathbf{d}}$ so that $V \sim \mathcal{CN}(Q^{-1}\mu_{\hat{R}_{\mathbf{x}\mathbf{d}}}, (QQ^*)^{-1}\sigma_{\hat{R}_{\mathbf{x}\mathbf{d}}}^2)$ that simplifies to $V \sim \mathcal{CN}(Q^{-1}\mu_{\hat{R}_{\mathbf{x}\mathbf{d}}}, \frac{1}{K})$, it is clear that

$$\hat{R}_{\mathbf{x}\mathbf{d}}R_{\mathbf{x}\mathbf{x}}^{-1}\hat{R}_{\mathbf{x}\mathbf{d}}^* = VV^* \quad (3.37)$$

is a non-central $\chi_2^2(\delta_{T_{\text{GL}}})$ with the non-centrality parameter

$$\delta_{T_{\text{GL}}} = (Q^{-1}\mu_{\hat{R}_{\mathbf{x}\mathbf{d}}})(Q^{-1}\mu_{\hat{R}_{\mathbf{x}\mathbf{d}}})^* = \frac{|\mu_{\hat{R}_{\mathbf{x}\mathbf{d}}}|^2}{R_{\mathbf{x}\mathbf{x}}} \simeq \frac{P_s}{P_s + P_n} = \frac{\rho}{\rho + 1}, \quad (3.38)$$

where the equivalence $R_{\mathbf{x}\mathbf{x}} = \|\alpha\|^2 + \sigma^2 = P_s + P_n$ was used in the latest approximation. Each of the underlying Gaussian variables that contains $T_{\text{GL}}(\mathbf{X})$ has the variance

$$\sigma_{T_{\text{GL}}}^2 = \frac{1}{2K}. \quad (3.39)$$

Notice that the input noise variance σ^2 is equally split in the real and the imaginary part and this fact is represented by the factor 2 in the denominator of $\sigma_{T_{\text{GL}}}^2$.

Particularizing the non-centrality parameter of $\chi_2^2(\delta_{T_{\text{GL}}})$ for each testing hypotheses, inserting (3.2) and (3.3) in (3.38), the test statistic is fully characterized:

$$T_{\text{GL}}(\mathbf{x}) \sim \begin{cases} \chi_2^2(\delta_{T_{\text{GL}}; \mathcal{H}_1}), & \text{in } \mathcal{H}_1, \\ \chi_2^2(\delta_{T_{\text{GL}}; \mathcal{H}_0} = 0), & \text{in } \mathcal{H}_0, \end{cases} \quad (3.40)$$

where

$$\delta_{T_{\text{GL}}; \mathcal{H}_1} = \frac{|\alpha|^2}{R_{\mathbf{x}\mathbf{x}}} \simeq \frac{P_s}{P_n} = \rho, \quad (3.41)$$

if $P_n \gg P_s$ or equivalently, $\rho \ll 1$. The distribution becomes a central χ_2^2 in \mathcal{H}_1 due to the absence of the satellite signal.

It is possible to find closed form solutions for both false alarm and detection probabilities, expressed as $P_{fa}(\gamma) = 1 - P_{\mathcal{H}_0}(T_{\text{GL}}(\mathbf{x}; \mathcal{H}_0) \leq \gamma)$ and $P_d(\gamma) = 1 - P_{\mathcal{H}_1}(T_{\text{GL}}(\mathbf{x}; \mathcal{H}_1) \leq \gamma)$, respectively, where $P_{\mathcal{H}_x}(\cdot)$ is the χ_2^2 CDF can be expressed as:

$$P_d(\gamma) = Q_1\left(\frac{\sqrt{\delta_{T_{\text{GL}}; \mathcal{H}_1}}}{\sigma_{T_{\text{GL}}}}, \frac{\sqrt{\gamma}}{\sigma_{T_{\text{GL}}}}\right), \quad (3.42)$$

$$P_{fa}(\gamma) = \exp\left\{\frac{-\gamma}{2\sigma_{T_{\text{GL}}}^2}\right\}, \quad (3.43)$$

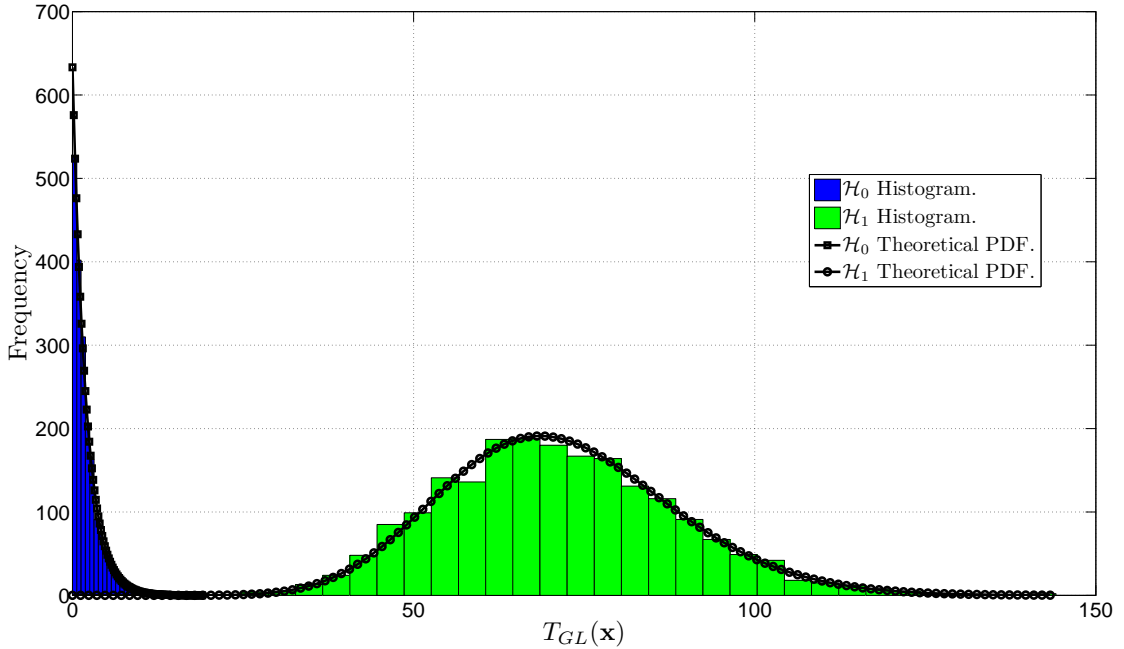


Figure 3.2: $T_{GL}(x)$ normalized histogram and theoretical PDF in both \mathcal{H}_1 and \mathcal{H}_0 acquisition hypotheses for Galileo E1 signal acquisition simulation.

where Q_1 is the generalized Marcum Q-function [Pro00] of order 1. This acquisition test statistic is a CFAR detector because P_{fa} does not depend on the noise power. The theoretical PDFs obtained in (3.40) were validated by Monte Carlo (MC) simulations. The test statistic histogram of $T_{GL}(x)$ was simulated for the acquisition of a Galileo E1 signal with $CN0 = 38$ dB-Hz in the absence of interfering signals and considering AWGN only. The baseband sampling frequency was set to 6 MHz and the acquisition bandwidth was set to 2 MHz. Each of the histograms contains 2000 realizations. Fig. 3.2 shows the results for both \mathcal{H}_1 and \mathcal{H}_0 hypotheses, concluding that the model is aligned with the simulations results. For the sake of simplicity, in order to use the normalized Marqum Q-function, both the histograms and the PDFs are normalized to $\sigma_{T_{GL}}^2 = 1$ expressed as $\bar{T}_{GL}(x) = 2KT_{GL}(x)$.

Furthermore, it is possible to compute the first two moments of $T_{GL}(x)$ by applying the chi-square properties $\mathbb{E}\{\chi_u^2(\delta)\} = u\sigma^2 + \delta$ and $\text{var}\{\chi_u^2(\delta)\} = 2(u\sigma^4 + 2\sigma^2\delta)$, with σ^2 as the underlying variance of each of the Gaussian squared variables composing the chi-square:

$$\mathbb{E}\{T_{GL}(x); \mathcal{H}_1\} = 2\frac{\sigma_{T_{GL}}^2}{2} + \delta_{T_{GL}} = \sigma_{T_{GL}}^2 + \delta_{T_{GL}}, \quad (3.44)$$

$$\mathbb{E}\{T_{GL}(x); \mathcal{H}_0\} = 2\frac{\sigma_{T_{GL}}^2}{2} = \sigma_{T_{GL}}^2, \quad (3.45)$$

$$\text{var}\{T_{GL}(x); \mathcal{H}_1\} = 2\left(2\frac{\sigma_{T_{GL}}^4}{4} + 2\sigma_{T_{GL}}^2\delta_{T_{GL}}\right) = \sigma_{T_{GL}}^2(\sigma_{T_{GL}}^2 + 4\delta_{T_{GL}}), \quad (3.46)$$

$$\text{var}\{T_{GL}(x); \mathcal{H}_0\} = 2\left(2\frac{\sigma_{T_{GL}}^4}{4}\right) = \sigma_{T_{GL}}^4. \quad (3.47)$$

Then, inserting the results in (3.14) and using both (3.38) and (3.39) the deflection coefficient is obtained:

$$d_{GL}^2 = \frac{\delta_{T_{GL}}^2}{\sigma_{T_{GL}}^4}. \quad (3.48)$$

The presented test function is a non-coherent detector, and it is affected by twice the noise power than the coherent detector [Hay88].

3.4 Joint Acquisition Strategy

In latest years the world has witnessed a rapid evolution of the existing GNSS and the emergence of new ones, such as the forthcoming European Galileo GNSS. As shown in Chapter 2, a variety of satellite constellations and signals will be available in the next years. Moreover, the mass market demands a multi-system receiver with short TTFF, low cost per unit, and low power consumption. Regarding this, there is a growing number of works dealing with the combined GPS and Galileo receiver possibilities in the literature, see e.g [CP-10, Sch05], and combined GPS/Glonass receivers are already available commercially, e.g., Apple's iPhone 4S integrates a GNSS receiver that enables the reception of GPS and Glonass signals [App12]. Furthermore, the new System on Chip (SoC) architectures include a combined GPS and Glonass receiver, such as the Qualcomm Snapdragon family [Qua12]. Consequently, a multi-system receiver has to deal with an increasing number of satellites in different constellations.

The acquisition operation is traditionally performed satellite-by-satellite, using a discrete search over a grid in the Doppler and delay dimensions, performing a correlation operation with a locally-generated satellite signal replica. The minimum amount of required correlations for a terrestrial low-speed GNSS receiver is in the order of $40 \cdot 10^3$ for a GPS C/A receiver and $160 \cdot 10^3$ for a Galileo E1 receiver, assuming 250 Hz of Doppler resolution and $\tau_{\text{step}} = 1 \mu\text{s}$ of code delay resolution at each bin⁴, with a Doppler search space $f_d \in [-5000, +5000] \text{ Hz}$ [Tsu00, p.37] and code delay search space $\tau_{\text{GPS}} \in [0, 1] \text{ ms}$ or $\tau_{\text{Galileo}} \in [0, 4] \text{ ms}$ for GPS C/A and Galileo E1, respectively. These quantities must be multiplied by the number of potentially in-view satellites of each constellation to obtain the total number of required correlators. Indeed, many approaches can be applied in order to reduce this number, for instance, the Fast Fourier Transform (FFT) based acquisition [Bor07]. However, the overall number of required correlators is still a meaningful measure of the associated computational cost. In addition, a combined GPS and Galileo receiver should perform the acquisition for all of the active satellites of both constellations. As a consequence, the acquisition operation could be a high resource-consuming task if a fast TTFF is required.

In this Section, we propose a novel approach intended to dramatically reduce the number of correlations required in the acquisition process. Instead of acquiring the satellites one-by-one, a joint satellite acquisition strategy is explored. The basis of the acquisition algorithm is the GLRT detector, derived in Section 3.3.2. The proposed method generates a local satellite signal replica which contains the sum of two or more (actually, this value is a design parameter) satellite codes and performs the grid search with this augmented local replica. The resulting grid is then analyzed with a test statistic function, thus resulting in a delay/Doppler grid with as many maxima as present satellites. Then, maxima are identified using an extra correlation per possible satellite. A tradeoff between the computational cost of the algorithm and the loss of acquisition sensitivity due to the presence of extra cross-correlation terms is identified.

3.4.1 Augmented local satellite signal replica

The new local satellite signal replica contains the sum of two or more satellite codes. It can be defined as:

$$\mathbf{r}(\check{f}_d, \check{\tau}) = \sum_{i=1}^A \mathbf{d}_i(\check{f}_d, \check{\tau}), \quad (3.49)$$

where A is the number of different satellite codes contained in $\mathbf{r}(\check{f}_d, \check{\tau})$. Notice that all the satellites codes present in the augmented local replica are sharing the same synchronization parameters. Inserting (3.49) in (3.33) it is possible to obtain a joint acquisition test function:

$$T_r(\mathbf{x}) = \max_{\check{f}_d, \check{\tau}} \left\{ \frac{|\frac{1}{K} \mathbf{x} \mathbf{r}(\check{f}_d, \check{\tau})^H|^2}{\hat{R}_{\mathbf{xx}}} \right\} > \gamma. \quad (3.50)$$

⁴The required number of correlations (N_g) is equal to the number of bins in the search grid, assuming a single-dwell acquisition $N_g = \frac{(f_{d,\max} - f_{d,\min})}{\tau_{\text{step}}} \frac{(\tau_{\max} - \tau_{\min})}{\tau_{\text{step}}}$.

Using $T_r(\mathbf{x})$ it is expected to detect up to A satellites simultaneously. This process can be represented as an iterative maximization of $T_r(\mathbf{x})$ over the parameter search set $\Omega = \{\check{f}_d \in [f_{\max}, f_{\min}], \check{\tau} \in [0, LT_c]\}$, where f_{\max}, f_{\min} are the maximum and minimum Doppler frequency respectively, and L is the PRN sequence length in chips. The first iteration is:

$$(\check{f}_{d,1}, \check{\tau}_1) = \arg \max_{\check{f}_d, \check{\tau} \in \Omega} T_r(\mathbf{x}) > \gamma, \quad (3.51)$$

the second iteration has to search in a subset $\Omega_2 = \Omega \setminus \{(\check{f}_1, \check{\tau}_1)\}$ ⁵

$$(\check{f}_{d,2}, \check{\tau}_2) = \arg \max_{\check{f}_d, \check{\tau} \in \Omega_2} T_r(\mathbf{x}) > \gamma, \quad (3.52)$$

finally we can write the general iterative formula as:

$$(\check{f}_{d,i}, \check{\tau}_i) = \arg \max_{\check{f}_d, \check{\tau} \in \Omega_i} T_r(\mathbf{x}) > \gamma, \quad (3.53)$$

where $\Omega_i = \Omega \setminus \{(\check{f}_1, \check{\tau}_1), \dots, (\check{f}_{i-1}, \check{\tau}_{i-1})\}$ is the subset of the remaining grid positions. Fig. 3.3 shows a sample of this effect for different values of A . The acquisition algorithm must determine the corresponding satellite *id* for each detected maximum. This ambiguity can be solved performing extra correlations on each $(\check{f}_{d,i}, \check{\tau}_i)$ maximum and comparing their outputs.

Fig. 3.4 shows a flow chart of the proposed acquisition algorithm implementation. From top to bottom, after the RF front-end, the signal is sampled, converted to base-band and arranged into a vector \mathbf{x} . The acquisition implementation is divided in two stages. The first one consists of a grid search algorithm that uses the augmented local signal replica and the test function $T_r(\mathbf{x})$. Several grid search strategies [Bor06] can be implemented here, having in mind that the target is to detect up to A maxima.

Once the grid search algorithm has located the maxima, the next stage is in charge of identifying the satellites' *id* associated with each maximum. To complete this operation, a recursive algorithm can be implemented. Starting from the synchronization parameters estimation of the highest detected maximum, we perform parallel correlations with all the local signals included in this particular set of A satellites. The most correlated local replica will give the satellite *id* associated to this particular maximum. Next maximum will be identified in the same manner but performing $(A - 1)$ correlations, and so on. This stage can be used also to confirm the detection, extending the acquisition time or refining the synchronization parameters.

Finally, the confirmed detections with their satellites identifications and the corresponding synchronization parameters estimations $(\hat{f}_{d,i}, \hat{\tau}_i)$, are sent to the tracking stage. The remaining undetected satellites will be searched performing a new algorithm cycle, starting the flow chart again.

3.4.2 Computational cost

The computational cost of a given acquisition algorithm can be measured in terms of the number of correlations needed in the operation [Bor07]. It is considered that the correlations are performed in time domain and the acquisition is performed over a single signal block, also known as *single-dwell* acquisition. The results can be extended to *multiple dwell* acquisition and to frequency-domain correlations. According to (3.50), the number of correlations needed by the acquisition algorithm considering a cold acquisition, can be expressed as:

$$N_c(A) = N_g \left\lceil \frac{M_s}{A} \right\rceil + \sum_{i=1}^A (A - i), \quad (3.54)$$

where $\lceil x \rceil = \max\{m \in \mathbb{Z} \mid m \leq x\}$ corresponds to the ceil operation and N_g is the number of different $(\check{f}, \check{\tau})$ pairs (bins) in the grid. A is the number of satellites present on \mathbf{r} and M_s is the

⁵In set theory notation, $\mathcal{A} \setminus \mathcal{B}$ denotes all elements of set \mathcal{A} that are not contained in set \mathcal{B} .

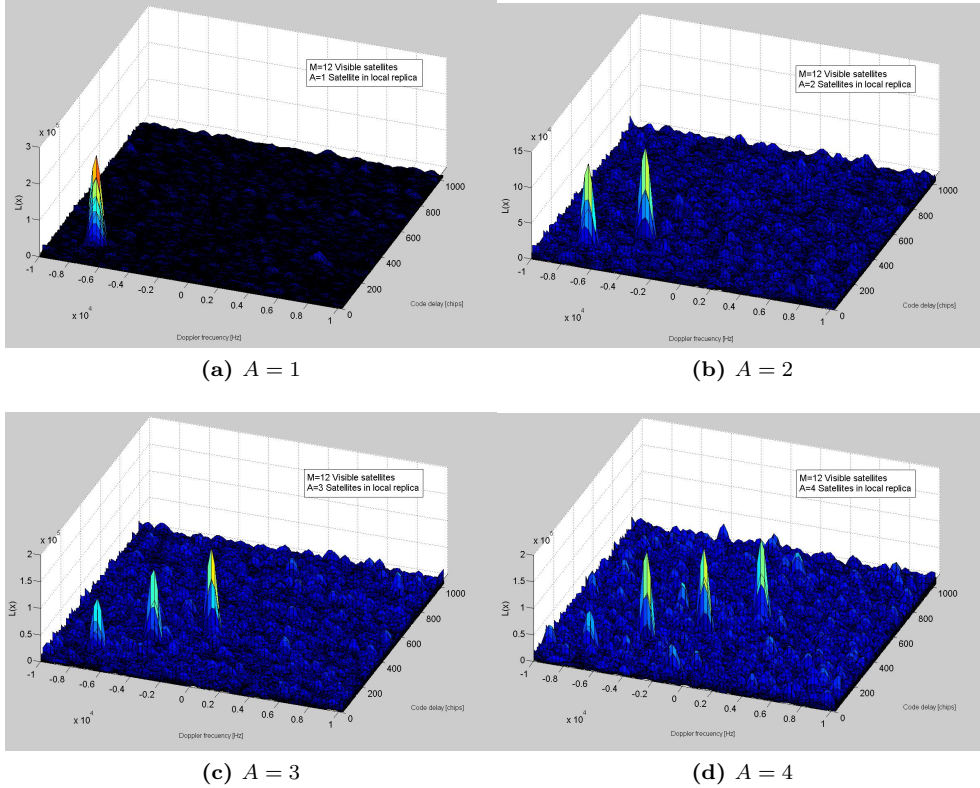


Figure 3.3: Simulated acquisition search grid for GPS L1 C/A signal with $M = 12$ visible satellites and equal CN0 = 45 dB-Hz, and different number of satellites present in local replica.

number of satellites in the GNSS signal. Fig. 3.5 shows an example of the evolution of $N_c(A)$ for different A values performing a GPS L1 C/A cold acquisition, assuming a constellation of 31 satellites and a search grid of $\check{f}_d \in [-5000, +5000]$ Hz with 250 Hz steps and $\check{\tau} \in [0, 1)$ ms with $1\mu\text{s}$ steps. The set Ω contains 40×1000 bins. The obtained correlation cost reduction with respect to conventional acquisition, that is $A = 1$, is about 50% for $A = 2$ and about 66% for $A = 3$.

3.4.3 Performance analysis

The PDF of $T_r(\mathbf{x})$ can be extracted reorganizing the terms in (3.50) as is shown in (3.55). Inserting (3.1) in (3.55), we obtain (3.56), where the term $\hat{R}_{\mathbf{x}\mathbf{r}}$ is distributed as a complex Gaussian random variable with mean $\mu_{\hat{R}_{\mathbf{x}\mathbf{r}}}$ and variance $\sigma_{\hat{R}_{\mathbf{x}\mathbf{r}}}^2$, defined as

$$\mu_{\hat{R}_{\mathbf{x}\mathbf{r}}} = \frac{1}{K} \sum_{i=1}^M \alpha_i \mathbf{d}_i(f_{d,i}, \tau_i) \mathbf{r}(\check{f}_d, \check{\tau})^H, \quad (3.57)$$

$$\sigma_{\hat{R}_{\mathbf{x}\mathbf{r}}}^2 = \frac{\hat{R}_{\mathbf{rr}} \hat{R}_{\mathbf{xx}}}{K} \simeq \frac{A \hat{R}_{\mathbf{xx}}}{K}. \quad (3.58)$$

The variance of $\hat{R}_{\mathbf{x}\mathbf{r}}$ increases by a factor of A because the power of the local augmented replica is proportional to the number of local PRN codes, that is $\hat{R}_{\mathbf{rr}} = \frac{1}{K} \mathbf{r} \mathbf{r}^H \simeq A$. On the other hand, it is assumed that the estimation of the input signal variance is performed with a large number of samples, which leads to consider $\hat{R}_{\mathbf{xx}} \simeq R_{\mathbf{xx}}$.

Following the same analysis as in the GLRT performance of Section 3.3.2.3, considering (3.56), the test statistics also have a quadratic form of a complex Gaussian variable, becoming

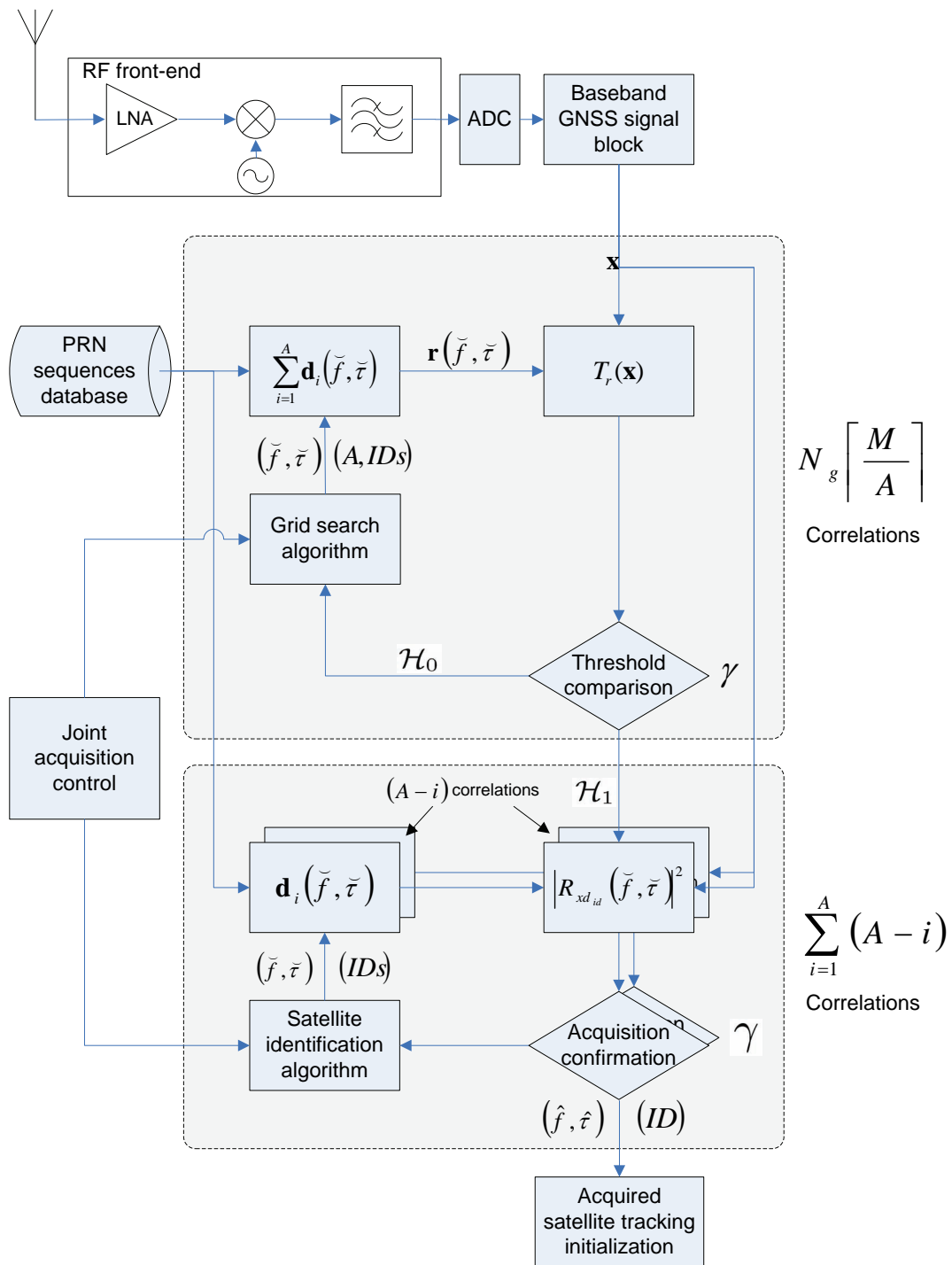


Figure 3.4: Proposed joint-acquisition algorithm flow chart.

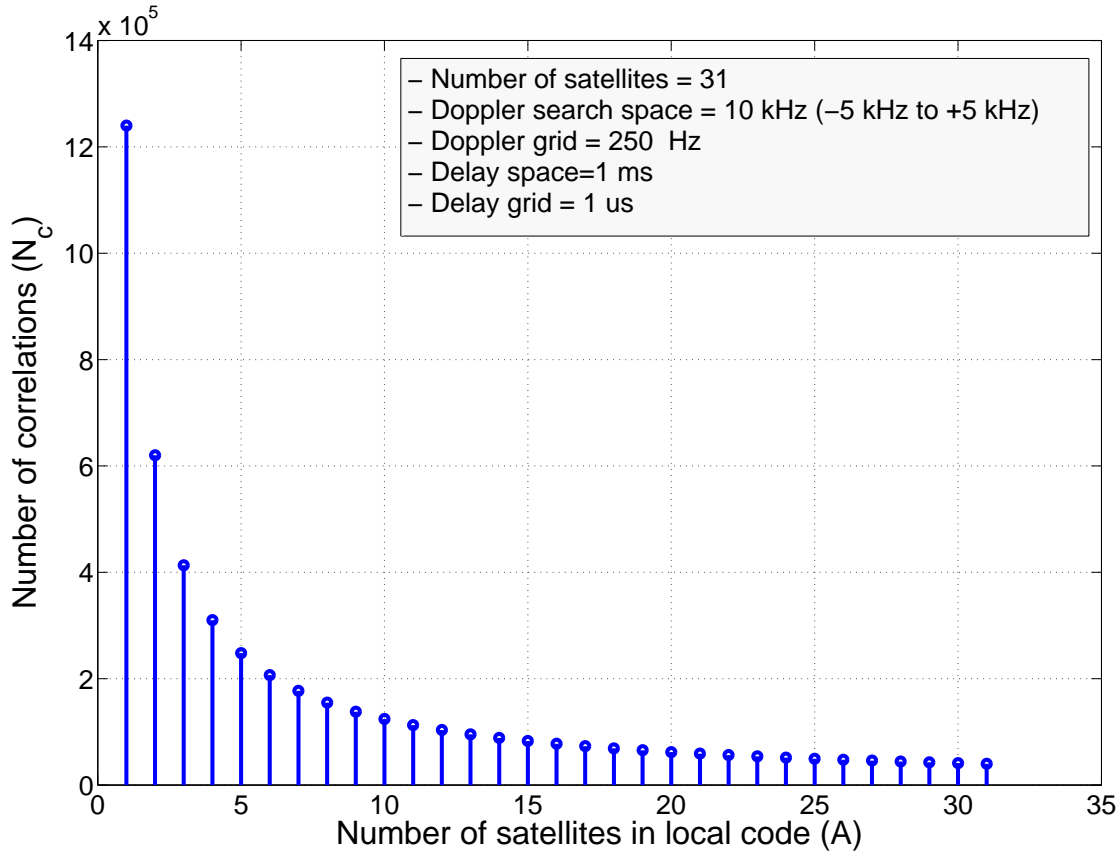


Figure 3.5: Number of correlations needed in single-dwell acquisition vs. the number of satellites present in local code replica for GPS L1 C/A.

$$T_r(\mathbf{x}) = \max_{\tilde{f}_d, \tilde{\tau}} \left\{ \left(\frac{1}{K} \mathbf{x} \mathbf{r}(\tilde{f}_d, \tilde{\tau})^H \right) \hat{R}_{\mathbf{xx}}^{-1} \left(\frac{1}{K} \mathbf{x} \mathbf{r}(\tilde{f}_d, \tilde{\tau})^H \right)^* \right\}, \quad (3.55)$$

$$T_r(\mathbf{x}) = \max_{\tilde{f}_d, \tilde{\tau}} \left\{ \underbrace{\left(\frac{1}{K} \sum_{i=1}^{M_s} \alpha_i \mathbf{d}_i(f_{d,i}, \tau_i) \mathbf{r}(\tilde{f}_d, \tilde{\tau})^H + \mathbf{n} \mathbf{r}(\tilde{f}_d, \tilde{\tau})^H \right)}_{\hat{R}_{\mathbf{xr}}} \hat{R}_{\mathbf{xx}}^{-1} \underbrace{\left(\frac{1}{K} \sum_{i=1}^{M_s} \alpha_i \mathbf{d}_i(f_{d,i}, \tau_i) \mathbf{r}(\tilde{f}_d, \tilde{\tau})^H + \mathbf{n} \mathbf{r}(\tilde{f}_d, \tilde{\tau})^H \right)^*}_{\hat{R}_{\mathbf{xr}}^*} \right\}, \quad (3.56)$$

a $\chi_2^2(\delta_{T_r})$, with the non-centrality parameter defined as

$$\delta_{T_r} = \frac{|\mu_{\hat{R}_{\mathbf{xr}}}|^2}{R_{\mathbf{xx}}}. \quad (3.59)$$

Particularizing the non-centrality parameter for each testing hypotheses, inserting (3.2) and (3.2) in (3.59), and using (3.49), we obtain δ , both for the alternative and for the null hypotheses on (3.60) and (3.61) respectively.

The autocorrelation of the desired satellite with the aligned local replica can be approximated by

$$\alpha_{id} \hat{R}_{\mathbf{s}_{id} \mathbf{s}_{id}} \simeq \alpha_{id}, \quad (3.62)$$

where we assume perfect alignment $f_d = \tilde{f}_d$ and $\tau = \tilde{\tau}$. On the other hand, the cross-correlation terms depend on the actual value of both synchronization parameters and the spreading codes structure. For instance, GPS L1 C/A signal uses a Gold type sequence, and according to

$$\delta_{T_r; \mathcal{H}_1} = \frac{1}{R_{\mathbf{xx}}} \left| \underbrace{\frac{1}{K} \alpha_{id} \mathbf{d}_{id}(f_{d,id}, \tau_{id}) \mathbf{d}_{id}(\check{f}_d, \check{\tau})^H}_{\text{signal autocorrelation}} + \underbrace{\sum_{\substack{i=1 \\ i \neq id}}^A \frac{1}{K} \alpha_{id} \mathbf{d}_{id}(f_{d,id}, \tau_{id}) \mathbf{d}_i(\check{f}_d, \check{\tau})^H}_{(A-1) \text{ cross-correlations}} + \underbrace{\sum_{\substack{i=1 \\ i \neq id}}^{M_s} \frac{1}{K} \alpha_i \mathbf{d}_i(f_{d,i}, \tau_i) \mathbf{r}(\check{f}_d, \check{\tau})^H}_{(M_s-1)A \text{ cross-correlations}} \right|^2, \quad (3.60)$$

$$\delta_{T_r; \mathcal{H}_0} = \frac{1}{R_{\mathbf{xx}}} \left| \underbrace{\sum_{\substack{i=1 \\ i \neq id}}^A \frac{1}{K} \alpha_{id} \mathbf{d}_{id}(f_{d,id}, \tau_{id}) \mathbf{d}_i(\check{f}_d, \check{\tau})^H}_{(A-1) \text{ cross-correlations}} + \underbrace{\sum_{\substack{i=1 \\ i \neq id}}^{M_s} \frac{1}{K} \alpha_i \mathbf{d}_{d,i}(f_{d,i}, \tau_i) \mathbf{r}(\check{f}_d, \check{\tau})^H}_{(M_s-1)A \text{ cross-correlations}} \right|^2. \quad (3.61)$$

[Gol67], the maximum cross-correlation value is⁶

$$|R_{\mathbf{ss}_\perp}| \leq 2^{\frac{N_r+2}{2}} + 1, \quad (3.63)$$

where N_r is the number of bits of the shift registers used by the Gold code generator. For GPS L1 C/A, $N_r = 10$ and $(|R_{\mathbf{ss}_\perp}|) \leq 65$. Table 3.1 shows some cross-correlation absolute values and their associate cumulative probabilities of occurrence, extracted from [Kap96, p.115]. Interestingly, neither the maximum nor the average cross-correlation value depend on the satel-

Cumulative probability of occurrence	Cross-Correlation for any two codes [dB]
0.23	-23.9
0.5	-24.2
1	-60.2

Table 3.1: GPS L1 C/A code Maximum cross-correlation power (zero Doppler Differences).

lites' *id*. On the contrary, Galileo E1-C uses a memory code, and the maximum and average cross-correlation values have to be computed directly from the sequences extracted from the reference document [Und10]. The empirical cross-correlation mean value of Galileo E1 codes was computed by the author obtaining $\{ |R_{\mathbf{ss}_\perp}|_{\text{Galileo E1}} \} = -24.9$ dB.

Due to the low cross-correlation values of the GNSS PRN sequences, it is possible to approximate $\delta_{\mathcal{H}_1}$ and $\delta_{\mathcal{H}_0}$ in the case of GPS L1 C/A signal as:

$$\delta_{\mathcal{H}_1} = \frac{|\alpha_{id}|^2}{R_{\mathbf{xx}}} + \frac{(MA-1)|\bar{\alpha}_i|^2|R_{\mathbf{ss}_\perp}|^2}{R_{\mathbf{xx}}} \simeq \frac{|\alpha_{id}|^2}{R_{\mathbf{xx}}} \quad (3.64)$$

$$\delta_{\mathcal{H}_0} = \frac{(MA-1)|\bar{\alpha}_i|^2|R_{\mathbf{ss}_\perp}|^2}{R_{\mathbf{xx}}} \leq \frac{(MA-1)10^{-23.9}}{R_{\mathbf{xx}}}, \quad (3.65)$$

where $\bar{\alpha}_i$ is the mean amplitude of the received satellites, and assuming $P_n \gg P_s$ it is possible to approximate $\frac{|\alpha_{id}|^2}{R_{\mathbf{xx}}} \simeq \rho$. According to the results, it is possible to identify that the presence of extra satellite codes on the local replica does not have an important effect in $\delta_{\mathcal{H}_1}$ if all the received satellites have similar CN0. Since the effect of extra satellites is present on the variance of the underlying complex Gaussian distribution that forms the chi-square distribution of $T(\mathbf{x})$, it is possible to write

$$\sigma_{T_r}^2 = \frac{A}{2K}, \quad (3.66)$$

where the variance increases quadratically with the number of satellites present in local replica, and consequently, the SNR is reduced in a factor $10 \log(A)$.

Summarizing, it is possible to write the distributions for both hypotheses:

⁶The symbol \perp is used here to indicate that the cross-correlation includes all the possible cases, which are the mismanagement of two signals with the same *id* but different synchronization parameters and/or two signals with different *id*'s.

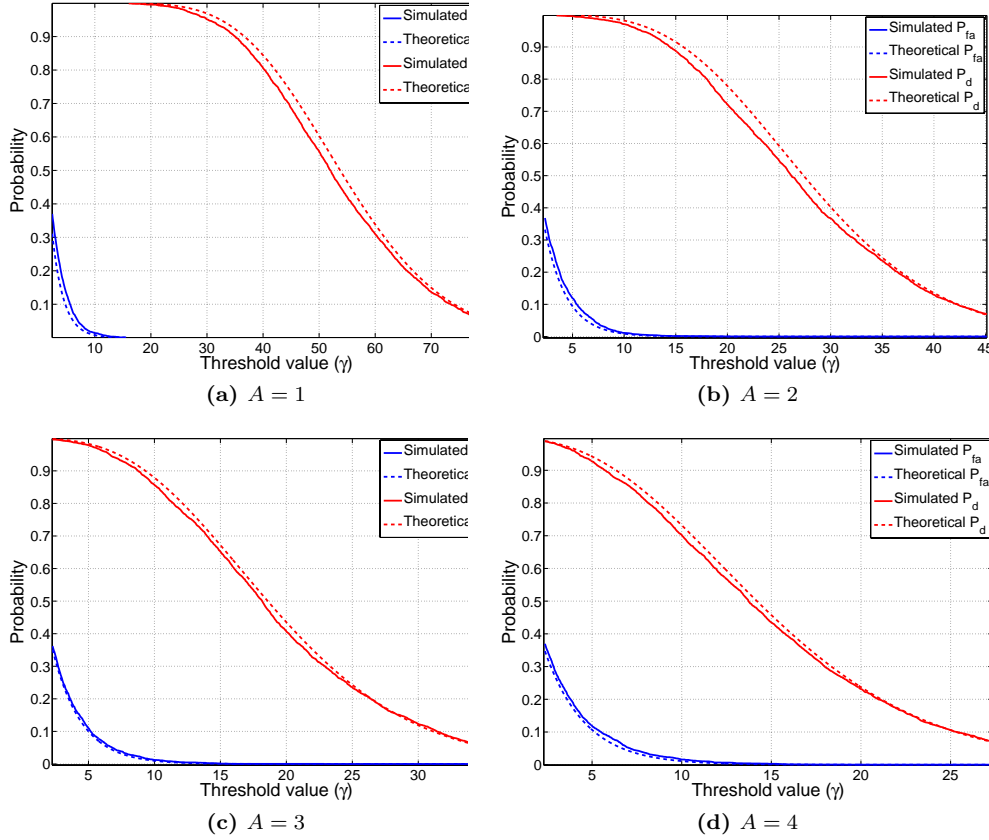


Figure 3.6: False alarm and detection probabilities for GPS L1 C/A signal with $M_s = 12$ visible satellites and a receiving signal to noise density ratio of $\text{CN0} = 44$ dB-Hz, and different number of satellites (A) present in local replica.

$$T_r(\mathbf{x}) \sim \begin{cases} \chi_2^2(\delta_{T_r; \mathcal{H}_1}), & \text{in } \mathcal{H}_1, \\ \chi_2^2(\delta_{T_r; \mathcal{H}_0}), & \text{in } \mathcal{H}_0, \end{cases} \quad (3.67)$$

and the expressions for both P_d and P_{fa} as

$$P_d(\gamma) = Q_1 \left(\frac{\sqrt{\delta_{T_r; \mathcal{H}_1}}}{\sigma_{T_r}}, \frac{\sqrt{\gamma}}{\sigma_{T_r}} \right) \quad (3.68)$$

$$P_{fa}(\gamma) = Q_1 \left(\frac{\sqrt{\delta_{T_r; \mathcal{H}_0}}}{\sigma_{T_r}}, \frac{\sqrt{\gamma}}{\sigma_{T_r}} \right), \quad (3.69)$$

Q_1 is the generalized Marcum Q-function [Pro00] of order 1. Fig. 3.6 shows the evolution of P_d and P_{fa} versus the threshold value and for different number of satellites in local replica.

3.4.4 Simulation results

The proposed acquisition function $T_r(\mathbf{x})$ was tested by means of MC simulations. Both GPS L1 C/A and Galileo E1 baseband signals with $M_s = 12$ visible satellites plus noise were generated, as described in (3.1). For the sake of simplicity, in GPS simulations, all satellites have the nominal CN0 available on the Earth surface according to [Win10], which is 44 dB-Hz. On the other hand, in Galileo simulations, due to the longer code period and thus, higher acquisition gain, the CN0 is reduced to 38 dB-Hz to be able to observe the performance effect of adding satellites to the local replica. The synchronization parameters f_d and τ were uniformly distributed along

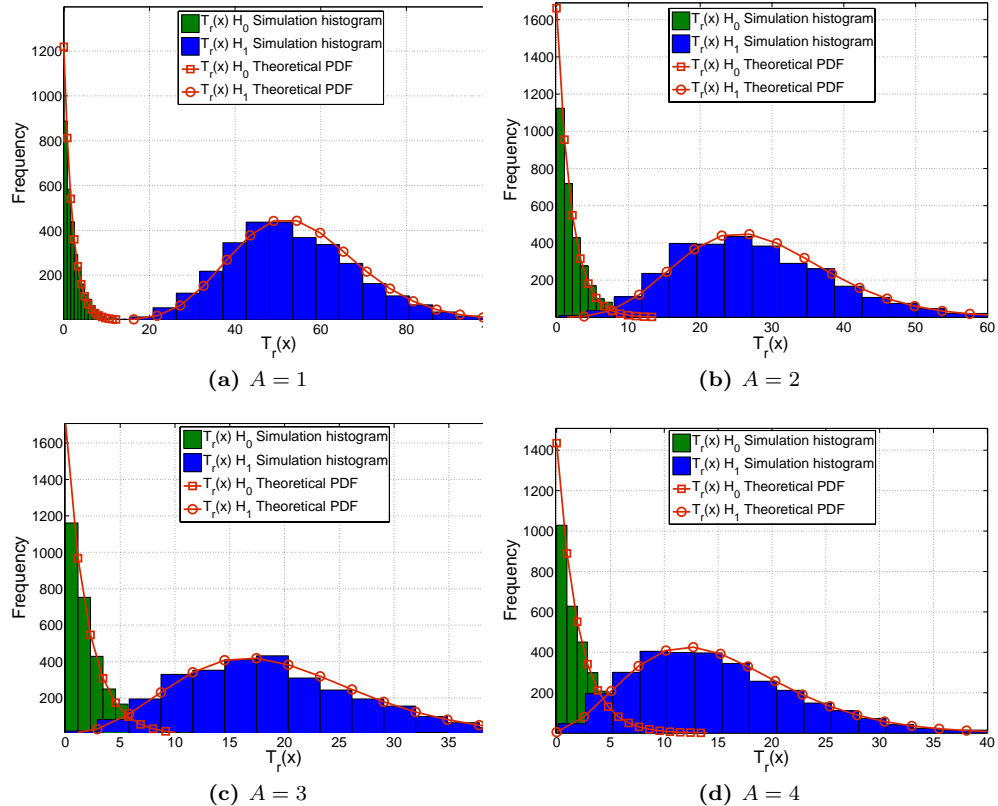


Figure 3.7: Histogram of $T_r(x|\mathcal{H}_1)$ and $T_r(x|\mathcal{H}_0)$ test statistics for GPS L1 C/A signal with $M_s = 12$ visible satellites and a receiving signal to noise density ratio of CN0 = 44 dB-Hz, and different number of satellites (A) present in local replica.

$[-5000, +5000]$ Hz. and $[0, 1]$ ms for GPS, and $[0, 4]$ ms for Galileo, respectively, with the constraint that all the satellites must have different synchronization parameters. The augmented satellite signal replica described in (3.49) was generated for both hypotheses with different number of local satellites. In the simulator, we set perfect alignment of the augmented local replica with one of the received satellites. That is, $\check{f}_d = f_d$ and $\check{\tau} = \tau$ as the true values in the \mathcal{H}_1 hypothesis, since we are interested in the performance of the detector itself. Although in practice, a grid search method should be used to estimate the synchronization parameters, as is described in Chapter 2. \mathcal{H}_0 is defined as the misalignment $(f_{d,id}, \tau_{id}) \neq (\check{f}_d, \check{\tau})$ of $\mathbf{r}(\check{f}_d, \check{\tau})$ with all the visible satellites. Table 3.2 shows a summary of the simulation parameters. Regarding Galileo E1 signal, we simulated acquisition with the E1-B signal component. Due to the fact that the Galileo E1 signal carries half the power on each B and C components, the minimum CN0 required by the acquisition process CN0 is increased in 3 dB with respect to the equivalent GPS C/A signal acquisition. Both simulated GPS L1 C/A and Galileo E1 signals contained neither navigation data nor tiered codes.

Parameter	Value	Units
Visible satellites (M_s)	12	–
Sampling frequency (f_s)	8	Msps
Baseband bandwidth	4	MHz.
GPS Signal	L1 C/A	–
Galileo Signal	E1	–
Acquisition time (GPS)	1	ms
Acquisition time (Galileo)	4	ms
Local satellites (A)	1 – 6	–
GPS Satellite's CN0	44	dB-Hz.
Galileo Satellite's CN0	38	dB-Hz.
Realizations (GPS)	3000	–
Realizations (Galileo)	2000	–
\mathcal{H}_1 hypothesis	$(f_{d,id}, \tau_{id}) = (\hat{f}_d, \hat{\tau})$	–
\mathcal{H}_0 hypothesis	$(f_{d,id}, \tau_{id}) \neq (\hat{f}_d, \hat{\tau})$	–

Table 3.2: Simulation parameters.

The proposed acquisition test function (3.50) was simulated for both hypotheses and for different number of satellites in the local replica. Fig. 3.7 shows the histograms in both hypotheses for different values of A . As the number of satellites present in the local replica increases, it also increases the variance and thus the two histograms became overlapped, which limits the performance of the acquisition.

The performance reduction can be observed quantitatively in the ROC curves of Fig. 3.8. The theoretical models are aligned with the histogram simulations. The theoretical ROC curves are slightly optimistic because we did not modeled the effect of the limited baseband bandwidth in the simulation.

The applicability of the joint acquisition strategy and the maximum number of satellites present in the local replica will depend basically on the satellites' CN0. In an open field scenario, the degradation of the acquisition sensibility can be affordable, and, specially in a software defined receiver, valuable resources and power could be saved using the proposed acquisition method. However, in low CN0 situations the GNSS receiver will need to switch to high sensitivity acquisition. Galileo codes have higher joint acquisition applicability potential due to their better correlation and cross-correlation properties.

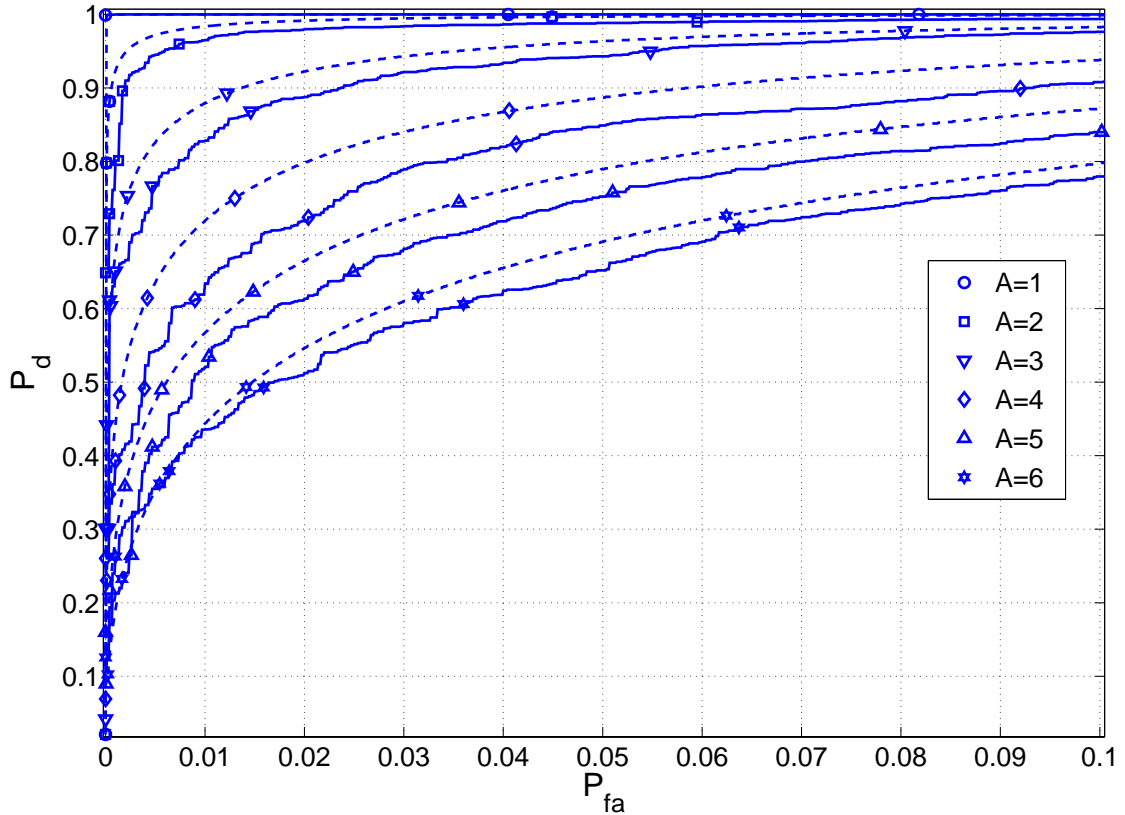


Figure 3.8: GPS L1 C/A $\text{CN}0 = 44 \text{ dB-Hz}$. Simulated and theoretical (dashed) acquisition ROC

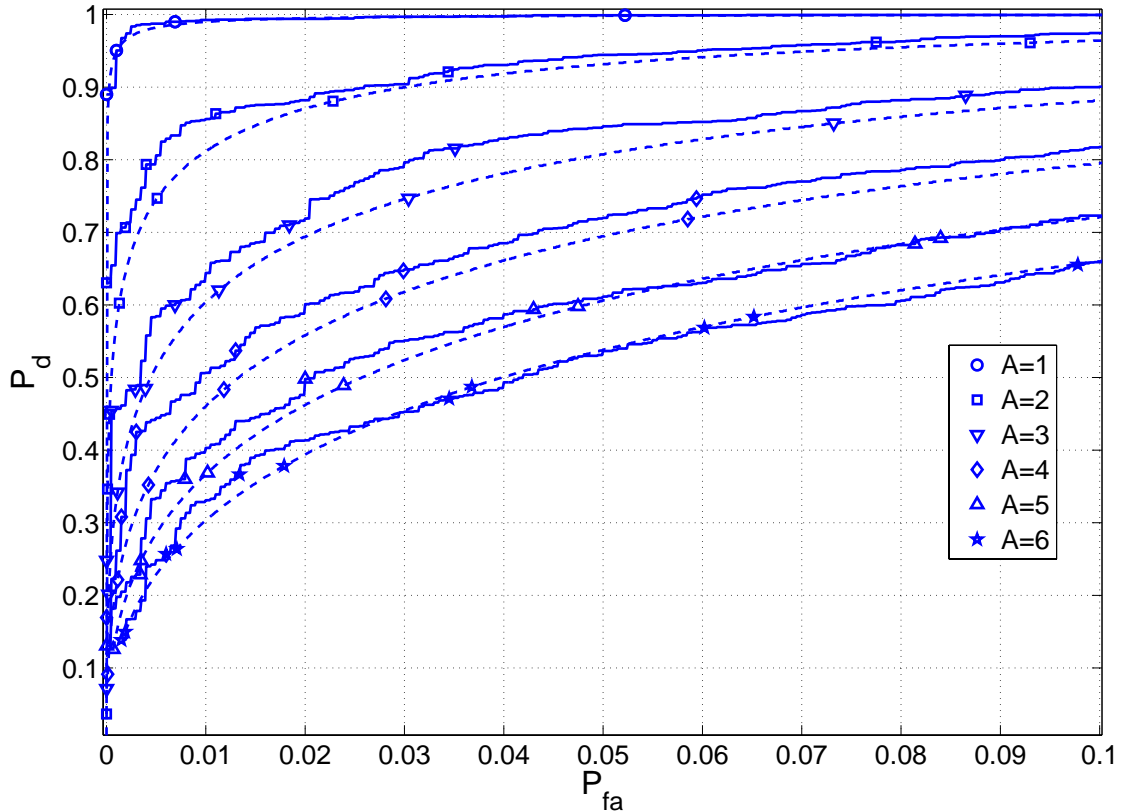


Figure 3.9: Galileo E1 $\text{CN}0 = 38 \text{ dB-Hz}$. Simulated and theoretical (dashed) acquisition ROC curves for different number of satellites present in the local signal replica.

3.5 The effect of the receiver bandwidth

The performance expressions derived in previous sections for selected acquisition algorithms does not take into account an important parameter of every GNSS receiver: the front-end bandwidth. This section is devoted to give some insight into the bandwidth effect on the acquisition process. The receiver RF front-end and the sampling frequency limits the available signal bandwidth and consequently, both the signal and noise power are also affected. The acquisition pre-correlation SNR can be defined as follows

$$\rho_{acq} = \frac{P'_s}{P'_n}, \quad (3.70)$$

where P'_s and P'_n are the satellite signal and the noise baseband power, respectively. Using the convolution property $\mathcal{F}\{x[n] * y[n]\} = X(f)Y(f)$, where $\mathcal{F}\{x[n]\} = X(f)$ is the Discrete-Time Fourier Transform (DTFT) of $x[n]$, and the Parseval's theorem [Pro00], P'_s can be computed as:

$$P'_s = P_s \int_{-\frac{1}{2}}^{\frac{1}{2}} G_s(f) |H_{FE}(f)|^2 df, \quad (3.71)$$

where $G_s(f)$ is the normalized Power Spectral Density (PSD) of the discrete-time satellite signal and $H_{FE}(f)$ is the DTFT of the front-end baseband-equivalent impulse response $h_{FE}[n]$. Considering the Galileo E1 MBOC(6,1,1/11) [Und10], the analytical expression for the PSD can be found in [Bet99]:

$$G_s(f) = \frac{10}{11} G_{BOC(1,1)} + \frac{1}{11} G_{BOC(6,1)} \\ G_{BOC(m,n)}(f) = \frac{1}{T_c} \left(\frac{\sin(\frac{\pi f F_s T_c}{N_B}) \sin(\pi f F_s T_c)}{\pi f F_s \cos(\frac{\pi f F_s T_c}{N_B})} \right)^2, \quad (3.72)$$

where $N_B = 2\frac{m}{n}$ is the BOC(m,n) modulation index relation. Using the same approach, the noise power can be expressed as:

$$P'_n = \frac{N_0}{2} B_{FE} \int_{-\frac{1}{2}}^{\frac{1}{2}} |H_{FE}(f)|^2 df, \quad (3.73)$$

where N_0 [W-Hz] is the antenna noise density and B_{FE} is the front-end pass-band bandwidth. Fig. 3.10 shows the theoretical and the simulated dependence of the SNR with the front-end cutoff frequency.

Considering now a band-limited satellite signal $\mathbf{d}' = \mathbf{d} * \mathbf{h}_{FE}$, using the Wiener-Khinchine theorem and the convolution properties [Pro00, p.72]⁷, we can compute the cross-correlation between \mathbf{d}' and \mathbf{d} as

$$R_{\mathbf{d}'\mathbf{d}}[\tau] = \int_{-\frac{1}{2}}^{\frac{1}{2}} G_s(f) H_{FE}(f) e^{j2\pi f \tau} df, \quad (3.74)$$

and therefore $P_s R_{\mathbf{d}'\mathbf{d}}[0] = P_s \int_{-0.5}^{0.5} G_s(f) H_{FE}(f) df$. Interestingly, if we consider the baseband-equivalent $H_{FE}(f)$ response of an ideal band-pass filter, then

$$P_s R_{\mathbf{d}'\mathbf{d}}[0] = P_s \int_{-\frac{B_{FE}}{2f_s}}^{\frac{B_{FE}}{2f_s}} G_s(f) df = P'_s. \quad (3.75)$$

Clipping the bandwidth of the received satellite signal makes also the correlation peak wider. Fig. 3.11 shows the evolution of MBOC(6,1,1/11) $R_{\mathbf{d}'\mathbf{d}}[\tau]$ function for different baseband bandwidths. It is obtained the 80% of the despread gain using $B_{FE} = 4$ MHz, which is the minimum usable passband bandwidth according to Nyquist-Shannon theorem [Pro00].

⁷ $\Phi_{yx}(\tau) = \int_{-\infty}^{\infty} \Phi_{yx}(f) e^{j2\pi f \tau} df$ and $\Phi_{yx}(f) = \Phi_{xx}(f)H(f)$, where $\Phi_{xy}(\tau)$ is the cross-correlation function and $\Phi_{xy}(f)$ is the cross-power density spectrum of two stochastic processes $x[n]$ and $y[n]$ defined as $y[n] = x[n] * h[n]$, respectively.

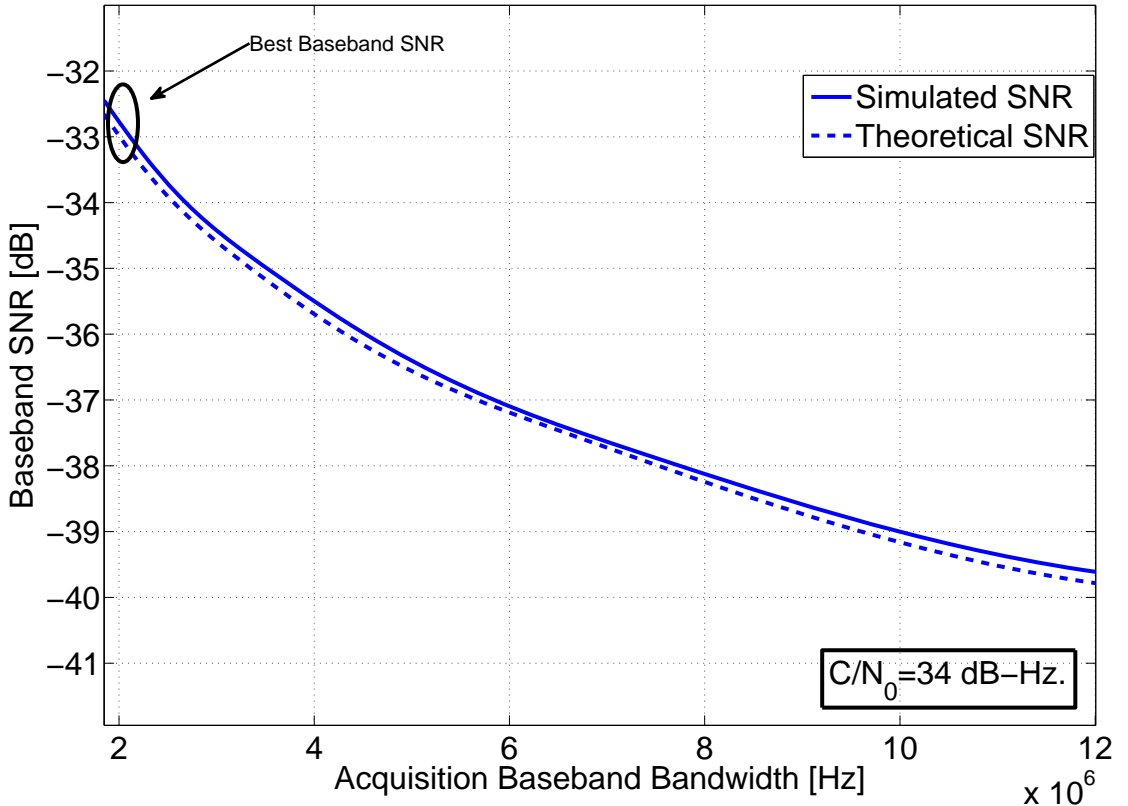


Figure 3.10: Theoretical and simulated Galileo E1 MBOC(6,1,1/11) SNR versus the baseband bandwidth.

Recalling the performance expressions for the GLRT-based detector of Section 3.3.2.3, front-end bandwidth affects both the P_{fa} and P_d and consequently the ROC is affected according to the values of the $\chi_2^2(\delta_{T_{GL}})$ non-centrality parameter (3.38)

$$\delta_{T_{GL}} = \frac{|\mu_{R_{xd}}|^2}{R_{xx}} \simeq \frac{P'_s}{P'_n} = \rho_{acq}, \quad (3.76)$$

which implies that the maximization of ρ_{acq} maximizes the acquisition performance.

3.5.1 Simulation results

In order to verify the theoretical study of the front-end bandwidth effects on the acquisition, the false alarm and the detection probabilities of the GLRT test function $T(\mathbf{x})_{GL}$ defined in (3.33) were evaluated by means of MC simulations. The results are valid for a single cell acquisition and can be easily extended to multiple cell search strategies [Bor06]. The simulated signal contains a single Galileo satellite on the E1 link with MBOC(6,1,1/11) modulation [Und10]. The sampling frequency F_s and T_{acq} was set to $F_s = 50\frac{1}{T_c} = 51.150$ MHz and $T_{acq} = 4$ ms, respectively. The ideal RF Band-Pass Filter (BPF) bandwidth was set to $B_{RF} = 24.552$ MHz. The baseband signal was filtered again with a 5 coefficients Butterworth Low-Pass Filter (LPF) with different 3 dB cutoff bandwidths. Each of the MC simulations contains 2000 independent realizations.

The effect of the acquisition bandwidth was simulated for a constant $CN_0 = 44$ dB-Hz and bandwidth sweep $2 \leq B_{bb} \leq 13$ MHz. Using the MC results, the P_{fa} and P_d curves and the ROC can be found in Fig. 3.12 and Fig. 3.13, respectively. The theoretical performance was computed using the analytical expressions for the P_{fa} and P_d defined in (3.42) and (3.43), respectively. Notice that there are slight differences between the theoretical curves and the MC curves. The main reason is the difference between the implemented LPF filter frequency response and the

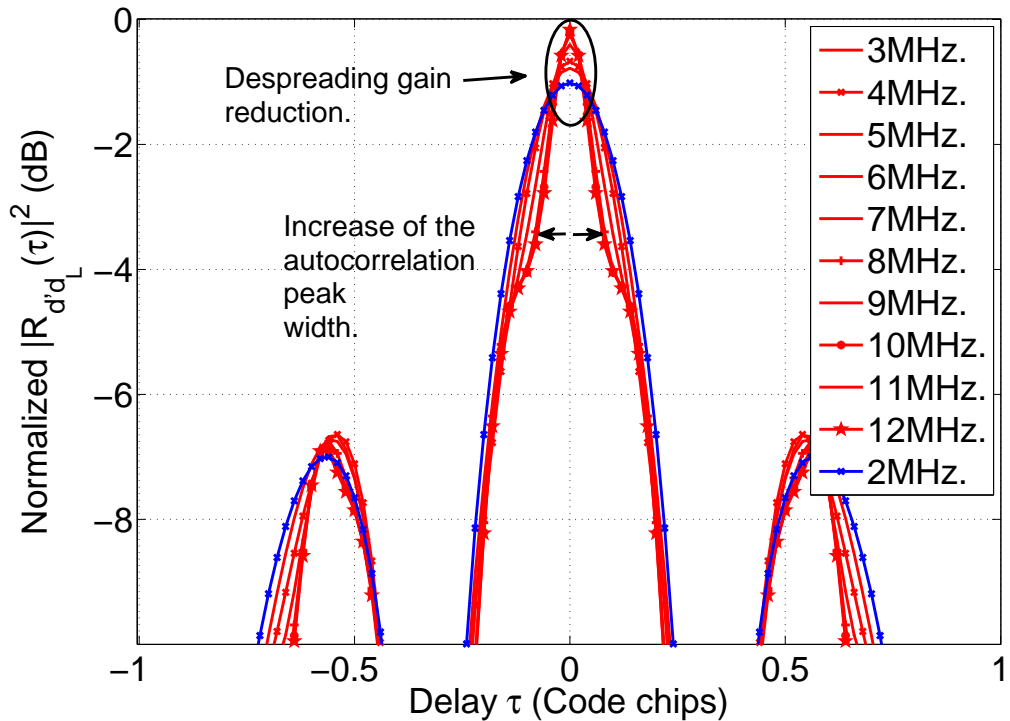


Figure 3.11: Autocorrelation of Galileo E1 MBOC(6,1,1/11) signal with the local replica versus τ for different baseband bandwidths.

theoretical LPF frequency response used in (3.71) and (3.73). Despite this effect, the results were aligned with the theory and the acquisition with the minimum bandwidth obtained the best performance.

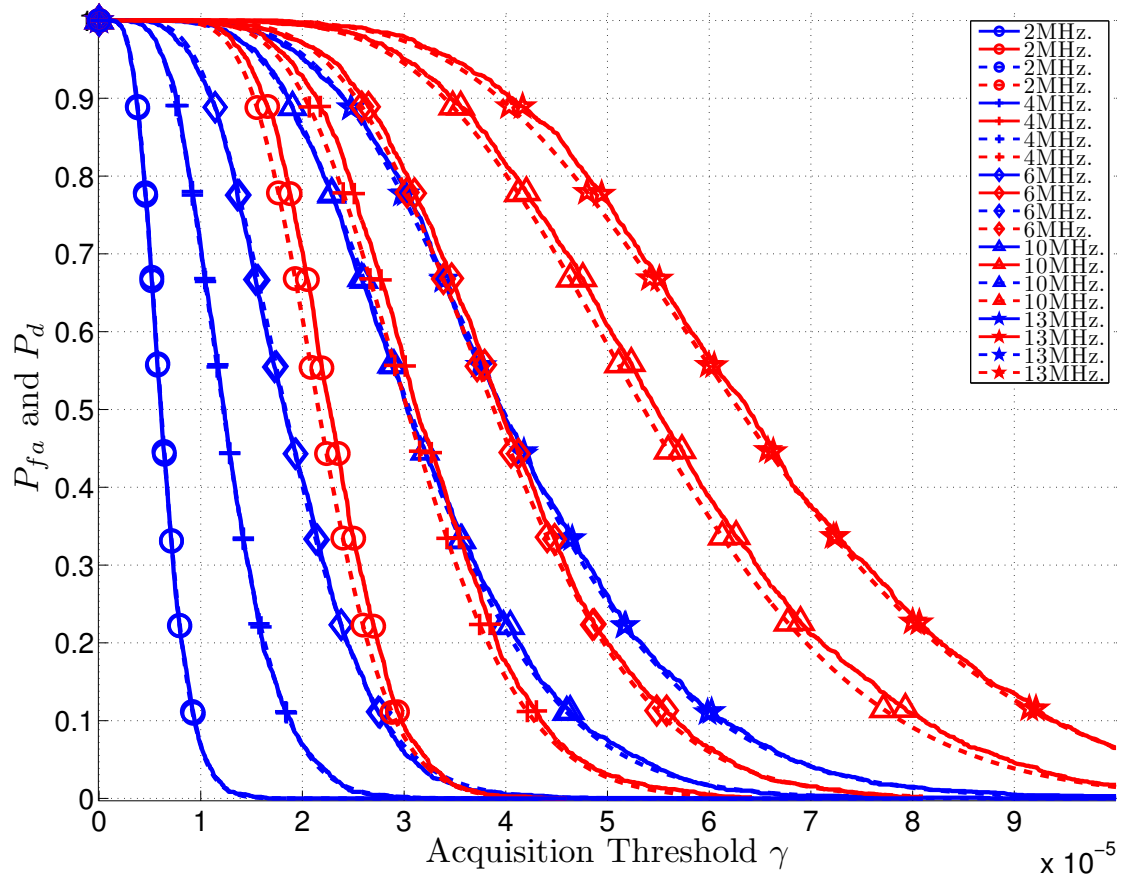


Figure 3.12: Theoretical and simulated P_{fa} (blue) and P_d (red) for single-antenna GLRT acquisition over different baseband bandwidths.

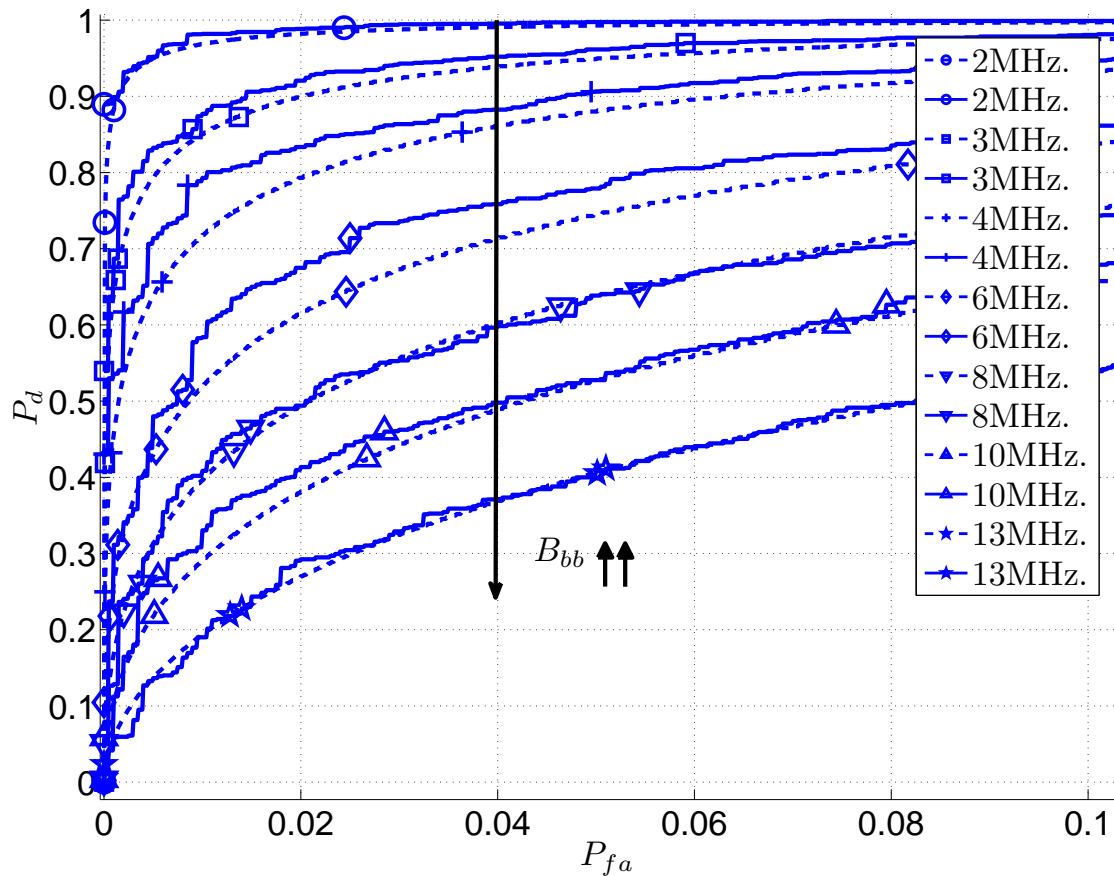


Figure 3.13: Theoretical and simulated ROC for single-antenna GLRT acquisition over different baseband bandwidths.

3.6 Acquisition schemes

In recent times, a number of papers and PhD Theses related to the GNSS acquisition have arisen. Most of them deal with the acquisition of new composite signals in single-antenna receivers. The combination of the pilot and data channel in the acquisition process improves the sensitivity due to the fact that it uses all the available signal power [Und10, Win08, Win05]. Major contributions include O'Driscoll's PhD Thesis [O'D07] where the GNSS acquisition problem is addressed both from the estimation and the detection theory. The optimum detector is derived and some acquisition techniques referred as coherent detector, non-coherent combining detector and differentially coherent detector are analyzed. In Shanmugam's PhD Thesis [Sha08] a similar approach was examined, focusing on the detection of the GPS L1 C/A signal. The proposed detectors are derived from the coherent MF detector using the GLRT and the concept of *estimator-correlator*.

In contrast, Borio [Bor08] focuses on the evaluation of a pre-defined Cross-Ambiguity Function (CAF) which is equivalent to the non-coherent MF detector. The use of the FFT parallelization techniques and the cell and the decision domain probabilities for the selected CAF are given. The second part of Borio's work is devoted to the effects of the interferences in the CAF and its mitigation techniques. An approach to combined acquisition of two GPS signal links can be found in Gernot's PhD Thesis [Ger09] and once again, the non-coherent MF is pre-defined as the detection test function.

In order to identify the available acquisition test functions, it is possible to classify them in categories using the presented detection theory framework. The acquisition schemes hereafter are defined for a pair of f_d and τ , referred to as *single cell* evaluation, and for a single captured signal block, referred to as *single-dwell* evaluation. The acquisition algorithm is in charge of creating a search strategy to test for the presence of a satellite signal in the whole signal space. In [Bor06] it can be found an analysis of the performance impact for different search strategies.

- **Coherent Matched Filter (CMF) detector :** derived in 3.3.1, assumes θ known, is the optimum detector according to the NP criterion. It is used as the upper bound for detectors' performance [Kay98]. Hereafter is recalled the test function:

$$T_{\text{MF}}(\mathbf{x}) = \Re\left\{\mathbf{x}\mathbf{s}_\theta^H\right\} > \gamma, \quad (3.77)$$

where \mathbf{s}_θ is defined in (3.15). Fig. 3.14 shows a conceptual block diagram.

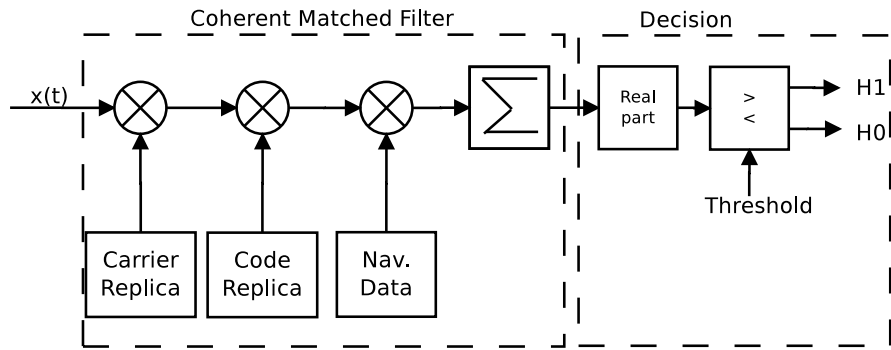


Figure 3.14: CMF detector block diagram.

- **Non-coherent Matched Filter (NCMF):** assumes all the receiver signal parameters known except the carrier phase ϕ_i . The test function can be derived from the *energy detector* [Kay93, Sch91] or applying the GLRT with $\hat{\phi}_{ML}$. It can be considered a simplification of the GLRT detector. The drawback is the complexity of designing a dynamic threshold, since the test statistic output depends both on the receiver's signal and noise power. The test function can be written as:

$$T_{\text{NCMF}}(\mathbf{x}) = |\mathbf{x}\mathbf{s}_\theta|^2 > \gamma, \quad (3.78)$$

where \mathbf{s}_θ is defined in (3.15). The NCMF is a non-coherent detector, and thus is affected by the terms of the real and imaginary noise components. It turns into an SNR loss with respect to the CMF. A recent work on this effect can be found in [Str07]. On the other hand, the influence of residual navigation data modulation can be found in [Dav88] and [O'D07].

Fig. 3.15 shows a conceptual block diagram.

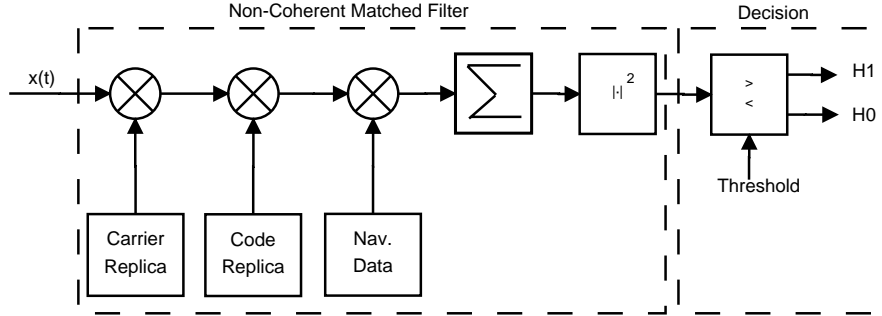


Figure 3.15: NCMF detector block diagram.

- **GLRT detector:** derived in Section 3.3.2, it assumes all the signal parameters unknown except the signal structure. The test function is based on the GLRT [Kay98, Sch91]. The test statistic is CFAR which makes the threshold γ independent of the noise power. Hereafter is recalled the test function

$$T_{\text{GL}}(\mathbf{x}) = \max_{f_d, \tau} \left\{ \frac{|\hat{R}_{\mathbf{x}\mathbf{d}}(f_d, \tau)|^2}{\hat{R}_{\mathbf{xx}}} \right\} > \gamma, \quad (3.79)$$

where $\hat{R}_{\mathbf{x}\mathbf{d}}(f_d, \tau)$ and $\hat{R}_{\mathbf{xx}}$ are defined in (3.25). Fig. 3.16 shows a conceptual block diagram.

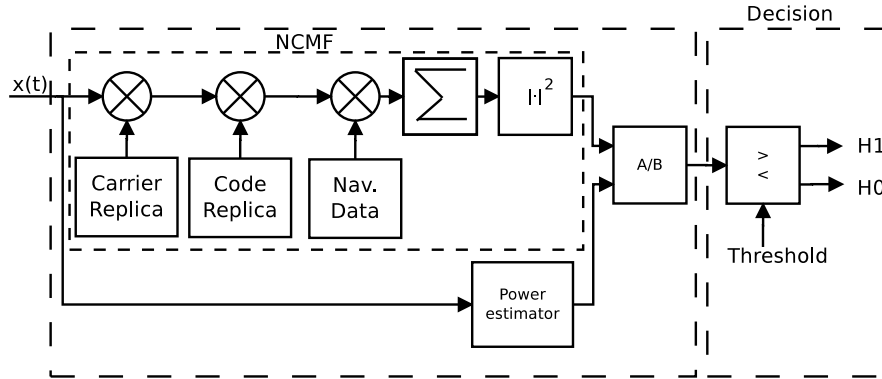


Figure 3.16: GLRT detector block diagram.

- **Post-Correlation Non-coherent Detector (PCND):** hybrid detector that uses a coherent MF block, usually with the length of one PRN code period, and a second block which is an energy detector. The energy detector accumulates non-coherently the correlations results. The target is to obtain a detector not affected by the unknown navigation data. The PCND is one of the widely used acquisition detectors for the GPS L1 C/A signal. Hereafter can be found the test function:

$$T_{\text{PCND}}(\mathbf{x}) = \max_{f_d, \tau} \sum_{t=nkT_s}^{N_{\text{dw}}} |\hat{R}_{\mathbf{x}\mathbf{d}}(t, f_d, \tau)|^2 > \gamma, \quad (3.80)$$

where N_{dw} is the number of dwells and $\hat{R}_{\mathbf{x}\mathbf{d}}(t, f_d, \tau)$ is defined in (3.25). The performance analysis is available in the GNSS literature [Par96, Kap05, Tsu00, Bor07]. A recent comparative of non-coherent detectors can be found in [Bor09a]. A variation of PCND was

presented in LoPresti's work [Pre09], where a Moving Average (MA) block was attached to the detector output to mitigate the effects of the secondary code sign transitions of new Galileo signals. Fig. 3.17 shows a possible block diagram.

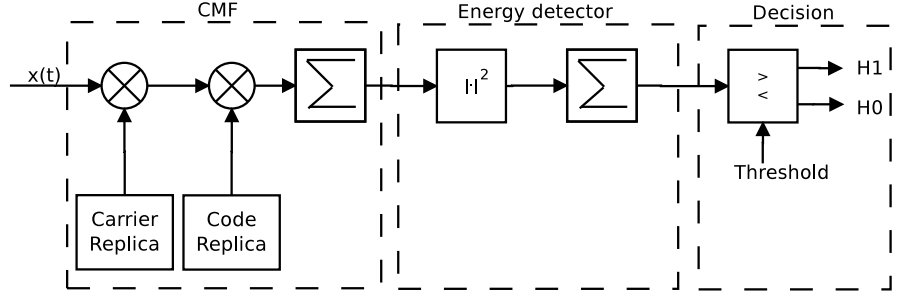


Figure 3.17: PCND detector block diagram.

- **Post-correlation differential detector (PCDD):** uses a different approach to avoid the navigation data phase variation. The first part of the detector is a coherent MF as in PCND. The concept consists of correcting the phase shifts of the MF using a delayed and conjugate output. It can also be viewed as a phase estimator. The reported power loss due to navigation data in GPS C/A signal is approximately 0.45 dB [Sch04]. A general derivation of PCDD is presented in [Ped04]. An extensive analysis of PCDD detector can be found in [O'D07]. Hereafter is recalled the test function

$$T_{\text{PCDD}}(\mathbf{x}) = \max_{f_d, \tau} \sum_{t=nkT_s}^{N_{\text{dw}}} \hat{R}_{\mathbf{x}\mathbf{d}}(t, f_d, \tau) \hat{R}_{\mathbf{x}\mathbf{d}}^*(t - KT_s, f_d, \tau) > \gamma, \quad (3.81)$$

where N_{dw} is the number of dwells and $\hat{R}_{\mathbf{x}\mathbf{d}}(t, f_d, \tau)$ is defined in (3.25). In Shanmugam's PhD Thesis, a novel detector based both on PCDD and PCND is proposed [Sha08]. Fig. 3.18 shows a possible block diagram for an implementation of this approach.

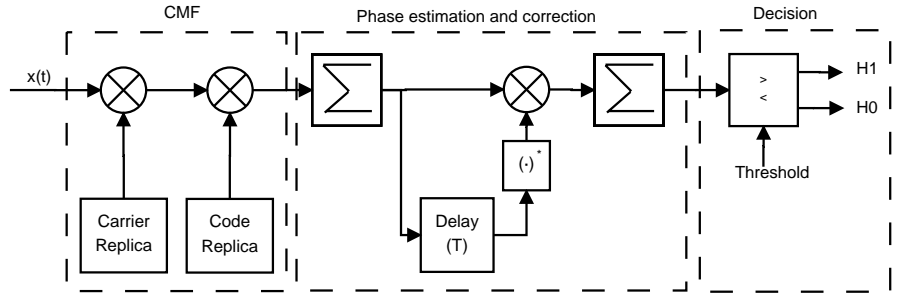


Figure 3.18: PCDD detector block diagram.

- **Pre-correlation differential detector (PDD) :** uses the same approach of PCDD but the phase correction is applied before the coherent MF block. The estimator works at chip period level instead of a PRN period level. It was first presented in [Coe92], were it is also referred to as *chip level differential detection* [Chu95]. Hereafter is recalled the test function:

$$T_{\text{PDD}}(\mathbf{x}) = \max_{f_d, \tau} \frac{1}{K} \sum_{k=0}^{K-1} \dot{\mathbf{x}}(k) \dot{\mathbf{d}}(k, \tau) > \gamma, \quad (3.82)$$

where $\dot{\mathbf{x}}(k) = \mathbf{x}_k \mathbf{x}_{k-L}^*$ and $\dot{\mathbf{d}}(k) = \mathbf{d}_k(\tau) \mathbf{d}_{k-L}^*(\tau)$, with $L = \lceil \frac{T}{T_s} \rceil$, and the vector subindex denotes the k -th vector component. Fig. 3.19 shows a possible block diagram. The delay T is a design parameter.

Assuming that both the carrier phase and the telemetry symbols are highly correlated over the PRN chip period, the detector's test statistic is independent of these signal parameters,

reducing the synchronization parameters search to τ . Unfortunately, the detector does not provide a Doppler frequency estimation.

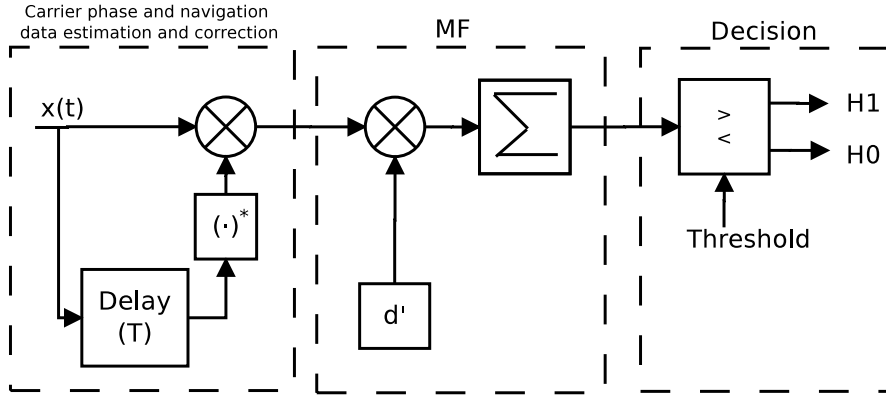


Figure 3.19: PDD detector block diagram.

An interesting comparative of the different detectors can be found in Table 3.3 extracted from [Sha08]. The sensitivity to dynamics is defined as the performance loss caused by a variation of the satellite signal parameters during the acquisition interval, and the SNR loss is defined as the equivalent signal SNR loss with respect to the optimal detector, which is the CMF.

Table 3.3: Comparative of detectors

Detector	Sensitivity to dynamics	SNR loss
CMF	High	Minimal
ICMF	Moderate	Moderate $\simeq 3$ dB
PCND	Moderate	Moderate
PCDD	Minimal	High
PDD	Minimal	High

Furthermore, the mentioned detectors have been applied to composite signals and a number of combination strategies can be found in the literature. A complete comparative of coherent, non-coherent and differentially coherent techniques applied to new GNSS signals can be found in [Bor09b]. Addressing the modernized GPS, the L5 signal acquisition algorithms are derived by Hegarty in [Heg03] and [Heg06], where optimal acquisition of GPS L5 signal was presented.

3.7 Performance degradation sources

In previous Sections the signal acquisition theoretical background was presented for a single-antenna receiver. The detector's performance expressions were obtained without considering any source of signal degradation except the thermal noise. In a real-life receiver, the acquisition operation is sensitive to a variety of performance degradation sources:

- **Signal attenuation:** a GNSS ground based user can experience weak signal conditions for a significant portion of time. The foliage attenuation or the urban canyon environment [Klu03, Ste05] are examples of weak signal environments. Furthermore, in the interior of a building the attenuation can reach values above 30 dB [Eng01, Mac02]. In these situations, the $CN0$ could take values around 17 dB-Hz. Increase the acquisition sensitivity requires to extend the integration time to raise the satellite signal from the noise floor [Tsu00]. The counterpart is the increase of T_{acq} and thus, the increase of TTFF. High Sensitivity GNSS (HS-GNSS) receivers can extend the integration time up to several seconds [Wat05].
- **Interferences:** the presence of an interference reduces the SNR and may destroy the optimality of Gaussian-based acquisition algorithms due to the non-Gaussian noise distribution arising from interference [Kay98]. Strong Continuous Wave Interference (CWI) or

narrow band interferences can seriously degrade the acquisition performance, or even completely block the acquisition [Des04]. Sources of GNSS interferences are briefly described in Section 2.2.3.

- **Multipath propagation:** reflection, diffraction and shadowing can produce long term and short term signal fadings due to constructive and destructive signal additions at the receiver point [War06]. The effect is similar to a time-varying signal attenuation during the acquisition integration time. It is important to highlight that, according to the results of a well-known measurement campaign and GNSS channel model [Ste04], the differential delays and Doppler shifts presented by the signal replicas with respect to the LOS are within a chip period and a Doppler bin. Consequently, the shift of the correlation peak caused by the multipath does not distort the acquisition coarse estimation of the synchronization parameters, even in indoor environments, as is stated in [En05].
- **Navigation data:** the presence of data modulation on the ranging signal limits the coherent integration time due the undetermined phase-shift transitions. In modern GNSS signals, a separate date-free pilot channel can be used to extend the coherent integration time. Non-coherent and differentially coherent techniques can also be used to extend the integration time, but they are subject to a sensitivity loss. In Section 3.6 it can be found several schemes of these techniques.
- **Receiver movement:** it causes the variation of the synchronization parameters during the integration time, becoming another limiting factor to be taken into account. High-dynamics applications are affected by this effect; examples include the use of a GNSS receiver for spacecraft navigation [Win04] or aviation applications.
- **Receiver clock drift:** it causes an apparent variation of the code delay and limits the coherent integration time. According to [Gag08], it was experimentally proven that, when ultra-stable oscillators are used (with Allan deviation frequency stability in the order of $\sigma_{osc}(\tau) \leq 1 \cdot 10^{-11}$), coherent integrations up to $T_{acq} = 60$ s are possible, without relevant losses due to the stability of the local frequency source. Furthermore, for this integration time, it is also reported that the satellite clock instabilities and atmospheric errors are essentially negligible.

From the aforementioned sources, the most harmful one is the presence of interferences in the received signal, as mentioned in Section 2.2.3. In this line, the noise term in (3.1) can be redefined as

$$\mathbf{n}(t) = \boldsymbol{\eta}(t) + \mathbf{i}(t), \quad (3.83)$$

where $\boldsymbol{\eta}(t)$ is the thermal noise contribution and $\mathbf{i}(t)$ is the interference contribution that can assume different expressions depending on the interference source. A suitable metric to evaluate the interference effects on signal acquisition, carrier tracking, and telemetry demodulation is the post-correlation SNIR [Kap05]. The acquisition SNIR is defined as

$$\varrho = \frac{\mathbb{E}^2\{T(\mathbf{x})\}}{\text{var}\{T(\mathbf{x})\}}, \quad (3.84)$$

where $T(\mathbf{x})$ is the acquisition test statistic. Particularizing $T(\mathbf{x})$ for the coherent MF correlator as in the optimum detector (3.16) and considering that the satellite signal is completely aligned with the local replica, the SNIR expression can be written as [Bor08]

$$\varrho_{MF} = \frac{P_s \left(\int_{-0.5}^{0.5} G_s(f) H_{FE}(f + f_d) df \right)^2}{\frac{N_0}{4} f_s \frac{1}{K} \int_{-0.5}^{0.5} |H_{FE}(f + f_d)|^2 G_s(f) df + \frac{P_i}{2} \frac{1}{K} \int_{-0.5}^{0.5} \bar{G}_i(f) G_s(f) df}, \quad (3.85)$$

where P_s is the baseband signal power, $G_s(f)$ is the normalized PSD of the satellite signal, $H_{FE}(f)$ is the DTFT of the baseband-equivalent front-end impulse response, N_0 is the thermal noise density at the front-end output, P_i is the baseband interference power, and $\bar{G}_i(f) =$

$\frac{1}{P_i} G_i(f + f_d) |H_{FE}(f + f_d)|^2$ is the normalized PSD of the filtered interference. Taking into account that $\frac{K}{T_s} = T_{acq}$ it is possible to re-arrange (3.85) in terms of *CN0* and *IN0* as

$$\varrho_{MF} = 2T_{acq} \left(\frac{P_s}{N_0} \right) \frac{\left(\int_{-0.5}^{0.5} G_s(f) H_{FE}(f + f_d) df \right)^2}{\frac{1}{2} \int_{-0.5}^{0.5} |H_{FE}(f + f_d)|^2 G_s(f) df + \left(\frac{P_i}{N_0} \right) \int_{-0.5}^{0.5} \bar{G}_i(f) G_s(f) df}. \quad (3.86)$$

By applying the same analysis for the GLRT detector defined in (3.33), the SNIR expression can be written as [Bet00]

$$\varrho_{GL} = T_{acq} \left(\frac{P_s}{N_0} \right) \frac{\left| \int_{-0.5}^{0.5} G_s(f) H_{FE}(f + f_d) df \right|^2}{\frac{1}{2} \int_{-0.5}^{0.5} |H_{FE}(f + f_d)|^2 G_s(f) df + \left(\frac{P_i}{N_0} \right) \int_{-0.5}^{0.5} \bar{G}_i(f) G_s(f) df} + 1. \quad (3.87)$$

The interference reduces the acquisition SNIR according to the Spectral Separation Coefficient (SSC) defined as [Bet02]

$$k_d = \int_{-0.5}^{0.5} \bar{G}_i(f) G_s(f) df, \quad (3.88)$$

which represents the projection of the normalized interference PSD over the normalized local code PSD. The more overlapped interference spectrum with the satellite signal spectrum, the more degradation is expected, specially if the overlap occurs at or near the maximum of the satellite signal PSD. In [Kap05] can be found a complete analysis of these effects using SSC metrics and considering the spectral characteristics of the interference, as defined in Section 2.2.3.

The GNSS Radio Frequency Interference (RFI) detection and mitigation has been addressed in several works. For instance, [War94] presents GPS sources of interference and their mitigation techniques. In [Bas03] the AGC was used as a possible interference mitigation tool. Even, new acquisition algorithms were specifically designed to deal with interferences, like the multi-correlation differential detection reported in [Sha07]. A recent CWI interference mitigation technique was presented in [Bal08b]. This technique identifies the satellites affected by the interference using both the satellite Doppler and the CWI frequency estimation in order to exclude them from the PVT solution, improving the receiver performance.

By far, one of the most successful RFI mitigation technique in single-antenna GNSS receivers is the use of notch filters to remove the unwanted signals prior to the traditional GNSS signal processing blocks. Notch filters are designed to excise the energy contained in the spectrum frequencies affected by interferences at expense of removing also a small fraction of the satellite signal spectrum. This side-effect limits the applicability of such filters to the mitigation of narrowband interferences, such as CWI.

According to [Bor08], the most important CWI mitigation notch-filters based algorithms can be classified in:

- adaptive transversal time-domain FIR filters,
- FFT-based FIR filters,
- constrained poles and zeros Infinite Impulse Response (IIR) notch filters,
- unconstrained zeros IIR notch filters.

Pulsed interferences can also be mitigated with adaptive filters, as reported in [Rai06]. However, the problem of wideband interferences remain unsolved, and the performance of these techniques is compromised in low SNR situations [Fu02]. All the aforementioned techniques have in common the use of time/frequency domain diversity to discriminate the unwanted signals. There is still another degree of freedom that can be exploited to mitigate the interferences; the spatial diversity.

In that sense, a single-antenna receiver can partially mitigate interferences using special antenna design to reject low elevation signals, such as the “choke-ring” antenna [Kun03], however this technique has inherent limitations and high-elevation interferences cannot be attenuated.

The application of antenna arrays to GNSS technology has been recently considered as a possible solution to the GNSS interference problem. Antenna arrays provide the spatial diversity needed to discriminate interference signals without the drawbacks of the time and frequency domain techniques. The array-based acquisition for interference mitigation is extensively discussed in the next Chapter, where novel algorithms are presented and analyzed.

3.8 Summary

This Chapter described the basics of the detection theory framework that is used to solve the GNSS acquisition problem from a single-antenna receiver point of view, providing the necessary background for our proposed improvements. Using the NP approach, both the optimum and the GLRT detector were derived and their performance was analyzed for the problem at hand.

The mass market demands a multi-system receiver with short TTFF, low cost per unit, and low power consumption. In response to this requirement, a novel acquisition algorithm was introduced in Section 3.4, intended to jointly acquire a set of GNSS satellites and thus, to dramatically reduce both the acquisition time and the required computational resources.

The new acquisition method shows a potential reduction of the 50% of the required correlators with a loss of 3 dB of SNR using a two-satellite local signal replica and a reduction of 66% with a loss of 5 dB of SNR with three-satellite local signal replica. These values are compared to the conventional acquisition method that uses a single satellite local signal replica. In an open field scenario, the reduction of the acquisition SNR can be affordable, and, specially in a software defined receiver, valuable resources and power could be saved using the proposed method.

Closed form performance expressions were obtained for all the detectors, and the effects of the front-end bandwidth were analyzed. In the analysis, it was shown that the acquisition performance is directly proportional to the available SNR, and consequently, it is inversely proportional to the front-end bandwidth. This conclusion is made patent taking into account that the PSD of the GNSS signals contains more than the 80 % of their power in the region between the first spectral nulls. The result is the opposite in the tracking performance, which is known to be directly proportional to the front-end bandwidth [Kap05].

In Section 3.6 a set of acquisition schemes used to increase the acquisition sensitivity or overcome the navigation data uncertainties were briefly introduced to exemplify a representative set of acquisition algorithms suitable for real-life GNSS receivers. Finally, in the last Section of this Chapter, the acquisition perturbations were discussed, focusing the analysis in the effects of the interferences as well as defining a performance metric. The existing single-antenna mitigation techniques and their limitations were emphasized, concluding that the effects of wideband interferences remains as one of the most harmful sources of acquisition performance degradation or even create a complete denial of the GNSS service situation.

Going further, the next Chapter explores the applicability of antenna arrays to obtain a possible solution to the acquisition interference problem.

The results presented in this Chapter were partially published in:

- [Arr10b] J. Arribas, C. Fernández-Prades, and P. Closas, “Receiver Operating Characteristic For Array-Based GNSS Acquisition”, *Proceedings of XVIII European Signal Processing Conference, EUSIPCO*, pp. 1082–1086, Aalborg, Denmark, August 2010.
- [Arr10a] J. Arribas, P. Closas, and C. Fernández-Prades, “Joint acquisition strategy of GNSS satellites for computational cost reduction”, *Proceedings of the 5th ESA Workshop on Satellite Navigation Technologies, NAVITEC’2010*, Noordwijk, The Netherlands, December 2010.

Chapter 4

Antenna Array-Based GNSS Signal Acquisition for Interference Mitigation

Let me tell you the secret that has led me to my goal. My strength lies solely in my tenacity.

Louis Pasteur.

ANTENNA array-based receivers can benefit from spatial-domain processing and thus, incorporate the spatial information to the time and frequency information in order to improve their performance [Mon80].

In GNSS, the capability of antenna arrays to reject interferences or jamming signals and the theoretical multipath mitigation potential is usually applied to signal tracking operation, and there exists an extensive bibliography on this topic, see, e.g., [Sec05, Sec00, FP06, Myr01, Kon07, O'B08, FP09b]. In tracking operation, beamforming algorithms may have access to an estimation of the satellite signal synchronization parameters, Direction Of Arrivals (DOAs), and array attitude [Tsu00]. Tracking depends on signal acquisition, and there is a number of situations in which the acquisition process can fail due to strong interferences, as stressed in Section 3.7, or high signal attenuation. Taking into account that the acquisition sensitivity is usually higher than tracking sensitivity [Mit08], it becomes a performance bottleneck specially in harsh environments [Des04, Bor10]. Surprisingly, to the best of our knowledge, the application of antenna arrays to GNSS signal acquisition has not yet received much attention.

In order to protect the acquisition stage and the rest of receiver operations, it is possible to filter out the interfering signals by performing a simple null-steering beamforming, such as a blind power minimization algorithm, as is described in [Zol95] and [Car05]. In [Tor08], it is proposed a method that recursively suppresses the interfering signals, which are considered stronger than the desired ones. However, these works neither analyze explicitly the acquisition performance improvement nor define an acquisition test statistic.

In the literature it can be found a number of papers considering DS-CDMA signal acquisition by antenna arrays with the assumption of the receiver capability to estimate the signal DOA, see, e.g., [Wan03, Pus08]. In these papers, the DOA is estimated using either a pilot signal or including the DOA in the acquisition search grid, and then use the estimated DOA information to recombine the outputs of correlators or matched filters. In a GNSS receiver, due to the extremely low receiving power of the satellite signals, it is difficult to estimate the DOA before signal correlation (or despread), and DOA-based beamforming techniques usually need a calibrated array. A receiver that performs a warm, hot or an assisted acquisition can provide prior DOA information to the acquisition algorithm, but the cold acquisition remains unprotected.

The work reported in [Ami05] proposes a solution based on Spectral Self-Coherence Restoral (SCORE) beamforming that maximizes the cross-correlation between the beamforming output signal and a reference signal generated from a different block of the received data and, consequently, it can be used before signal acquisition. Unfortunately, the SCORE algorithm does not provide an estimation of the signal synchronization parameters.

A DS-CDMA acquisition method that combines a Minimum Mean Square Error (MMSE) beamformer with independent matched filters on each antenna element was presented in [Zha03] and its performance in jamming environments was analyzed in [Pus07]. However its derivation and the associated analysis were done for DS-CDMA communication systems, and it does not account for the particularities of the GNSS signal acquisition.

In this Chapter, the antenna array-based acquisition process is addressed taking a statistical approach in contrast to the beamforming approach that is deterministic. Following an outline analogous to the single-antenna acquisition analysis of the previous Chapter, here, the NP detection theory in the form of GLRT is used to obtain a new detector which is able to mitigate uncorrelated interferences. The key statistical feature is the assumption of an arbitrary and unknown covariance noise matrix, which attempts to capture the statistical behavior of the interferences and other non-desirable signals, while exploiting the spatial dimension provided by antenna arrays.

It is included an analysis of the statistical properties of the detector, its interference mitigation capability, and the effect of realistic conditions in the receiver performance, providing the preliminary hardware requirements for a possible implementation of the algorithm. In addition, the theoretical performance bound for a single-dwell GNSS signal acquisition, referred to as the performance of the *clairvoyant detector* [Kay98] is derived for the GNSS array-signal model.

Realistic conditions include signal quantization effects caused by ADCs, the effect of limited coherent acquisition time, and the impact of signal synchronization errors. These are analyzed in terms of the covariance matrix estimation errors and the acquisition performance. Theoretical results are supported by extensive MC simulations for several scenarios.

The Chapter is organized as follows: Section 4.1 presents the antenna array signal model and Section 4.2 derives the optimum detector. Section 4.3 presents the GLRT detector applied to GNSS acquisition, as well as proposing a novel test statistic. The detector's properties are analyzed and closed form expressions for the performance are given considering two possible scenarios: the white noise assumption is considered in Section 4.4 and the colored noise assumption is considered in Section 4.5. The later includes a complete analysis of the interference rejection capability of the algorithm based on a geometric interpretation of signal and interference subspaces.

Towards a possible implementation, Section 4.7 analyzes the performance of the proposed algorithm under realistic conditions, namely finite sample size, signal quantization effects, and signal synchronization errors. Section 4.8 validates the theoretical results by Monte Carlo simulations simulations and Section 4.9 concludes the Chapter.

4.1 Array signal model

Considering that a signal from a GNSS satellite is received with a N -element antenna array, the discrete baseband signal model is defined as:

$$\mathbf{X}(t) = \mathbf{h}\mathbf{d}(t, f_d, \tau) + \mathbf{N}(t), \quad (4.1)$$

where

- $\mathbf{X}(t) = [\mathbf{x}(t - (K - 1)T_s) \dots \mathbf{x}(t)] \in \mathbb{C}^{N \times K}$ is referred as the *space-time data matrix*, where $\mathbf{x}(t) = [x_1(t) \dots x_N(t)]^T$ is defined as the antenna array baseband snapshot, each row corresponds to one antenna, and K is the number of captured snapshots. The acquisition time can be defined as $T_{acq} = KT_s$ where $F_s = 1/T_s$ is the sampling frequency.

- $\mathbf{h} = [h_1 \dots h_N]^T \in \mathbb{C}^{N \times 1}$ is the non-structured channel model, which includes both the channel and the array response. The channel vector assumes the role of the spatial signature but does not impose any structure. The arbitrary structure of \mathbf{h} , which is considered constant during T_{acq} , is not only parameterized by the satellite signal DOA and the location of antennas, but also may include other unmodeled phenomena.
- $\mathbf{d}(t, f_d, \tau) = [s(t - (K - 1)T_s - \tau)e^{j2\pi f_d(t-(K-1)T_s)} \dots s(t - \tau)e^{j2\pi f_d t}] \in \mathbb{C}^{1 \times K}$ is the discrete version of the satellite baseband signal at the front-end output after the digital downconversion, with normalized power and known structure $s(t)$, defined in Chapter 2, received with a propagation delay τ and a Doppler frequency f_d , which are also considered constant during T_{acq} . In our analysis, without losing generality, a telemetry-free signal is considered.
- $\mathbf{N}(t) = [\mathbf{n}(t - (K - 1)T_s) \dots \mathbf{n}(t)] \in \mathbb{C}^{N \times K}$ is a complex, circularly symmetric Gaussian vector process with a zero-mean, temporally white and spatially colored with an arbitrary (also unknown) spatial covariance matrix $\mathbf{Q} \in \mathbb{C}^{N \times N}$ that models both the noise and other non desirable terms such as interferences:

$$\mathbb{E}\{\mathbf{n}(t_n)\} = \mathbf{0}, \quad (4.2)$$

$$\mathbb{E}\{\mathbf{n}(t_n)\mathbf{n}^T(t_m)\} = \mathbf{0}, \quad (4.3)$$

$$\mathbb{E}\{\mathbf{n}(t_n)\mathbf{n}^H(t_m)\} = \sigma^2 \mathbf{I} + \boldsymbol{\Sigma} = \mathbf{Q}\delta_{t_n,t_m}, \quad (4.4)$$

where it is considered that the noise have double-sided spectral density $\sigma^2 = \frac{N_0}{2}$ W/Hz, \mathbf{I} stands for the identity matrix, $\boldsymbol{\Sigma}$ models the covariance matrix of interferences and spurious signals, and δ_{t_n,t_m} stands for the Kronecker delta.

For notation convenience, in the rest of the Chapter we group the received satellite signal parameters in a vector $\boldsymbol{\theta}_a = [\mathbf{h}^T, f_d, \tau]^T$. We focus on a single satellite's signal, thus neglecting the contribution of the rest of satellites. This assumption is realistic, considering that GNSS systems use pseudorandom noise codes with a high processing gain and relatively small cross-correlation among satellite codes. Therefore, the influence of other satellites can be considered as Gaussian noise and included in the thermal noise term since those signals are well below the noise floor [Tsu00].

4.2 Antenna array optimum detector

By applying the detection theory analogously as in the single-antenna acquisition of Section 3.2, it is possible to define the array signal model for both hypotheses as

$$\mathcal{H}_1 : \mathbf{X}(t) = \mathbf{h}\mathbf{d}(t, f_d, \tau) + \mathbf{N}(t), \quad (4.5)$$

$$\mathcal{H}_0 : \mathbf{X}(t) = \mathbf{N}(t), \quad (4.6)$$

and using the NP approach, the LRT is defined as

$$L(\mathbf{X}) = \frac{p(\mathbf{X}; \mathbf{Q}, \boldsymbol{\theta}_a, \mathcal{H}_1)}{p(\mathbf{X}; \mathbf{Q}, \mathcal{H}_0)} > \gamma, \quad (4.7)$$

where γ is the detection threshold, $p(\mathbf{X}; \mathbf{Q}, \boldsymbol{\theta}_a, \mathcal{H}_1)$ and $p(\mathbf{X}; \mathbf{Q}, \mathcal{H}_0)$ stand for the conditional PDF of \mathbf{X} for \mathcal{H}_1 and \mathcal{H}_0 hypotheses, respectively. The PDF for \mathcal{H}_1 is parameterized by the signal parameter vector $\boldsymbol{\theta}_a$ and by the covariance noise matrix \mathbf{Q} , and the PDF for \mathcal{H}_0 is parametrized only by \mathbf{Q} .

If it is assumed that all the parameters of the LRT are known, then the optimum detector from (4.5) and (4.6) arises:

$$L_{NP}(\mathbf{X}) = \frac{\frac{1}{\pi^{NK} \det(\mathbf{Q})^K} \exp \left\{ -\text{Tr}\{\mathbf{Q}^{-1}\mathbf{C}\} \right\}}{\frac{1}{\pi^{NK} \det(\mathbf{Q})^K} \exp \left\{ -\text{Tr}\{\mathbf{Q}^{-1}\hat{\mathbf{R}}_{xx}\} \right\}} > \gamma, \quad (4.8)$$

where the PDF of a complex multivariate Gaussian vector for K snapshots is used. The matrix \mathbf{C} is defined as¹:

$$\mathbf{C} = \hat{\mathbf{R}}_{\mathbf{xx}} - \hat{\mathbf{r}}_{\mathbf{xd}} \mathbf{h}^H - \mathbf{h} \hat{\mathbf{r}}_{\mathbf{xd}}^H + \mathbf{h} \hat{R}_{\mathbf{dd}} \mathbf{h}^H, \quad (4.9)$$

and the autocorrelation and cross-correlation matrices are:

- $\hat{\mathbf{R}}_{\mathbf{xx}} = \frac{1}{K} \mathbf{X} \mathbf{X}^H$ is the estimation of the autocorrelation matrix of the array snapshots, also known as the Sample Covariance Matrix (SCM), if $E\{\mathbf{x}\} = \mathbf{0}$,
- $\hat{\mathbf{r}}_{\mathbf{xd}} = \frac{1}{K} \mathbf{X} \mathbf{d}^H$ is the estimation of the cross-correlation vector between the array snapshot matrix and the DS-CDMA signal,
- $\hat{R}_{\mathbf{dd}} = \frac{1}{K} \mathbf{d} \mathbf{d}^H$ is the estimation of the DS-CDMA signal autocorrelation. Considering that \mathbf{d} has normalized power, then it is possible to write $\hat{R}_{\mathbf{dd}} \simeq 1$.

Simplifying terms and by applying the natural logarithm in (4.8) the following expression is obtained:

$$\begin{aligned} \ln(L_{NP}(\mathbf{X})) &= \text{Tr}\{\mathbf{Q}^{-1}(\hat{\mathbf{R}}_{\mathbf{xx}} - \mathbf{C})\} \\ &= \text{Tr}\{\mathbf{Q}^{-1}(\hat{\mathbf{R}}_{\mathbf{xx}} - \hat{\mathbf{R}}_{\mathbf{xx}} + \hat{\mathbf{r}}_{\mathbf{xd}} \mathbf{h}^H + \mathbf{h} \hat{\mathbf{r}}_{\mathbf{xd}}^H - \mathbf{h} \hat{R}_{\mathbf{dd}} \mathbf{h}^H)\} \\ &= \text{Tr}\{\mathbf{Q}^{-1}(\hat{\mathbf{r}}_{\mathbf{xd}} \mathbf{h}^H + \mathbf{h} \hat{\mathbf{r}}_{\mathbf{xd}}^H - \mathbf{h} \hat{R}_{\mathbf{dd}} \mathbf{h}^H)\} > \ln(\gamma), \end{aligned} \quad (4.10)$$

where $\text{Tr}\{\cdot\}$ stands for the trace operator. The latter expression can be further simplified by grouping the non-data dependent terms in the threshold, obtaining

$$\ln(L_{NP}(\mathbf{X})) = \text{Tr}\{\mathbf{Q}^{-1}(\hat{\mathbf{r}}_{\mathbf{xd}} \mathbf{h}^H + \mathbf{h} \hat{\mathbf{r}}_{\mathbf{xd}}^H)\} > \ln(\gamma) + \mathbf{Q}^{-1} \mathbf{h} \mathbf{h}^H, \quad (4.11)$$

where the trace invariance under cyclic permutation property, $\text{Tr}\{\mathbf{ABC}\} = \text{Tr}\{\mathbf{CAB}\} = \text{Tr}\{\mathbf{BCA}\}$, for matrices with appropriate dimensions, and the complex number property $A + A^* = 2\Re\{A\}$ is used to get a compact expression for the test function

$$T_{NP}(\mathbf{X}) = \Re\{\mathbf{h}^H \mathbf{Q}^{-1} \hat{\mathbf{r}}_{\mathbf{xd}}\} > \underbrace{\frac{\ln(\gamma) + \mathbf{Q}^{-1} \mathbf{h} \mathbf{h}^H}{2}}_{\gamma'}. \quad (4.12)$$

This expression is the Generalized Matched Filter [Kay98].

Since the expression $z = \mathbf{h}^H \mathbf{Q}^{-1} \hat{\mathbf{r}}_{\mathbf{xd}}$ is a linear transformation of a complex Gaussian vector $\hat{\mathbf{r}}_{\mathbf{xd}}$, whose probability distribution is

$$\hat{\mathbf{r}}_{\mathbf{xd}} \sim \begin{cases} \mathcal{CN}(0, \frac{\mathbf{Q}}{K}), & \text{in } \mathcal{H}_0, \\ \mathcal{CN}(\mathbf{h} R_{\mathbf{dd}}, \frac{\mathbf{Q}}{K}), & \text{in } \mathcal{H}_1, \end{cases} \quad (4.13)$$

then, the moments of z are

$$E\{z; \mathcal{H}_0\} = \mathbf{h}^H \mathbf{Q}^{-1} E\{\hat{\mathbf{r}}_{\mathbf{xd}}; \mathcal{H}_0\} = 0, \quad (4.14)$$

$$E\{z; \mathcal{H}_1\} = \mathbf{h}^H \mathbf{Q}^{-1} E\{\hat{\mathbf{r}}_{\mathbf{xd}}; \mathcal{H}_1\} = \mathbf{h}^H \mathbf{Q}^{-1} \mathbf{h}, \quad (4.15)$$

$$\text{var}\{z\} = \mathbf{h}^H \mathbf{Q}^{-1} E\{\hat{\mathbf{r}}_{\mathbf{xd}} \hat{\mathbf{r}}_{\mathbf{xd}}^H; \mathcal{H}_0\} \mathbf{Q}^{-1} \mathbf{h} = \frac{\mathbf{h}^H \mathbf{Q}^{-1} \mathbf{h}}{K}, \quad (4.16)$$

where it is assumed the ideal case of $E\{\hat{R}_{\mathbf{dd}}\} \simeq 1$ and

$$E\{\hat{\mathbf{r}}_{\mathbf{xd}} \hat{\mathbf{r}}_{\mathbf{xd}}^H; \mathcal{H}_0\} = \text{var}\{\hat{\mathbf{r}}_{\mathbf{xd}}\} = \frac{\mathbf{Q}}{K}. \quad (4.17)$$

¹For the sake of notation simplicity, we drop the $\mathbf{d}(t, f_d, \tau)$ dependency on t , f_d and τ .

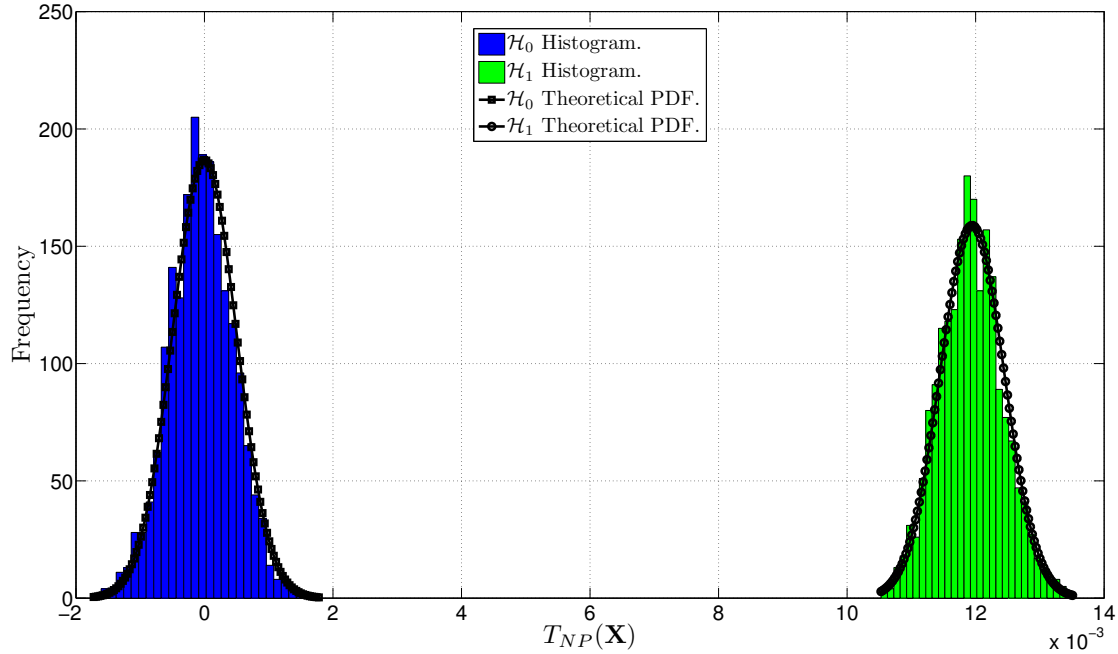


Figure 4.1: $T_{NP}(\mathbf{X})$ histogram and theoretical PDF in both \mathcal{H}_1 and \mathcal{H}_0 acquisition hypotheses for Galileo E1 signal acquisition simulation.

Now we have fully characterized $T_{NP}(\mathbf{X})$

$$T_{NP}(\mathbf{X}) \sim \begin{cases} \mathcal{N}(0, \sigma_{T_{NP}}^2), & \text{in } \mathcal{H}_0, \\ \mathcal{N}(\mu_{T_{NP}}, \sigma_{T_{NP}}^2), & \text{in } \mathcal{H}_1, \end{cases} \quad (4.18)$$

where

$$\mu_{T_{NP}}(\mathbf{Q}, \mathbf{h}) = \Re\{\mathbb{E}\{z; \mathcal{H}_1\}\} = \mathbf{h}^H \mathbf{Q}^{-1} \mathbf{h}, \quad (4.19)$$

and

$$\sigma_{T_{NP}}^2(\mathbf{Q}, \mathbf{h}, K) = \text{var}\{\Re\{z\}\} = \frac{\mathbf{h}^H \mathbf{Q}^{-1} \mathbf{h}}{2K}. \quad (4.20)$$

Notice that the optimum detector receives half of the input noise power. Closed form expressions for P_{fa} and P_d are

$$P_{fa}(\gamma') = 1 - \Phi\left(\frac{\gamma'}{\sigma_{T_{NP}}(\mathbf{Q}, \mathbf{h}, K)}\right), \quad (4.21)$$

and

$$P_d(\gamma') = 1 - \Phi\left(\frac{\gamma' - \mu_{T_{NP}}(\mathbf{Q}, \mathbf{h})}{\sigma_{T_{NP}}(\mathbf{Q}, \mathbf{h}, K)}\right), \quad (4.22)$$

where $\Phi(\cdot)$ stands for the CDF of the Gaussian distribution [Mui82]. The obtained performance is the upper bound performance for any NP detector. The theoretical PDFs obtained in (4.18) were validated by MC simulations. The test statistic histogram of $T_{NP}(\mathbf{X})$ was simulated for the acquisition of a Galileo E1 signal with $CN0 = 44$ dB-Hz in the absence of interfering signals and considering AWGN only, received with 8-elements circular antenna array. The baseband sampling frequency was set to 6 MHz and the acquisition bandwidth was set to 2 MHz. Each of the histograms contains 2000 realizations. Fig. 4.1 shows the results for both \mathcal{H}_1 and \mathcal{H}_0 hypotheses, concluding that the model is aligned with the simulations results.

4.2.1 Sensitivity analysis

In the previous analysis, the theoretical performance upper bound was obtained in terms of $\mu_{NP}(\mathbf{Q}, \mathbf{h})$ and $\sigma_{NP}(\mathbf{Q}, \mathbf{h}, K)$. The aim of this subsection is to associate the performance to

the satellite pre-correlation SNR, and consequently, obtain the sensitivity lower bound of any detector for a desired P_{fa} and P_d in the absence of interferences or jamming signals.

Before the analysis, it is useful to define the following terms:

- $\mathbf{h}^H \mathbf{h} = |\mathbf{h}|^2 = NP_s$ assuming that each antenna element is receiving the same signal power P_s and there are no coupling effects between antenna elements,
- $\sigma^2 = P_n$ is the thermal noise power present at each antenna element, and
- $\rho = \frac{P_s}{P_n}$ is the SNR at the antenna terminals.

In the sensitivity analysis, it is considered only the AWGN contribution, and thus, the correlation matrix is diagonal. Taking it into account, it is possible to rewrite the expressions for $\mu_{NP}(\mathbf{Q}, \mathbf{h})$ inserting $\mathbf{Q} = \sigma^2 \mathbf{I}$ in (4.19) and (4.20), obtaining:

$$\mu_{T_{NP}}(N, \rho) = \frac{NP_s}{P_n} = N\rho, \quad (4.23)$$

and

$$\sigma_{T_{NP}}^2(N, \rho, K) = \frac{NP_s}{2KP_n} = \frac{N\rho}{2K}, \quad (4.24)$$

which fully characterizes the sensitivity of the detector when there is no interferences or colored noise present.

A closed form expression for the sensitivity can be obtained inserting (4.23) and (4.24) in (4.22) and (4.21). The new expressions for the detector's performance are

$$P_{fa}(\gamma') = 1 - \Phi\left(\frac{\gamma'}{\sqrt{\frac{N\rho}{2K}}}\right) = Q\left(\frac{\gamma'}{\sqrt{\frac{N\rho}{2K}}}\right), \quad (4.25)$$

and

$$P_d(\gamma') = 1 - \Phi\left(\frac{\gamma' - N\rho}{\sqrt{\frac{N\rho}{2K}}}\right) = Q\left(\frac{\gamma' - N\rho}{\sqrt{\frac{N\rho}{2K}}}\right), \quad (4.26)$$

where $Q(\cdot)$ stands for the Q-function [Sim06]. Using the inverse of the Q-function and solving both equations for the threshold γ' , it is possible to write

$$\sqrt{\frac{N\rho}{2K}} Q^{-1}(P_{fa}) = \sqrt{\frac{N\rho}{2K}} Q^{-1}(P_d) + N\rho, \quad (4.27)$$

where finally, solving the equation for ρ we get

$$\rho_{min}(P_d, P_{fa}) = \frac{1}{2KN} (Q^{-1}(P_{fa}) - Q^{-1}(P_d))^2, \quad (4.28)$$

which is the minimum SNR required to obtain the desired performance. The sensitivity, consequently, can be written as the minimum CN0 needed to obtain the performance

$$\text{CN0}_{min}(P_d, P_{fa}) = 10 \log_{10}(\rho_{min}(P_d, P_{fa}) B_{RF}), \quad (4.29)$$

where B_{RF} is the RF front-end passband bandwidth.

Table 4.1 shows the relation of the sensitivity with the probabilities of false alarm and detection for an $N = 8$ element antenna array.

4.3 GLRT approach

In order to obtain a feasible array-based acquisition algorithm, it is assumed that the satellite synchronization parameters $\boldsymbol{\theta}_a$ are unknown by the receiver.

$T_{NP}(\mathbf{X})$	$P_d = 0.80$	$P_d = 0.90$	$P_d = 0.99$
$P_{fa} = 0.001$	22.12 dB-Hz	23.01 dB-Hz	24.92 dB-Hz
$P_{fa} = 0.01$	20.22 dB-Hz	21.42 dB-Hz	23.62 dB-Hz
$P_{fa} = 0.1$	16.82 dB-Hz	18.42 dB-Hz	21.42 dB-Hz

Table 4.1: Sensitivity of the clairvoyant detector for different P_{fa} and P_{fa} , with $N = 8$ elements circular antenna array, $f_s = 6$ MSPS, $T_{acq} = 4$ ms, and $\hat{R}_{dd} = 1$.

Considering the above conditions and the array signal model given in Section 4.1, it is possible to apply the NP criterion to obtain the GLRT test statistic, expressed as

$$L_{GL}(\mathbf{X}) = \frac{p(\mathbf{X}; \hat{\mathbf{Q}}_{\mathcal{H}_1}, \hat{\boldsymbol{\theta}}_a, \mathcal{H}_1)}{p(\mathbf{X}; \hat{\mathbf{Q}}_{\mathcal{H}_0}, \mathcal{H}_0)} > \gamma, \quad (4.30)$$

where $\hat{\boldsymbol{\theta}}_a$ is the MLE of $\boldsymbol{\theta}_a$ assuming that \mathcal{H}_1 is true. Since the covariance noise matrix is also unknown, $\hat{\mathbf{Q}}_{\mathcal{H}_1}$ and $\hat{\mathbf{Q}}_{\mathcal{H}_0}$ should be also obtained. A similar detector was developed in a well-known paper by E. J. Kelly [Kel86] for radar applications.

4.3.1 Maximum Likelihood Estimators

The derivation of the MLE of both $\boldsymbol{\theta}_a$ and $\mathbf{Q}_{\mathcal{H}_1}$ can be found in [FP06]; hereafter we recall only the most relevant results. We need to find the estimators that maximize $p(\mathbf{X}; \hat{\mathbf{Q}}_{\mathcal{H}_1}, \hat{\boldsymbol{\theta}}_a, \mathcal{H}_1)$. For this purpose, the negative log-likelihood function of a complex multivariate Gaussian snapshot vector \mathbf{x} for K observations can be defined as:

$$\Lambda_1(\mathbf{Q}_{\mathcal{H}_1}, \mathbf{h}, f, \tau) = \ln(\det(\mathbf{Q}_{\mathcal{H}_1})) + \text{Tr}\{\mathbf{Q}_{\mathcal{H}_1}^{-1} \mathbf{C}\}, \quad (4.31)$$

where we neglected the irrelevant constants and the matrix \mathbf{C} already defined in (4.9).

Minimizing (4.31) with respect to each parameter:

$$\hat{\mathbf{Q}}_{\mathcal{H}_1}, \hat{\mathbf{h}}, \hat{f}_d, \hat{\tau}|_{ML} = \arg \min_{\mathbf{Q}_{\mathcal{H}_1}, \mathbf{h}, f_d, \tau} \left\{ \Lambda_1(\mathbf{Q}_{\mathcal{H}_1}, \mathbf{h}, f_d, \tau) \right\}, \quad (4.32)$$

the resulting estimators are summarized here:

$$\hat{\mathbf{Q}}_{ML}^{\mathcal{H}_1} = \mathbf{C}|_{\mathbf{h}=\hat{\mathbf{h}}_{ML}, f=\hat{f}_{ML}, \tau=\hat{\tau}_{ML}} \quad (4.33)$$

$$\hat{\mathbf{Q}}_{ML}^{\mathcal{H}_0} = \hat{\mathbf{R}}_{\mathbf{xx}}, \quad (4.34)$$

$$\hat{\mathbf{h}}_{ML} = \hat{\mathbf{r}}_{\mathbf{xd}} \hat{R}_{dd}^{-1}|_{\mathbf{Q}_{\mathcal{H}_1}=\hat{\mathbf{Q}}_{\mathcal{H}_1,ML}, f=\hat{f}_{ML}, \tau=\hat{\tau}_{ML}}, \quad (4.35)$$

$$\hat{f}_{ML}, \hat{\tau}_{ML} = \arg \min_{f_d, \tau} \ln(\det(\mathbf{W}(f_d, \tau))), \quad (4.36)$$

where $\mathbf{W}(f_d, \tau) = \hat{\mathbf{R}}_{\mathbf{xx}} - \hat{\mathbf{r}}_{\mathbf{xd}}(f_d, \tau) \hat{R}_{dd}^{-1} \hat{\mathbf{r}}_{\mathbf{xd}}(f_d, \tau)^H$. Notice that $\mathbf{W}(f_d, \tau)$ is the SCM of the noise spatiotemporal matrix \mathbf{N} .

4.3.2 Acquisition test function

Using the obtained estimators, it is possible to express $L_{GL}(\mathbf{X})$ using (4.30) and the PDF of a complex multivariate Gaussian vector for K snapshots²

$$L_{GL}(\mathbf{X}) = \frac{\frac{1}{\pi^{NK} \det(\hat{\mathbf{Q}}_{\mathcal{H}_1})^K} \exp \left\{ -\text{Tr}\{\hat{\mathbf{Q}}_{\mathcal{H}_1}^{-1} \mathbf{C}\} \right\}}{\frac{1}{\pi^{NK} \det(\hat{\mathbf{Q}}_{\mathcal{H}_0})^K} \exp \left\{ -\text{Tr}\{\hat{\mathbf{Q}}_{\mathcal{H}_0}^{-1} \hat{\mathbf{R}}_{\mathbf{xx}}\} \right\}}, \quad (4.37)$$

²For the sake of simplicity of the notation, we drop the $(\cdot)_{ML}$ subindex in the estimations.

and, inserting (4.33) and (4.34) in (4.37), whereas neglecting the constant multiplicative terms, it is obtained a simplified equivalent test statistic function as

$$T_{\text{GL}}(\mathbf{X}) = \frac{\det(\hat{\mathbf{R}}_{\mathbf{xx}})}{\det(\mathbf{W}(\hat{f}_d, \hat{\tau}))} > \gamma. \quad (4.38)$$

Further simplification can be done using the Sylvester's determinant theorem $\det(\mathbf{A} + \mathbf{c}\mathbf{r}) = \det(\mathbf{A})(1 + \mathbf{r}\mathbf{A}^{-1}\mathbf{c})$ for any invertible matrix \mathbf{A} and column and row vectors \mathbf{c} and \mathbf{r} , respectively, with appropriate dimensions. Resulting in

$$T_{\text{GL}}(\mathbf{X}) = \frac{\det(\hat{\mathbf{R}}_{\mathbf{xx}})}{\det(\hat{\mathbf{R}}_{\mathbf{xx}})(1 - \hat{\mathbf{r}}_{\mathbf{xd}}^H(\hat{f}_d, \hat{\tau})\hat{R}_{\mathbf{dd}}^{-1}\hat{\mathbf{R}}_{\mathbf{xx}}^{-1}\hat{\mathbf{r}}_{\mathbf{xd}}(\hat{f}_d, \hat{\tau}))} > \gamma. \quad (4.39)$$

This expression contains the MLE for f_d and τ defined in (4.36). Inserting the ML minimization in (4.39) leads to the final test statistic expression:

$$T_{\text{GL}}(\mathbf{X}) = \max_{f_d, \tau} \frac{1}{1 - \hat{\mathbf{r}}_{\mathbf{xd}}^H(\hat{f}_d, \hat{\tau})\hat{R}_{\mathbf{dd}}^{-1}\hat{\mathbf{R}}_{\mathbf{xx}}^{-1}\hat{\mathbf{r}}_{\mathbf{xd}}(\hat{f}_d, \hat{\tau})} = \quad (4.40)$$

$$= \max_{f_d, \tau} \left\{ \hat{\mathbf{r}}_{\mathbf{xd}}^H(f_d, \tau)\hat{R}_{\mathbf{dd}}^{-1}\hat{\mathbf{R}}_{\mathbf{xx}}^{-1}\hat{\mathbf{r}}_{\mathbf{xd}}(f_d, \tau) \right\} > \gamma, \quad (4.41)$$

and the result is compared with the detection threshold, completing the GLRT detector's design. Equation (4.41) could be solved performing an exhaustive grid search in the entire (f_d, τ) synchronization parameter space, and similar grid search strategies used in the conventional single-antenna acquisition [Tsu00] can be applied. It is possible to make a geometric interpretation of the detector identifying the projection matrix $\mathbf{P}_{\mathbf{X}^H} = \mathbf{X}^H(\mathbf{X}\mathbf{X}^H)^{-1}\mathbf{X}$, and then writing $T_{\text{GL}}(\mathbf{X}) = \max_{f_d, \tau} \left\{ (\mathbf{d}\mathbf{d}^H)^{-1}\mathbf{d}(f_d, \tau)\mathbf{P}_{\mathbf{X}^H}\mathbf{d}(f_d, \tau)^H \right\}$, which is the maximization of the signal projection over the subspace spanned by the received data. The proposed detector is consequently analogous to the estimator proposed in [FP09b].

4.4 White noise assumption

Let's suppose that the noise term \mathbf{n} in the signal model is defined as AWGN with a diagonal covariance matrix $\mathbf{Q} = \sigma^2\mathbf{I}$ and unknown variance σ^2 . In this particular case it is possible to obtain a test statistic expression $T_{\text{Wh}}(\mathbf{X})$ inserting the covariance noise model in (4.41) as follows

$$T_{\text{Wh}}(\mathbf{X}) = \max_{f_d, \tau} \left\{ \frac{\hat{\mathbf{r}}_{\mathbf{xd}}^H(f_d, \tau)\hat{\mathbf{r}}_{\mathbf{xd}}(f_d, \tau)}{\hat{\sigma}^2} \right\} > \gamma, \quad (4.42)$$

where it is assumed $\hat{R}_{\mathbf{dd}} \simeq 1$ and $\hat{R}_{\mathbf{xx}} \simeq \sigma^2\mathbf{I}$. This expression is equivalent to maximize the Euclidian norm of the cross-correlation vector, formulated as $\|\hat{\mathbf{r}}_{\mathbf{xd}}(f_d, \tau)\|^2$, where $\|\cdot\| = \sqrt{\mathbf{u}^H \mathbf{u}}$, and $(\cdot)^H$ denotes conjugate transpose, normalized by the estimation of the noise variance (or power). Since it is not possible to obtain a closed expression for \hat{f}_d and $\hat{\tau}$, a grid based search is still needed to find the function maximum.

4.4.1 Performance analysis

The performance analysis can be completed taking into account that the resulting array-based acquisition is equivalent to perform a GLRT acquisition independently over each antenna element and adding the results, expressed as

$$T_{\text{Wh}}(\mathbf{X}) = \max_{f_d, \tau} \left\{ \frac{\|\hat{\mathbf{r}}_{\mathbf{xd}}(f_d, \tau)\|^2}{\hat{\sigma}^2} \right\} = \max_{f_d, \tau} \sum_{i=1}^N T_{\text{GL}}(\mathbf{x}_i, f_d, \tau), \quad (4.43)$$

where \mathbf{x}_i is the received signal vector for the i -th antenna element and $T_{\text{GL}}(\mathbf{x}, f_d, \tau)$ is defined in (3.33).

Since $T_{\text{GL}}(\mathbf{x}_i, f_d, \tau) \sim \chi_2^2(\delta_{T_{\text{GL}},i})$, the sum of N $\chi_2^2(\delta_{T_{\text{GL}}})$ random variables is distributed as $\chi_{2N}^2(\delta_{T_{\text{Wh}}})$, where the new non-centrality parameter and the underlying Gaussian variance are

$$\delta_{T_{\text{Wh}}} = \sum_{i=1}^N \delta_{T_{\text{GL}},i}, \quad (4.44)$$

$$\sigma_{T_{\text{Wh}}}^2 = \sigma_{T_{\text{GL}}}^2 = \frac{1}{2K}. \quad (4.45)$$

Notice that the variance is the same as in $T_{\text{GL}}(\mathbf{x})$ due to the array noise variance normalization factor. As a consequence, the detector's distributions for both hypotheses are:

$$T_{\text{Wh}}(\mathbf{X}) \sim \begin{cases} \chi_{2N}^2(\delta_{T_{\text{Wh}}, \mathcal{H}_1}), & \text{in } \mathcal{H}_1, \\ \chi_{2N}^2(\delta_{T_{\text{Wh}}, \mathcal{H}_0}), & \text{in } \mathcal{H}_0, \end{cases} \quad (4.46)$$

notice that $\delta_{T_{\text{Wh}}, \mathcal{H}_0} = 0$ due to the absence of the searched satellite signal, expressed as $\mathbf{h} = \mathbf{0}$.

The false alarm probability can be expressed as $P_{fa}(\gamma) = 1 - P_{\mathcal{H}_0}(T_{\text{Wh}}(\mathbf{X}) \leq \gamma)$, where $P_{\mathcal{H}_0}(T_{\text{Wh}}(\mathbf{X}) \leq \gamma)$ is the χ_{2N}^2 CDF. A closed form expression can be written as:

$$P_{fa}(\gamma) = \exp \left\{ \frac{-\gamma}{2\sigma_{T_{\text{Wh}}}^2} \right\} \sum_{k=0}^{N-1} \frac{1}{k!} \left(\frac{\gamma}{2\sigma_{T_{\text{Wh}}}^2} \right)^k. \quad (4.47)$$

Finally, the detection probability can be computed as $P_d(\gamma) = 1 - P_{\mathcal{H}_1}(T_{\text{Wh}}(\mathbf{X}) \leq \gamma)$, where $P_{\mathcal{H}_1}(T_{\text{Wh}}(\mathbf{X}) \leq \gamma)$ is the CDF of a non-central chi-square χ_{2N}^2 :

$$P_d(\gamma) = Q_N \left(\frac{\sqrt{\delta_{T_{\text{Wh}}}}}{\sigma_{T_{\text{Wh}}}}, \frac{\sqrt{\gamma}}{\sigma_{T_{\text{Wh}}}} \right), \quad (4.48)$$

where Q_N is the generalized Marcum Q-function [Pro00] of order N .

The deflection coefficient can be obtained using 3.14 and the results of the statistical moments of a chi-square, already defined in Section 3.3.2.3:

$$d_{T_{\text{Wh}}}^2 = \frac{\delta_{T_{\text{Wh}}}^2}{\sigma_{T_{\text{Wh}}}^4}. \quad (4.49)$$

Assume a situation where the satellite signal power is equal in each antenna element. Therefore, the chi-square non-centrality parameter can be expressed as $\delta_{T_{\text{Wh}}} = N\delta_{T_{\text{GL}}}$. The array gain can be patent computing the ratio between the deflection coefficient of the single-antenna GLRT detector and the proposed detector:

$$\Delta g = \frac{d_{T_{\text{Wh}}}^2}{d_{T_{\text{GL}}}^2} = \frac{N\delta_{T_{\text{GL}}}^2}{\delta_{T_{\text{GL}}}^2} = N, \quad (4.50)$$

the result can be expressed in terms of the array SNR gain using (3.41)

$$\delta_{T_{\text{Wh}}}^2 \simeq N \frac{P_s}{P_n} = N\rho, \quad (4.51)$$

which is the well known array gain upper bound [Mon80]. It is remarkable the fact that the performance of the array-based acquisition GLRT test function for the white noise assumption is independent of the signal DOA or the array attitude. Obviously, the DOA affects the received signal power due to the individual antenna array elements gain patterns.

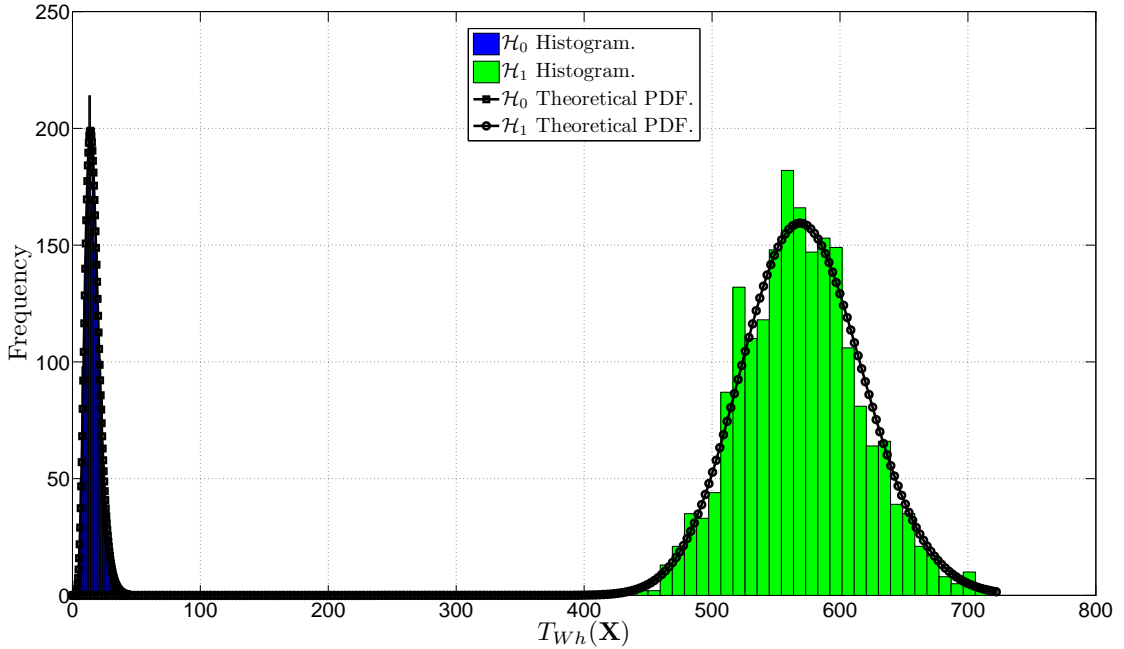


Figure 4.2: $T_{Wh}(\mathbf{X})$ normalized histogram and theoretical PDF in both \mathcal{H}_1 and \mathcal{H}_0 acquisition hypotheses for Galileo E1 signal acquisition simulation.

In order to validate the theoretical PDF obtained in (4.46), the test statistic histogram of $T_{Wh}(\mathbf{X})$ was simulated for the acquisition of a Galileo E1 signal with $CN0 = 44$ dB-Hz in the absence of interfering signals considering AWGN only, received with 8-element circular antenna array. The baseband sampling frequency was set to 6 MHz and the acquisition bandwidth was set to 2 MHz. Each of the histograms contains 2000 realizations. Fig. 4.2 shows the results for both \mathcal{H}_1 and \mathcal{H}_0 hypotheses, concluding that the model is aligned with the simulations results. Notice that in order to use the normalized Marqum Q function, both the histograms and the PDFs are normalized to $\sigma_{T_{Wh}}^2 = 1$ expressed as $\bar{T}_{Wh}(\mathbf{X}) = 2KT_{Wh}(\mathbf{X})$.

4.5 Colored noise assumption

In Section 4.4, the array receiver noise was modeled both temporally and spatially white, an assumption that leads to obtain a GLRT-based acquisition test function that is equivalent to perform a non-coherent MF acquisition independently over each antenna element and sum up the results. As a consequence, the test function does not exploit the array spatial diversity, and thus, does not offer protection against interferences.

In this Section, the key statistical feature is the assumption of an arbitrary and unknown covariance noise matrix \mathbf{Q} defined in (4.4), which attempts to capture the statistical behavior of the interferences and other non-desirable signals, while exploiting the spatial dimension provided by antenna arrays.

Considering the above conditions, both the performance and the interference rejection capabilities of the proposed detector are analyzed.

4.5.1 Performance analysis

Inserting the signal model (4.1) in (4.41) and assuming that the maximization over (f_d, τ) is able to obtain the absolute maximum of the function, it is possible to write:

$$T_{\text{GL}}(\mathbf{X}) = \hat{R}_{\mathbf{dd}}^{-1} \left(\underbrace{\frac{(\mathbf{d}\mathbf{d}^H \mathbf{h}^H + \mathbf{d}\mathbf{N}^H)}{K}}_{\hat{\mathbf{r}}_{\mathbf{x}\mathbf{d}}^H} \hat{\mathbf{R}}_{\mathbf{xx}}^{-1} \underbrace{\frac{(\mathbf{h}\mathbf{d}\mathbf{d}^H + \mathbf{N}\mathbf{d}^H)}{K}}_{\hat{\mathbf{r}}_{\mathbf{x}\mathbf{d}}} \right), \quad (4.52)$$

where $\hat{\mathbf{r}}_{\mathbf{x}\mathbf{d}} \sim \mathcal{CN}(\hat{R}_{\mathbf{dd}} \mathbf{h}, \frac{\mathbf{R}_{\mathbf{xx}}}{K})$ if \mathbf{d} is uncorrelated with \mathbf{N} . It is known that the distribution of a quadratic form $\mathbf{z}^H \Sigma^{-1} \mathbf{z}$ is a non-central chi-square $\chi_{2N}^2(\delta)$ with $2N$ degrees of freedom and $\delta = \boldsymbol{\mu}^H \Sigma^{-1} \boldsymbol{\mu}$, where $\mathbf{z} \in \mathbb{C}^{N \times 1}$ and $\mathbf{z} \sim \mathcal{CN}(\boldsymbol{\mu}, \Sigma)$. Notice that the presence of Σ^{-1} acts as a *whitening* transformation, and thus, the resulting distribution is independent of the structure of Σ . The proof can be found in [Mui82, p.26].

Assuming $\mathbf{z} = \hat{\mathbf{r}}_{\mathbf{x}\mathbf{d}}$ and $\Sigma = \hat{\mathbf{R}}_{\mathbf{xx}} \simeq \mathbf{R}_{\mathbf{xx}}$, which is the case of the ideal conditions, it is possible to state that $T_{\text{GL}}(\mathbf{X}) \sim \chi_{2N}^2(\delta_{T_{\text{GL}}})$. The chi-square non-centrality parameter can be expressed as:

$$\delta_{T_{\text{GL}}}(\hat{\mathbf{R}}_{\mathbf{xx}}, \mathbf{h}) = \hat{R}_{\mathbf{dd}} \mathbf{h}^H \hat{\mathbf{R}}_{\mathbf{xx}}^{-1} \mathbf{h} \simeq \mathbf{h}^H \mathbf{R}_{\mathbf{xx}}^{-1} \mathbf{h}, \quad (4.53)$$

that depends on $\hat{R}_{\mathbf{dd}}$, $\mathbf{R}_{\mathbf{xx}}^{-1}$, and the signal channel vector \mathbf{h} . Considering normalized power in the signal \mathbf{d} and the use of all the available satellite bandwidth, it is possible to assume $\hat{R}_{\mathbf{dd}} \simeq 1$, as is shown in Section 3.5.

Summarizing, the distributions of the test function for both hypotheses are:

$$T_{\text{GL}}(\mathbf{X}) \sim \begin{cases} \chi_{2N}^2(\delta_{T_{\text{GL}}; \mathcal{H}_1}), & \text{in } \mathcal{H}_1, \\ \chi_{2N}^2(\delta_{T_{\text{GL}}; \mathcal{H}_0}), & \text{in } \mathcal{H}_0, \end{cases} \quad (4.54)$$

notice that $\delta_{T_{\text{GL}}; \mathcal{H}_0} = 0$ because the searched satellite signal is not present, and thus $\mathbf{h} = \mathbf{0}$ in this case.

It is possible to write closed form expressions for both false alarm and detection probabilities, expressed as $P_{fa}(\gamma) = 1 - P_{\mathcal{H}_0}(T(\mathbf{X}; \mathcal{H}_0) \leq \gamma)$ and $P_d(\gamma) = 1 - P_{\mathcal{H}_1}(T(\mathbf{X}; \mathcal{H}_1) \leq \gamma)$ respectively, where $P_{\mathcal{H}_0}(\cdot)$ and $P_{\mathcal{H}_1}(\cdot)$ are the central and non-central χ_{2N}^2 CDF respectively:

$$P_{fa}(\gamma) = \exp \left\{ \frac{-\gamma}{2\sigma_{T_{\text{GL}}}^2} \right\} \sum_{k=0}^{N-1} \frac{1}{k!} \left(\frac{\gamma}{2\sigma_{T_{\text{GL}}}^2} \right)^k, \quad (4.55)$$

$$P_d(\gamma) = Q_N \left(\frac{\sqrt{\delta_{T_{\text{GL}}}(\hat{\mathbf{R}}_{\mathbf{xx}}, \mathbf{h})}}{\sigma_{T_{\text{GL}}}}, \frac{\sqrt{\gamma}}{\sigma_{T_{\text{GL}}}} \right), \quad (4.56)$$

where $\sigma_{T_{\text{GL}}}^2 = \frac{1}{2K}$ and Q_N is the generalized Marcum Q-function [Mui82] of order N . This result is valid only if:

- The noise term \mathbf{N} can be modeled as AWGN, with the conditions defined in the signal model (Section 4.1).
- The acquisition time is adequate to assume $\hat{\mathbf{R}}_{\mathbf{xx}} \simeq \mathbf{R}_{\mathbf{xx}}$.
- The maximization involved in $T_{\text{GL}}(\mathbf{X})$ is able to obtain the absolute maximum of the function without errors.

Otherwise, the performance of the detector will be degraded as we show in Section 4.7. Under the above conditions, two consequences can be identified:

- The proposed detector is CFAR because P_{fa} does not depend on $\mathbf{R}_{\mathbf{xx}}$.
- The interference rejection capability relies on the spatial diversity of the signal and the interferences, as it is shown in Section 4.5.1.3.

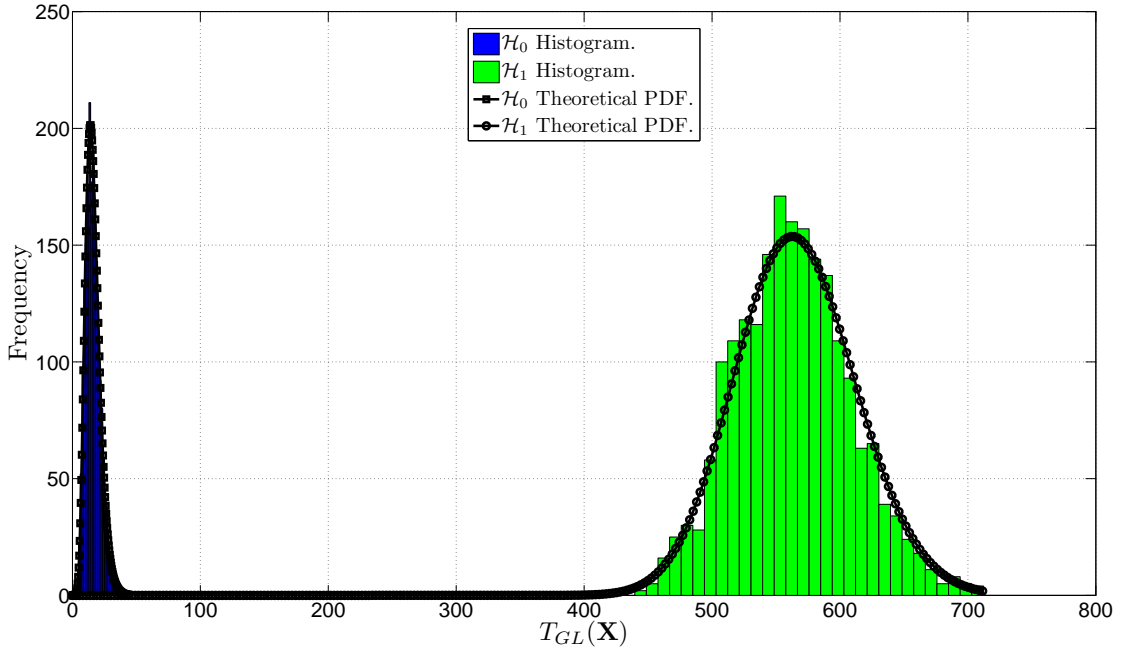


Figure 4.3: $T_{GL}(\mathbf{X})$ normalized histogram and theoretical PDF in both \mathcal{H}_1 and \mathcal{H}_0 acquisition hypotheses for Galileo E1 signal acquisition simulation.

In order to validate the theoretical PDF obtained in (4.54), the test statistic histogram of $T_{GL}(\mathbf{X})$ was simulated for the acquisition of a Galileo E1 signal with $CN0 = 44$ dB-Hz in the absence of interfering signals considering AWGN only, received with 8-element circular antenna array. The baseband sampling frequency was set to 6 MHz and the acquisition bandwidth was set to 2 MHz. Each of the histograms contains 2000 realizations. Fig. 4.3 shows the results for both \mathcal{H}_1 and \mathcal{H}_0 hypotheses, concluding that the model is aligned with the simulations results. Notice that in order to use the normalized Marqum Q function, both the histograms and the PDFs are normalized to $\sigma_{T_{GL}}^2 = 1$ expressed as $\bar{T}_{GL}(\mathbf{X}) = 2KT_{GL}(\mathbf{X})$.

4.5.1.1 Uniformly Most Powerful test condition

Considering the test statistics expression of (4.41), distributed as (4.54), the detector can be tested against the UMP condition using the Karlin-Rubin Theorem defined in Section 3.2.2. The first step is to check $T_{GL}(\mathbf{X})$ against the MLR condition by defining the ratio of the test function PDFs parameterized by δ

$$\frac{p(T_{GL}(\mathbf{X}); \delta_2)}{p(T_{GL}(\mathbf{X}); \delta_1)} = \frac{p(\chi_{2N}^2(\delta_2))}{p(\chi_{2N}^2(\delta_1))}, \quad (4.57)$$

where $\delta_1 = \delta_{T_{GL}}(\hat{\mathbf{R}}_{\mathbf{xx}}, \mathbf{h}_1)$ and $\delta_2 = \delta_{T_{GL}}(\hat{\mathbf{R}}_{\mathbf{xx}}, \mathbf{h}_2)$ are two possible values for the non-centrality parameter of the chi-square defied in (4.53). It is known in the literature that the ratio of two exponential-class PDFs is monotone non-decreasing for all $\delta_2 > \delta_1$, the proof can be found in [Kar56]. As a consequence, the MLR condition for $T_{GL}(\mathbf{X})$ is positive.

Now, if we define the test condition as $\mathcal{H}_0 : \delta \leq \delta_0$ versus $\mathcal{H}_1 : \delta > \delta_0$, where $\delta_0 = 0$ because the desired satellite signal is not present in \mathcal{H}_0 , then we accept \mathcal{H}_1 if $T_{GL}(\mathbf{X}) > \gamma$. According to Karlin-Rubin theorem, this test is a UMP test of level $\beta = P_d(\gamma)$, where $P_d(\cdot)$ was defined in (4.56).

4.5.1.2 Sensitivity analysis

In the previous analysis, the theoretical performance of the detector was obtained in terms of $\delta_{T_{GL}}(\hat{\mathbf{R}}_{\mathbf{xx}}, \mathbf{h})$ and $\sigma_{T_{GL}}(K)$. The aim of this section is to associate the performance to the

$T_{\text{GL}}(\mathbf{X})$	$P_d = 0.80$	$P_d = 0.90$	$P_d = 0.99$
$P_{fa} = 0.001$	25.62 dB-Hz	26.32 dB-Hz	27.72 dB-Hz
$P_{fa} = 0.01$	24.42 dB-Hz	25.22 dB-Hz	26.82 dB-Hz
$P_{fa} = 0.1$	22.32 dB-Hz	23.32 dB-Hz	25.42 dB-Hz

Table 4.2: GLRT detector's sensitivity for selected P_{fa} and P_{fa} , with $N = 8$ elements circular array, $f_s = 6$ MSPS, $T_{\text{acq}} = 4$ ms, and $\hat{R}_{\text{dd}} = 1$.

satellite's SNR, and consequently, to obtain the sensitivity of the detector in the absence of interferences or jamming signals.

The CFAR condition of $T_{\text{GL}}(\mathbf{X})$ makes P_{fa} independent of the input noise and interferences power, and, according to (4.56), P_d depends on $\delta_{T_{\text{GL}}}(\hat{\mathbf{R}}_{\mathbf{xx}}, \mathbf{h})$. Assuming only AWGN at the input, inserting $\mathbf{R}_{\mathbf{xx}} = \sigma^2 \mathbf{I}$ in (4.53), it is possible to write $\delta_{T_{\text{GL}}; \mathcal{H}_1}$ in terms of ρ as

$$\delta_{T_{\text{GL}}; \mathcal{H}_1} = \frac{\mathbf{h}^H \mathbf{h}}{\sigma^2} = N\rho, \quad (4.58)$$

that fully characterizes the sensitivity of the detector in AWGN. Notice that $\delta_{T_{\text{GL}}} = \delta_{T_{\text{Wh}}}$ in this case, and thus, both detectors obtain the same performance.

Unfortunately, there is no direct inverse for the generalized Marcum Q-function, and consequently, it is difficult to obtain a closed form expression for the sensitivity. Table 4.5.1.2 shows the theoretical sensitivity values for selected P_{fa} and P_d , computed by a numerical evaluation of (4.55) and (4.56).

4.5.1.3 Interference rejection capability

As shown in (4.56) and (4.53), P_d relies on $\delta_{T_{\text{GL}}}(\hat{\mathbf{R}}_{\mathbf{xx}}, \mathbf{h})$. Assuming $E\{\hat{\mathbf{R}}_{\mathbf{xx}}\} \simeq \mathbf{Q}$, in this section, it is considered a scenario where a set of M uncorrelated³ interferences impinge into the array through a channel matrix $\mathbf{H}_i = [\mathbf{h}_{i,1}, \dots, \mathbf{h}_{i,M}] \in \mathbb{C}^{N \times M}$ and an interference basis function matrix $\mathbf{D}_i = [\mathbf{d}_{i,1}^T, \dots, \mathbf{d}_{i,M}^T]^T \in \mathbb{C}^{M \times K}$, where $\mathbf{d}_{i,i} \in \mathbb{C}^{1 \times K}$ is the i -th interference arbitrary baseband signal structure. Considering the noise as AWGN for the sake of simplicity, it is possible to write the noise plus interferences term as

$$\mathbf{N} = \mathbf{H}_i \mathbf{D}_i + \mathbf{N}_w, \quad (4.59)$$

where \mathbf{N}_w is the thermal AWGN with zero mean and variance σ^2 . Due to the particular structure of \mathbf{Q} , it can be separated in the interferences and noise subspaces:

$$\mathbf{Q} = \mathbf{U} \boldsymbol{\Lambda} \mathbf{U}^H + \sigma^2 \mathbf{I} = \mathbf{U} (\boldsymbol{\Lambda} + \sigma^2 \mathbf{I}) \mathbf{U}^H, \quad (4.60)$$

where \mathbf{U} is an unitary matrix whose columns are the eigenvectors of \mathbf{Q} , \mathbf{I} stands for the identity matrix, and $\boldsymbol{\Lambda} = \text{diag}\{\lambda_1, \dots, \lambda_N\}$, where λ_i are the eigenvalues of the interferences subspace. In the modeled scenario, the interferences' eigenvalues dominate \mathbf{Q} , assuming $\min_{\lambda \neq 0} \lambda \gg \sigma^2$. Notice that the covariance matrix is positive definite and thus it cannot contain negative eigenvalues.

Now, it is possible to obtain the expression for \mathbf{Q}^{-1} as:

$$\mathbf{Q}^{-1} = \mathbf{U} (\boldsymbol{\Lambda}^{-1} + \sigma^{-2} \mathbf{I}) \mathbf{U}^H, \quad (4.61)$$

from which it is clear that, in \mathbf{Q}^{-1} , the interference nullspace eigenvectors have dominant associated eigenvalues and, on the contrary, the interference space eigenvectors have small associated eigenvalues.

The interferences covariance matrix $\mathbf{U} \boldsymbol{\Lambda} \mathbf{U}^H$ usually does not have a full rank. Here it is assumed that the thermal noise has enough power to make \mathbf{Q} invertible, otherwise, rank-extending techniques can be used, e.g., diagonal loading [Car88].

³Uncorrelated between them and uncorrelated with the satellite signal.

It is useful to express $\mathbf{U}\Lambda\mathbf{U}^H$ in terms of the interference signal model

$$\mathbf{U}\Lambda\mathbf{U}^H = \mathbf{H}_i \mathbf{R}_{\mathbf{D}_i \mathbf{D}_i} \mathbf{H}_i^H \simeq \mathbf{H}_i \mathbf{H}_i^H, \quad (4.62)$$

where $\mathbf{R}_{\mathbf{D}_i \mathbf{D}_i} = E\{\mathbf{D}_i \mathbf{D}_i^H\}$ is the interference basis functions autocorrelation matrix, which can be approximated to $\mathbf{R}_{\mathbf{D}_i \mathbf{D}_i} \simeq \mathbf{I}$ if the interferences are uncorrelated in time domain. Inserting (4.62) in (4.61), it is possible to write

$$\begin{aligned} \mathbf{Q}^{-1} &= (\mathbf{H}_i \mathbf{R}_{\mathbf{D}_i \mathbf{D}_i} \mathbf{H}_i^H + \sigma^2 \mathbf{I})^{-1} \\ &= \sigma^{-2} \mathbf{I} - \sigma^{-4} \mathbf{H}_i (\mathbf{I} + \sigma^{-2} \mathbf{H}_i^H \mathbf{H}_i)^{-1} \mathbf{H}_i^H \\ &\simeq \sigma^{-2} (\mathbf{I} - \mathbf{H}_i (\mathbf{H}_i^H \mathbf{H}_i)^{-1} \mathbf{H}_i^H), \end{aligned} \quad (4.63)$$

where the matrix inversion lemma⁴ was used, and assuming that the interferences' power are orders of magnitude above the AWGN power, then it is possible to approximate $\mathbf{I} + \sigma^{-2} \mathbf{H}_i^H \mathbf{H}_i \simeq \sigma^{-2} \mathbf{H}_i^H \mathbf{H}_i$. The latter expression in (4.63) can be rewritten as

$$\mathbf{Q}^{-1} = \sigma^{-2} \mathbf{P}_{\mathbf{H}_i}^\perp, \quad (4.64)$$

where $\mathbf{P}_{\mathbf{H}_i}^\perp = (\mathbf{I} - \mathbf{H}_i (\mathbf{H}_i^H \mathbf{H}_i)^{-1} \mathbf{H}_i^H)$ is the projection matrix over the orthogonal subspace to the interference subspace, spanned by the columns of \mathbf{H}_i .

The impact of the presence of interferences in the detector's performance can be analyzed inserting (4.64) in (4.53) to obtain a new expression for the test statistic non-centrality parameter:

$$\delta_{T_{GL}}(\sigma^2, \mathbf{h}, \mathbf{H}_i) = \frac{\mathbf{h}^H \mathbf{P}_{\mathbf{H}_i}^\perp \mathbf{h}}{\sigma^2} = \frac{\mathbf{h}^H \mathbf{h}}{\sigma^2} - \frac{\mathbf{h}^H \mathbf{P}_{\mathbf{H}_i} \mathbf{h}^H}{\sigma^2}, \quad (4.65)$$

where $\mathbf{P}_{\mathbf{H}_i} = \mathbf{H}_i (\mathbf{H}_i^H \mathbf{H}_i)^{-1} \mathbf{H}_i^H$ is the projection matrix over the interference subspace. The geometric interpretation is that $\delta_{T_{GL}}(\sigma^2, \mathbf{h}, \mathbf{H}_i)$ is inversely proportional to the spatial correlation of the satellite signal subspace and the interferences subspace. It is remarkable the fact that the detector's performance does not depend on the power of interference signals⁵. In the worst case⁶ if the satellite signal subspace is located inside the interference subspace, then $\delta_{T_{GL}}(\sigma^2, \mathbf{h}, \mathbf{H}_i) = 0$.

Consider the particular case of a single interference impinging into the array. Particularizing (4.64) for $M = 1$, leads to

$$\mathbf{Q}^{-1} = \sigma^{-2} \mathbf{P}_{\mathbf{h}_i}^\perp = \sigma^{-2} (\mathbf{I} - \mathbf{h}_i (\mathbf{h}_i^H \mathbf{h}_i)^{-1} \mathbf{h}_i^H), \quad (4.66)$$

and, inserting (4.66) in (4.53), the following expression is obtained

$$\delta_{T_{GL}}(\sigma^2, \mathbf{h}, \mathbf{h}_i) = \frac{\mathbf{h}^H \mathbf{P}_{\mathbf{h}_i}^\perp \mathbf{h}}{\sigma^2} = \frac{\mathbf{h}^H \mathbf{h}}{\sigma^2} - \frac{|\mathbf{h}^H \mathbf{h}_i|^2}{\sigma^2 \mathbf{h}_i^H \mathbf{h}_i}, \quad (4.67)$$

which is the projection of the signal steering vector over the subspace orthogonal to the interference steering vector, and normalized by the noise power σ^2 . Now, considering that:

- $\mathbf{h}_i^H \mathbf{h}_i = |\mathbf{h}_i|^2 = N P_i$, assuming that each antenna element is receiving the same interference power P_i and there is no coupling effects between antenna elements.
- $|\mathbf{h}^H \mathbf{h}_i|^2 = |\mathbf{h}|^2 |\mathbf{h}_i|^2 |\bar{\mathbf{h}}^H \bar{\mathbf{h}}_i|^2$, where (\cdot) stands for unitary vector,

it is possible to rewrite (4.67) as

$$\begin{aligned} \delta_{T_{GL}}(\rho, N, \bar{\mathbf{h}}, \bar{\mathbf{h}}_i) &= \frac{N P_s}{P_n} - \frac{N^2 P_i P_s |\bar{\mathbf{h}}^H \bar{\mathbf{h}}_i|^2}{N P_i P_n} \\ &= N \rho (1 - |\bar{\mathbf{h}}^H \bar{\mathbf{h}}_i|^2). \end{aligned} \quad (4.68)$$

⁴ $(\mathbf{A} + \mathbf{U}\mathbf{C}\mathbf{V}^H)^{-1} = \mathbf{A}^{-1} - \mathbf{A}^{-1}\mathbf{U}(\mathbf{C}^{-1} + \mathbf{V}\mathbf{A}^{-1}\mathbf{U})^{-1}\mathbf{V}\mathbf{A}^{-1}$.

⁵ Notice that in this analysis we do not consider the signal quantization effects, which will be addressed in Section 4.7.

⁶ The worst case is defined when both $T(\mathbf{X} : \mathcal{H}_0)$ and $T(\mathbf{X} : \mathcal{H}_1)$ PDFs are totally overlapped and consequently the detector is unable to discriminate between them.

Using (4.68), it is evident that the performance of the detector is maximized when the signal and the interference have orthogonal steering vectors. In that case, $\delta_{T_{GL}} = N\rho$ is the array maximum available SNR. Fig. 4.4 shows the evolution of $\delta_{T_{GL}}(\rho, N, \bar{\mathbf{h}}, \bar{\mathbf{h}}_i)$ in the proposed scenario, using a circular array with isotropic antenna elements. The 3-dimensional plots show the value of $\delta_{T_{GL}}(\rho, N, \bar{\mathbf{h}}, \bar{\mathbf{h}}_i)$ for all possible signal DOAs. The array acquisition performance depends also on the number of antenna elements. The distance between adjacent elements was kept constant and equal to half-wavelength in all the configurations. An increase in the number of antenna elements enables narrower interference null-steering patterns [Mon80], and thus increases the detector's performance.

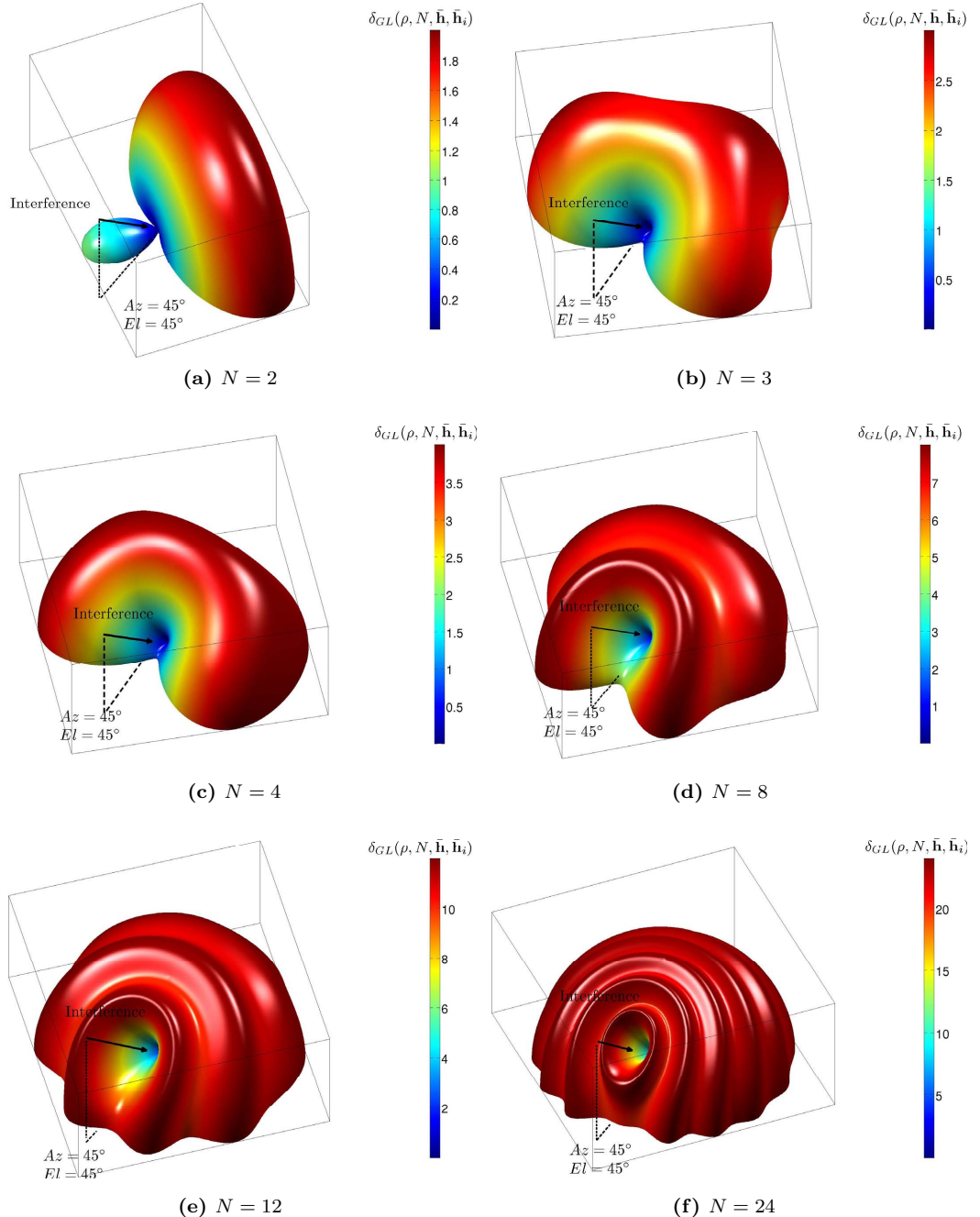


Figure 4.4: Evolution of $\delta_{T_{GL}}(\rho, N, \bar{\mathbf{h}}, \bar{\mathbf{h}}_i)$ in the presence of an uncorrelated interference impinging into the array from $Az = 45^\circ$ and $El = 45^\circ$, with $\rho = 1$.

4.6 Acquisition after beamforming

Beamforming is the combination of radio signals from a set of small non-directional antennas to simulate a large directional antenna. Digital Beamforming (DBF) with antenna arrays consists of several antennas, whose outputs are controlled in phase and gain, i.e., multiplied by complex weights, in order to achieve a gain pattern that can be manipulated electronically. Then, all the weighted signals are combined to obtain a single output.

As we highlighted in previous sections, in the acquisition stage it is difficult to provide both the signal DOA information and the array attitude required by some beamforming algorithms, such as the Minimum Variance Distortionless Response (MVDR) beamformer [Mon80] that minimizes the output noise variance subject to a unity gain constraint in the desired look direction⁷. However, it is possible to filter out the interferences prior to the acquisition using the so called *blind null-formers* as described in [Zol95, McD04, Car05, Xia09] among others. In these works, the beamformer tries to minimize the interference power at the output, which is fed to a conventional GNSS receiver. The performance metrics are usually given in terms of input and output SNIR, signal phase response, and positioning accuracy and precision.

In this Section, we analyze the performance of the GLRT acquisition algorithm developed in Section 3.3.2 when it is executed after a generic beamformer processor. In contrast to the available literature, here we provide the acquisition performance metrics in terms of the probability of detection and false alarm, and in that sense, closed form expressions are obtained. Simulations validate the theoretical analysis.

4.6.1 Performance of the GLRT detector after beamforming

The beamformer output signal model can be written as

$$\mathbf{y} = \mathbf{w}^H \mathbf{X}, \quad (4.69)$$

where $\mathbf{w} \in \mathbb{C}^{N \times 1}$ is the beamformer weights vector and \mathbf{X} is the array snapshots matrix already defined in (4.1). The spatially-filtered output of the beamformer can be fed to a conventional GNSS receiver equipped with the GLRT acquisition algorithm. Inserting (4.69) into (3.29) the acquisition test function can be rewritten as:

$$T_{\text{DBF}}(\mathbf{X}) = \max_{f_d, \tau} \frac{\hat{R}_{\mathbf{yd}}^H(f_d, \tau) \hat{R}_{\mathbf{yd}}(f_d, \tau)}{\hat{R}_{\mathbf{yy}}} > \gamma, \quad (4.70)$$

where⁸

$$\hat{R}_{\mathbf{yd}} = \frac{1}{K} \mathbf{y} \mathbf{d}^H = \mathbf{w}^H \frac{1}{K} \mathbf{X} \mathbf{d}^H = \mathbf{w}^H \hat{\mathbf{r}}_{\mathbf{xd}} \quad (4.71)$$

and

$$\hat{R}_{\mathbf{yy}} = \frac{1}{K} \mathbf{y} \mathbf{y}^H = \mathbf{w}^H \hat{\mathbf{R}}_{\mathbf{xx}} \mathbf{w}. \quad (4.72)$$

Fig. 4.5 shows a simplified block diagram of the acquisition after a generic beamformer processor.

In order to obtain the performance expressions for (4.70) the first step is to obtain the statistical moments of the cross-correlation between the beamformer output and the local code replica:

$$\mu_{\hat{R}_{\mathbf{yd}}} = E\{\hat{R}_{\mathbf{yd}}\} = \mathbf{w}^H E\{\hat{\mathbf{r}}_{\mathbf{xd}}\} = \mathbf{w}^H R_{\mathbf{dd}} \mathbf{h}, \quad (4.73)$$

⁷also known as *Capon's beamformer* [Cap69].

⁸For the sake of simplicity of the notation, we omit the maximization operation of the acquisition test function over the signal synchronization parameters (f_d, τ) and its dependency in the rest of the Section.

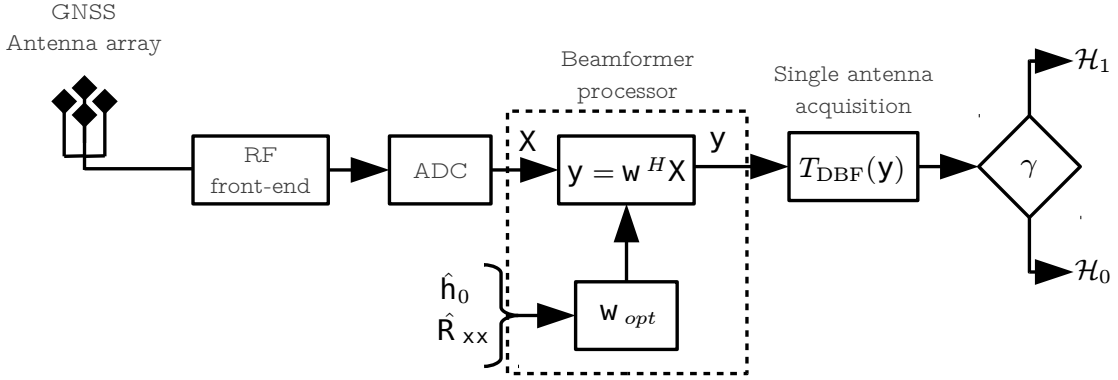


Figure 4.5: Acquisition after generic beamforming.

where $E\{\hat{r}_{xd}\}$ was already obtained in Section 4.5.1 and

$$\sigma_{R_{yd}}^2 = \text{var}\{\hat{R}_{yd}\} = E\{(\hat{R}_{yd} - \mathbf{w}^H R_{dd}\mathbf{h})(\hat{R}_{yd} - \mathbf{w}^H R_{dd}\mathbf{h})^H\} = \quad (4.74)$$

$$= E\{(\mathbf{w}^H \hat{r}_{nd})(\mathbf{w}^H \hat{r}_{nd})^H\} = \mathbf{w}^H E\{\hat{r}_{nd} \hat{r}_{nd}^H\} \mathbf{w} = \quad (4.75)$$

$$= \mathbf{w}^H \frac{\mathbf{R}_{nn}}{K} \mathbf{w} \simeq \mathbf{w}^H \frac{\mathbf{R}_{xx}}{K} \mathbf{w}, \quad (4.76)$$

where the latter approximation is valid only for low signal power values, as in the case of GNSS signals. From the results it is possible to express \hat{R}_{yd} as a complex Gaussian variable $\hat{R}_{yd} \sim \mathcal{CN}(\mu_{\hat{R}_{yd}}, \sigma_{\hat{R}_{yd}}^2)$.

On the other hand, $T_{DBF}(\mathbf{X})$ can be analyzed as a quadratic form of \hat{R}_{yd} by applying the same procedure presented in (3.37). Then it is possible to obtain the distribution of the test statistic as a Chi-square random variable $\chi_2^2(\delta_{T_{DBF}})$. We particularize the non-centrality parameter for each testing hypotheses, inserting (3.2) and (3.3) in (3.38):

$$T_{DBF}(\mathbf{X}) \sim \begin{cases} \chi_2^2(\delta_{T_{DBF}; \mathcal{H}_1}), & \text{in } \mathcal{H}_1, \\ \chi_2^2(\delta_{T_{DBF}; \mathcal{H}_0} = 0), & \text{in } \mathcal{H}_0, \end{cases} \quad (4.77)$$

where

$$\delta_{T_{DBF}; \mathcal{H}_1} = \frac{\|\mu_{\hat{R}_{yd}}\|^2}{\hat{R}_{yy}} = \frac{\mathbf{w}^H R_{dd} \mathbf{h} \mathbf{h}^H R_{dd}^* \mathbf{w}}{\mathbf{w}^H \mathbf{R}_{xx} \mathbf{w}}, \quad (4.78)$$

and the underlying Gaussian variance is

$$\sigma_{T_{DBF}}^2 = \frac{1}{2K}. \quad (4.79)$$

From the results, it is possible to find closed form solutions for both false alarm and detection probabilities, expressed as $P_{fa}(\gamma) = 1 - P_{\mathcal{H}_0}(T_{DBF}(\mathbf{x}; \mathcal{H}_0) \leq \gamma)$ and $P_d(\gamma) = 1 - P_{\mathcal{H}_1}(T_{DBF}(\mathbf{x}; \mathcal{H}_1) \leq \gamma)$, respectively, where $P_{\mathcal{H}_x}(\cdot)$ is the χ_2^2 CDF can be expressed as:

$$P_d(\gamma) = Q_1 \left(\frac{\sqrt{\delta_{T_{DBF}; \mathcal{H}_1}}}{\sigma_{T_{DBF}}}, \frac{\sqrt{\gamma}}{\sigma_{T_{DBF}}} \right), \quad (4.80)$$

$$P_{fa}(\gamma) = \exp \left\{ \frac{-\gamma}{2\sigma_{T_{DBF}}^2} \right\}, \quad (4.81)$$

where Q_1 is the generalized Marcum Q-function [Pro00] of order 1. This acquisition test statistic is a CFAR detector because P_{fa} does not depend on the noise power.

4.6.2 Power minimization beamformer

In the previous analysis we assumed both generic and deterministic beamforming weights to obtain the acquisition performance expressions. In this Section we particularize the beamformer with one of the widely used interference mitigation algorithm suitable to be applied to GNSS receivers in the acquisition stage: the *power minimization* beamformer [Zol95].

The power minimization approach presupposes that the GNSS signals are well below the noise floor, and thus, the contribution in the array covariance matrix is negligible. The algorithm tries to minimize the beamformer output power pointing nulls in the directions where interfering signals are present. The design equation can be written as:

$$\begin{aligned} & \min_{\mathbf{w}} \mathbf{w}^H \mathbf{R}_{\mathbf{x}\mathbf{x}} \mathbf{w} \\ & \text{s.t. } \mathbf{w}^H \mathbf{h}_0 = 1, \end{aligned} \quad (4.82)$$

where the steering vector in the constraint is defined as $\mathbf{h}_0 = [1 \ 0 \dots 0]^T \in \mathbb{C}^{N \times 1}$. In other words, the beamformer minimizes the output power while not weighting a reference antenna. The weights used to form the beams on the auxiliary elements are then determined by minimizing the mean square value of the difference between the reference antenna output and the output of the auxiliary beam [Zol95].

The power minimization beamformer can be seen as a **particular case of the MVDR beamformer**, where it is used the above defined steering vector instead of the satellite signal DOA, which is supposed to be unknown at the acquisition stage. This problem can be solved by applying the Lagrange multipliers method, obtaining:

$$\Lambda(\mathbf{w}, \lambda) = \mathbf{w}^H \mathbf{R}_{\mathbf{x}\mathbf{x}} \mathbf{w} + \lambda(\mathbf{w}^H \mathbf{h}_0 - 1), \quad (4.83)$$

where λ is the Lagrange parameter. Minimizing the new cost function $\Lambda(\mathbf{w}, \lambda)$ the optimal set of weights is found as:

$$\mathbf{w}_{\text{opt}} = \frac{\mathbf{R}_{\mathbf{x}\mathbf{x}}^{-1} \mathbf{h}_0}{\mathbf{h}_0^H \mathbf{R}_{\mathbf{x}\mathbf{x}}^{-1} \mathbf{h}_0}, \quad (4.84)$$

which is the well-known MVDR beamformer solution in case we are using \mathbf{h}_0 for pointing the radiation diagram towards the expected DOA.

A single-antenna receiver can use the beamformer output \mathbf{y} to acquire GNSS signals. The GLRT test function can be rewritten by inserting (4.84) in the cross-correlation and autocorrelation estimators of (4.72) and (4.71) respectively, obtaining:

$$\hat{R}_{\mathbf{yy}} = \left(\frac{\mathbf{R}_{\mathbf{x}\mathbf{x}}^{-1} \mathbf{h}_0}{\mathbf{h}_0^H \mathbf{R}_{\mathbf{x}\mathbf{x}}^{-1} \mathbf{h}_0} \right)^H \hat{\mathbf{R}}_{\mathbf{x}\mathbf{x}} \left(\frac{\mathbf{R}_{\mathbf{x}\mathbf{x}}^{-1} \mathbf{h}_0}{\mathbf{h}_0^H \mathbf{R}_{\mathbf{x}\mathbf{x}}^{-1} \mathbf{h}_0} \right) = \quad (4.85)$$

$$= \frac{1}{\mathbf{h}_0^H \mathbf{R}_{\mathbf{x}\mathbf{x}}^{-1} \mathbf{h}_0}, \quad (4.86)$$

and finally by a straightforward manipulation of (4.70), a simplified version of the test function is obtained for the MVDR beamformer case:

$$\begin{aligned} T_{\text{MVDR}}(\mathbf{X}) &= (\mathbf{h}_0^H \mathbf{R}_{\mathbf{x}\mathbf{x}}^{-1} \mathbf{h}_0) \hat{\mathbf{r}}_{\mathbf{x}\mathbf{d}}^H \left(\frac{\mathbf{R}_{\mathbf{x}\mathbf{x}}^{-1} \mathbf{h}_0}{\mathbf{h}_0^H \mathbf{R}_{\mathbf{x}\mathbf{x}}^{-1} \mathbf{h}_0} \right) \left(\frac{\mathbf{R}_{\mathbf{x}\mathbf{x}}^{-1} \mathbf{h}_0}{\mathbf{h}_0^H \mathbf{R}_{\mathbf{x}\mathbf{x}}^{-1} \mathbf{h}_0} \right)^H \hat{\mathbf{r}}_{\mathbf{x}\mathbf{d}} = \\ &= \frac{\hat{\mathbf{r}}_{\mathbf{x}\mathbf{d}}^H (\mathbf{R}_{\mathbf{x}\mathbf{x}}^{-1} \mathbf{h}_0) (\mathbf{R}_{\mathbf{x}\mathbf{x}}^{-1} \mathbf{h}_0)^H \hat{\mathbf{r}}_{\mathbf{x}\mathbf{d}}}{\mathbf{h}_0^H \mathbf{R}_{\mathbf{x}\mathbf{x}}^{-1} \mathbf{h}_0}. \end{aligned} \quad (4.87)$$

The latter expression can be interpreted in terms of the geometric projection over the interferences subspace using the approximation of $\mathbf{R}_{\mathbf{x}\mathbf{x}}^{-1} \simeq \sigma^{-2} \mathbf{P}_{\mathbf{H}_i}^\perp$ obtained in (4.64):

$$T_{\text{MVDR}}(\mathbf{X}) = \frac{1}{\sigma^2} \frac{|\hat{\mathbf{r}}_{\mathbf{x}\mathbf{d}}^H \mathbf{P}_{\mathbf{H}_i}^\perp \mathbf{h}_0|^2}{\|\mathbf{h}_0^H \mathbf{P}_{\mathbf{H}_i}^\perp\|^2}, \quad (4.88)$$

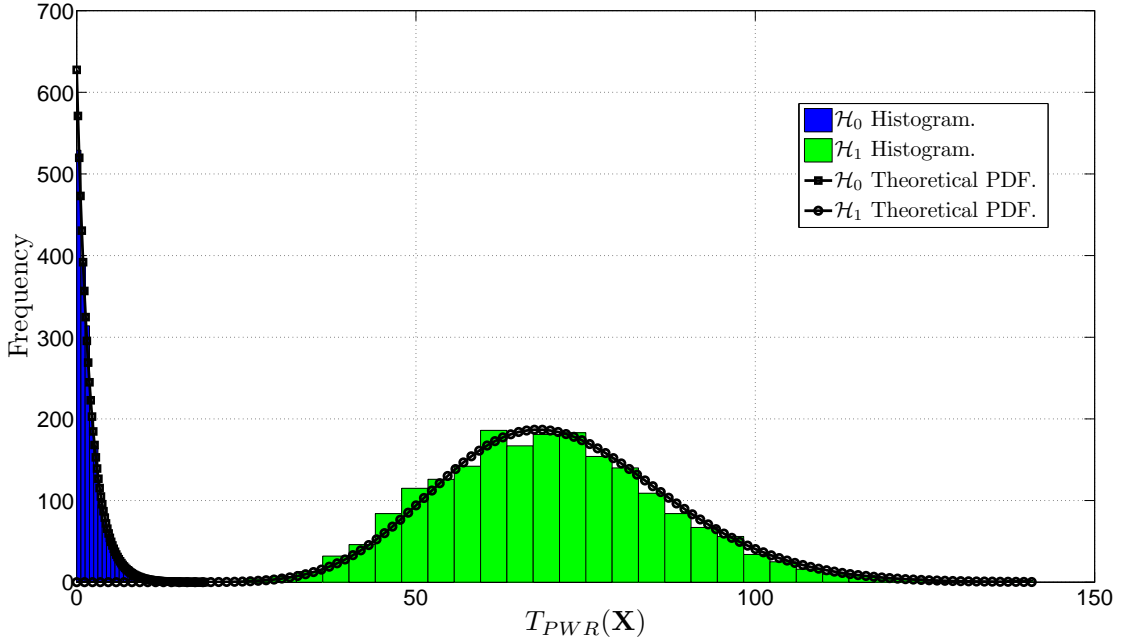


Figure 4.6: $T_{\text{PWR}}(\mathbf{X})$ normalized histogram and theoretical PDF in both \mathcal{H}_1 and \mathcal{H}_0 acquisition hypotheses for Galileo E1 signal acquisition simulation.

where $\mathbf{P}_{\mathbf{H}_i}^\perp$ is the projection matrix to the subspace orthogonal to the interference subspace. Moreover, the Chi-square non-centrality parameter of $T_{\text{MVDR}}(\mathbf{X})$ can be expressed also in terms of geometric projections as:

$$\delta_{T_{\text{MVDR}}} = \frac{|R_{\mathbf{dd}}|^2}{\sigma^2} \frac{|\mathbf{h}_0^H \mathbf{P}_{\mathbf{H}_i}^\perp \mathbf{h}|^2}{\|\mathbf{h}_0^H \mathbf{P}_{\mathbf{H}_i}^\perp\|^2}. \quad (4.89)$$

The performance of the detector in the absence of interferences can be obtained setting $\mathbf{P}_{\mathbf{H}_i}^\perp = \mathbf{I}$ in (4.88) and assuming $|R_{\mathbf{dd}}|^2 \simeq 1$. In this scenario, the detector can be rewritten as:

$$T_{\text{MVDR}}(\mathbf{X}) = \frac{\sigma^{-2}}{\|\mathbf{h}_0^H \mathbf{h}_0\|^2} \|\mathbf{r}_{\mathbf{x}\mathbf{d}}^H \mathbf{h}_0\|^2. \quad (4.90)$$

Assuming $\mathbf{h}_0 = [1 \ 0 \dots \ 0]$, which is the *power minimization* constraint, the beamformer only activates the reference antenna. In this particular case, the test function for the power minimization beamformer can be written as $T_{\text{PWR}}(\mathbf{X}) = T_{\text{GL}}(\mathbf{x}_1, f_d, \tau)$, where $T_{\text{GL}}(\mathbf{x}_1, f_d, \tau)$ is the single-antenna GLRT acquisition defined in (3.33) and \mathbf{x}_i is the received signal vector for the i -th antenna antenna element. The power minimization approach does not exploit the signal DOA information and the resulting acquisition does not benefit from the available array gain, in contrast to the algorithm proposed in Section 4.5.

In order to validate the theoretical PDF obtained in (4.77), the test statistic histogram of $T_{\text{PWR}}(\mathbf{X})$ was simulated for the acquisition of a Galileo E1 signal with $CN0 = 44$ dB-Hz in the absence of interfering signals considering AWGN only. The baseband sampling frequency was set to 6 MHz and the acquisition bandwidth was set to 2 MHz. Each of the histogram bins averages 2000 realizations. The acquisition time was set to one PRN code period ($T_{\text{acq}} = 4$ ms). Fig. 4.6 shows the results for both \mathcal{H}_1 and \mathcal{H}_0 hypotheses, concluding that the performance expressions are aligned with the simulations results. Notice that, in order to use the normalized Marqum Q function, both the histograms and the PDFs are normalized to $\sigma_{T_{\text{PWR}}}^2 = 1$ expressed as $\bar{T}_{\text{PWR}}(\mathbf{X}) = 2KT_{\text{PWR}}(\mathbf{X})$.

The performance of the acquisition after the power minimization beamformer ($T_{\text{PWR}}(\mathbf{X})$) algorithm was compared to the optimum acquisition defined in (4.12) ($T_{\text{NP}}(\mathbf{X})$) and the proposed GLRT acquisition ($T_{\text{GL}}(\mathbf{X})$) algorithm defined in (4.40). In addition, we included the

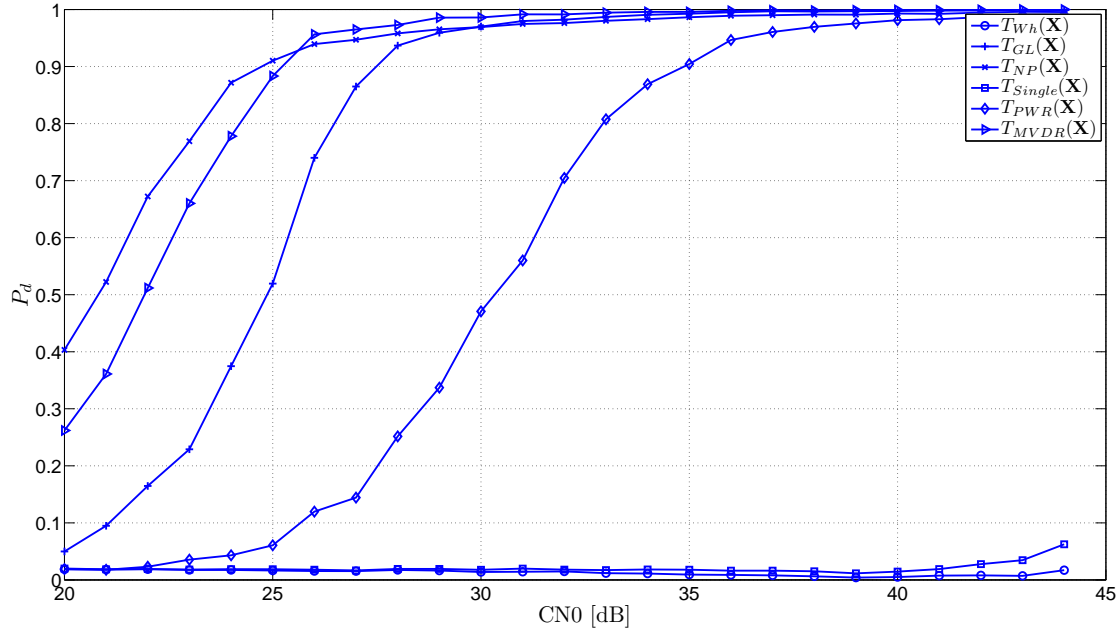


Figure 4.7: Galileo E1 acquisition P_d vs. satellite CN0 in the presence of wideband interference for different algorithms and no DOA estimation error in the MVDR beamformer ($T_{MVDR}(\mathbf{X})$).

performance of the acquisition after the MVDR beamformer considering different cases where the signal DOA is estimated with and without errors.

Simulation results shows the P_d versus the satellite CN0 in a simulated Galileo E1 scenario. In the scenario, a wideband, noise-like, in-band interference impinges into an $N = 8$ elements circular array (half wavelength separation between elements) with uniformly distributed random DOA and $IN0 = 85$ dB-Hz. The baseband sampling frequency was set to 6 MHz and the acquisition bandwidth was set to 2 MHz. For each CN0 value, the simulation contains 10000 realizations. The acquisition time was set to one PRN code period ($T_{acq} = 4$ ms) and the P_{fa} was set to 0.001 for all the algorithms.

Fig. 4.7 shows the resulting plot considering no pointing error in the MVDR beamformer. In Fig. 4.8 is considered a DOA estimation mean pointing error of 15° degrees with a variance of 5° , in both Azimuth and Elevation coordinates. Finally, Fig. 4.9 plots the simulation results for the case of an estimation DOA error of 20° .

From the results it can be inferred that the GLRT algorithm for the colored noise case enjoys a higher performance than the power minimization beamformer algorithm due to the array gain, which is aligned with the theoretical performance expressions. On the other hand, the *clairvoyant detector* presents the upper performance bound as stated in Section 4.2.

Interestingly, the acquisition after the MVDR beamformer is severely affected by moderate pointing errors. A pointing error of 20° in this configuration reduces the MVDR performance and it is overtaken by the proposed GLRT acquisition algorithm. This is one of the main drawbacks of the beamforming algorithms that require signal DOA information; on the one hand, it requires both calibrated and oriented array (or an estimation of the array attitude), and, on the other hand, it requires a good signal DOA estimation [Mon80]. If one of the two requirements fail, then, the algorithm will make a pointing error and thus the acquisition performance will be reduced.

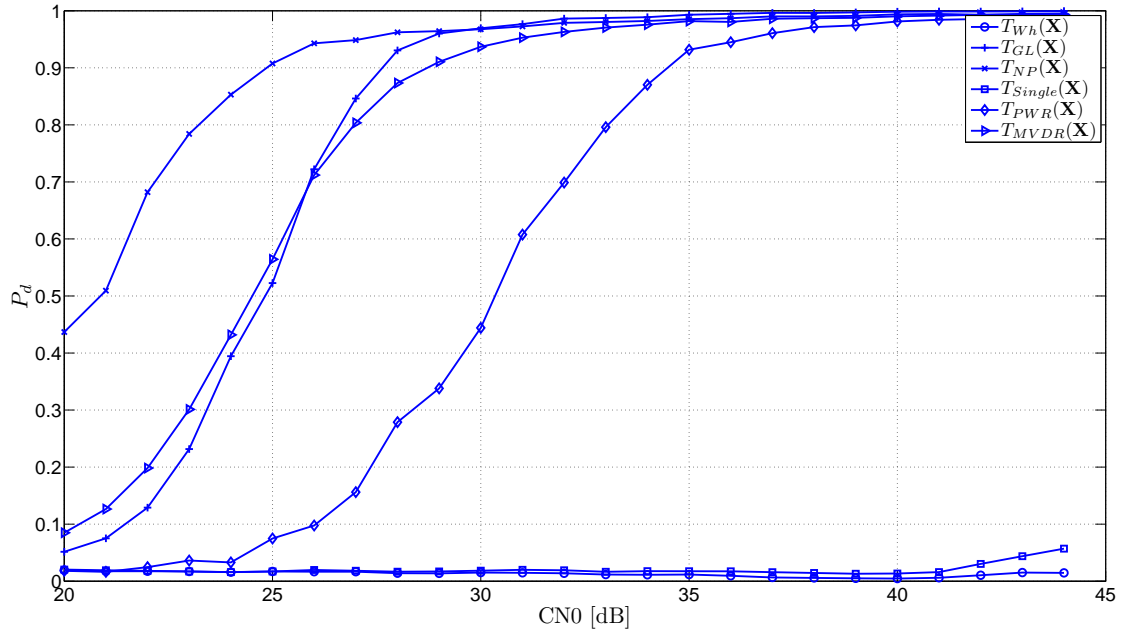


Figure 4.8: Galileo E1 acquisition P_d vs. satellite CN0 in the presence of wideband interference for different algorithms and 15° DOA estimation mean pointing error in the MVDR beamformer ($T_{MVDR}(\mathbf{X})$).

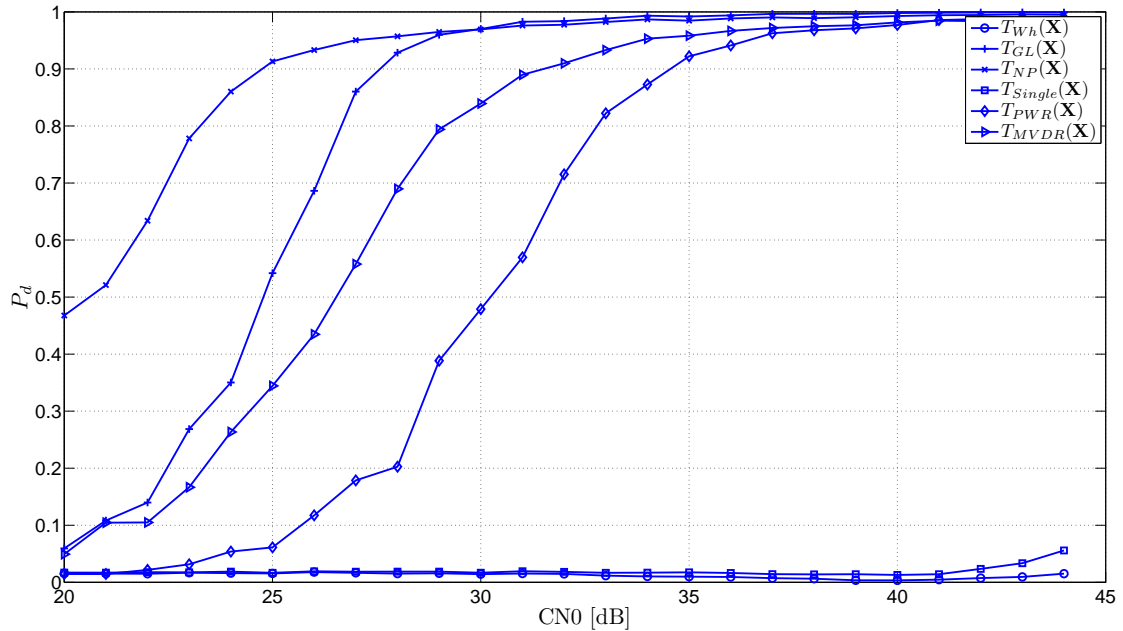


Figure 4.9: Galileo E1 acquisition P_d vs. satellite CN0 in the presence of wideband interference for different algorithms and 20° DOA estimation mean pointing error in the MVDR beamformer ($T_{MVDR}(\mathbf{X})$).

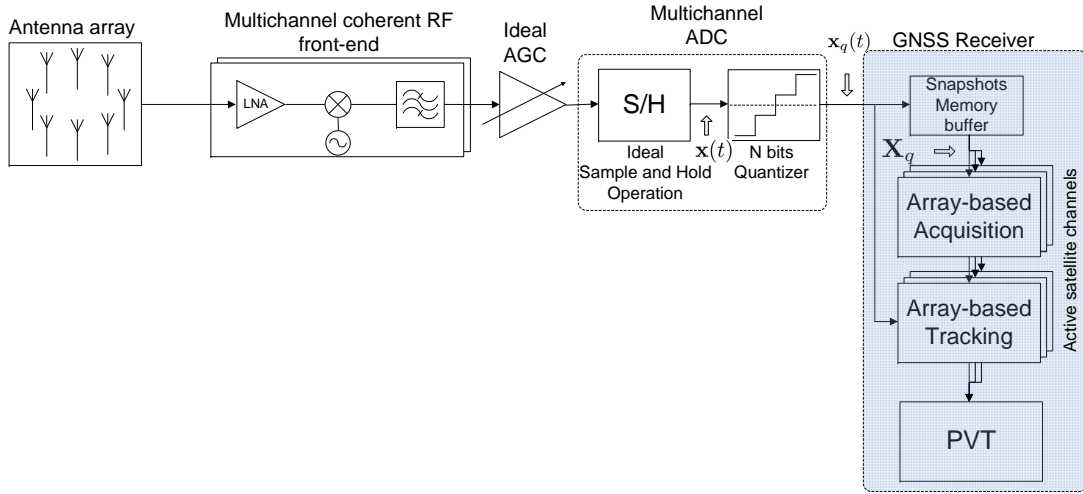


Figure 4.10: GNSS receiver block diagram, as simulated.

4.7 Performance in realistic conditions

The theoretical analysis of previous sections assumes ideal conditions. In this section the performance of the detectors is analyzed under realistic conditions, namely:

- **finite sample size:** the acquisition operation assumes that the signal synchronization parameters remain constant during the coherent acquisition time, which might not hold in long acquisition periods. In addition, the receiver hardware has limited resources to store the required data. Both restrictions limit the amount of available snapshots,
- **signal quantization effects:** the quantization or roundoff occurs when a signal is represented numerically with a finite number of bits. The antenna array front-end has typically an ADC for each antenna element, which obtains a quantized version of the input. This analysis considers an ideal sample-and-hold operation and uniform quantization, and
- **satellite signal synchronization errors:** the proposed acquisition test function involves a maximization on (f_d, τ) , performed usually by a grid search. In this analysis, we consider the effect of a finite number of grid search bins and, as a consequence, the presence of errors on the satellite synchronization parameters estimation.

The effects of the realistic conditions on the acquisition can be classified in

- presence of errors in the estimation of \mathbf{R}_{xx} , and
- perturbations of the cross-correlation vector \mathbf{r}_{xd} .

Fig. 4.10 shows a block diagram of the proposed GNSS receiver simulation. From left to right, the output of the antenna array elements is fed to a multichannel front-end, which is in charge of amplifying and downconverting synchronously all the antenna elements signals. Next, an ideal AGC is inserted to normalize the signal power. All antenna element channels are driven by the same gain, computed by the AGC, to avoid distortions in the signals' spatial signature. This simplified model isolates the quantization effects (which is the main interest of the analysis) from the possible artifacts caused by a saturation condition in the ADC. The normalized output of the AGC is inserted in an ideal sample-and-hold block and is uniformly quantized using N_b bits (actually, N_b is a design parameter) with a basic mid-tread quantizer [Wid08]. Finally, the quantized version of $\mathbf{x}(t)$, referred to as $\mathbf{x}_q(t)$, is recorded in a memory buffer during T_{acq} , obtaining the quantized version of the spatiotemporal matrix, represented by \mathbf{X}_q . At this point, a software-based GNSS receiver performs the signal processing operations with double-precision floating point resolution.

4.7.1 A Metric to measure the presence of errors in $\hat{\mathbf{R}}_{\mathbf{xx}}$

It is interesting to define a suitable metric to determine how much $\hat{\mathbf{R}}_{\mathbf{xx}}$ is affected by the quantization noise and other possible error sources. The covariance matrix belongs to a set of Hermitian positive definite matrices, which is a convex cone⁹, defined as $\mathcal{S} = \{\mathbf{R} \in \mathbb{C}^{N \times N} : \mathbf{R}^H = \mathbf{R}, \mathbf{R} \succ \mathbf{0}\}$. This set can be described using differential geometry to state definitions inside the set as is described hereafter.

For any two points \mathbf{R}_1 and \mathbf{R}_2 inside \mathcal{S} , the *geodesic distance* is the length of the geodesic curve that connects them [Ede98]. The geodesic distance is defined as:

$$\text{dist}_g(\mathbf{R}_1, \mathbf{R}_2) = \|\mathbf{M}\|_F, \quad (4.91)$$

where $\|\mathbf{M}\|_F = \sqrt{(\sum_i |\ln(\lambda_i)|^2)}$ stands for the logarithmic version of the Frobenius norm and λ_i represents the i -th eigenvalue of matrix $\mathbf{R}_1^{-\frac{1}{2}} \mathbf{R}_2 \mathbf{R}_1^{-\frac{1}{2}}$, and $\mathbf{M} = \ln(\mathbf{R}_1^{-\frac{1}{2}} \mathbf{R}_2 \mathbf{R}_1^{-\frac{1}{2}})$.

The geodesic distance is able to detect differences both in the eigenvectors and in the eigenvalues of $\mathbf{R}_{\mathbf{xx}}$ and $\hat{\mathbf{R}}_{\mathbf{xx}}$, consequently, it is eligible to measure possible perturbations in the covariance matrix estimation, as we show in the sequel.

4.7.2 Acquisition time effect in $\hat{\mathbf{R}}_{\mathbf{xx}}$

The SCM, defined in (4.9), is known to have a central Wishart distribution with $2K$ degrees of freedom [Mui82], thus, the elements in $\hat{\mathbf{R}}_{\mathbf{xx}}$ are distributed as a chi-square χ_{2K}^2 . The statistical moments of $\hat{\mathbf{R}}_{\mathbf{xx}} \sim \frac{1}{K} \mathcal{W}_N(\mathbf{R}_{\mathbf{xx}}, 2K)$ are

$$\mathbb{E}\{\hat{\mathbf{R}}_{\mathbf{xx}}\} \simeq \mathbf{R}_{\mathbf{xx}} \text{ when } K \rightarrow \infty \quad (4.92)$$

$$\text{var}\{\hat{\mathbf{R}}_{\mathbf{xx},i,j}\} = \frac{1}{K}(c_{i,j}^2 + c_{ii}c_{jj}), \quad (4.93)$$

where $\hat{\mathbf{R}}_{\mathbf{xx},i,j}$ is the element corresponding to the i -th row and the j -th column of $\hat{\mathbf{R}}_{\mathbf{xx}}$, and $c_{i,j}^2$ is the cross-correlation for the i and j antenna elements pair. As the number of available snapshots K increases, the degrees of freedom increase and $\text{var}\{\hat{\mathbf{R}}_{\mathbf{xx},i,j}\}$ decreases. It is also known that the SCM is a biased estimator of $\mathbf{R}_{\mathbf{xx}}$, but is approximately unbiased for a large number of snapshots. A Wishart matrix can be considered a Gaussian matrix using the central limit Theorem when it has a large number of degrees of freedom [Mui82]. In GNSS receivers, specially in slow-varying interference scenarios, the assumption is valid when using several milliseconds of coherent signal to estimate the SCM, see, e.g., [Tsu00]. This assumption leads us to consider $\hat{\mathbf{R}}_{\mathbf{xx}} \simeq \mathbf{R}_{\mathbf{xx}}$, assuming no quantization or roundoff effects.

To measure the dependence of T_{acq} and the quality of the estimation of $\hat{\mathbf{R}}_{\mathbf{xx}}$, the geodesic distance $\text{dist}_g(\mathbf{R}_{\mathbf{xx}}, \hat{\mathbf{R}}_{\mathbf{xx}})$, defined in (4.91), was computed for different T_{acq} in Fig. 4.11. The distance reached zero asymptotically with the increase of T_{acq} , even in the presence of strong CWI.

⁹In linear algebra, a convex cone is a subset of a vector space that is closed under linear combinations. When the definition is applied to the set of all symmetric positive semidefinite matrices $\{\mathbf{A} \in \mathcal{S}^N : \mathbf{y}^T \mathbf{A} \mathbf{y} > 0, \forall \|\mathbf{y}\| = 1\}$ of particular dimension N , this set \mathcal{S}^N is called the positive semidefinite cone, formed by the intersection of an infinite number of halfspaces in the vectorized variable. The positive definite (full-rank) matrices comprise the cone interior, while all singular positive semidefinite matrices (having at least one 0 eigenvalue) reside on the cone boundary [Dat05].

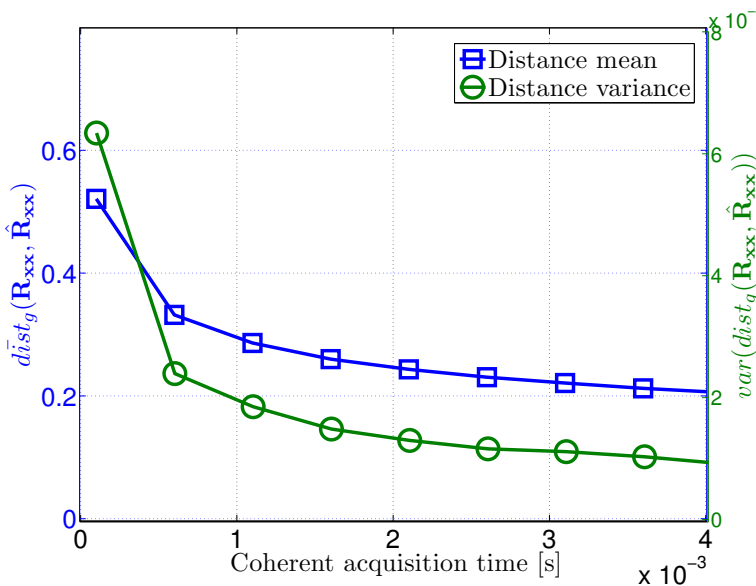


Figure 4.11: $\bar{dist}_g(\mathbf{R}_{xx}, \hat{\mathbf{R}}_{xx})$ vs. T_{acq} with a CW interference impinging into the array with $IN0 = 85$ dB-Hz. $\hat{\mathbf{R}}_{xx}$ was computed using 64-bits double floating-point resolution and the conditions of Table 4.4.

4.7.3 Signal quantization effects in $\hat{\mathbf{R}}_{xx}$

Assuming that the receiver performs the matrix multiplications without rounding or overflows, the presence of errors due to the signal quantization in $\hat{\mathbf{R}}_{xx}$ can be modeled as

$$\begin{aligned}\hat{\mathbf{R}}_{\mathbf{x}_q \mathbf{x}_q} &= \frac{1}{K} \left(\underbrace{(\mathbf{X} + \mathbf{X}_e)}_{\mathbf{x}_q} \underbrace{(\mathbf{X} + \mathbf{X}_e)^H}_{\mathbf{x}_q^H} \right) \\ &= \frac{1}{K} \mathbf{X} \mathbf{X}^H + \frac{1}{K} (2\Re\{\mathbf{X} \mathbf{X}_e^H\} + \mathbf{X}_e \mathbf{X}_e^H),\end{aligned}\quad (4.94)$$

where \mathbf{X}_e models the additive Pseudo Quantization Noise (PQN) [Wid08] matrix. The elements of the PQN noise matrix can be considered uncorrelated to the quantized signal and uniformly distributed with zero mean and variance

$$\sigma_q^2 = \frac{q^2}{12}, \quad (4.95)$$

where $q = \frac{V}{N_b}$ is the quantization granularity, V is the ADC dynamic range in volts, and N_b is the ADC resolution in number of bits. The PQN model is valid only when the Characteristic Function (CF) of the signal satisfies the Widrow quantizing Theorems 1 and 2 [Wid56]. A necessary condition is that the CF must be bandlimited. In the presented signal model, the noise is normally-distributed, and the associated Gaussian CF can be considered approximately bandlimited. For this case, the PQN model can be applied if $q \leq \sigma^2$. For coarse quantization granularity, the assumption of independence of the quantization noise is no longer valid. An approximation using the Sheppard's corrections can be used to obtain the variance of the quantized signal, see, e.g. [Wid08, p.84].

The AGC affects this analysis in the sense that it modifies the noise variance σ^2 present in the ADC input, specially when strong interference signals are present. In this case, the AGC reduces the gain, preventing ADC saturation, and then it is possible that the quantization granularity no longer holds the condition for the PQN model.

Considering that the quantized signal holds the PQN conditions, the expectation of (4.94) can be written as

$$E\{\hat{\mathbf{R}}_{\mathbf{x}_q \mathbf{x}_q}\} = \mathbf{R}_{xx} + \mathbf{R}_e, \quad (4.96)$$

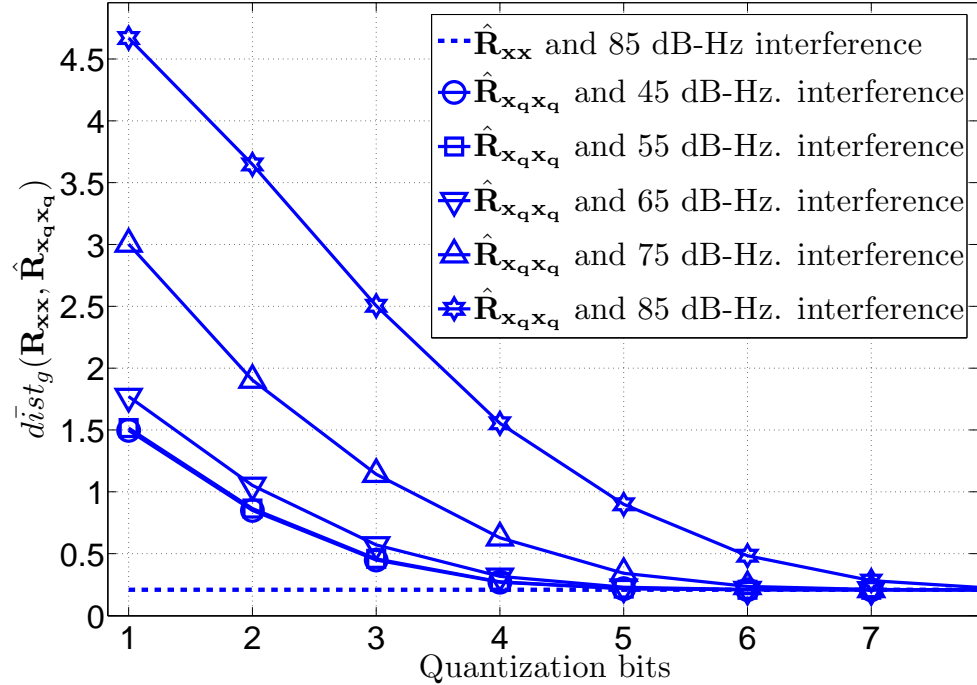


Figure 4.12: $\text{dist}_g(\mathbf{R}_{\mathbf{xx}}, \hat{\mathbf{R}}_{\mathbf{x}_q \mathbf{x}_q})$ vs. different quantization bits and a CW interference impinging into the array with different IN_0 .

where the cross-correlation term $\frac{1}{K} 2\Re\{\mathbf{E}\{\mathbf{XX}_e\}\} = 0$. The covariance matrix of the PQN is a diagonal matrix expressed as

$$\mathbf{R}_e = \sigma_q^2 \mathbf{I}. \quad (4.97)$$

Now, inserting (4.96) in (4.91) leads to

$$\text{dist}_g(\mathbf{R}_{\mathbf{xx}}, \hat{\mathbf{R}}_{\mathbf{x}_q \mathbf{x}_q}) = \|\mathbf{I} + \mathbf{R}_{\mathbf{xx}}^{\frac{-1}{2}} \mathbf{R}_e \mathbf{R}_{\mathbf{xx}}^{\frac{-1}{2}}\|_F, \quad (4.98)$$

where the eigenvalues of \mathbf{M} are $\lambda_i = 1 + \text{eig}(\mathbf{R}_{\mathbf{xx}}^{\frac{-1}{2}} \mathbf{R}_e \mathbf{R}_{\mathbf{xx}}^{\frac{-1}{2}})$.

In the case of a diagonal covariance matrix $\mathbf{R}_{\mathbf{xx}} = \sigma^2 \mathbf{I}$, inserting it in (4.98), a direct relation between $\text{dist}_g(\mathbf{R}_{\mathbf{xx}}, \hat{\mathbf{R}}_{\mathbf{x}_q \mathbf{x}_q})$ and the associated PQN variance σ_q^2 can be established

$$\sigma_q^2 = \sigma^2 \left(\exp \left(\frac{\text{dist}_g(\mathbf{R}_{\mathbf{xx}}, \hat{\mathbf{R}}_{\mathbf{x}_q \mathbf{x}_q})}{\sqrt{N}} \right) - 1 \right), \quad (4.99)$$

where the definition of $\|\cdot\|_F$ stated in Section 4.7.1 was used.

The signal quantization effect can be seen in Fig. 4.12, where the matrix distance between $\mathbf{R}_{\mathbf{xx}}$ and $\hat{\mathbf{R}}_{\mathbf{x}_q \mathbf{x}_q}$ was computed for different number of quantization bits simulations and for different CW interference IN_0 ¹⁰. The stronger is the interference, the more bits are needed to obtain a good estimation of $\mathbf{R}_{\mathbf{xx}}$. Notice that the matrix distance minimum is bounded by the value of T_{acq} , as stated in Section 4.7.2, which is set to 4 ms in this simulation. The impact of the covariance matrix estimation distance in the overall performance of the detector is shown in Section 4.8.

¹⁰Defined as the ratio of interference power to white-noise spectral density.

4.7.4 Signal quantization effects in $\hat{\mathbf{r}}_{\mathbf{x}\mathbf{d}}$

Assuming that the local signal replica is generated using floating point resolution and the cross-correlation operations are computed without rounding or overflows, it is possible to apply the PQN model also in $\hat{\mathbf{r}}_{\mathbf{x}\mathbf{d}}$ as

$$\hat{\mathbf{r}}_{\mathbf{x}_q \mathbf{d}} = \frac{1}{K} \mathbf{X} \mathbf{d}^H + \frac{1}{K} \mathbf{X}_e \mathbf{d}^H, \quad (4.100)$$

where \mathbf{X}_e is the PQN matrix defined in the previous Section. Inserting (4.100) in (4.41), assuming that $\hat{\mathbf{R}}_{\mathbf{x}\mathbf{x}}^{-1} \simeq \mathbf{R}_{\mathbf{x}\mathbf{x}}^{-1}$, the quantized version of the test function is

$$T_{\text{GL}}(\mathbf{X}_q) = \underbrace{\hat{\mathbf{r}}_{\mathbf{x}\mathbf{d}}^H \mathbf{R}_{\mathbf{x}\mathbf{x}}^{-1} \hat{\mathbf{r}}_{\mathbf{x}\mathbf{d}}}_{T_{\text{GL}}(\mathbf{X})} + \underbrace{\hat{\mathbf{r}}_{\mathbf{x}_e \mathbf{d}}^H \mathbf{R}_{\mathbf{x}\mathbf{x}}^{-1} \hat{\mathbf{r}}_{\mathbf{x}_e \mathbf{d}}}_{T_{\text{GL}}(\mathbf{X}_e)}, \quad (4.101)$$

where the cross-correlation terms $\hat{\mathbf{r}}_{\mathbf{x}\mathbf{d}}^H \mathbf{R}_{\mathbf{x}\mathbf{x}}^{-1} \hat{\mathbf{r}}_{\mathbf{x}_e \mathbf{d}}$ and $\hat{\mathbf{r}}_{\mathbf{x}_e \mathbf{d}}^H \mathbf{R}_{\mathbf{x}\mathbf{x}}^{-1} \hat{\mathbf{r}}_{\mathbf{x}\mathbf{d}}$ are neglected due to the independence of $\hat{\mathbf{r}}_{\mathbf{x}\mathbf{d}}$ and $\hat{\mathbf{r}}_{\mathbf{x}_e \mathbf{d}}$. The non-quantized version of the test function is distorted with an independent quantization noise term. The resulting PDF of $T_{\text{GL}}(\mathbf{X}_q)$ is the sum of the chi-square $T_{\text{GL}}(\mathbf{X}) \sim \chi_{2N}^2(\delta_{T_{\text{GL}}})$ distribution, modeled in Section 4.5.1 plus a central chi-square $T_{\text{GL}}(\mathbf{X}_e) \sim \chi_{2N}^2$, which models the PQN. The performance of the detector is affected and a quantitative analysis by simulations can be found on Section 4.8.

4.7.5 Satellite signal synchronization errors

The aim of this section is the identification of the effects of signal synchronization errors in the detector's performance. It is considered that the signal is not quantized and all the operations are performed without rounding or overflows and using all the available satellite signal bandwidth. It is also assumed a single-dwell acquisition using a coherent block of signal with T_{acq} equal to one spreading code period. In these conditions, the maximization of $T_{\text{GL}}(\mathbf{X})$ in (4.41) involves the computation of $\hat{\mathbf{r}}_{\mathbf{x}\mathbf{d}}(\hat{f}_d, \hat{\tau})$, which can be interpreted as a vector of N correlators or matched filters outputs:

$$\hat{\mathbf{r}}_{\mathbf{x}\mathbf{d}}(\hat{f}_d, \hat{\tau}) = [\hat{R}_{\mathbf{x}_1 \mathbf{d}}(\hat{f}_d, \hat{\tau}) \dots \hat{R}_{\mathbf{x}_N \mathbf{d}}(\hat{f}, \hat{\tau})]^T, \quad (4.102)$$

where $\hat{R}_{\mathbf{x}_i \mathbf{d}}(\hat{f}_d, \hat{\tau}) = \frac{1}{K} \mathbf{x}_i \mathbf{d}(\hat{f}_d, \hat{\tau})$ is the correlator output for the i -th antenna element.

This maximization can be performed by a grid search operation similar to the classical single-antenna matched filter based acquisition [Tsu00], and thus it is possible to use the results for the single-antenna acquisition to analyze the performance losses due to satellite signal synchronization errors.

In the definition of the grid search, the uncertainty region of the synchronization parameters (f_d, τ) shall be defined based on the specific GNSS constellation, frequency band, and receiver dynamics. In the case of a static receiver for GPS L1 C/A and Galileo E1 Open Service signal, the Doppler search space should be $\tilde{f} \in [+5000, -5000]$ Hz [Tsu00, p.37] and the time delay search space should be the entire code period, which for GPS L1 C/A is $\tilde{\tau}_{\text{GPS}} \in [0, 1]$ ms, and for Galileo E1 is $\tilde{\tau}_{\text{Gal}} \in [0, 4]$ ms [Und10].

The average error of the signal synchronization parameters estimation will depend on the size of the search grid bin, defined both by $\Delta \tilde{f}_d$ and $\Delta \tilde{\tau}$. The choice of $\Delta \tilde{\tau}$ depends on the autocorrelation properties of the satellite signal.

For GPS L1 C/A the typical value is $\Delta \tilde{\tau}_{\text{GPS}} = T_c$, which guarantees a maximum misalignment of $\tau_e = |\tau - \hat{\tau}| \leq 0.5T_c$ and consequently, according to the GPS L1 C/A autocorrelation function, the signal autocorrelation loss is limited to $\alpha_{\text{ACF}}(\tau_e) \leq 3$ dB [Tsu00].

On the contrary, the Galileo E1 CBOC signal has a multiple-peak autocorrelation function that requires $\Delta \tilde{\tau}_{\text{Gal}} = \frac{T_c}{4}$ to guarantee $\tau_e = |\tau - \hat{\tau}| \leq 0.125T_c$ and thus, the signal autocorrelation loss is below 3 dB. In the literature it can be found a number of single-antenna acquisition techniques specially designed for the new CBOC-based GPS and Galileo signals, see, e.g. [Bor09b] that can be applied to the proposed grid search.

GNSS	Search space	Grid bin	Synchronization errors	ρ'
GPS L1 C/A	$\check{f} \in [+5, -5]$ kHz. $\check{\tau} \in [0, 1)$ ms	$\Delta\check{f} \leq \frac{2}{3T_{acq}}$ $\Delta\check{\tau} = \frac{T_c}{2}$	$f_e \leq \frac{\Delta\check{f}}{2}$ $\tau_e \leq 0.25T_c$	$\rho' \geq \rho - 6$ dB
Galileo E1	$\check{f} \in [+5, -5]$ kHz. $\check{\tau} \in [0, 4)$ ms	$\Delta\check{f} \leq \frac{2}{3T_{acq}}$ $\Delta\check{\tau} = \frac{T_c}{4}$	$f_e \leq \frac{\Delta\check{f}}{2}$ $\tau_e \leq 0.125T_c$	$\rho' \geq \rho - 6$ dB

Table 4.3: Grid search signal synchronization errors and their equivalent SNR loss.

Regarding the frequency search space, the choice of $\Delta\check{f}_d$ depends on the frequency response of a matched filter, which is known to have a closed expression for the correlation loss

$$\alpha_{MF}(f_e, T_{acq})|_{\tau_e=0} = \left| \frac{\sin(\pi f_e T_{acq})}{\pi f_e T_{acq}} \right|^2, \quad (4.103)$$

where $f_e = |f_d - \hat{f}_d| \leq \frac{\Delta\check{f}_d}{2}$. The frequency response is a sinc-shaped curve, and increasing T_{acq} makes the sinc main lobe narrower, and thus $\Delta\check{f}$ should be able to limit $\alpha_{MF}(f_e, T_{acq})|_{\tau_e=0}$. A criterion commonly used is to limit $\alpha_{MF}(f_e, T_{acq})|_{\tau_e=0} \leq 3$ dB and then $\Delta\check{f}_d \leq \frac{2}{3T_{acq}}$.

Both the effect of τ_e and f_e can be expressed as an equivalent loss of the SNR:

$$\rho' = \rho - (\alpha_{ACF}(\tau_e) + \alpha_{MF}(f_e, T_{acq})) \geq \rho - 6 \text{ dB}, \quad (4.104)$$

if the above conditions for the grid search hold. Table 4.3 summarizes the effects of the synchronization errors on the acquisition SNR, and consequently, the effect on the acquisition performance.

In addition to the grid search errors, the signal acquisition is affected by the navigation data bits transition. The reader is referred to [O'D07] among other references for the effects on single-antenna receivers, which can be extended to the array-based acquisition considering the operation of N parallel correlators or matched filters as stated in (4.102).

4.8 Simulation results

In order to verify the theoretical study, the performance of the proposed test functions was evaluated by means of MC simulations in a variety of scenarios. Table 4.4 shows the common parameters for all the simulations. A satellite signal level of $CN0 = 24$ dB-Hz. was selected, which is close to the sensitivity level according to Table 4.2, in order to be able to evaluate the performance of the detectors by means of ROC curves.

Table 4.4: Simulation parameters

Parameter	Value	Units
Signal type	Galileo E1-B ¹ (no telemetry)	–
Signal $CN0$	24	dB-Hz.
Signal DOA	$Az = 120^\circ$, $El = 45^\circ$	
CW interference	1	kHz.
Wideband interference	2	MHz.
Interference DOA	random DOA ²	–
Interference $IN0$	45-85	dB-Hz.
Array geometry	8 elements Circular ³	–
Sampling frequency	6	Msps
Sampling resolution ⁴ (ideal conditions)	64	bits
Sampling resolution ⁵ (realistic conditions)	1 to 8	bits
T_{acq}	4	ms
Acquisition baseband bandwidth ⁶	2	MHz.
Independent realizations	2000	–

¹ According to [Und10].² Uniform distribution for elevation and azimuth, $El \in [0, 90]$ and $Az \in [0, 360]$ degrees.³ Half-wavelength separation between isotropic elements.⁴ IEEE floating point format 64 bits double-precision.⁵ Fixed-point format.⁶ The acquisition baseband bandwidth was set according to the optimal acquisition bandwidth values stated in [Arr10b].

In the simulations, the synchronization parameters estimations were set $\hat{f}_d = f_d$ and $\hat{\tau} = \tau$ as the true values in the \mathcal{H}_1 hypothesis to show the performance of the detector test function without signal synchronization errors. Although in a real receiver, a grid search method should be used to estimate the synchronization parameters [Tsu00], which results in a loss of performance, as stated in Section 4.7.5.

4.8.1 Ideal conditions

Summarizing the theoretical analysis, Table 4.5 summarizes the expressions for test statistics and both detection and false alarm probabilities of the presented detectors. In this section, the simulations were performed in the absence of signal quantization or roundoff effects.

The test statistic histogram for $T_{GL}(\mathbf{X})$ detector is simulated in the presence of strong CWI with $IN0 = 80$ dB-Hz impinging into the array with a random DOA. Fig. 4.13 shows the results compared to the theoretical PDF curves defined in (4.54). As it can be observed, the detector was able to distinguish between the two hypotheses and the histograms are aligned with the theoretical PDF curves. Regarding the \mathcal{H}_1 histogram, their associated theoretical PDFs curves are slightly optimistic because that do not take into account the effects of the limited bandwidth in \hat{R}_{dd} .

In Fig. 4.14 the ROC performance curves of the detector are compared to the clairvoyant detector ($T_{NP}(\mathbf{X})$) and the white noise version of GLRT ($T_{Wh}(\mathbf{X})$). The simulation scenario was identical to the previous one, however, the CWI impinges the array with different $IN0 = 45 - 85$ dB-Hz values. The same simulation was done for an uncorrelated wideband interference impinging into the array, and generated using a Gaussian pseudorandom number generator. The latter can be found in Fig. 4.15. Examining both figures some conclusions can be extracted:

	NP $T_{NP}(\mathbf{X})$	GLRT white $T_{Wh}(\mathbf{X})$	GLRT colored $T_{GL}(\mathbf{X})$
$T(\mathbf{X})$	$\Re\{\mathbf{h}^H \mathbf{Q}^{-1} \hat{\mathbf{r}}_{xd}\}$	$\max_{f_d, \tau} \left\{ \frac{\hat{\mathbf{r}}_{xd}^H(f_d, \tau) \hat{\mathbf{r}}_{xd}(f_d, \tau)}{\hat{R}_{dd} \hat{\sigma}^2} \right\}$	$\max_{f_d, \tau} \left\{ \frac{\hat{\mathbf{r}}_{xd}^H(f_d, \tau) \hat{\mathbf{R}}_{xx}^{-1} \hat{\mathbf{r}}_{xd}(f_d, \tau)}{\hat{R}_{dd}} \right\}$
$P_{fa}(\gamma)$	$1 - \Phi\left(\frac{\gamma}{\sigma_{NP}}\right)$	$\exp\left\{\frac{-\gamma}{2\sigma_{T_{Wh}}^2}\right\} \sum_{k=0}^{N-1} \frac{1}{k!} \left(\frac{\gamma}{2\sigma_{T_{Wh}}^2}\right)^k$	$\exp\left\{\frac{-\gamma}{2\sigma_{T_{GL}}^2}\right\} \sum_{k=0}^{N-1} \frac{1}{k!} \left(\frac{\gamma}{2\sigma_{T_{GL}}^2}\right)^k$
$P_d(\gamma)$	$1 - \Phi\left(\frac{\gamma - \mu_{T_{NP}}}{\sigma_{T_{NP}}}\right)$	$Q_N\left(\frac{\sqrt{\delta_{T_{Wh}}}}{\sigma_{T_{Wh}}}, \frac{\sqrt{\gamma}}{\sigma_{T_{Wh}}}\right)$	$Q_N\left(\frac{\sqrt{\delta_{T_{GL}}}}{\sigma_{T_{GL}}}, \frac{\sqrt{\gamma}}{\sigma_{T_{GL}}}\right)$
Par.	$\mu_{T_{NP}}(\mathbf{Q}, \mathbf{h}) = \mathbf{h}^H \mathbf{Q}^{-1} \mathbf{h},$ $\sigma_{T_{NP}}^2(\mathbf{Q}, \mathbf{h}, K) = \frac{\mathbf{h}^H \mathbf{Q}^{-1} \mathbf{h}}{2K}$	$\delta_{T_{Wh}}(\hat{\sigma}^2, \mathbf{h}) = \frac{\mathbf{h}^H \mathbf{h}}{\hat{\sigma}^2},$ $\sigma_{T_{Wh}}^2(K) = \frac{1}{2K}$	$\delta_{T_{GL}}(\hat{\mathbf{R}}_{xx}, \mathbf{h}) = \mathbf{h}^H \hat{\mathbf{R}}_{xx}^{-1} \mathbf{h},$ $\sigma_{T_{GL}}^2(K) = \frac{1}{2K}$

Table 4.5: Performance expressions for the detectors in ideal conditions.

- the performance of $T_{GL}(\mathbf{X})$ detector is aligned with the theoretical model. The proposed detector offers efficient protection against uncorrelated point source interferences. In that sense, even with the presence of high power interference values of $IN0 = 85$ dB-Hz, the reduction of the P_d is below 10%,
- the performance of both algorithms is almost equal in low power interference conditions, a fact that is aligned with the theoretical analysis, however when the interference reach $IN0 \geq 55$ dB-Hz, the performance of $T_{Wh}(\mathbf{X})$ is dramatically reduced. A conventional single-antenna¹¹ matched filter based GNSS acquisition has the same response to a directional interference as $T_{Wh}(\mathbf{X})$. Therefore, the performance improvement with respect to a single-antenna receiver has been assessed, and
- the wideband interference rejection capability of $T_{GL}(\mathbf{X})$ is slightly worse than the CW interference counterpart. One factor that should be taken into account is the level of correlation between the wideband interference and the satellite signal.

Finally, we simulated the detector's performance vs. the number of antenna elements in a scenario with strong wideband jammer impinging into the array with $IN0 = 85$ dB-Hz. Fig. 4.16 shows the resulting ROC curves. The protection against the interference increases dramatically with the number of antenna elements, which is aligned with the theoretical analysis of Section 4.5.1.3.

The interference protection offered by the detectors was compared to the single-antenna MF acquisition and the white noise version of GLRT detector.

Fig. 4.17 shows the detector's P_d versus the number of impinging interferences (N_{int}), for a selected $P_{fa} = 0.001$. In the simulation, we used the parameters listed in Table 4.4, without considering quantization effects, and for a satellite's signal with $CN0 = 44$ dB-Hz. Each of the interfering signals is a noise-like wideband interference with $IN0 = 76$ dB-Hz and random DOA. From the results it is possible to state that the proposed detector offers an excellent protection against uncorrelated wideband interferences in contrast to conventional single-antenna MF. The interference-rejection capability is maintained until the subspace generated by the interferences completely overlaps the signal subspace. In this situation ($N_{int} > 7$), the array run out of its degrees of freedom.

¹¹Not using any time-domain or frequency-domain interference rejection technique, like notch-filter based techniques.

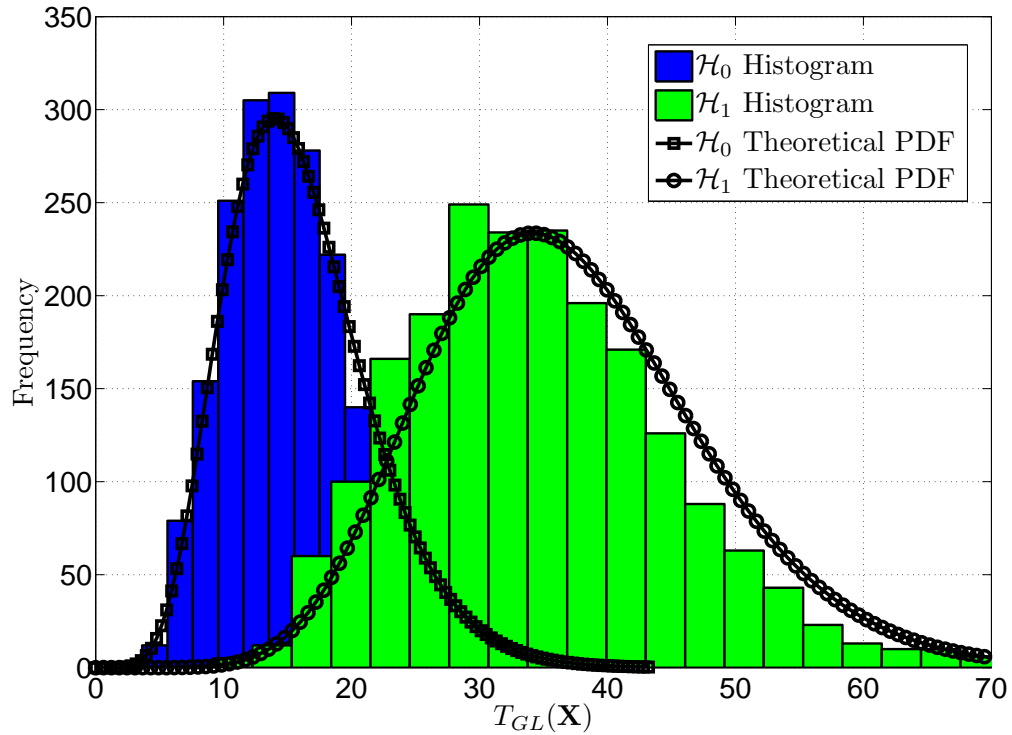


Figure 4.13: $T_{GL}(X)$ histogram in ideal conditions, in an scenario with a CWI impinging into the array with no INR.

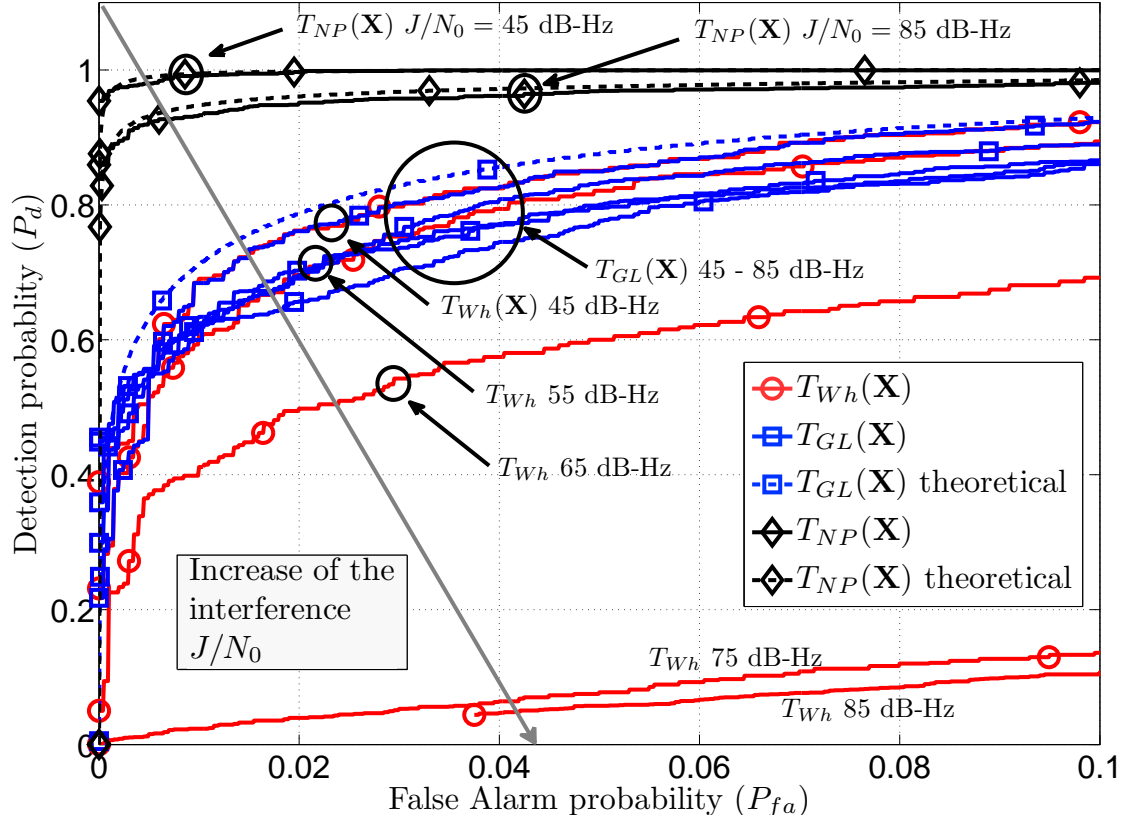


Figure 4.14: $T_{NP}(X)$, $T_{GL}(X)$, and $T_{Wh}(X)$ ROCs performance in ideal conditions, in an scenario with an in-band CW interference impinging into the array with different $IN0 = \{45, 55, 65, 75, 85\}$ dB-Hz. For clarity reasons some theoretical and simulated curves are omitted.

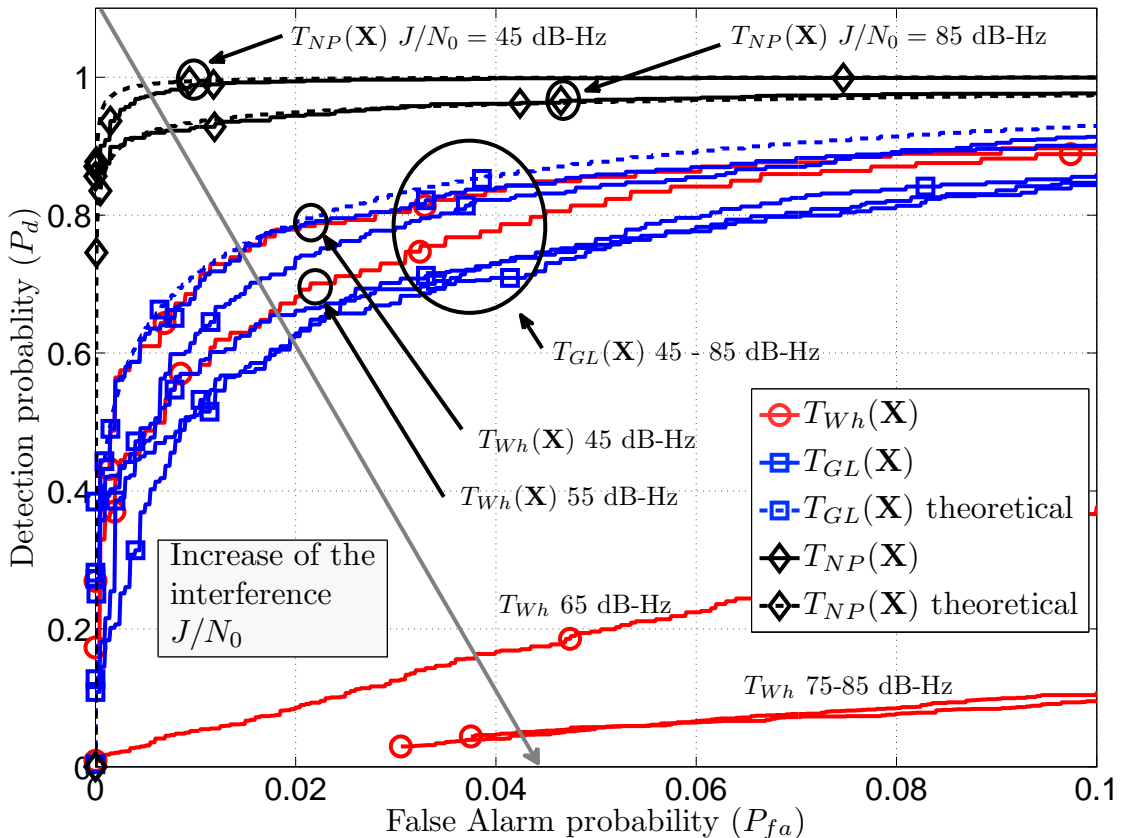


Figure 4.15: $T_{NP}(\mathbf{X})$, $T_{GL}(\mathbf{X})$, and $T_{Wh}(\mathbf{X})$ ROCs performance in ideal conditions, in an scenario with an uncorrelated wideband interference impinging into the array with different $IN0 = \{45, 55, 65, 75, 85\}$ dB-Hz. For clarity reasons some theoretical and simulated curves are omitted.

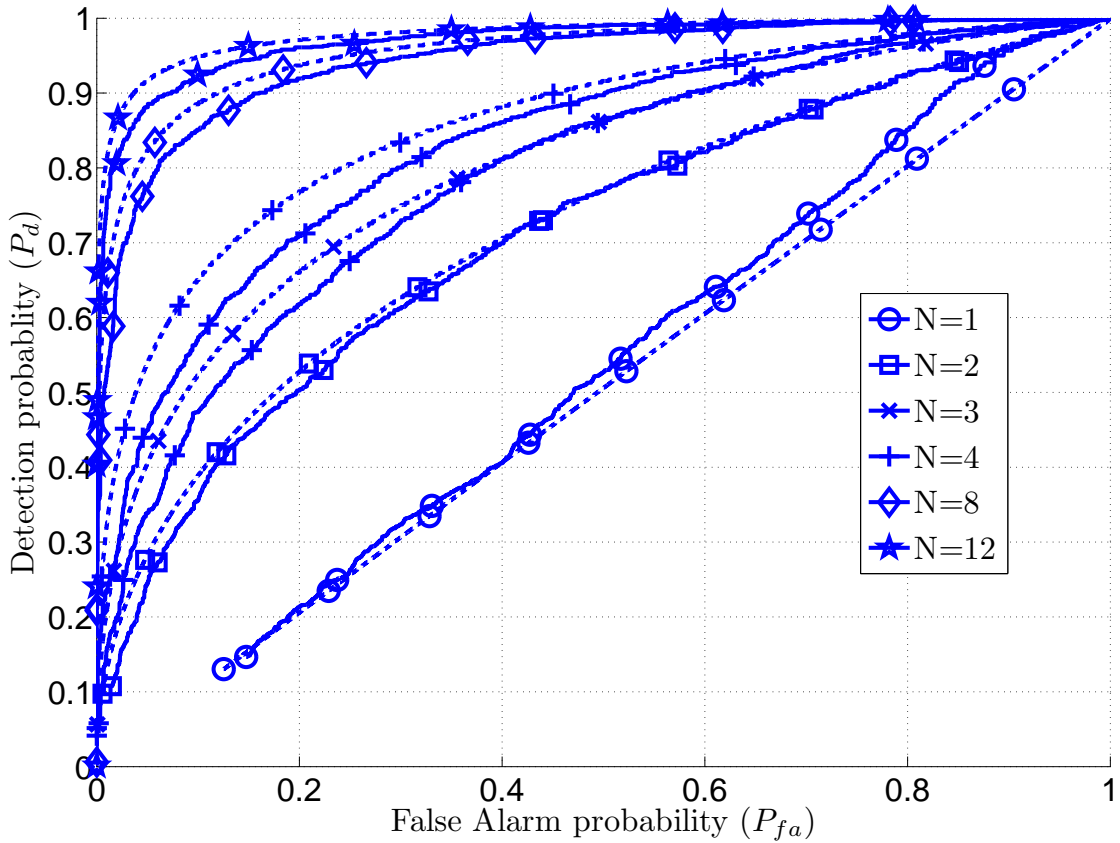


Figure 4.16: Acquisition performance of $T_{GL}(\mathbf{X})$ for $N = 1 - 12$ antenna elements, with a wideband interference impinging into the array with $IN0 = 85$ dB-Hz. The $T_{GL}(\mathbf{X})$ theoretical ROC curves are plotted in dashed lines.

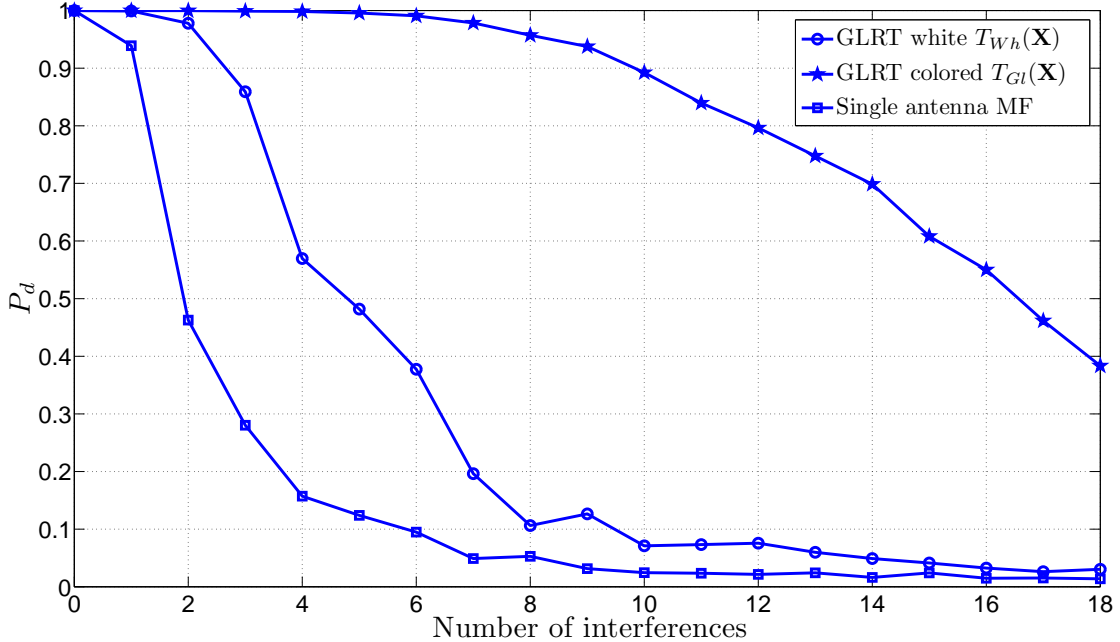


Figure 4.17: Evolution of the P_d for a fixed $P_{fa} = 0.001$ in the presence of an increasing number of wideband interferences. Each of the points contains 4000 independent realizations.

4.8.2 Realistic conditions

Regarding the realistic conditions defined in Section 4.7, two different simulations were performed for $T_{\text{GL}}(\mathbf{X})$, with the parameters described in Table 4.4:

- **the effect of $\text{dist}_g(\mathbf{R}_{\mathbf{xx}}, \hat{\mathbf{R}}_{\mathbf{xx}})$ in the acquisition performance:** in this experiment, an intentionally distorted version of $\hat{\mathbf{R}}_{\mathbf{xx}}$ using (4.96) and (4.97) was generated in order to simulate different $\text{dist}_g(\mathbf{R}_{\mathbf{xx}}, \hat{\mathbf{R}}_{\mathbf{xx}})$ values. The snapshots matrix and the detector test statistic operations were performed without quantizations or overflows, as in the ideal conditions case. Additionally, the simulation scenario includes a strong wideband jammer with Interference-to-Noise-density Ratio $IN0 = 85$ dB-Hz. Fig. 4.18 shows the resulting ROC curves, and
- **the effect of 1-8 bits Uniform Quantization and a comparison with the 1-8 bits PQN model:** the effect of the snapshot matrix quantization described in Section 4.7.4 was simulated for different ADC resolutions. Moreover, the PQN model was also simulated adding to the ideal snapshots matrix a uniformly-distributed pseudorandom noise, described in (4.94). The scenario also includes a strong in-band CW jammer with $IN0 = 85$ dB-Hz. Fig. 4.19 shows the resulting ROC curves.

From the results it can be seen that the matrix distance $\text{dist}_g(\mathbf{R}_{\mathbf{xx}}, \hat{\mathbf{R}}_{\mathbf{xx}})$ plays a critical role for the performance in the presence of interferences or jamming signals, which is aligned with the theoretical analysis of Section 4.5.1.3. Observing the simulation of $\text{dist}_g(\mathbf{R}_{\mathbf{xx}}, \hat{\mathbf{R}}_{\mathbf{xx}})$ vs. different quantization bits in Fig. 4.12, it is possible to establish a relation between the ADC resolution and the performance of the acquisition when an estimation of the covariance matrix is used. The effect of the snapshots quantization in the acquisition performance shown in Fig. 4.19 indicates that the detector reaches the same performance as the floating-point resolution case when a minimum of 5 quantization bits are used, assuming the ideal AGC described in Section 4.7.

Another simulation was performed in order to show how the ADC resolution affects the detector's performance in an open sky, $CN0 = 44$ dB-Hz scenario, where a single in-band CWI impinges the array with a range of $IN0 = 70 - 136$ dB-Hz. The rest of simulation parameters are defined in Table 4.4. We plotted P_d subject to a $P_{fa} = 0.001$ in Fig. 4.20.

From the results it is possible to draw some important conclusions:

- in the presence of strong interferences, the increase of the ADC resolution does not improve the performance of the detectors that do not take into account the spatial dimension of the problem ($T_{\text{MF}}(\mathbf{X})$ and $T_{\text{Wh}}(\mathbf{X})$). In this case, the interference power exceeds the processing gain before the ADC quantization effects appears, and
- the GLRT detector for the colored noise ($T_{\text{GL}}(\mathbf{X})$) increases its performance proportionally to the increment of the dynamic range of the ADC. The rationale is that with a higher ADC resolution, the effective bits available for the satellite signal also increase, and consequently, for the same AGC gain, there are more effective signal bits. As a result, higher interference power is required to reduce the AGC gain and thus reduce the effective signal bits. It is possible to write an expression for the equivalent $IN0$ protection as the increase of the dynamic range:

$$\Delta_{DR} = 20 \log \left(\frac{2^{N_{b_2}}}{2^{N_{b_1}}} \right), \quad (4.105)$$

where N_{b_1} and N_{b_2} is the previous and the actual ADC resolution, respectively. Particularizing it for $N_{b_1} = 2, N_{b_2} = 4$, $\Delta_{DR} = 12$ dB, and for $N_{b_1} = 4, N_{b_2} = 8$, $\Delta_{DR} = 24$ dB, which is aligned with simulation results of Fig. 4.20.

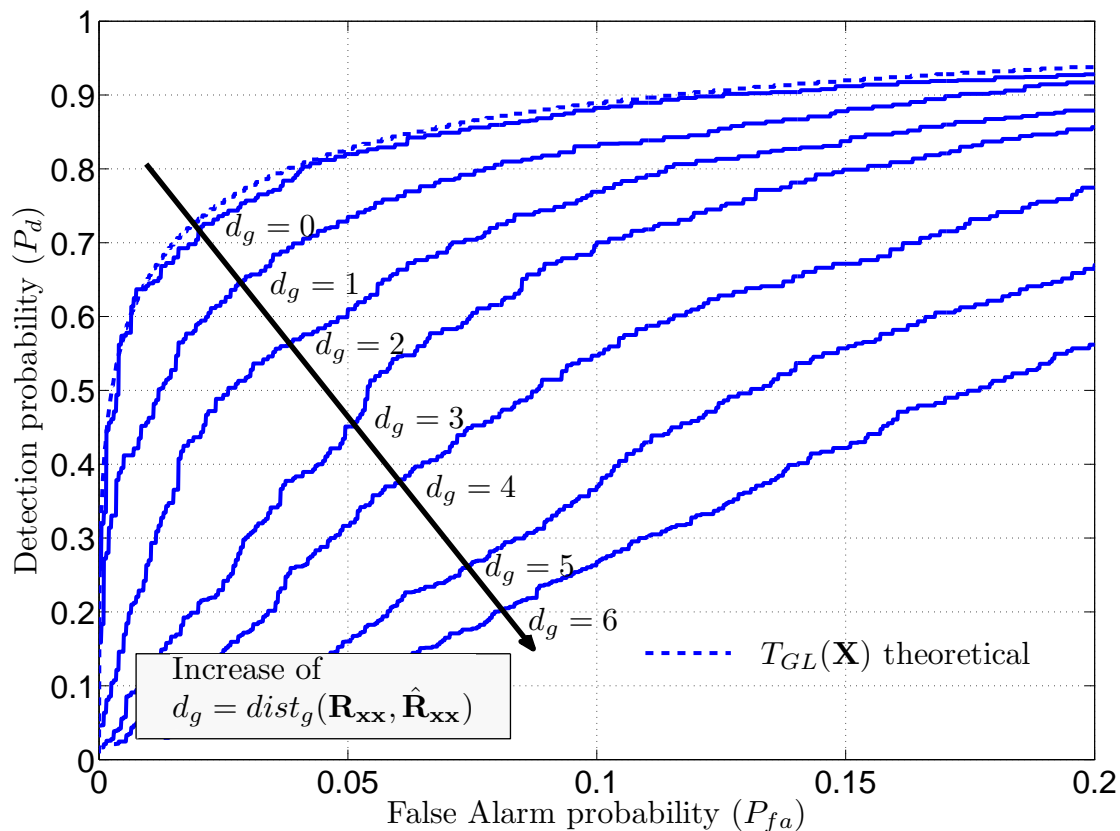


Figure 4.18: Effect of the $dist_g(\mathbf{R}_{xx}, \hat{\mathbf{R}}_{xx})$ in the acquisition performance of $T_{GL}(\mathbf{X})$, with a CWI impinging into the array with $IN0 = 85$ dB-Hz.

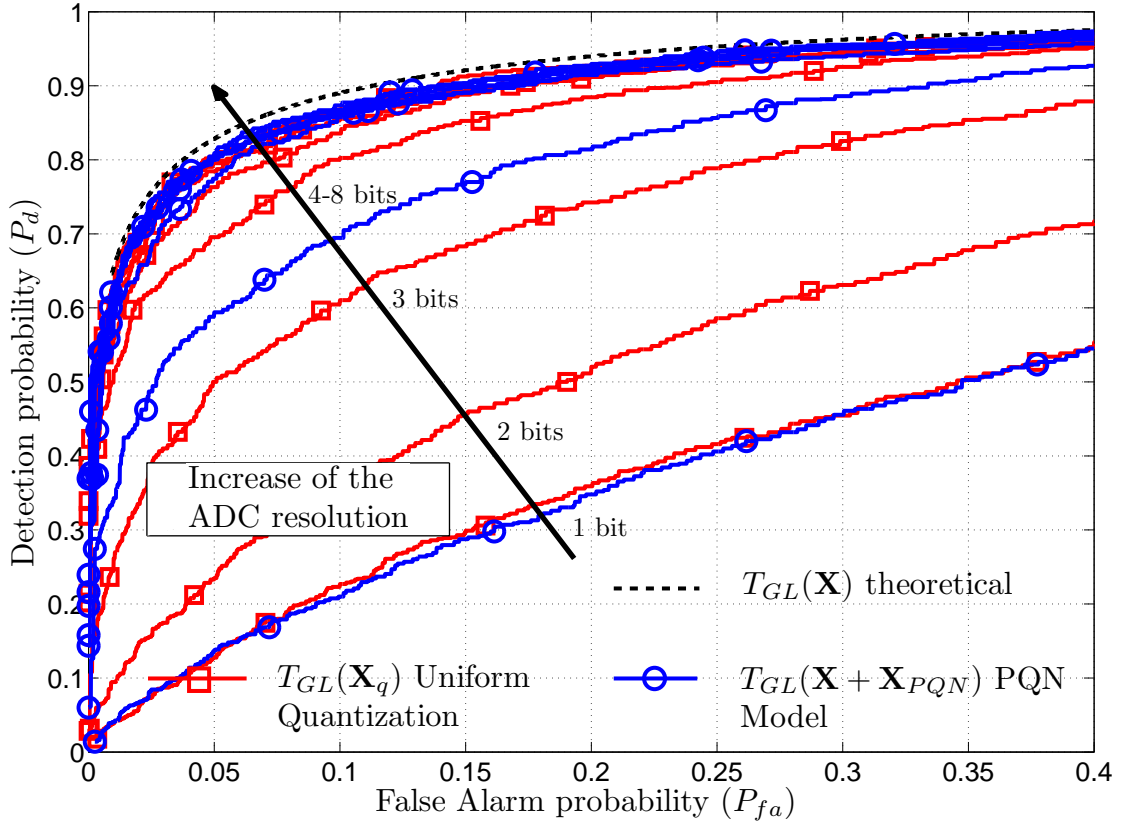


Figure 4.19: Acquisition performance of $T_{GL}(\mathbf{X}_q)$ for 1-8 bits uniform quantization and 1-8 bits PQN model, with a CW interference impinging into the array with $IN_0 = 85$ dB-Hz.

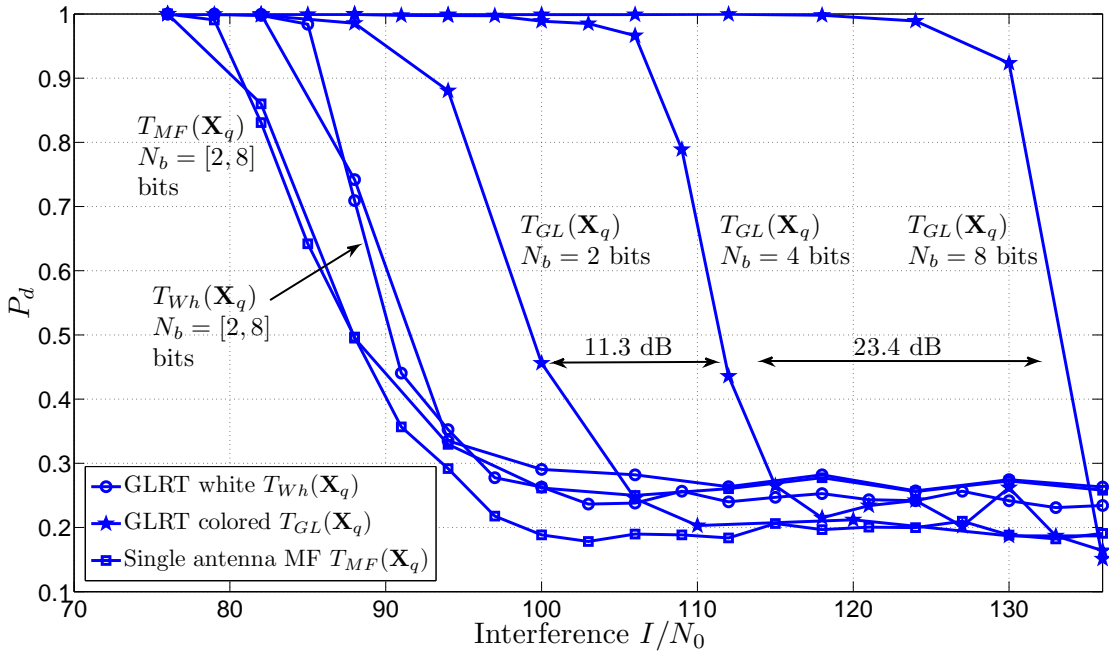


Figure 4.20: P_d in an scenario with satellite $CN_0 = 44$ dB-Hz, and single CW interference impinging into the array with $IN_0 = 70 - 136$ dB-Hz, for $P_{fa} = 0.001$ and different quantization bits $N_b = 2 - 8$ bits.

4.9 Summary

In this Chapter, we proposed a statistical approach for the antenna array-based GNSS signal acquisition problem. We used the NP detection framework and the GLRT to obtain a new GNSS detector which is able to mitigate temporally uncorrelated point source interferences even if the array is unstructured and moderately uncalibrated. The key statistical feature is the assumption of an arbitrary and unknown covariance noise matrix, which attempts to capture the statistical behavior of the interferences and other non-desirable signals, while exploiting the spatial dimension provided by antenna arrays. Closed form expressions for the detection and false alarm probabilities were provided and the performance and the interference rejection capability were modeled and compared to their theoretical bound.

The proposed detector was proven to be a UMP test detector and has CFAR properties. Both properties are highly valuable in a cold acquisition situation where there is neither information of the satellites' direction of arrival, that prevents from applying spatial-based beamforming, nor the receiving signals power, that makes difficult to set an acquisition threshold. The protection against interference effects was modeled by means of signal and interference subspace projections. The impact of the number of antenna elements and the effect of narrowband and wideband interferences were also analyzed and simulated. Results show that the detector offers a superior interference protection in both interference cases. The proposed array-based acquisition algorithm was also compared to conventional acquisition techniques performed after blind null-steering beamformer approaches, such as the power minimization algorithm.

Additionally, the detector performance was examined under realistic conditions, modeled as the presence of errors in the covariance matrix estimation due to finite sample size, residual synchronization errors, and signal quantization effects. From the results we can conclude that the signal quantization plays a key role in the performance of the proposed detector. In that sense, the relation between the ADC resolution and the interference mitigation capability was found. Theoretical results were supported by Monte Carlo simulations.

Going further towards a proof-of-concept prototype of the proposed acquisition algorithms, next chapter is devoted to develop a novel real-time array-based GNSS receiver platform with a two-fold main target: to examine the real-time implementation feasibility and to explore their performance in real-life scenarios, taking into account all the unmodeled phenomena such as the antenna-array elements radiation patterns and front-end non-linearities among others.

The results presented in this chapter were partially published in:

- [FP09a] C. Fernández-Prades, J. Arribas, and P. Closas, “The decoupling of DOA/Synchronization parameters in colored noise environments”, *Proceedings of NEWCOM++ ACoRN Joint Workshop*, Barcelona (Spain), April 2009.
- [Arr10b] J. Arribas, C. Fernández-Prades, and P. Closas, “Receiver Operating Characteristic For Array-Based GNSS Acquisition”, *Proceedings of XVIII European Signal Processing Conference, EUSIPCO*, pp. 1082–1086, Aalborg, Denmark, August 2010.
- [Arr11b] J. Arribas, C. Fernández-Prades, and P. Closas, “Array-Based GNSS Acquisition In The Presence Of Colored Noise”, *Proceedings of the 36th IEEE International Conference on Acoustics, Speech, and Signal Processing, ICASSP’11*, Prague, Czech Republic, May 2011.
- [Arr12b] J. Arribas, C. Fernández-Prades, and P. Closas, “Antenna Array Based GNSS Signal Acquisition for Interference Mitigation”, accepted in *IEEE Transactions on Aerospace and Electronic Systems*, 2012.

Chapter 5

Design and implementation of a real-time array-based GNSS receiver platform

A man who carries a cat by the tail learns something he can learn in no other way.

Mark Twain.

DIVIDE and conquer is a key strategy of every complex design. The design and implementation of a real-time array-based GNSS receiver platform is a challenging task that involves several engineering fields. On the one hand, the platform is composed of an analog section, which includes the antenna array elements, a multichannel coherent RF front-end, and a digital-to-analog conversion stage, and, on the other hand, it contains a digital signal processing section in charge of executing the desired GNSS algorithms in real-time, which includes the design and implementation of digital filters, correlators, and matrix operations among others.

In the literature can be found some efforts towards the implementation of GNSS array platforms. One of the first mentions was the High Gain Advanced GPS Receiver (HAGR), reported by the NAVSYS corporation in [Cor02]. The HAGR platform was a digital beam steering receiver designed for GPS satellite radio navigation and other spread spectrum applications, available for both L1/L2 civil and military signals with an array configuration up to 16 channels. However, it was a commercial product and very few design and implementation details are available. Following the commercial military products line, in November 2011 QinetiQ and NovAtel announced the first COTS anti-jamming smart antenna appropriate for land vehicles. The system uses NovAtel's patented seven element Controlled Reception Pattern Antennas (CRPA) to receive GNSS signals in the L1 and L2 bands. Interference mitigation is achieved by applying QinetiQ's proprietary digital beamforming algorithms to the signals, giving protection against narrow-band and broad-band sources. Again, neither hardware implementation nor algorithms details are available.

Recently, there is a growing number of works devoted to the implementation of specific beamforming algorithms such as the time-referenced Least Mean Squares (LMS) or the MVDR algorithms, see e.g., [Fu02, Lor05, Kon07, Cun09, FP11b], among others, but the proposed platforms assume that the GPS signal is acquired before the beamforming operation in all the scenarios, and thus, are suitable only for tracking operation leaving the acquisition phase unprotected.

At this time of writing (February 2012), the Institute of Communications and Navigation of the German Aerospace Center (DLR) is pushing a novel array-based receiver architecture intended to be used in a Galileo SoL receiver [Cun09]. Aligned with this, an ambitious project was started in 2010, named BaSE (Bavarian security receiver) project, where a consortium

consisting of six Bavarian (Germany) companies and research institutes was formed to investigate core technologies, acquire necessary know-how, and develop a high-end Galileo PRS receiver prototype [Rue11]. The receiver is designed to operate in the Galileo E1 and E6 frequency bands, making use of the Galileo PRS signal components. Special attention is given to robust acquisition and tracking of the BOC_c-modulated PRS signals. Effective suppression of jamming and interference is achieved by combining different approaches, such as the application of an adaptive, two frequency antenna array with a post-correlation beamforming. The acquisition algorithm used in BaSE extends the traditional time delay and Doppler frequency grid search space by adding the signal spatial dimension, i.e., signal DOA [Hü11]. Additionally, the BaSE receiver makes use of a combination of the array antenna acquisition with interference mitigation, applying frequency-domain adaptive filtering techniques. The presented prototype is able to operate with a four-elements antenna array.

This Chapter deals with the design trade-offs and implementation complexities to obtain a GPS L1 / Galileo E1 working prototype, intended to demonstrate the implementation feasibility of the novel array-based acquisition algorithms proposed in this Dissertation. The platform includes an eight-elements antenna array, the associated circuitry, and the algorithms implementation. This effort is rewarded with a valuable research tool that enables the algorithm validation with real GNSS signals and shortens the time required to obtain a proof-of-concept prototype.

The Chapter is organized as follows: Section 5.1 deals with the design of a phase-coherent GNSS multichannel RF front-end, which in charge of providing the digital processing block of the array platform with the snapshot vector. The front-end design includes all the hardware components from the antenna array elements to the analog-to-digital conversion. Based on the results, Section 5.2 provides the front-end requirements.

The complete design is validated by computer simulations in Section 5.3 and the composing COTS are selected and tested in Section 5.4. Section 5.5 deals with the particularities of the local oscillator and its distribution network. A single-channel prototype is validated in Section 5.6 and performance measurements are given. Finally, Section 5.7 deals with the issues of the integration of all the front-end channels in a single Printed Circuit Board (PCB) and introduces the multichannel prototype.

The second part of this Chapter is devoted to the digital section of the platform. It starts with the Field Programmable Gate Array (FPGA) interface to the front-end ADCs in Section 5.8.1. A detailed description of the digital signal processing block diagram can be found in Section 5.8. It covers implementation details of the signal conditioning and the implemented array-based acquisition platform. The algorithms developed in Chapter 4 were implemented to work in real-time. The platform is validated in Section 5.10 by means of calibration measurements in an anechoic chamber. Finally, the performance of the implemented acquisition algorithms were tested in Section 5.11 in a variety of challenging scenarios, and Section 5.12 concludes the Chapter.

5.1 Multichannel coherent front-end: design fundamentals

We refer to the term RF front-end to define all the analog circuitry between the antenna and the ADC stage. In the literature, several textbook references focus on the GNSS receiver from a system point of view, see e.g., [Par96, Tsu00, Kap05, Bor07] among others. However, in these references, the front-end design and implementation is usually overlooked.

Most of the commercial GNSS front-ends are made into Application Specific Integrated Circuits (ASICs) to obtain better performance, reduced size, and cost. An exhaustive GNSS ASIC front-end analysis and design can be found in [Men09]. In addition, several research papers are available to the reader, see, e.g. [Pia98, Clo99, Psi03, Spa06] among others. A good reference textbook for the particularities of GNSS antenna design can be found in [Moe09].

Other competent textbook sources, which are focused on more general topics, include communications antenna design and analysis, see, e.g. [Bal03] among others. Communications front-end components and system design and analysis can be found in [Poz98, Poz01, Gil03b].

The Section starts with an overall system analysis of the array platform to introduce the operating context of the front-end. Section 5.1.1 briefly review the GNSS signals specifications and the antenna-array working principles. In Section 5.1.2, it can be found the system block diagram as a starting point to characterize each of the front-end components in the subsequent sections, such as antenna elements, amplifiers, filters, mixers, and local oscillators. In this sense, each of them is characterized stressing the key performance parameters. Section 5.1.9 introduces the ADC specifications, which completes the front-end analysis.

5.1.1 Radio Frequency antenna array signal model

Considering the signals coming from M GNSS satellites, each of the transmitted signal is received in an N -elements antenna array, each antenna receives a different replica of this signal, with a different delay depending on the array geometry and the direction of arrival. Using a local coordinate system (for example east–north–up or $[e, n, u]$ system with origin in a reference point, usually the phase center of the whole array), we can express the delay between array elements Δt_{mn} , where subindex m refers to a given source and subindex n refers to a given antenna, as the dot product of the wave vector \mathbf{k}_m (with modulus $\frac{2\pi}{\lambda_c}$ and direction pointing to the signal source, defined by its azimuth θ_m and elevation ψ_m) and the position of the antenna center of phase, \mathbf{r}_n :

$$\Delta t_{mn} = \mathbf{k}_m \cdot \mathbf{r}_n = \frac{2\pi}{\lambda_c} (\cos(\theta_m) \cos(\psi_m), \sin(\theta_m) \cos(\theta_m), \sin(\psi_m)) \cdot (r_e, r_n, r_u)^T. \quad (5.1)$$

Generalizing this example for M sources and N antennas in an arbitrary geometry, the time delay of each source caused in each antenna can be computed and expressed in a matrix form

$$\mathbf{G} = \exp \{j\pi \mathbf{K} \mathbf{R}\}^T, \quad (5.2)$$

where $\mathbf{K} \in \mathbb{R}^{M \times 3}$ is the wavenumber matrix, defined as

$$\mathbf{K} = \begin{pmatrix} \cos(\theta_1) \cos(\psi_1) & \sin(\theta_1) \cos(\theta_1) & \sin(\psi_1) \\ \vdots & \vdots & \vdots \\ \cos(\theta_M) \cos(\psi_M) & \sin(\theta_M) \cos(\theta_M) & \sin(\psi_M) \end{pmatrix}, \quad (5.3)$$

having its rows pointing towards the corresponding emitter, being θ_i the angle of the source i defined anticlockwise from the e axis on the en plane and ψ_i the angle with respect to the en plane, see Fig. 5.1. On the other hand,

$$\mathbf{R} = \begin{pmatrix} r_{e_1} & \dots & r_{e_N} \\ r_{n_1} & \dots & r_{n_N} \\ r_{u_1} & \dots & r_{u_N} \end{pmatrix} \in \mathbb{R}^{3 \times N} \quad (5.4)$$

is the matrix of sensor element positions normalized to units of half wavelengths with respect to the e , n and u axes.

This set of incoming signals and their corresponding delay at each antenna can be expressed by a vector signal model, where each row corresponds to one antenna:

$$\mathbf{x}_{RF}(t) = \Re \{\mathbf{G}(\boldsymbol{\psi}, \boldsymbol{\theta}) \mathbf{\Gamma} \mathbf{d}(t)\} + \mathbf{n}(t), \quad (5.5)$$

where

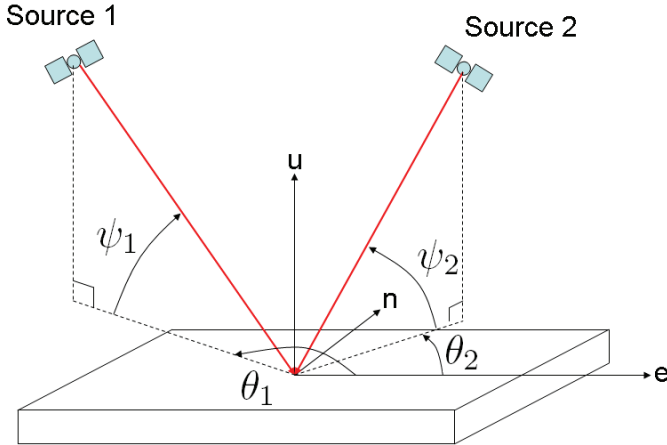


Figure 5.1: Definition of Directions of Arrival angles.

- $\mathbf{x}_{RF}(t) \in \mathbb{R}^{N \times 1}$ is the received signal vector,
- $\mathbf{G}(\psi, \boldsymbol{\theta}) \in \mathbb{C}^{N \times M}$ is the spatial signature matrix related to array geometry and Directions Of Arrival (DOAs),
- $\psi = [\psi_1, \dots, \psi_M]^T$ and $\boldsymbol{\theta} = [\theta_1, \dots, \theta_M]^T$ are vectors containing the elevation and azimuth angles of the M incoming signals,
- $\boldsymbol{\Gamma} = \text{diag}(\boldsymbol{\alpha}) \in \mathbb{R}^{M \times M}$ is a diagonal matrix with the elements of the amplitude vector $\boldsymbol{\alpha} = [\sqrt{2P_1}, \dots, \sqrt{2P_M}]$, along its diagonal, where P_i is the received signal power for the i -th satellite at the antenna terminals,
- $\mathbf{d}(t) = \begin{bmatrix} s_{T,1}(t - \tau_1(t))e^{j(2\pi f_c(t - \tau_1(t)))} \\ \vdots \\ s_{T,M}(t - \tau_M(t))e^{j(2\pi f_c(t - \tau_M(t)))} \end{bmatrix} \in \mathbb{C}^{M \times 1}$, where f_c is the carrier signal, $s_{T,i}$ is the complex baseband transmitted signal with unitary power, defined in Section 2.1, and $\tau_i(t)$ is the time-varying delay for the i -th satellite, respectively, and
- $\mathbf{n}(t) \in \mathbb{R}^{N \times 1}$ represents additive noise and all other disturbing terms.

In this model, the *narrowband array assumption* has been made. This assumption considers that the time required for the signal to propagate along the array is much smaller than inverse of its bandwidth. So, a phase shift can be used to describe the propagation from one antenna to another. Current navigation signals are reported to be emitted with a bandwidth of ≤ 40 MHz, as described in Chapter 2, which inverse is ≥ 25 ns or ≥ 7.5 m in spatial terms. The array is expected to be much smaller, since the carrier half wavelength is on the order of 10 cm, so the assumption seems reasonable. However, it must be pointed out that this signal model becomes invalid for large arrays.

5.1.2 System block diagram

Fig. 5.2 presents the overall system block diagram of the proposed GNSS antenna array platform. From left to right, the first element is the antenna array, which is composed of eight antenna elements distributed in a circular shape with half-wavelength separation between them¹. Each of the antenna terminal elements is connected to a dedicated front-end channel. The multichannel front-end is in charge of selecting the GNSS link and adapting the received antenna signals in both frequency and amplitude to be digitized by the ADC. It is composed of a RF amplification and filtering stage, a frequency downconversion stage, and an IF amplification and filtering stage.

¹Notice that the distribution of the array elements is a design decision that does not affect the platform hardware architecture.

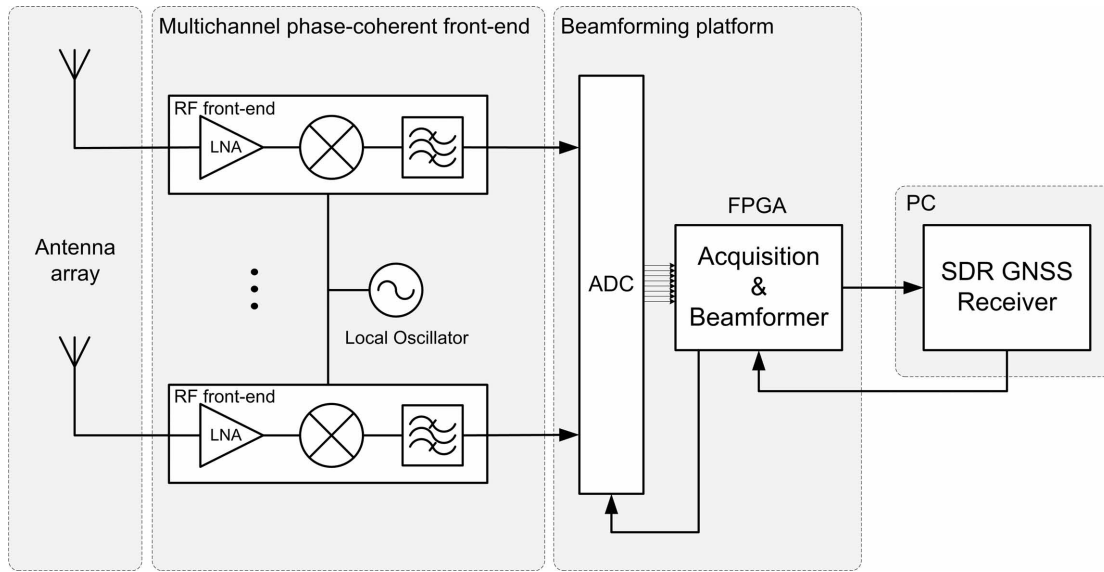


Figure 5.2: Simplified system block diagram.

It is known that most of the adaptive array algorithms require a calibrated array, which in turn, require phase coherence between antenna array channels [Mon80]. A common Local Oscillator (LO) is used for all the heterodyne stages in order to meet this requirement. Moreover, in order to avoid an extra phase rotation to the input signals, the sample clock is also phase coherent with the LO signal.

The frequency translation process could be made with multiple mixing stages forming a super heterodyne receiver [Pia98]. The downconversion is mainly needed to bring the signal to the ADC operating frequency range, but is also needed to distribute the signal amplification and to reduce the filter implementation costs [Men09]. On the other hand, there is a rising number of works covering direct RF sampling GNSS front-ends, where the ADC is digitizing the RF directly, see e.g., [Psi03].

The front-end output is fed to a multichannel ADC, which is able to sample all the channels simultaneously, providing the FPGA with the array snapshot vector. In order to use the full dynamic range of the ADC in a variety of input power levels, it is necessary to implement an AGC. The sample clock can be generated by the FPGA or can be applied from a high quality external source. The FPGA logic is in charge of downconverting the front-end signal from IF to baseband and executing the acquisition algorithm, as is described in Section 5.8.

Finally, the beamformer output is sent to a GNSS software receiver running on a PC², where all the digital signal processing chain and the associated PVT computation is performed. The reader is referred to Chapter 6 for a detailed description of the GNSS software receiver developed in this Dissertation.

A detailed block diagram of a single-channel front-end is shown in Fig. 5.3. The front-end includes the active antenna element, several Low Noise Amplifiers (LNAs), a RF BPF, a frequency mixer, an IF BPF, and finally an IF Variable Gain Amplifier (VGA) to dynamically adjust the signal gain. Next Sections are devoted to characterize each of the aforementioned building blocks.

5.1.3 Antenna elements

The antenna element is in charge of capturing the power of the electromagnetic waves generated by each of the GNSS satellites. The received power available at the i -th antenna element

²Actually, it is possible to use an FPGA-based embedded processor to execute the software defined receiver

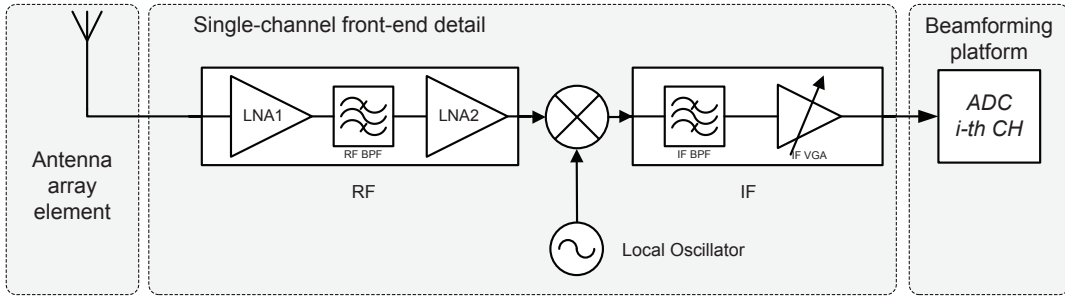


Figure 5.3: Detailed front-end block diagram for one antenna element.

terminals (P_i) is equal to the received power density (W) times the effective area (A_E) [Bal03]

$$P_i(\psi, \theta) = W A_E(\psi, \theta), \quad (5.6)$$

where

- $W = \frac{P_T G_T}{4\pi R^2 L_A}$ [W/m²], where P_T and G_T is the satellite transmitted power and the satellite antenna gain, respectively, R is the distance of the radio link path, and L_A is the power loss due to the propagation through the atmosphere,
- $A_E = \frac{G_R(\psi, \theta)\lambda_c^2}{4\pi}$, where λ_c is the carrier signal wavelength and $G_R(\psi, \theta)$ is the antenna element gain at the direction (ψ, θ) .

Since GNSS signals should come from any direction above the horizon, the antenna element radiation pattern should provide nearly full sky coverage [Kap05]. A commonly used antenna technology is the patch antenna [Bal03]. The gain offered by a patch antenna at L1/E1 GNSS radio link, for elevations higher than 10° can be considered on average $G_R = 0$ dBi, independent of the signal DOA [Mis06]. For the sake of simplicity, in the subsequent analysis, this assumption is taken into account. We considered the minimum available signal power at the Earth surface (according with the ultimate GPS and Galileo signal interface specifications documents), as shown in Table 2.1 and 2.2, which is a conservative choice.

For the particular case of GPS L1 CA, inserting the nominal signal power $W_{GPS} = -159$ dBW/m² and the carrier wavelenght $\lambda_{GPS} = 0.19$ m in (5.6), we obtain $A_E = 1.0066$ m² and $P_i \simeq -159$ dBW. Recalling the thermal noise formula introduced in Section 2.3.4.1, it is possible to compute the satellite CN0 present at the antenna terminals as

$$CN_0 = \frac{P_i}{kT_a}, \quad (5.7)$$

where $k = 1.3806 \times 10^{-23}$ J/K and T_a is the antenna sky temperature [Bal03]. Considering the GNSS frequency band and patch antenna technology, a typical T_a value is 100 K according to [Kap05]³. For the GPS L1 CA signal, we obtain $CN_0 = 49.6$ dB-Hz. A similar computation for Galileo E1, the minimum available CN0 at the Earth surface is $CN_0 = 48.5$ dB-Hz.

Considering now an array of N antenna elements arranged in a circular shape, with half-wavelength separation between elements, the following key points should be carefully analyzed:

- the individual antenna element radiation pattern: plays a critical role in beamforming algorithms because it modifies the array response. This is specially important when the algorithm requires a calibrated array and does not take into account differences between array elements,
- the individual antenna element polarization: it should be taken into account that all the current GNSS signals are transmitted using RHCP, and the reflected signals, such as multipath replicas, have the opposite polarization. Thus, using a RHCP polarization in the antenna array elements offers an extra attenuation of 3 dB to those unwanted signals,

³Notice that the antenna temperature is often assumed to be 290 K, which is the standard room temperature. However, according with the measured sky temperature values at 1575.42 MHz, 100 K is a better approximation.

- coupling between antenna elements: has a direct impact in the array performance modifying the array autocorrelation matrix [Tre02], and
- the antenna array phase center: it modifies the carrier phase of the satellite signals and it should be taken into account specially when the array is used for precise positioning, see, e.g., [Kun10] among other sources.

It is possible to compensate the differences between antenna elements in the digital domain using calibration signals responses, but the calibration depends on the signal DOA and other parameters such as the array physical temperature, making the calibration process cumbersome, see, e.g., [Chu09].

In order to minimize this problem, antenna radiation pattern differences between elements should be reduced, on the one hand, in the fabrication process and, on the other hand, in the array integration. Fig. 5.4 shows a suitable antenna elements integration. All the elements are placed sharing the same orientation in order to keep the wavefront impinging into each of them by the same DOA.

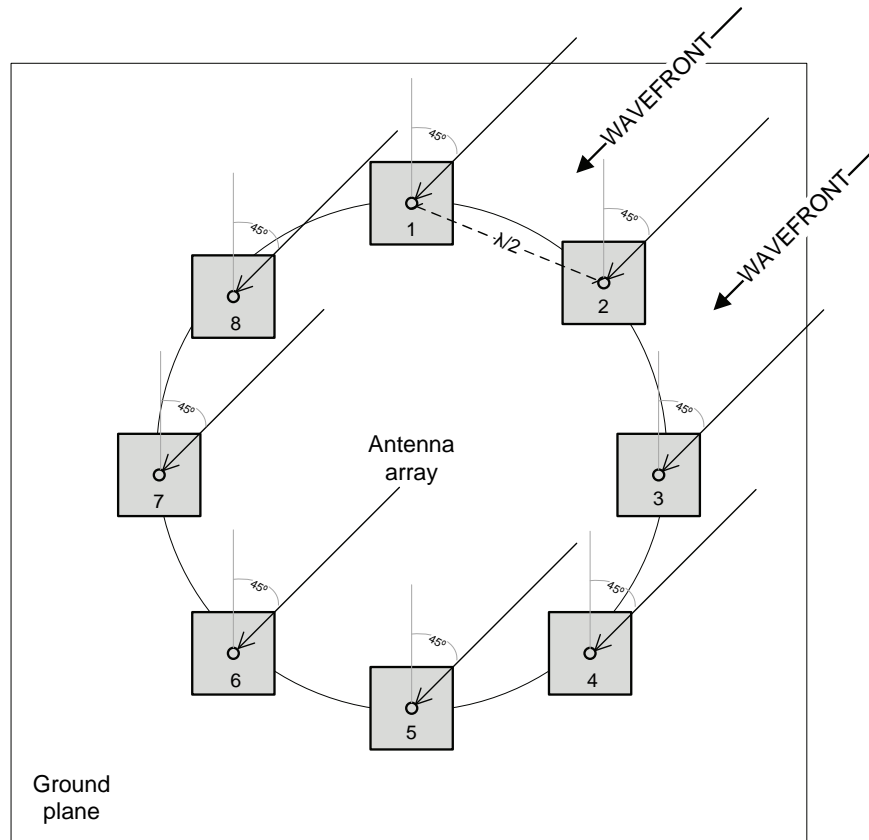


Figure 5.4: Arrangement of antenna array elements.

5.1.4 Low Noise Amplifier

The LNA is one of the most critical building block of a GNSS front-end. It amplifies the RF input signal with the minimum possible distortion. The performance of this device constraints the whole receiver sensitivity [Men09]. Fig. 5.5 shows the LNA symbol and the most relevant parameters. A simple amplifier non-linear model can be expressed as

$$x_{\text{LNA}}(t) = \sum_{k=1}^K a_k x_{\text{RF}}(t)^k + n_{\text{LNA}}(t), \quad (5.8)$$

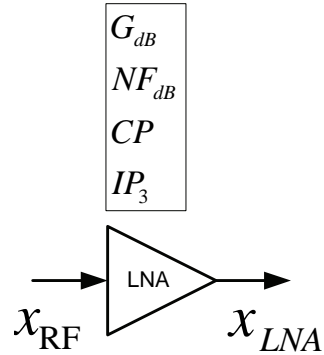


Figure 5.5: Low Noise Amplifier symbol.

where $a_i \dots a_k \in \mathbb{R}$ are the amplification constant terms and n_{LNA} is the noise generated by the LNA device operation. An ideal linear amplifier can be modeled with $K = 1$ and $G_{dB} = 10 \log a_1$, where G_{dB} is the signal gain. However, a real amplifier produces additive noise and non-linear terms, such as the third-order intermodulation (IM_3) terms ($k = 3$).

If the amplifier is excited with two or more signals with different frequencies, the output has a collection of new frequencies as a result of the non-linear amplification terms:

$$x_{\text{LNA}} = a_1 f_1 + a_1 f_1 + a_2(f_1 \pm f_2) + a_3(2f_1 \pm f_2) + a_3(2f_2 \pm f_1) + \dots, \quad (5.9)$$

where f_1 and f_2 are the input frequencies. These new signals are called *intermodulation products*. Fig. 5.6 shows a spectrum plot of the most significant intermodulation products. The IM_3 terms are particularly harmful because their frequency can be very close to the fundamental one.

It is possible to approximate the amplifier behavior by defining the noise figure and non-linearity parameters, such as the Compression Point (CP) and the third-order Interception Point (IP3), and analyze its effects on the GNSS receiver operations as is shown hereafter.

5.1.4.1 Noise Figure

A device increases the noise floor proportionally to their associated Noise Figure (NF), which is defined as the difference in dB between the actual noise power at the device output and the thermal noise power at the device input:

$$F = \frac{P_{n \text{ out}}}{P_n} = \frac{\rho_{\text{in}}}{\rho_{\text{out}}}, \quad (5.10)$$

$$NF = 10 \log(F), \quad (5.11)$$

where $P_{n \text{ out}}$ is the noise power at the device output, P_n is the input noise power, ρ_{in} is the SNR at the device input, ρ_{out} is the SNR at the device output, F is the noise factor, and NF is the noise figure. For a system composed of two or more cascaded components, it is useful to compute the overall noise factor using the well-known Friis formula

$$F = F_1 + \frac{F_2 - 1}{G_1} + \frac{F_3 - 1}{G_1 G_2} + \dots + \frac{F_n - 1}{G_1 G_2 \dots G_n}, \quad (5.12)$$

where F_i and G_i are the noise factor and the gain for the i -th component respectively. If the first stage gain is sufficiently high, the noise figure contributions of the subsequent stages are negligible. Consequently, the antenna LNA plays a critical role in the overall noise figure.

In order to evaluate the effects of the NF on the GNSS receiver, it should be considered two different operations that define the minimum required signal CN0:

- satellite telemetry demodulation,

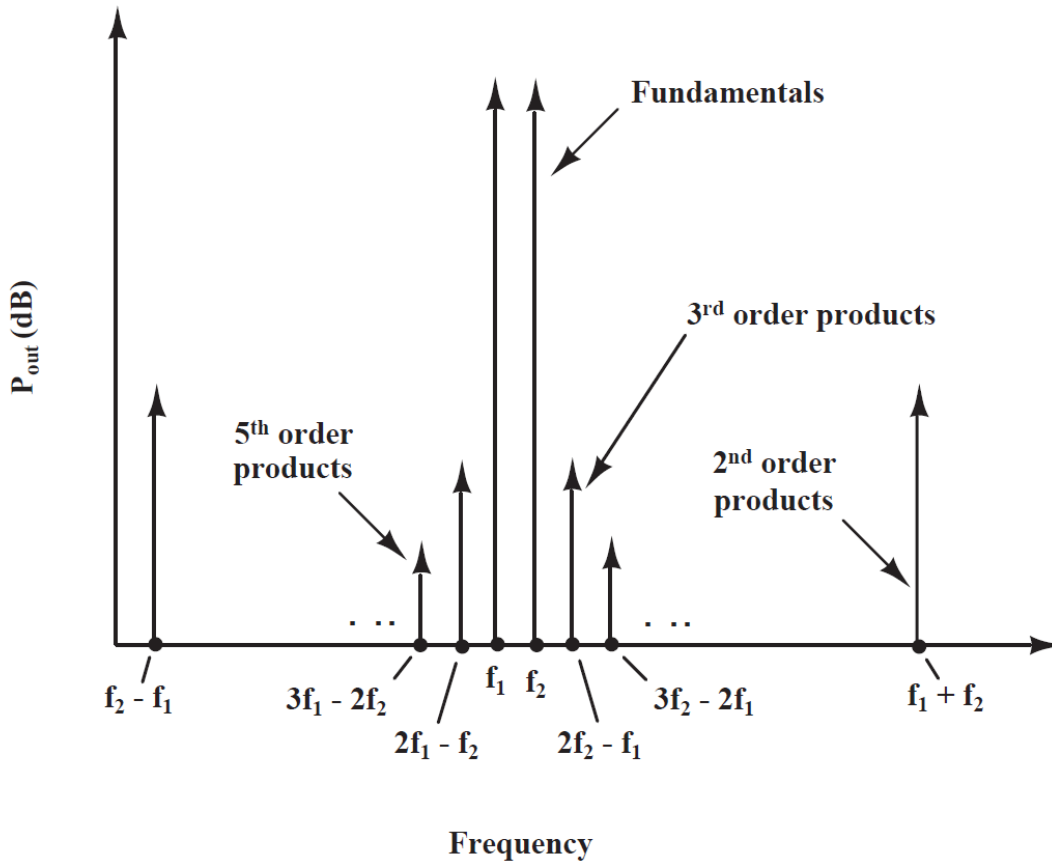


Figure 5.6: Graphical representation of intermodulation products [Gil03a].

- positioning solution.

The telemetry demodulation probability of error depends on the signal modulation technique. A common technique used in GNSS signals is the BPSK. Considering only AWGN, the probability of bit-error of a BPSK signal demodulation can be computed as [Men09]

$$P_{E,\text{BPSK}} = \text{erfc} \sqrt{\frac{2C}{N_0 f_{bit}}}, \quad (5.13)$$

where $\text{erfc}(\cdot)$ stands for the complementary Gaussian error function. It depends both on the signal CN0 at the demodulator input and on the telemetry bit rate f_{bit} . In the particular case of the GPS L1 C/A signal, $f_{bit} = 50$ bps. It is possible to relate the CN0 with the Bit Error Rate (BER) using (5.13). According to [Par96], the minimum required CN0 at the demodulator input (which in a digital receiver, it is the CN0 at the front-end output) is $CN_0 \geq 27$ dB-Hz⁴. However, this lower bound only assures the correct reception of the navigation message. The receiver positioning precision depends also on the CN0 value as we show in the sequel.

The receiver's positioning performance can be measured for several parameters, one of the most common performance parameters is the Root Mean Square (RMS) code tracking error, because it is directly related to the pseudorange error and the positioning precision [Kap05]. A complete performance analysis can be found in [Gre07], hereafter are given the most relevant results. For the case of GPS C/A signal, it is possible to derive the theoretical error bound for an unbiased code delay ML estimator [Wei94]. The obtained expression is

$$\sigma_{\hat{\tau}_{ML}} = \frac{3.444 \times 10^{-4}}{\sqrt{(CN0)B_{bb}T}}, \quad (5.14)$$

⁴Considering a maximum BER of 10^{-5} required for a GPS receiver [Par96].

where $\sigma_{\hat{\tau}_{ML}}$ is the standard deviation for the MLE of the code delay τ , B_{bb} is the receiver's baseband bandwidth, and T is the observation time interval. This expression is the Cramér-Rao bound (CRB), and it is valid only for a satellite signal in AWGN, in the absence of multipath.

Considering the aforementioned conditions, it is possible to obtain the code tracking ranging error in meters using the signal propagation speed⁵. Fig. 5.7 shows the evolution of the RMS error vs. the CN0 for different B_{bb} .

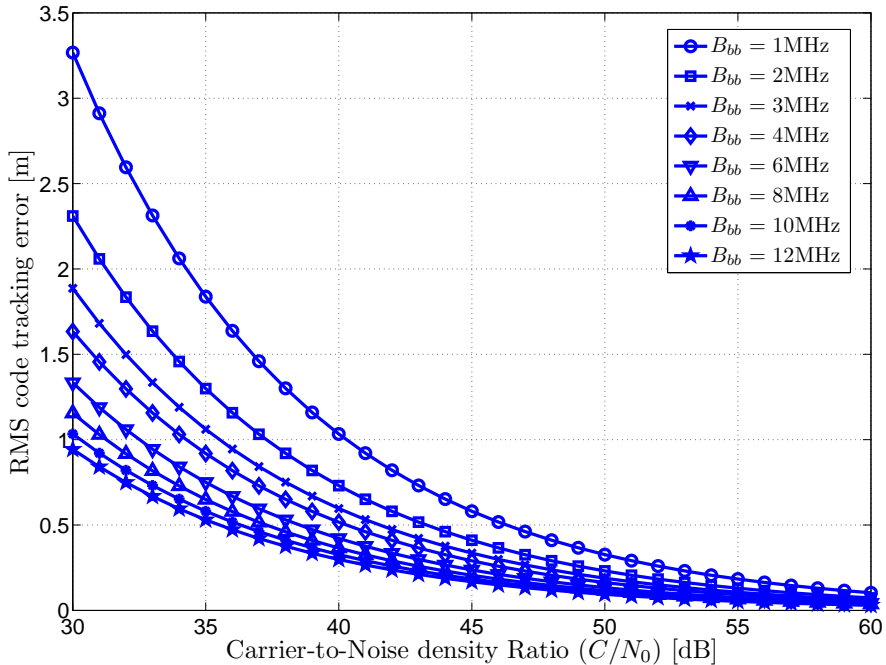


Figure 5.7: GPS C/A RMS code tracking error CRB vs. input CN0, observation time $T = 1$ s and baseband bandwidth $B_{bb} = 1 - 12$ MHz.

It is important to take into account that the differential improvement in precision decreases exponentially with the increase of B_{bb} , up to the maximum available bandwidth according to the signals specifications introduced in Table 2.1 and 2.2. In practice, B_{bb} depends on the positioning precision required by the GNSS application⁶. The available CN_0 also affects the precision, thus, the front-end NF also degrades the receiver positioning performance.

Notice that the above analysis is valid only for single antenna receivers. An antenna array receiver can improve the satellite CN0 up to their associated array processing gain as shown in (4.50). The platform is intended to be used as a testbed for different receiver algorithms, included single-antenna algorithms, thus we consider the CN0 improvement as an optional processing gain and it is not taken into account in the front-end requirement analysis.

In order to find the front-end NF requirement, it is necessary to define the GNSS receiver minimum acceptable CN0, which at the same time depends on the desired positioning performance. Considering the nominal GPS L1 C/A receiver $CN_0 = 49$ dB-Hz at the antenna terminals, shown in Section 5.1.3, it is possible to compute the relation of the front-end NF with the theoretical code tracking ranging error, as is shown on Fig. 5.8.

The NF is a decisive parameter specially in low signal power situations. For instance, in places with high buildings and narrow streets, such as in urban environments, the satellite's CN_0 can fall down to 15 dB-Hz [Ste04]. Lower NF also contributes to a shorter signal acquisition time, since it provides higher SNR and thus, higher signal detection probability as is shown in Chapter 3.

⁵We consider $v_p = 3 \times 10^8$ m/s.

⁶The typical COTS automotive GPS receivers baseband bandwidth is 2 MHz.

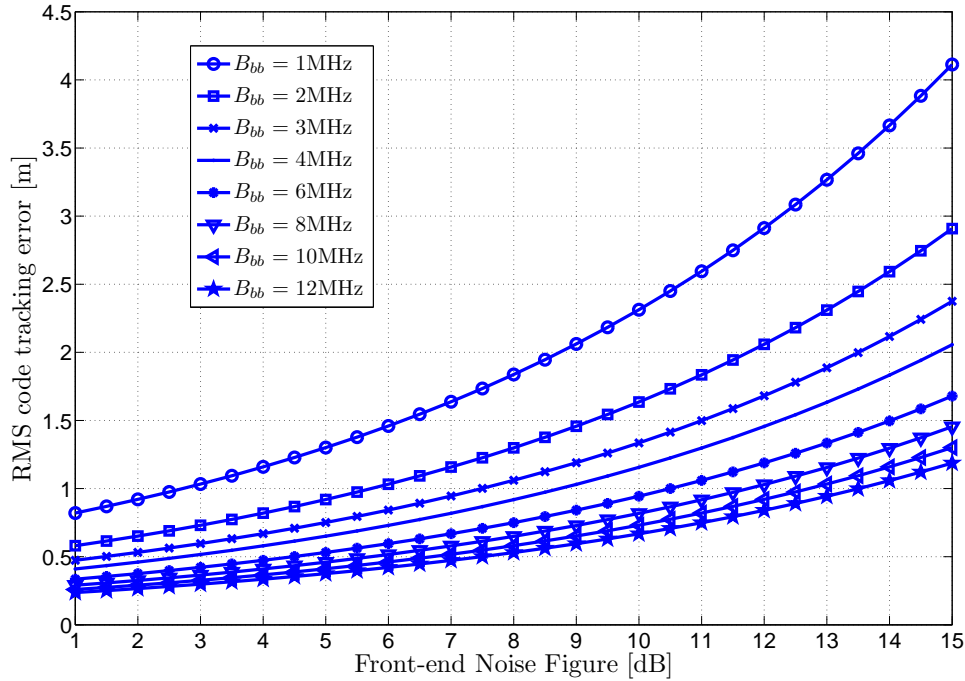


Figure 5.8: GPS C/A RMS code tracking error vs. front-end F_{dB} , observation time $T = 1\text{s}$, input $CN_0 = 49\text{ dB}$, and baseband bandwidth $B_{bb} = 1 - 12\text{ MHz}$.

5.1.4.2 Linearity parameters

Several measures of linearity can be found in the literature; hereafter are briefly listed the most informative ones:

- **1 dB Compression Point (CP):** gain compression in an active electronic circuit is a reduction in “differential” or “slope” gain caused by nonlinearity of the transfer function of the device. It is defined as the input power that causes the output power 1 dB lower than the expected output power. Considering only the fundamental and the third-order terms, inserting $x_{RF}(t) = V \cos(wt)$ in (5.8), we can write

$$x_{LNA}(t) = a_1 V \cos(wt) + a_3 V \cos^3(wt) = \left(a_1 V + \frac{3}{4} a_3 V^3 \right) \cos wt + \frac{1}{4} a_3 V^3 \cos(3wt), \quad (5.15)$$

where the first term contains the linear gain and the intermodulation products, at the fundamental frequency w and the second term contains energy in the 3rd harmonic. If we compute the signal gain at the fundamental frequency w we have

$$G = \frac{a_1 V + \frac{3}{4} a_3 V^3}{V} = a_1 \left(1 + \frac{3}{4} \frac{a_3}{a_1} V^2 \right), \quad (5.16)$$

from the result it is clear that if $\frac{a_3}{a_1} < 0$, then the gain compresses with the increase of the signal amplitude. Using (5.16), it is possible to find the signal amplitude where the gain has dropped 1 dB,

$$20 \log \left(1 + \frac{3}{4} \frac{a_3}{a_1} V^2 \right) = -1, \quad (5.17)$$

where solving the equation for V it is possible to obtain

$$V_{CP_{lin}}^2 = \frac{4}{3} \left| \frac{a_1}{a_3} \right| 0.11, \quad (5.18)$$

which is the 1 dB CP input power considering only the third order distortion. Notice that it is possible to compute the CP point input power as $P_{1dB} = 10 \log(V_{CP_{lin}}^2)$.

- **Third-Order intercept point (IP3):** it is the theoretical point at which the desired signal and the third-order intermodulation products are equal in amplitude [Gil03a]. For the case of one signal present at the input, using (5.15) it is possible to find IP3 as

$$a_1 V = \frac{3}{4} a_3 V^3, \quad (5.19)$$

$$V_{IP3_{lin}}^2 = \frac{4}{3} \frac{a_1}{a_3},$$

where it is possible to compute the IP3 input power as $P_{IP3} = 10 \log(V_{IP3_{lin}}^2)$. By inserting the obtained ratio $\frac{a_1}{a_3}$ into (5.18) the relation between with IP3 and CP arises:

$$P_{IP3} = P_{1dB} + 9.6 \text{ dB}, \quad (5.20)$$

notice that $10 \log(0.11) \simeq -9.6$ and all the values are given in units of signal input power.

Fig. 5.9 shows graphically the relations between the defined compression point and third-order intercept point.

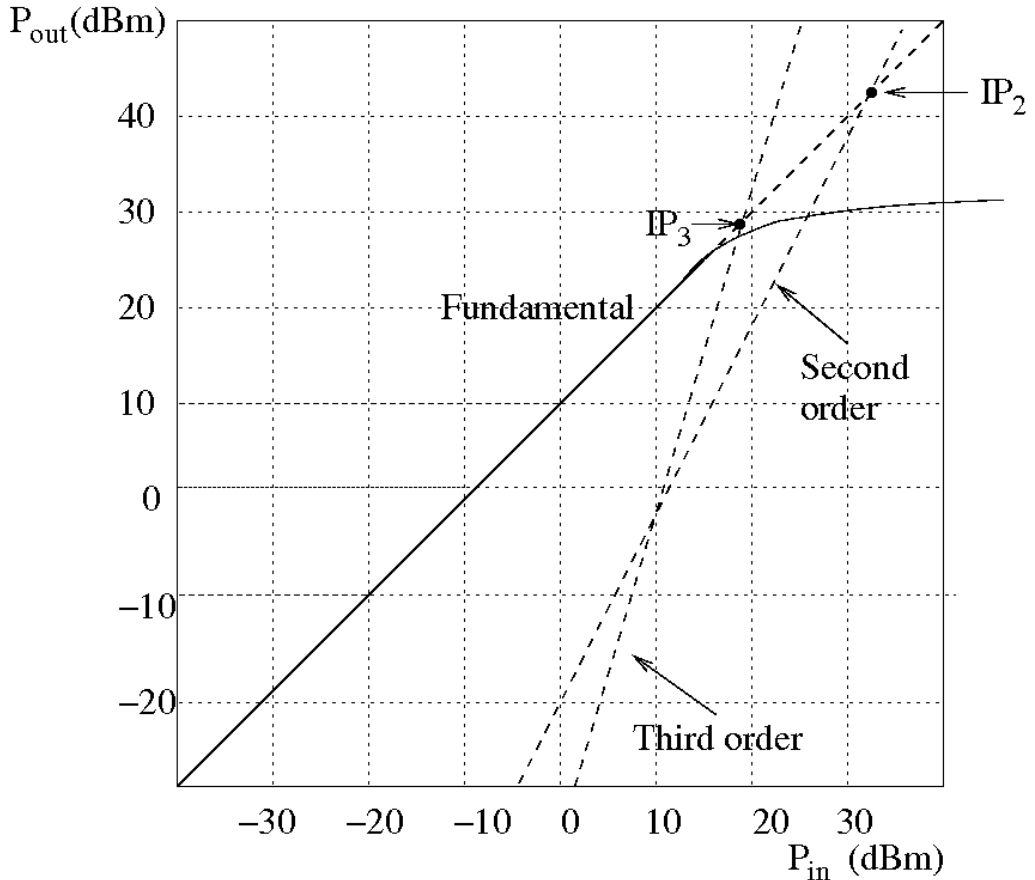


Figure 5.9: Compression point and Interception Points definitions [Gil03b].

The front-end linearity requirements considering only the GNSS signals are not critical since the received signal power is below the noise power and almost constant [Kap05]. However, external interferences have much higher power and could drive the front-end into non-linear regions, therefore the linearity requirements are imposed by the interference robustness requirements.

In a GNSS receiver, the linearity is defined as the limit of the highest interference power that the receiver can handle before it begins to perform incorrectly [Men09]. The ADC dynamic

range impose the upper bound for the admissible signal power. The front-end should be able to behave linearly at least in the input dynamic range that the ADC can handle without saturation.

The presence of in-band interferences reduces the CN0, even if the receiver behaves linearly. For the GPS L1 BPSK modulation, it is possible to write the equivalent CN0 in the presence of an in-band interference as [Men09]

$$CN0_{eq} = \frac{1}{\frac{1}{CN0} + \frac{J/S}{QR_c}}, \quad (5.21)$$

where $CN0$ is the original CN0, J/S is the jammer-to-signal power ratio, R_c [chips/sec] is the chipping rate of the GPS PRN code, and Q is the spread spectrum processing gain adjustment factor. An antenna array based receiver is capable to mitigate the in-band interference effects by using of spatial filtering techniques as shown in Chapter 4. The above formula does not take this improvement into account.

5.1.5 Frequency mixer

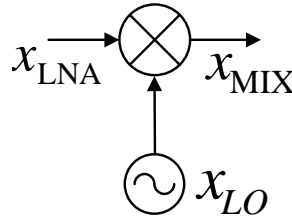


Figure 5.10: Frequency mixer symbol.

Mixers are 3-port active or passive devices that use a non-linear component such as a diode or transistor to archive *frequency conversion* of an input signal [Hin84]. The mixer symbol is shown in Fig. 5.10 and the signal model can be written as:

$$x_{IF}(t) = C_1 x_{RF}(t) + C_2 x_{LO}(t) + C_3 x_{RF}(t)x_{LO}(t) + n_{MIX}(t), \quad (5.22)$$

where C_1 is the RF feedthrough, C_2 is the LO feedthrough, and C_3 is the conversion gain. The spurious terms such as intermodulation products are grouped in the noise term $n_{MIX}(t)$. A *double balanced* mixer has $C_1 = 0$ and $C_2 = 0$ by design, however, some RF and LO leakage is expected and should be taken into account, specially in a GNSS receiver, where the LO signal could be in the order of 130 dB more powerful than the satellite's signal.

The RF signal is converted to IF by means of an *analog multiplication* expressed as the trigonometric identity

$$\cos(2\pi f_{RF}) \cos(2\pi f_{LO}) = \frac{1}{2} \cos(2\pi(f_{RF} + f_{LO})t) + \frac{1}{2} \cos(2\pi(f_{RF} - f_{LO})t), \quad (5.23)$$

where the frequency relations can be:

- $f_{RF} + f_{LO} = f_{IF}$ for a sum mixer,
- $f_{RF} - f_{LO} = f_{IF}$ if $f_{RF} > f_{LO}$ (low-side mixer), or
- $f_{RF} - f_{LO} = -f_{IF}$ if $f_{RF} < f_{LO}$ (high-side mixer), where the negative sign in IF means that the signal is phase-inverted.

A IF filter is in charge of selecting the desired frequency and attenuating the non-desired frequencies at the mixer output. On the other hand, if a frequency is present at RF port centered at:

- $f_{IMG} = f_{RF} - 2f_{IF}$ for a sum mixer,

- $f_{\text{IMG}} = f_{\text{RF}} - 2f_{\text{IF}}$ for a low-side mixer, or
- $f_{\text{IMG}} = f_{\text{RF}} + 2f_{\text{IF}}$ for a high-side mixer,

then the mixer will map the f_{IMG} signal into f_{IF} , overlapping f_{RF} . In practice, f_{IMG} should be removed at the mixer RF port by means of an *image rejection filter*. These are the primary image frequencies, but due to the mixer non-linear nature, the higher order harmonics mixer products could be mapped also to f_{IF} as follows:

- $f_{\text{IF}} = nf_{\text{LO}} + mf_{\text{IMG}}$ for a sum mixer,
- $f_{\text{IF}} = nf_{\text{LO}} - mf_{\text{IMG}}$ for a low-side mixer, or
- $-f_{\text{IF}} = nf_{\text{LO}} - mf_{\text{IMG}}$ for a high-side mixer.

where n and m are integer values. In addition to these spurious responses, active mixers specially suffer from gain compression and intermodulation products like the amplifiers, as they include active devices in its implementation. Since GNSS signals do not contribute with noticeable power, the mixer linearity specifications should take into account possible in-band and out-of-band interfering signals, as we will see in Section 5.2.

5.1.6 Reference and local signal oscillators

The reference oscillator is another critical component of a GNSS receiver because it has a direct impact on range measurements, since all other frequency synthesizers and the ADC sampling clock are phase-locked to it, and hence mirrors its performance [Kap05]. The most important oscillator performance parameters and their impact on the GNSS receiver are briefly listed here:

- **accuracy:** is the difference between the actual frequency and the specified frequency. It causes an apparent Doppler frequency bias for all the visible satellites,
- **stability:** is the relative change in frequency (Δf) with respect to the nominal value (f_0) during an interval of time. It is expressed as a fraction ($\Delta f/f_0$). There are two types of stability values; the *long term stability* for 1 day period and the *short term stability* for 1 second period. Short term stability limits the coherent integration time, and thus, affects the performance of high sensitivity receivers [Gag08]. Moreover, the oscillator stability also limits the maximum acquisition to tracking transition time, as we will see in Appendix 6.A, and
- **phase noise:** is a measure of fluctuation of carrier phase as a function of frequency due to various stochastic processes. It is expressed as a signal power ratio with respect to the oscillator fundamental frequency power versus the frequency offset, often expressed as a spectral density (dBc-Hz). If the phase noise have high offset (> 10 kHz) is effectively filtered by the low-pass response of the correlators. However, close-in phase noise induces an apparent high-dynamic motion, and thus the tracking loop bandwidth should be increased to avoid cycle slips, which in turn increases the pseudorange measurement noise [Kap05]. According to [Men09, p.56], for a combined GPS L1 and Galileo E1 front-end, a suitable LO phase noise specification is $PN_{\text{LO}} \leq -60$ dBc-Hz for 1 kHz and $PN_{\text{LO}} \leq -90$ dBc-Hz for 100 kHz.

5.1.7 RF and IF filters

As shown in the last Section, a super heterodyne front-end requires at least two filters:

- a RF filter to prevent f_{IMG} from entering into the mixer input, and
- an IF filter designed to filter out the non-desired mixer responses.

The available front-end bandwidth is the combination of both filters frequency response.

The performance of a band-pass filter can be measured in terms of the quality factor defined as:

$$Q = \frac{f_c}{B_p}, \quad (5.24)$$

where f_c is the filter center frequency and B_p is the filter pass-band bandwidth measured for 3 dB of attenuation. Let's assume a GNSS L1/E1 front-end designed for a 4 MHz of bandwidth and $f_{IF} = 70$ MHz.

$$Q_{RF} = \frac{1575.42 \cdot 10^6}{4 \cdot 10^6} = 393.8, \quad (5.25)$$

$$Q_{IF} = \frac{70 \cdot 10^6}{4 \cdot 10^6} = 17.5. \quad (5.26)$$

From these results, it is clear that an efficient solution is to have wideband filters at RF to relax its performance specifications, and sharp-cutoff filters at IF. However, wider RF filters could become a problem in harsh interference environments, where high-power transmissions are located nearby the GNSS central frequency, such as the situations described in Section 2.2.3. The interfering signals could produce non-desired intermodulation products and front-end desensitization⁷. The frequency plan should be carefully designed to avoid such issues.

The phase stability and the group delay are two crucial performance parameters specially for high-end GNSS receivers. Depending on the filter technology some trade-offs are identified:

- cavity resonators: enjoy high Q-factor, constant group delay, and low insertion loss (≤ 1 dB), but the device is large and sensitive to thermal and vibration stress. It is an expensive solution.
- ceramic filters: provide a reasonable Q-factor in small size. The group delay is acceptable for GNSS applications and the insertion loss is moderate ($1 - 2 \leq$ dB).
- Surface Acoustic Wave (SAW) filters: enjoy high Q-factor even at high frequencies at expenses of high insertion loss (2 – 10 dB). Since this solution converts the electric signal to acoustic wave and vice-versa [Mor07], it has a large group delay (in the order of tens of ns for RF filters and in the order of one μ s for IF filters) with variations over changes in temperature [Ada03]. A side effect of this phenomena is that SAW filters do not have a constant impedance, and thus they are difficult to impedance match. As a consequence, SAWs filters are unacceptable for high-end GNSS applications.

It is important to highlight that the adverse effects caused by group delay ripple, phase responses, and impedance mismatches of the front-end have a direct impact in the tracking performance. The main adverse effect is the so called *component-induced multipath* in the pseudorange measurements. However, the shift of the correlation peak caused by the induced multipath does not distort the acquisition coarse estimation of the synchronization parameters if differential delays caused by the component-induced multipath with respect to the LOS are limited within a chip period⁸, as stated in [En05]. Since the platform primary goal is the implementation and testing of array-based acquisition algorithms, SAW filters become a suitable option.

5.1.8 Intermediate Frequency amplifier

The filtered mixer signal output should be amplified again in order to reach the power values required by the ADC. Since the LNA does not offer high gain due to the demanding NF requirements, the IF amplifier is usually a high-gain stage. This is particularly important in GNSS receivers, where the gain requirements at the IF amplification stage could be higher than 40 dB.

Since the mixer produces several out-of-band signals, the IP3 of this stage must be high enough to not degrade the front-end performance, specially important in the presence of high power interfering signals at the antenna input. A technique commonly used to relax the amplifier requirements is to partition the required gain in several cascaded stages. It is preferred that the

⁷Receiver desensitization occurs when a strong off-channel signal overloads a receiver front-end and thus reduces the sensitivity to weaker on-channel signals.

⁸For GPS L1 C/A and Galileo E1, $\Delta\tau \leq 1 \mu$ s.

AGC is implemented also at IF amplification stage, due to the fact that it is easy to design and implement VGA at lower frequencies.

An additional task of this stage is to adapt the impedance and the front-end output connection type to the particularities of the ADC (i.e., unbalanced to balanced).

5.1.9 Analog-to-Digital conversion

As described in Section 5.1.2, the front-end output is fed to the ADC block. The ultimate goal of the front-end is to adapt the satellites signals in order to be conveniently sampled. The ADC characteristics constraints the front-end design, and thus they should be carefully analyzed as a previous step.

The ADC digitizes the output signal of the front-end in time, in a process referred to as sampling, and in magnitude, in a process referred to as quantization. The target is to obtain a discrete version of the analog signal without losing information [Opp00]. Considering the particularities of GNSS signal, the following ADC specifications should be analyzed:

- **sampling frequency:** according with the Nyquist-Shannon theorem, the sampling frequency should be at least twice the signal passband bandwidth⁹ (B_p) in order to not loss information ($f_s \geq 2B_p$). In practice, the ADC should use a suitable sampling frequency to accommodate the signal stopband¹⁰ (B_s), much more restrictive to prevent the aliasing [Kap05]. Due to the limitations of the front-end filters implementation, $B_s > B_p$ and thus, $f_s \geq 2B_s$. Otherwise, some signal degradation due to the aliasing is expected.

The sampled IF signal can be written as

$$x_{IF}[n] = x_{IF}(t) \Big|_{t=nT_s}, \quad (5.27)$$

where $T_s = \frac{1}{f_s}$ is the sampling period. In GNSSs, the sampling frequency typically is set from 2 to 20 times the chip rate, depending on the required receiver performance.

If f_{IF} is greater than the half of the sampling frequency, then the sampling process acts as a frequency translation stage [Opp00]. This property is used in a technique referred to as IF sampling. In [Ber08] IF sampling was used to sample the signal and downconvert it to BB using a simplified Numerically Controlled Oscillator (NCO). The idea behind this process is to properly choose both f_{IF} and f_s to meet the following relations

$$f_{IF} = kf_s \pm \frac{f_s}{4}, \forall k \in \mathbb{Z} | k \geq 1 \quad (5.28)$$

$$f_s \geq 2B_p, \quad (5.29)$$

which ensures that a non-overlapped signal alias is centered at $f_s/4$. In the digital domain, the downconversion to baseband process can use the frequency-shifting property of the Fourier transform of a signal, i.e., $Z(f \pm f_0) \leftrightarrow^F z[n]e^{\mp j2\pi f_0 n T_s}$. For the particular case of $f_0 = f_s/4$, it results in multiplying the alias by $e^{-j\frac{\pi}{2}n}$. The latter is a straightforward operation with cyclic values $\{1, -j, -1, j\}$, with $j^2 = -1$, which can be implemented using multiplexers, avoiding complex multipliers and thus saving valuable resources on the FPGA.

Therefore, each antenna channel is downconverted, extracting Inphase (I) and Quadrature (Q) baseband components from

$$\begin{aligned} \mathbf{x}_{BB}[n] &= \mathbf{x}_{IF}[n]e^{-j\frac{\pi}{2}n} \\ &= [\mathbf{x}_{IF}[0], -j\mathbf{x}_{IF}[1], -\mathbf{x}_{IF}[2], j\mathbf{x}_{IF}[3], \dots], \end{aligned} \quad (5.30)$$

as the real and imaginary parts of $\mathbf{x}_{BB}[n]$, defined as $\mathbf{x}_{BB,I}[n]$ and $\mathbf{x}_{BB,Q}[n]$, respectively.

⁹Measured at 3 dB of attenuation.

¹⁰The stopband minimum attenuation is 20 dB.

- **Analog bandwidth:** Is the analog input frequency at which the spectral power of the discrete fundamental frequency is reduced by 3 dB. When IF sampling technique is used, the analog bandwidth should be greater than the signal IF plus half of the signal bandwidth.
- **Resolution:** The ADC resolution is defined as the number of discrete values to quantize the amplitude of each signal sample. It is usually given in number of bits used by the output sample word. Due to the DS-CDMA modulation technique used in the majority of GNSS signals, the ADC resolution can be reduced dramatically. The effects of the ADC resolution in MF DS-CDMA demodulator was first studied in [Cha82]. Regarding the GPS L1 C/A signal, Table 5.1 shows the SNR degradation versus the ADC resolution, assuming Gaussian noise and the absence of interferences. Based on the results, the SNR degradation is negligible when 4 or more bits are used.

ADC resolution	SNR degradation $f_s \geq 2B_s$	SNR degradation $f_s = 2B_p$
1 bit	1.96 dB	3.5 dB
2 bits	0.55 dB	1.2 dB
3 bits	0.16 dB	0.6 dB
4 bits or more	≤ 0.16	≤ 0.6 dB

Table 5.1: GPS L1 C/A SNR degradation vs. ADC resolution assuming Gaussian noise [Par96].

However, if an interference signal is present, the ADC can be saturated and the satellite signal can be masked. A recent work on the effects of the quantization in presence of CWI can be found in [Bal08a].

- **Effective Number Of Bits (ENOB):** is a measure of the quality of a digitized signal. ENOB specifies the number of bits in the digitized signal above the noise floor, and thus the effective ADC resolution is reduced with respect to the ADC nominal resolution.
- **Input range:** The ADC has a limited analog voltage input range, mapped to cover all the quantization levels. Typically the input range is in the order of 1 – 2 V peak-to-peak (Vpp) [Men09]. If the ADC is connected to a signal source, discarding the ADC input current, the signal power needed to exercise all the input bits is defined as

$$P_{\text{FSR}} = \frac{V_{\text{FSR}}^2}{Z_{\text{ADC}}}, \quad (5.31)$$

where P_{FSR} is the full-scale ADC signal input power, V_{FSR} is the full scale voltage, usually defined as the RMS differential voltage across the ADC inputs, and Z_{ADC} is the ADC input impedance.

When a multibit ADC is used, it is important to take into account that the GNSS signal can be received without significant losses using only 3-4 quantization bits as stated before. It is possible to use this condition for a two-fold objective:

- to relax the required front-end gain, and
- to increase the robustness to interferences.

The power required at the ADC terminals can be computed as:

$$P_{\text{ADC}} \geq 10 \log \left(\frac{(V_{\text{LSB}} 2^{i-1})^2}{Z_{\text{ADC}}} \right), \quad (5.32)$$

where the input voltage needed to excite the Least Significant Bit (LSB) is $V_{\text{LSB}} = \frac{V_{\text{FSR}}}{2^{N_b}}$ considering a Full-Scale Range (FSR) voltage V_{FSR} , ADC resolution of N_b bits, i active bits. The tradeoffs imposed by the ADC specifications are discussed in the next Section.

5.2 Front-end requirements and specifications

In previous Sections we reviewed the characterization of a generic front-end building blocks, highlighting the most important performance parameters and its effects on a GNSS receiver. In

Equipment	Common f_{IF}
Satellite equipment	70 MHz
Terrestrial microwave equipment	250 MHz, 70 MHz
Radar	30 MHz, 70 MHz
RF test equipment	160 MHz, 70 MHz, 21.4 MHz

Table 5.2: Commonly used intermediate frequencies.

k value	Spectrum inversion	f_s [MHz]
$k = 1$	NO	$f_{\text{IF}} = f_s + \frac{f_s}{4} = f_{\text{IF}}$ $f_s = 56$
$k = 1$	YES	$f_{\text{IF}} = f_s - \frac{f_s}{4} = f_{\text{IF}}$ $f_s = 93.33$
$k = 2$	NO	$f_{\text{IF}} = 2f_s + \frac{f_s}{4} = f_{\text{IF}}$ $f_s = 31.11$
$k = 2$	YES	$f_{\text{IF}} = 2f_s - \frac{f_s}{4} = f_{\text{IF}}$ $f_s = 40$
$k = 3$	NO	$f_{\text{IF}} = 3f_s + \frac{f_s}{4} = f_{\text{IF}}$ $f_s = 21.53$
$k = 3$	YES	$f_{\text{IF}} = 3f_s - \frac{f_s}{4} = f_{\text{IF}}$ $f_s = 25.45$

Table 5.3: f_s candidates for different k values and $f_{\text{IF}} = 70$ MHz.

this Section, we propose an specific front-end architecture and we provide its requirements as well the specifications for each of the composing elements.

The first design decision to be made is the selection of the RF link, because it gives the core requirements of the front-end. As shown in Fig. 2.3 in Chapter 2, currently, the L1/E1 link carries both the GPS SPS and the Galileo Open Service, which are intended for current and forthcoming civil positioning services, and in the case of GPS, the L1 link is widely used. Based on these facts, the front-end is designed to receive both signals, centered at $f_c = 1575.42$ MHz.

One of the most important steps in any front-end design is the radio frequency planning. As we have seen in previous Sections, the front-end is in charge of downconverting the f_{RF} to a f_{IF} suitable to be sampled with the ADC. The selected architecture is a single conversion super-heterodyne receiver, as shown in the block diagram of Fig. 5.3. Since f_{RF} is defined by the GNSS radio link, f_{IF} is a design parameter that constraints the local oscillator and several other components. One of the most critical component is the IF passband filter which contributes to the front-end selectivity. In that sense, there exists several commonly used f_{IF} frequencies where it is possible to find specific filter components, as is shown in Table 5.2.

Based on this fact, we selected an intermediate frequency of $f_{\text{IF}} = 70$ MHz due to the availability of COTS filters of a variety of bandwidths at this frequency. The IF sampling technique constraints f_s based on (5.28). Table 5.3 shows the possible f_s candidates. In addition, f_s also defines the system bandwidth, which at the same time limits the receiver performance as we have seen in Fig. 5.7. Considering this trade-off, in order to alleviate the ADC requirements, the best choice for the sampling frequency is $f_s = 40$ MHz. The frequency plan is shown in Table 5.4. The maximum available baseband bandwidth set by the frequency plan is $B_{bb} = f_s/4 = 10$ MHz, which enables the reception of both GPS L1 CA and Galileo E1 signals.

Along with the defined frequency plan, a receiver front-end should have at least the following specifications¹¹:

- passband and stopband bandwidths,
- gain,

¹¹It is assumed that the electrical characteristics such as input/output impedance and power supply voltages/currents are also defined and meet the antenna-array platform requirements.

Frequency [Hz]	Value [MHz]
RF frequency (f_{RF})	1575.42
IF frequency (f_{IF})	70
Sampling frequency (f_s)	40
Maximum passband bandwidth (B_p)	$f_s/2 = 20$
Maximum baseband bandwidth (B_{bb})	$B_p/2 = 10$
LO frequency (f_{LO})	$f_{\text{RF}} - f_{\text{IF}} = 1505.42$
Image frequency (f_{IM})	$f_{\text{RF}} - 2f_{\text{IF}} = 1435.42$

Table 5.4: Front-end frequency plan.

- NF, and
- linearity parameters (CP and IP3).

5.2.1 Passband and stopband bandwidths

From the frequency plan shown in Table 5.4, the sampling frequency is defined as $f_s = 40$ MHz. In order to avoid aliasing, according to the Nyquist criterion, the stopband should be defined as $B_s = f_s/2 = 20$ MHz. As a consequence of this constraint, the passband bandwidth is upper bounded by $B_p \leq B_s$. On the other hand, the lower bound of B_p depends on the desired receiver positioning precision. In practice, a suitable trade-off between B_{bb} and positioning precision is $B_{bb} = 6$ MHz. The associated RMS tracking error is bounded to $\sigma_{\hat{\tau}_{ML}} < 1.5$ m for $CN_0 > 30$ dB-Hz (see (5.14)).

Based on the aforementioned constraints, a suitable front-end bandwidth specification is to have a passband $B_p = 2B_{bb} \geq 12$ MHz while keeping a stopband $B_s \leq 20$ MHz, which comprises the two main lobes of the Galileo E1 Binary Offset Carrier (BOC)(1,1) signal as well as the main lobe of the GPS L1 CA-code with its two side lobes. The CN0 correlation loss caused by front-end limited bandwidth is less than 0.7 dB for both signals [Kap05].

5.2.2 Gain

The required front-end gain depends on the ADC resolution, dynamic range, and the minimum number of active bits needed to guarantee the desired GNSS signal quality. The power required at the ADC terminals (P_{ADC}) can be computed using (5.32). The front-end is in charge of rising the input signal power to P_{ADC} . Since the GNSS signals power is well below the thermal noise power, in absence of interferences, the thermal noise excites the ADC, consequently, the associated front-end gain can be computed as

$$G_{\text{FE}} \geq P_{\text{ADC}} - P_n,$$

$$G_{\text{FE}} \geq 10 \log \left(\frac{\left(\frac{(V_{\text{LSB}} 2^{i-1})^2}{Z_{\text{ADC}}} \right)}{kT_a B_p} \right), \quad (5.33)$$

where the thermal noise power at the antenna terminals $P_n = kT_a B_p$ is already defined in Section 5.1.3.

Particularizing (5.32) for an ADC, with $V_{\text{FSR}} = 2$ V, $Z_{\text{ADC}} = 50$ Ω, and $N_b = 12$. Fig. 5.11 shows the associated P_{ADC} required to activate each of the bits. As shown in Section 5.1.9, four active bits ($i = 4$) assures almost no quantization losses in the absence of interferences. In this case, the required ADC input power is $P_{\text{ADC}} \geq -35$ dBm. Considering $B_p = 12$ MHz and $T_a = 100$ K, the noise power available at the antenna terminals is $P_n = -107.8$ dBm. The **minimum front-end gain** is therefore $G_{\text{FE}} \geq 72.8$ dB. Fig. 5.12 shows the required front-end gain versus the number of active bits.

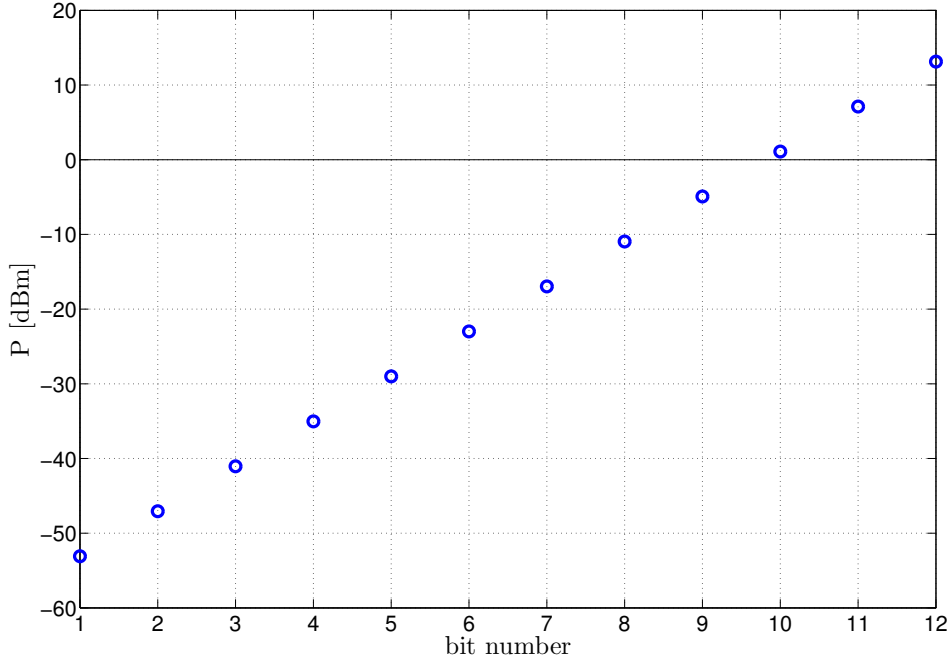


Figure 5.11: Required input power ($P_{\text{bit-}i}$) vs. ADC active bits for $V_{\text{FSR}} = 2$, $Z_{\text{ADC}} = 50 \Omega$, and $N_b = 12$.

In addition to the interference saturation protection provided by using a high resolution ADC, the front-end should be designed to keep a constant RMS amplitude at the output. The AGC circuit is in charge of this operation by means of dynamically modify the last stage amplifier gain [Men09]. An example of AGC implementation can be found in [Clo99]. The interference mitigation capability of AGC circuits is studied in [Bal08b] and [Bas03] among other sources.

5.2.3 Noise figure and linearity parameters

Recalling the results of Section 5.1.4.1, the overall NF of the front-end depends on the required receiver precision, which in turn gives the required satellite CN0 at the ADC terminals. Recalling (5.14), it is possible to write

$$\sigma_{\hat{\tau}_{ML,\max}} = \frac{3.444 \times 10^{-4}}{\sqrt{\left(\frac{(CN0)}{F_{FE}}\right) B_{bb} T}}, \quad (5.34)$$

where, if both the integration time (T) and the bandwidth (B_{bb}) are fixed by the receiver, there are three degrees of freedom: the code delay error bound, the satellite CN0, and the front-end noise factor. By setting $CN0 = 49$ dB, which is the nominal satellite CN0 at the antenna terminals computed in Section 5.1.3, and defining a code delay error bound $\sigma_{\hat{\tau}_{ML,\max}}$, it is possible to compute the $F_{FE,\max}$. However, in practice, by improving the front-end NF not only improves the receiver precision, but also improves the sensitivity of the receiver, in the sense that the receiver will obtain the desired precision in lower CN0 conditions, i.e., low satellite elevation or urban canyon environments [Ste05].

For the particular case of GPS L1 CA signal, setting the baseband bandwidth to $B_{bb} = 6$ MHz and $\sigma_{\hat{\tau}_{ML}} \leq 1.5$ m, it is possible to use the results of Fig. 5.8 to identify the NF requirement, which in this case is $NF_{FE,\max} = 14$ dB.

In [Men09], a maximum noise figure of $NF_{FE,\max} \leq 4$ dB has been defined to guarantee the signal acquisition and tracking even in harsh environments [Men09]. By establishing this

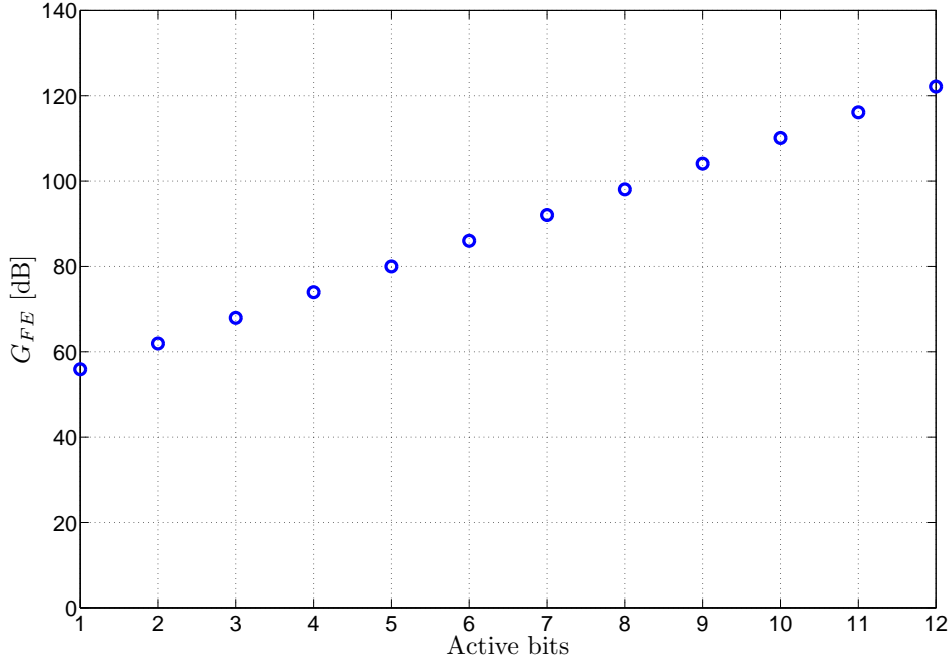


Figure 5.12: Front-end gain (G_{FE}) vs. ADC active bits for $V_{FSR} = 2$, $Z_{ADC} = 50 \Omega$, and $N_b = 12$.

feasible specification, it is possible to reduce the minimum required CN0 from 49 dB to 35 dB. The receiver can operate with lower CN0, but at expenses of higher $\sigma_{\tau_{ML}}$.

Regarding the linearity parameters, as shown in previous Sections, the ADC FSR input power defined in (5.31) imposes the upper bound for the admissible in-band interference power. A suitable linearity requirement is that the front-end should be able to handle at least the input dynamic range that the ADC can handle without saturation. The interference power at antenna terminals without saturating the ADC thus can be computed as

$$P_{int\ max} = P_{FSR} - G_{FE}, \quad (5.35)$$

where P_{FSR} is the maximum admissible ADC power (full scale power). For this particular front-end design, the front-end gain specification was set to $G_{FE} \geq 72.8$ dB in Section 5.2.2. Considering an ADC with $V_{FSR} = 2$ Vpp, $N_b = 12$, we obtain $P_{FSR} = 19.1$ dBm thus, $P_{int\ max} = -53.7$ dBm. Notice that the front-end AGC is not taken into account, and it is supposed that G_{FE} is the maximum available front-end gain, which is the worst case in terms of the linearity of the electronic components. This requirement constraints both the CP and the IP3 of all the front-end building blocks. A classical design criterion is to limit the $P_{CP} \geq P_{int\ max}$ in order to assure a linear operation for the worst case scenario. Consequently, $P_{IP3} \geq (P_{int\ max} + 9.6)$.

5.2.4 Specifications summary and detailed block diagram

Summarizing the results of this Section, Table 5.5 shows the front-end specifications, considering a code delay error bound $\sigma_{\tau_{ML}} \leq 1.5$ and a satellite signal $CN0 \geq 35$ dB-Hz, for a GPS L1 CA receiver using a correlation period $T = 1$ ms.

Fig. 5.13 proposes a detailed block diagram for each of the front-end channels. From left to right, the front-end is composed of the following blocks:

- **Active antenna:** each of the antenna elements of the antenna array is composed of a patch antenna plus an integrated LNA, which is referred to as *active antenna*. Since this is the first component of the RF chain, the LNA should have a low NF because this is the

Requirement	Design parameter	Proposed Value
Input frequency	f_{RF}	1575.42 MHz
Output frequency	f_{IF}	70 MHz
ADC dynamic range	V_{FSR}	2 Vpp
ADC resolution	N_b	12 bits
Conversion Gain	G_{FE}	≥ 72.8 dB
Bandpass bandwidth	B_p	≥ 12 MHz
Stopband bandwidth	B_s	≤ 20 MHz
Local Oscillator phase noise		≤ -60 dBc-Hz @ 1 kHz ≤ -90 dBc-Hz @ 100 kHz
Noise figure	NF_{FE}	≤ 4 dB
Image frequency rejection	L_{IMG}	≥ 40 dB
CP	P_{CP}	≥ -53.7 dBm
IP3	P_{IP3}	≥ -44.1 dBm

Table 5.5: Front-end channel design specifications summary.

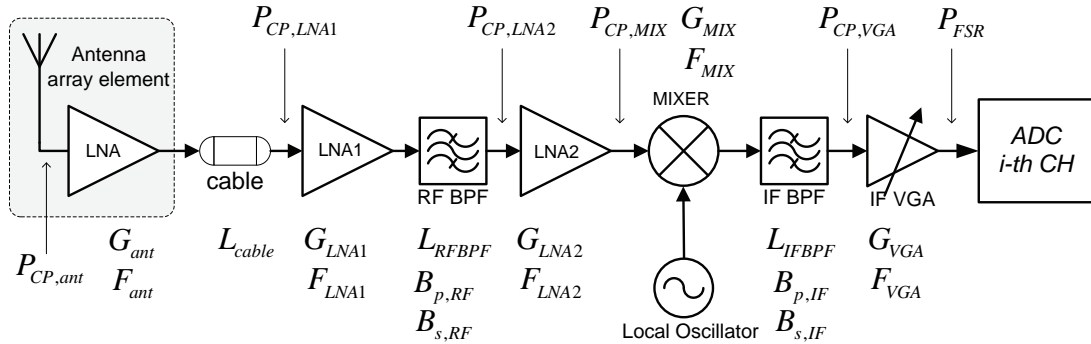


Figure 5.13: Proposed front-end architecture and performance parameters.

most contributing block to the overall front-end noise (see (5.36)). A commercial GNSS active antennas comparative can be found in [Wor10]. The average gain and noise figure for a COTS GNSS active antenna are considered in the design.

- **RF cable losses:** the active antenna output is connected to the multichannel front-end board by means of a RG174 cable. Table 5.6 shows the signal attenuation values provided by the manufacturer. For $f_{RF} = 1575.42$ MHz the attenuation is in the order of 1.4 dB/m. Considering 2.5 meters cable from the antenna to the front-end, $L_{RF_cable} = 4$ dB of attenuation is considered, including the cable connectors. In the schematic, the cable loss is represented by an attenuator.
- **RF amplification 1st stage:** a high-gain LNA rises the signal level to suitable levels for the mixer input. It can be made with a single stage or with a cascade set-up of amplifiers to get an overall gain of 30–50 dB, depending on the downconversion and IF amplification gain [Pia98]. In our design we chose a two-stage cascaded amplification and filtering block to relax the specifications.

Frequency [MHz]	Max. Attenuation [dB/100m]
50	20
100	28
1000	94
1800	140

Table 5.6: RG174 cable losses for IF and RF frequencies.

Parameter	Value
Center frequency	1575.42 MHz
Insertion loss (L_{RF_BPF})	≤ 2 dB
B_p	≥ 12 MHz
B_s	≤ 100 MHz
Stopband min. attenuation	≥ 20 dB
Image frequency rejection	≥ 40 dB

Table 5.7: RF SAW bandpass filter parameter values.

Parameter	Value
Center frequency	70 MHz
Insertion loss (L_{IF_BPF})	≤ 15 dB
B_p	≥ 12 MHz
B_s	≤ 20 MHz
Stopband min. attenuation	20 dB

Table 5.8: IF SAW bandpass filter parameter values.

According to [Men09] the state-of-the-art GNSS LNA has a NF between 0.8 dB and 3.8 dB and signal gain between 13 dB and 22 dB, however, at this time of writing (February 2012) there are available COTS GNSS LNAs with a NF ≤ 0.8 dB. The first amplification stage is represented by *LNA1* in the schematic. In the design we considered $G_{LNA1} \geq 15$ dB and $NF_{LNA1} \leq 2$ dB.

- **RF bandpass filter:** the bandpass filter is in charge of selecting the GNSS radio link frequency band and to limit the RF bandwidth. Additionally, the filter should reject the mixer image frequency and the possible out-of-band interferences. Thus, it is possible to relax the stopband bandwidth requirement taking into account that the final front-en bandwidth will be defined by the IF filter as discussed in 5.1.7. Considering the trade-offs, we selected a SAW filter due its availability. SAW filters have a good image rejection, attenuation of out-of-band interferences of $L_{RF_stopband} \geq 40$ dB, and insertion loss of $L_{RF_BPF} \leq 2$ dB. However, the design is compatible with a ceramic filter in order to improve the group delay response.

Table 5.7 summarizes the considered values for this component.

- **RF amplification 2nd stage:** the RF filter output is fed to a general purpose amplifier, represented by *LNA2*. At this point it is possible to relax the noise figure specifications because this is the second amplification cascaded device. We considered $G_{LNA2} \geq 15$ dB of amplification with $NF_{LNA2} \leq 4$.
- **Downconversion:** the downconversion stage uses a frequency mixer and a local oscillator to translate the signal carrier from the RF frequency a lower IF, preserving the modulation structure. According with the statements of Section 5.1.5, in this design, an active mixer is selected, referred to as *MIX* in the schematic. We considered an average performance mixer with $G_{MIX} \geq 5$ dB of amplification with $NF_{MIX} \leq 10$.
- **IF bandpass filter:** in order to select the desired IF a BPF is used. Here can be used either SAW technology, ceramic filter technology, or conventional lumped components. The frequency response of the IF filter defines and shapes the noise bandwidth to be amplitude-quantized by the ADC [Men09]. By using standard $f_{IF} = 70$ MHz, it is possible to find SAW filters for the required bandwidth, which offers great image rejection capability. However, the SAW filter technology have high insertion losses at low frequencies. In the design it is considered the parameters of a COTS SAW filter, with the insertion loss $L_{IF_BPF} \leq 15$ dB and the stopband attenuation of $L_{IF_stopband} \geq 40$ dB. Table 5.8 summarizes the filter parameter values.
- **IF amplification and AGC:** an extra amplification is applied to the signal before it

Parameter	Ant	Cable	LNA1	RF BPF	LNA2	MIX	IF BPF	VGA
G [dB]	≥ 15	—	≥ 20	—	≥ 15	≥ 5	—	≥ 35
L [dB]	—	≤ 4	—	≤ 2	—	—	≤ 10	—
NF [dB]	≤ 2	—	≤ 10	—	≤ 10	≤ 10	—	≤ 10

Table 5.9: Proposed gain/loss distribution and noise figure values.

Component	Compression point	Computed value
Antenna LNA	$P_{CP,ant} \geq P_{CP,LNA1} - G_{ant} + L_{cable}$	≥ -55.9 dBm
LNA1	$P_{CP,LNA1} \geq P_{CP,LNA2} - G_{LNA1} + L_{RF_BPF}$	≥ -44.9 dBm
LNA2	$P_{CP,LNA2} \geq P_{CP,MIX} - G_{LNA2}$	≥ -25.9 dBm
Mixer	$P_{CP,MIX} \geq P_{CP,VGA} - G_{MIX} + L_{IF_BPF}$	≥ -10.9 dBm
VGA	$P_{CP,VGA} \geq P_{FSR} - G_{VGA}$	≥ -15.9 dBm

Table 5.10: Compression point design specifications.

reach the ADC. This stage is usually composed of a VGA. The selected gain range is $G_{VGA} = 0 - 35$ dB.

A summary of the selected parameters considered in the preliminary design can be found in Table 5.9. By applying the Friis formula (5.12) it is possible to obtain the overall noise factor as:

$$F_{FE} = F_{ant} + \frac{L_{cable} - 1}{G_{ant}} + \frac{F_{LNA1} - 1}{\frac{G_{ant}}{L_{cable}}} + \frac{L_{RF_BPF} - 1}{\frac{G_{ant}G_{LNA1}}{L_{cable}}} + \frac{F_{LNA2} - 1}{\frac{G_{ant}G_{LNA1}}{L_{cable}L_{RF_BPF}}} + \frac{F_{MIX} - 1}{\frac{G_{ant}G_{LNA1}G_{LNA2}}{L_{cable}L_{RF_BPF}}} + \frac{L_{IF_BPF} - 1}{\frac{G_{ant}G_{LNA1}G_{LNA2}G_{MIX}}{L_{cable}L_{RF_BPF}}} + \frac{F_{VGA} - 1}{\frac{G_{ant}G_{LNA1}G_{LNA2}G_{MIX}}{L_{cable}L_{RF_BPF}L_{IF_BPF}}}, \quad (5.36)$$

where the respective amplifier, mixer, and filter parameters can be found in Fig. 5.13. The equation shows clearly that if G_{ant} is sufficiently high, the overall receiver noise factor is close to F_{ant} , and the noise introduced by subsequent blocks are negligible. The front-end gain should be distributed between the amplifiers taking into account also the implementation feasibility: i.e., high gain amplifiers usually have also high noise figure and low CP and IP3. In addition, the gain should be distributed also between the RF chain and the IF chain in order to avoid possible oscillations caused by parasitic feedback [Gil03b]. Aligned to this, Table 5.9 proposes a suitable set of values for the gain and NF parameters of the front-end components based on the available technology.

The overall front-end gain is $G_{FE} \geq 74$ dB and the noise figure is $NF_{FE} \leq 2.47$ dB. Both values meet the requirements with a margin of 1.2 dB and -1.53 dB for the gain and NF respectively.

The overall front-end CP and IP3 specifications were obtained in last Section using (5.35). It is possible to derive the linearity specifications for each individual component starting from the component closer to the ADC using the P_{FSR} value. Table 5.10 shows the design equations and the computed values for the selected gain / loss distribution of Table 5.9, considering that the front-end is connected to an ADC with $N_b = 12$ bits and $V_{FSR} = 2$ Vpp. Based on that information, we describe in the next Section a front-end design that is validated by computer simulations using Electronic Design Automation (EDA) software, as a previous step to implement each of the front-end building blocks.

5.3 Simulations and design validation

The complete chain was simulated using the Agilent ADS software [Agi11] by using two different techniques:

Frequency	Phase noise
1 kHz	-50 dBc
10 kHz	-93 dBc
100 kHz	-118 dBc

Table 5.11: Simulated local oscillator phase noise.

- **harmonic balance:** is a highly accurate frequency-domain analysis technique for obtaining the steady state solution of nonlinear circuits and systems. The harmonic balance method assumes that the input stimulus consists of a few steady-state sinusoids. Therefore the solution is a sum of steady state sinusoids that includes the input frequencies in addition to any significant harmonics or mixing terms. This technique is suitable to compute quantities such as IP3, Total Harmonic Distortion (THD), and inter-modulation distortion components[Ag11], and
- **S-Parameters:** the Agilent S-parameter simulation controller computes the scattering parameters (S-parameters) of a component, circuit, or subnetwork. It is possible to simulate the variations in swept-frequency S-parameters, simulate group delay or linear noise. In addition, it is possible to simulate the effects of frequency conversion on small-signal S-parameters in a circuit employing a mixer [Ag11]. This is also known as analyzing a frequency-translating network. This technique is suitable to compute the front-end conversion gain, bandwidth, noise figure, and compression point, among other specifications.

The S-parameters describe the electrical behavior of linear electrical networks when undergoing various steady state stimuli by electrical signals [Poz01]. Fig. 5.14 shows a representation of a 2-ports network with the labels of the incident and the reflected waves. It is possible to write their relationships using the S-parameters matrix:

**Figure 5.14:** S-parameters incident and reflected waves representation.

$$\begin{pmatrix} b_1 \\ b_2 \end{pmatrix} = \begin{pmatrix} S_{11}S_{12} \\ S_{21}S_{22} \end{pmatrix} \begin{pmatrix} a_1 \\ a_2 \end{pmatrix} \quad (5.37)$$

The simulated block diagram for one channel is depicted in Fig. 5.15. The local oscillator phase noise was also simulated and the phase noise values for several frequencies can be found in Table 5.11. In the simulations an ideal AGC that uses an analog control input is selected.

Fig. 5.16a shows the front-end conversion gain vs. the RF input frequency, represented by the $S(2,1)$ parameter. Based on the results, the gain in the GNSS L1/E1 link is $G_{FE} = 73.9$ dB and $B_p = 17.8$ MHz. The stopband bandwidth is around 20 MHz. Both performance parameters match the design specifications of Table 5.5. The NF simulation results can be found in Fig. 5.16b. The front-end enjoys a noise figure of $NF_{FE} = 2.178$ dB which is aligned with the design specification maximum value of 4 dB. The output phase noise was also simulated and the results can be found in Fig. 5.17. The phase noise is mainly dependent of the local oscillator phase noise, as we will see in the next Sections. Finally, the image frequency rejection was simulated and Fig. 5.18 shows the results.

Table 5.12 summarizes the simulated front-end specifications. In the sequel, each of the front-end modules are mapped to the suitable COTS components towards a complete prototype implementation.

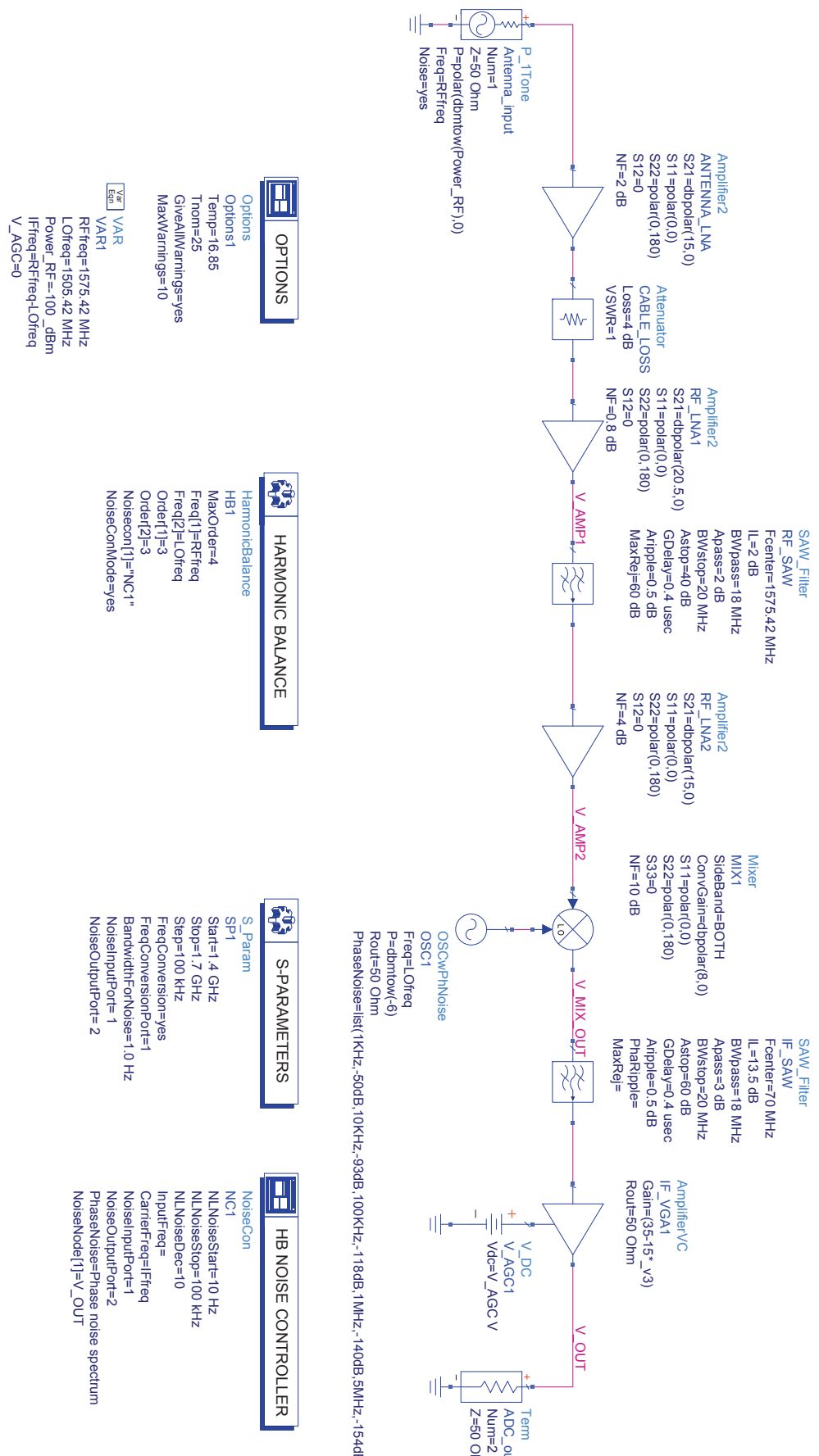


Figure 5.15: Generic GNSS front-end diagram.

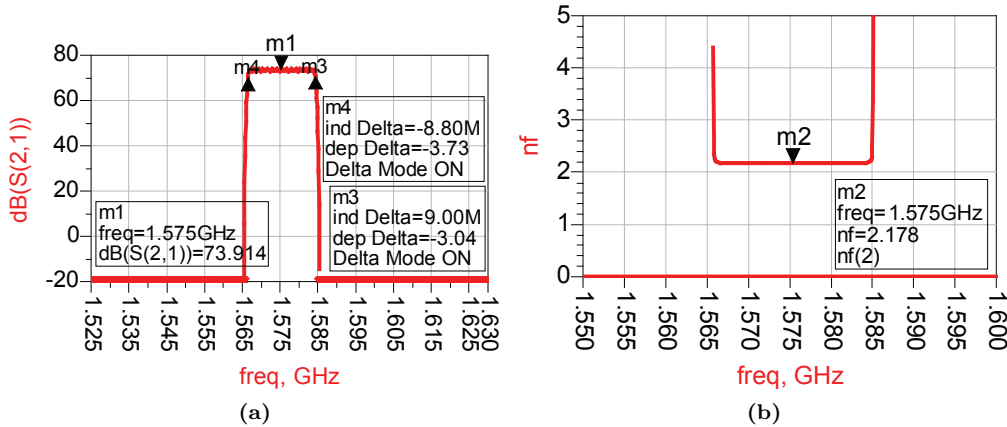


Figure 5.16: Simulated front-end gain and noise figure.

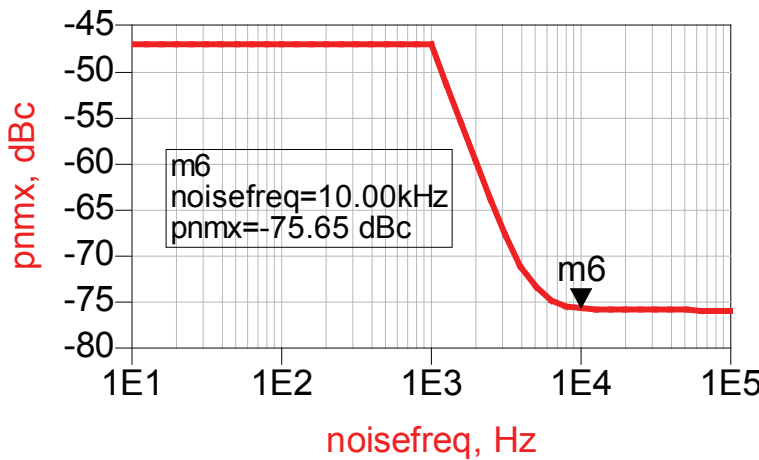


Figure 5.17: Simulated front-end phase noise.

5.4 Part selection and implementation measurements

In this section, the front-end high-level schematic of Fig. 5.13 is mapped into available COTS components considering the design specifications. Each of the building blocks, such as LNAs, mixers, and filters are implemented individually in order to measure the performance parameters in a controlled test bench. This preliminary procedure helps the detection of implementation issues such as impedance matching problems between devices or power supply incompatibilities.

5.4.1 Antenna array elements

Each of the antenna array elements consists of a commodity compact GPS L1 active antenna model Garmin GA27c [GA205]. The manufacturer specifications are listed in Table 5.13.

Fig. 5.19a shows a picture of the antenna element. It is composed of a ceramic patch-type antenna [Bal03, p.727] mounted over a circuit board which contains the LNA circuit. Notice that the both G_{ant} and NF_{ant} meet the design specifications listed in Table 5.5. According to (5.36) the overall front-end noise figure will be close to NF_{ant} . However, there is no information available regarding the linearity parameters of the antenna LNA, thus, it will be obtained using anechoic chamber measurements.

The internal distribution can be seen in Fig. 5.19b. All the elements are placed sharing the same orientation in order to keep the wavefront impinging into each of them by the same DOA

Parameter	Design specification	Simulation result
RF frequency (f_{RF})	1575.42 MHz	1575.42 MHz
IF frequency (f_{IF})	70 MHz	70 MHz
Passband bandwidth (B_p)	≥ 12 MHz	17.8 MHz
Stopband bandwidth (B_{bb})	≤ 20 MHz	20 MHz
Conversion Gain (G_{FE})	≥ 72.8 dB	73.9 dB
Noise figure (NF_{FE})	≤ 4 dB	2.178 dB
Image rejection (L_{img})	≥ 40 dB	60.2 dB
Phase noise (10kHz)	≤ -60 dB	-75.65 dB

Table 5.12: Simulated front-end performance values compared to design specifications.

Specification or feature	Manufacturer Value	Front-end specification
Manufacturer	GARMIN	
Antenna	GA27c	
Dimensions (mm)	50x71x17	
Mount	Magnetic	
Connector (modified)	SMA	
Impedance	$50\ \Omega$	
Power	5Vdc@30mA max.	
G_{ant}	15 dB	
Cable length (m)	2.5	
Cable type	RG-174	
Cable loss	4 – 5 dB	≤ 4 dB
NF_{ant}	2 dB	≤ 2 dB
$P_{CP,ant}$	NOT AVAILABLE	≥ -55.9 dBm
Gain Pattern	+1.5 dB @90 deg. -1 dB @45 deg. -6 dB @10 deg.	
Axial Ratio	3 dB @90 deg.	
Interferences attenuation	15 dB @1575.42 \pm 50 MHz 25 dB @1575.42 \pm 100 MHz	
Operating Temp.	-55/+85 deg. Celsius	

Table 5.13: GA27c active antenna specifications summary.

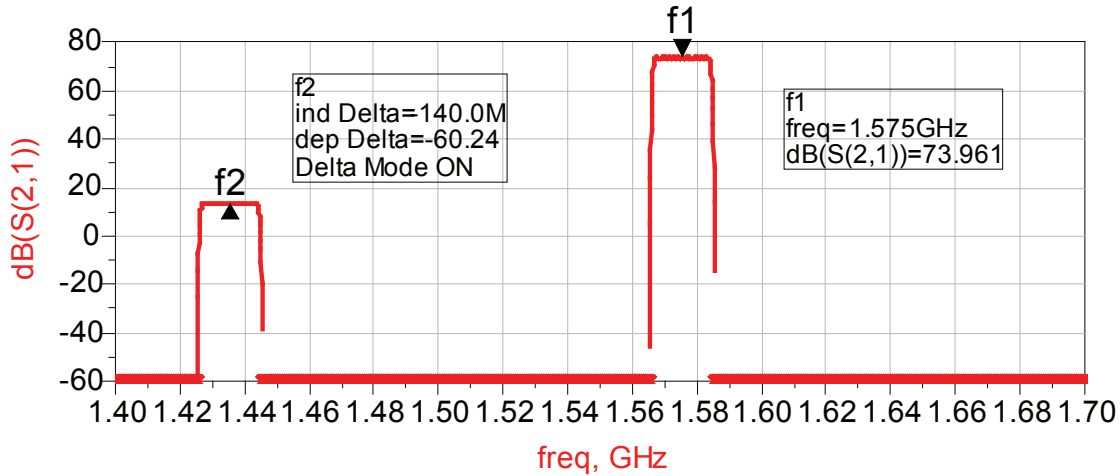


Figure 5.18: Simulated front-end GNSS link gain and image frequency rejection.

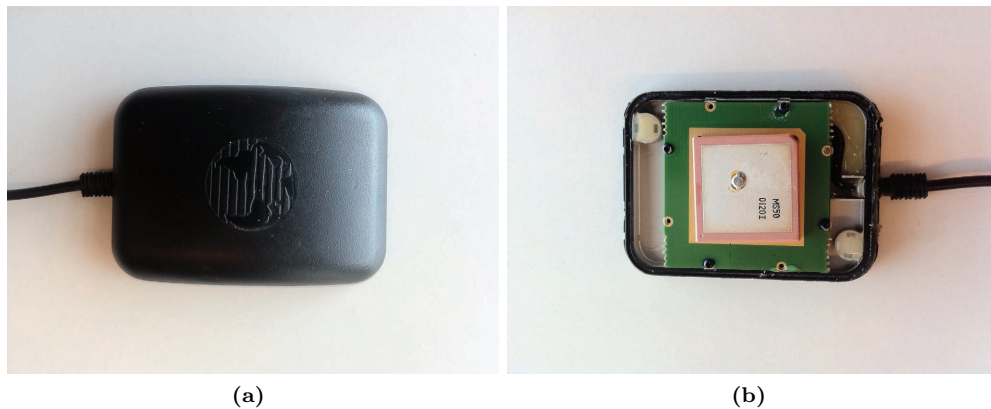


Figure 5.19: Garmin GA27c active antenna.

and thus, minimize the radiation pattern differences between elements as described in Section 5.1.3.

The antenna array prototype is shown in Fig. 5.20. The individual antenna elements radiation patterns were measured in an anechoic chamber. As is shown in Fig. 5.21, there exist important differences between elements. Some of the possible causes are the coupling effect between neighbors elements, aging, and slight differences in the fabrication process. Since the proposed acquisition algorithm enjoys protection against array calibration errors as shown in Chapter 4, the uncalibrated array is an excellent opportunity to validate the theoretical results.

5.4.2 RF low noise amplifier and RF bandpass filter

5.4.2.1 Prototype design and implementation

The RF LNA amplification and filtering stage is composed of two cascaded LNA monolithic integrated circuits and a SAW filter intercalated between them. The first amplifier is in charge of providing high gain at minimum noise figure. For this application we select the Maxim MAX2659 [Max09], which is specifically designed for GPS, Galileo and Glonass applications. It is designed in SiGe¹² technology. The device achieves $G_{\text{RF,LNA1}} = 20.5 \text{ dB}$ with $NF_{\text{RF,LNA1}} = 0.8 \text{ dB}$. In

¹²The SiGe (silicon-germanium) technology enables the fabrication of low current and high frequency high performance transistors, with more flexible band gap tuning than silicon-only technology [Oue02].

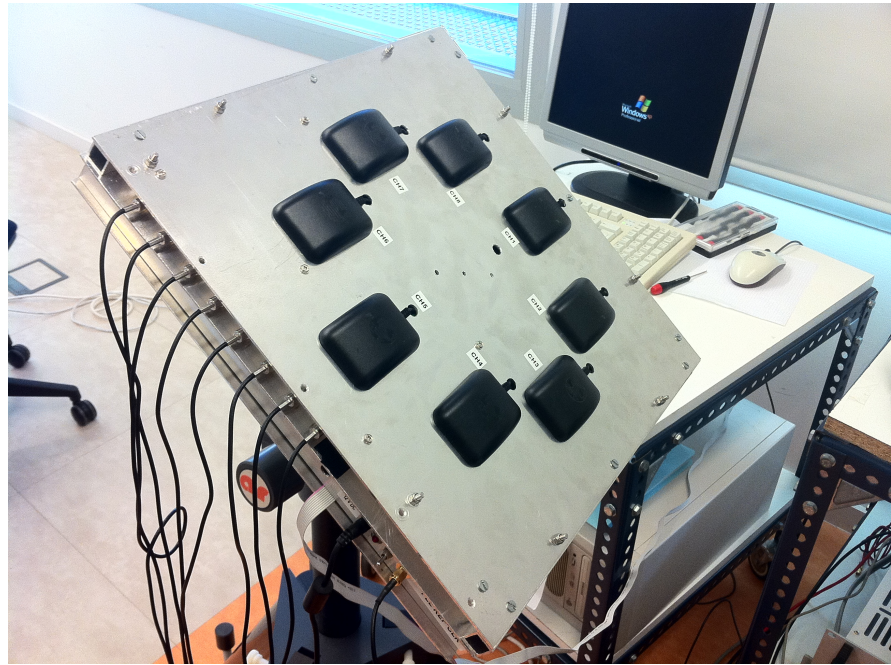


Figure 5.20: Antenna array prototype.

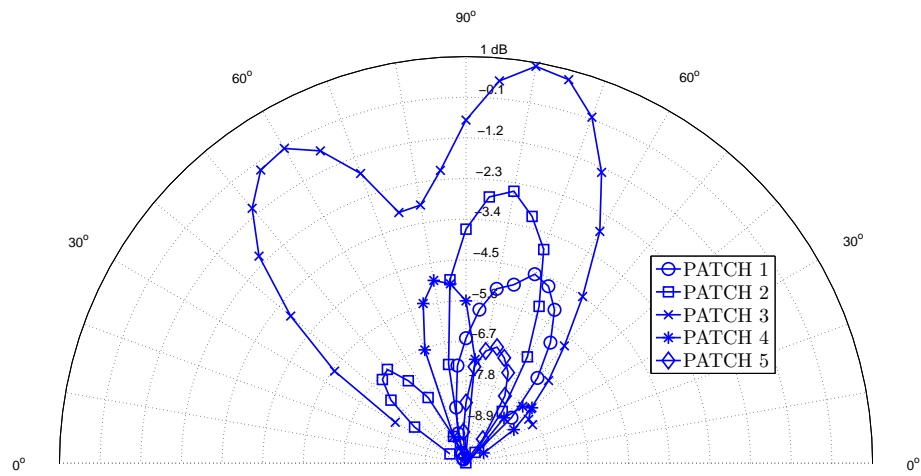


Figure 5.21: Differences between radiation patterns of some antenna elements in elevation.

addition, the LNA enjoys good CP and IP3 of $P_{CP,RF,LNA1} = -12$ dBm and $P_{IP3,RF,LNA1} = -5$ dBm, respectively. A summary of the specifications and features are listed in Table 5.14.

Specification or feature	Manufacturer Value	Front-end specification
Manufacturer	Maxim semiconductors	
Input frequency	1575.42 MHz	1575.42 MHz
G_{LNA1}	20.5 dB	≥ 20 dB
NF_{LNA1}	0.8 dB	≤ 4 dB
$P_{CP,LNA1}$	-12 dBm	≥ -44.9 dBm
$P_{IP3,LNA1}$	-5 dBm	≥ -35.3 dBm
Input/Output type	Single ended	
Input/output impedance	$50\ \Omega$	
Supply voltage	1.6 to 3.3 V DC	
Supply current	4.1 mA	

Table 5.14: MAX2659 1st RF LNA specifications summary.

The MAX2659 output is fed to a Murata SAFSE1G57KA0T90 [Mur07] SAW bandpass filter which is in charge of selecting the GNSS L1/E1 link bandwidth. Table 5.15 shows the manufacturer specifications, although the measured performance shows that the device has higher bandwidth and it is suitable for the prototype.

Specification or feature	Manufacturer Value	Front-end specification
Manufacturer	Murata Manufacturing Co., Ltd	
Filter type	Passband SAW filter	
Nominal center frequency	1575.42 MHz	1575.42 MHz
Insertion Loss	1.1 dB @ 1574.42 - 1576.42 MHz	≤ 2 dB
Ripple deviation	0.1 dB @ 1574.42 - 1576.42 MHz	
Absolute attenuation	33 dB @ 100 - 960 MHz 35 dB @ 1205 - 1215 MHz 40 dB @ 1385 - 1395 MHz 38 dB @ 1710 - 1990 MHz 40 dB @ 1990 - 2500 MHz	≥ 40 dB @ $f_{IMG} = 1435.42$ MHz
Image frequency att. (1435.42 MHz)	40 dB	≥ 40 dB
Group delay	15 ns	$\leq 1\mu s$
Group delay variation	10 ns	$\leq 1\mu s$
Input/Output impedance	$50\ \Omega$	

Table 5.15: SAFSE1G57KA0T90 SAW filter specifications summary.

Finally, the filtered output is fed to a general purpose DC-to-Microwave amplifier Maxim MAX2650 [Max03a] to compensate the filter insertion losses and to add extra gain to the amplification stage. MAX2650 specifications summary can be found in Table 5.16.

A prototype of the whole RF amplification and filtering stage was designed and built in a separate PCB board in order to verify the module's standalone performance. It is included a bias T network¹³ in order to provide the power supply voltage to the active antenna element. The detailed schematic can be found in Fig. 5.22. Fig. 5.23 shows the PCB layout and 5.24 shows a picture of the implementation.

5.4.2.2 Measurements

S-parameters measurements were performed using Rohde & Schwarz ZVA 24 Vector Network Analyzer [Roh11] for a frequency sweep from 1.5 – 1.7 GHz. The input-output ports impedance

¹³A bias T network is diplexer [Poz01]. The low frequency port is used to set the bias voltage; the high frequency port passes the radio frequency signals but blocks the biasing levels; the combined port connects to the device to be powered.

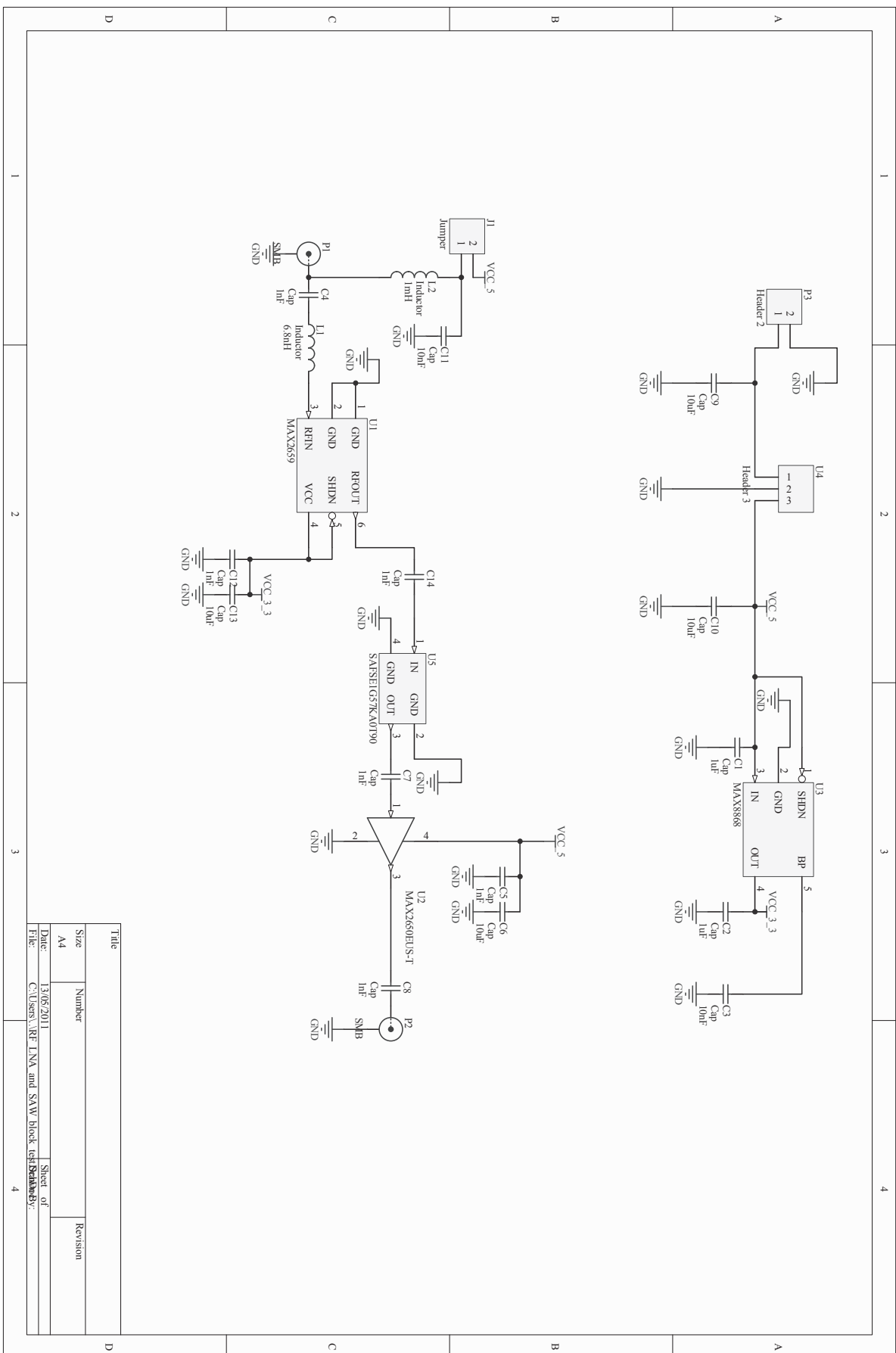
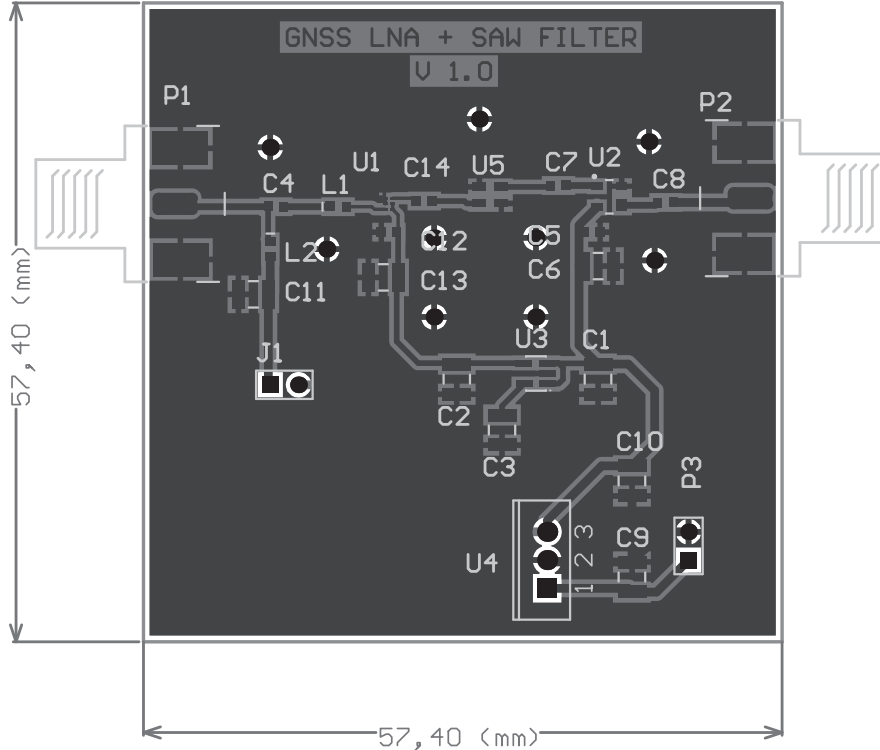


Figure 5.22: RF LNA prototype schematic.

Specification or feature	Manufacturer Value	Front-end specification
Manufacturer	Maxim semiconductors	
Input frequency range	DC to 1600 MHz	1575.42 MHz
G_{LNA2} @ 1500 MHz	12.5 dB	≥ 15 dB
NF_{LNA2} @ 1500 MHz	4.5 dB	≤ 10 dB
$P_{CP,LNA2}$ @ 1500 MHz	-3 dBm	≥ -25.9 dBm
Input/Output type	Single ended	
Input/output impedance	50 ohms	
Supply voltage	4.5 to 5.5 V DC	
Supply current	17.7 mA	

Table 5.16: MAX2650 2nd RF LNA specifications summary.**Figure 5.23:** RF LNA prototype PCB.

matching measurements can be found in Fig. 5.25a and 5.25b, which shows the S_{11} and S_{22} magnitude parameters, respectively. A minimum of -10 dB of return loss was measured on all ports. The measured amplification gain magnitude and phase (S_{21} parameter) can be found in 5.26a and 5.26b, respectively.

The device linearity was also tested using the vector analyzer. In the experiment, an input power sweep for -50 to -20 dBm was performed for an unmodulated 1575.42 MHz carrier signal. The output power was recorded by the analyzer and the results can be found in Fig. 5.27. A 1 dB compression point was identified for $P_{IN} = -31$ dBm.

Finally, the noise figure was measured using an Agilent N8975A noise figure analyzer [Agi05c]. In the experiment, a calibrated noise source Agilent [Agi05b] was connected to the signal input and the amplifier output was connected directly to the analyzer. The noise figure and the gain measured by the noise analyzer are plotted in Fig. 5.28.

The measured performance values for the RF amplification and filtering stage are summarized in Table 5.17.

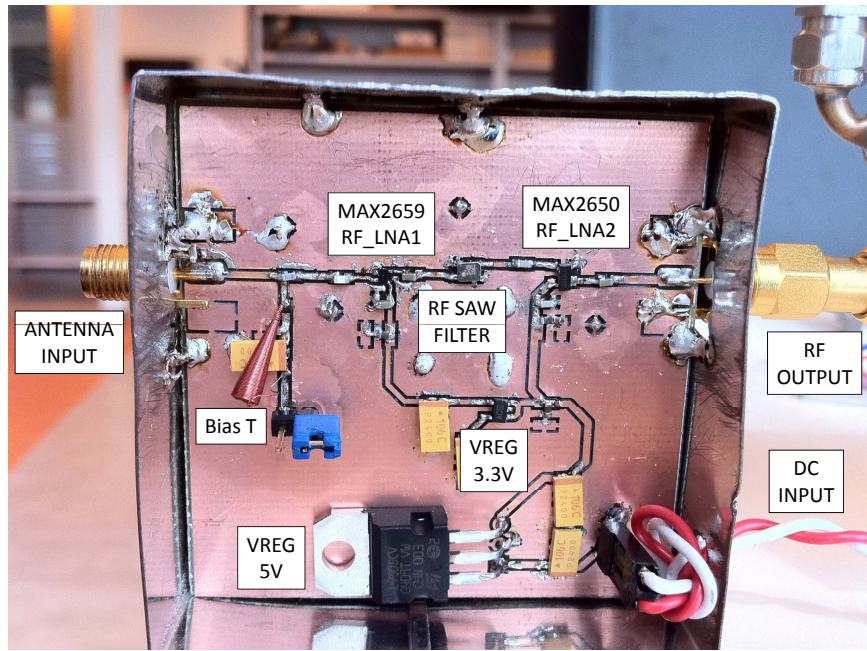
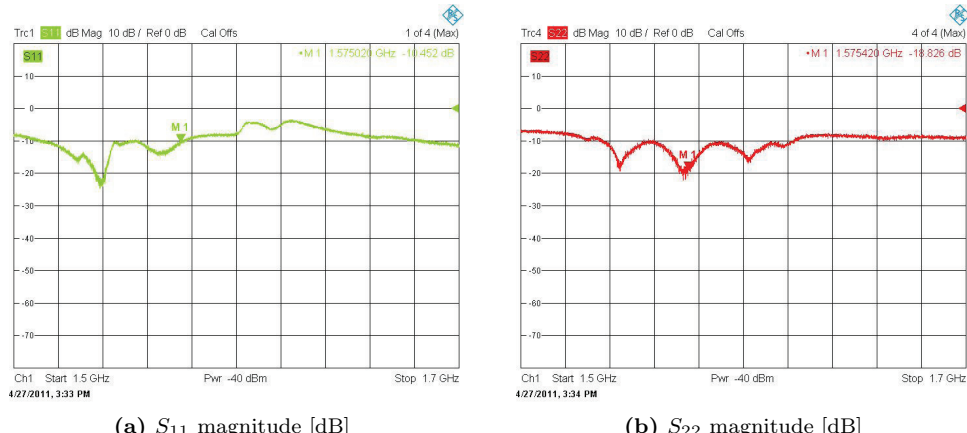


Figure 5.24: RF LNA prototype picture.

Parameter	Measured value	Front-end specification
Center frequency	1575.42 MHz	1575.42 MHz
$G_{\text{LNA1+RF_BPF+LNA2}}$	29 dB	$20.5 - 2 + 15 = 33.5$ dB
Passband bandwidth	40 MHz	≥ 12 MHz
Stopband bandwidth	70 MHz	≤ 100 MHz
$N\bar{F}_{\text{LNA1+RF_BPF+LNA2}}$	1.8 dB	≤ 4 dB
$P_{CP,\text{LNA1+RF_BPF+LNA2}}$	-31.1 dBm	≥ -44.9 dBm
Input/Output type	Single ended	
Input/output impedance	50 ohms	
Supply voltage	7 to 12 V DC	
Supply current	≤ 60 mA	

Table 5.17: RF LNA and RF filtering measured specifications summary.



(a) S_{11} magnitude [dB]

(b) S_{22} magnitude [dB]

Figure 5.25: RF LNA input-output matching measurements.

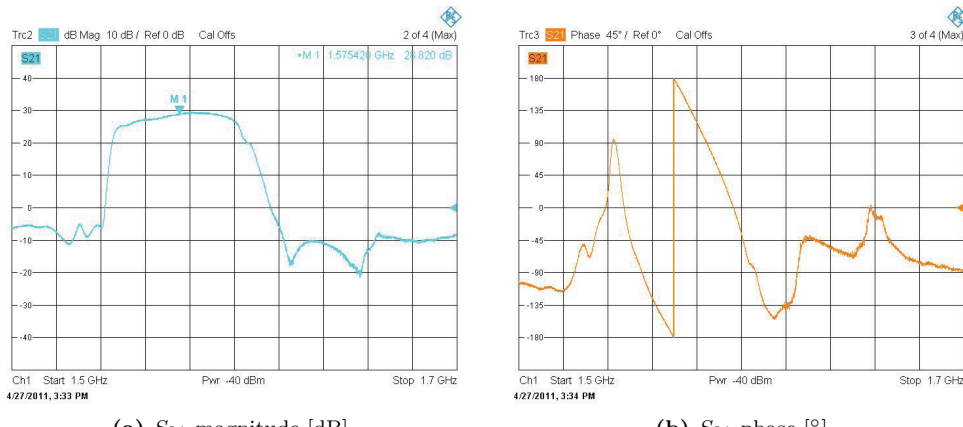


Figure 5.26: RF LNA amplification magnitude and phase measurements.

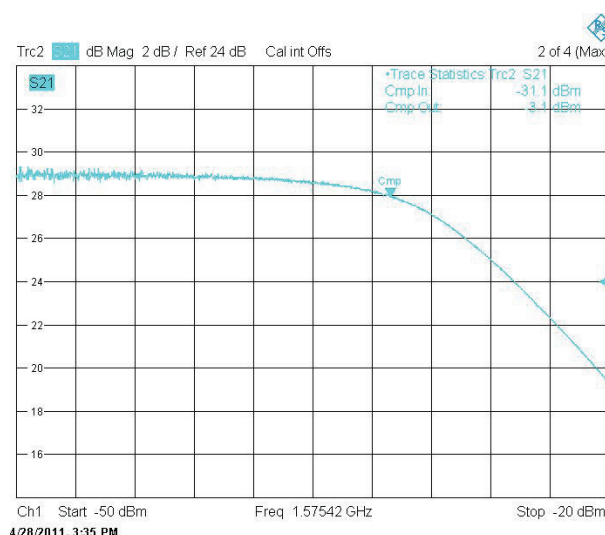


Figure 5.27: RF LNA prototype compression measurements.

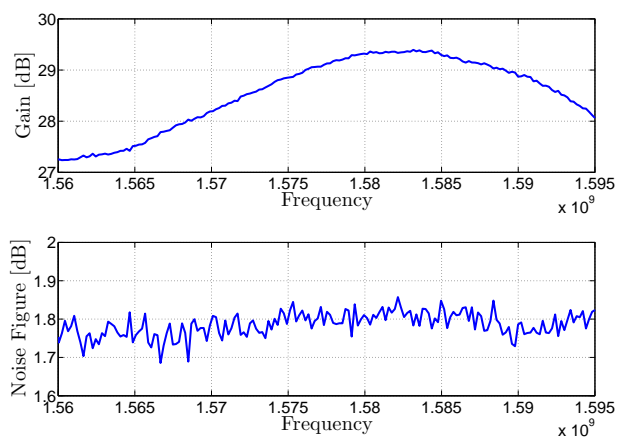


Figure 5.28: RF LNA prototype noise figure measurements.

5.4.3 RF mixer and IF bandpass filter

There are three basic implementations for both active and passive mixers [Poz01]:

- Unbalanced mixers
- Single-balanced mixers
- Double-balanced mixers

Double-balanced mixer offers superior interport isolation, which contributes to alleviate the IF filter requirements. The proposed prototype is based on an active double-balanced mixer.

5.4.3.1 Prototype design and implementation

A Gilbert cell active mixer is suitable because it presents a higher gain and lower noise than passive ones [Gil68]. The MAX2681 [Max03b] is a double-balanced Gilbert-cell low-noise down-converter mixer designed for low-voltage, low-current operation. It is designed in SiGe technology. The MAX2681 can be used with input frequencies between 400 MHz and 2500 MHz, to downconvert to IFs between 10 MHz to 500 MHz. The input RF for a GPS receiver is 1575.42 MHz. Assuming a 70 MHz IF, and high-side LO injection ($f_{LO} = 1645.42$ MHz), the MAX2681 achieves +10.5 dB of gain, has a noise figure of 9.6 dB, and an input third-order intercept point of -0.8 dBm, according to the manufacturer application note [Max02]. Table 5.18 summarizes the specifications.

Specification or feature	Manufacturer Value	Front-end specification
Manufacturer	Maxim semiconductors	
Input frequency range	400 MHz to 2500 MHz	1575.42 MHz
G_{MIX} @ 1575.42 MHz	10.5 dB	≥ 10 dB
NF_{MIX} @ 1575.42 MHz	9.6 dB	≤ 10 dB
$P_{CP,MIX}$ @ 1575.42 MHz	-10.4 dBm	≥ -10.9 dBm
$P_{IP3,MIX}$ @ 1575.42 MHz	-0.8 dBm	≥ -1.3 dBm
Required LO power	-8 to 0 dBm	
Input/Output type	Single ended	
Input/output impedance	Matching network required	
Supply voltage	2.7 to 5.5 V DC	
Supply current	8.7 mA	

Table 5.18: MAX2681 mixer specifications summary.

The mixer output is filtered by a Sawtek 854669 IF passband SAW filter [Tri05] whose specifications can be found in Table 5.19. The use of the state-of-the-art SAW technology in low frequency applications, such as IF filtering, offers high selectivity, but at expenses of high insertion losses.

A prototype of the mixing stage was designed and built in a separate PCB board in order to verify the module's standalone performance. The detailed schematic can be found in Fig. 5.29. Fig. 5.30 shows the PCB layout and Fig. 5.31 shows a picture of the prototype implementation.

5.4.3.2 Measurements

S-parameters measurements were performed using Rohde & Schwarz ZVA 24 Vector Network Analyzer [Roh11] for a frequency sweep from 1.55 – 1.59 GHz. The analyzer was configured in frequency conversion mode. During the measurements, the LO signal was generated using an additional output port of the same instrument.

Fig. 5.16a shows the front-end conversion gain vs. RF input frequency, represented by the $b2/a1$ magnitude parameter (see, (5.37)). Based on the results, the gain in the GNSS L1/E1

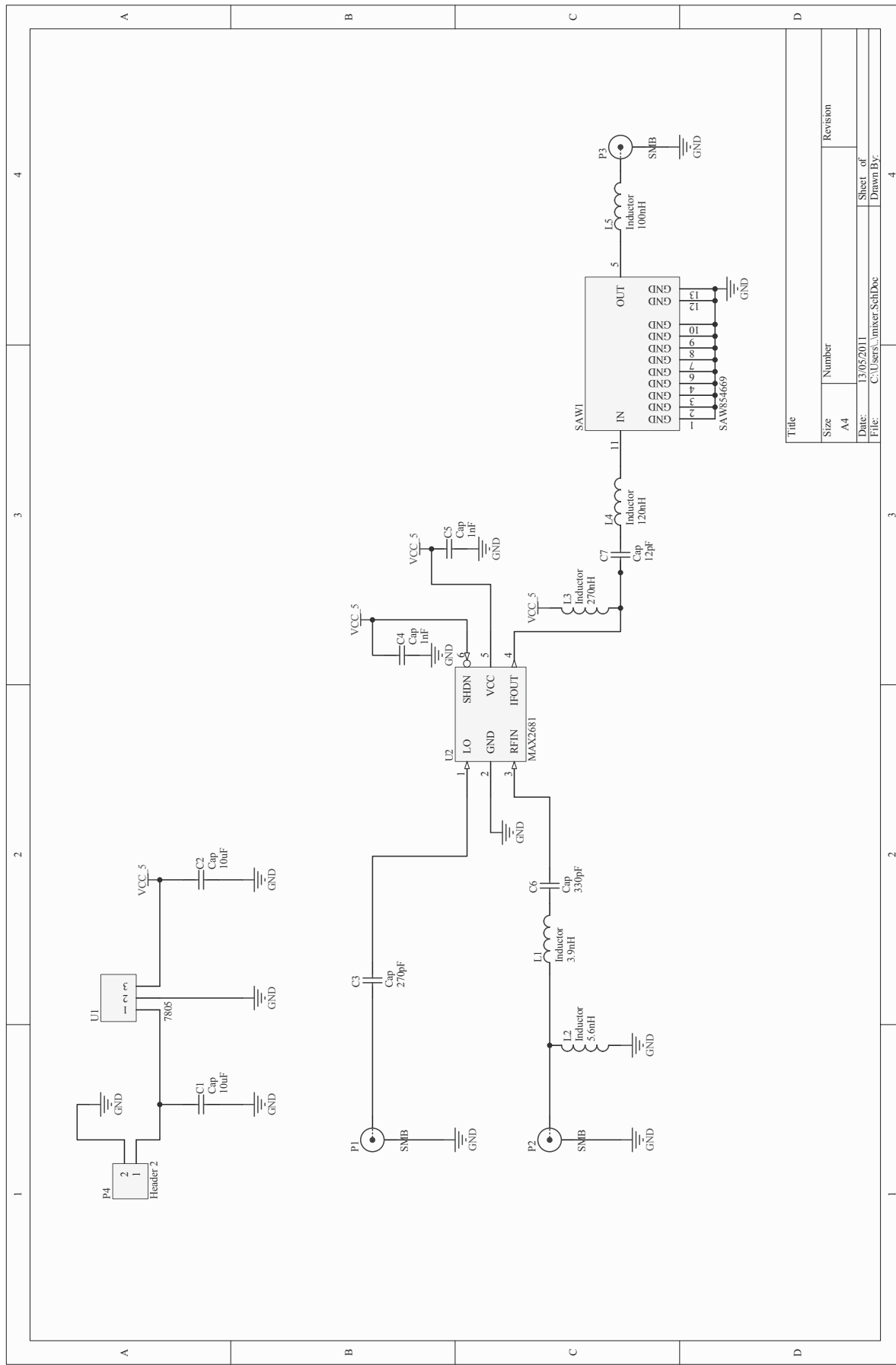
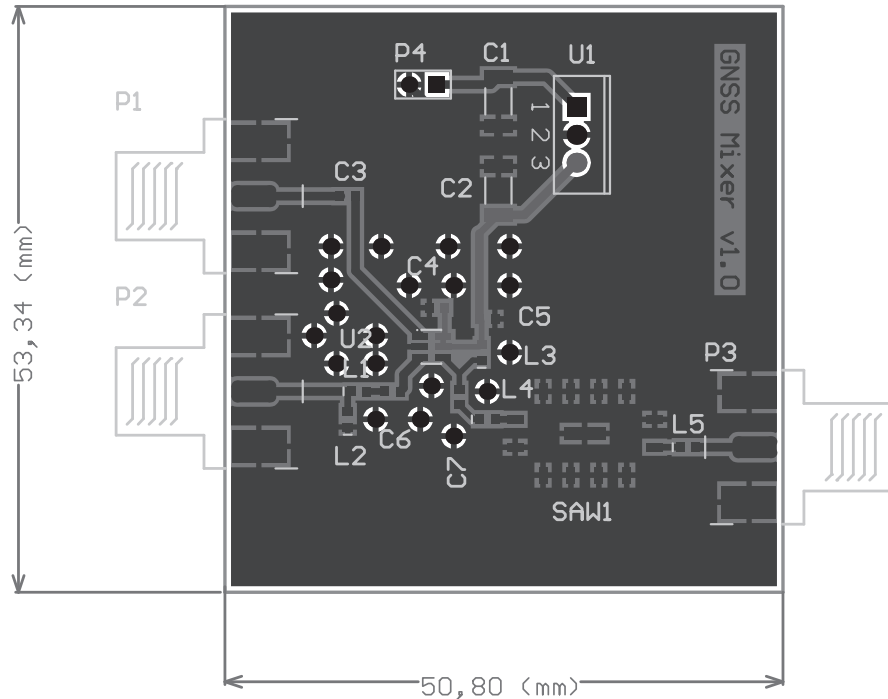


Figure 5.29: Mixer and IF filter prototype schematic.

Specification or feature	Manufacturer Value	Front-end specification
Manufacturer	Sawtek,. Inc	
Filter type	Passband SAW filter	
Nominal center frequency	70 MHz	70 MHz
Insertion Loss	13.5 dB	≤ 10 dB (*)
Passband ripple	0.7 dB	
1 dB bandwidth	17.55 MHz	
3 dB bandwidth	18.5 MHz	≥ 12 MHz
40 dB stopband bandwidth	23.4 MHz	≤ 20 MHz (20 dB att.)
Group delay	1.07 μ s	
Group delay variation (61.9 - 78.1) MHz	70 ns	$\leq 1\mu$ s
Input/Output impedance	50 ohms	

Table 5.19: Sawtek 854669 70 MHz SAW filter specifications summary.**Figure 5.30:** Mixer and IF filter prototype PCB.

link is $G_{MIX} = -2.553$ dB. Although the selected mixer has a conversion gain of 13.5 dB, the SAW filter insertion losses gives overall conversion losses of 2.553 dB.

The measured conversion passband bandwidth is $B_p = 18.5$ MHz. The 20 dB stopband bandwidth is ≤ 20 MHz, which matches the design requirements.

Fig. 5.32 and 5.33 shows the b_2/a_1 parameter using two possible LO frequencies of 1505.42 MHz and 1645.42 MHz, respectively. Based on the measurement results, the mixer frequency response is almost the same in both experiments, but the 1505.42 MHz option offers 1 dB more of conversion gain.

The device linearity was also tested using the vector analyzer. In the experiment, an input power sweep from -40 to -10 dBm was performed for an unmodulated 1575.42 MHz carrier signal. The output power was recorded by the analyzer and the results can be found in Fig. 5.34. A 1 dB compression point was identified for $P_{IN} = -18.4$ dBm.

Finally, the noise figure was measured using an Agilent N8975A noise figure analyzer [Agi05c]. In the experiment, a calibrated noise source Agilent [Agi05b] was connected to the signal input

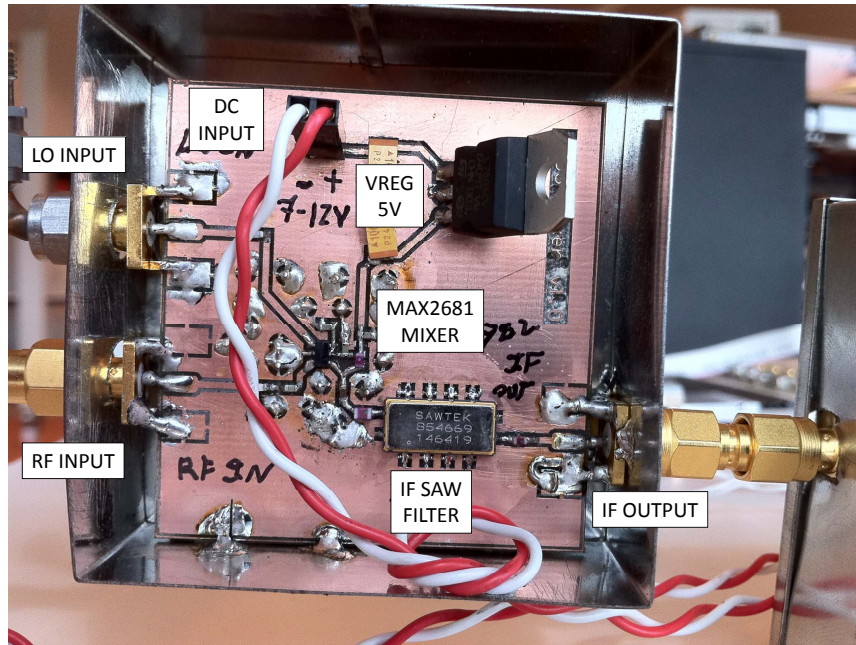


Figure 5.31: Mixer and IF filter prototype picture.

and the mixer output was connected directly to the analyzer. The instrument was configured in *system downconverter mode*, which takes into account the frequency conversion output IF. Fig. 5.35 shows the instrument mode configuration screen and the device under test connection scheme. The measured noise figure is plotted in Fig. 5.36

The measured performance values for the frequency downconversion stage are summarized in Table 5.20. Comparing the values to the manufacturer specifications, we realize that the mixer CP is out of specs. The prototype mixer reach the compression point 7.5 dB earlier than the front-end design specification, consequently, the interference protection offered by the front-end will be reduced as we will see in the next Section. Regarding the conversion gain combined with the IF filtering stage, the extra gain provided by the mixer compensates the high insertion loss of the SAW filter, thus, the implementation meets the gain specifications.

Parameter	Measured value	Front-end specification
Input frequency	1575.42 MHz	1575.42 MHz
Output frequency	70 MHz	70 MHz
3 dB Passband bandwidth	18.5 MHz	≥ 12 MHz
20 dB Stopband bandwidth	20 MHz	≤ 20 MHz
G_{MIX+IF_BPF}	-2.55 dB	≥ -5 dB
NF_{MIX+IF_BPF}	10.2 dB	—
$P_{CP,MIX+IF_BPF}$	-18.4 dBm	≥ -10.9 dBm(*)
LO frequency	1505.42 MHz or 1645.42 MHz	
Required LO power	-8 to 0 dBm	
Input/Output type	Single ended	
Input/output impedance	50 ohms	
Supply voltage	7 to 12 V DC	
Supply current	≤ 60 mA	

Table 5.20: RF mixer and IF bandpass filter measured specifications summary.

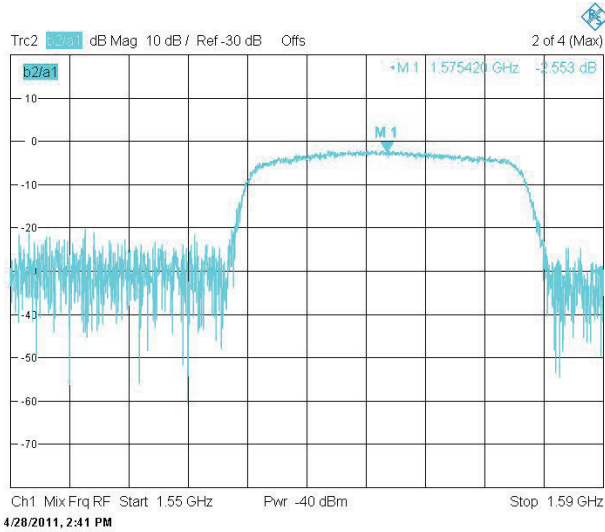


Figure 5.32: Mixer prototype gain measurement for $f_{LO} = 1505.42$ MHz and $P_{LO} = -5$ dBm.

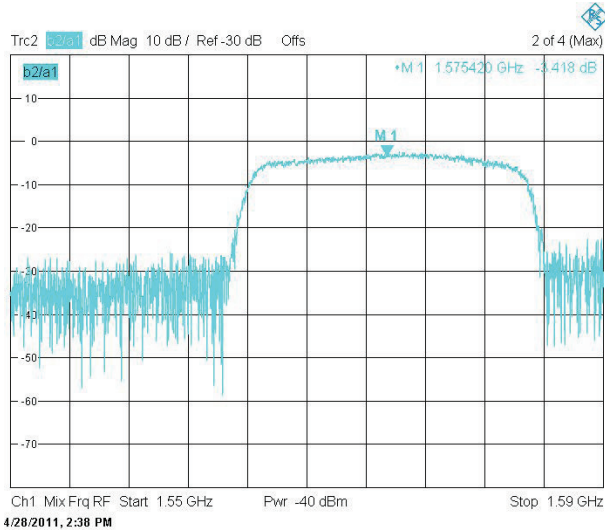


Figure 5.33: Mixer prototype gain measurement for $f_{LO} = 1645.42$ MHz and $P_{LO} = -5$ dBm.

5.4.4 IF variable gain amplifier

The IF amplification stage core is a low-frequency VGA. Variable gain amplifiers can be designed using two different techniques:

- varying the device's bias voltage, or
- using a variable attenuator at the input of a fixed gain amplifier.

It is known that the variable attenuator technique offers a linear response to the VGA control input, which simplifies the AGC algorithm. Depending on the control input nature, VGAs can be classified in two categories:

- analog control input: the gain is proportional to the voltage or intensity applied to a control pin. Usually this type of device needs calibration, or
- digital control input: The gain is proportional to the gain control code. It is factory-calibrated.

Since the multichannel ADC is controlled by an FPGA and the AGC algorithm is implemented using the internal FPGA logic, a digitally controlled VGA is suitable for this design.

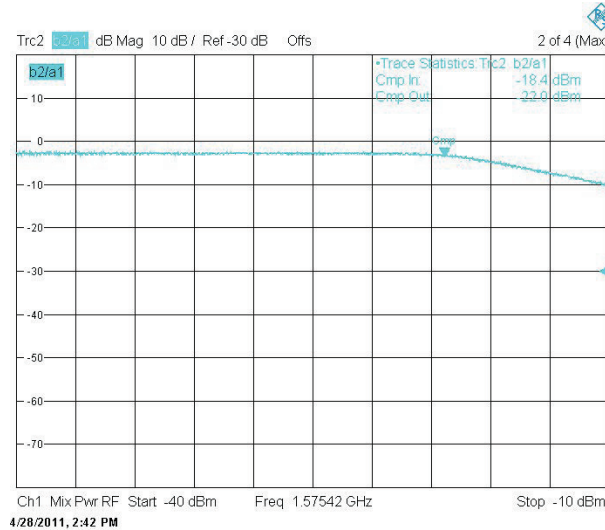


Figure 5.34: Mixer prototype compression point measurement.

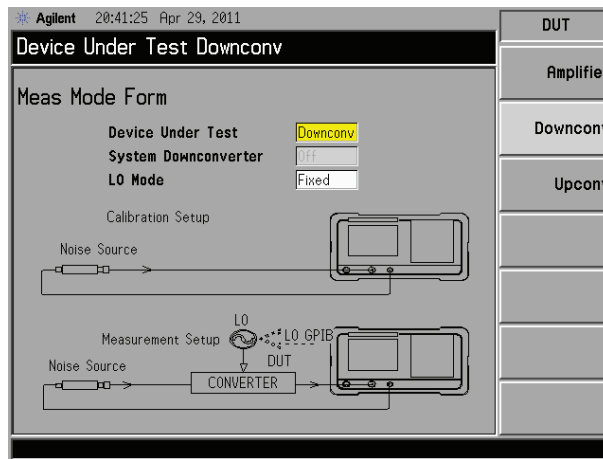


Figure 5.35: Mixer prototype noise figure analyzer configuration.

Other derived key benefits are the possibility to transmit the same digital control input for all the channels without losses or tolerances.

5.4.4.1 Prototype design and implementation

The selected VGA is the Analog Devices AD8369 [Ana02]. It is a high performance digitally controlled VGA for use from low frequencies up to 600 MHz at all gain codes. The device has a nominal NF of 7 dB at maximum gain, and the output IP3 is 19.5 dBm at 70 MHz.

The gain range at 200 ohms load is -10 dB to 35 dB in 3 dB steps. The gain control uses 4 bits and implements a variable attenuator. Digital control of the AD8369 is archived using either a serial or parallel interface. Fig. 5.37 shows the internal block diagram, and Table 5.21 summarizes the manufacturer specifications.

A prototype of the IF VGA stage was designed and built in a separate PCB board in order to verify the module's standalone performance. The detailed schematic can be found in Fig. 5.38. Fig. 5.39 shows the PCB layout and 5.40 shows a picture of the prototype implementation.

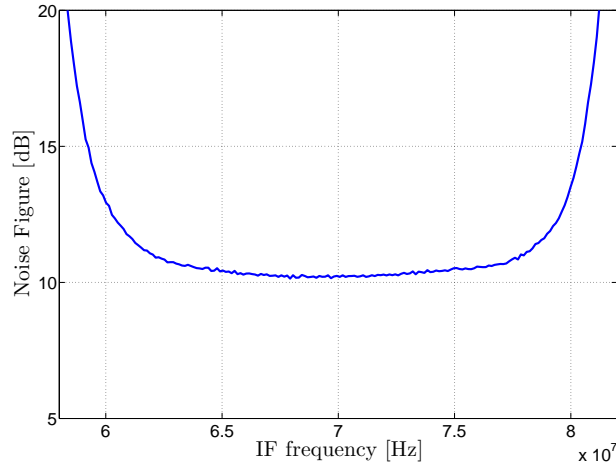


Figure 5.36: Mixer prototype noise figure measurement.

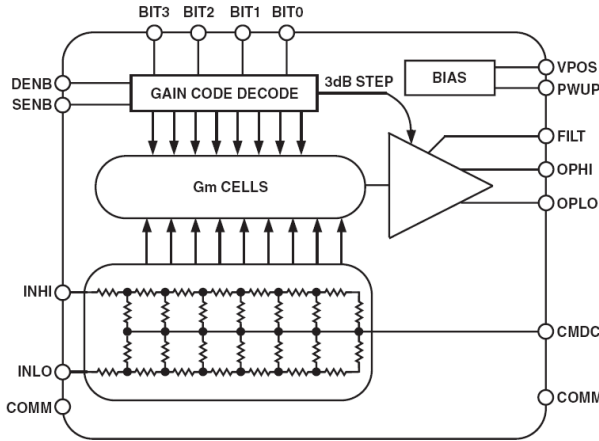


Figure 5.37: AD8369 functional block diagram.

Specification or feature	Manufacturer Value	Front-end specification
Manufacturer	Analog devices	
Input frequency	LF to 600 MHz	70 MHz
Gain range	-5 to 40 dB for 1 kΩ load -10 to 35 dB for 200 Ω load	0 to 35 dB
Gain step	3 dB	
NF_{VGA}	7 dB @ maximum gain	≤ 10 dB
$P_{IP3,VGA}$	19.5 dBm @ 70 MHz and 1 kΩ load	≥ -6.3 dBm
Input/Output type	Differential	
Input/output impedance	200 Ω	
Control interface	4 bit parallel or 3 wire serial interface	
Supply voltage	3.0 to 5.5 V DC	
Supply current	37 mA	

Table 5.21: AD8369 IF VGA specifications summary.

5.4.4.2 Measurements

S-parameters measurements were performed using Rohde & Schwarz ZVA 24 Vector Network Analyzer [Roh11] for a frequency sweep of 40 – 100 MHz and the VGA was set to the maximum gain. Fig. 5.41 shows the measured S_{11} magnitude, S_{21} magnitude, S_{21} phase, and S_{22}

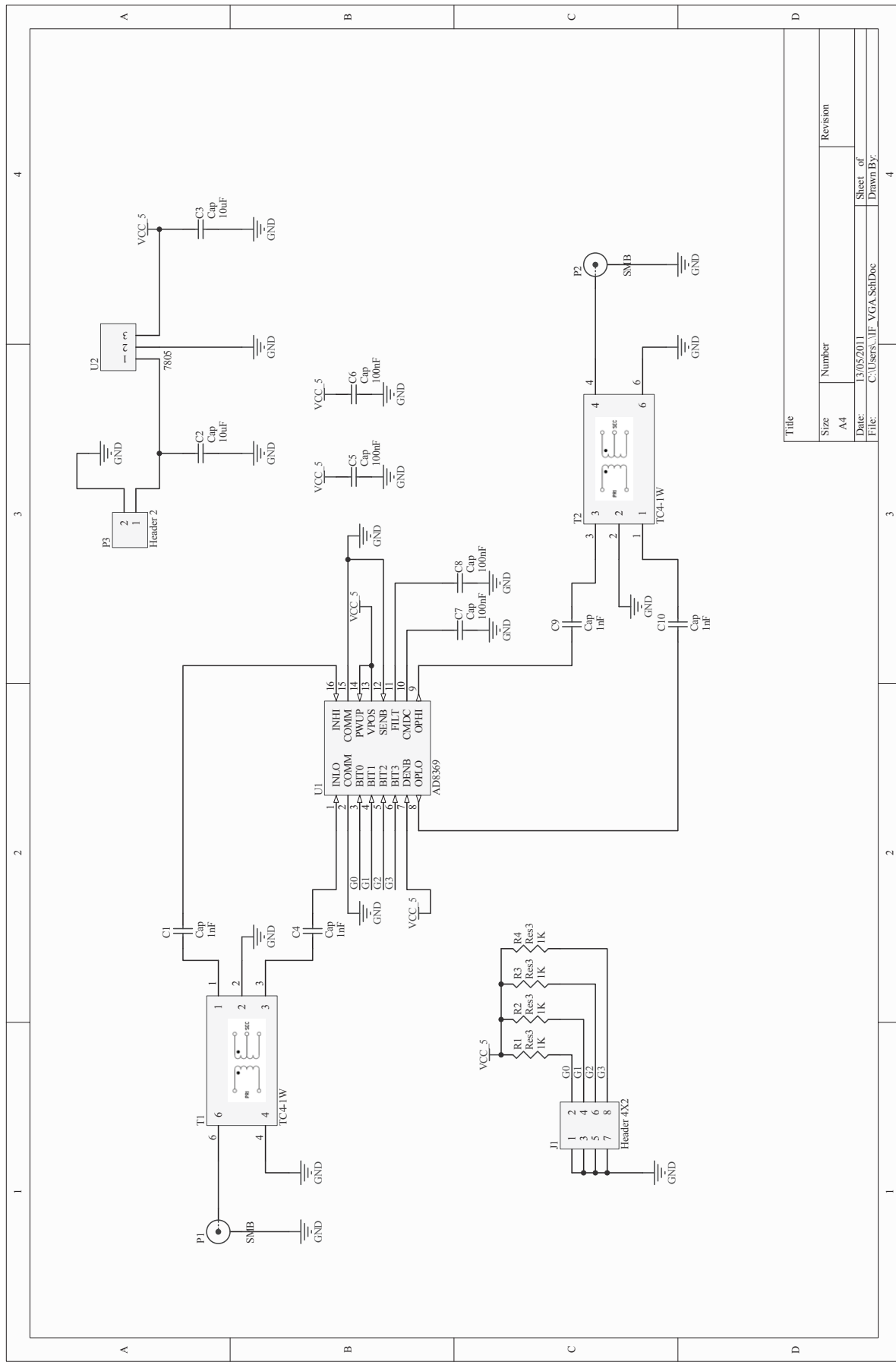


Figure 5.38: IF VGA prototype schematic.

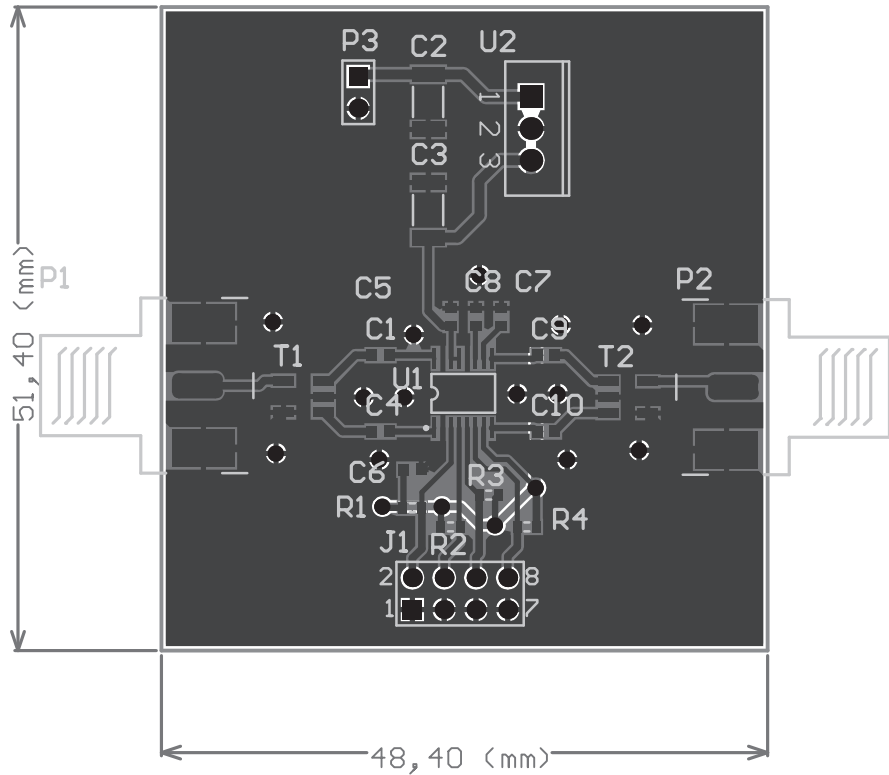


Figure 5.39: IF VGA prototype PCB.

magnitude.

The device linearity was also tested using the vector analyzer. In the experiment, an input power sweep for -40 to -5 dBm was performed for an unmodulated 70 MHz carrier signal. The output power was recorded by the analyzer and the results can be found in Fig. 5.42. A 1 dB compression point was identified for $P_{IN} = -7.1$ dBm.

Finally, the noise figure was measured using an Agilent N8975A noise figure analyzer [Agi05c]. In the experiment, a calibrated noise source Agilent [Agi05b] was connected to the signal input and the VGA output was connected directly to the analyzer. The VGA gain code was set to the maximum value. The measured gain and the noise figure is plotted in Fig. 5.43. The measured performance values for IF amplification stage are summarized in Table 5.22.

Parameter	Measured value	Front-end specification
Center frequency	70 MHz	70 MHz
Gain range	-15 to 33 dB	0 to ≥ 35
Bandwidth	LF to 600 MHz	≥ 12 MHz
NF_{VGA}	8.7 dB @ maximum gain	≤ 10 dB
$P_{CP,VGA}$	-7.1 dBm @ maximum gain	≥ -15.9 dBm
Input/Output type	Single ended	
Input/output impedance	50Ω	
Supply voltage	7 to 12 V DC	
Supply current	≤ 60 mA	

Table 5.22: IF amplification measured performance values summary.

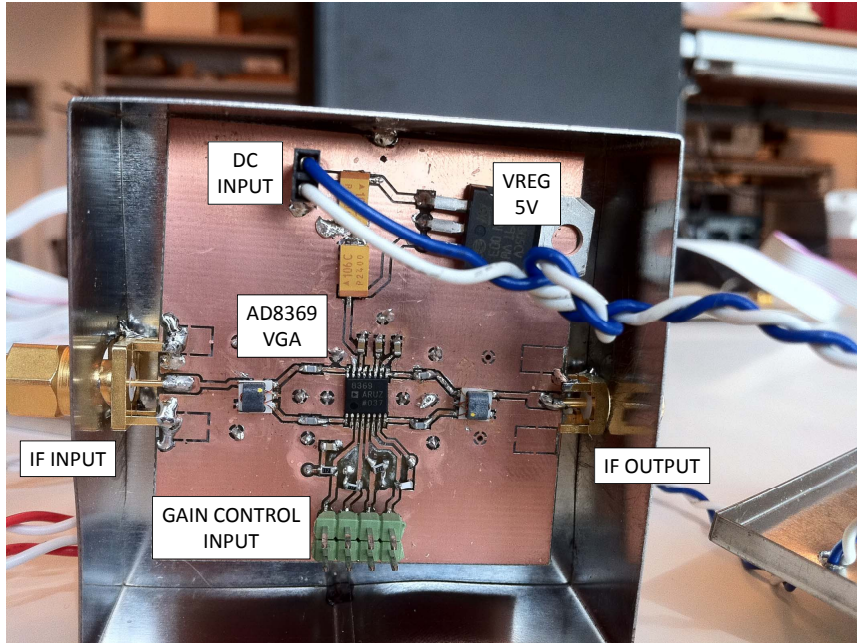


Figure 5.40: IF VGA prototype picture.

5.5 Local oscillator

5.5.1 Frequency synthesizer

A suitable source of the shared LO signal is a frequency synthesizer [Ban06]. In the most common configuration, it is composed of a Voltage Controlled Oscillator (VCO), a PLL, and a loop filter, as shown in Fig. 5.44.

The PLL is able to generate an output signal whose phase is related to the phase of the input *reference* signal. In order to keep the phase coherence between the ADC sample clock and the frequency downconversion, a PLL reference input should be provided by the FPGA.

The synthesizer should be properly designed to operate in the LO frequency range and the output power should be enough to drive all the mixers simultaneously. The selected frequency synthesizer is the National Semiconductors LMX2531LQ1570E [LMX07], whose specifications are briefly summarized in Table 5.23. Fig. 5.45 shows the high level block diagram for LMX2531.

An evaluation module that can be used as a working prototype is available directly from the manufacturer [LMX08]. The evaluation board includes all the external components required by the Integrated Circuit (IC) and the Sub-Miniature version A (SMA) connectors needed for proper operation. Fig. 5.46 shows a picture of the PCB.

The manufacturer also provides a control software that can be executed in a Personal Computer (PC) connected to the PLL evaluation board using the PC parallel port. The control software can program all the registers of the PLL and allows the user to dynamically adjust the operating modes. A screen capture and settings are shown in Fig. 5.47. The functionality provided by the control software can be integrated into the FPGA functionality as a hardware initialization function.

5.5.2 Distribution network

As we have seen in Section 5.1, the local oscillator signal should be fed to each of the mixer LO input ports. Considering the beamforming application, the LO distribution network requirements are therefore:

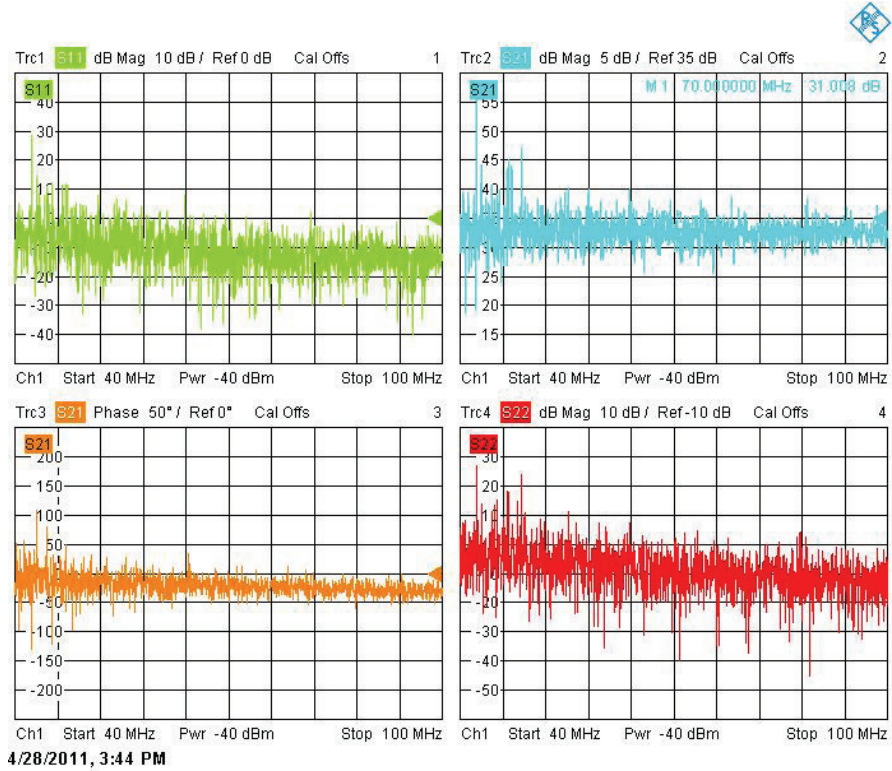


Figure 5.41: IF VGA prototype measured S-parameters.

- to minimize both the power and the phase differences between output ports,
- to minimize the input to output losses, and
- to isolate the LO ports

A suitable power divider that meet the requirements is the Wilkinson divider/combiner [Poz01, p.363]. The Wilkinson divider network can achieve isolation between the output ports while maintaining a matched condition on all ports. The power division is theoretically lossless at matched frequencies. The theoretical S parameters matrix is:

$$S = \frac{-j}{\sqrt{2}} \begin{pmatrix} 0 & 1 & 1 \\ 1 & 0 & 0 \\ 1 & 0 & 0 \end{pmatrix} \quad (5.38)$$

The circuit is designed and simulated using the Agilent ADS software [Agi11]. The design process starts with a 1:2 Wilkinson divider at LO frequency. The operation frequency is tuned using the integrated electromagnetic simulator Momentum [Agi11]. Fig. 5.49 shows the 1:2 primitive schematic and the electromagnetic simulator parameters.

The 1:2 is extended then to 1:4 division using the designed 1:2 Wilkinson primitive. An additional electromagnetic simulation is done to fine-tune the operation frequency. Finally the 1:4 primitive is used to build the final 1:8 Wilkinson divisor. Fig. 5.50 and Fig. 5.51a shows the electromagnetic simulator schematic and the PCB board layout respectively.

The PCB prototype was built using Arlon 25N substrate [AM11], which is a low-loss microwave substrate. Fig. 5.51b shows a picture of the prototype with the SMA connectors.

The performance of the divider was measured using a Rohde & Schwarz vector network analyzer [Roh11] over a range of frequencies from 1400 MHz to 1700 MHz. Fig. 5.52 shows the simulated and measured overall attenuation between the input port and one of the output ports.

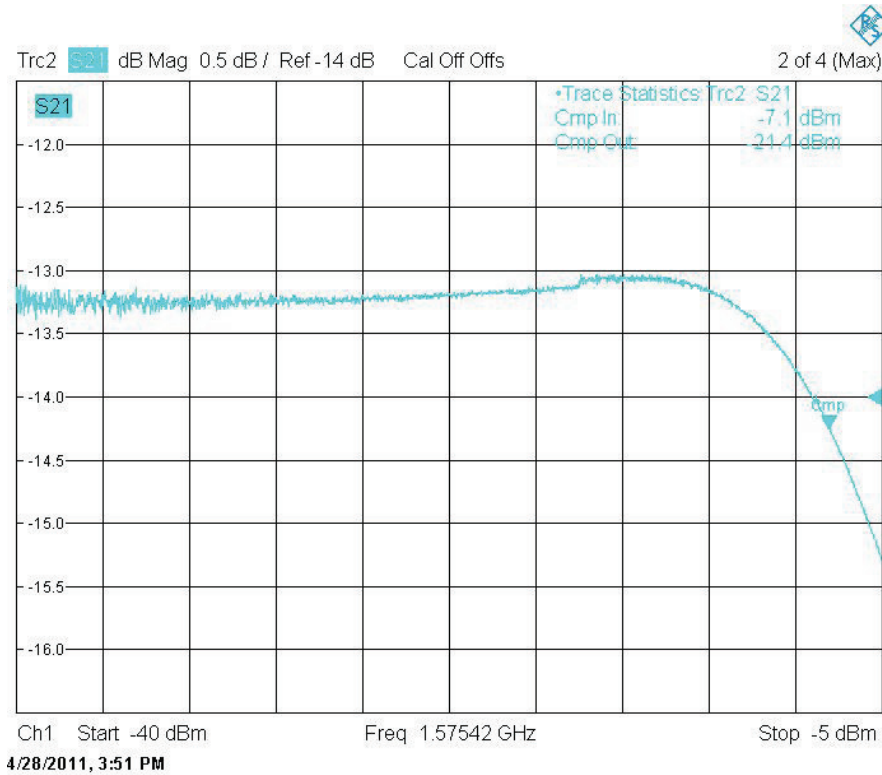


Figure 5.42: IF VGA prototype measured compression point.

The attenuation is in the order of 9.4 dB which almost match the theoretical simulation performance. The power differences between outputs are shown in Fig. 5.53. From the results can be extracted that an amplitude tolerance of 0.2 dB should be expected.

Finally, the unwrapped phase differences between outputs are shown in Fig. 5.54.

Table 5.24 shows the prototype specifications

5.5.3 Measurements results

In the last Sections, the performance of the standalone PLL and the LO power divider was measured. In this Section we measure the performance of the complete frequency synthesizer including the LO distribution network.

As we mentioned in Section 5.1.6, one of the most critical parameters to be measured is the phase noise. Phase noise analysis is the frequency domain representation of rapid, short-term, random fluctuations in the phase of a waveform, caused by time domain instabilities [Ban06].

In the experiment, the PLL reference signal was generated using an Agilent [Agi05a] generator configured for $f_{\text{ref}} = 10$ MHz. The phase noise of the synthesizer was measured using an Agilent E4448A PSA Series spectrum analyzer [Agi04]. The instrument was configured in phase noise measurement mode. Fig. 5.55 shows the phase noise measured for a frequency range of 100 Hz to 1 MHz with respect the carrier frequency $f_{\text{LO}} = 1505.42$ MHz. In addition, the carrier power was also measured.

5.6 Single-channel prototype validation

The complete front-end system design and implementation was validated by means of a realistic single-channel prototype. Fig. 5.56 shows a self-explanatory detailed picture of the set-up. Due

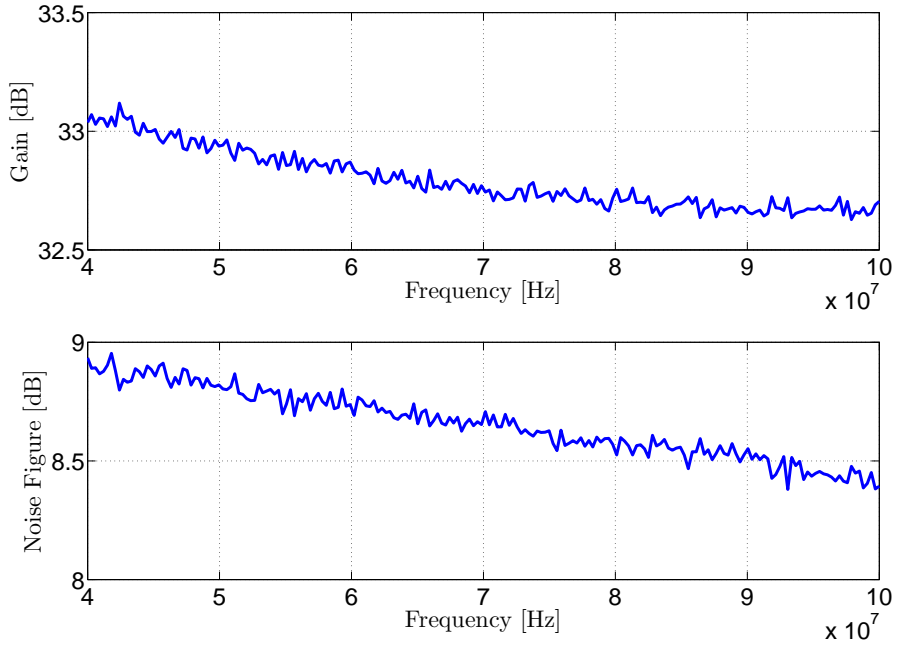


Figure 5.43: IF VGA prototype measured noise figure.

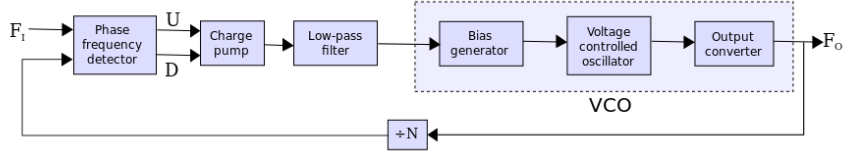


Figure 5.44: PLL generic block diagram.

to the limitations of the active antenna element, the antenna LNA was not included in the measurements. In all measurements, the front-end VGA gain was set to the maximum value, which is the worst case due to the device nonlinearity.

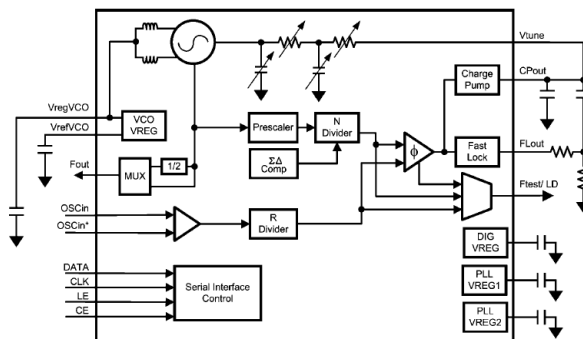
5.6.1 S Parameters

S-parameters measurements were performed using Rohde & Schwarz ZVA 24 Vector Network Analyzer [Roh11] for a frequency sweep from 1.54 – 1.59 GHz. Fig. 5.57 shows a picture of the set-up.

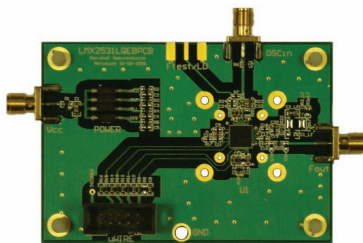
The analyzer was configured in frequency conversion mode. During the measurements, the LO signal was generated using the frequency synthesizer and the LO distribution network, as described in Section 5.5. Due to the calibration requirements of the analyzer, the stimulus output power was set to -40 dBm. A 40 dB attenuator was intercalated in order to reduce the power to the front-end acceptable input levels.

Fig. 5.58 shows the front-end conversion gain vs. RF input frequency, represented by the $b2/a1$ magnitude parameter (see, (5.37)). Based on the results, the gain in the GNSS L1/E1 link is $G_{FE} = 18 + 40 = 58$ dB. Using the results, the 3 dB passband bandwidth was also measured.

Specification	Manufacturer Value	Front-end
Operating output frequency	1500 - 1650 MHz	1505.42 MHz
PLL type	Fractional-N Delta Sigma Modulation up to 4th Order	
Registers programming interface	three-wire Microwire serial	
Reference frequency input range	5 - 80 MHz	
Reference frequency sensitivity	0.5 - 2.0 Vpp	
VCO type	Integrated tank inductor	
Phase noise	10 kHz, -93 dBc, 100 kHz -118 dBc, 1 MHz, -140 dBc, 5 MHz, -154 dBc	$\leq -90 \text{ dBc-Hz}$, 100 kHz

Table 5.23: National Instruments LMX2531 PLL specifications.**Figure 5.45:** LMX2531 block diagram.

Specification	Value
Power divider ratio	1:8
Operating frequency	1400 - 1700 MHz
Input-to-output attenuation	9.4 dB
Output power tolerance	0.2 dB
Output phase tolerance	8 degrees

Table 5.24: Wilkinson 1:8 prototype specifications.**Figure 5.46:** LMX2531 Evaluation Module PCB.

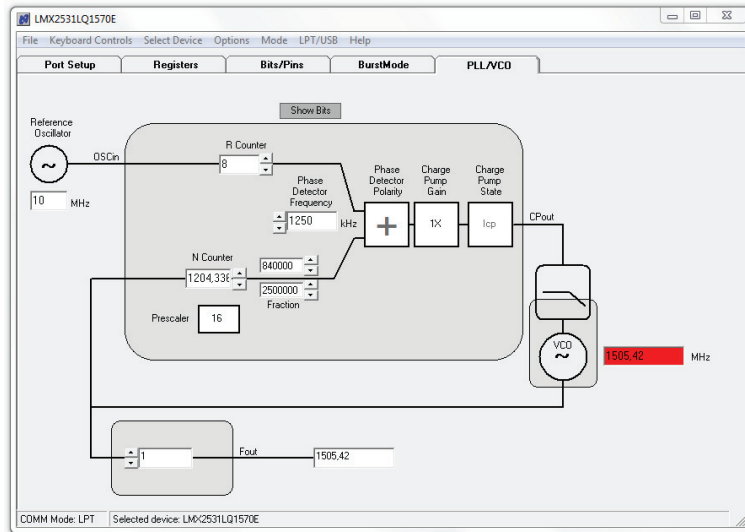


Figure 5.47: PLL control software and register settings for LMX2531EVM.

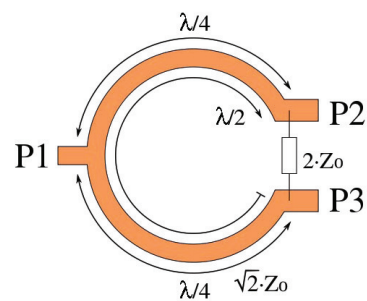


Figure 5.48: Two ports Wilkinson divider theoretical schematic.

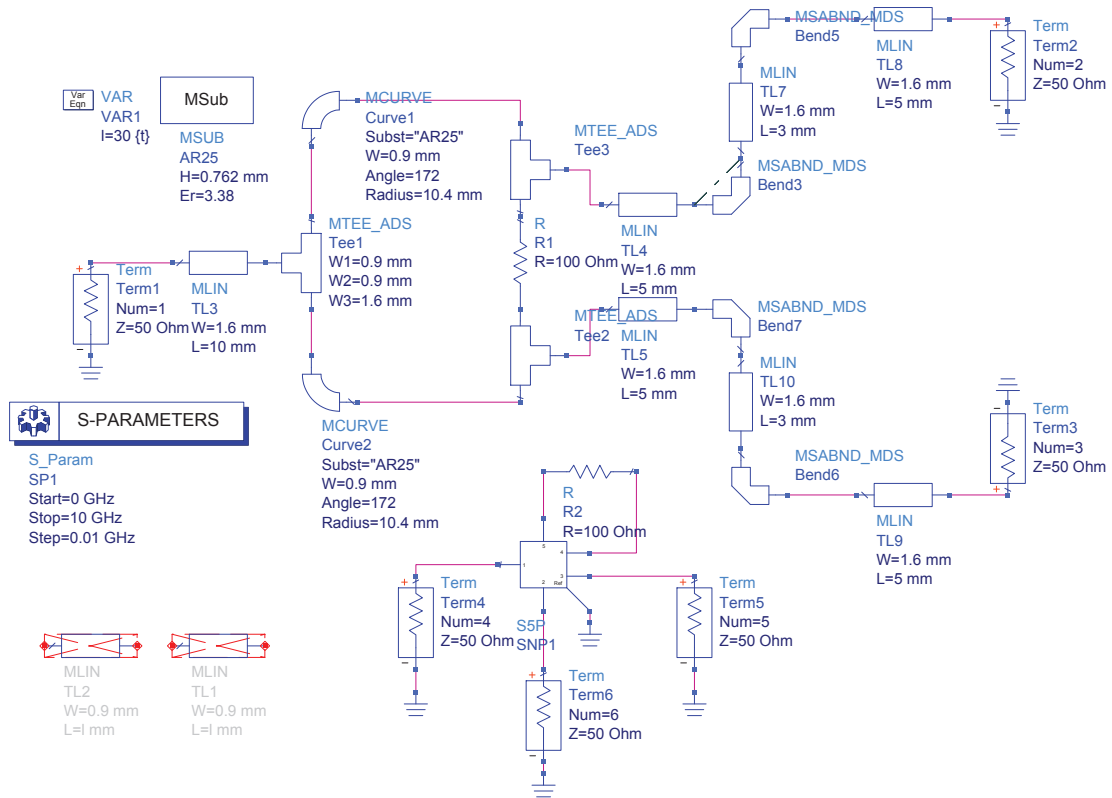


Figure 5.49: Two ports Wilkinson divider schematic and electromagnetic simulation model.

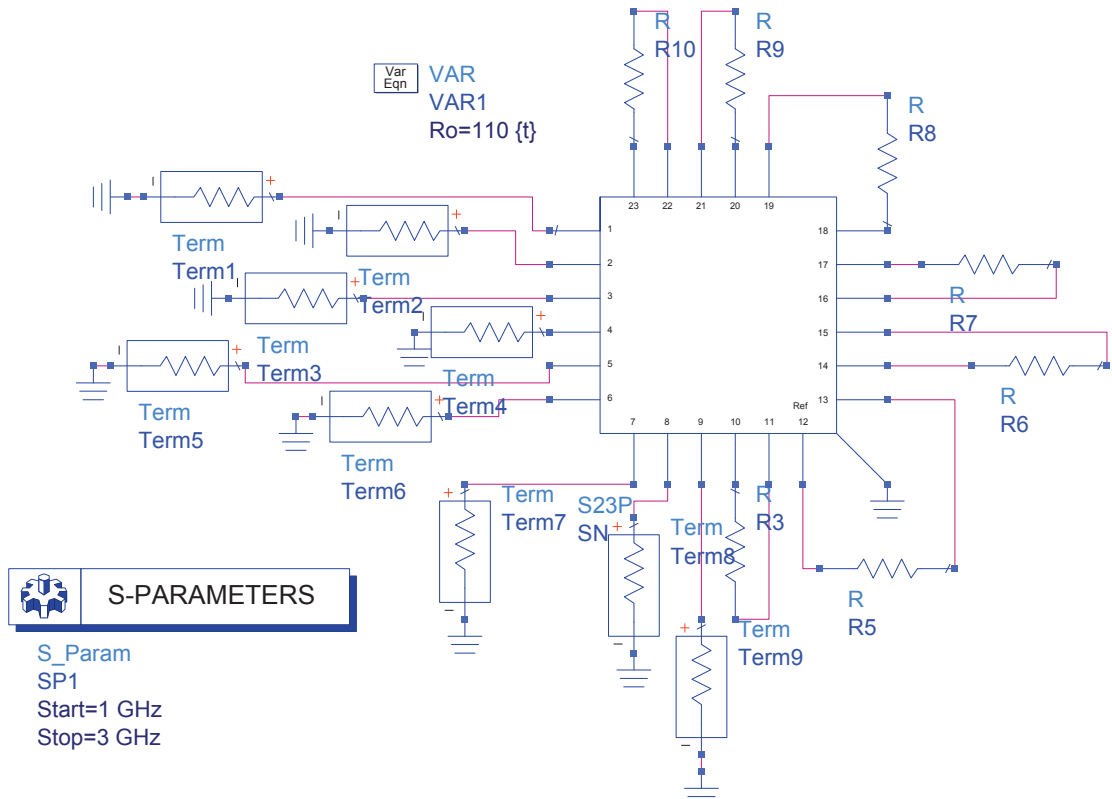


Figure 5.50: Eight ports Wilkinson divider electromagnetic simulation model.

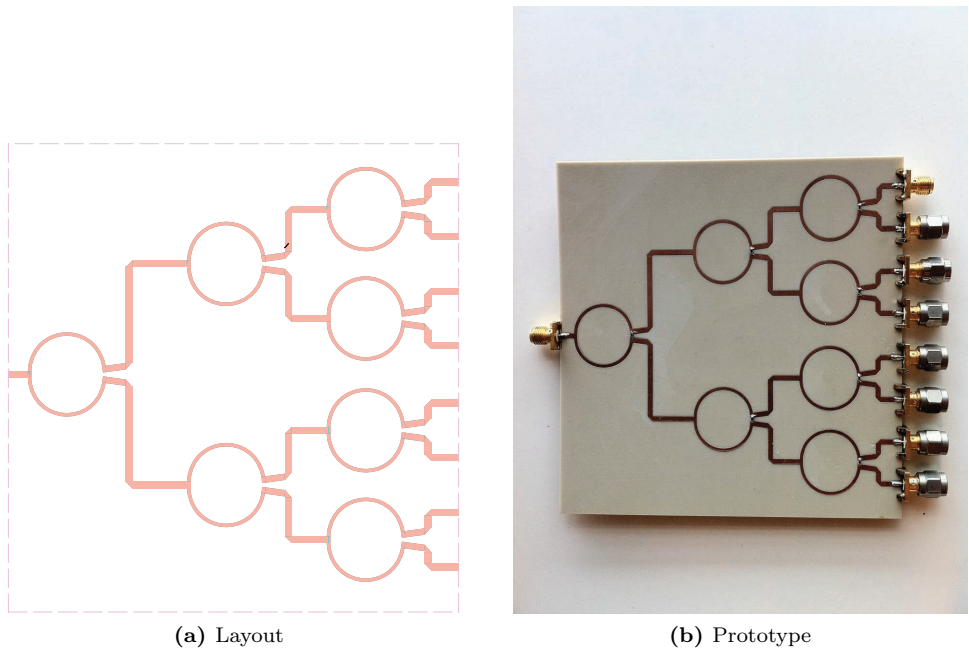


Figure 5.51: Eight ports Wilkinson PCB layout and prototype.

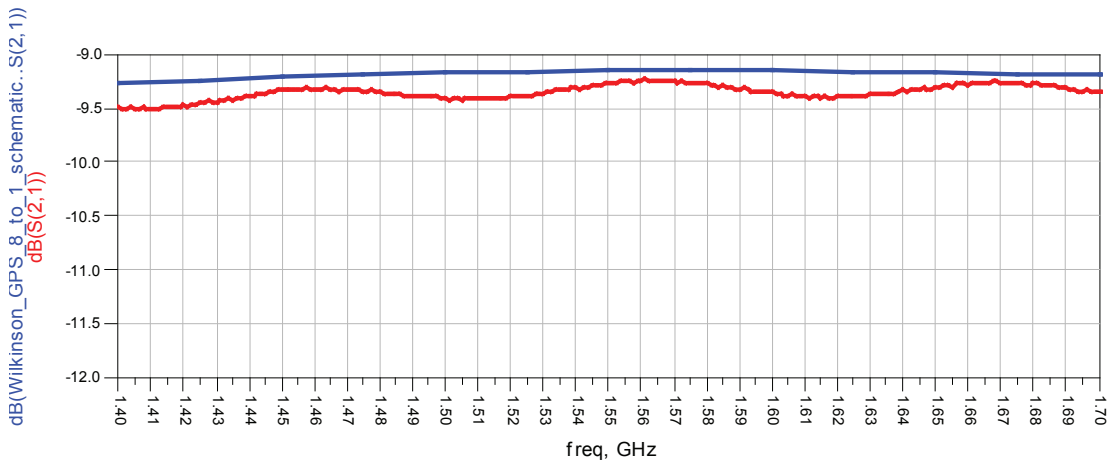


Figure 5.52: Simulated(blue) and measured(red) eight ports Wilkinson Input to output attenuation.

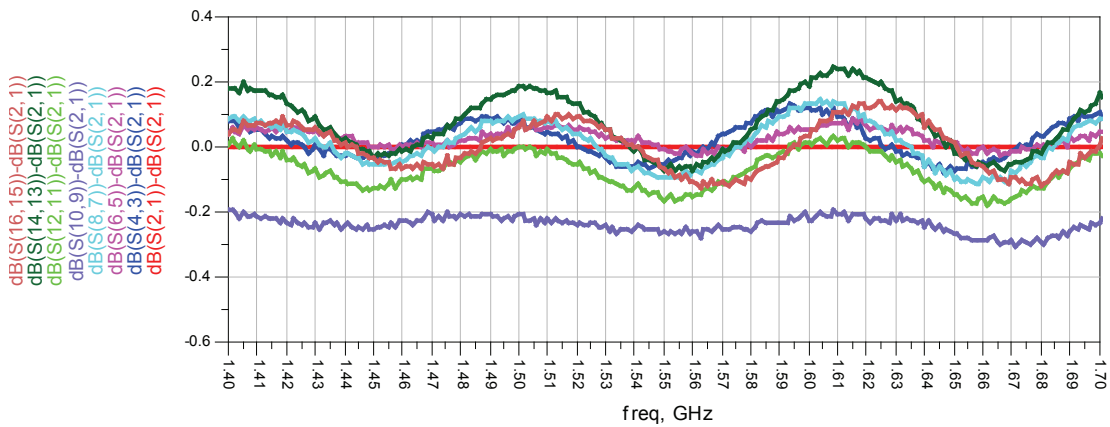


Figure 5.53: Eight ports Wilkinson measured output signal power differences.

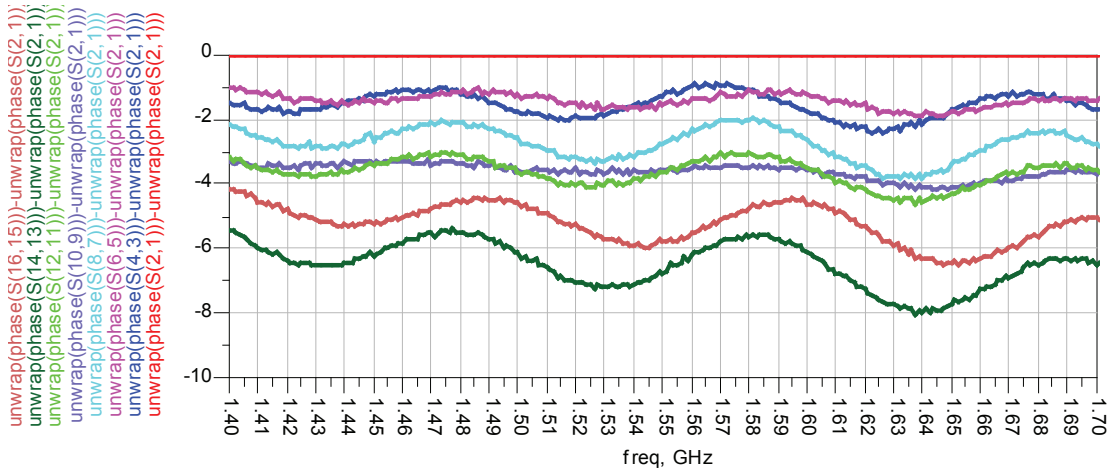


Figure 5.54: Eight ports Wilkinson measured output signal phase differences.

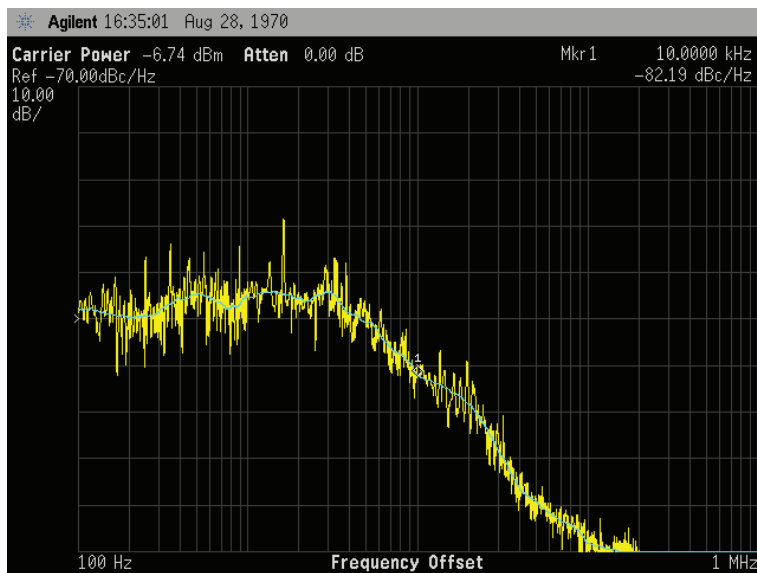


Figure 5.55: Measured phase PLL phase noise after the Wilkinson power divider for $f_{OL} = 1505.42$ MHz.

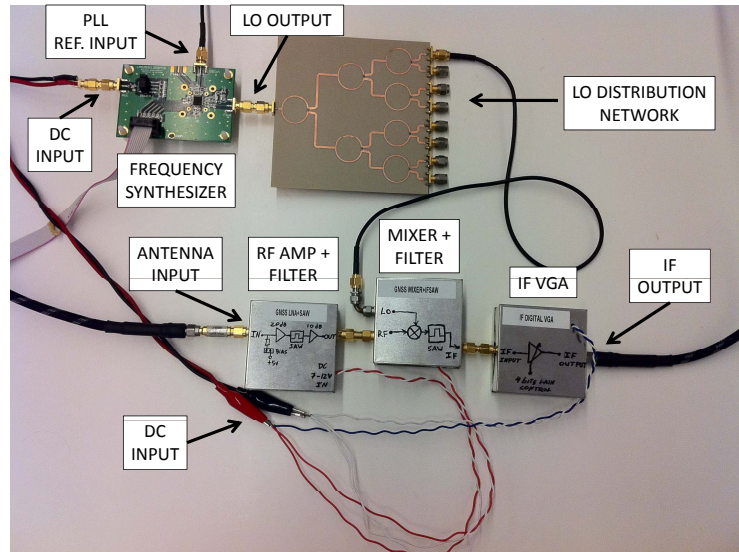


Figure 5.56: Single-channel front-end and local oscillator network prototype picture.

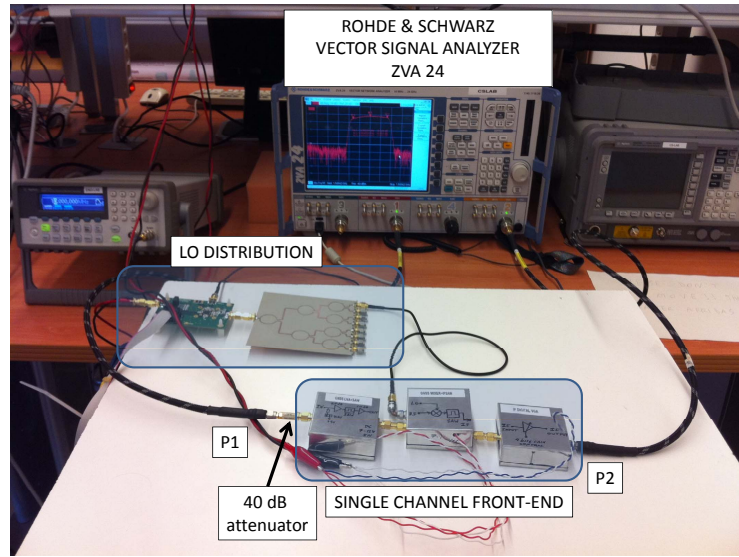


Figure 5.57: Single-channel front-end prototype S parameters measurement set-up.

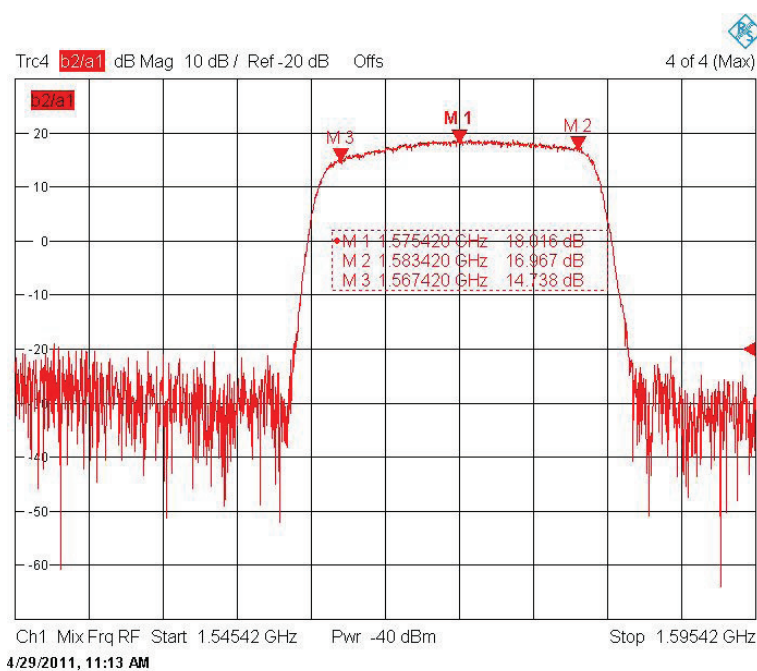


Figure 5.58: Single-channel front-end prototype gain and bandwidth.

5.6.1.1 Linearity

The front-end linearity was also measured using the vector analyzer. In the experiment, an input power sweep for -40 to -5 dBm was performed for an unmodulated 1575.42 MHz carrier signal. Due to the use of a 40 dB input attenuator, the real input power sweep range is from -80 to -45 dBm. The output power was recorded by the analyzer and the results can be found in Fig. 5.59. A 1 dB compression point was identified for $P_{IN} = -15.3 - 40 = -65.3$ dBm.

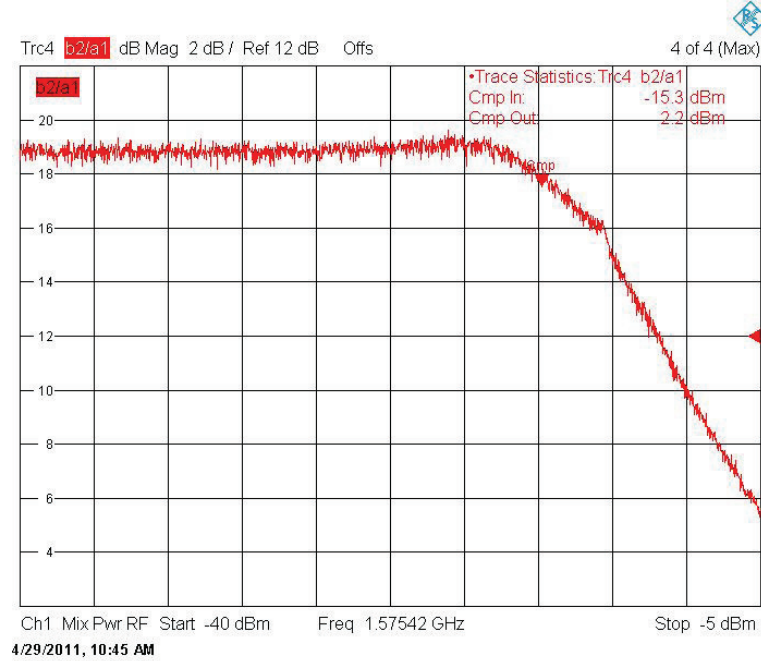


Figure 5.59: Single-channel front-end prototype measured compression point.

5.6.2 Noise Figure

The complete front-end noise figure, excluding the active antenna, was measured using an Agilent N8975A noise figure analyzer [Agi05c]. In the experiment, a calibrated noise source Agilent [Agi05b] was connected directly to the signal input and the mixer output was connected directly to the analyzer as is shown in Fig. 5.60. The instrument was configured in *system downconverter mode*, which takes into account the frequency conversion output IF. The measured noise figure is plotted in Fig. 5.61. The conversion gain measure by the noise analyzer can be found in Fig. 5.62. There is a difference of 2 dB in the measured gain, likely caused by small input/output impedance mismatch, which specially affects to the noise analysis.

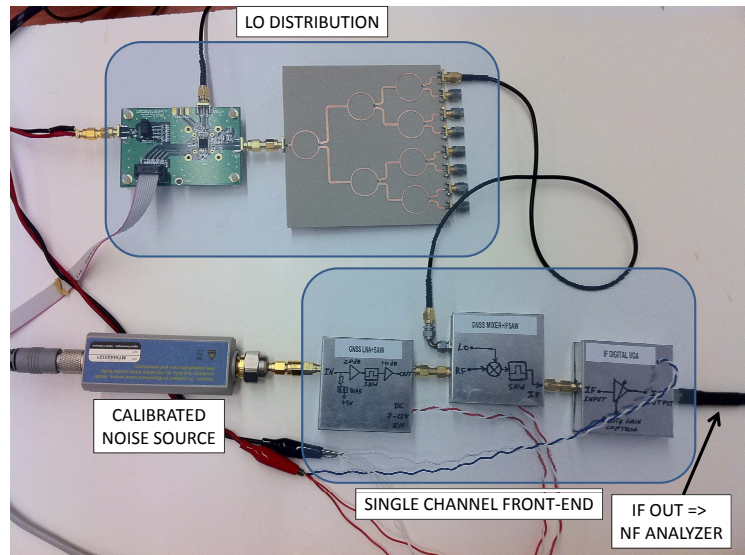


Figure 5.60: Single-channel front-end prototype noise figure measurement set-up.

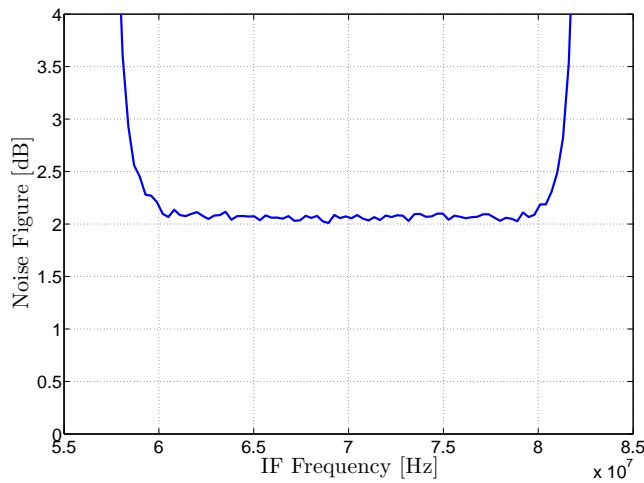


Figure 5.61: Single-channel front-end prototype measured noise figure.

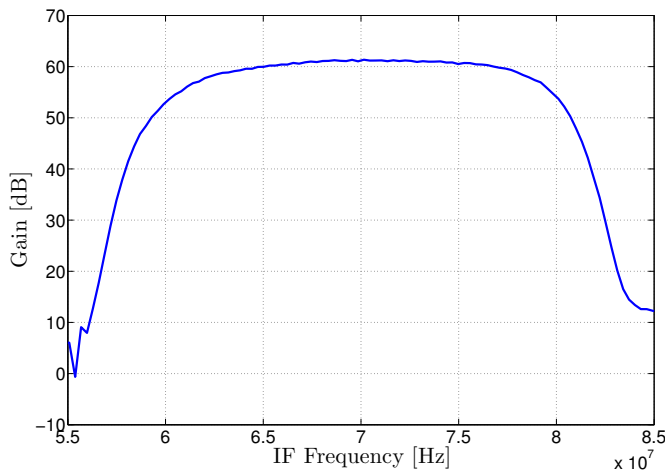


Figure 5.62: Single-channel front-end prototype measured gain (using N8975A).

5.6.3 Phase noise

In this experiment, an RF carrier signal was generated by an Agilent E4438C ESG Vector Signal Generator [Agi06] at $f_{RF} = 1575.42$ MHz and $P_{RF} = -80$ dBm. The RF signal was fed into the front-end output and the IF output was connected to an Agilent E4448A PSA Series spectrum analyzer [Agi04]. The instrument was configured in phase noise measurement mode. Fig. 5.63a shows the phase noise measured for a frequency range of 100 Hz to 1 MHz with respect to the carrier frequency $f_{IF} = 70$ MHz. Fig. 5.63b shows the carrier frequency drift and the power at IF. The front-end enjoys of a very good overall phase noise of -65 dBc at 1 kHz, -82 dBc at 10 kHz, and -115 dBc at 100 kHz, which is aligned with the front-end specifications of Table 5.5.

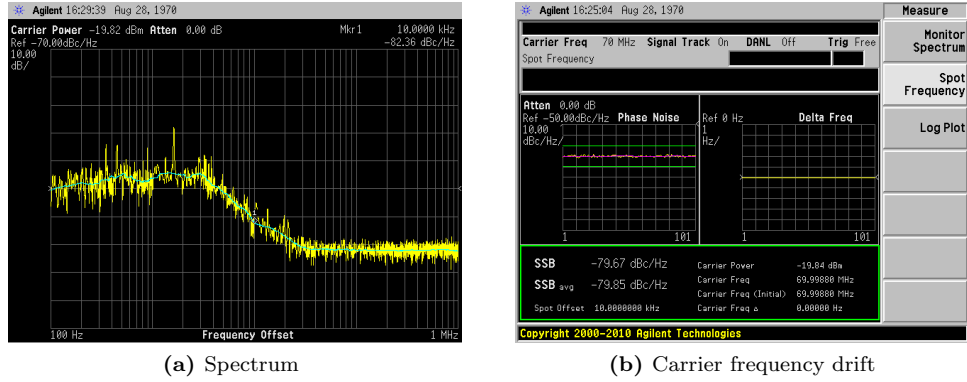


Figure 5.63: Single-channel front-end prototype measured phase noise.

5.6.4 Output spectrum

Finally, the front-end prototype output spectrum was measured in order to validate the front-end response to weak signals. In the experiment, an RF carrier signal was generated by an Agilent E4438C ESG Vector Signal Generator [Agi06] at $f_{RF} = 1575.42$ MHz and $P_{RF} = -100$ dBm. The output spectrum was measured for both the presence and the absence of the carrier signal. Fig. 5.64a and 5.64b show the results, respectively. It is possible to observe the front-end bandwidth and noise floor, which is approximately $P_N \simeq -64$ dBm, measured at front-end output. No noticeable spurious signals are present and the measured front-end gain at f_{RF} is $G_{RF} = -39.8 + 100 = 60.2$ dB without taking into account cable and connectors losses, which is aligned with the front-end requirements.

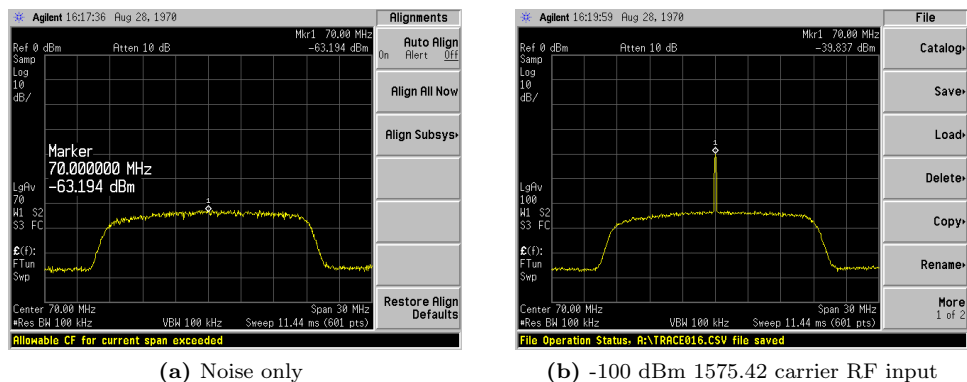


Figure 5.64: Measured output spectrum.

5.6.5 Analog-to-Digital conversion

Based on the bandwidth requirements and the frequency plan, considering the COTS components available, the selected ADC for the beamforming platform is the Texas Instruments ADS5273 [Tex05a]. The ADC features eight-channels, 12 bits per channel, encapsulated in a single integrated circuit. Table 5.25 shows the most relevant features and specifications.

Specification or feature	Manufacturer Value	Front-end
Number of channels	8	8
Resolution	12 bits	12 bits
Operational sampling frequency	20 - 70 MSPS	≥ 40 MSPS
V_{FSR}^1	2.03 Vpp	2 Vpp
Full-Scale input power ² (P_{FSR})	19.1 dBm	19.1 dBm
SFDR for $f_{IF} = 70$ MHz	78 dBc	
SINAD for $f_{IF} = 70$ MHz	65 dBFS	
SNR for $f_{IF} = 70$ MHz	65 dBc	
Interface	Serialized LVDS ³	

¹ Differential Full-Scale input voltage range using internal reference.

² Assuming 50 ohms load.

³ Low Voltage Differential Signaling.

Table 5.25: ADS5273 features, extracted from [Tex05a].

The device is a Texas Instruments ADS5273, that contains 8-channel, 12 bits per sample ADC in a single integrated circuit [Tex05a]. The manufacturer specifications can be found in Table 5.25. An ADS527xEVM evaluation module that contains all the required external components and the connectors was used to facilitate the implementation [Tex05b]. However, a custom adapter board, shown in Fig. 5.65, was designed in order to integrate the native ADS527xEVM connector into a Xilinx FMC XM105 Debug Card [Xil10a], enabling the compatibility with the FPGA Mezzanine Card (FMC) connector. The FMC connector is an American National Standards Institute (ANSI) standard that provides a standard mezzanine card form factor, connectors, and modular interface to an FPGA located on a base board. Decoupling the I/O interfaces from the FPGA simplifies I/O interface module design while maximizing carrier card reuse [Nak10]. A detailed description of the digital interface with the ADC can be found in Section 5.8.1. Both the ADC and the ML605 boards are conveniently installed in a 1U rack unit, as is shown in Fig. 5.66.

The input range and the ADC resolution were measured at IF injecting a carrier signal centered at $f_{IF} = 71$ MHz directly to the evaluation module SMA connectors. The sample clock was set to $f_s = 40$ MHz and the FPGA was used to determine the active bits for different input power levels. The results were recorded and in Fig 5.67 can be found a comparative to the theoretical values of the input range computed using (5.32) versus the active bits. The theoretical model is aligned with the device measurements.

A further step was done to evaluate the effectiveness of the front-end. In this measurement, the complete single-channel front-end was connected to an ADC input port and the input range was measured again following the aforementioned procedure. Fig. 5.68a shows the results and Fig. 5.68b shows the front-end equivalent gain, obtained by subtracting the IF previously measured input range for each of the resolution values. The results are consistent with the front-end measured specifications. In addition, it is possible to conclude that the ADC driven by the front-end obtains its maximum gain when it is used at the resolution of 6 – 11 bits.

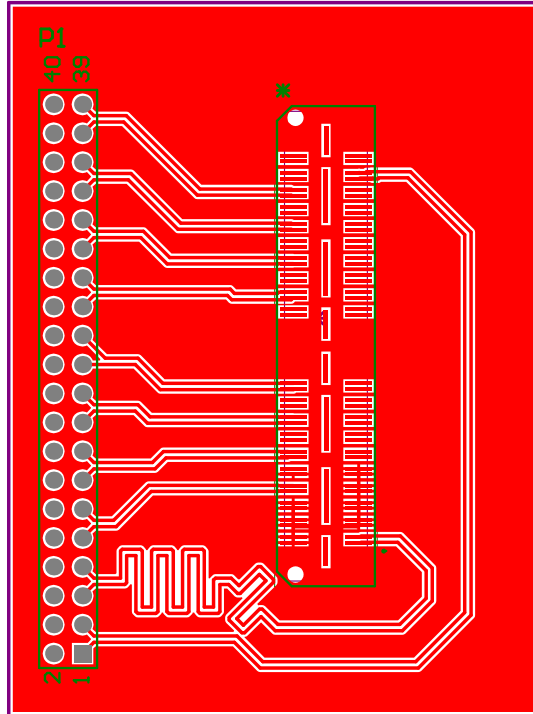


Figure 5.65: ADC custom adapter board for FPGA digital interface.

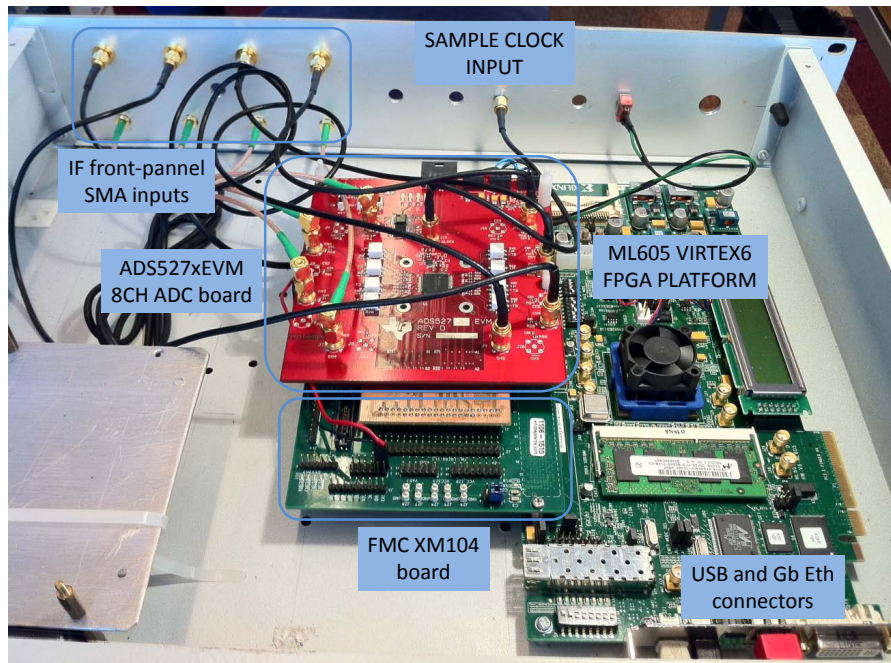


Figure 5.66: ADC board and FPGA platform rack.

5.6.6 Prototype performance summary

Table 5.26 summarizes the single-channel front-end prototype measured performance values and the design specifications. The front-end linearity is compromised by the active mixer as we have identified in Section 5.4.3, thus, both the CP and IP3 are out of specifications. However, considering a possible in-band interference signal present at the antenna terminals with $P_{int} = P_{CP,FE}$, which is equivalent to have an Interference-to-Noise density ratio (IN0) in the order of 113 dB-Hz

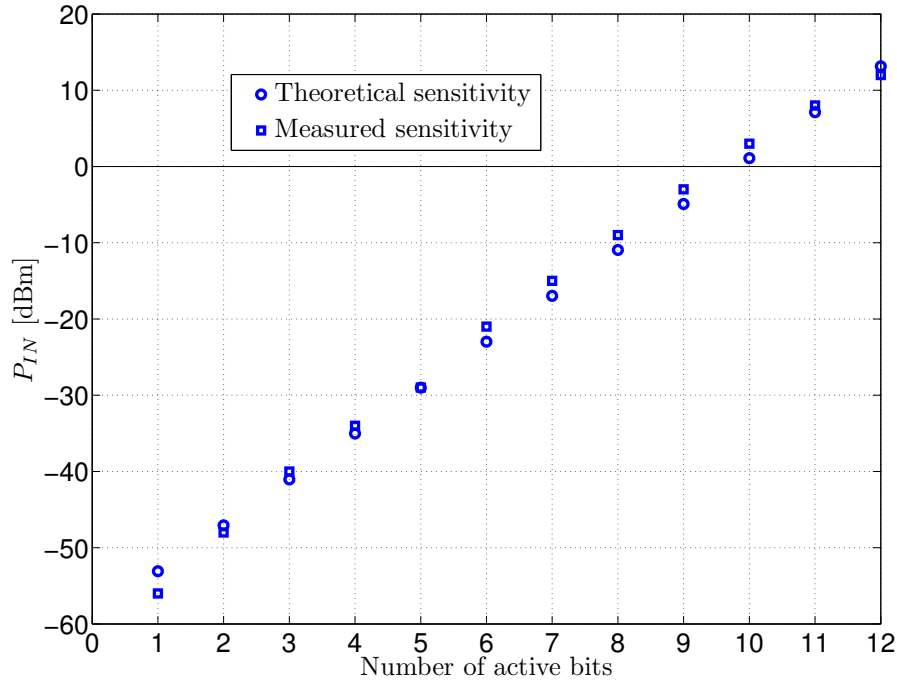


Figure 5.67: ADC active bits vs. input power at IF.

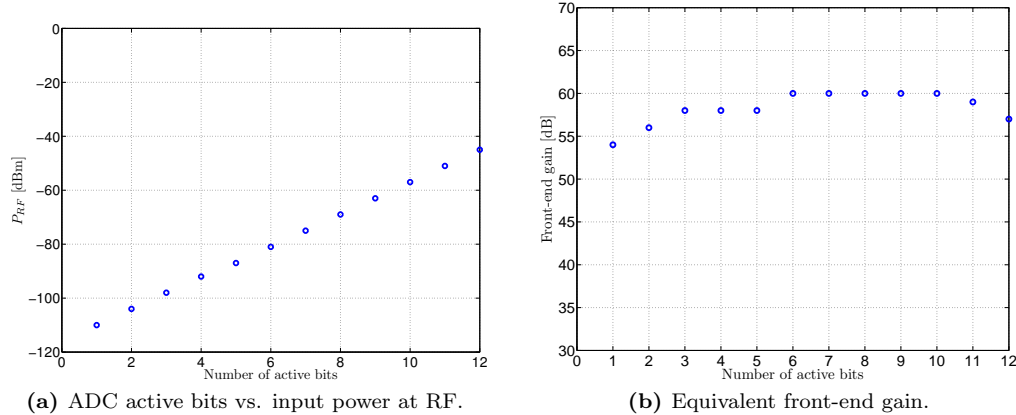


Figure 5.68: Front-end and ADC verification test.

for $T_a = 100$ K, the front-end linearity is sufficient to test the interference mitigation capability of the proposed acquisition algorithms implementation as shown in the simulation results of Chapter 4. On the other hand, the IF frequency deviation from the specified value should be taken into account by the GNSS receiver in order to correct the Doppler frequency estimations. Finally, the front-end stopband bandwidth (B_s) is 2 MHz wider than the specification, and this issue will produce aliasing on the high frequencies in GNSS E1/L1 bandwidth. However, since the B_s is measured at 20 dB of attenuation, it is expected that the spurious signals have an attenuation greater than 10 dB due to the filter slope.

5.7 Multichannel extension

In the last section, a single-channel front-end was implemented and the performance parameters were measured. This Section is devoted to integrate eight front-end channels in a single PCB to complete the array front-end prototype. The Section not only deals with the PCB design

Parameter	Simulated Value	Measured Value	Specification
RF frequency	1575.42 MHz	1575.42 MHz	1575.42 MHz
IF frequency	70 MHz	69.9988 MHz	70 MHz (*)
Passband bandwidth (B_p)	17.8 MHz	17.5 MHz	≥ 12 MHz
Stopband bandwidth (B_s)	20 MHz	22 MHz	≤ 20 MHz (*)
G_{FE}	73.9 dB	$58 + G_{ant} = 73$ dB	≥ 72.8 dB
N_{FE}	2.178 dB	2.18 dB	≤ 72.8 dB
$P_{CP,FE}$	—	-65.3 dBm	≥ -44.9 dBm (*)
$P_{IP3,FE}$	—	$-65.3 + 9.6 = -54.7$ dBm	≥ -35.3 dBm (*)
Image rejection	60.2 dB	57 dB	≥ 40 dB
Phase noise (10 kHz)	-75.65 dBc	-82 dBc	—

Table 5.26: Simulated and measured front-end performance compared the design specifications summary.

particularities but also provides a compact implementation of the antenna array elements and front-end enclosure, designed to improve the overall performance reducing both the coupling between elements and the cable losses.

5.7.1 PCB design

High frequency PCBs require specific design techniques to avoid undesired effects such as signal coupling between tracks and impedance mismatches. In the literature can be found several references to cope with this situation, e.g. [Wad91] and [Bur00]. Hereafter are highlighted some good practices in RF PCB design:

- Signal return currents follow the PCB path of least impedance. For high frequency signals this means that the current follows the least inductance path. Long paths may cause coupling effects and signal losses. A suitable solution is to provide always a return path using a low-impedance ground plane placed in a separate layer connected to the desired component ground points using via connections.
- Long signal tracks must have controlled impedance: this is specially important in PCB traces longer than a critical length computed as $L_{\text{critical}} = \frac{1}{\lambda_{\text{carr}}}$, where λ_{carr} is the wavelength in the PCB medium. The formula can be expressed as:

$$L_{\text{critical}} = \frac{\lambda_{\text{carr}}}{16} = \frac{c}{f} \frac{1}{\sqrt{\epsilon_{eff}}} \frac{1}{16}, \quad (5.39)$$

where c is the speed of light, f is the signal center frequency, ϵ_{eff} is the effective dielectric constant of the PCB substrate. For FR4¹⁴ substrate, $\epsilon_{eff} \approx 4.34$ for $f = 1$ GHz. The critical length for a signal centered at $f_c = 1575.42$ MHz is $L_{\text{critical}} = 5.7$ mm. Consequently, the PCB tracks of the RF section composed by the LNAs, RF bandpass filter, and the mixer input should be designed with controlled impedances. The effective wavelength also affects the ground vias separation criterion. A convenient rule is to place vias at $\frac{\lambda_{\text{carr}}}{20}$ distance [Bur00].

- Low level analog, RF/Microwave, and digital sections must be separated. Divide the RF section into groups, placing the high frequency components nearest connectors, and isolate channels using both sufficient separation and ground planes.
- The LO signals should be carefully routed in order to avoid coupling and cross-talk and, if phase alignment is required between channels, the length of the LO signal path for each mixer should be the same.

The prototype PCB was designed with the Altium Designer software suite [Lim12]. The suite features an EDA software package for printed circuit board, FPGA and embedded software

¹⁴FR4 is a composite material composed of woven fiberglass cloth with an epoxy resin binder.

design, and associated library and release management automation. It has useful features to assist the RF board designer, such as track length and impedance calculator.

The PCB replicates a single-channel design in a side-by-side structure to complete the 8-channels front-end. Fig. 5.69 shows the top-level schematic and Fig. 5.70 shows the final PCB design. Following the aforementioned rules, the RF LNAs are placed in the top, next to the SMA connectors. The tiny μ DFN package and its footprint picture are shown in Fig. 5.71. Fig. 5.72 shows the soldering detail of the RF SAW filter. Both components were soldered using a hot air soldering station and an optical microscope.

5.7.2 Array implementation

In order to minimize the RF cable losses, the front-end is integrated into the antenna array aluminum structure. Fig. 5.74 shows a picture of the complete 8-channels front-end PCB prototype mounted inside the antenna array frame. All the connectors are SMA type with RG174 RF cable due to their small size and flexibility. A stacked structure keeps the LO synthesizer, the Wilkinson divider, and the power supply circuit separated and appropriately shielded. Fig. 5.75 shows a picture of the LO generation and distribution compartment.

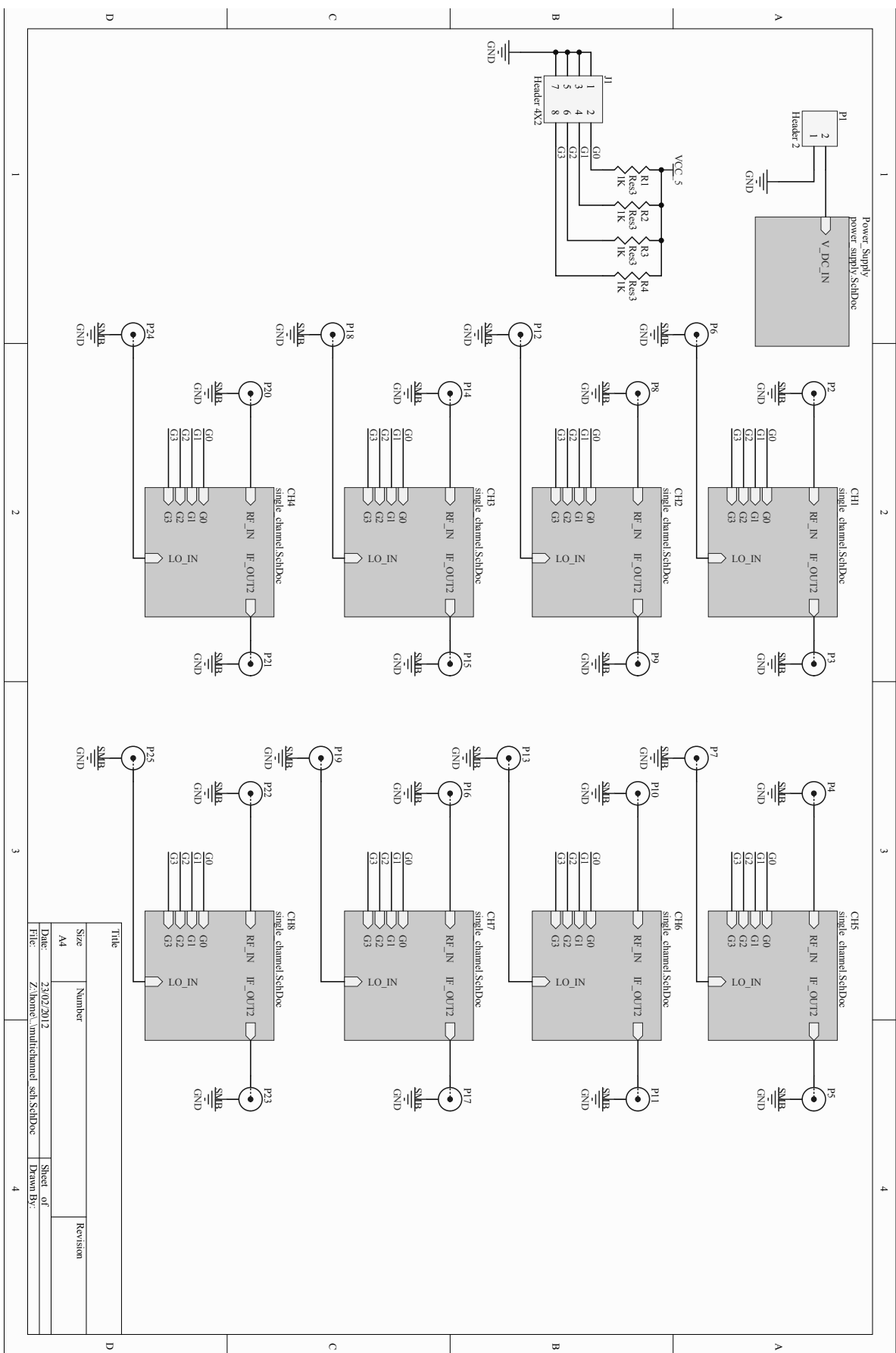


Figure 5.69: Multichannel front-end top-level schematic.

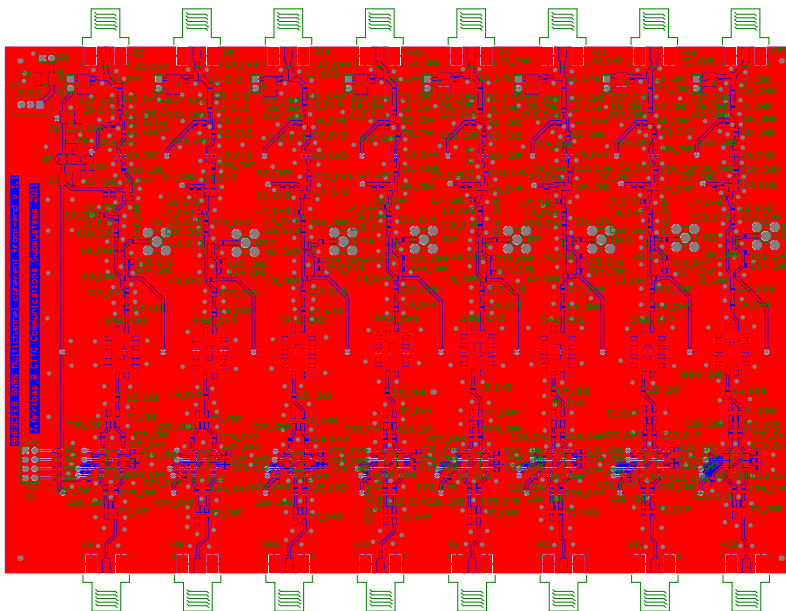


Figure 5.70: Multichannel front-end PCB design.

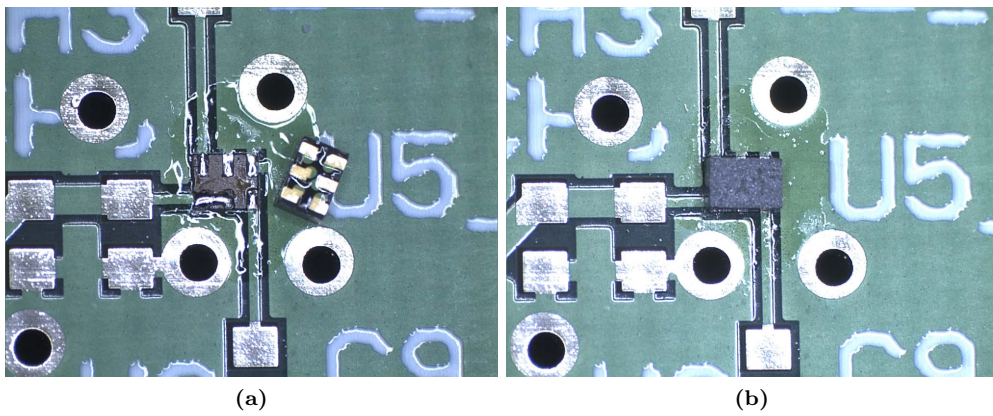


Figure 5.71: RF LNA SMD footprint and soldering detail.

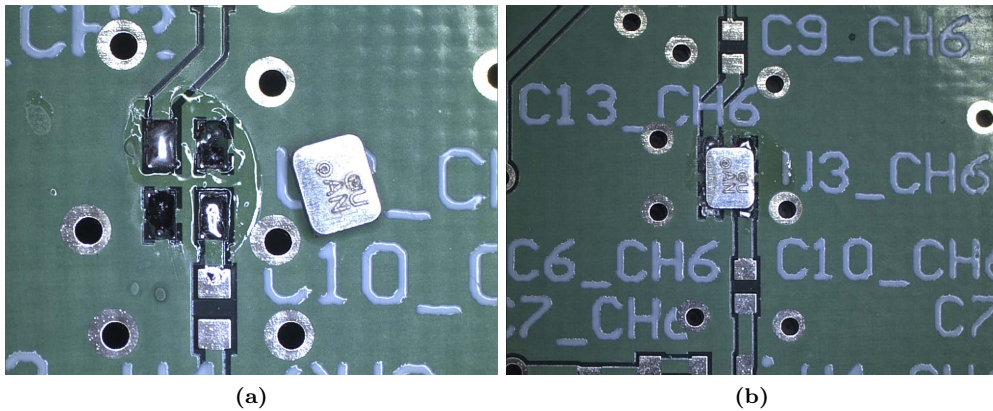


Figure 5.72: RF SAW filter SMD footprint and soldering detail.

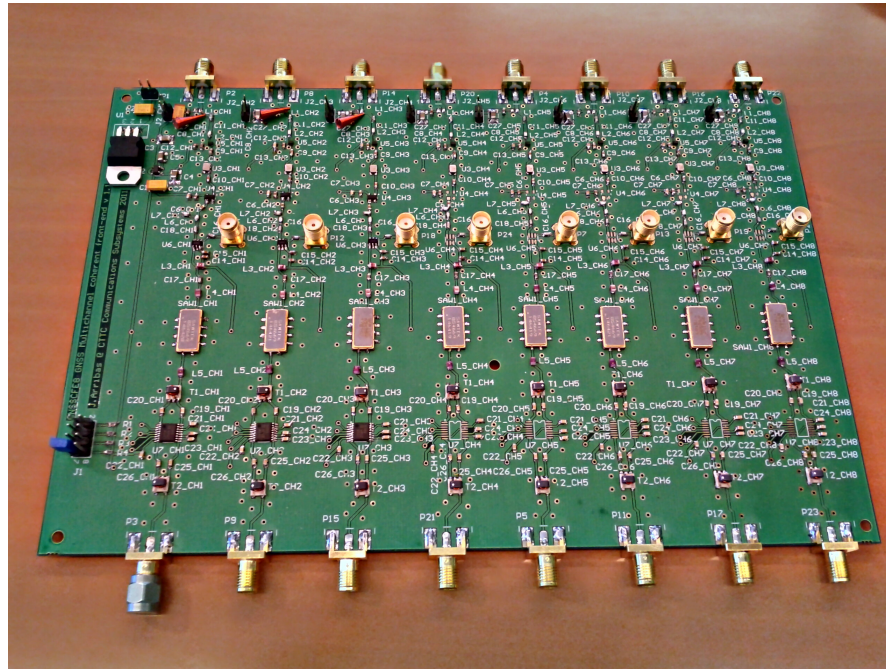


Figure 5.73: Multichannel front-end PCB picture.

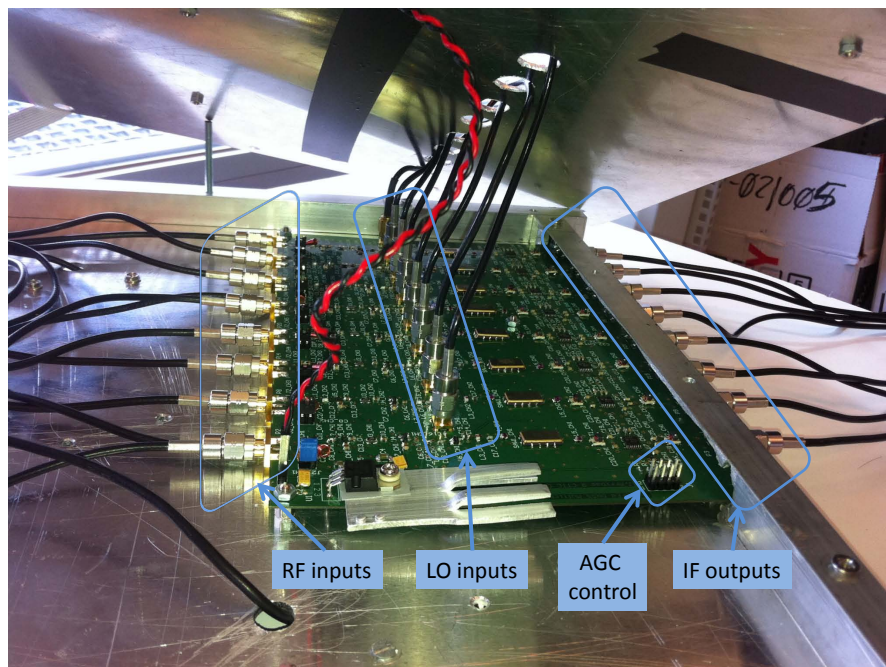


Figure 5.74: Multichannel front-end board mounted in the antenna array frame.

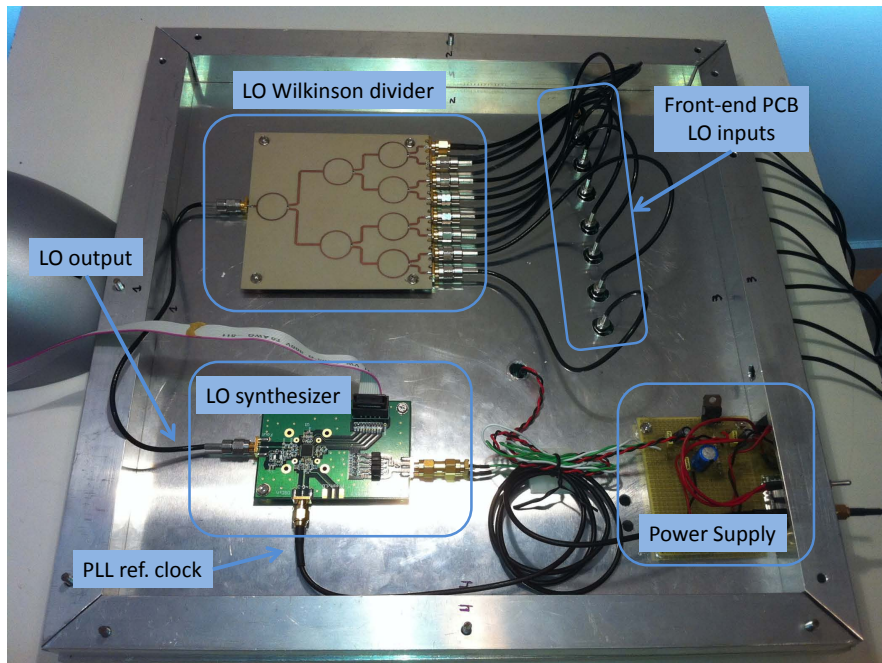


Figure 5.75: LO synthesizer and Wilkinson divider.

5.8 FPGA Processing

The core of the platform is based on a Xilinx ML605 board populated with a Virtex-6 XC6VLX240T FPGA [Xil11j]. The number of logic slices is 37680 and the DSP48E¹⁵ units are 768, which enables the implementation of complex signal processing algorithms.

The Xilinx ML605 Hardware Platform [Xil11g] is a general purpose development board with onboard 512 MB DDR3 memory and a number of convenient I/O ports, such as Gigabit Ethernet, USB master-slave ports, and USB-to-UART bridge. This platform also implements the emerging standard VITA 57.1.1 FMC connector [VME08], which enables the interconnection of a variety of devices and expansion modules, sharing the same physical connector [Nak10].

5.8.1 FPGA interface with multichannel ADC

As mentioned in Section 5.6.5, the ADC block is in charge of sampling the output of the 8 front-end channels simultaneously at a suitable rate. The implementation is based on the ADS527x-EVM Evaluation Module of Texas Instruments, a board based on the ADS5273 [Tex05a] eight-channel ADC integrated circuit, supporting a sample frequency up to 70 Msps with 12 bits of resolution per sample.

The ADS5273 provides eight pairs of Low Voltage Differential Signaling (LVDS) [LVD01] serial data output lines plus two extra LVDS signals for clock managing. LVDS is a differential signaling system, which means that it transmits two different voltages which are compared at the receiver. The transmitter injects a current, typically of 3.5 mA, into one wire or the other, depending on the logic level to be sent. The current passes through a resistor of about $100\ \Omega$ at the receiving end, then returns in the opposite direction along the other wire. From Ohm's law, the voltage difference across the resistor is therefore about 350 mV. The receiver senses the polarity of this voltage to determine the logic level. This technology provides low power dissipation (about 1.2 mW at the load resistor) and high speed. In point-to-point applications, the fastest LVDS devices can operate at 2 Gbps.

In the prototype, the sampling frequency was set to $f_s = 40$ Msps. That means that each digital output will transmit at a bit rate of $40 \times 12 = 480$ Mbps. The sample clock is provided by an external signal generator model Agilent 33250A [Agi05a].

The detailed diagram for the ADC block interface can be found in Fig. 5.76. The ADS5273 internally generates two new clock signals to allow the synchronization of the sample capture logic implemented at the FPGA. These two signals are denoted as "SAMPLE_CLOCK_IN" and "BIT_CLOCK_IN" in Fig. 5.76. "SAMPLE_CLOCK_IN" is a delayed version of the "SAMPLE_CLOCK" and their rising edge marks the beginning of the transmission of a new sample. The signal denoted as "BIT_CLOCK_IN" have six times the "SAMPLE_CLOCK_IN" frequency and their rising and falling edge marks the middle of each bit that forms the sample word. Since the sample resolution is 12 bits, during the period of the "SAMPLE_CLOCK_IN" there are 6 rising edges and 6 falling edges, forming a Double Data Rate (DDR) clock. The electrical connections from the ADC board to the FPGA are based on the differential signal expansion connectors of the ML605 evaluation platform through a Xilinx FMC XM105 Debug Card [Xil10a] plus a custom adapter board (See Section 5.6.5).

The FPGA logic reads the signal samples from the ADC outputs and converts it from serial to parallel using a specifically programmed logic, dumping the data samples into a 12×8 bits register that contains the snapshots $\mathbf{x}_{IF}[n] = \mathbf{x}_{IF}(t) \Big|_{t=nT_s}$, where $T_s = \frac{1}{f_s}$ is the sampling period. In the FPGA logic design, it is recommended to regenerate the incoming clocks using a Digital Clock Manager (DCM) in order to reduce the clock jitter, the clock skew for the internal logic and to assure a 50% duty cycle.

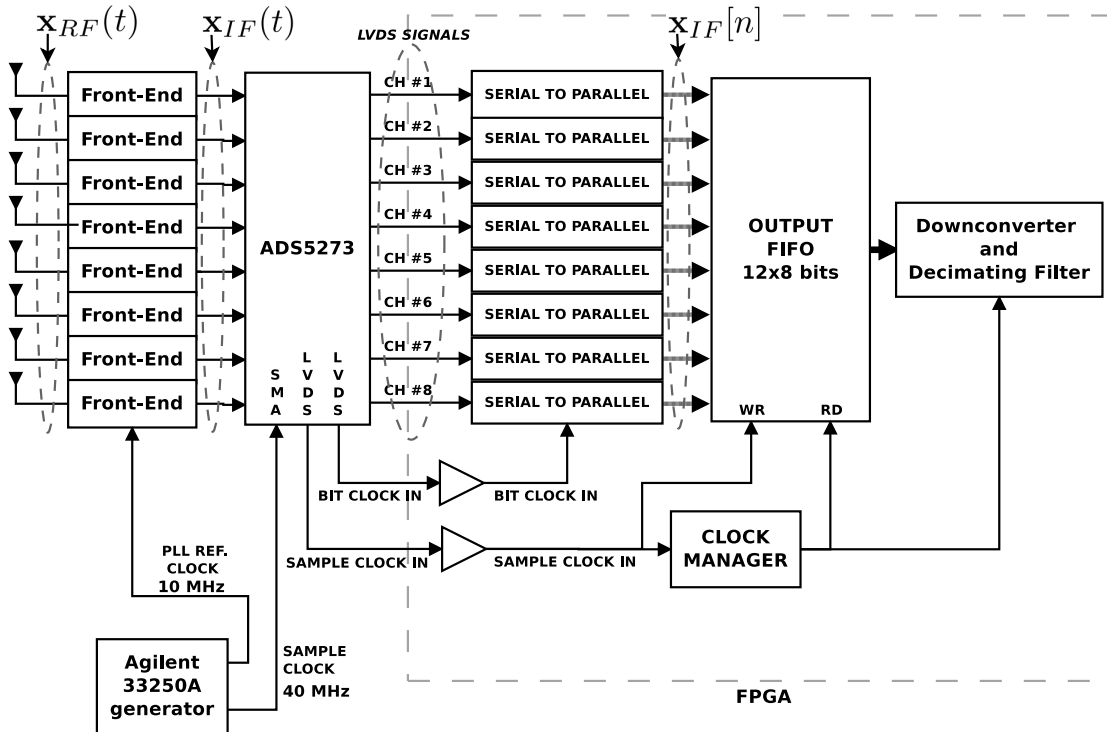


Figure 5.76: ADC FPGA interface block diagram.

5.8.2 GNSS array platform block diagram

The block diagram of the proposed digital processing architecture is shown in Fig. 5.77. From left to right, each of the f_{IF} output channels of the antenna array front-end is sampled synchronously by the ADC board at $f_s = 40$ Msps. The sample clock is provided externally by an Agilent 33250A function generator [Agi05a], which also provides the 10 MHz reference clock for the front-end LO frequency synthesizer. The FPGA logic circuitry reads the digital samples coming from the ADC and performs a digital downconversion from f_{IF} to baseband using the algorithm described in Section 5.1.9. In this step, in order to reduce the sample rate, the digital downconverter stage implements a decimation filter. Considering the bandwidth requirements of the proposed acquisition algorithms described in Chapter 4, the decimation factor in this implementation was set to 8, and thus, the obtained baseband sample rate is $f_{s,bb} = \frac{40}{8} = 5$ Msps.

The baseband samples are fed to a calibration correction block, which compensates the differences both in phase and in amplitude between channels. The reader is referred to Section 5.10.1 for more information on the calibration process.

At this point, the calibrated snapshots are fed both to the real-time spatial-filter processing block and to the array acquisition hardware accelerator. The spatial-filter block can implement a wide range of beamforming algorithms, such as the power minimization beamformer described in Section 4.6.2. The resulting spatially-filtered single output sample stream is fed to the Gigabit Ethernet module, which is in charge of grouping the signal samples into Ethernet packets. A PC receives the packets, and the samples can be stored for post-processing, or processed in real-time by a software receiver. For a detailed information on the spatial filter and Ethernet transmission the reader is referred to Section 5.84.

As seen in Chapter 4, acquisition algorithms require the computation of the autocorrelation and the cross-correlation vectors of the received snapshots, as well as inversions of matrices and other sophisticated matrix algebra operations that require floating point precision. The

¹⁵Each DSP48E slice contains a 25×18 multiplier, an adder, and an accumulator.

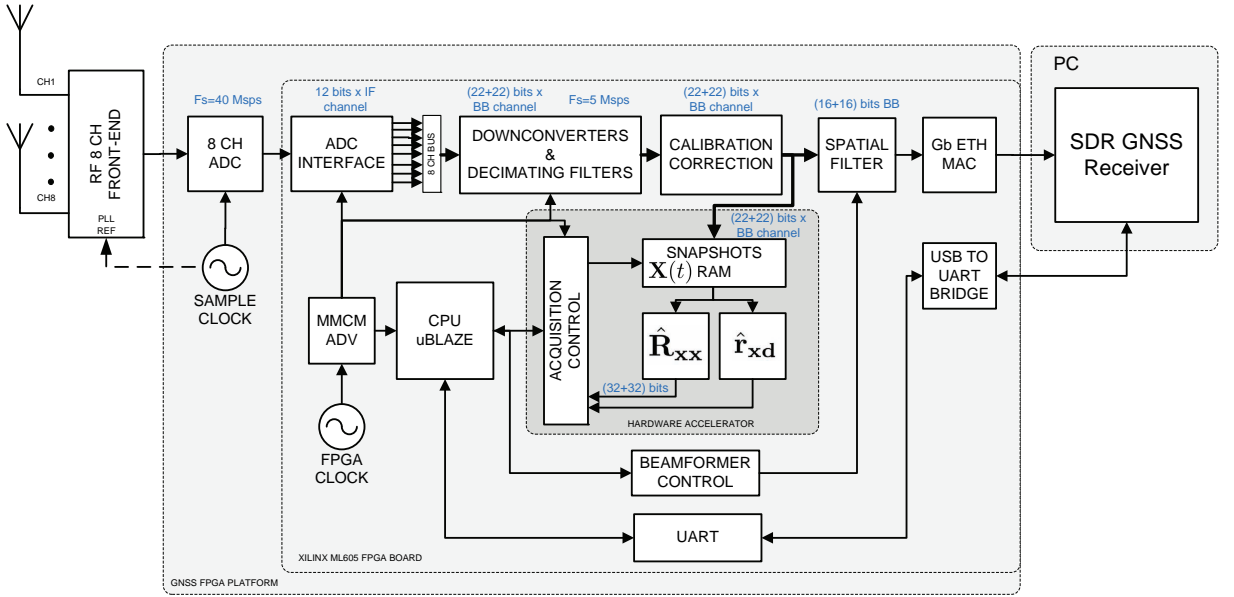


Figure 5.77: Digital beamforming platform detailed block diagram.

computation can be split in logic circuitry blocks implemented in Very High Speed Integrated Circuit Hardware Description Language (VHDL), or in an embedded processor that provides floating point capabilities and higher-level programming. For this prototype, the embedded software processor is implemented using a software processor core, which is used both for the acquisition and for the spatial-filter algorithms.

A soft processor is a Central Processing Unit (CPU) wholly developed using logic synthesis that can be implemented in a semiconductor device containing programmable logic such an FPGA. That is to say, the FPGA emulates, using logic circuitry, a processor that can be used as conventionally. Currently there are a number of soft cores available in the market, both developed by major vendors in the field of reconfigurable devices, like Xilinx and Altera, or developed by the open source community. As examples, we can mention MicroBlaze by Xilinx [Xil11f], Nios II by Altera [Alt09], LEON3 by Aeroflex Gaisler [LEO], and OpenRISC 1200 and aeMB from OpenCores [OCO]. In our prototype, the soft processor of choice has been the Xilinx MicroBlaze, an established soft-core IP.

MicroBlaze is a 32-bit Reduced Instruction Set Computer (RISC) architecture soft processor core with 32 general purpose registers, an Arithmetic Logic Unit (ALU), and an instruction set which is very similar to the RISC-based DLX architecture described in [Hen06, Pat08]. It supports both on-chip block RAM and/or external memory. The MicroBlaze soft processor has been implemented with an IEEE-754 compatible single-precision Floating-Point Unit (FPU), which connects directly to the MicroBlaze instruction execution pipeline, working at 125 MHz. A set of Xilinx peripherals are connected to the processor using the Advanced eXtensible Interface (AXI) bus, including a RAM memory Double Data Rate (DDR) controller which gives access to a 512 MB RAM onboard memory module, an Universal Serial Bus (USB) controller for the communication to a PC, and an interrupt controller with a timer to provide a high-precision time counter.

The acquisition hardware accelerator module is directly connected to the software processor by means of a dedicated FIFO-style connection called Fast Simplex Link (FSL) bus [Xil10b]. In that sense, the processor has access to the portion of the acquisition algorithm implemented in VHDL using a specifically developed peripheral. The selected development environment was the Xilinx ISE Design Suite 13.1 [Inc11].

In addition, the algorithms could require external data to perform warm, hot or an assisted acquisition [Kap05]. The data could be the estimated DOAs of satellite signals and synchronization parameters coming from the software-defined GNSS receiver running in an external device,

or from external sensors.

On the other hand, the acquisition results obtained by the platform should be sent to the GNSS software receiver. This bidirectional feedback channel is implemented using a software defined Universal Asynchronous Receiver-Transmitter (UART) connected to a USB-to-UART bridge.

The most critical operation by far is the transition from acquisition to tracking. Since the tracking process resides in an external device, it is expected a time delay in the transition, caused both by the acquisition operation latency and the feedback channel latency. It is important to keep a global sample time reference to correct the acquisition values at tracking start time [Sch99]. In that sense, the platform implements a sample timestamp counter which is sent within the Gigabit Ethernet sample stream.

The next sections are devoted to give details about the implementation of the selected acquisition algorithms, starting from the low level hardware accelerators that extracts the autocorrelation matrix and the cross-correlation vector, to the high level operations performed in the software processor.

5.8.3 Real-time GNSS signal acquisition

Considering the acquisition algorithms proposed in Chapter 4, the tests functions are composed of common estimators that require to operate with the snapshots matrix, simple matrix algebra operations, and high-level matrix operations such as matrix inversions. In this section, each of the required operations is analyzed and a real-time implementation is proposed.

Computationally-expensive operations such the autocovariance matrix and cross-correlation vector estimations are implemented using custom VHDL logic blocks in Sections 5.8.3.1 and 5.8.3.2. Complex operations that require floating-point precision are implemented in Section 5.8.3.3 using a high-level programming language in a software defined processor.

5.8.3.1 Autocovariance matrix estimation

The autocovariance matrix estimator implements the SCM formula in a two step process, comprised of a correlation step represented by a complex multiplication, and a discrete-time integration accumulation. The SCM formula can be expanded as

$$\begin{aligned} \hat{\mathbf{R}}_{\mathbf{xx}} &= \frac{1}{K} \mathbf{XX}^H = \\ &= \frac{1}{K} \left[\sum_{k=1}^K \mathbf{x}(k) x_1^*(k), \dots, \sum_{k=1}^K \mathbf{x}(k) x_N^*(k) \right] = \\ &= \frac{1}{K} \begin{bmatrix} \sum_{k=1}^K x_1(k) x_1^*(k) & \dots & \sum_{k=1}^K x_1(k) x_N^*(k) \\ \vdots & \ddots & \vdots \\ \sum_{k=1}^K x_N(k) x_1^*(k) & \dots & \sum_{k=1}^K x_N(k) x_N^*(k) \end{bmatrix}, \end{aligned} \quad (5.40)$$

where $\mathbf{x}(k) = [x_1(k), \dots, x_N(k)]^T$ is the snapshot captured at sample index k , $x_j(k)$ is the baseband signal sample for the j -th antenna element, $(\cdot)^*$ stands for complex conjugate operator, K is the number of snapshots used to estimate $\mathbf{R}_{\mathbf{xx}}$, and N is the number of antenna elements.

A conceptual schematic of the SCM estimator for $N = 8$ is shown in Fig. 5.78. The multiplication phase is, in principle, composed of N^2 complex multipliers corresponding to each of the possible combinations of the antenna elements. The product is fed to N^2 accumulators,

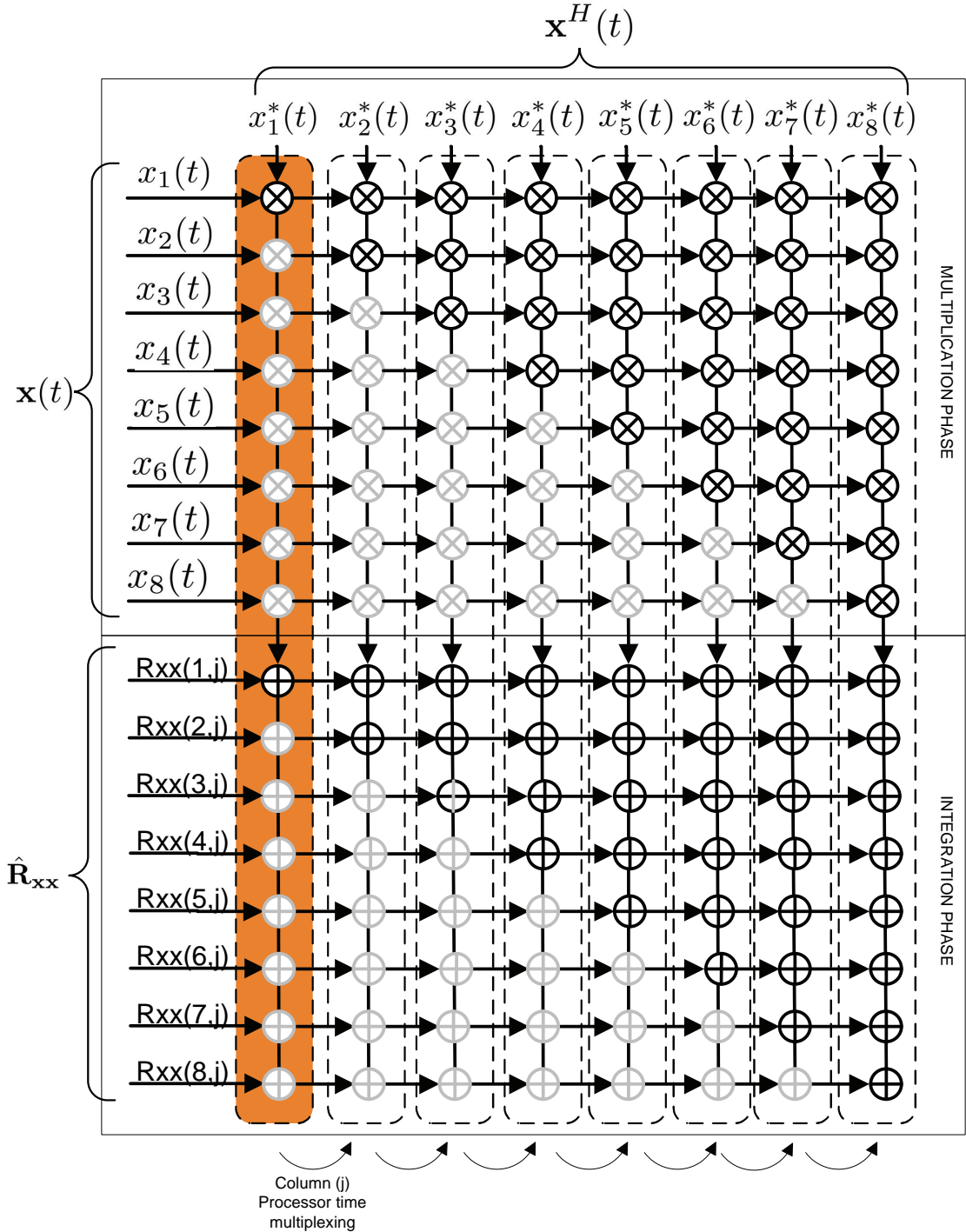


Figure 5.78: Conceptual schematic of $\hat{\mathbf{R}}_{xx}$ computation.

which performs the integration. Taking into account the hermitian structure of the covariance matrix, it is possible to reduce by $\frac{N+1}{2N}$ the number of required multipliers and accumulators.

Further reduction is possible using only N multipliers and sharing them for all matrix columns. For each multiplier, one of the operands remains constant during each time instant (row operand), and the other operand is switching between columns (column operand). In the schematic, the so-called row processor performs N operations per snapshot. The implementation of this approach is feasible without increasing the processing time thanks to the use of a faster processing clock in comparison to the sample clock.

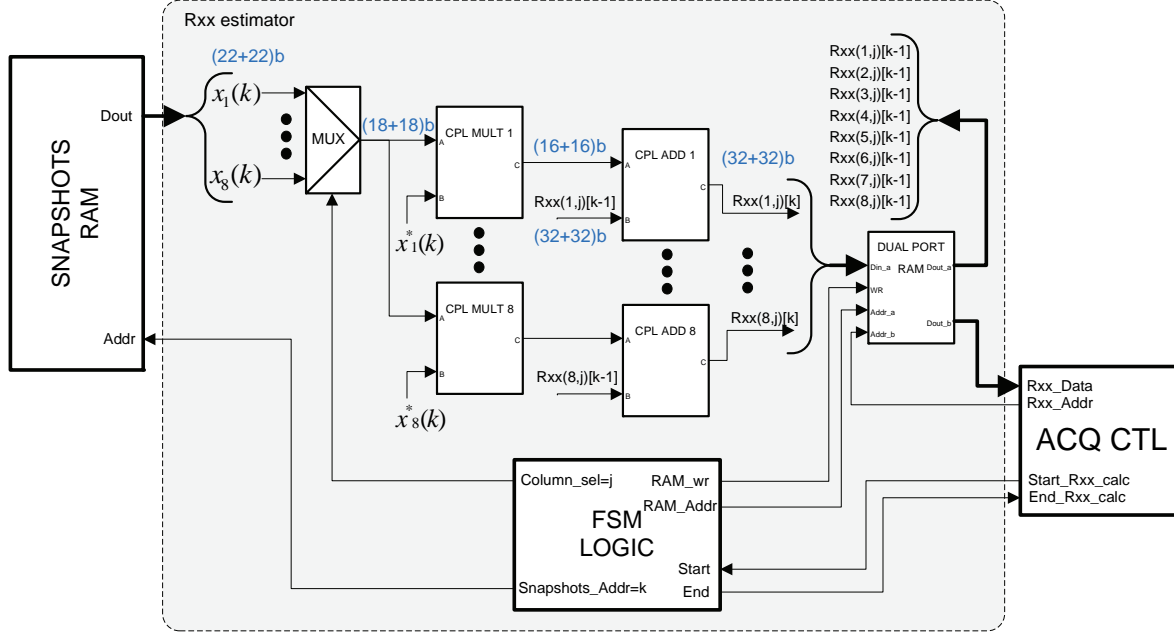


Figure 5.79: Schematic of the real-time logic for $\hat{\mathbf{R}}_{\mathbf{xx}}$.

The implemented real-time logic schematic is shown in Fig. 5.79, particularized for $N = 8$. From left to right, the snapshots matrix \mathbf{X} is contained in a Random Access Memory (RAM) memory [Xil11b], whose data output is fed to a complex multiplexer [Xil11d], which is in charge of selecting the active column. The multiplexed output is connected to the first operand of all multipliers. The second operand is the complex conjugate version of $x_1(t), \dots, x_8(t)$, depending on the row. At this point, the product of each multiplier is fed to an accumulator [Xil11a], and the result is stored in a dual port RAM memory [Xil11b]. For each snapshot read from RAM, the active column goes from 1 to 8 performing the multiply and accumulate operations. The number of required snapshots is a design parameter limited only by the snapshot RAM size.

Finally, when all snapshots are processed, the embedded processor can have access to the estimated matrix using the secondary read-only port of the $\hat{\mathbf{R}}_{\mathbf{xx}}$ RAM.

The process is orchestrated by a Finite State Machine (FSM) in charge of generating control signals and RAM addresses. It is possible to compute the processing time for N antennas, K snapshots, and FPGA clock frequency f_{clk} using the following formula:

$$T_{\hat{\mathbf{R}}_{\mathbf{xx}}} = T_{\text{cap}} + T_{\text{pro}}, \quad (5.41)$$

where $T_{\text{cap}} = \frac{1}{f_s} K$ is the time needed to capture K snapshots, $T_{\text{pro}} = \frac{1}{f_{\text{clk}}} NK$ is the processing time. For the particular case of $N = 8$, $K = 5000$, $f_s = 5$ MHz, and $f_{\text{clk}} = 100$ MHz, the estimation lasts $T_{\hat{\mathbf{R}}_{\mathbf{xx}}} = 2.3$ ms.

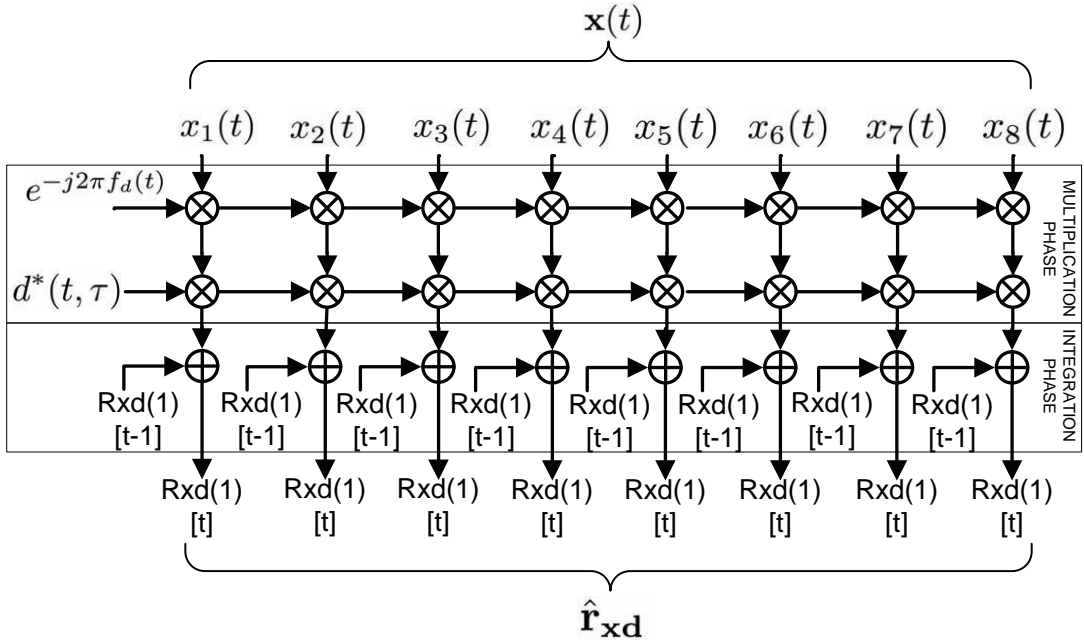


Figure 5.80: Conceptual schematic of $\hat{\mathbf{r}}_{\mathbf{xd}}$ computation.

5.8.3.2 Cross-correlation vector estimation

The cross-correlation vector estimator implements the correlation between the incoming snapshots and a locally-generated satellite PRN replica. The process comprises a Doppler wipe-off step, a code correlation step, and an integration step. The estimator formula can be expanded as

$$\begin{aligned}\hat{\mathbf{r}}_{\mathbf{xd}}(\check{f}_d, \check{\tau}) &= \frac{1}{K} \mathbf{X} \mathbf{d}(\check{f}_d, \check{\tau})^H = \\ &= \left[\sum_{k=1}^K x_1(k) e^{-j2\pi \check{f}_d k} d^*(k, \check{\tau}), \dots, \sum_{k=1}^K x_N(k) e^{-j2\pi \check{f}_d k} d^*(k, \check{\tau}) \right],\end{aligned}\quad (5.42)$$

where $x_j(k)$ is the baseband signal sample for the j -th antenna element at sample index k and the trial value for the signal Doppler bin is defined as $\check{f}_d \in [F_{dmin}, F_{dmax}]$, where F_{dmin}, F_{dmax} is the minimum and maximum expected Doppler shift, respectively. The local PRN replica at sample index k with time delay $\check{\tau}$ is represented by $d(k, \check{\tau})$. The code delay trial values are defined as $\check{\tau} \in [0, T_{PRN}]$, and T_{PRN} is the GPS C/A PRN period or the Galileo E1 PRN period.

A conceptual schematic is shown in Fig. 5.80, for the particular case of $N = 8$. The implemented real-time logic schematic is depicted in Fig. 5.81. From left to right, the snapshots matrix \mathbf{X} is contained in a RAM memory [Xil11b], shared with the $\hat{\mathbf{R}}_{\mathbf{xx}}$ module. Each of the snapshot components is fed to the first operand of a complex multiplier. The second operand, common to all the multipliers is connected to the output of a programmable Direct Digital Synthesizer (DDS) [Xil11e], which generates the Doppler wipe-off oscillator signal.

Next, the multipliers outputs are fed to a BPSK demodulator module, which performs the despread using the output of a GPS C/A PRN generator module and the Doppler-free snapshots. The PRN generator block implements directly the Gold Code shift registers structure for the GPS C/A PRN signal [Win10], and it can be reconfigured for all the available satellites ID's. Each the code-free outputs of the BPSK demodulators is integrated by means of accumulator blocks [Xil11a], which adds the new value to the old one, and the result is stored in a dual port RAM memory [Xil11b]. Finally, when all snapshots are processed, the embedded processor can have access to the estimated cross-correlation vector using the secondary read-only port of the $\hat{\mathbf{r}}_{\mathbf{xd}}$ RAM.

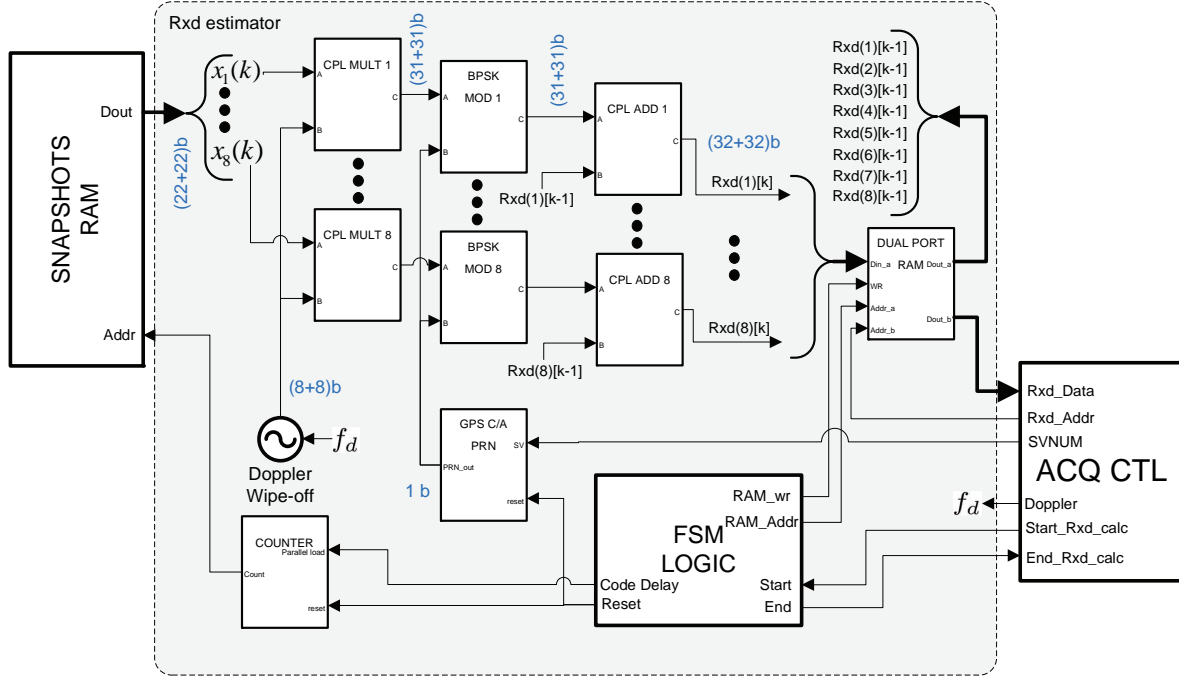


Figure 5.81: Schematic of the real-time logic for \hat{r}_{xd} .

The processor selects both the Doppler frequency bin \tilde{f}_d and the satellite ID. The FSM logic performs the $\tilde{\tau}$ sweep over the entire τ space, by means of a circular time-shift of the snapshots. In the implementation, a counter with a parallel load capability is used to select the current $\tilde{\tau}$ and generate the snapshot RAM addresses. It is possible to compute the processing time using the following formula

$$T_{\hat{r}_{\text{xd}}} = T_{\text{cap}} + T_{\text{pro}} N_{\tau \text{bins}}, \quad (5.43)$$

where $T_{\text{cap}} = \frac{1}{f_s} K$ is the time needed to capture K snapshots, $T_{\text{pro}} = \frac{1}{f_{\text{clk}}} K$ is the processing time for one $\tilde{\tau}$ value, and $N_{\tau \text{bins}}$ is the number of different $\tilde{\tau}$ bins. For the particular case of $K = 5000$, $f_s = 5$ MHz, $f_{\text{clk}} = 100$ MHz, and $N_{\tau \text{bins}} = 1023$, which correspond to a 1 chip resolution for GPS C/A PRN, the estimation lasts $T_{\hat{r}_{\text{xd}}} = 85.4$ ms. The acquisition operation delay plus the acquisition to tracking transition delay is measured by the software receiver. The tracking pull-in operation is in charge of correcting the synchronization parameter values given by acquisition using this information, as we will see in Section 6.4.2.6.

5.8.3.3 High-level operations

As shown in this section, the low level operations required for statistics extraction can be efficiently implemented using hardware accelerators. However, the acquisition algorithms require high level operations as well, such as matrix inversions. Since the GNSS platform described in this work is intended to be used as a research tool, it is also important to provide a flexible acquisition implementation, which can be easily modified or compared to other algorithm implementations. A suitable solution is to use an embedded processor.

In this prototype, we use the Xilinx Embedded Development Kit (EDK), a complement of the Xilinx ISE suite [Inc11], to program the embedded processor. The Software Development Kit (SDK) provides a high-level C++ programming framework to implement complex acquisition algorithms.

Fig. 5.82 shows the processor software flowchart. From top to bottom, after the reset, the program performs a complete initialization process, including the initialization of external

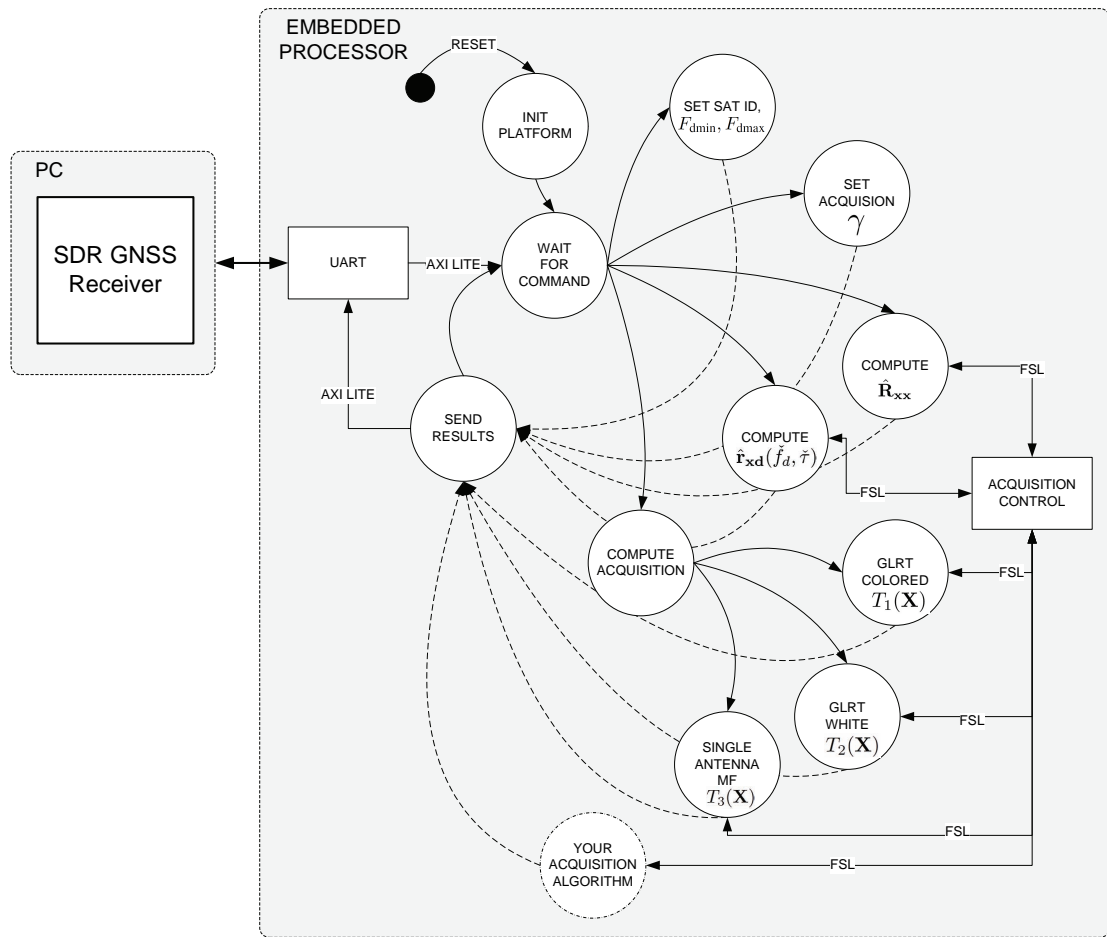


Figure 5.82: Embedded processor acquisition software flowchart.

Operation ($N = 8$)	Value
Complex matrix multiplication	0.1 ms
Complex matrix inverse	0.6 ms
$T_{\text{GL}}(\mathbf{X})$ algorithm operations	0.643 ms
$T_{\text{GL}}(\mathbf{X})$ code delay sweep	57 ms
$T_{\text{GL}}(\mathbf{X})$ complete Doppler/delay grid	1200 ms

Table 5.27: Acquisition operations time performance for $T_{\text{GL}}(\mathbf{X})$.

devices such as the front-end frequency synthesizer registers. At this point, a process waits for new commands coming from the PC by means of the USB-to-UART bridge.

It is possible to configure the satellite ID, the Doppler search space, the number of grid points, and the acquisition threshold using specific commands. For debug purposes, it is possible to trigger the estimation and read the results for both $\hat{\mathbf{R}}_{\mathbf{xx}}$ and $\hat{\mathbf{r}}_{\mathbf{xd}}(\check{f}_d, \check{\tau})$, directly from Matlab scripts, using a serial port driver.

Acquisition algorithms can be implemented by the GNSS software receiver. In this work, we have implemented three different acquisition algorithms using different test functions and sharing the same hardware accelerators:

- **GLRT colored** is the acquisition algorithm described in Section 4.5, whose test function is defined in (4.52).
- **GLRT white** is the white noise version of the GLRT for the unstructured array signal model, described in Section 4.4, whose test function is defined in (4.42).
- **Single antenna MF** is the non-coherent matched filter commonly used in single-antenna receivers [Kap05]. The test function is defined in (3.33).

Fig. 5.83 shows the software flowchart for the GLRT colored acquisition. From top to bottom, the first step consists of computing $\hat{\mathbf{R}}_{\mathbf{xx}}$ using the hardware accelerator. The Microblaze processor performs the required matrix operations. The Microblaze software obtains $\hat{\mathbf{R}}_{\mathbf{xx}}^{-1}$ by using a real matrix inversion [Zie79]. This inversion is computed using the Gaussian elimination algorithm [Gol96].

Once the SCM is inverted, the Doppler search loop starts using the configured parameters. In this implementation, the $\hat{\mathbf{r}}_{\mathbf{xd}}$ estimator is called for each of \check{f}_d bins in the grid. The hardware accelerator is in charge of executing the delay search over the entire $\check{\tau}$ space. Next, the test function is executed and the absolute maximum value is found. The associated \check{f}_d and $\check{\tau}$ are preserved. This operation is repeated for each Doppler value.

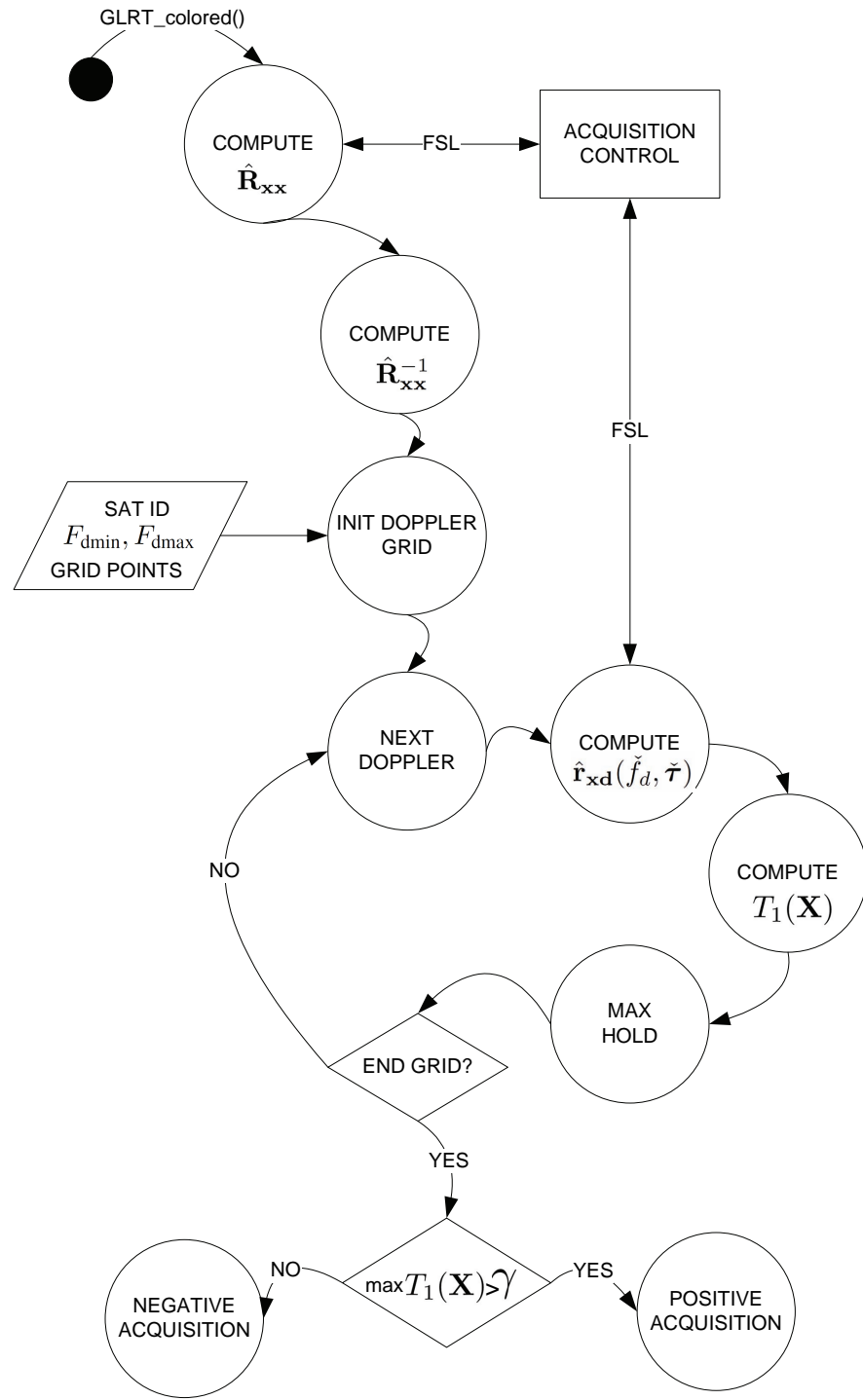
Finally, when the grid loop ends, the maximum is compared to the configured threshold and a decision is made. In case of positive acquisition, the associated synchronization parameters are sent to the PC.

Table 5.27 shows the time performance values obtained by the GLRT colored acquisition implementation ($T_{\text{GL}}(\mathbf{X})$ Eq. (4.52)). The delay search space was set to $\check{\tau} \in [0, 1023]$ chips with 1 chip resolution, and the Doppler frequency search space was set to $\check{f}_d \in [-5000, 5000]$ Hz with frequency bin resolution of 500 Hz.

5.9 FPGA interface with GNSS software receivers

The signal coming from the spatial filter block is sent in real-time to a GNSS SDR receiver running in a commodity PC by means of a dedicated Gigabit Ethernet bus [Nor03]. A special type of frame has been designed to minimize the overhead imposed by network protocols, and the corresponding driver has been implemented with the Xilinx LogiCORE IP Virtex-6 FPGA Embedded Tri-Mode Ethernet MAC Wrapper core [Xil10c].

Fig. 5.84 shows the Ethernet frame header fields and the payload generated by the platform. Only the Medium Access Control (MAC) 802.3 frame is used. The payload area is divided in the

Figure 5.83: $T_{GL}(\mathbf{X})$ acquisition software flowchart.

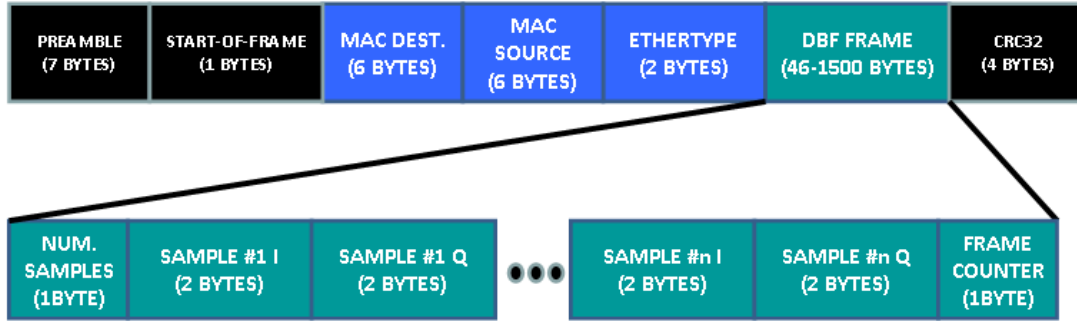


Figure 5.84: GNSS array platform custom Ethernet frame.

following fields: the first byte of the payload indicates the amount of signal samples contained in the frame, next bytes contain the signal samples using a standard two-complement 16 bits signed little-endian¹⁶ integer format both for the real and for the imaginary part (thus forming a 32 bits complex number), and the last byte of the payload is a frame counter to allow the detection of missing frames at the PC.

In order to properly design the frame, there is a trade-off between the frame rate and the number of samples per frame. Long frames reduces CPU utilization at the PC (mostly due to interrupt reduction) and increases throughput by allowing the system to concentrate on the data samples in the frames, instead of handling the frames containing the data. However, these long frames increase the time that the PC has to wait for retrieving data, since the whole frame has to be received before data samples could be extracted from the Ethernet frame. In addition, long frames require also higher memory buffers.

Defining r_f as the amount of frames transmitted per second, and r_s as the rate of transmitted samples per second, it is possible to write:

$$r_f = \frac{r_b}{OH \times 8 + GF \times b}, \quad (5.44)$$

$$r_s = r_f \times GF, \quad (5.45)$$

where $r_b = 10^9$ bits per second is the physical speed of the Ethernet bus, $b = 32$ is the number of bits per sample, $OH = 26 + 2 + 219$ is the amount of extra bytes imposed by the MAC protocol headers (26 bytes, see Fig. 5.84), plus the platform frame extra bits (2 bytes), plus the inter-frame delay bytes imposed by the Marvell Alaska 88E1111 Gigabit Ethernet transceiver [Mar04] (equivalent to 219 bytes, according to our working experience), and GF is the number of data samples per frame (also known as grouping factor). Since the rate of transmitted samples per second has to be equal or higher to the output rate of the beamformer (defined as $r_o = \frac{f_s}{D}$, in samples per second), the designed value for GF is the solution to:

$$\max_{GF} r_f(GF) \quad (5.46)$$

subject to $r_s \geq r_o$

In our prototype, $r_o = 25$ Msps. Considering $r_f = R_o$ and using equations (5.44) and (5.45), we get

$$GF_{\min} = \frac{r_{s\min} \times OH \times 8}{r_b - r_{s\min} \times b} = 247 \text{ samples per frame}, \quad (5.47)$$

for the particular case of the presented platform.

In order to relax time constraints at the PC for handling interruptions, we set $GF = 255$ samples per frame.

¹⁶The least significant byte value is at the lowest memory address.

At the PC, device drivers make network cards to generate an interrupt whenever the card needs attention (e.g., for informing the operating system that there is an incoming packet to handle). In case of high traffic rate, the operating system spends most of its time handling interrupts, leaving little time for other tasks. This problem is referred to as *interrupt livelock* [Mog96], and it could provoke packet losses than will be seen as signal glitches, or phase discontinuities, that can affect the GNSS software receiver performance. In order to avoid so, we have adopted the strategy proposed in [Der04, NTO08], that implies a Linux kernel patching and recompilation, as a solution for signal capturing at the PC.

A suitable Ethernet driver wrapper was designed to connect the array platform output stream with the GNURadio open source software defined radio framework [GRa]. The reader is referred to Chapter 6 for a detailed description.

5.10 Platform validation

At this point the complete array platform is designed and fully implemented. The next step is to validate each of the components in order to assure that the platform meets the design requirements and guarantee a bug-free operation. The validation includes setting up a controlled operation environment where both the analog and digital components are tested in a variety of conditions. The validation follows the RF signal logic path, starting with the antenna array and front-end calibration in Section 5.10.1 and ending with the digital signal processing FPGA implementation tests in Section 5.10.2.

5.10.1 Antenna array and RF front-end calibration

The antenna array and the RF front-end was tested in an anechoic chamber, where a -40 dBm unmodulated carrier calibration signal was generated by an Agilent E4438C generator [Agi06]. The generator calibration carrier frequency was set to $f_{\text{cal}} = f_c + f_{\text{ref}}$, where f_{ref} is a frequency shift from the nominal carrier frequency. In the experiment, f_{ref} was set to 10 kHz. The calibration signal was transmitted by a ETS-Lindgren model 3164 horn type antenna [ETS09] with vertical polarization. Notice that the antenna-array elements have circular polarization, thus, a 3 dB of signal losses due the polarization mismatch is expected.

The wavefront impinges into the array by the broadside DOA (azimuth $\theta = 0^\circ$, elevation $\psi = 90^\circ$). In this set-up, the platform FPGA code was modified to include a Chipscope logic analyzer core [Xil11c] at the baseband snapshot output. This modification enables the capture of snapshots using the Xilinx USB platform cable [Xil11h] and a commodity PC. In addition, this procedure also verifies the correct operation of both the ADC interface and the digital down converter logic.

The amplitude and phase calibration procedure includes the following steps:

1. Capture a snapshot matrix $\mathbf{X}_{\text{raw}} \in \mathbb{C}^{N \times K}$ with sufficient samples to capture at least one signal period of the baseband version of the calibration signal. The minimum number of snapshots is consequently $K \geq \lfloor \frac{f_{\text{ref}}}{f_s} \rfloor$.
2. Compute the amplitude normalization vector as $\mathbf{a}_{\text{cal}} = [\frac{1}{\sqrt{\hat{P}_1}}, \dots, \frac{1}{\sqrt{\hat{P}_N}}] \in \mathbb{R}^{1 \times N}$, where $\hat{P}_i = \frac{1}{K} \sum_0^{K-1} x_i x_i^*$ is the estimation of the input power for the i -th antenna channel.
3. Normalize the snapshots using \mathbf{a}_{cal} .
4. Estimate the phase shifts between the reference channel and rest of the channels. In our calibration process, we used the ML estimator for time delay between two signals [Kna76], which involves the maximization of the discrete cross-correlation between the reference

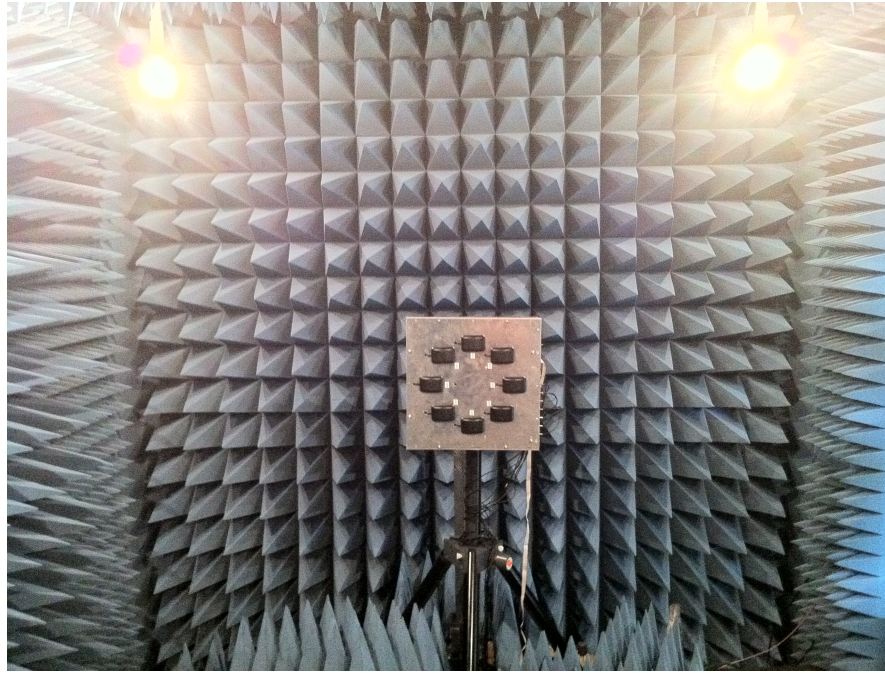


Figure 5.85: Antenna array and front-end calibration setup in an anechoic chamber.

antenna element and the rest of antenna elements:

$$\hat{\Delta k}_i = \arg \max_{\Delta k_i} \left\{ \begin{array}{l} \sum_{k=1}^{K-\Delta k_i} \Re\{x_1(k)\} \Re\{x_i(k + \Delta k_i)\} \Delta k_i \geq 0 \\ \sum_{k=1}^{K+\Delta k_i} \Re\{x_i(k)\} \Re\{x_1(k - \Delta k_i)\} \Delta k_i < 0, \end{array} \right. \quad (5.48)$$

where $\hat{\Delta k}_i$ is the estimated time delay in samples for the i -th antenna element. The phase correction vector can be created as

$$\boldsymbol{\phi}_{\text{cal}} = \left[e^{-j2\pi \frac{\hat{\Delta k}_1 f_{\text{ref}}}{f_s}}, \dots, e^{-j2\pi \frac{\hat{\Delta k}_N f_{\text{ref}}}{f_s}} \right] \in \mathbb{C}^{1 \times N}. \quad (5.49)$$

5. Finally, the calibration matrix can be defined as

$$\mathbf{G}_{\text{cal}} = \text{diag}(\mathbf{a}_{\text{cal}}) \text{diag}(\boldsymbol{\phi}_{\text{cal}}), \quad (5.50)$$

where $\text{diag}(\cdot)$ is a diagonal matrix with the elements of the vector. The calibrated snapshot matrix is defined as

$$\mathbf{X}_{\text{cal}} = \mathbf{G}_{\text{cal}} \mathbf{X}. \quad (5.51)$$

Notice that this calibration matrix only compensates the amplitude and phase differences between antenna elements and front-end channels. The possible signal coupling between antenna elements and the inter-channel cross-talk remain uncalibrated.

Fig. 5.85 shows a picture of the anechoic chamber setup. As shown in Fig. 5.86a, the uncalibrated snapshots have important amplitude and phase differences between antenna channels. After applying the calibration matrix, Fig. 5.86b shows that the reference signal is completely aligned in amplitude and phase in all the antenna channels after the calibration. Notice that this basic calibration procedure is valid only for the broadside direction and for the specific f_{cal} RF frequency. Differences between antenna elements radiation patterns makes the calibration data dependent on the signal DOA, as mentioned in Section 5.1.3. In addition, the frequency response of the front-end makes the calibration data dependent of f_{cal} .

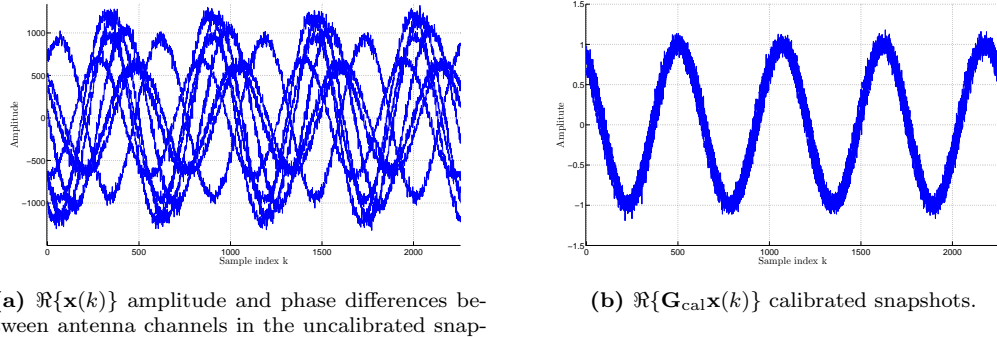


Figure 5.86: Uncalibrated and calibrated snapshots plots for $f_{\text{ref}} = 10$ kHz.

In order to verify the array calibration, the array response was tested using a single satellite GPS L1 C/A signal generated by an Agilent E4438C generator [Agi06] equipped with GPS Personality [Agi07]. During the experiment different signal DOAs were tested, and the array response was evaluated by means of post-processing the captured snapshots matrices.

For each signal DOA, a spectral Multiple Signal Classification (MUSIC) algorithm [Tre02, p.1158] was executed in order to estimate its azimuth $\theta \in [0^\circ, 360^\circ)$ and its elevation $\psi \in [0^\circ, 90^\circ)$. The MUSIC test function can be defined as

$$(\hat{\theta}, \hat{\psi}) = \arg \max_{\theta, \psi} \frac{1}{\mathbf{v}(\theta, \psi)^H (\mathbf{I} - \mathbf{u}\mathbf{u}^H) \mathbf{v}(\theta, \psi)}, \quad (5.52)$$

where $\mathbf{v}(\theta, \psi) \in \mathbb{C}^{N \times 1}$ is the signal steering vector defined by its azimuth θ and elevation ψ , $\mathbf{u} \in \mathbb{C}^{N \times 1}$ is the eigenvector associated with the most powerful eigenvalue of $\hat{\mathbf{R}}_{\mathbf{xx}}$, and $\mathbf{I} \in \mathbb{R}^{N \times N}$ stands for the identity matrix. Fig. 5.87a, 5.87b, 5.87c, 5.87d shows the evolution of the MUSIC test function over the entire space of θ and ψ for different signal DOAs. Fig. 5.88 shows the elevation estimation root square error for two different DOA azimuths of 0° and 180° . Notice that in the calibration direction ($\theta = 0^\circ, \psi = 0^\circ$) the pointing error is minimum. However, the calibration is DOA dependent and consequently, the array remains uncalibrated for other DOAs. The array response registered an average pointing error of 10° in both θ and ψ . Possible causes are the non-homogeneous antenna elements response and coupling effects between antenna elements, among others.

5.10.2 Acquisition hardware accelerators

The hardware accelerators implementation was verified using unit tests for each component. This is specially important in FPGA-based implementations, due to high compilation time and debug complexity presented when the design is tested in a real device. On the other hand, VHDL simulators offer the possibility to test and debug the VHDL code efficiently.

Each VHDL entity was tested using a dedicated VHDL test bench. Simulations using the Xilinx I-SIM [Xil11i] were performed in order to verify and debug the implementation. Fig. 5.89 shows the test procedure. From left to right, the VHDL test bench creates the input stimulus required by the acquisition component, such as the sampling clock, the FPGA clock and the control signals. Next, the Component Under Test (CUT) is instantiated and their snapshots data input are connected to a RAM emulator, where the snapshots are read from a file. This file can be created using either a real signal capture, using Chipscope, or using Matlab generated snapshots.

The CUT output is recorded in a file and, after the simulation, a Matlab script analyzes and compares the results to their theoretical values. A pass / fail decision is made.

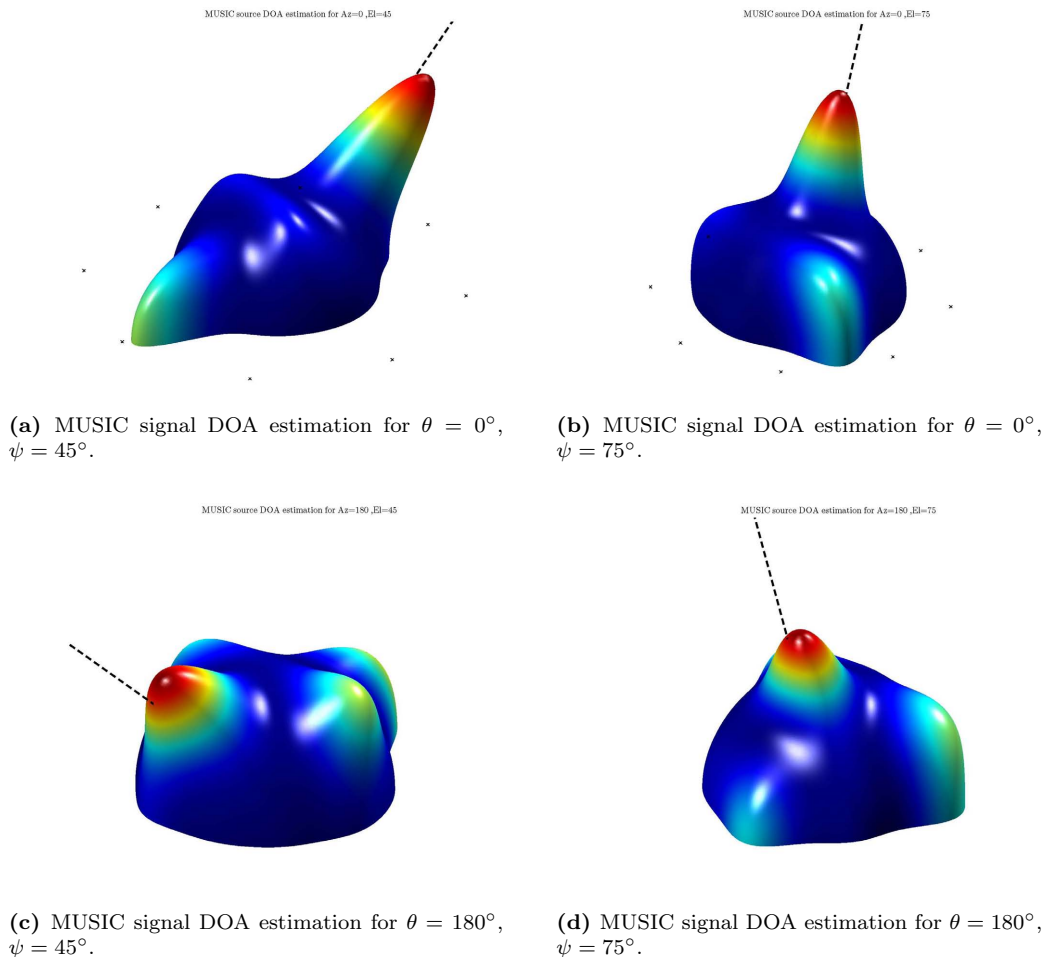


Figure 5.87: Calibration validation using MUSIC DOA estimation.

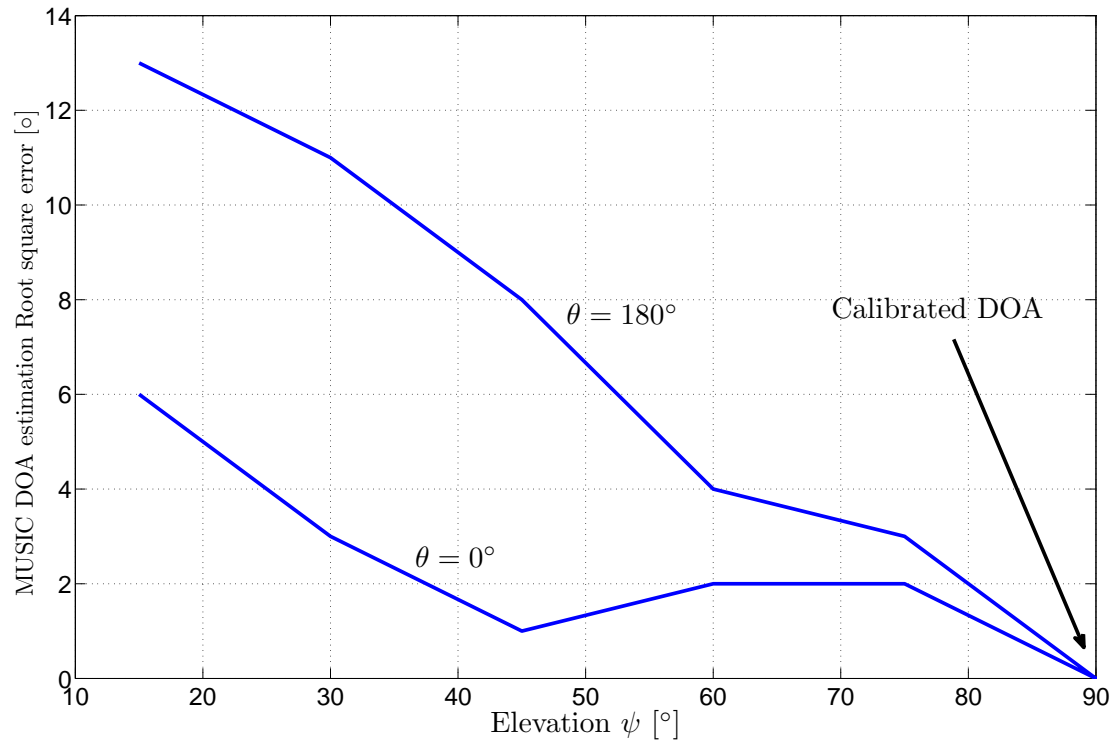


Figure 5.88: DOA elevation estimation pointing error for $\theta = 0^\circ$ and $\theta = 180^\circ$.

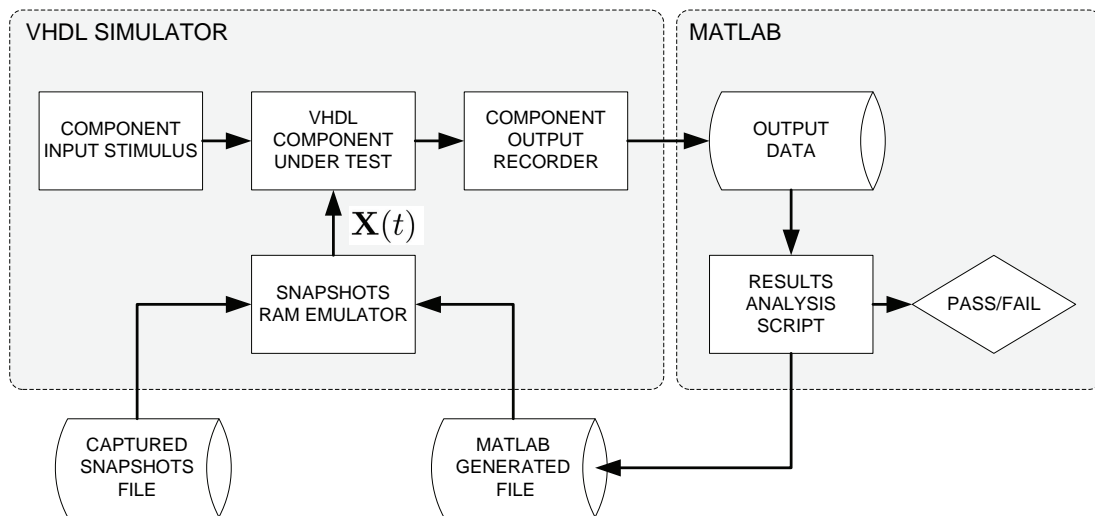


Figure 5.89: VHDL components testing methodology.

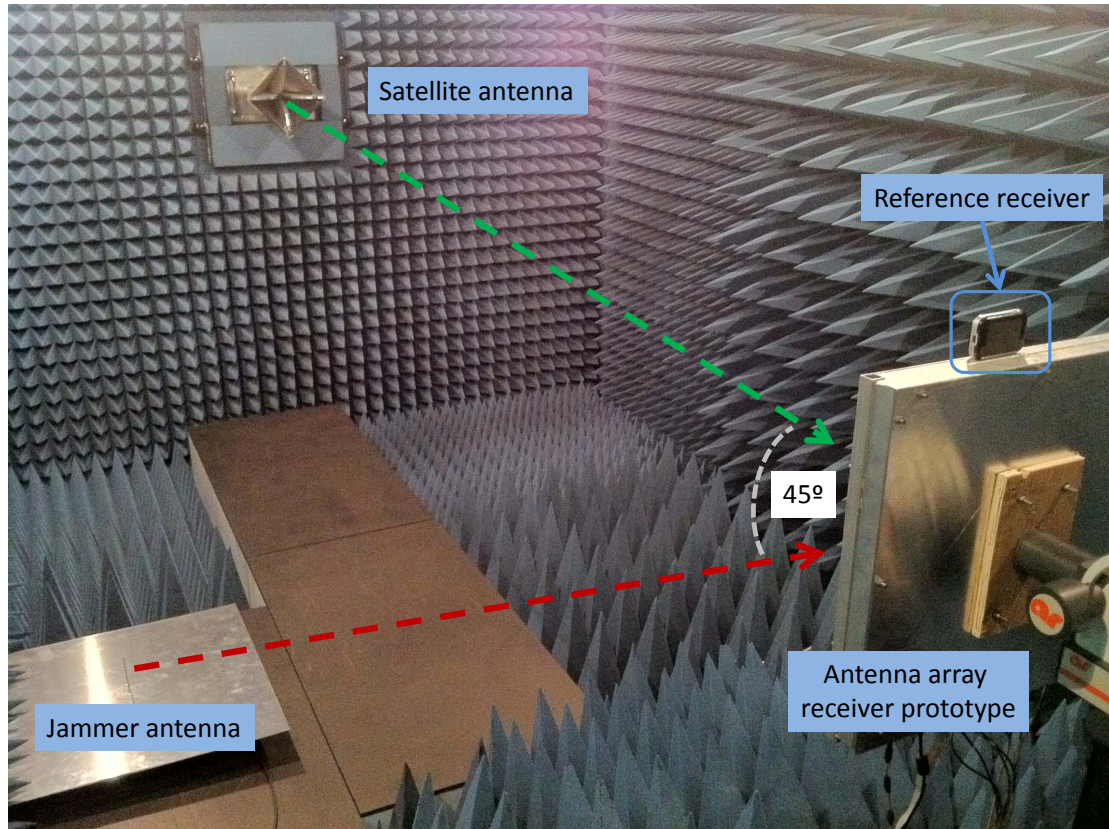


Figure 5.90: Picture of the interference scenario setup.

5.11 Anechoic chamber measurement set-up and results

With a functional GNSS array platform prototype, the performance of the implemented acquisition algorithms was tested in harsh interference environments conditions. The test functions defined in Section 5.8.3.3 were executed using 1 ms of captured snapshots.

The worst case was defined as an scenario where a strong uncorrelated in-band interference impinges into the array with different DOA. Fig. 5.90 shows a picture of the anechoic chamber setup. The satellite signal is transmitted using the horn antenna, with DOA set to $\theta = 0^\circ$ and $\psi = 90^\circ$, simulating a realistic situation where a high elevation satellite is received. The interference is transmitted using an auxiliary monopole antenna with an approximated DOA of $\theta = 45^\circ$ and $\psi = 45^\circ$, which simulates a moderate elevation jammer or a communication signal coming from nearby communication tower. The satellite signal power and the interference (or jammer) power is given in terms of CN0 and IN0 respectively, measured at the IF output of the front-end. The AGC function was turned off and the front-end was configured at maximum gain.

In both scenarios, the interference and the satellite GPS L1 C/A signal were generated by two Agilent E4438C generators [Agi06], one of them was equipped with GPS Personality [Agi07]. The satellite CN0 was set 44 dB-Hz, which was measured using a Sirf Star III [Cam10] as a reference receiver.

Two in-band interference scenarios were tested:

- **continuous wave interference:** In this scenario, a Continuous Wave (CW) jammer impinges into the array with $f_{int} = 1575.43$ MHz and $IN0 = 133$ dB-Hz. The frequency spectrum measured at IF terminals is shown in Fig. 5.91d. The resulting test statistics values in the Doppler/delay search grid is shown in Fig. 5.91a, 5.91b, and 5.91c for $T_{GL}(\mathbf{X}(t, \tilde{f}_d, \tilde{\tau}))$, $T_{Wh}(\mathbf{X}(t, \tilde{f}_d, \tilde{\tau}))$, and $T_{GL}(\mathbf{x}(t, \tilde{f}_d, \tilde{\tau}))$ respectively. From the results it seems clear that the GLRT for the colored noise model is able to mitigate the interference,

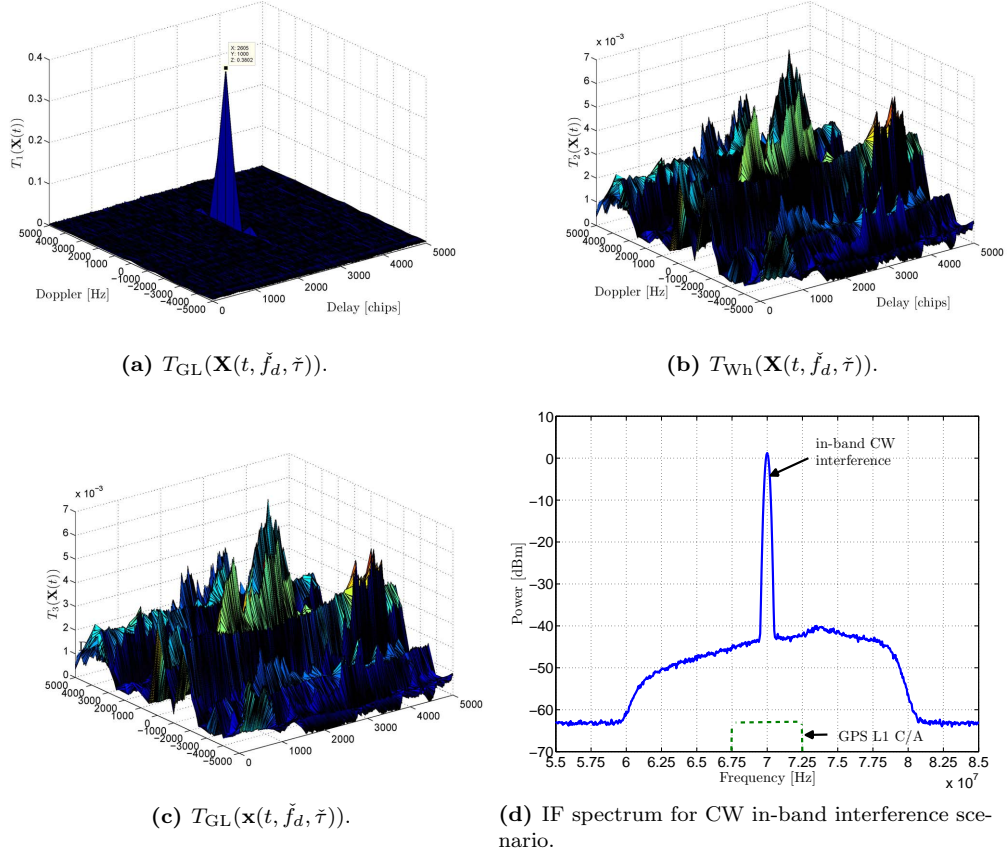


Figure 5.91: Doppler and delay grid search plot for in-band CW interference scenario.

and the grid maximum peak is plainly visible. However, the white version of the GLRT and the single antenna MF are unable to overcome the interference.

- **4G/LTE interference:** This experiment simulates a situation where an LTE-like signal coming from a nearby base station is interfering the GPS L1 C/A signal. It is known the concern about the interferences that the deployment of Lightsquared's 4G network could cause, specially when it uses the 1552.7 MHz band [Bou11], as it was stressed in Section 2.2.3.

Since the RF front-end prototype is equipped with highly selective SAW filters, in our setup, the interference generator is unable to reach the interference power levels required to interfere the GPS L1 band with the out-of-band spurious emissions.

In order to test the protection against a possible wideband interference, a simulated LTE base station downlink signal [3gp11] with 5 MHz of channel bandwidth impinges into the array with $f_{\text{int}} = 1575.42$ MHz and $IN0 = 133$ dB-Hz. In this situation, the interference is superposed over the entire acquisition bandwidth.

The frequency spectrum measured at IF terminals is shown in Fig. 5.92d. The resulting test statistics values in the Doppler/delay search grid are shown in Fig. 5.92a, 5.92b, and 5.92c for $T_{\text{GL}}(\mathbf{X}(t, \tilde{f}_d, \tilde{\tau}))$, $T_{\text{Wh}}(\mathbf{X}(t, \tilde{f}_d, \tilde{\tau}))$, and $T_{\text{GL}}(\mathbf{x}(t, \tilde{f}_d, \tilde{\tau}))$ respectively. From the results it is possible to state that the GLRT colored offers good protection against wideband uncorrelated interferences, while the GLRT white version and the single antenna MF remain unprotected.

In order to define an interference protection metric offered by the proposed acquisition with respect to other acquisition algorithms, we used the deflection coefficient defined in 3.14 of Section 3.2.3 to measure the detectors performance. This quantity measures the effectiveness of

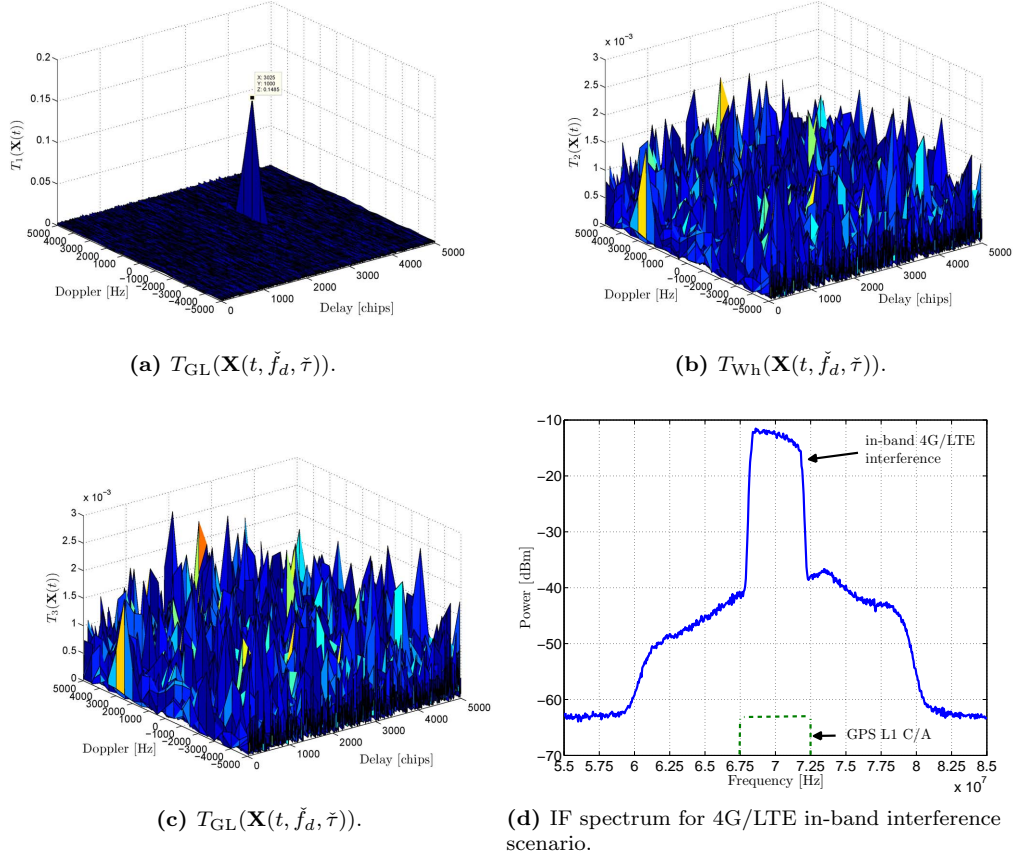


Figure 5.92: Doppler and delay grid search plot for in-band 4G/LTE interference scenario.

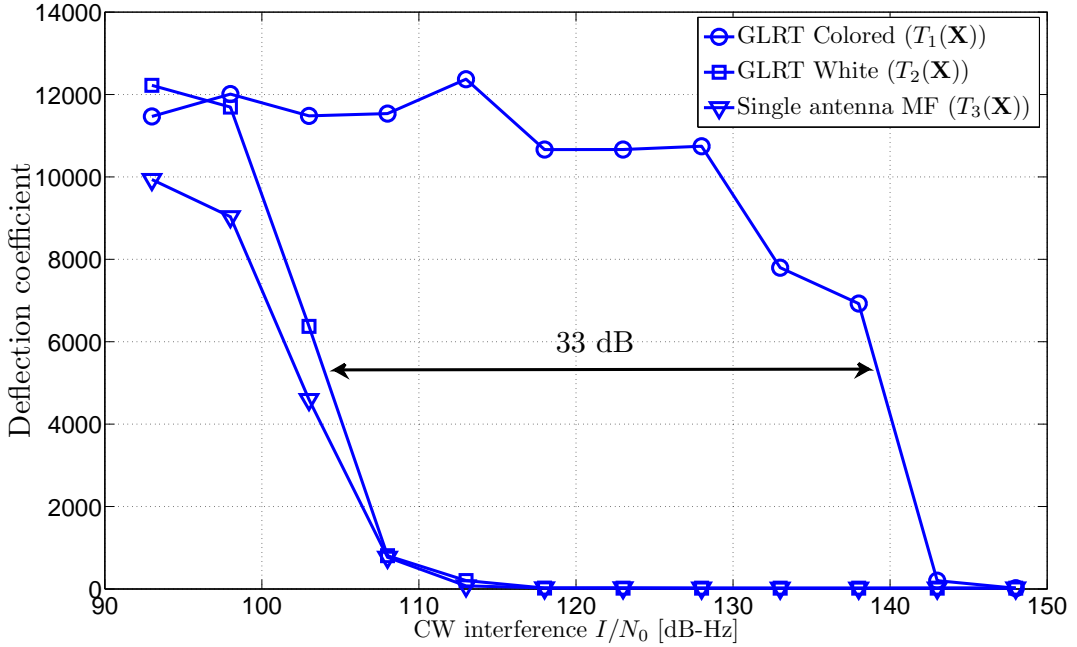


Figure 5.93: Deflection coefficient evolution in CW interference scenario.

the quadratic statistic in separating the two hypotheses, although is not directly related to the error probability. In the measurements, the expectations operators and the variance operator were substituted by its sample mean and sample variance respectively.

Fig. 5.93 shows the evolution of the estimated deflection coefficients in the CW interference scenario for a ($IN_0 = 90 - 150$ dB-Hz) sweep. From the results its is possible to infer that the acquisition based on the GLRT for colored noise offers a jammer or interference protection of 33 dB with respect to the single antenna MF and the white version of the GLRT.

The deflection coefficient measurement was done also for the LTE interference scenario. Fig. 5.94 shows the results. The GLRT colored offers 25 dB of protection for wideband in-band interferences with respect to the single antenna MF and the white version of the GLRT.

It is important to take into account that the front-end reached the compression point at the highest power region of the interference power sweep ($IN_0 = 135 - 150$ dB-Hz). This situation degrades the performance of the acquisition algorithms, and thus, a better performance is expected enabling the AGC to avoid the front-end saturation.

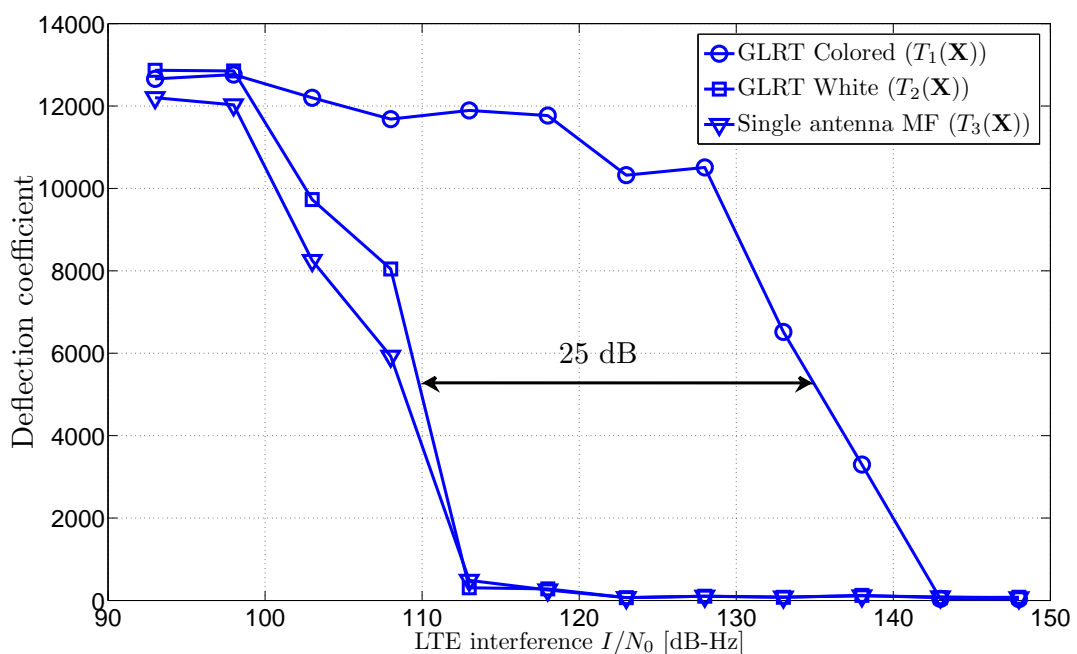


Figure 5.94: Deflection coefficient evolution in LTE interference scenario.

5.12 Summary

In this Chapter we presented the design and the implementation of a novel FPGA-based GNSS real-time antenna-array receiver platform, intended to be used as a reliable research tool tightly coupled with software defined GNSS receivers.

A complete signal reception chain including the eight-elements antenna array and the multichannel coherent RF front-end for the GPS L1/ Galileo E1 was designed, implemented and tested. The digital section of the platform was also verified. The design trade-offs and the implementation technology limitations were carefully analyzed and taken into account.

As a proof-of-concept, the problem of GNSS vulnerability to interferences was addressed using the presented platform. In that sense, the array-based acquisition algorithms introduced in Chapter 4 were implemented and tested under realistic conditions. The performance of the algorithms were compared to single antenna acquisition techniques, measured under strong in-band interference scenarios, including narrow band interferers and LTE-like communication signals.

The results show, on the one hand, the real-time implementation feasibility using COTS components, and on the other hand, that the proposed acquisition algorithm, based on the GLRT for colored noise model, offers excellent protection against uncorrelated directional interferences, even if the array is moderately uncalibrated, which is aligned with the theoretical results.

The antenna-array platform was designed to work tightly coupled with a SDR running in a PC in order to provide the necessary resources to complete the GNSS receiver operations. In this context, next chapter introduces the GNSS-SDR: an open-source, software defined GNSS receiver project that provides a tool for testing purposes.

The results presented in this chapter were partially published in:

- [Arr09b] J. Arribas, C. Fernández-Prades, D. Bernal, and J. A. Fernández-Rubio, “Plataforma de conformación de haz digital para receptores GNSS en tiempo real”, *Proceedings XXIV Simposium Nacional de la Unión Científica Internacional de Radio (URSI 2009)*, Santander (Spain), September 2009.
- [Arr09a] J. Arribas, D. Bernal C., Fernández-Prades, P. Closas, and J. A. Fernández-Rubio, “A novel real-time platform for digital beamforming with GNSS software defined receivers”, *Proceedings of the ION GNSS 2009, Savannah, GA (USA)*, September 2009.
- [FP09c] C. Fernández-Prades, P. Closas, and J. Arribas, “Implementation of digital beamforming in GNSS receivers”, *Proceedings of the 4th European Workshop on GNSS Signals and Signal Processing*, Oberpfaffenhofen, München (Germany), December 2009.
- [Arr11a] J. Arribas, C. Fernández-Prades, and P. Closas, “Antenna Array Based GNSS Signal Acquisition: Real-time Implementation and Results”, *Proceedings of the ION GNSS 2011, Portland, Oregon (USA)*, September 2011.

Chapter 6

Real-time GNSS Software Defined Receiver

I do not fear computers. I fear the lack of them.

Isaac Asimov.

IN the previous Chapter we presented a novel array-based GNSS receiver platform, focusing the efforts in the particularities of the multichannel front-end and the associated high-speed, real-time signal processing implemented using FPGAs. However, the FPGA platform was designed to demonstrate the implementation feasibility of array-based acquisition algorithms. We left the rest of the receiver operations (mainly, tracking, navigation message decoding, and PVT solution) to a conventional (single-antenna) receiver processing the spatially-filtered signal sample stream.

In this Chapter, we close the loop by designing and implementing a software defined receiver. We focus the efforts on digital signal processing, understood as the process between the ADC and the computation of code and phase observables, including the demodulation of the navigation message. We purposely omit data processing, understood as the computation of the navigation solution from the observables and the navigation message, since there are a number of well-established libraries and applications for that, such as GPSTk [Tol04, Sal10]. With this consideration in mind, the receiver is able to generate observables and navigation data in standard-compliant output files. Nevertheless, for the sake of completeness, we included a basic PVT algorithm implementation.

In this context, we introduce an open-source, real-time GNSS software defined receiver (so-named GNSS-SDR) that features shared memory techniques to manage efficiently the data flow between receiver blocks, the use of hardware-accelerated instructions for time-consuming vector operations like carrier wipe-off and code correlation, and the availability to compile and run on multiple software platforms and hardware architectures.

The Chapter starts with Section 6.1, highlighting the relevance of software receivers made patent in recent times. The software development methodology is introduced in Section 6.2. With the aim of “not reinventing the wheel”, the well-established concept of software design patterns, widely used by software developers, is introduced in Section 6.2.2 and a complete set of use cases is presented. Furthermore, in order to provide a solid development framework, Section 6.2.3 establishes the computer programming style rules, as well as defining C++ as the preferable programming language for the project at hand. Important features beyond the receiver’s source code, such as the development ecosystem, which includes a website (www.gnss-sdr.org) with instructions for users and developers, a set of communication tools, and a revision control system and quality assurance, are also considered in this Section.

The second part of the Chapter is devoted to the GNSS-SDR software design. Section 6.3.1 briefly introduces the widely-used GNU Radio framework that provides the signal processing

runtime and processing blocks to implement software radio applications. It constitutes the GNSS-SDR backbone. The main characteristics and goals of the proposed software receiver and the overall receiver architecture can be found in Section 6.3. We identify the most useful signal sources and data output formats in this Section.

Then, we move the focus to the implementation aspects of the receiver: Section 6.4.1 starts with details about the receiver code structure and the different abstraction layers involved in the control plane. The control plane is in charge of providing the configuration options and signal samples flow management to the receiver signal processing blocks. Using this highly modular and scalable framework, the receiver signal processing plane is detailed in Section 6.4.2. The implementation details of a set of acquisition, tracking, observables computation, navigation message decoding, and basic PVT algorithms are given.

Finally, the performance of the developed software is analyzed in Section 6.5, where the receiver operation is tested in both synthetic and real-life scenarios and Section 6.6 concludes the Chapter.

6.1 Introduction to GNSS software receivers

The first commercial GPS device was first offered for sale in 1981. The TI 4100 NAVSTAR navigator [War82] was a big ($37.3 \times 44.5 \times 21.1$ cm) and heavy (≥ 1.5 kg) device that required more than 90 W of power to operate. Nowadays, location has become an embedded feature not only on medium and high-end mobile phones, but also on other portable devices such as digital cameras and portable gaming consoles. This massive deployment of GNSS receivers requires a high level of integration, a low cost, a small size and a low power consumption, which has pushed the leading GNSS IC manufacturers such as Qualcomm Inc., Broadcom Corporation, Cambridge Silicon Radio (CSR, merged with SiRF in 2009), Texas Instruments Inc., STMicroelectronics, u-Blox AG, Maxim or MediaTek to offer single-chip solutions easy to integrate in multi-function devices. Consequently, the RF front-end and the baseband processing are jointly implemented in monolithic ICs, tiny black boxes leaving the user no possibility to interact or to modify the internal architecture or the algorithmics.

Developers of location services and applications are interested in using the location information provided by GNSS but not in how the position has been obtained. Moreover, most of the mobile operating systems provide an abstraction layer to hide all the complexities involved in the access to the positioning device. The developer typically has access to the geographic coordinates, the estimated speed and heading, and the estimated accuracy (see e.g., Apple iOS location framework REF or the Android location Application Programming Interface (API) REF). This abstraction layer simplifies a lot the job of the application developer, but leaves no way to observe or modify any internal aspect of the receiver.

As an opposite driving force, as we have seen in Chapter 2, the advent of a number of new GNSS (Galileo, COMPASS), the modernization of existing ones (GPS L2C and L5, Glonass L3OC) and the deployment of augmentation systems (both satellite-based, such as WAAS in the USA, EGNOS in Europe, and MSAS in Japan; and ground-based, such as WiFi positioning and Assisted GNSS provided by cellular networks) depict an unprecedented landscape for receiver designers [FP11c]. In the forthcoming years, many new signals, systems and frequency bands will be available for civil use, and their full exploitation will require a thoughtful redesign of the receiver's architecture and inner algorithms. New available signals pose the challenge of multisystem, multiband receivers' design, including issues such as interference countermeasures, high-precision positioning for the mass-market, assisted GNSS, and tight hybridization with other technologies.

In addition to being black boxes hidden by an abstraction layer, current mass-market GNSS ICs are clearly constrained in terms of reconfigurability, flexibility, and capacity to be upgraded. This fact has headed receivers' designers to the software radio paradigm, in which an analog front-end performs the RF to intermediate frequency (or directly to baseband) conversion prior to the ADC. All remaining signal and data processing, including the hybridization with other

systems, are defined in the software domain. This approach provides the designers with a high degree of flexibility, allowing full access and possibility of modification in the whole receiver chain.

The last decade has witnessed a rapid evolution of GNSS software receivers. Since the first GPS SPS software receiver described in [Ako97], where the concept of bandpass sampling (or intentional aliasing) was introduced, several works were devoted to architectural and implementation aspects [Kru01, Cha01, Led03, Hec06, Hur09, Hum11, Mit09, Hob10, Li10]. Textbooks [Tsu00, Bor07] increased the awareness of the community about the great benefits provided by software receivers with respect to the traditional hardware-oriented approach, providing Matlab implementations of a complete GPS receiver, and [Pet09b, Pri11] provide discussions about high-level architecture design.

Today, there are solutions available at academic and commercial levels, usually not only including programming solutions but also the development of dedicated RF front-ends. As examples, we can mention the GSNRx (GNSS Software Navigation Receiver [Pet09b]) developed by the Position, Location, And Navigation (PLAN) Group of the University of Calgary; the ipexSR, a multi-frequency (GPS C/A and L2C, EGNOS and GIOVE-A E1-E5a) software receiver developed by the Institute of Geodesy and Navigation at the University FAF Munich [Ang07, Sto10] or N-Gene, a fully software receiver developed by the Istituto Superiore Mario Boella (ISMB) and Politecnico di Torino that is able to process in real-time the GPS and Galileo signals broadcast on the L1/E1 bands, as well as to demodulate the differential corrections broadcast on the same frequency by the EGNOS system. This receiver is able to process in real-time more than 12 channels, using a sampling frequency of approximately 17.5 MHz with 8 bits per sample [Fan09].

6.2 Software development methodology

After a brief review of the GNSS SDR challenges and objectives in the introductory section, this Section aims to provide the basis to attain the objective of well-written software receiver. The goal is to provide a suitable framework to develop a flexible, efficient, and maintainable software-based receiver, using the state-of-the-art software design techniques. The overview starts defining the appropriate notation and describing the design patterns applied to the problem at hand, and it finishes with the definition of the development ecosystem where the developers' community work together.

6.2.1 Software design notation

As a previous step before entering into design details, we briefly define the software design notation that is used in the rest of the Chapter. The notation should let software designers represent modules, interfaces, hidden information, concurrency, message passing, invocation of operations, and overall program structure in a comprehensive and standardized way. A key aspect of an object-oriented software design is the class hierarchy. This is represented using the Unified Modeling Language (UML) standard. Additionally, since the software receivers usually implement state machines, an extension of UML for FSM is also defined here.

6.2.1.1 UML notation for class diagrams

We used a simplified version of the UML standard [UML11]. Classes are described as rectangles with three sections:

- the upper part holds the name of the class,
- the middle part contains the attributes of the class, and
- the bottom part gives the methods or operations the class can take or undertake.

The attributes and methods sections of a class lists each of the class's members on a separate line. To specify the visibility of a class member there are defined the following notations that must be placed before the member's name :

- (+) Public.
- (-) Private.
- (#) Protected.
- (~) Package.
- (/) Derived.
- (underline) Static.

The class methods or operations are documented using the following notation:

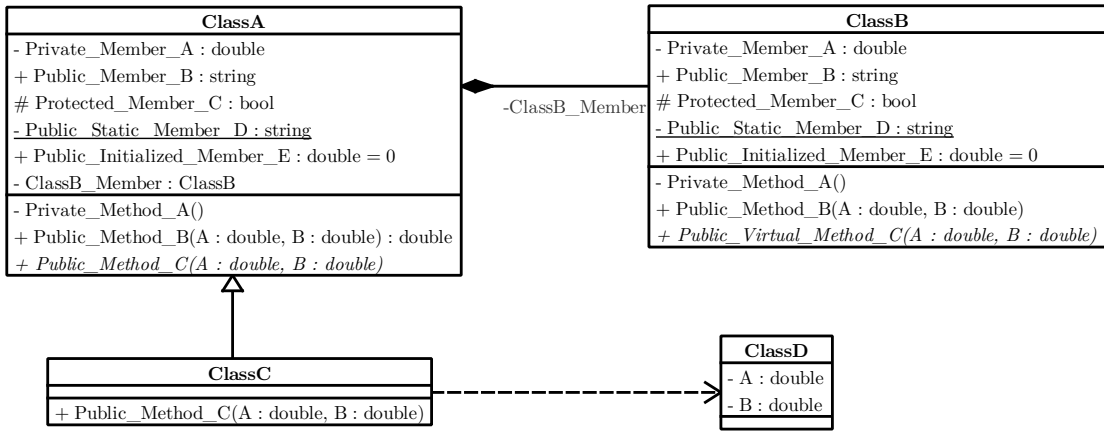
```
name(parameter_list) : type_of_value_returned
```

If a method or operation is *pure virtual*¹ it is denoted using *italics*. If the class is completely virtual, its name is also denoted in *italics*.

The class relationships are represented using:

- **dependency**: a dashed line with an arrow head from ClassA to ClassB represents the dependency. This relationship simply means that ClassA somehow depends upon ClassB, for instance, importing a library that uses the ClassB.
- **composition**: If the class dependency is established holding a member of the parent class, that is, ClassA has a public or private class member of ClassB, the relationship is represented using a solid line with a solid diamond-shaped head.
- **generalization**: when ClassA inherits from ClassB, we say that ClassA is the subclass of ClassB and ClassB is the superclass (or parent class) of ClassA. The UML modeling notation for inheritance (or generalization) is a solid line with a closed arrowhead pointing from the subclass to the superclass.

Fig. 6.1 shows an exemplifying diagram of class relations in UML.



Diaograma diaograma de clase Página **Figure 6.1:** Class relations in UML diagram.

6.2.1.2 UML notation for finite state machines

UML statecharts preserves the general form of the traditional state diagrams. The UML state diagrams are directed graphs in which nodes denote states and connectors denote state transitions. A basic UML FSM can be described using the following elements [UML11]:

¹In object-oriented programming, a virtual function or virtual method is a function or method whose behavior must be overridden within an inheriting class by a function with the same signature.

- **events:** is something that happens that affects the system. In UML, the term event refers to the type of occurrence rather than to any concrete instance of that occurrence. An event can have associated parameters, allowing the event instance to convey not only the occurrence of some interesting incident but also quantitative information regarding that occurrence.
- **states:** capture the relevant aspects of the system's history in an efficient way. A state can abstract away all possible (but irrelevant) event sequences and capture only the relevant ones.
- **transitions:** when an event instance is dispatched, the state machine responds by performing actions. Switching from one state to another is called *state transition*, and the event that causes it is called the triggering event. The transitions, represented as arrows, are labeled with the triggering events followed optionally by the list of executed actions.
- **entry and exit actions:** every state in a UML statechart can have optional entry actions, which are executed upon entry to a state, as well as optional exit actions, which are executed upon exit from a state. Entry and exit actions are associated with states, not transitions. Regardless of how a state is entered or exited, all its entry and exit actions will be executed. Because of this characteristic, UML statechart behave like Moore state machines.

Fig. 6.2 shows an exemplifying UML statechart. In the figure, the reset event switch the initial state to *State_0*. At this time, the state machine executes the entry action *Action_A*. If an event *Event_A* arrives, then the state machine executes the exit action *Action_B* and switch its state to *State_1*.

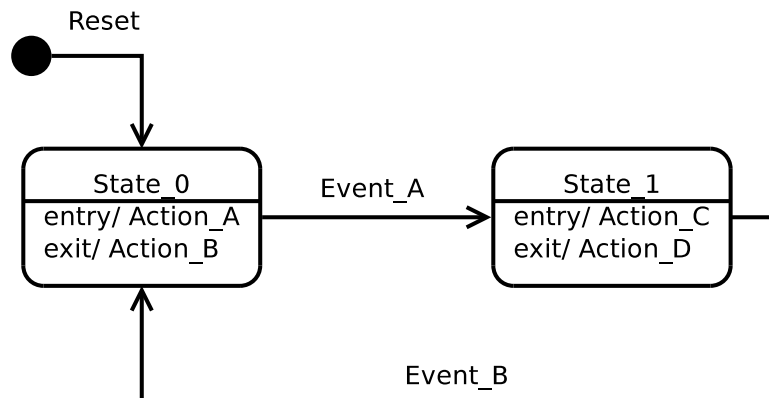


Figure 6.2: Sample FSM statechart UML diagram.

6.2.2 Design Patterns for GNSS Software Receivers

An introduction to software design patterns in the context of GNSS receivers can be found in [FP10a, FP11a], hereafter we recall the most relevant concepts, definitions, and use cases.

The concept of software design pattern was firstly introduced in [Gam95], a book that rapidly became a fundamental reference on the topic. Software design patterns are descriptions of solutions to common software problems arising in different contexts, capturing recurring structures and dynamics among software participants to facilitate reuse of successful, thoughtfully proven designs.

They generally codify expert knowledge of design strategies, constraints and best practices. Following a pattern helps to resolve key design forces such as flexibility, extensibility, dependability, predictability, scalability, and efficiency. They are not code recipes but generalized solutions to commonly occurring problems, showing relationships and interactions between classes or objects but without specifying the final application instantiations.

The work in [Dou02] took these concepts further, and explored their applicability to real-time systems. Other references are [Sch00], dealing with concurrency issues, [Sha04], that introduced the object pool pattern, and [Ker04], that advocates using patterns for improving an existing design.

Patterns can be classified into *architectural*, when they apply to large-scale organization of subsystems and components, how they are constructed or how are they managed, and *mechanistic*, when they are more local in scope and define mechanisms for object collaboration. This latter type can be subdivided into categories of *creational* (patterns that deal with object creation mechanisms), *structural* (identifying ways to realize relationships between entities), or *behavioral* (identifying common communication patterns between objects that increase flexibility).

A software GNSS receiver can take profit of those design patterns as follows:

- **Architectural patterns:** are related to the system organization into sets of sequential transformational elements (where actual signal processing is performed), and how to handle concurrency and memory management. They solve and delineate some essential cohesive elements of the software architecture. The following architectural patterns are candidates to be applied in GNSS-SDR software:
 - **Channel pattern:** GNSS algorithms process the input data stream, applying the same set of operational transformations, such as acquiring or tracking the signal of different satellites. It is desirable an architectural structure that improves throughput capacity (i.e., the number of satellites to be tracked) with the replication of architectural units, allowing efficient parallel processing of data. The Channel Architecture pattern [Dou02] is well suited to the sequential transformation of data from one state or form to another. It is possible to group all the signal processing related to a single satellite into a channel subsystem. A channel can be thought of as a pipe that sequentially transforms data from an input value to an output value.
 - **State machine pattern:** it should be possible for an object to alter its behavior when its internal state changes. In GNSS this happens during the acquisition to tracking transitions and vice-versa or in the decoding of the navigation message. A State Machine [Sha06] pattern makes the state-dependent behavior to be localized in the state classes. The transition logic is separated from the behavior in a particular state and the state classes should only notify a context of a particular event. This pattern does not contain redundant interfaces for the context and the state classes they all implement the same interface. The implementation of an interface is trivial and could be generated automatically. Transitions could be implemented as a simple index lookup. Also note that the automata interface is implemented by the context and by the state classes. This allows making certain compile-time consistency check.
 - **Message queuing pattern:** in most multi-threaded systems, threads must synchronize and share information with others. Two primary things must be accomplished. First, the tasks must synchronize to permit sharing of the information, for instance concurrent access to the signal sample flow or the output of an acquisition module. Second, the information must be shared in such a way that there is no chance of corruption or race conditions (condition in which a result depends on the order of execution, but the order of execution cannot be predicted). The Message Queuing pattern [Dou02] provides a simple means for threads to communicate information among one another. Each thread owns a message queue that stores messages received asynchronously. When the thread is active, it reads messages from the queue and processes them, usually by dispatching them to an internal object. Each queue is protected by a mutual exclusion semaphore, since the queue itself is a shared resource (shared between the owning thread and the thread objects that want to send it messages), it must be protected from simultaneous access. This is a well-known approach to the producer-consumer problem that frequently arise in multi-threaded systems, particularly used to decouple processes that produce and consume data at different rates.

- **Smart pointer pattern:** when dealing with pointers, precise management is easy to forget about when dealing with all possible execution paths. Inevitably, somewhere a pointer is destroyed (or goes out of scope), but the memory is not properly freed (a memory leak), memory is released but nevertheless accessed (dangling pointer), or memory is accessed but not properly allocated (uninitialized pointer). These problems are notoriously difficult to identify using standard means of testing and peer reviews. The basic solution of the Smart Pointer pattern is to reunify the pointer into an object that contains the actual pointer as an attribute, as well as constructor, destructor, and access operations, thus preventing inappropriate use.
- **Mechanistic patterns:** are related to the definition of object collaboration mechanisms. The following architectural patterns are candidates to be applied in GNSS-SDR software:
 - **Factory method pattern:** one of the most attractive features of a software receiver is the possibility of interchanging algorithms (for instance, different implementations of signal acquisition and tracking) and observe its impact in the whole system, or establish fair comparisons among them. The creation of such objects often requires complex processes not appropriate to include within a composing object. The object's creation may lead to a significant duplication of code, may require information not accessible to the composing object, or may not provide a sufficient level of abstraction. A suitable solution is the definition of an interface for creating generic algorithm objects, but let subclasses decide which class to instantiate. The Factory Method [Gam95] lets a class defer instantiation to subclasses. Factory Methods eliminate the need to bind application-specific classes into the code, provide hooks for subclasses (thus making more flexible the creation of objects inside a class with a factory method than creating an object directly, for instance the addition of a new tracking method), and connect parallel class hierarchies (thus localizing knowledge of which classes belong together).
 - **Strategy pattern:** it is easy to add a dependency on a class; for instance, the implementation of an specific signal processing algorithm can be encapsulated into a library. However, the inverse is not that easy and getting rid of an unwanted dependency can turn into complicated refactoring work or even worse, blocking the user from reusing the code in another context. This kind of problem can be solved by means of the Strategy pattern [Gam95], which defines a family of algorithms, encapsulates each one, and makes them interchangeable, letting the algorithms vary independently from clients that use them. The solution follows the key principle of a reusable object-oriented design is: program to an interface, not an implementation [Gam95]. Isolating the interface from the implementation means the implementation can vary, and that is a healthy dependency relationship. This approach gives the developer flexibility, but it also separates the really valuable part, the design, from the implementation, which allows clients to be decoupled from the implementation. In fact, an abstract class gives you more flexibility when it comes to evolution. You can add new behavior without breaking clients.
 - **Template method pattern:** when we want to improve the implementation of a certain part of an algorithm, it is desirable to not have to reprogram the complete algorithm implementation. An efficient solution is to define the operation skeleton of an algorithm, deferring some steps to subclasses. The Template Method pattern [Gam95] lets subclasses redefine certain steps of an algorithm without changing the algorithm's structure. Template Methods are a fundamental technique for code reuse. They are particularly important in class libraries, because they are the means for factoring out common behavior in library classes.

6.2.3 Computer Programming Style

In the previous Section, we highlighted how software patterns can help in the reuse of proven software designs and architectures, preserving crucial design information, and guiding design

choices for application developers. In this section, we focus the attention on the coding style guidelines, which become an important topic in every community-maintained software.

If design patterns provides conceptual solutions for different problems, coding styles provides an efficient (and reusable) way to implement them. Since the seminal work by Kernighan et al. in 1974 [Ker74], there is a clear concern on the style in writing software and its impact in the final quality of the product. Following programming guidelines and code conventions not only helps to avoid introducing errors, but cuts maintenance costs and favours effective code reuse.

Generic programming is a well-established style in which algorithms are written in terms of to-be-specified-later types that are then instantiated when needed for specific types provided as parameters. Software entities created under this paradigm are known as parameterized types [Gam95], or *templates* when using C++. Templates are used by a compiler to generate temporary source code, which is merged by the compiler with the rest of the source code and then compiled. This mechanism, known as static polymorphism, along with being a way of pre-evaluating some of the code at compile-time rather than at run-time, also reverts in more optimized code, smaller executables, shorter runtimes, and lesser memory requirements, avoiding the overhead of run-time polymorphism.

Compile-time execution refers to the ability of a compiler, that would normally compile a function to machine code and execute it at run time, to execute the function at compile time. Since in a software receiver working in real-time performance is critical, we should maximize compile-time work (which usually is not an issue), and even in an offline, not time-restricted signal processing this methodology provides benefits such as syntax and semantic analysis, code generation, timings, and earlier bug detection.

As a necessarily non-comprehensive list of good coding practices, we can mention the need of clear functional and detailed specifications (requirements, architecture, analysis, design, and testing) before jumping into programming, the observation of naming conventions (set of rules for choosing the character sequence to be used for identifiers which denote variables, types, classes, etc.), code documentation, and the absence of magic numbers (unnamed or ill-documented numerical constant values). References [Mey01], [Mey05], and [Mey96] provide a wide-scope list of good coding practices.

6.2.3.1 C++ as a suitable programming language for GNSS SDR receivers

Since programming styles are often designed for a specific programming language, we first discuss the choice of C++ for the GNSS software receiver presented in this Dissertation. The rationale relies, on the one hand, on the fact that C++ is a dominant language that makes it much easier to recruit experienced programmers, and, on the other hand, on the availability of a number of well-written, peer-reviewed libraries (see, e.g., Boost libraries [Abr04, Kar05]), and advanced compilers.

Although it allows *close to the metal* programming (thus addressing efficiency), C++ also adds layers of abstraction that make possible the use of templates. Moreover, a new version of the language, named C++11, has been recently approved as an ISO (International Organization of Standardization) standard [ISO11]. This ensures that decades from now, today's standard conforming C++ programs will run with minimal modifications, just as an older C++ programs do today. It also ensures portability and the availability of compilers. This new version provides facilities for writing concurrent code (e.g., for multi-core machines) in a type safe-manner, smart pointers, new memory-optimized ways of object handling, and tons of new core and library features that are very convenient for software radio applications.

6.2.3.2 Development ecosystem

Infrastructure for project management and code development is of equal importance than programming style. A set of efficient and easy-to-use tools helps managers and developers to keep tight to objectives and schedule, avoiding improper communication and facilitating feedback among users and developers.

- *Project management tool*: This includes scheduling, resource allocation, collaboration software, communication, quality management and documentation or administration systems. When web-based, it should be accessed from any type of computer, ease of access-control, and multi-user. Storage “in the cloud” of relevant documents is suggested.
- *Version control system*: An application that automates the process of keeping an annotated history of the project, allowing reversion of code changes, change tracking, and bug tracking is essential. As examples we can mention Subversion² [SVN] and git [GIT]. Trac [TRA] and redmine [RED] are web-based tools that integrates well.
- *Integrated Development Environment (IDE)*: Admitting that each developer has his/her own preference, a full-featured IDE increases productivity. Usually, an IDE consists of a source code editor, an interface to a compiler and/or an interpreter, build automation tools, and a debugger, but modern ones also provide integration with the version control system, a class browser, an object inspector, and a class hierarchy diagram. Eclipse [ECL] is a free and open source option.
- *Build tool*: The build process should be easily maintained and highly portable. When not thought out well, development time shifts towards build system tweaking instead of source file coding. There are several tools that automatize the process, such as bjam [BJA] and CMake [CMa]. Regarding the compiler, we suggest the GNU Compiler Collection (gcc) [GCC], a multi-platform, world-class optimizing compiler that closely follows language standards.
- *Communication*: An email distribution list uses to be an efficient communication tool among developer team members. When needed, can be complemented with net-meetings and personal instant messaging. In these cases, emailed minutes of meeting are useful to keep logging of discussions and decisions.

6.3 GNSS-SDR design

Hereafter we present a software project, so-called GNSS-SDR and accessible from the website www.gnss-sdr.org, that implements the concepts presented so far. The design and implementation is heavily based on the GNU Radio [GRa], a well-established framework that provides the signal processing runtime and processing blocks to implement software radio applications. Frameworks are a special case of software libraries - they are reusable abstractions of code wrapped in a well-defined API, yet they contain some key distinguishing features that separate them from normal libraries: the overall program’s flow of control is not dictated by the caller, but by the framework; and it can be extended by the user usually by selective overriding or specialized by user code providing specific functionality. Software frameworks aim to facilitate software development by allowing designers and programmers to devote their time to meeting software requirements rather than dealing with the more standard low-level details of providing a working system, thereby reducing overall development time.

In case of GNU Radio, it incorporates many of the design patterns described in Section 6.2.2. From an architectural point of view, a GNSS-SDR application can be seen as a factory with different working lines where we put raw data at the input and we get processed data at the output. This raw data is, in our case, the continuous stream of signal samples and the processed data is the position of the receiver updated constantly and regularly. This simplification describes quite effectively the GNSS-SDR architecture. Since the designer should focus in solving the problem of introducing the raw data into the application, distributing it through the factory line, and gathering the results at the other end. It is an efficient implementation of the *Channel architecture pattern* and it becomes one of the main contributions to the GNSS-SDR architecture.

Adopting this approach has several benefits, namely that the architecture can be easily mapped with a hardware implementation of any signal processing device, it implies a degree

²Although we provide web references, we suggest readers interested in the forthcoming mentioned software tools, denoted in sans-serif, to look for the most updated information in the web search engine of their choice.

of modularity that is required by SDR applications, the concepts involved do not require deep knowledge of software engineering concepts and can be used in an interdisciplinary environment, and the fact that using a design pattern introduces a component of standardization that is always desired for software design.

The user can build a receiver by creating a graph where the nodes are signal processing blocks and the lines represent the data flow between them. GNU Radio incorporates a *scheduler* that assigns working threads to each block that allows automatic scheduling in multicore processors, hiding all the complexity behind a simple and robust API. It uses *shared memory* to manage efficiently the flow of data between blocks, and offers a large set of well-programmed blocks that provide implementations for very common signal processing tasks. In contrast, GNU Radio does not provide any standard way to provide control over the blocks.

Hereafter can be found an overview of the GNU Radio architecture, focused in the real-time scheduler which is the core component of the proposed receiver implementation.

6.3.1 GNU Radio architecture

GNU Radio uses a modular, block-based architecture with a hybrid Python/C++ programming model. Python provides a high-level abstraction layer that enables the implementation of complex interactions between blocks, similar to a block diagram design, while signal processing functionality that requires high-performance and low-level programming is implemented in C++. One of the interesting features of the GNU Radio framework is the extensive library of community-maintained and tested functional blocks. The pre-defined blocks provide signal processing functionality, encapsulate sources and sinks of data and provide simple type conversions.

The blocks, written in C++, have an automatically-generated Python “wrapper” or interface that allows them to be manipulated, connected, and utilized in Python. However, the GNSS-SDR receiver provides its own overlay layer to the plain GNU Radio framework, thus replacing the Python functionality with a pre-defined block diagram and particularized for the GNSS receiver requirements, as we will see in Section 6.3.2.2.

The GNU Radio software architecture is composed of the following core modules:

- *GR_block*: encapsulates the computational phase which implements the data or signal processing functions such as filter, decimator, or custom implementations like GNSS correlators. Depending on the exact function, a block may have one or multiple data/signal input stream(s) and/or output stream(s).
- *GR_buffer*: is used internally to connect the blocks together. It uses the shared memory³ technique to minimize the memory requirements and to maximize the data throughput between blocks. It implements a thread-safe, single writer, multi-reader shared ring buffer.
- *flowgraph*: is a set of interconnected *GR_blocks*.
- *GR_top_block*: is used to define the links between *GR_blocks*, instantiates one or more flow graphs, and assign an scheduler to each of them. *GR_top_block* is also in charge to initiate and stop the flow graph activity.
- *scheduler*: is used by GNU Radio for allocating computational resource among *GR_blocks* within a flow graph at runtime. There are two types of scheduler: single threaded scheduler and thread-per-block (TPB) scheduler. TPB scheduler can exploit the multitasking capability of modern multi-core and hyperthreading processors. It is enabled by default in current versions of GNU Radio.

GNU Radio processes data as a stream of homogeneous items. These items are typically built-in C++ standard types such as floats, doubles or complex values but may include any C++ element for which the function `memcpy()` is a valid constructor. This includes the valuable option of interchanging data between blocks using structures and classes.

³In computing, shared memory is memory that may be simultaneously accessed by multiple programs with an intent to provide communication among them or avoid redundant copies. Shared memory is an efficient means of passing data between programs or threads.

The GNU Radio flow graph computations can be jointly modeled as a Kahn process [Kah74, Kah77]. A Kahn process describes a model of computation where processes are connected by communication channels to form a network. Processes produce data elements or tokens and send them along a communication channel where they are consumed by the waiting destination process. Communication channels are the only method processes may use to exchange information. Kahn requires that execution of a process be suspended when it attempts to get data from an empty input channel. A process may not, for example, examine an input to test for the presence or absence of data. At any given point, a process is either enabled or it is blocked waiting for data on only one of its input channels: it cannot wait for data from one channel or another. Systems that obey Kahn's mathematical model are determinate: the history of tokens produced on the communication channels does not depend on the execution order [Kah74]. With a proper scheduling policy, it is possible to implement SDR process networks holding two key properties:

- **Non-termination:** understood as an infinite running flow graph process without deadlocks situations, and
- **Strictly bounded:** the number of data elements buffered on the communication channels remains bounded for all possible execution orders.

The reader is referred to Parks, PhD dissertation for an analysis of process networks scheduling [Par95].

The GNU Radio scheduler assures that GNU Radio flow graph satisfies Kahn model rules. It breaks each data stream into finite length vectors and feeds these vectors one at a time into each block in the flow graph using the algorithm described in Algorithm 1.

Algorithm 1 GNU Radio Scheduling loop [GNU06].

```

while GR_top_block running do
    for  $i = 1, \dots, \text{NBLOCKS}$  do
        if sufficient room in output port buffers and data at input ports of block  $i$  then
            call general_work() on block  $i$ 
        end if
    end for
end while

```

In the algorithm, each block provides a `general_work()` function that is called by the scheduler. The function processes one vector of data per input. The size of the vectors depends on many factors, in particular, the data type associated to block inputs, and it can also vary from call to call for a given block. It is possible to specify the minimum amount of data in each input required to execute a particular block `general_work()` function. The rate of data flowing into the block can vary between different input streams, but the rate of data flowing out of a block must be constant across all output streams.

Fig. 6.3 shows an illustrative flow graph block diagram with all the underlying elements. The blocks are interconnected by means of dedicated memory buffers, created by the GNU Radio runtime using the `GR_buffer` class. The data stream is emitted from output ports and read into input ports. Every block declares fixed unit sizes on each of its input ports that are necessary to support one atomic operation of the block's processing task (the `general_work()` method). The block also has a fixed unit size for the data conveyed to its output ports in one atomic operation. These unit sizes are known to the scheduler at the initialization process, and the scheduler arranges memory mappings to hold the data that will be exchanged across connections. For the duration of the flow graph configuration, the mappings are static: both the location and size of memory allocations are fixed. The scheduler is also responsible for memory management during runtime, that is, arranging for the storage and access of intermediate data products as transmission data flows through the signal processing chain. The scheduler exercises this management function in part via delegation to helper classes such as `GR_buffer` or `GR_buffer_reader`.

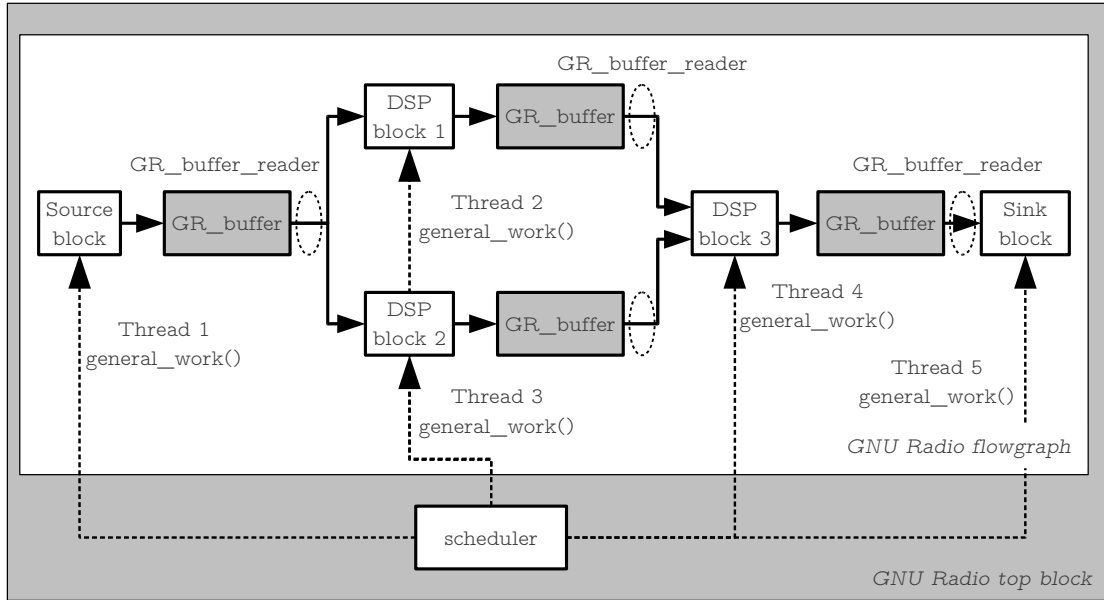


Figure 6.3: GNU Radio scheduler illustrative flow graph.

6.3.2 GNSS-SDR architecture

The proposed receiver provides an interface to different RF front-ends and implements all the receiver chain up to the navigation solution. Its design allows any kind of customization, including interchangeability of signal sources, signal processing algorithms, interoperability with other systems, output formats, and offers interfaces to all the intermediate signals, parameters and variables.

The receiver runs in a commodity personal computer and provides interfaces through USB and Ethernet buses to a variety of either commercially available or custom-made RF front-ends, adapting the processing algorithms to different sampling frequencies, intermediate frequencies and sample resolutions. This makes possible rapid prototyping of specific receivers intended, for instance, to geodetic applications, observation of the ionospheric impact on navigation signals, GNSS reflectometry, signal quality monitoring, or carrier phase based navigation techniques.

Testing is conducted both by the systematic functional validation of every single software block (following a test-driven developing approach and using unit testing as a verification and validation methodology as described in Section 6.2.3), and by experimental validation of the complete receiver using both real and synthetic signals. In the sequel, each of the receiver sections are described, following the satellite signal logic path.

6.3.2.1 Signal sources

An appealing feature for a software receiver is the possibility of working in real-time with real signals, when the processor is fast enough, or in an offline mode (post-processing) working with raw signal samples stored in a file, when the complexity of the implementation prevents from a real-time processing. Signals might also need to be created by synthetic signal generators in order to conduct experiments with controlled parameters.

Ideally, an all-software receiver should perform digitization right after the antenna. Due to technological constraints, there is still the need for amplification and downconversion before the ADC, the so-called RF front-end, as we saw in Chapter 5. We also need an interface between the ADC output and the PC (or other general-purpose processor) in which the software receiver is running. This “hardware portion” of the receiver can be implemented with commercial off-the-shelf components or taking advantage of existing RF application-specific ICs, or with custom-designed front-ends, such as the GNSS array platform presented in this Dissertation.

There are several signal grabbers commercially available. For instance, the Universal Software Radio Peripheral (USRP) [Ett10] is a general-purpose family of computer-hosted hardware for software radios that, equipped with a DBSRX daughterboard [Ett11] that can be used as a customizable RF front-end for GNSS receivers. Other more-specific, lower cost solutions are usually composed of an antenna, a RF IC front-end, a Complex Programmable Logic Device (CPLD) that arranges sample bits in bytes, and a USB 2.0 microcontroller, such as the SiGe GN3S Sampler v2, based on the SiGe 4120 GPS IC [SiG09], or the recently appeared One Talent GNSS receiver family SdrNav [GNS], among others.

In summary, the two main requirements for the software receiver in terms of signal sources can be defined as:

- it should allow both real-time (when possible) and off-line operations, and
- it should be able to use a variety of signal sources (files and RF front-ends).

6.3.2.2 Core components

The software architecture has to resolve design forces that sometimes can be antithetical, such as flexibility vs robustness, or portability vs efficiency. With the objective of attaining real-time in mind, efficiency should be addressed specially in those blocks that work with high data rates (mainly, signal conditioning, Doppler removal, and correlation), while other blocks working at medium rate (tracking, extraction of navigation parameters) or low rate (measurement generation, navigation solution) can be implemented targeting robustness and reliability.

The receiver's general block diagram is depicted in Fig. 6.4. It consists of a **Control Plane** in charge of managing the whole receiver and the interactions with the underlying operating system, external applications, and user-machine interface; and a **Signal Processing Plane** that extracts information from raw signal samples.

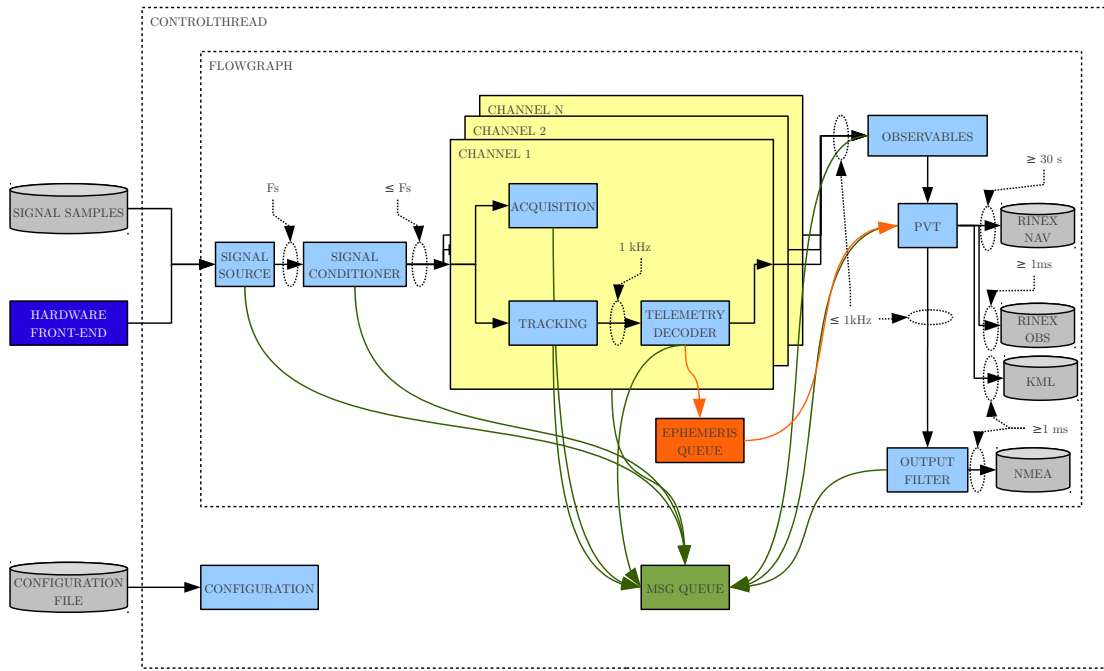


Figure 6.4: Diagram of the modules that form the GNSS software receiver. Each module accepts multiple implementations, which can be selected by the user.

The nature of a GNSS receiver imposes some requirements in the architecture design. Since the composition of the received signals will change over time (initially, some satellites will be visible, and after a while, some satellites will not be visible anymore and new ones will show up), some channels will lose track of their signals and some new channels will have to be instantiated

to process the new signals. This means that the receiver must be able to activate and deactivate the channels dynamically, and it also needs to detect these changes during runtime.

In that sense, there is a need to design a communication mechanism within the signal processing blocks and the control plane. The Message Queuing pattern approach (see Section 6.2.2) is a suitable solution to this problem.

There is a control thread running in parallel to the flow graph that receives notifications by means of a thread-safe message queue and triggers changes in the application. Some of these notifications are sent directly from the processing blocks using the same instance of the queue. For instance, an acquisition block that finishes its processing and detects a satellite's signal, sends a notification to the control thread via a message queue indicating its success. The control thread will then change the internal configuration of the channel and pass the results of the acquisition process (i.e., detection of in-view satellite and rough estimations of its code delay and Doppler shift) to the tracking blocks. The behavior of the receiver is controlled by state-machines (see Section 6.2.2), where the stimulus are the messages coming from different signal processing blocks. Based on pre-defined reactions, the receiver activates or deactivates satellite channels or triggers the computation of the navigation solution.

In parallel to the control plane, signal processing blocks process the input data stream, concurrently applying the same set of operational transformations. Hence, a Channel Architecture pattern (see Section 6.2.2) is used to efficiently group and replicate each of the signal processing blocks related to a single satellite into a channel subsystem. The architecture of the signal processing plane is heavily based on the GNU Radio framework shown in Section 6.3.1, however, in order to isolate the signal processing blocks interface from its implementation, GNSS-SDR provides an abstraction overlay to the plain GNU Radio framework as follows:

1. Each of the signal processing blocks inside the flow graph is defined by an abstract interface: (i.e., signal source, signal conditioner, acquisition, tracking, telemetry decoder, observables, PVT, and output filter). Consequently, there is a common set of exposed interfaces used by the control plane that enables the receiver to easily interchange signal processing algorithms or upgrade the existing ones. This is an effective case of use of the Strategy pattern described in Section 6.2.2.
2. The particular implementation of an algorithm requires the implementation of an *adapter*, which is associated to a signal processing block interface. The adapter provides the link from the GNSS-SDR architecture to the underlying GNU Radio signal processing block. The receiver is able to select the desired algorithm in run-time, according to a configuration file, by means of a block Factory Method pattern as described in Section 6.2.2.
3. The DSP algorithm is implemented customizing a GNU Radio block, which uses the GNU Radio scheduler described in Section 6.3.1 to perform the required tasks and to generate the outputs to the subsequent blocks. The adapter acts as a container, while the GNU Radio signal processing block has access to the data stream of the preceding blocks (i.e., signal samples coming from the signal conditioner or tracking products).

The rationale to implement the aforementioned overlay is twofold:

- provide independence between the implementation particularities required by a GNSS SDR receiver, such as flexibility and reconfigurability, from the complexities associated to a high performance software radio framework, such as memory allocation/alignment, data type conversion, or thread synchronization, and
- minimize the learning curve required to write and test new algorithms or functionalities. It is possible to focus the work in the algorithm itself and leave the integration task to the receiver architecture. New algorithms can be selected with a straightforward modification of the configuration file.

The reader is referred to Section 6.4.1 and Section 6.4.2 for further insight into the control plane and signal processing plane implementation, respectively.

6.3.2.3 Data outputs

Most geodetic processing software for GNSS data use a well-defined set of observables:

- the pseudorange (code) measurement, equivalent to the difference of the time of reception (expressed in the time frame of the receiver) and the time of transmission (expressed in the time frame of the satellite) of a distinct satellite signal,
- the carrier-phase measurement of one or more carriers (actually being a measurement on the beat frequency between the received carrier of the satellite signal and a receiver-generated reference frequency), and
- the observation time being the reading of the receiver clock at the instant of validation of the carrier-phase and/or the code measurements.

The Receiver Independent Exchange Format (RINEX) is a data interchange format for raw satellite navigation system data, covering observables and the information contained in the navigation message broadcast by satellites. The most common version at present is 2.10, which enables storage of measurements from pseudorange, carrier-phase and Doppler systems for GPS or GLONASS, along with data from EGNOS and WAAS SBAS, simultaneously.

The need for improving the handling of the data files in case of files containing tracking data of more than one satellite system, each one with different observation types, led to significant modifications of the structure of data record. At this time of writing (February 2012), the newest version is 3.01 [Gur09], and includes defined formats for the modernized GPS signals, GLONASS, Galileo and SBAS. Hence, observable and navigation RINEX files are one of the output formats of the proposed software receiver.

Commercial receivers usually do not provide access to such intermediate information but offer direct access to the PVT solution and almanac data. The National Marine Electronics Association (NMEA) 0183 is the standard output format for commercial GPS receivers, and there is a plethora of compliant software available for handling and displaying such information. GNSS-SDR provides this output format for the PVT block module.

Finally, another interesting format to export geographic data is Keyhole Markup Language (KML), directly importable by software applications such as Google Earth, Google Maps, and Google Maps for mobile. KML is an open standard officially named the OpenGIS KML Encoding Standard (OGC KML), and it is maintained by the Open Geospatial Consortium, Inc. (OGC).

In summary, the requirements for the software receiver in terms of data outputs can be defined as:

- RINEX.
- NMEA.
- KML.

Fig. 6.5 shows a representative diagram of the possible user interactions with GNSS-SDR. The flexibility of the receiver is not only limited to the aforementioned standard output formats, but opens a myriad of custom interactions such as:

- Intermediate signals analysis by means of logging the internal variables and states to hard disk files.
- Real-time link to positioning and scientific applications.
- Data exchange to and from IMU units.
- Data exchange to and from instrumentation equipment.

6.4 GNSS-SDR Implementation

The GNSS receiver is written in C++ language, as discussed in Section 6.2.3.1. The receiver implementation contributes with several novel features such as the use of shared memory techniques

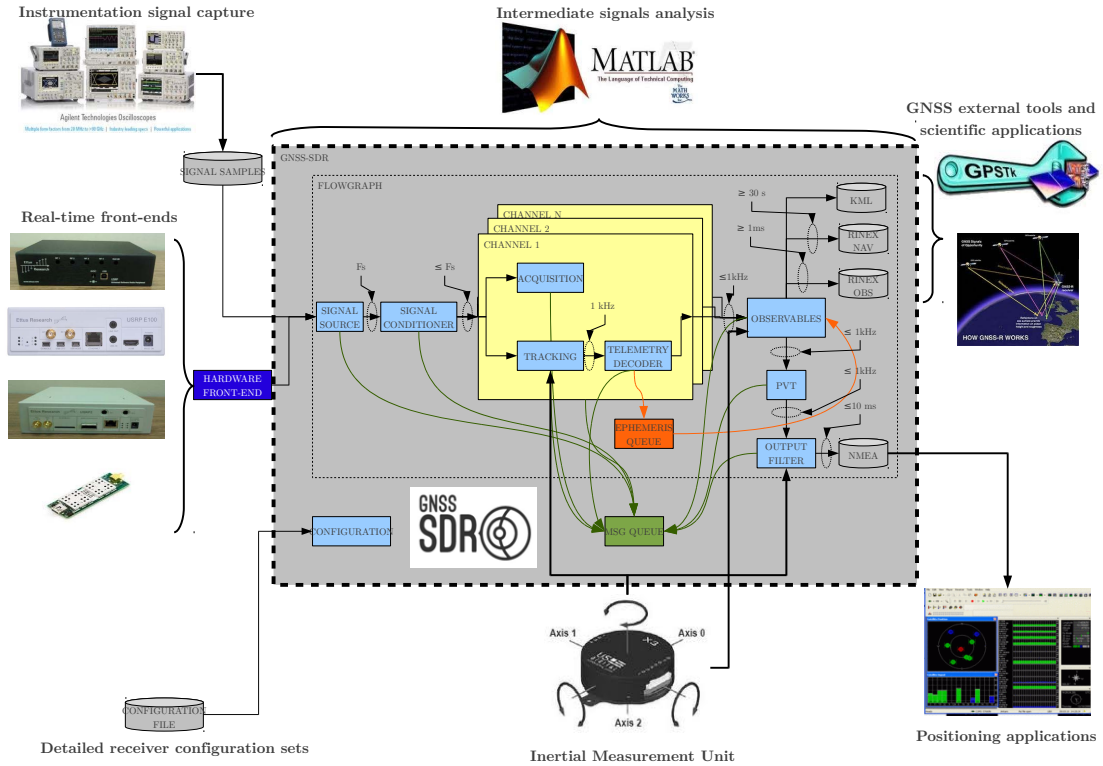


Figure 6.5: GNSS-SDR user interoperability diagram.

to manage efficiently the data flow between receiver blocks, the use of hardware-accelerated instructions for time-consuming vector operations like carrier wipe-off and code correlation, and the availability to compile and run on multiple software platforms and hardware architectures. This Section aims to provide the implementation details.

GNSS-SDR's main method initializes the logging library⁴, processes the command line flags⁵, if any, provided by the user, and instantiates a `ControlThread`⁶ object. Its constructor reads the configuration file, creates a control queue and creates a flow graph according to the configuration. Then, the program's main method calls the `run()` method of the instantiated object, an action that connects the flow graph and starts running it.

After that, and until a stop message is received, it reads control messages sent by the receiver's modules through a thread-safe queue and processes them. Finally, when a stop message is received, the main method executes the destructor of the `ControlThread` object, which deallocates memory, does other cleanup and gracefully exits the program.

As introduced in the previous Section (see Fig. 6.4), the software receiver is split into a **Control Plane** and a **Signal Processing Plane**. In the following subsections we provide details about their implementation.

6.4.1 Control plane

The Control Plane is in charge of creating a flow graph according to the configuration and then managing the modules. Configuration allows users to define in an easy way their own custom receiver by specifying the flow graph (type of signal source, number of channels, algorithms to be used for each channel and each module, strategies for satellite selection, type of output format,

⁴ At the time of writing, GNSS-SDR makes use of the Google C++ open source logging library [GLO]

⁵ At the time of writing, GNSS-SDR makes use of the Google C++ open source commandline flags library [GFL]

⁶ Actual name classes are denoted in sans-serif, while the signal processing block modules are denoted in *italics* fonts.

etc.). Since it is difficult to foresee what future module implementations will be needed in terms of configuration, we used a very simple approach that can be extended without a major impact in the code. This can be achieved by simply mapping the names of the variables in the modules with the names of the parameters in the configuration.

Properties are passed around within the program using the `ConfigurationInterface` class. There are two implementations of this interface: `FileConfiguration` and `InMemoryConfiguration`.

`FileConfiguration` reads the properties (pairs of property name and value) from a file and stores them internally. `InMemoryConfiguration` does not read from a file; it remains empty after instantiation and property values and names are set using the `set` property method. `FileConfiguration` is intended to be used in the actual GNSS-SDR application whereas `InMemoryConfiguration` is intended to be used in tests to avoid file-dependency in the file system. Classes that need to read configuration parameters will receive instances of `ConfigurationInterface` from where they will fetch the values. For instance, parameters related to `SignalSource` should look like this:

```
; This is a comment line
SignalSource.parameter1=value1
SignalSource.parameter2=value2
```

The name of these parameters can be anything but one reserved word: `implementation`. This parameter indicates in its value the name of the class that has to be instantiated by the factory for that role. For instance, if we want to use the implementation `DirectResampler` for module `SignalConditioner`, the corresponding line in the configuration file would be

```
SignalConditioner.implementation=DirectResampler
```

The system is very versatile and easily extensible since the configuration is just a set of property names and values without any meaning or syntax. The application defines a simple accessor class to fetch the configuration pairs of values and passes them to a factory class called `GNSSBlockFactory`. This factory decides which class needs to be instantiated and which parameters should be passed to the constructor, according to the configuration. Hence, the factory encapsulates the complexity of blocks' instantiation. With this approach, adding a new block that requires new parameters will be as simple as adding the block class and modifying the factory to be able to instantiate it. This loose coupling between the blocks' implementations and the syntax of the configuration enables extending the application capacities in a high degree. It also allows to produce fully customized receivers, for instance a testbed for acquisition algorithms, and to place observers at any point of the receiver chain.

The `GNSSFlowgraph` class is responsible for preparing the graph of blocks according to the configuration, running it, modifying it during run-time and stopping it. Blocks are identified by its role. This class knows which roles it has to instantiate and how to connect them to configure the generic graph that is shown in Fig. 6.4. It relies on the configuration to get the correct instances of the roles it needs and then it applies the connections between GNU Radio blocks to make the graph ready to be started. The complexity related to managing the blocks and the data stream is handled by GNU Radio's `gr_top_block` class. `GNSSFlowgraph` wraps the `gr_top_block` instance so we can take advantage of the GNSS block factory, the configuration system and the processing blocks.

This class is also responsible for applying changes to the configuration of the flow graph during run-time, dynamically reconfiguring channels: it selects the strategy for selecting satellites. This can range from a sequential search over all the satellites' ID to smarter approaches that determine what are the satellites most likely in-view based on rough estimations of the receiver position in order to avoid searching satellites in the other side of the Earth.

This class internally codifies actions to be taken on the graph. These actions are identified by simple integers. `GNSSFlowgraph` offers a method that receives an integer that codifies an action, and this method triggers the action represented by the integer. Actions can range from changing internal variables of blocks to modifying completely the constructed graph by adding/removing blocks. The number and complexity of actions is only constrained by the number of integers available to make the codification. This approach encapsulates the complexity of preparing a complete graph with all necessary blocks instantiated and connected. It also makes good use of

the configuration system and of the GNSS block factory, which keeps the code clean and easy to understand.

It also enables updating the set of actions to be performed to the graph quite easily. The `ControlThread` class is responsible for instantiating the `GNSSFlowgraph` and passing the required configuration. Once the flow graph is defined and its blocks connected, it starts to process the incoming data stream. The `ControlThread` object is then in charge of reading the control queue and processing all the messages sent by the the processing blocks via the thread-safe message queue.

6.4.2 Signal processing plane

As introduced in Section 6.3.2.2, GNSS-SDR provides an abstraction layer to the GNU Radio framework. Fig. 6.6 shows the general class hierarchy for the GNU Radio signal processing blocks. The entity `gr_basic_block` is the abstract base class for all signal processing blocks, a bare abstraction of an entity that has a name and a set of inputs and outputs. It is never instantiated directly; rather, this is the abstract parent class of both `gr_hier_block2`, which is a recursive container that adds or removes processing or hierarchical blocks to the internal graph, and `gr_block`, which is the abstract base class for all the processing blocks. A signal processing flow is constructed by creating a tree of hierarchical blocks, which at any level may also contain terminal nodes that actually implement signal processing functions. Class `gr_top_block` is the top-level hierarchical block representing a flow graph. It defines GNU Radio runtime functions used during the execution of the program: `run()`, `start()`, `stop()`, `wait()`, etc.

In GNSS-SDR, a subclass called `GNSSBlockInterface` is the common interface for all the GNSS-SDR modules, as shown in Fig. 6.7. It defines pure virtual methods, that are required to be implemented by a derived class. Subclassing `GNSSBlockInterface`, we defined interfaces for all the receiver blocks shown in Fig. 6.4. This hierarchy, shown in Fig. 6.8, provides the definition of different algorithms and different implementations, which will be instantiated according to the configuration. This strategy allows multiple implementations sharing a common interface, achieving the objective of decoupling interfaces from implementations: it defines a family of algorithms, encapsulates each one, and makes them interchangeable. Hence, we let the algorithm vary independently from the program that uses it. Hereafter, we describe `GNSSBlockInterface` subclasses. They are, again, abstract interfaces that defer instantiation to their own subclasses. Furthermore, the particular implementation for some of the built-in GNSS-SDR algorithms are shown.

6.4.2.1 Signal source

The Signal Source module is in charge of implementing the hardware driver, that is, the portion of the code that communicates with the RF front-end and receives the samples coming from the ADC. This communication is usually performed through USB or Ethernet buses, but can also be made using internal Peripheral Component Interconnect (PCI) bus. Since real-time processing requires a highly optimized implementation of the whole receiver, this module also allows to read samples from a file stored in a hard disk, and thus processing without time constraints. Relevant parameters of those samples are the intermediate frequency (or baseband I&Q components), the sampling rate and number of bits per sample, that must be specified by the user in the configuration file.

The main features to be implemented in a signal source when it is connected to an RF front-end are briefly listed hereafter:

1. Instantiate the hardware driver: this includes the initialization of the associated buses and the execution of the firmware loading procedure (when needed). The hardware initialization and the set up of all the operational parameters such as the sampling frequency, analog filter bandwidth, and RF center frequency are performed in this step.

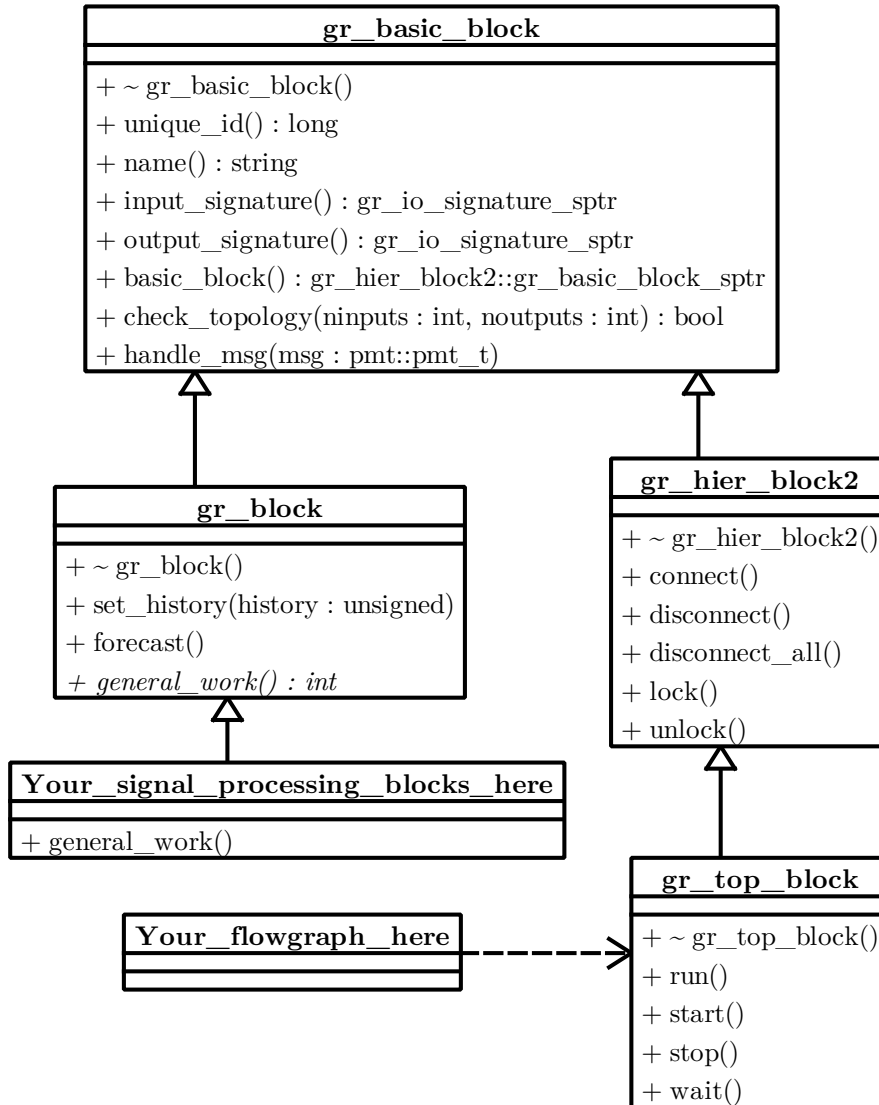


Figure 6.6: GNU Radio class hierarchy for the signal processing blocks.

2. Start the real-time signal sample streaming: it is orchestrated by the GNU Radio scheduler, which is in charge to call the `general_work()` function implemented by the associated GNU Radio block.
3. Detect and notify sample buffer overruns: this is the most critical operation of the signal source. Once the real-time sample streaming is initiated, the signal source block has to detect overruns in the sample buffer. A buffer overrun situation occurs when the hardware driver tries to write a new sample into the input buffer and there is no space left on it. In this situation, the new sample is discarded.

The underlying cause is that the SDR flow graph is not able to process (or consume) the samples at the required speed set by the selected front-end sampling frequency. In GNSS receivers the consequences of a buffer overrun are dramatic; the most relevant one is the immediate loss of tracking of all the observed satellites due to the apparent random slip of the PRN code phase. Overrun situations prevent the real-time operation of the receiver and should be notified to the user.

4. Stop the front-end operation and safely close the hardware communications when the program stops.

At this time of writing (February 2012) GNSS-SDR provides the following signal source

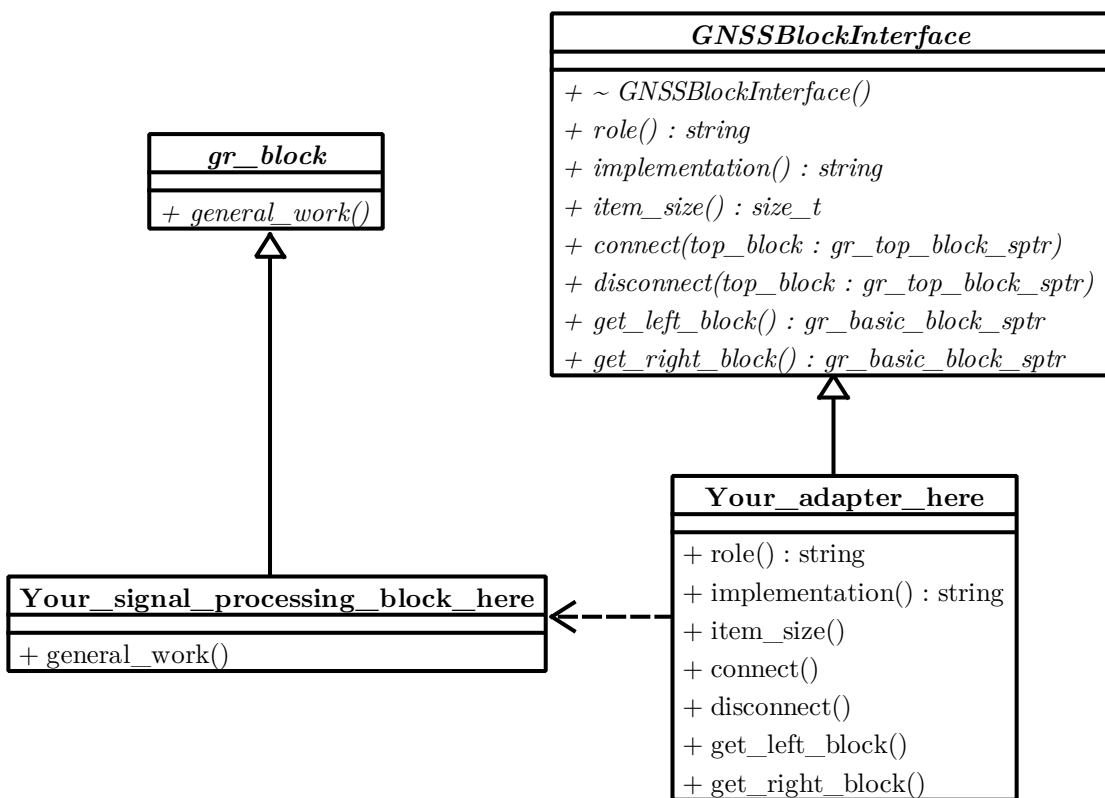


Figure 6.7: GNSS-SDR generic interface for signal processing blocks.
Diagrama: diagrama de clase Página

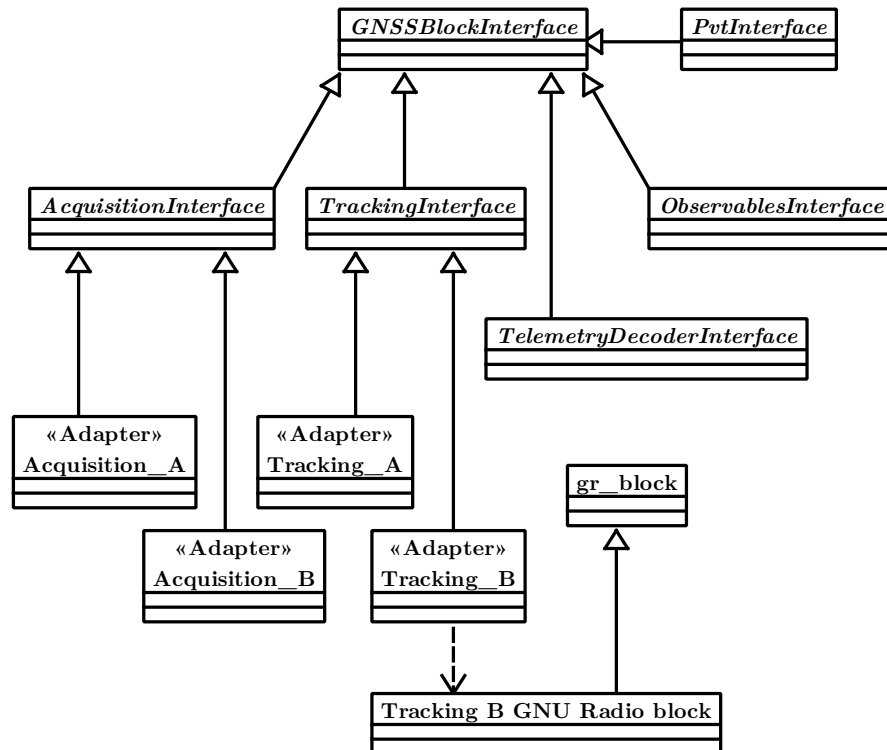


Figure 6.8: Receiver's class hierarchy.
Diagrama: diagrama de clase Página

implementations:

- FileSignalSource: it is an interface to GNU Radio baseband signal sample files.
- UhdSignalSource: it implements an interface to GNU Radio Universal Hardware Driver (UHD) block [GRa] that provides a complete support for the Universal Software Radio Peripheral (USRP) hardware family [Ett10] and its associated front-end daughter boards [Ett11].
- Gn3sSignalSource: it is a driver implementation for the GPS USB SiGe GN3S Sampler v2, based on the SiGe 4120 GPS IC [SiG09].

6.4.2.2 Signal conditioner

In order to provide compatibility with a variety of RF front-ends, GNSS-SDR implements a signal conditioner block that is in charge of providing a simplified interface to the input signal. The signal conditioner adapts the signal and performs an optional resampling. The block acts as a facade between the signal source and the satellite channels. In case of multi-band front-ends, this module would be in charge of providing a separated data stream for each band. At this time of writing (February 2012) GNSS-SDR provides signal conditioning only for baseband sample streams. It is planned the support of IF sampling front-ends with a software-based real-time IF to baseband conversion.

Fig. 6.9 shows the internal diagram of the signal conditioner block. From left to right it is composed of:

1. Data type adapter: is in charge of homogenizing the input samples of different front-ends with different ADC resolutions and data types to a common resolution and data type used by all the GNSS-SDR signal processing blocks. The preferred data type for signal samples in GNSS-SDR is the C++ standard type `std::complex<short int>`, which provides 16 bits of resolution for the In-phase and Quadrature components. The rationale is to optimize both the shared-memory buffers requirements and the speed of the operations, while not degrading the GNSS signal quality. The choice of 16 bits was made taking into account that most of the front-end ADCs have a resolution between 1 to 12 bits. The dynamic range offered is more than the required for GNSS applications. The extra resolution can be used to protect the receiver from interfering signals, as shown in Section 4.7.
2. Input filter: filters the adapted input signal in order to prevent aliasing in the resampling process.
3. Resampler: adapts the hardware sampling frequency to the GNSS-SDR internal sampling frequency. It is an user choice that can be specified using the configuration file.

It is possible to configure all the filter parameters and the internal sampling frequency using

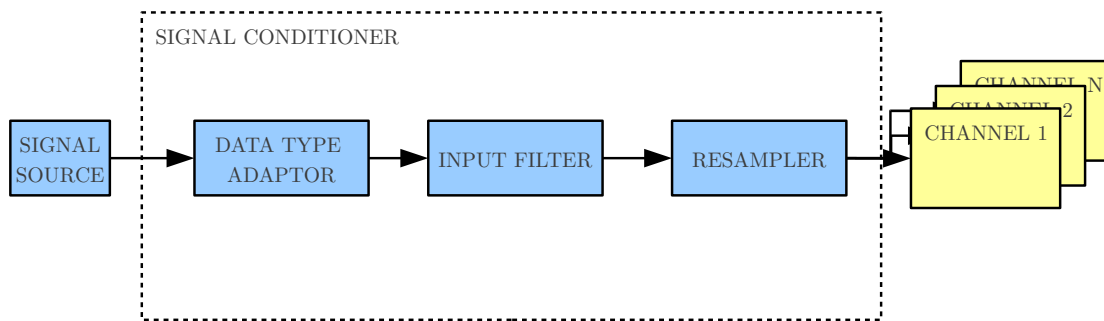


Figure 6.9: Internal view of signal conditioner block.

6.4.2.3 Channel

A Channel encapsulates all signal processing devoted to a single satellite. Thus, it is a large composite object which encapsulates the acquisition, tracking and telemetry decoding modules.

As a composite object, it can be treated as a single entity, meaning that it can be easily replicated. Since the number of channels is selectable by the user in the configuration file, this approach helps improving the scalability and maintainability of the receiver.

The channel module with the help of the flowchart container module is in charge of managing the interplay between acquisition and tracking (see Section 2.3.4 for more information on the GNSS synchronization process). The mathematical abstraction used to design this logic is modeled in an FSM, as shown simplified in Fig. 6.10. For the implementation, we used the Boost.Statechart library [BSC], which provides desirable features such as support for asynchronous state machines, multi-threading, type-safety, error handling and compile-time validation.

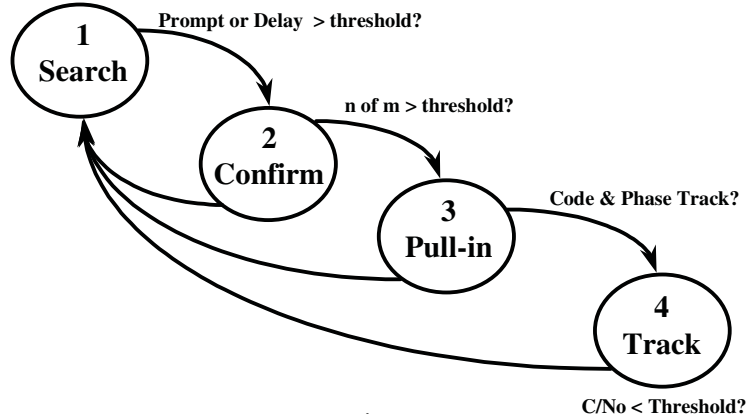


Figure 6.10: Simplified version of the channel states [Cha01].

At the time of writing (February 2012), we provide an implementation that works with the GPS L1 C/A signal. It provides multiple configuration options to facilitate the algorithm performance testing, such as the assignment of arbitrary PRN IDs to each of the available channels, thus, forcing the acquisition of a particular satellite. For more information the reader is referred to [Est12].

More complex channel implementations could accommodate more sophisticated strategies such as the joint acquisition strategy introduced in Section 3.4 or vector tracking loops involving signals from more than one satellite and optimizations performed directly in the position domain [Clo10b].

6.4.2.4 Acquisition

The first task of a GNSS receiver is to detect the presence or absence of in-view satellites. This is done by the acquisition process as introduced in Section 2.3.4. `AcquisitionInterface` is the common interface for all the acquisition algorithms and their corresponding implementations.

The concrete algorithms' interface is defined in the implemented adapters. It may vary depending on the use of information external to the receiver, such as in assisted GNSS. Software-based acquisition methods can consist of a serial search or a parallel frequency search based on the FFT [Bor07]. The implementations can make use of specialized and highly optimized libraries such as FFTW [Fri05], using coherent or non-coherent integration [Tsu00], or even taking advantage of signals from different frequency bands [Ger11]. For more information of the GNSS-SDR acquisition implementation, the reader is referred to [Est12].

From an SDR flow graph point of view, the acquisition block processes the input sample stream and obtains a coarse estimation of the detected signal synchronization parameters. This

information should be fed to the tracking block in order to initialize the tracking algorithm. At this point some challenging questions arise:

- how the acquisition blocks exchange information with their associated tracking blocks?, and
- how the tracking block can check if the acquisition information is still valid?

GNSS-SDR solves efficiently both problems using a common structure to exchange information between GNSS signal processing blocks, as shown in the next Section.

6.4.2.5 Signal synchronization information exchange

GNSS-SDR provides custom structures to manage the GNSS related information allowing an efficient and flexible way to exchange information between blocks.

On the one hand, all the information related to an specific satellite signal is grouped in `Gnss_Signal` class, which in turn has a class member of their related GNSS satellite, represented with the class `Gnss_Satellite`. In Fig. 6.11 can be found the UML diagram of both entities, showing in detail the information fields. The receiver make use of these structures to identify the current satellite assigned to each of the composing elements of the channel (acquisition, tracking, and telemetry decoder) and to sign their associated outputs as we show hereafter.

On the other hand, the signal synchronization information produced and consumed between GNSS blocks is packed in a common class entity: the `gnss_synchro` class. Fig. 6.12 shows the associated UML class diagram. It is important to highlight that every synchronization data has an associated *sample stamp* value. The sample stamp is generated from an absolute sample counter instantiated in each of the signal processing blocks independently and reseted at the receiver start operation. Sample stamp is analogous to a time stamp and provides critical information to measure the internal delays between the receiver state transitions such as acquisition to tracking transition or in the computation of pseudoranges.

The flexibility of the GNU Radio framework allows us the customization of GNU Radio blocks to make use of `gnss_synchro` structures as input/output data types.

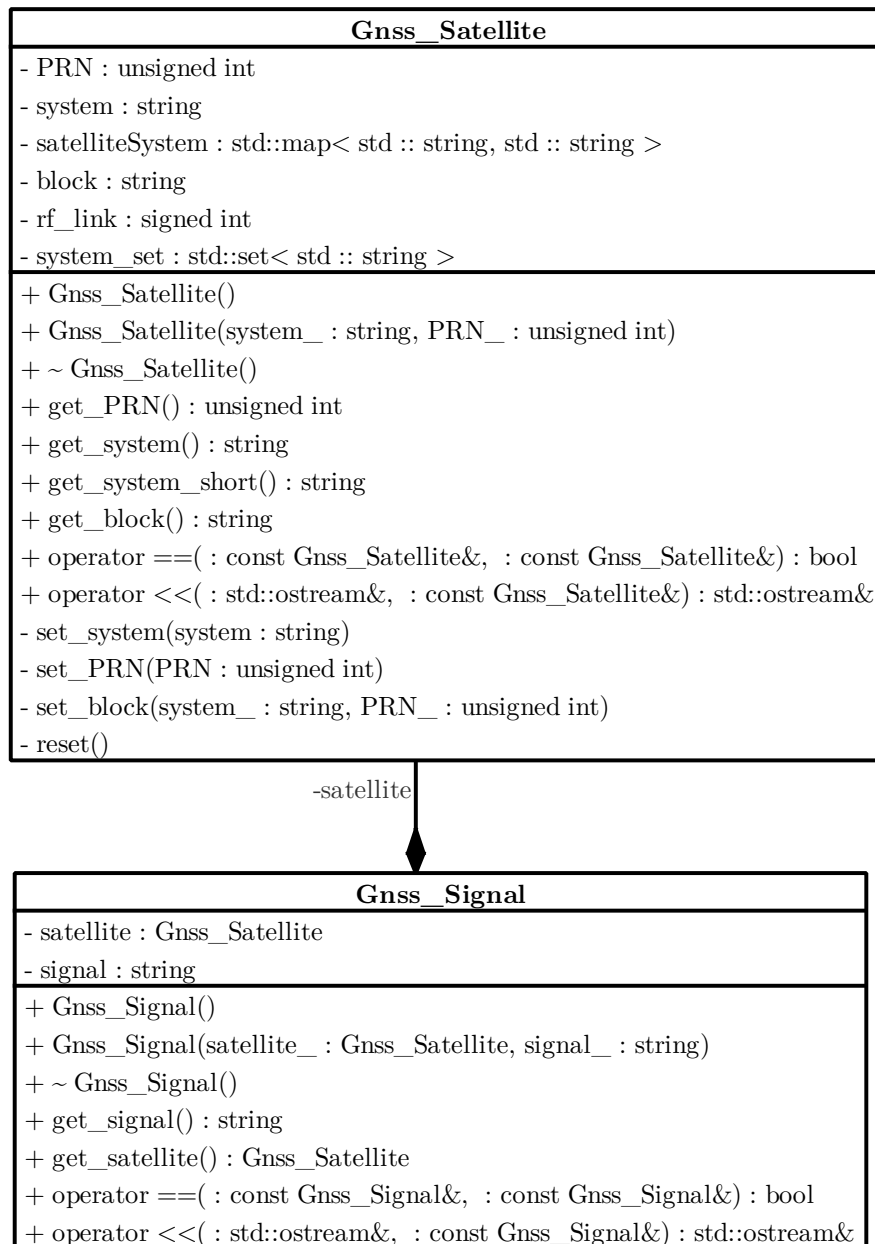


Figure 6.11: UML diagram of the `Gnss_Satellite` and `Gnss_Signal` classes.

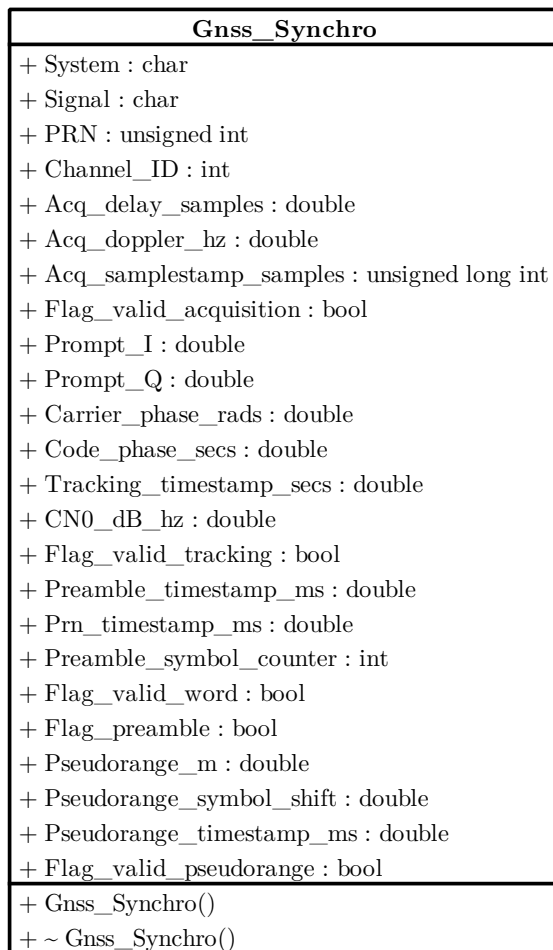


Figure 6.12: UML diagram of the `gnss.synchro` class.

6.4.2.6 Tracking

When a satellite is declared present in a channel, the parameters estimated by the acquisition module are then fed to the receiver tracking module, which represents the second stage of the signal processing unit. Tracking aims to perform a local search for accurate estimates of code delay and carrier phase, and follows their eventual variations as introduced in Section 2.3.4.2.

Possible algorithms for code delay tracking include the DLL and its multiple variants, along

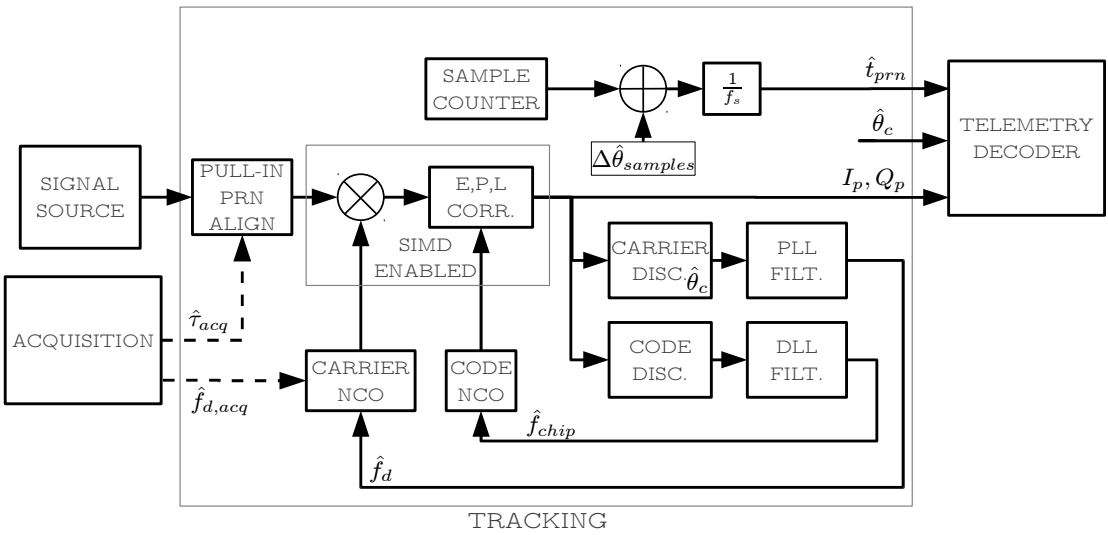


Figure 6.13: GNSS-SDR tracking module internal block diagram.

Fig. 6.13 shows the internal block diagram of the GNSS-SDR tracking DLL/PLL implementation. From left to right, acquisition and tracking exchange information using shared memory with a common instance of the `gnss_synchro` class. The FSM implemented in the `GNSSFlowgraph` orchestrates the read/write operations. Since the time spent in the transition from acquisition to tracking is unknown, tracking blocks make use of the acquisition sample stamp information (also included in `gnss_synchro`) to measure the transition delay and correct the acquisition PRN code phase values prior to close the tracking loops. This step is called *tracking pull-in*, and it aligns the incoming PRN satellite signal with a locally-generated PRN signal. The algorithm is detailed in Appendix 6.A.

It is worth mentioning that, in this particular implementation, the local PRN sequence always starts with the first chip, thus, the correlation of a PRN period is always aligned with telemetry bit transitions⁷ at the tracking block.

The rest of the blocks are the usual tracking blocks present in a conventional receiver, as described in 2.3.4.2, with the exception of the computation of the PRN start time stamp estimation \hat{t}_{prn} . This variable tracks the exact time stamp associated to the initial chip of each PRN period of the satellite signal. It can be written as:

$$\hat{t}_{prn}(n) = (k_{trk}(n) + \Delta\hat{\theta}_{samples}(n)) \frac{1}{f_s}, \quad (6.1)$$

⁷For instance, in GPS L1 CA each bit lasts 20 symbols, equivalent to 20 PRNs, and the transitions are aligned with the PRN starting chip.

where n is the tracking loop counter, $k_{trk}(n) \in \mathbb{N}$ is the tracking sample counter, reseted at the receiver start, f_s is the sampling frequency, and

$$\Delta\hat{\theta}_{samples}(n) = \tilde{K}_{prn}(n) - \text{round}(\tilde{K}_{prn}(n)), \quad (6.2)$$

is the remainder code phase due to the sample rounding error, expressed in samples. The tracking algorithm adjust dynamically the correlation length to match the estimated PRN code length as $\tilde{K}_{prn}(n) = \left(\frac{\tilde{T}_{prn}(n)}{f_s} \right)$, where $\tilde{T}_{prn}(n)$ is the estimated code period. The sample counter is increased in each tracking loop with

$$k_{trk}(n) = k_{trk}(n-1) + \text{round}(\tilde{K}_{prn}(n)), \quad (6.3)$$

consequently, the samples consumed in the loop count n are $\text{round}(\tilde{K}_{prn})$. This parameter is passed to the GNU Radio scheduler using the function `consume_each()`.

GNSS-SDR was designed using modular structures that allows to recycle code between different algorithm implementations. Basic operations are packed in classes that allows the customization of its behavior by means of parametrized constructors or tunning functions. At this moment GNSS-SDR tracking module is equipped with the following helper classes:

- **Correlator:** performs the signal Carrier wipe-off operation and Early, Prompt, and Late correlations.
- **CN0_estimators:** includes a set of CN0, carrier lock, and code lock detectors (see e.g., [Pin08, Par96] for the algorithm details).
- **Tracking_2nd_DLL_filter:** implements a second order DLL filter according to [Bor07].
- **Tracking_2nd_PLL_filter:** implements a second order PLL filter according to [Bor07].
- **Tracking_FLL_PLL_filter:** implements a hybrid PLL-DLL filter according to [Kap05].
- **Tracking_discriminators:** includes a set of PLL and DLL discriminators [Kap05].

Among them, it is wort to insight into the **Correlator** class that performs by far the most time-consuming task of the entire receiver. In order to reach real-time, **Correlator** makes use of the Vector-Optimized Library of Kernels (VOLK), recently included in the GNU Radio framework [VOL].

The aim of VOLK library is to facilitate the programmer access to the Single Instruction, Multiple Data (SIMD) instruction set present on most of the modern computer architectures [Hor90]. Basic SIMD instructions performs the same operation on multiple data simultaneously, thus, exploiting data level parallelism. Specific implementations of SIMD architectures found in x86 processors are the Streaming SIMD Extensions (SSE) family designed by Intel and introduced in 1999 in their Pentium III series processors and evolved to SSE4.2 in the newest Core i-series processors [SSE]. VOLK comes with a profiler that builds a configuration file for the best SIMD architecture for the particular processor where it is executed.

For the sake of completeness, the tracking pull-in algorithm is detailed in Appendix 6.A.

6.4.2.7 Telemetry decoder

Most of GNSS signal links are modulated by a navigation message. It contains the time the message was transmitted, orbital parameters of satellites, and an almanac (information about the general system health, rough orbits of all satellites in the network as well as data related to error correction) as introduced in Section 2.3.4.3.

Navigation data bits are structured in words, pages, subframes, frames and superframes. Sometimes, bits corresponding to a single parameter are spread over different words, and values extracted from different frames are required for proper decoding. Some words are for synchronization purposes, others for error control, and others contain actual information. There are also error control mechanisms, from parity checks to FEC encoding and interleaving, depending on the system. Details on the structure of the navigation message are reported in the related interface specification documents: see Chapter 2 for more information about the available GNSSs.

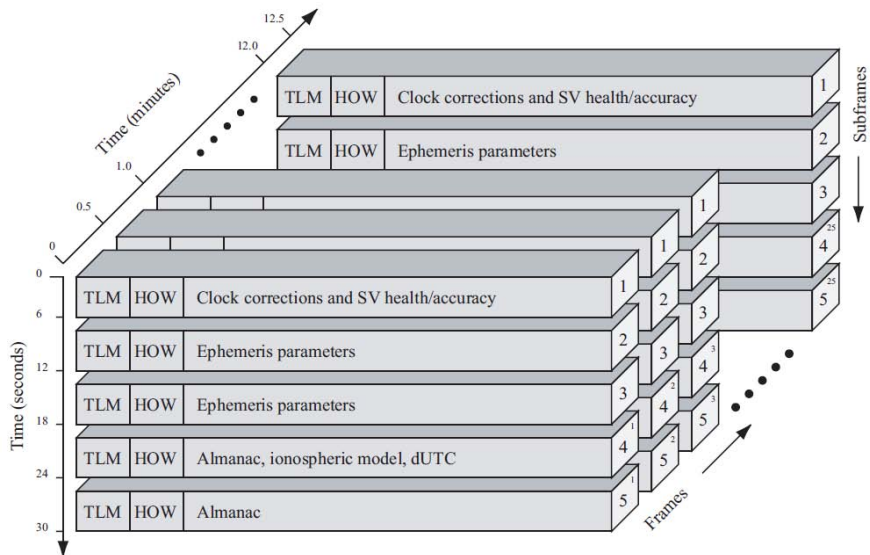


Figure 6.14: GPS C/A navigation message structure [Bor07].

Fig. 6.14 shows the GPS L1 C/A navigation message structure. Each subframe last 6 seconds. A base structure composed of 5 different subframes is transmitted every $6 * 5 = 30$ seconds. The First three subframes contains basic parameters related to the current tracked satellite, allowing a fast TTFF. Subframes 4 and 5 transmit extended information related to the ionospheric model and clock corrections and the ephemeris almanac for the rest of the GPS constellation. The complete navigation message is repeated every 12.5 minutes [Win10].

GNSS-SDR provides a GPS L1 C/A telemetry decoder interface implementation as shown in Fig. 6.15. From left to right, the first element is a BPSK demodulator which obtains the telemetry symbols stream using the *In-phase* component of the *prompt* tracking correlator output. Next, the symbols are mapped to bits, bits are assigned to words, and finally the words are processed by a FSM. The preamble detector block is in charge of correlating the incoming symbols stream with the local preamble symbol sequence. In case of a positive detection, it turns on the reset signal to synchronize the rest of the blocks and the symbol counter.

The symbol counter tracks the symbol number associated to the current tracking t_{prn} . This information is necessary solve the PRN *integer ambiguity problem* [Kap05] and compute the pseudoranges, as is shown in the next Section.

All the frame navigation frame decoding complexity is managed by a finite state machine implemented with the Boost.Statechart library [BSC]. Fig. 6.16 shows the associated simplified UML statechart.

Class hierarchy for these implementations mimics the architecture already presented for

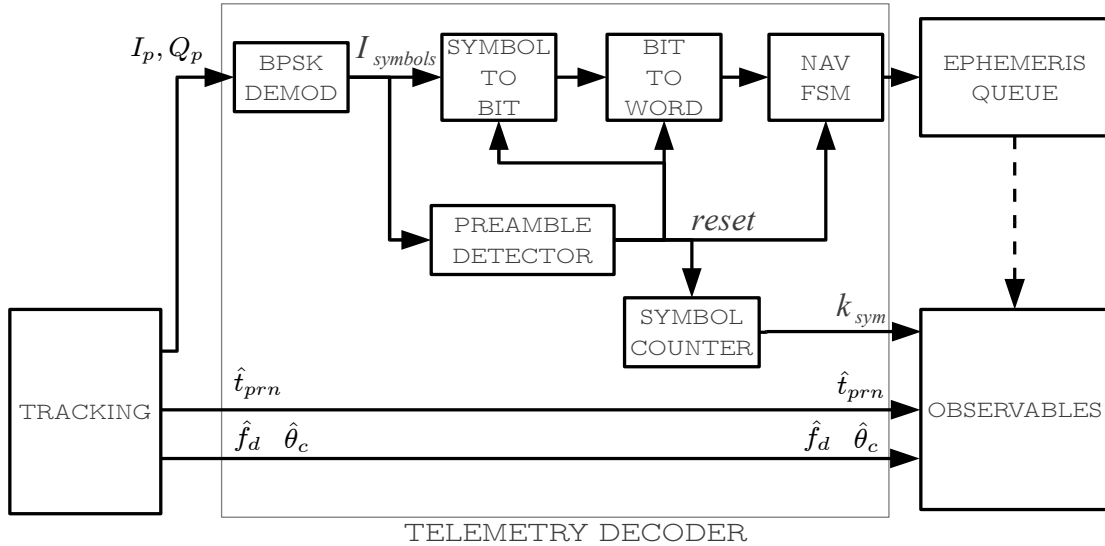


Figure 6.15: GNSS-SDR telemetry decoder module internal block diagram.

acquisition and tracking: a `TelemetryDecoderInterface` provides a single interface for decoding the navigation message of different systems. The particular implementation of GPS C/A decoder is contained in `GpsL1CaTelemetryDecoder` class, which inherits from `TelemetryDecoderInterface`.

Summarizing, the telemetry decoder module produces two different output informations:

- Telemetry synchronization: associates the tracking information to the current telemetry symbol number with respect to the preamble. This information is recorded in the `gnss_synchro` object, and it is sent to the observables block along with the tracking output data.
- Navigation record: the telemetry decoder receives the navigation message structures and checks for their consistency. In GNSSs, the transmission speed is usually low, in the order of 50 – 100 bps. For instance, in GPS, a navigation message frame record is received every 30 seconds. This is in contrast to the tracking signal synchronization estimation which has a cadence in the order of milliseconds. In order to efficiently send the navigation information to the PVT block, GNSS-SDR implements a thread-safe queue of navigation information structure. In the case of GPS, the class `Gps_Navigation_Message` is the navigation record container. Every telemetry block of all the channels has the producer role, and the PVT block is the only consumer.

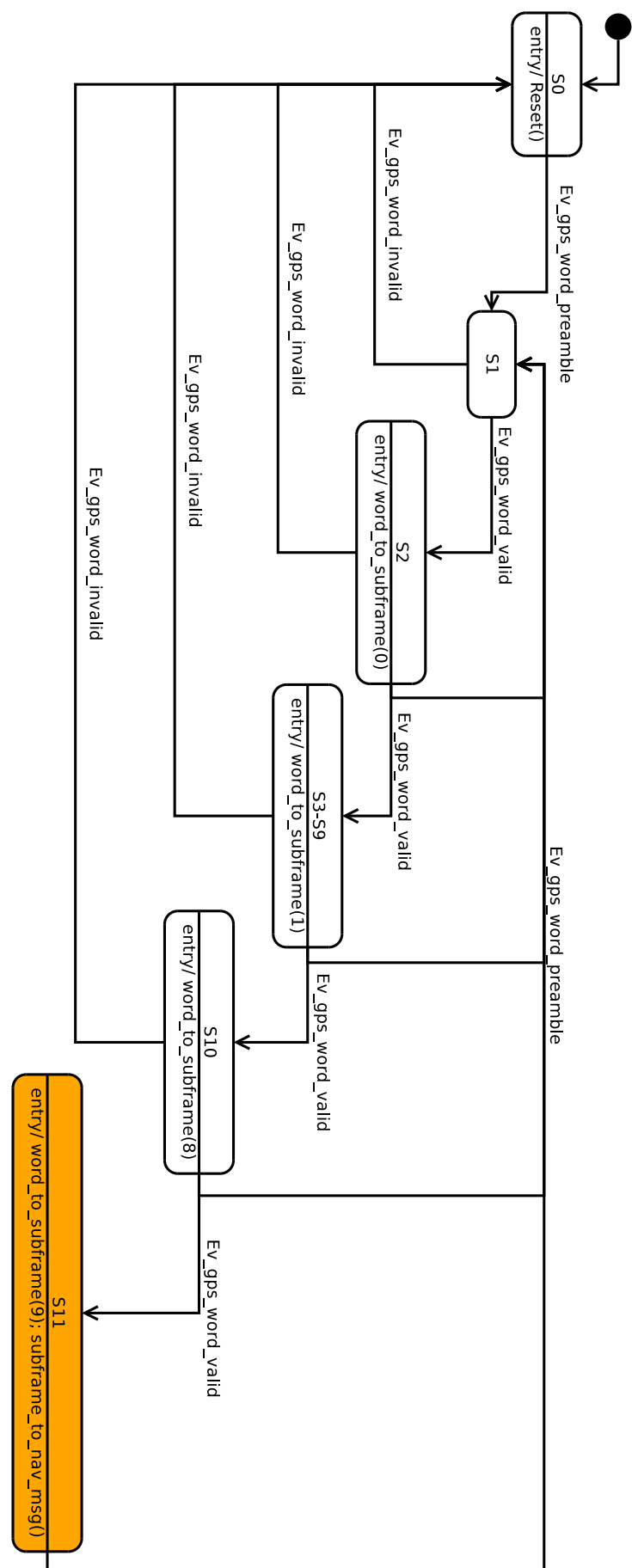


Figure 6.16: GNSS-SDR GPS C/A telemetry word to navigation message subframe decoder FSM UML diagram.

6.4.2.8 Observables

GNSS systems provide different kinds of observations. As shown in Section 2.3.4.4, the most commonly used are the code phase observations, also called pseudoranges. The *pseudo* comes

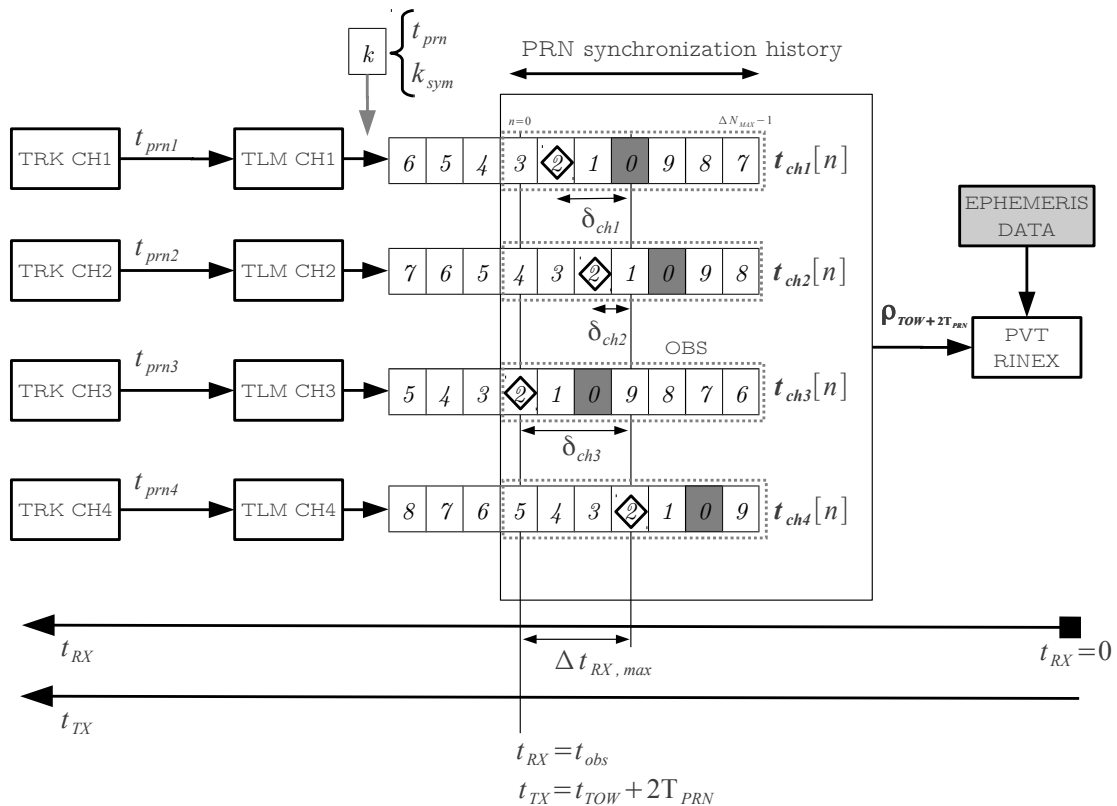


Figure 6.17: GNSS-SDR pseudorange estimation using common transmission time.

Fig. 6.17 shows the detailed operation of the GNSS-SDR observables module and the interactions with the rest of the receiver's blocks. From left to right, each satellite signal is tracked in an independent channel, represented by the *TRK* blocks. As described in Section 6.4.2.6, the tracking algorithm aligns the incoming signal with a locally-generated reference that starts always with the first chip of the PRN sequence. After the correlation of a complete PRN period, each of the tracking blocks makes an output with an estimation of the PRN start time stamp t_{prn_i} , where i is the channel index. For the sake of simplicity, we drop the tracking loop index n in the formulation.

Each tracking output also contains the *prompt* correlator signal associated with t_{prn_i} . Both outputs are fed to the corresponding telemetry decoding modules, represented by *TLM* block. At this point, the *prompt* signal is demodulated and the preambles are detected, as described in Section 6.4.2.7. The telemetry decoder identifies the current symbol number with respect to the preamble start symbol (i.e., for the GPS L1 CA signal, the preamble period is $T_{pre} = 6$ s and the PRN period is $T_{prn} = 1$ ms; thus, there are $K_{sym} = 6000$ symbols between preambles⁸). For

⁸Notice that here it is used the nominal PRN period (T_{prn}), at transmission side, without Doppler, in contrast to the receiver PRN period \bar{T}_{prn} which is measured at the receiver side, and it is modulated by the Doppler effect.

the sake of simplicity, we reduced the number of symbols to 10 in Fig. 6.17. In the telemetry output we have each t_{prn_i} associated with the corresponding symbol k_{sym_i} .

The observables module collects these data from all channels and computes the pseudoranges using the common transmission time algorithm [Rao12]. The algorithm is based on the fact that all satellites broadcast data synchronously but, due to different propagation delays $\tau_{prop,i}$, the user does not receive the data from every satellite synchronously. As described in Section 2.3.4.4, considering the GPS L1 CA and the Galileo E1 signals, $T_{prn} < \tau_{prop,i}$, and, in consequence, the measurement of t_{prn_i} is affected by the so-called *integer ambiguity problem* [Kap05]. In order to solve this ambiguity, the observables module has to compare t_{prn_i} corresponding to the same telemetry symbol. In practice, this is implemented using a small memory buffer for each channel to keep a record of the synchronization information. Since the maximum differential delay between ToAs is 20 ms according to the GPS orbit model described in [Tsu00, p.32], for a receiver operated in or near the Earth surface, the buffer length was set to $\Delta N_{max} = 20$.

At observation time t_{obs} , the most delayed channel is identified, finding the minimum k_{sym_i} , represented by a diamond shape in Fig. 6.17. The required history shift to align the rest of the channels to this symbol is $\Delta N_i = k_{sym_i} - k_{sym,min}$. Once the symbols are aligned, it is possible to compute the ToAs differences using the associated PRN start timestamps t_{prn_i} as:

$$\hat{\delta}_i = t_{prn_i} - t_{prn,min}, \quad (6.4)$$

where the channel with the minimum t_{prn_i} (nearest satellite) is the reference. Now it is possible to compute the pseudorange distance as follows

$$\hat{\rho}_i = c\delta_i + \rho_{ref}, \quad (6.5)$$

where c is the speed of light constant⁹ and $\rho_{ref} = c\tau_{prop,ref}$ is the pseudorange relative to the reference channel. Since it is not possible to obtain τ_{ref} due to the differences between satellite and receiver clocks, the first pseudorange set uses the mean propagation time between for the GNSS constellation, which in the case of GPS is $\bar{\tau}_{prop} = 68.802$ ms. After solving the PVT set of equations of the form described in 2.6.5 (i.e., by using the Bancroft's algorithm [Ban85]), it is possible to replace $\bar{\tau}_{prop}$ with the particular propagation delay using the computed receiver clock offset (see, e.g., [Str97, Lei04]). This operation takes place in the *PVT* block.

It is worth pointing out that the PVT block requires, on the one hand, the complete ephemeris set for each satellite, obtained using the *ephemeris queue* as described in Section 6.4.2.7, and, on the other hand, it needs the transmission time t_{TX} for the current pseudoranges set. The transmission time is sent periodically in the navigation message, which in GPS it is the *tTOW* value. It is contained in the Hand Over Word (HOW) telemetry frame field¹⁰, as shown in Fig. 6.14. However, the receiver should extend the *tTOW* time to the current transmission time using the following equation

$$t_{TX} = t_{TOW} + k_{sym,min} T_{prn}, \quad (6.6)$$

where t_{TX} is the transmission time associated with the current pseudorange set. It is used to find the satellites' positions, solving Kepler's equations [Lei04].

The output information for the pseudorange data fits again in the `gnss_synchro` object, where it is added to the tracking and telemetry decoder information, completing the signal synchronization information available for each of the satellites in track.

6.4.2.9 PVT

On the one hand, the PVT block reads the navigation information sent by telemetry decoder blocks using the `Gps_Navigation_Message` objects queue. It keeps a complete, up-to-date set of navigation parameters such as ephemeris records, clock corrections, and health status of all the visible satellites. In addition, the PVT block keeps an updated record of the GNSS constellation

⁹In the particular case of GPS $c_{GPS} \stackrel{def}{=} 299792458.0$ m/s.

¹⁰It actually contains a truncated version of Time Of Week (TOW) [Win10].

almanac. On the other hand, PVT block has access to the complete pseudorange set using the outputs of the observables block, contained in `gnss_synchro` class objects.

By combining both informations, this block is in charge of writing the observables files in the form of RINEX log files [Gur09]. As described in Section 6.3.2.3, RINEX standard-compliant files pave the way to high accuracy positioning, since they can be directly used by applications and libraries that implement the corresponding positioning algorithms. The integration with libraries and software tools that are able to deal with multi-constellation data such as GPSTk or gLAB [Sal10,HP10b] appears as a viable solution for high performance, completely customizable GNSS receivers.

Although data processing for obtaining high-accuracy PVT solutions is out of the scope of GNSS-SDR, we provide a module that can compute a simple LS solution [Bor07] and leaves room for more sophisticated positioning methods. The implemented LS solver makes use of the Armadillo C++ open source linear algebra library [ARM]. The computed position is logged in KML standard-compliant file.

The logging interval of both RINEX and KML files can be modified using the configuration file, as described in Section 6.4.1. Next Section is devoted to the receiver performance analysis, where it can be found practical examples of the GNSS-SDR operation.

6.5 GNSS-SDR Performance

In order to validate the GNSS-SDR implementation, the complete GPS L1 CA receiver chain was tested using both simulated and real-life signals. The receiver was used in real-time mode and in post-processing mode for a variety of configurations.

We evaluated the receiver performance using standard positioning accuracy and precision measurements, represented with position scatter plots and confidence regions. Two of the most commonly used confidence measurements are the Distance Root Mean Square (DRMS) and the Circular Error Probability (CEP). Table 6.1 lists the particular computation formulas for the position confidence regions [Nov03].

Accuracy measures	Formula	Confidence region probability
2D DRMS	$\sqrt{\sigma_x^2 + \sigma_y^2}$	65%
2D 2DRMS	$2\sqrt{\sigma_x^2 + \sigma_y^2}$	95%
2D CEP	$0.62\sigma_y + 0.56\sigma_x$, accurate when $\frac{\sigma_y}{\sigma_x} > 0.3$	50%
2D R95	$R(0.62\sigma_y + 0.56\sigma_x)$, with $R = 2.08$ when $\frac{\sigma_y}{\sigma_x} = 1$	95%
3D DRMS	$\sqrt{\sigma_x^2 + \sigma_y^2 + \sigma_z^2}$	65%
3D 2DRMS	$2\sqrt{\sigma_x^2 + \sigma_y^2 + \sigma_z^2}$	95%

Table 6.1: Position accuracy measurements [Nov03].

In the tests, we used the obtained receiver position local East North Up (ENU) coordinates¹¹ to compute the performance measurements. In addition, we decided to use the obtained receiver mean ENU position as the true position since in some cases (i.e., real-life scenarios), this information is not available, following the same procedure introduced in [Har01]. As a consequence, the confidence regions obtained are indicators of the receiver precision. The receiver accuracy was measured, when possible, computing the error between the true position (i.e, the position configured in a GNSS signal simulator) and the obtained position.

¹¹The local ENU coordinates are formed from a plane tangent to the Earth's surface fixed to a specific location. The east axis is labeled x, the north y, and the up z.

In the sequel can be found both the receiver configurations and the performance results.

6.5.1 Receiver configuration

As introduced in this Chapter, the software receiver is able to operate in post-processing mode and in real-time mode. The post-processing configuration parameters are listed in Table 6.2.

Configuration parameter	Value
Sampling frequency	4 MSPS
Number of channels	12
Number of channels in acquisition	12
Signal Source	File_Signal_Source
Signal conditioner	Pass_Through
Acquisition algorithm	GPS_L1_CA_PCPS_Acquisition
Acquisition threshold	70
Tracking algorithm	GPS_L1_CA_DLL_PLL_Tracking
Tracking parameters	$b_{PLLW} = 40$ Hz, $b_{DLLW} = 2$ Hz, Filter order 3
Telemetry decoder algorithm	GPS_L1_CA_Telemetry_Decoder
Observables algorithm	GPS_L1_CA_Observables
PVT algorithm	GPS_L1_CA_PVT

Table 6.2: GNSS-SDR post-processing configuration.

The real-time mode requires enabling the corresponding signal source in the configuration file in order to initialize and obtain access to the connected front-end. Using this file, it is also possible to configure several front-end parameters, such as the gain, the RF frequency and bandwidth, and the sampling frequency.

The required computer processing power depends mainly on the number of active satellite channels and on the configured sampling frequency. In that sense, there is a trade-off between the positioning precision and the computer requirements. A minimum of four satellite channels are required to solve the PVT equation, as introduced in Section 6.4.2.9. Regarding the sampling frequency, considering the GPS L1 CA signal bandwidth, a minimum of 2 MSPS is required to compute the pseudoranges. If the computer resources are not sufficient to process the signal sample stream in real-time, the hardware driver sends a buffer overrun signal, thus, alerting the user of the problem.

Notice that prior to use the real-time mode, it is mandatory to enable compile-time optimizations using the *release* option of the compiler. This option disables all debug symbols and logging mechanisms, thus, a highly-optimized executable is obtained.

At this time of writing (April 2012), the current version of GNSS-SDR was able to operate in real-time using the configuration listed in Table 6.2 with the variations of Table 6.3.

Computer CPU	Intel Core 2 Quad Q9400@2.66 MHz
RAM Memory	4 Gb
Operating System	Linux Ubuntu 10.10 (maverick)
Front-end	USRP 1 + DBSRX2
Front-end center frequency	1575.42 MHz
Front-end Gain	60 dB
Sampling frequency	2 MSPS
Number of channels	6
Number of channels in acquisition	1
Signal Source	UHD_Signal_Source

Table 6.3: GNSS-SDR real-time configuration.

6.5.2 Simulated scenarios

6.5.2.1 Agilent E4438C GPS personality

The Agilent E4438C generator [Agi06] equipped with GPS Personality [Agi07] simulates a multi-satellite GPS signal for GPS receiver testing. This firmware option provides the capability to verify functionality of embedded GPS chips in mobile consumer products such as cellular phones and handheld receivers. The predefined scenarios can be loaded to the instrument using the scenario files.

In this test, a USRP1 board equipped with a DBSRX2 front-end daughter board was connected directly to the Agilent generator RF output. The front-end was used both to capture GNSS signals to disk and to feed the GNSS-SDR in real-time. The generator parameters are listed in Table 6.4. The scenario position is defined by the associated geographical coordinates, expressed in the World Geodetic System (WGS) 84 geodetic system [WGS97].

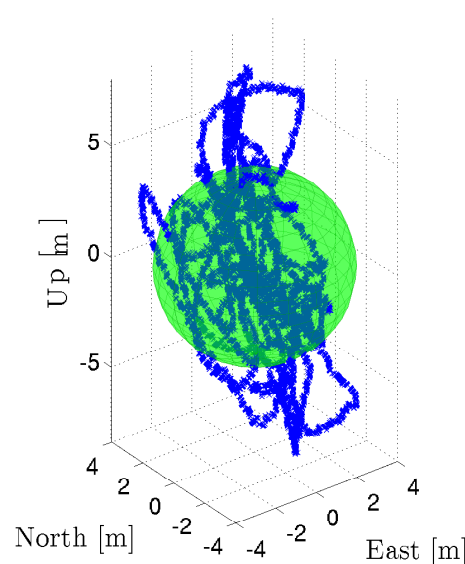
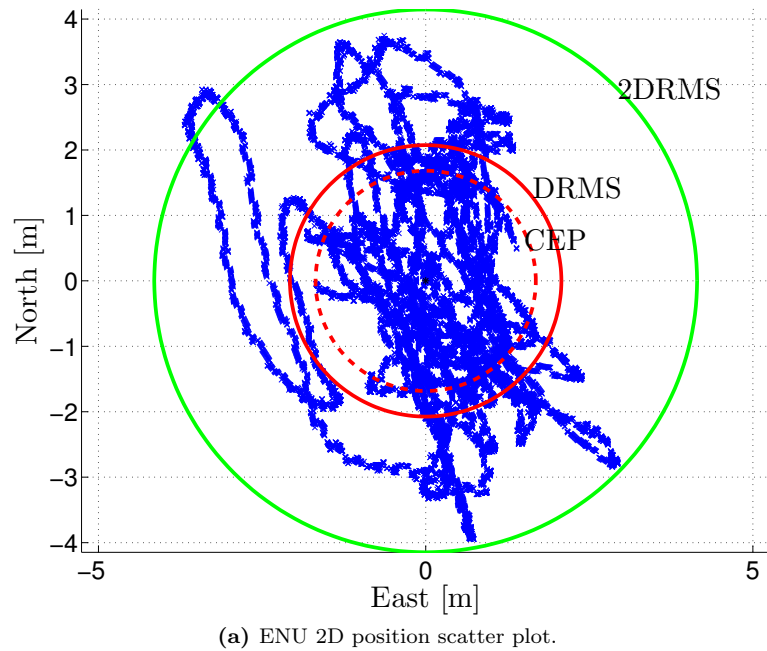
Parameter	Value
Scenario file	NEWYORK.GPS
Carrier frequency	1575.42 MHz
Output power	-80 dBm
Visible satellites PRN	1,3,6,7,16,20,23,31
Latitude	40.7484638888889 N
Longitude	-73.9860000000000 W
Height	330 m
Initial date	20-Sep-2007 15:30:00
Initial Dilution Of Precisions (DOPs)	
GDOP	2.282
PDOP	2.027
HDOP	1.665
VDOP	1.157
TDOP	1.048

Table 6.4: Agilent E4438C GPS Personality simulated scenario parameters.

The GNU Radio UHD tools were used to capture 160 seconds of signal into a file. The GNSS-SDR was executed in post-processing mode using the configuration parameters listed in Table 6.2. The receiver was able to acquire and track 6 satellites with a TTFF of 44 s. The PVT averaging was set to 1000 ms and 30 seconds of positioning results were used to compute the performance parameters. Fig. 6.18a shows the 2D scatter plot and Fig. 6.18b shows the analogous 3D scatter plot. From the results, the CEP, DRMS, and 2DRMS 2D confidence intervals were computed, obtaining the values of 1.6827 m, 2.0735 m, and 4.1471 m respectively. The 3D confidence region DRMS and 2DRMS was also computed, obtaining 4.0055 m and 8.0110 m, respectively.

Since this a simulated scenario, the true position is a known parameter. It is possible to compute the positioning error and thus the receiver accuracy in this particular set-up. Fig. 6.19 shows the ENU errors committed by the GNSS-SDR in PVT results for the 30 seconds interval. It is clear that the computed altitude (*Up* coordinate) is more affected and biased than the 2D position in the local plane, which is aligned with the DOP values.

Finally, a qualitative position accuracy test is shown in Fig. 6.20, where the obtained KML file was opened using Google Earth REF. It is possible to compare the receiver position evolution with respect to the true position reported by the signal simulator.



(b) ENU 3D position scatter plot

Figure 6.18: GNSS-SDR precision in the Agilent New York GPS simulated scenario.

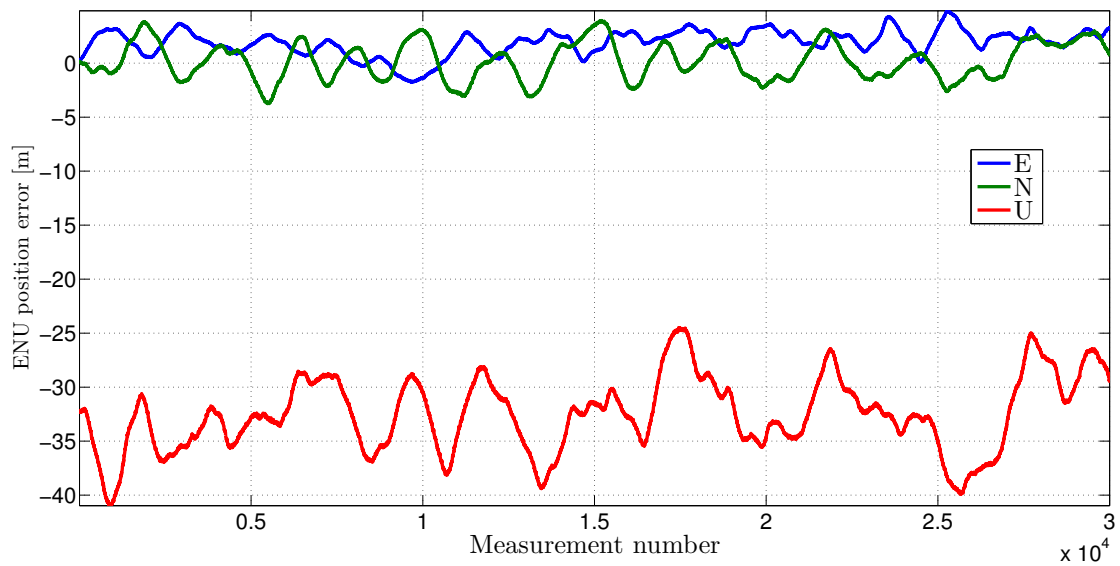


Figure 6.19: GNSS-SDR ENU position error in the Agilent New York GPS scenario.



Figure 6.20: Google Earth KML 3D position evolution in the Agilent New York GPS scenario.

6.5.2.2 Spirent GSS6700

The GSS6700 Multi-GNSS Simulator from Spirent has been developed for R&D, integration and verification testing of devices that use commercial GPS, Glonass, and Galileo signals [Spi09]. The GSS6700 provides 12 channels of one, two or three GNSS constellations. It supports GPS/SBAS L1, Glonass L1 and Galileo E1 OS signals. The simulator was configured for a static GPS L1 CA scenario with a known reference position, listed in Table 6.5.

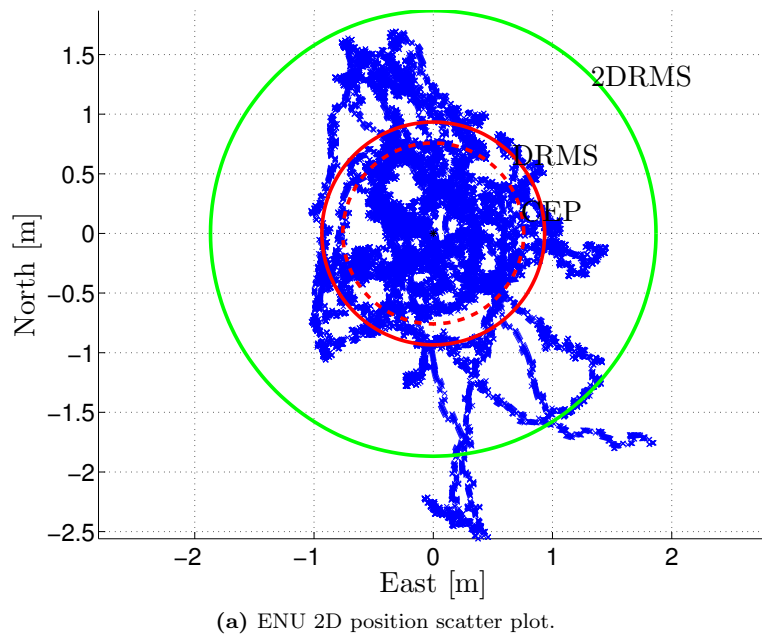
Using the same procedure as in the previous test, 160 seconds of signal was captured and processed with GNSS-SDR.

Parameter	Value
Mode	GPS L1 C/A
Visible satellites PRN	9,14,17,18,22,26,29
Latitude	41.29999999997026 N
Longitude	2.16666000000409 E
Height	100 m
Initial DOPs	
GDOP	1.934
PDOP	1.845
HDOP	1.231
VDOP	1.187
TDOP	1.014

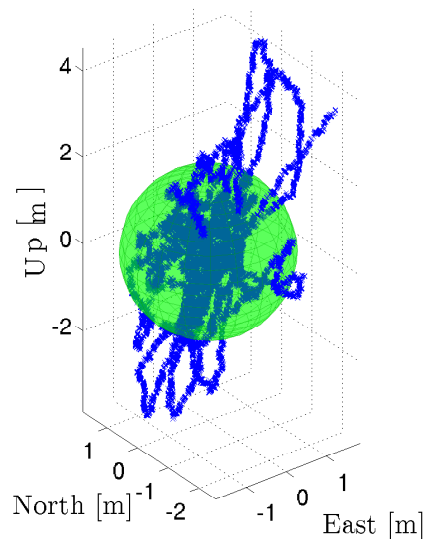
Table 6.5: Spirent GSS6560 simulated scenario parameters.

The receiver was able to acquire and track 7 satellites with a TTFF of 39 s. The PVT averaging was set to 1000 ms and 30 seconds of positioning results were used to compute the performance parameters. Fig. 6.21a shows the 2D scatter plot and Fig. 6.21b shows the analogous 3D scatter plot. From the results, the CEP, DRMS, and 2DRMS 2D confidence intervals were computed, obtaining the values of 0.7584 m, 0.9339 m, and 1.8679 m respectively. The 3D confidence region DRMS and 2DRMS was also computed, obtaining 1.7771 m and 3.5542 m, respectively.

In this case, it is also possible to compute the positioning error. Fig. 6.19 shows the ENU errors committed by the GNSS-SDR in PVT results for the 30 seconds interval. Again, the computed altitude is more affected and biased than the 2D position in the local plane, which is aligned with the DOP values.



(a) ENU 2D position scatter plot.



(b) ENU 3D position scatter plot

Figure 6.21: GNSS-SDR precision in the Spirent simulated scenario.

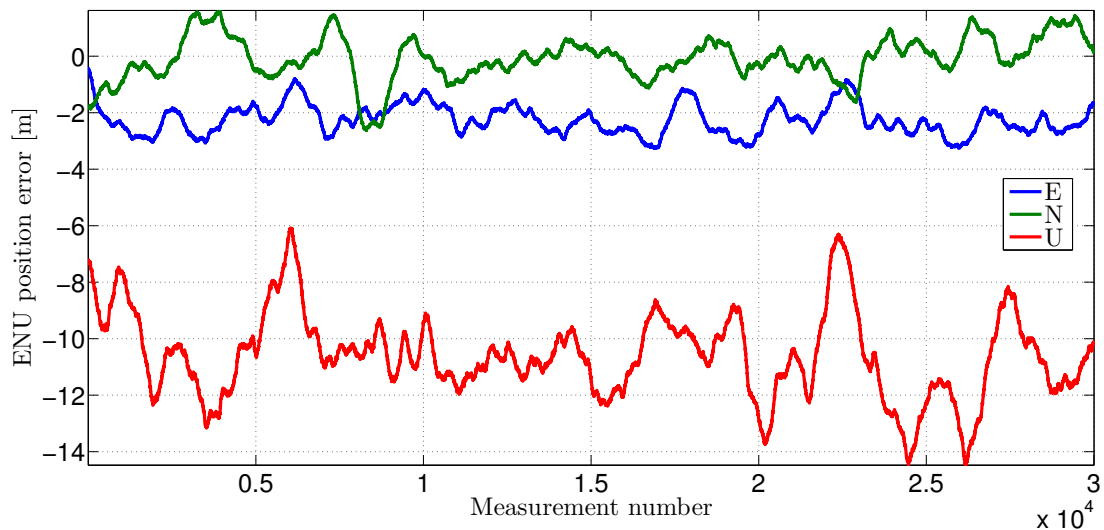


Figure 6.22: GNSS-SDR accuracy in the Spirent GPS simulated scenario.

6.5.3 Real-life signals

As a final test, the GNSS-SDR receiver was used to obtain a position in a real-life scenario. In this set-up, a Novatel GPS-600 active antenna [Nov01] was used with the USRP1 + DBSRX2 front-end to capture 160 s of signal. The capture location was the top of a building roof at the Centre Tecnològic de Telecomunicacions de Catalunya, located in Castelldefels (Barcelona, Spain). The scenario parameters are listed in 6.6.

Parameter	Value
Capture date	2012-Mar-17 05:20:15
Visible satellites PRN	9,15,17,18,26,27,28
Latitude (approximated)	41.27508455590000 N
Longitude (approximated)	1.98774803621805 E
Height	30 m
Initial DOPs	
GDOP	3.707
PDOP	3.192
HDOP	2.474
VDOP	2.016
TDOP	1.884

Table 6.6: CTTC roof-top antenna USRP + DBSRX2 scenario.

The receiver was able to acquire and track 7 satellites with a TTFF of 48 s. The average reported satellites CN0 are listed in Table 6.7.

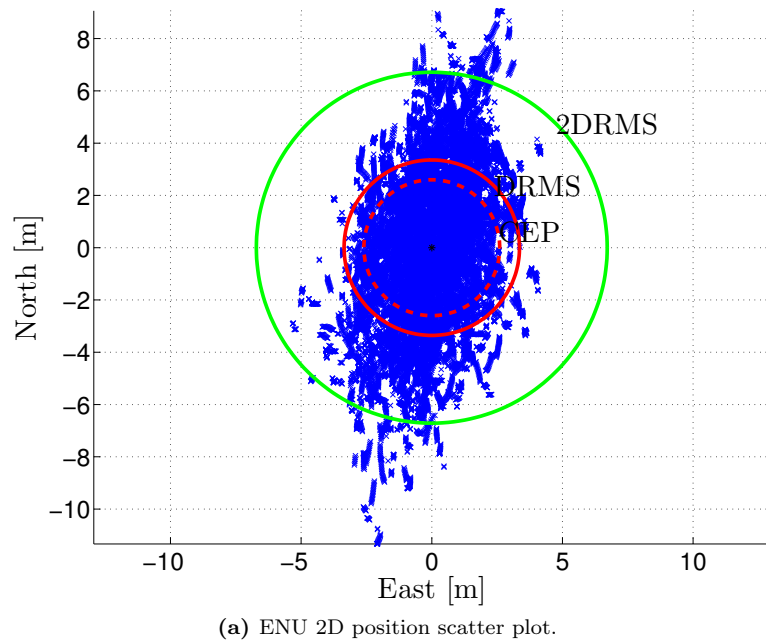
Channel	PRN	CN0
CH 0	GPS PRN 9 (Block IIA)	45.8 dB-Hz
CH 1	GPS PRN 15 (Block IIR-M)	48.5 dB-Hz
CH 2	GPS PRN 26 (Block IIA)	46.4 dB-Hz
CH 3	GPS PRN 27 (Block IIA)	46.5 dB-Hz
CH 4	GPS PRN 28 (Block IIR)	43.3 dB-Hz
CH 5	GPS PRN 17 (Block IIR-M)	39.5 dB-Hz
CH 6	GPS PRN 18 (Block IIR)	40.5 dB-Hz

Table 6.7: Satellites' CN0s reported by GNSS-SDR in a real-life scenario.

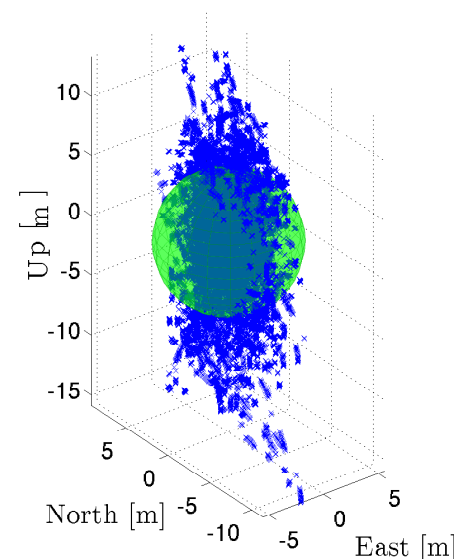
Two different PVT averaging values were tested using the captured file. In the first run, the averaging was set to 100 ms. Fig. 6.23a shows the 2D scatter plot and Fig. 6.23b shows the analogous 3D scatter plot. From the results, the CEP, DRMS, and 2DRMS 2D confidence intervals were computed, obtaining the values of 2.5987 m, 3.3566 m, and 6.7131 m respectively. The 3D confidence region DRMS and 2DRMS was also computed, obtaining 5.5646 m and 11.1293 m, respectively.

In the second run, the PVT averaging was set to 1000 ms. Fig. 6.24a shows the 2D scatter plot and Fig. 6.24b shows the analogous 3D scatter plot. From the results, the CEP, DRMS, and 2DRMS 2D confidence intervals were computed, obtaining the values of 1.5291 m, 1.9083 m, and 3.8166 m respectively. The 3D confidence region DRMS and 2DRMS was also computed, obtaining 3.6076 m and 7.2152 m, respectively. It is clear that the PVT averaging increases the receiver precision, at expenses of lower position update rate.

Finally, a qualitative position accuracy test is shown in Fig. 6.25, where the obtained KML files were rendered by Google Earth [GOO]. The yellow curve shows the position evolution for the 100 ms PVT averaging case and the red curve shows the 1000 ms PVT averaging case.

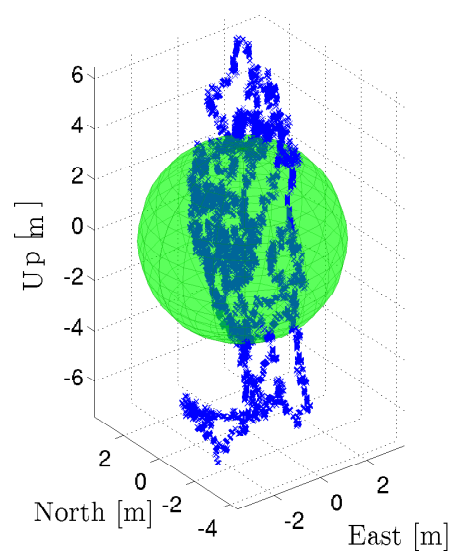
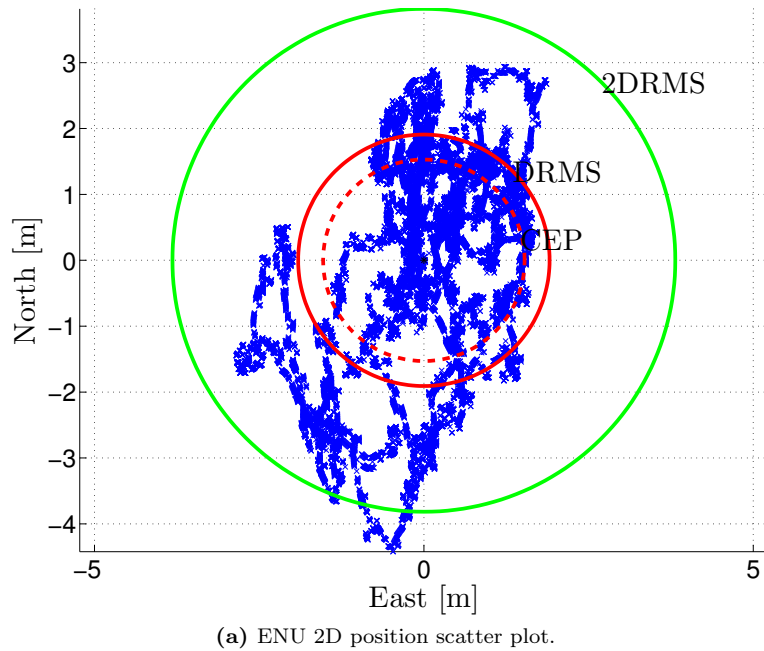


(a) ENU 2D position scatter plot.



(b) ENU 3D position scatter plot

Figure 6.23: GNSS-SDR precision obtained in a real-life scenario using 100 ms of PVT averaging.



(b) ENU 3D position scatter plot

Figure 6.24: GNSS-SDR precision obtained in a real-life scenario using 1000 ms of PVT averaging.



Figure 6.25: Google Earth KML 3D position evolution in a real-life scenario.

6.6 Summary

This Chapter presented an open source GNSS software defined receiver, discussing aspects about its design and implementation. The proposed software receiver targets multi-constellation/multi-frequency architectures, pursuing the goals of efficiency, modularity, interoperability, and flexibility demanded by user domains that require non-standard features, such as intermediate signals or data extraction and algorithms interchangeability.

The so-called GNSS-SDR is a real-time GNSS software defined receiver that contributes with several novel features. Among them, the use of software design patterns and shared memory techniques to manage efficiently the data flow between receiver blocks, the use of hardware-accelerated instructions for time-consuming vector operations like carrier wipe-off and code correlation, and the availability to compile and run on multiple software platforms and hardware architectures.

In addition, the receiver provides a full-featured data exporting options. It enables the algorithm testing either by using the low-level binary log of each of the composing modules (i.e., acquisition, tracking, telemetry decoding, observables, and PVT) or by using the end-user RINEX standard-compliant observables and navigation files. RINEX files pave the way to high accuracy positioning, since they can be directly used by applications and libraries that implement the corresponding positioning algorithms.

Although data processing for obtaining high-accuracy PVT solutions is out of the scope of GNSS-SDR, we provide a module that can compute a simple least squares solution and leaves room for more sophisticated positioning methods, such as the integration with inertial sensors. The computed position is logged in KML standard-compliant file. The receiver is also intended to be a framework for algorithm testing and an educational tool. The website available at www.gnss-sdr.org provides information and detailed instructions, as well as a link to the source code.

The complete receiver operation was tested in both simulated and real-life scenarios, using both the post-processing mode and the real-time mode. The obtained positioning precision and accuracy measurements were reported. At this time of writing (April 2012), the receiver enjoys of a 2-dimensional Distance Root Mean Square (DRMS) error lower than 2 meters for a GPS L1 C/A scenario with 8 satellites in lock and a Horizontal Dilution Of Precision (HDOP) of 1.2.

The results presented in this chapter were partially published in:

- [Sol09] M. Solé, J. Arribas, C. Fernández-Prades, D. Bernal, and J. A. Fernández-Rubio, “Correlador doble delta para GPS en tiempo real”, in *Proceedings XXIV Simposium Nacional de la Unión Científica Internacional de Radio (URSI 2009)*, Santander (Spain), September 2009.
- [FP10a] C. Fernández-Prades, C. Avilés, L. Esteve, J. Arribas, and P. Closas, “Design patterns for GNSS software receivers”, in *Proceedings of the 5th ESA Workshop on Satellite Navigation Technologies, NAVITEC’2010*, Noordwijk, The Netherlands, December 2010.
- [FP11a] C. Fernández-Prades, J. Arribas, and P. Closas, “GNSS-SDR: an open source tool for researchers and developers”, in *Proceedings of the ION GNSS 2011, Portland, Oregon (USA)*, September 2011.

Appendix 6.A Tracking pull-in algorithm

Tracking corrects the acquisition code delay estimation value according to the prior information: the transition time from acquisition to tracking and the acquisition Doppler frequency. The first step is to model the transition delay estimation as

$$\hat{t}_{\text{Acq-Trk}} = (k_{\text{Trk}} - k_{\text{Acq}})f_s^{-1} = t_{\text{Acq-Trk}} + t_{\text{Err}}, \quad (6.7)$$

where $k_{\text{Trk}} \in \mathbb{N}$ and $k_{\text{Acq}} \in \mathbb{N}$ are the current tracking sample stamp and the sample stamp at the acquisition instant, respectively, f_s is the sampling frequency, and t_{Err} is the term that absorbs the accumulated sampling clock error during the transition interval.

The next step is to compute the effects of the satellite and the receiver movement in the code frequency, according to the estimated Doppler reported by the acquisition module. The general formula for the Doppler effect [Dop42] can be written as:

$$\tilde{f} = \left(\frac{C + v_r}{C + v_s} \right) f_0, \quad (6.8)$$

where \tilde{f} is the observed frequency, C is the velocity of waves in the medium, v_r is the velocity of the receiver relative to the medium (positive if the receiver is moving towards the source), v_s is the velocity of the source relative to the medium; positive if the source is moving away from the receiver, and f_0 is the emitted frequency. Particularizing (6.8) for the GNSS carrier frequency we obtain:

$$\begin{aligned} f_c + \hat{f}_{d,\text{Acq}} &= \nu f_c, \\ \nu &= \frac{f_c + \hat{f}_{d,\text{Acq}}}{f_c} = 1 + \frac{\hat{f}_{d,\text{Acq}}}{f_c}, \end{aligned} \quad (6.9)$$

where $\hat{f}_{d,\text{Acq}} = f_{d,\text{Acq}} + f_{d,\text{Err}}$ is the Doppler estimation reported by acquisition, $f_{d,\text{Err}}$ is the error committed in the estimation, $\nu = \frac{C+v_r}{C+v_s}$ is the ratio between the satellite and the observer speeds, and f_c is the carrier frequency at RF. Using the above results, it is possible to obtain the modified chip frequency by inserting (6.9) in (6.8) as follows:

$$\tilde{f}_{\text{chip}} = \nu f_{\text{chip}} = f_{\text{chip}} + \frac{\hat{f}_{d,\text{Acq}}}{f_c} f_{\text{chip}}, \quad (6.10)$$

where f_{chip} is the nominal chip frequency. This effect is known as the *Code Doppler* effect [Kap05], which is independent from the carrier Doppler effect introduced in Section 2.2.1. In [Tsu00, p.37] can be found the Code Doppler upper bound for a static GPS L1 C/A receiver located in the Earth surface as $|f_{d,\text{code}}| = |\tilde{f}_{\text{chip}} - f_{\text{chip}}| \leq 3.2$ Hz. This value is an order of magnitude less than the maximum Carrier Doppler value in the same situation ($|f_d| \leq 4.9$ kHz. [Tsu00, p.37]). However, it is important to stress that Code Doppler has to be taken into account specially when long coherent integrations over several PRN code periods are required, such in weak signal acquisition situations as stated in [Lin02] or [O'D07], or when we need to infer the current code synchronization information from an estimation given in the past, such as the problem at hand, as we show in the sequel.

By extending the new chip period $\tilde{T}_{\text{chip}} = \frac{1}{\tilde{f}_{\text{chip}}}$ to the PRN code period we get

$$\tilde{T}_{\text{code}} = \tilde{T}_{\text{chip}} L_{\text{PRN}}, \quad (6.11)$$

where L_{PRN} is the code length in chips and \tilde{T}_{code} is the modified PRN code period. Finally, the code phase correction to be applied to the acquisition delay estimation is found as

$$\Delta \tilde{T}_{\text{code}} = \text{mod}(\hat{t}_{\text{Acq-Trk}}, \tilde{T}_{\text{code}}) \quad (6.12)$$

$$k_{\text{CORR}} = \text{round}((\tilde{T}_{\text{code}} - \Delta \tilde{T}_{\text{code}})f_s), \quad (6.13)$$

where $\Delta\tilde{T}_{\text{code}}$ is the remainder fractional part of the PRN sequence period in the transition delay $\hat{t}_{\text{Acq-Trk}}$, obtained using the modulus operator $\text{mod}(x, y)$. The difference with respect to the PRN code period in samples is k_{CORR} , and therefore, it is the correction that should be applied to the code phase reported by the acquisition module. It is approximated to the nearest integer using the rounding operator $\text{round}(\cdot)$. The tracking pull-in operation corrects the code delay reported by the acquisition using k_{CORR} and closes the tracking loops. Notice that the proposed code phase correction assumes that the code Doppler shift remains constant during the transition period. According to [Tsu00, p.40], the maximum rate of change of the Carrier Doppler frequency for the GPS L1 C/A is in the order of 0.936 Hz/s, which in turn it becomes 0.0006 Hz/s for the maximum rate of change Code Doppler frequency.

Using (6.10) and the transition time estimation of (6.7) it is possible to compute the code delay offset expressed in chips units caused by the transition and identify the estimation errors as

$$\begin{aligned}\Delta\hat{K}_{\text{chips}} &= \hat{f}_{\text{chip}}\hat{t}_{\text{Acq-Trk}} = \\ &= \left(1 + \frac{\hat{f}_{d,\text{Acq}}}{f_c}\right)f_{\text{chip}}(t_{\text{Acq-Trk}} + t_{\text{Err}}) = \\ &= \underbrace{\left(1 + \frac{f_{d,\text{Acq}}}{f_c}\right)f_{\text{chip}}t_{\text{Acq-Trk}}}_{\text{true value}} + \underbrace{\frac{f_{d,\text{Err}}}{f_c}f_{\text{chip}}t_{\text{Acq-Trk}}}_{\text{Doppler error } (\varepsilon_{\text{Doppler}})} + \underbrace{\left(1 + \frac{\hat{f}_{d,\text{Acq}}}{f_c}\right)f_{\text{chip}}t_{\text{Err}}}_{\text{clock error } (\varepsilon_{\text{Clk}})}.\end{aligned}\quad (6.14)$$

From the above expression it is possible to identify the two main sources of error in $\Delta\hat{K}_{\text{chips}}$ and their effects, as the Doppler acquisition estimation error term ($\varepsilon_{\text{Doppler}}$) and the transition time estimation error term (ε_{Clk}).

On the one hand, the effect of $\varepsilon_{\text{Doppler}}$ is shown in Fig. 6.26, where we plot the error evolution for a range of $f_{d,\text{Err}} = 10 - 500$ Hz acquisition Doppler errors versus the transition time. This term does not take into account the effect of the code Doppler variation during the transition time interval, but as shown previously, is has a very limited effect compared to the acquisition Doppler estimation error, and thus, it can be neglected.

On the other hand, the effect ε_{Clk} is shown in Fig. 6.27 for different sample clock accuracies expressed in Parts Per Million (PPM)¹².

The curves in both figures were computed for GPS L1 C/A signal with $f_s = 4$ MSPS, $f_c = 1575.42$ MHz and $f_{\text{chip}} = 1.023$ MHz.

From the results it is clear that the sample clock error has a dramatic effect in the acquisition to tracking transition, which is the main limitation factor as stated in Schamus' work [Sch99]. Schamus also proposed a method to estimate the sample clock frequency offset and then compensate it in the Code Delay prediction formula. Results show that using the clock error compensation it is possible to reach acquisition to tracking transitions up to 30 seconds in SDR GPS L1 C/A receiver, considering a maximum allowable Code Delay estimation error of half-chip for the tracking start operation.

¹²For instance, a non-compensated crystal oscillator has an accuracy in the order of 20 to 50 PPS. The USRP 1 [Ett10] on-board oscillator has an accuracy of 20 PPS.

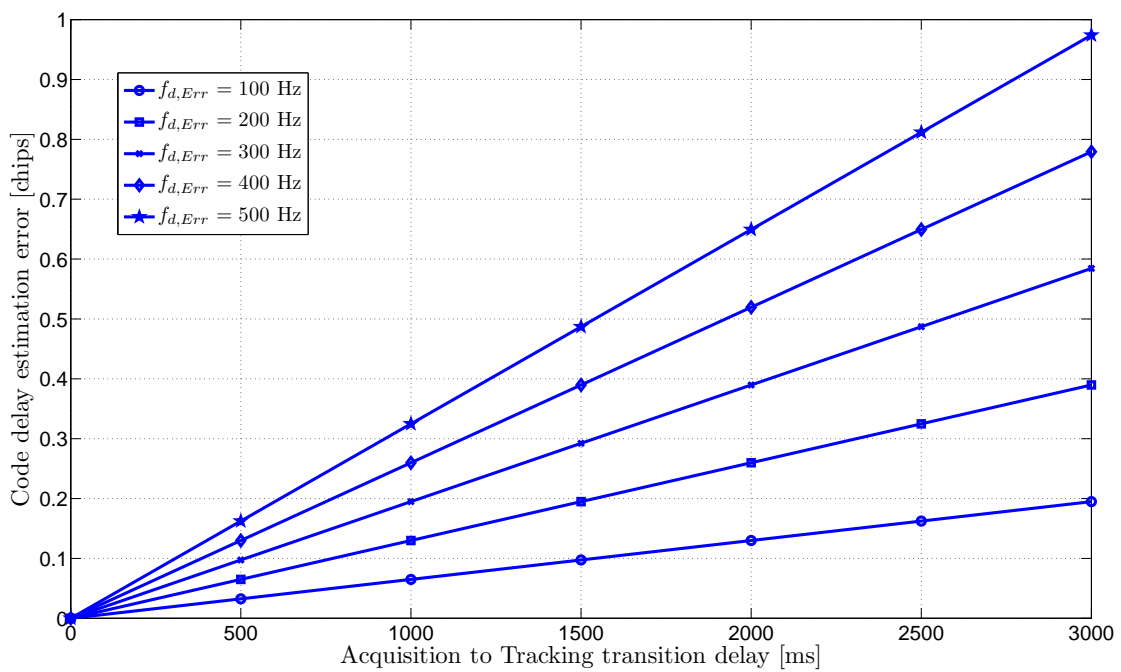


Figure 6.26: Code delay estimation error term in ΔK_{chips} due to acquisition Doppler estimation error.

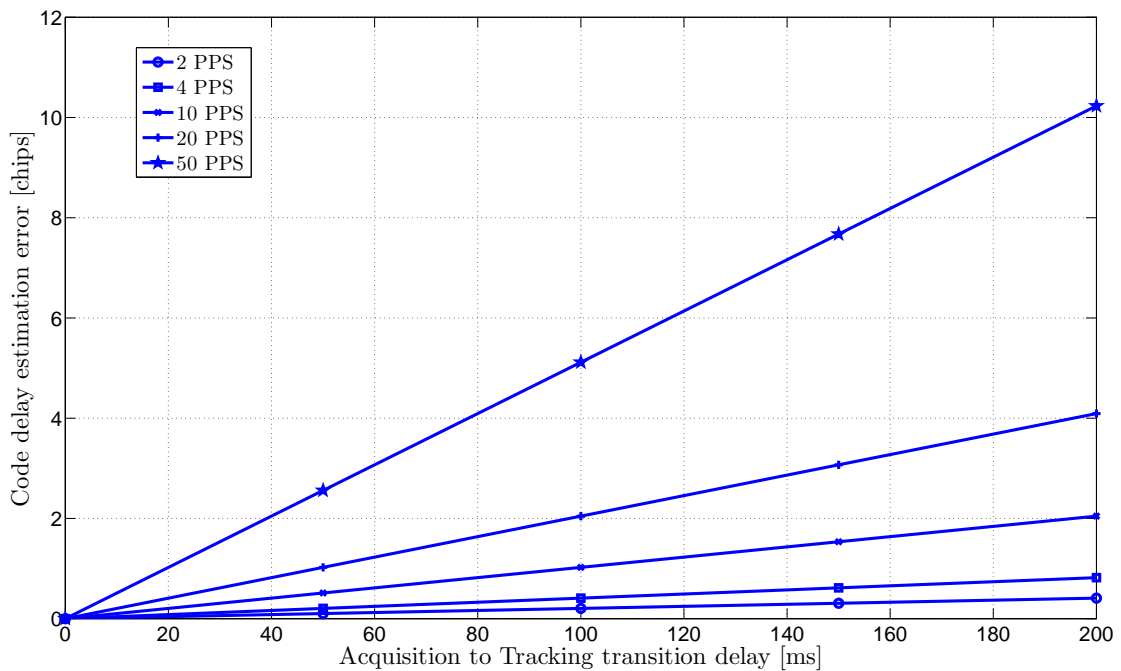


Figure 6.27: Code delay estimation error term in ΔK_{chips} due to acquisition Doppler estimation error.

Chapter 7

Conclusions and Directions for Future Research

I wanted to change the world. But I have found that the only thing one can be sure of changing is oneself.

Aldous Huxley.

THIS Dissertation has dealt with one of the most critical and challenging signal processing problems in a GNSS receiver: the signal acquisition. We analyzed the potential of antenna arrays and spatial-domain processing to mitigate the effects of interfering signals as well as to improve the acquisition performance. Based on the results, we proposed a novel array-based acquisition algorithm using a well-established statistical detection theory framework, and, going further, we demonstrated both the real-time implementation feasibility and the performance in realistic scenarios. Additionally, we completed the receiver chain by designing and implementing a GNSS software-defined receiver that works in real-time and contributes with several new features.

The present Chapter summarizes the conclusions and contributions arose by the research reported in the foregoing chapters. In addition, a list of topics that may be the subject for future research is also suggested.

The work has begun with an overview of a generic global navigation system in **Chapter 2**, providing some details about the navigation signals structure of both the American GPS and the European Galileo systems. The signal propagation channel was modeled stressing the interference problem, and several potential interfering sources are listed. We identified that RFIs (either intentional or unintentional) remain as the most important cause of performance degradation, specially in the acquisition operation, since it has the lowest sensitivity of the whole receiver operations, and, consequently, acquisition becomes a performance bottleneck.

In **Chapter 3** we focused the analysis of the GNSS signal acquisition as a detection problem, using the NP detection theory framework and the single-antenna acquisition signal model. The NP approach was used here to derive both the optimum detector (known as *clairvoyant detector*) and the GLRT detector. The GLRT detector assumes no prior knowledge of the satellite signal synchronization parameters. In this Chapter we also proposed a new detector test statistic intended to jointly acquire a set of GNSS satellites, which contributes in reducing both the acquisition time and the required computational resources with respect to traditional techniques.

The effects of the front-end bandwidth were also included in the performance analysis. The performance expressions show that, in the acquisition operation, the detection probability is directly proportional to the available SNR. Increasing the acquisition bandwidth in a BPSK or CBOC modulation, such as the used by the GPS L1 C/A or by the Galileo E1 signals, contributes to the SNR degradation when the cut-off frequency overpasses the main spectrum lobe, since

the GNSS signals power are well below the noise floor. As a consequence, the acquisition with the minimum bandwidth obtained the best results.

At the conclusion of this PhD Thesis, there remain some research related to this topic which might be worth exploring:

- Improve the joint acquisition algorithm by using multi-user interference mitigation techniques to minimize the cross-correlation terms of the detected satellites.

It is known that a single-antenna receiver can make use of time and frequency diversity to mitigate interferences, even though the performance of these techniques is compromised in low SNR conditions or in the presence of wideband interferences. On the other hand, antenna arrays receivers can benefit from spatial-domain processing, and thus mitigate the effects of interfering signals. The spatial diversity has been traditionally applied to the signal tracking operation of GNSS receivers. However, initial tracking conditions depend on signal acquisition. Surprisingly, the application of antenna arrays to GNSS signal acquisition has not yet received much attention. In **Chapter 4**, we investigated the application of antenna arrays to this problem and we proposed a possible solution by extending the GLRT to the GNSS array signal model to obtain an original detector which is able to mitigate temporally uncorrelated interferences even if the array is unstructured and moderately uncalibrated. The key statistical feature was the assumption of an arbitrary and unknown covariance noise matrix, which attempts to capture the statistical behavior of the interferences and other non-desirable signals, while exploiting the spatial dimension provided by antenna arrays. Closed form expressions for the detection and false alarm probabilities were provided. The performance and the interference rejection capability were modeled and compared to their theoretical bound, established by deriving the *clairvoyant detector* for the unstructured array signal model.

The proposed detector was proven to be a UMP test detector and has CFAR properties. Both properties are highly valuable in a cold acquisition situation, where there is neither information of the satellites' direction of arrival, that prevents from applying spatial-based beamforming, nor the receiving signals power, that makes difficult to set an acquisition threshold. The protection against interference effects was modeled by means of signal and interference subspace projections. The impact of the number of antenna elements and the effect of narrowband and wideband interferences were also analyzed and simulated. Results show that the detector offers a superior interference protection in both interference cases, with respect to state-of-the-art algorithms. The proposed array-based acquisition algorithm was also compared to conventional acquisition techniques performed after blind null-steering beamformer approaches, such as the power minimization algorithm. Results shown again that the proposed algorithm improves the acquisition performance, specially in harsh interference scenarios. Ultimately, we compared the proposed algorithm performance to a conventional acquisition after the MVDR beamformer, which requires a prior estimation of the signal DOA and the array attitude. We concluded that the MVDR is severely affected by moderate pointing errors and/or array miss-calibration, while the GLRT detector remains insensible to this situation.

Additionally, the detector performance was examined under realistic conditions, modeled as the presence of errors in the covariance matrix estimation due to finite sample size, residual synchronization errors, and signal quantization effects. From the results we can conclude that the signal quantization plays a key role in the performance of the proposed detector. In that sense, the relation between the ADC resolution and the interference mitigation capability was found. Theoretical results were supported by Monte Carlo simulations.

Some future research lines of this topic which might be worth exploring are:

- Explore the application of the Bayesian approach to the acquisition problem; it might be possible to estimate prior PDFs for the synchronization parameters and integrate them in the GLRT detector. In addition to the previous state information available in a warm or in a hot acquisition, the receiver could be assisted using a communication network, (i.e., using A-GNSS information). The array-based acquisition algorithm could be enhanced to obtain shorter TTFF and better performance.
- The integration of inertial sensors in the receiver might provide valuable information in the acquisition stage. The array attitude could be estimated by using IMU data combined

with last available tracking and PVT information. Ultimately, an hybridization between array-based acquisition and tracking might be possible, since both algorithms are related in the sense that acquisition contains prior information suitable for tracking initialization and vice-versa.

Going further towards a proof-of-concept prototype of the proposed acquisition algorithms, **Chapter 5** was devoted to develop a novel real-time array-based GNSS receiver platform with a two-fold main target: to examine the real-time implementation feasibility and to explore their performance in real-life scenarios, taking into account all the unmodeled phenomena such as the antenna-array elements radiation patterns and front-end non-linearities, among others. The platform is intended to be used as a research tool tightly coupled with software defined GNSS receivers. A complete signal reception chain, including the antenna array and the multichannel phase-coherent RF front-end for the GPS L1/ Galileo E1 was designed, implemented and tested. The details of the digital processing section of the platform, such as the array signal statistics extraction modules, are also provided. The design trade-offs and the implementation complexities were carefully analyzed and taken into account. As a proof-of-concept, the problem of GNSS vulnerability to interferences was addressed using the presented platform. The array-based acquisition algorithms introduced in this Dissertation were implemented and tested under realistic conditions. The performance of the algorithms was compared to single antenna acquisition techniques, measured under strong in-band interference scenarios, including narrow/wide band interferers and communication signals. The platform performance results were aligned with the theoretical and simulated one, thus, completing the algorithm validation.

The presented platform enables a myriad of expansion possibilities, hereafter can be found some ideas for a future work:

- The platform can be enhanced by integrating an IMU. The inertial measurements should be synchronized to the array snapshots stream using the sample clock. This data should be used by both acquisition and tracking algorithms to estimate the array attitude.
- Design and implementation of dual-band antenna elements patches to cover both the GPS L1 / Galileo E1 1575.42 MHz and the GPS L5 Galileo E5a 1176.45 MHz links, which provide a complete SoL signals coverage of two of the most evolved GNSS. The multichannel front-end and the FPGA processing should be extended to accommodate both links in each channel.
- Explore the integration of array elements and front-end calibration procedures.
- Explore the application of open source soft processors such as the Aeroflex Gaisler LEON3 [LEO] to replace the Microblaze implementation. Ultimately, it should be possible to integrate the GNU Radio framework and the GNSS-SDR software receiver in the soft processor.

The platform was designed to demonstrate the implementation feasibility of array-based acquisition algorithms, leaving the rest of the receiver operations (mainly, tracking, navigation message decoding, code and phase observables, and basic PVT solution) to a SDR receiver running in a PC, processing in real-time the spatially-filtered signal sample stream coming from the platform using a Gigabit Ethernet bus data link. In **Chapter 6**, we close the loop by designing and implementing such software receiver.

The proposed software receiver targets multi-constellation/multi-frequency architectures, pursuing the goals of efficiency, modularity, interoperability, and flexibility demanded by user domains that require non-standard features, such as intermediate signals or data extraction and algorithms interchangeability. In this context, we introduced an open-source, real-time GNSS software defined receiver (so-named GNSS-SDR) that contributes with several features such as the use of software design patterns and shared memory techniques to manage efficiently the data flow between receiver blocks, the use of hardware-accelerated instructions for time-consuming vector operations like carrier wipe-off and code correlation, and the availability to compile and run on multiple software platforms and hardware architectures.

The GNSS software receiver probably envisages a countless topics for future work and extensions. For instance,

- Upgrade the implemented receiver algorithms to support the existing GLONASS L1 and the forthcoming Galileo E1 signals. Since the receiver structure is highly modular, it should be possible to implement the acquisition, tracking, and telemetry decoding modules for Galileo and/or GLONASS while keeping the compatibility with the former GPS implementation. The receiver could provide combined GPS and Galileo observables and thus, enhanced PVT precision is expected. Additionally, it could be possible to implement the support for SBAS signals, such as EGNOS or WAAS.
- Explore the integration options of the available COTS IMU devices. This includes, on the one hand, the development of new device drivers or the integration of the existing ones, and, on the other hand, the accommodation of the inertial measurements in the signal processing chain. One critical point is the ability to synchronize the signal sample stream and the IMU measurements in order to be used by the algorithms at different levels of integration (e.g., loose, tight, and ultra-tight integration).
- Explore the implementation options of Signals of Opportunity positioning [Fis05]. Since most of the PCs are usually equipped with communication devices such as wifi, 3G or LTE network cards, the software-based GNSS receiver running on it may have access to ToA information or to the reception power of these signals. Furthermore, it should be possible to obtain GNSS assistance information using specific protocols, such as the Radio Resource Location Services Protocol (RRLP) for 3G networks or the 3GPP LTE Positioning Protocol (LPP).



Figure 7.1: The Claus Hypothesis.

Bibliography

- [3gp11] “3GPP TS 36.104: Base Station (BS) radio transmission and reception v.8.12.0”, Tech. rep., LTE 3GPP, June 2011.
- [Abr04] D. Abrahams, and A. Gurtovoy, *C++ Template Metaprogramming: Concepts, Tools, and Techniques from Boost and Beyond*, Addison Wesley Professional, Reading, MA, 2004.
- [Ada03] D. Adams, “The Effects of SAW Group Delay Ripple on GPS and Glonass Signals.”, Tech. rep., NovAtel Inc., Calgary, Alberta, 2003.
- [Agi04] Agilent Technologies, *Agilent E4448A 3 Hz to 50 GHz PSA Series spectrum analyzer*, October 2004.
- [Agi05a] Agilent Technologies, *Agilent 33250A 80 MHz function / Arbitrary Waveform generator datasheet*, October 2005.
- [Agi05b] Agilent Technologies, *Agilent N4001A 10 MHz - 26.5 GHz SNS-Series Noise Source datasheet*, Dec. 2005.
- [Agi05c] Agilent Technologies, *Agilent N8973A, N8974A, N8975A NFA Series Noise Figure Analyzers datasheet*, Dec. 2005.
- [Agi06] Agilent Technologies, *Agilent E4438C ESG Vector Signal Generator datasheet*, Dec. 2006.
- [Agi07] Agilent Technologies, *Agilent GPS Personality for the E4438C ESG Vector Signal Generator Option 409. Product Overview*, Oct. 2007.
- [Agi11] Agilent technologies, “Advanced Design System ADS EEsoft web page”, May 2011, <http://www.agilent.com/find/eesof>.
- [Ako97] D. Akos, *A Software Radio Approach to Global Navigation Satellite System Receiver Design*, PhD Thesis, College of Engineering and Technology, Ohio University, August 1997.
- [Alt09] Altera, San Jose, CA, *Nios II Processor Reference Handbook*, March 2009.
- [AM11] Microwave Materials Division Arlon-MED, “Arlon 25N Ceramic Hydrocarbon Thermoset Laminates, Microwave Low Loss PCB substrate”, May 2011, <http://www.arlon-med.com/25N25FR.pdf>.
- [Ami05] M. G. Amin, and W. Sun, “A Novel Interference Suppression Scheme for Global Navigation Satellite Systems Using Antenna Array”, *IEEE Journal on Selected Areas in Communications*, vol. 23, no. 5, pp. 999–1012, May 2005.
- [Ana02] Analog Devices, Inc., Norwood, MA, *AD8369 Datasheet. 45 dB Digitally Controlled VGA LF to 600 MHz*, January 2002.
- [Ang07] M. Anghileri, T. Pany, D. Sanromà-Güixens, J. H. Won, A. Sicramaz-Ayaz, C. Stöber, I. Krämer, and D. Dötterböck, “Performance evaluation of a multi-frequency GPSGalileoSBAS software receiver”, *Proceedings of the 20th International Technical Meeting of the Satellite Division of the Institute of Navigation (ION GNSS'07)*, pp. 2749–2761, 2007.

- [App12] Apple Inc., *Apple iPhone 4S specifications*, February 2012, <http://www.apple.com/iphone/specs.html>.
- [ARM] “The Armadillo C++ linear algebra library”, Retrieved: February 28, 2012, <http://arma.sourceforge.net/>.
- [Arr09a] J. Arribas, D. Bernal C., Fernández-Prades, P. Closas, and J. A. Fernández-Rubio, “A novel real-time platform for digital beamforming with GNSS software defined receivers”, *Proceedings of the ION GNSS 2009, Savannah, GA (USA)*, September 2009.
- [Arr09b] J. Arribas, C. Fernández-Prades, D. Bernal, and J. A. Fernández-Rubio, “Plataforma de conformación de haz digital para receptores GNSS en tiempo real”, *Proceedings XXIV Simposium Nacional de la Unión Científica Internacional de Radio (URSI 2009)*, Santander (Spain), September 2009.
- [Arr10a] J. Arribas, P. Closas, and C. Fernández-Prades, “Joint acquisition strategy of GNSS satellites for computational cost reduction, NAVITEC’2010.”, *Proceedings of the 5th ESA Workshop on Satellite Navigation Technologies, NAVITEC’2010*, Noordwijk, The Netherlands, December 2010.
- [Arr10b] J. Arribas, C. Fernández-Prades, and P. Closas, “Receiver Operating Characteristic For Array-Based GNSS Acquisition”, *Proceedings of XVIII European Signal Processing Conference, EUSIPCO*, pp. 1082–1086, Aalborg, Denmark, August 2010.
- [Arr11a] J. Arribas, C. Fernández-Prades, and P. Closas, “Antenna Array Based GNSS Signal Acquisition: Real-time Implementation and Results”, *Proceedings of the ION GNSS 2011, Portland, Oregon (USA)*, September 2011.
- [Arr11b] J. Arribas, C. Fernández-Prades, and P. Closas, “Array-Based GNSS Acquisition In The Presence Of Colored Noise”, *Proceedings of the 36th IEEE International Conference on Acoustics, Speech, and Signal Processing, ICASSP’11*, Prague, Czech Republic, May 2011.
- [Arr12a] J. Arribas, P. Closas, C. Fernández-Prades, M. Cuntz, M. Meurer, and A. Konovaltsev, “Advances in the theory and implementation of GNSS antenna array receivers”, *Microwave and Millimeter Wave Circuits and Systems*, Chap. 9, John Wiley & Sons Limited, 2012, in press.
- [Arr12b] J. Arribas, C. Fernández-Prades, and P. Closas, “Antenna Array Based GNSS Signal Acquisition for Interference Mitigation”, *accepted in IEEE Transactions on Aerospace and Electronic Systems*, 2012.
- [Ash06] V. Ashkenazi, “Geodesy and satellite navigation”, *Inside GNSS*, vol. 1, no. 3, pp. 44–49, 2006.
- [Bal03] C.A. Balanis, *Antenna Theory*, John Wiley & Sons Inc, 2003.
- [Bal08a] A. T. Balaei, D. Akos, and A. G. Dempster, “Quantization degradation of GNSS signal quality in the presence of CW RFI”, 2008.
- [Bal08b] A. T. Balaei, B. Motella, and A. Dempster, “A preventative approach to mitigating CW interference in GPS receivers”, *GPS Solutions*, vol. 12, pp. 199–209, 2008.
- [Ban85] S. Bancroft, “An algebraic solution of the GPS equations”, *IEEE Transactions on Aerospace and Electronic System*, vol. 21, pp. 56–59, 1985.
- [Ban06] D. Banerjee, *PLL Performance, Simulation, and Design*, Dog Ear Publishing, LLC, Indianapolis, IN, 4th ed., 2006.
- [Bar92] R. J. Barton, and H. V. Poor, “On generalized signal-to-noise ratios in quadratic detection”, *Mathematics of Control, Signals, and Systems (MCSS)*, vol. 5, no. 1, pp. 81–91, 1992.
- [Bas03] F. Bastide, D. Akos, C. Macabiau, and B. Roturier, “Automatic gain control (AGC) as an interference assessment tool”, *Proceedings of ION GPS 2003*, pp. 2042–2053, Portland, Oregon, September 2003.

- [BEI06] “Submission of the updated information of Compass system to the Fourth Resolution 609 (WRC-03), RG/036/2006”, Tech. rep., Radio Regulatory Department, Ministry of Information Industry, China, 2006.
- [Bei11] “BeiDou Navigation Satellite System Signal In Space Interface Control Document (Test Version)”, Tech. rep., China Satellite Navigation Office, December 2011.
- [Bel63] P. A. Bello, “Characterization of randomly time-variant linear channels”, *IEEE Journal on Selected Areas in Communications*, vol. 11, pp. 360–393, 1963.
- [Ben99] S. Benedetto, and E. Biglieri, *Principles of digital transmission: With wireless applications*, Kluwer Academic Plenum Publishers, New York, 1999.
- [Ber08] D. Bernal, P. Closas, and J. A. Fernández-Rubio, “Digital IQ demodulation in array processing: Theory and implementation”, *Proc. XVI European Signal Processing Conference, EUSIPCO*, Lausanne, Switzerland, August 2008.
- [Bes04] F. Bestid, E. Chatre, C. Macabiau, and B. Roturier, “GPS L5 and Galileo E5a/E5b signal-to-noise density ratio degradation due to DME/TACAN signals: Simulations and theoretical derivation”, *ION National Technical Meeting*, pp. 1049–1062, San Diego, CA, January 2004.
- [Bet99] J. W. Betz, “The offset carrier modulation for GPS modernization”, *Proceedings of the ION GNSS 1999 (USA)*, September 1999.
- [Bet00] J. W. Betz, “Effect of narrowband interference on GPS code tracking accuracy”, *ION National Technical Meeting*, pp. 16–27, Anaheim, CA, January 2000.
- [Bet01] J. W. Betz, “Effect of partial-band interference on receiver estimation of C=N0: theory”, *ION National Technical Meeting*, pp. 817–828, Long Beach, CA, January 2001.
- [Bet02] J. W. Betz, and D. B. Goldstein, “Candidate Designs for an Additional Civil Signal in GPS Spectral Bands”, *Proceedings of The Institute of Navigation National Technical Meeting*, San Diego, CA, January 2002.
- [Bet04] J. W. Betz, and B. M. Titus, “Intersystem and intrasystem interference with signal imperfections”, *IEEE Position Location and Navigation Symposium (PLANS)*, pp. 558–565, Monterey, CA, April 2004.
- [BJA] “Boost.build v2 User Manual”, Retrieved: October 21, 2010, <http://www.boost.org/boost-build2/doc/html/index.html>.
- [Bor06] D. Borio, L. Camoriano, and L. Lo Presti, “Impact of the acquisition searching strategy on the detection and false alarm probabilities in a CDMA receiver”, *Position, Location, And Navigation Symposium, PLANS’06*, pp. 1100–1107, April 2006.
- [Bor07] K. Borre, D. M. Akos, N. Bertelsen, P. Rinder, and S. H. Jensen, *A Software-Defined GPS and Galileo Receiver. A Single-Frequency Approach*, Applied and Numerical Harmonic Analysis, Birkhäuser, 2007.
- [Bor08] D. Borio, *A statistical theory for GNSS signal acquisition*, PhD Thesis, Politecnico Di Torino, Torino, Italy, May 2008.
- [Bor09a] D. Borio, and D. Akos, “Noncoherent Integrations for GNSS Detection: Analysis and comparisons”, *IEEE Transactions on Aerospace and Electronics Systems*, vol. 45, no. 1, pp. 360–375, January 2009.
- [Bor09b] D. Borio, C. O’Driscoll, and G. Lachapelle, “Coherent, noncoherent, and differentially coherent combining techniques for acquisition of new composite GNSS signals”, *IEEE Transactions on Aerospace and Electronic Systems*, vol. 45, no. 3, pp. 1227–1240, July 2009.
- [Bor10] D. Borio, “GNSS Acquisition in the Presence of Continuous Wave Interference”, *IEEE Transactions on Aerospace and Electronics Systems*, vol. 46, no. 1, pp. 47–60, January 2010.

- [Bou11] P. Boulton, R. Borsato, B. Butler, and K. Judge, “GPS Interference Testing Lab, Live, and LightSquared”, *Inside GNSS*, vol. 6, no. 4, pp. 32–45, July 2011.
- [BSC] “The Boost Statechart Library”, Retrieved: August 29, 2011, www.boost.org/doc/libs/release/libs/statechart/doc/index.html.
- [Buc97] T. Buck, and G. Sellick, “GPS RF interference via a TV signal”, *ION GPS International Technical Meeting*, pp. 1497–1501, Kansas City, MO, September 1997.
- [Bur00] L. M. Burns, “RF & Microwave Design Techniques for PCBs”, *Proceedings of the PCB design conference west*, Santa Clara, CA, March 2000.
- [Cam10] Cambridge Silicon Radio (CSR) plc., *SiRFstarIII GSC3e/LPx and GSC3f/LPx datasheet*, March 2010.
- [Cap69] J. Capon, “High-resolution frequency-wavenumber spectrum analysis”, *Proceedings IEEE*, vol. 8, no. 57, pp. 1408–1418, August 1969.
- [Car88] B. D. Carlson, “Covariance matrix estimation errors and diagonal loading in adaptive arrays”, *IEEE Transactions on Aerospace and Electronic Systems*, vol. 24, no. 4, pp. 397–401, July 1988.
- [Car05] G. Carrie, F. Vincent, T. Deloues, D. Pietin, and A. Renard, “A New Blind Adaptive Antenna Array for GNSS Interference Cancellation”, *The Thirty-Ninth Asilomar Conference on Signals, Systems and Computers, 2005*, pp. 1326–1330, November 2005.
- [Cas01] G. Casella, and R. L. Berger, *Statistical Inference, Second Edition*, Duxbury Press, Pacific Grove, CA, USA, 2001.
- [Cen02] Coordination Scientific Information Center, “Global navigation satellite system - GLONASS - interface control document 5.0”, Tech. rep., Moscow, 2002.
- [Cha82] H. Chang, “Presampling filtering, sampling and quantization effects on the digital matched filter performance”, *Proceedings of the international Telemetering Conference*, pp. 889–915, San Diego, CA, 1982.
- [Cha01] V. Chakravarthy, J. Tsui, D. Lin, and J. Schamus, “Software GPS receiver”, *GPS Solutions*, vol. 5, no. 2, pp. 63–70, October 2001.
- [Chu95] C. Chung, “Differentially coherent detection technique for direct-sequence code acquisition in a rayleigh fading mobile channel”, *IEEE Transactions on Communications*, pp. 1116–11, 1995.
- [Chu09] C. M. Church, and I. J. Gupta, “Calibration of GNSS Adaptive Antennas”, *Proceedings of the 22nd International Meeting of the Satellite Division of The Institute of Navigation (ION GNSS)*, pp. 344–350, Savannah, GA, September 2009.
- [Clo99] M. Cloutier, T. Varelas, C. Cojocaru, and F. Balteanu, “A 4-dB NF GPS Receiver Front-End with AGC and 2-b A/D”, *Proceedings of the IEEE Custom Integrated Circuits Conference*, pp. 205–208, San Diego, May 1999.
- [Clo09a] P. Closas, *Bayesian Signal Processing Techniques for GNSS Receivers: From multipath mitigation to positioning*, PhD Thesis, Universitat Politècnica de Catalunya (UPC), Barcelona, Spain, June 2009.
- [Clo09b] P. Closas, C. Fernández-Prades, and J. A. Fernández-Rubio, “Cramér-Rao Bound Analysis of Positioning Approaches in GNSS Receivers”, *IEEE Transactions on Signal Processing*, vol. 57, no. 10, pp. 3775–3786, October 2009.
- [Clo10a] P. Closas, J. Arribas, and C. Fernández-Prades, “Testing for normality of UWB-based distance measurements by the Anderson-Darling statistic”, *Proceedings of Future Networks & Mobile Summit (FUNEMS)*, Florence (Italy), June 2010.
- [Clo10b] P. Closas, and C. Fernández-Prades, “Bayesian nonlinear filters for direct position estimation”, *Proc. of IEEE Aerospace Conference*, pp. 1–12, Big Sky, MT, March 2010.

- [CMa] “CMake”, Retrieved: October 21, 2010, <http://www.cmake.org/>.
- [Coe92] A. Coenen, and D. Van Nee, “Novel fast GPS/GLONASS code-acquisition technique using low update rate FFT”, *IEEE Electronics Letters*, pp. 863–865, 1992.
- [Cor02] NAVSYS Corporation, “High gain advanced GPS receiver. white paper”, September 2002.
- [CP-10] “Combined performances for open GPS/Galileo receivers”, Tech. rep., EU-US Cooperation on Satellite Navigation / Working Group C, July 2010.
- [CP03] J. P. Cabrera-Plaza, and T. Burger, “Inter-system interference experiments for Galileo and GPS in L1 (1575.42 MHz)”, *European Navigation Conference (ENC)*, Graz, Austria, April 2003.
- [Cum01] D. Cummings, “Aggregate ultra wideband impact on global positioning system receivers”, *IEEE Radio and Wireless Conference RAWCON*, pp. 101–104, August 2001.
- [Cun09] M. Cuntz, L. A. Greda, M. Heckler, A. Konovaltsev, and M. Meurer, “Architecture of a Real-Time Safety of Life Receiver”, *Proceedings of the ION GNSS 2009, Savannah, GA (USA)*, September 2009.
- [Dat05] J. Dattorro, *Convex Optimization and Euclidean Distance Geometry*, Meboo Publishing USA, Palo Alto, California, 2005.
- [Dav88] L. D. Davission, J. Iinatti, and H. Saarnisaari, “Fast Single-Element PN Acquisition for the TDRSS MA System”, *IEEE Transactions on Communications*, vol. 36, no. 11, pp. 1226–1235, 1988.
- [Der04] L. Deri, “Improving passive packet capture: Beyond device polling”, *Proceedings of the 4th International System Administration and Network Engineering Conference, SANET’04*, Amsterdam, The Netherlands, Sept. 2004.
- [Des04] S. Deshpande, and M. E. Cannon, “Interference effects on the GPS signal acquisition”, *Proceedings of ION NTM 2004*, pp. 1026–1036, Anaheim, CA, January 2004.
- [Dhi10] A. Dhital, P. Closas, C. Fernández-Prades, J. Arribas, F. Sottile, M. A. Spirito, Z. Xiong, M. Kieffer, E. Lagunas, and M. Nájar, “Evaluation of tracking algorithms using the NEWCOM++ WPRB database measurements”, *Demo at the Future Networks & Mobile Summit (FUNEMS)*, Florence (Italy), June 2010.
- [Dig09] F. Diggelen, *A-GPS: Assisted GPS, GNSS, and SBAS*, Artech House, 2009.
- [Dop42] C. Doppler, “Über das farbige Licht der Doppelsterne und einiger anderer Gestirne des Himmels (On the colored light of the double stars and certain other stars of the heavens)”, *Abh. Kniglich Bhmischen Ges. Wiss.*, vol. 2, pp. 467–482, 1842.
- [Dou02] B. P. Douglass, *Real-Time Design Patterns: Robust Scalable Architecture for Real-Time Systems*, Addison Wesley, Upper Saddle River, NJ, 2002.
- [ECL] “Eclipse”, Retrieved: October 21, 2010, <http://www.eclipse.org/>.
- [Ede98] A. Edelman, T. A. Arias, and S. T. Smith, “The geometry of algorithms with orthogonality constraints”, *SIAM J. Matrix Anal. Appl.*, vol. 20, pp. 303–353, 1998.
- [Eno05] H. A. El-natour, A. C. Escher, C. Macabiau, and M. L. Boucheret, “Impact of Multipath and Cross-Correlation on GPS acquisition in Indoor Environments”, *ION National Technical Meeting*, San Diego, CA, January 2005.
- [Ene09] European Commission Directorate-General for Energy, and Transport, “EGNOS Service Definition Document: Open Service EGN-SDD OS V1.0”, Tech. rep., 2009.
- [Eng01] P. Enge, A. Fan, A. Tiwari, A. Chou, W. Mann, A. Sahai, J. Stone, and B. Van Roy, “Improving GPS coverage and continuity: Indoors and downtown”, *Proceedings of International Technical Meeting*, pp. 3067–3076, Salt Lake City, UT, September 2001.
- [Est12] L. Esteve, *Contribución al desarrollo de un receptor GNSS definido por software*, Master Thesis, Escola Tècnica Superior d’Enginyeria de Telecomunicació de Barcelona (ETSETB), Universitat Politècnica de Catalunya (UPC), Barcelona, Spain, 2012.

- [ETS00] “Digital cellular telecommunications system (Phase 2+); GSM Cordless Telephony System (CTS), Phase 1; CTS-FP Radio subsystem ETSI EN 302 408 V8.0.1”, Tech. rep., European Telecommunications Standards Institute (ETSI), 2000.
- [ETS04] “Electromagnetic compatibility and Radio spectrum Matters (ERM); Transmitting equipment for the digital television broadcast service, Terrestrial (DVB-T), ETSI EN 302 296 V1.1.1”, Tech. rep., European Telecommunications Standards Institute (ETSI), 2004.
- [ETS09] ETS-LINDGREN, *Diagonal Dual Polarized Horns, Model 3164 Series*, January 2009, <http://www.ets-lindgren.com/manuals/3164-04.pdf>.
- [Ett10] Ettus Research, *USRP motherboard datasheet. Universal Software Radio Peripheral. The foundation for complete software radio systems*, October 2010, http://www.ettus.com/downloads/ettus_ds_usrp_v7.pdf.
- [Ett11] Ettus Research, *TX and RX daughterboards for the USRP software radio system*, August 2011, http://www.ettus.com/downloads/ettus_daughterboards.pdf.
- [Fan09] M. Fantino, A. Molino, and M. Nicola, “N-Gene GNSS receiver: Benefits of software radio in navigation”, *Proceedings of the European Navigation Conference - Global Navigation Satellite Systems (ENC-GNSS)*, Naples, Italy, May 2009.
- [Far99] J. A. Farrell, and M. Barth, *The Global Positioning System & Inertial Navigation*, McGraw-Hill, 1999.
- [FCC99] “FCC Public Notice DA 99-2130”, Tech. rep., Federal Communications Commission (FCC), 1999.
- [FCC11] “LightSquared Technical Working Group final report”, Tech. rep., Federal Communications Commission, Washington, D.C., June 2011.
- [Fis05] K. A. Fisher, *The navigation potential of signals of opportunity-based time difference of arrival measurements*, PhD Thesis, Air Force Institute of Technology, March 2005.
- [Fon98] F. Pérez Fontán, M. A. Vázquez Castro, E. Kubista, A. Paraboni, B. Arbesser-Rastburg, S. Buonomo, and J. Poiares Baptista, “A methodology for the characterization of environmental effects on Global Navigation Satellite System (GNSS) propagation”, *International Journal of Satellite Communications*, vol. 1, no. 16, pp. 1–22, 1998.
- [FP06] C. Fernández-Prades, *Advanced Signal Processing Techniques for GNSS Receivers*, PhD Thesis, Universitat Politècnica de Catalunya (UPC), Barcelona, Spain, May 2006.
- [FP09a] C. Fernández-Prades, J. Arribas, and P. Closas, “The decoupling of DOA/Synchronization parameters in colored noise environments”, *Proceedings of NEWCOM++ ACoRN Joint Workshop*, Barcelona (Spain), April 2009.
- [FP09b] C. Fernández-Prades, and P. Closas, “Synchronization of GNSS signals with unstructured antenna arrays by a multivariate minimization of the generalized variance”, *16th International Conference on Digital Signal Processing*, Santorini, Greece, July 2009.
- [FP09c] C. Fernández-Prades, P. Closas, and J. Arribas, “Implementation of digital beamforming in GNSS receivers”, *Proceedings of the 4th European Workshop on GNSS Signals and Signal Processing*, Oberpfaffenhofen, München (Germany), December 2009.
- [FP10a] C. Fernández-Prades, C. Avilés, L. Esteve, J. Arribas, and P. Closas, “Design patterns for GNSS software receivers”, *Proceedings of the 5th ESA Workshop on Satellite Navigation Technologies, NAVITEC’2010*, Noordwijk, The Netherlands, December 2010.
- [FP10b] C. Fernández-Prades, P. Closas, and J. Vilà-Valls, “Non-linear filtering for ultra-tight gnss/ins integration”, *Proceedings of the IEEE International Conference on Communications (ICC 2010)*, pp. 1–5, Cape Town (South Africa), May 2010.
- [FP11a] C. Fernández-Prades, J. Arribas, and P. Closas, “GNSS-SDR: an open source tool for researchers and developers”, *Proceedings of the ION GNSS 2011, Portland, Oregon (USA)*, September 2011.

- [FP11b] C. Fernández-Prades, P. Closas, and J. Arribas, “Eigenbeamforming for Interference Mitigation in GNSS Receivers”, *Proceedings of the International Conference on Localization and GNSS (ICL-GNSS)*, Tampere (Finland), June 2011.
- [FP11c] C. Fernández-Prades, L. Lo Presti, and E. Falleti, “Satellite Radiolocation From GPS to GNSS and Beyond: Novel Technologies and Applications for Civil Mass-Market”, *Proceedings of the IEEE. Special Issue on Aerospace Communications and Networking in the Next Two Decades: Current Trends and Future Perspectives*, vol. 99, no. 11, pp. 1882–1904, November 2011.
- [Fri05] M. Frigo, and S. G. Johnson, “The design and implementation of fftw3”, *Proceedings of the IEEE*, vol. 93, no. 2, pp. 216–231, July 2005, special issue on Program Generation, Optimization, and Platform Adaptation.
- [Fu02] Z. Fu, A. Hornbostel, J. Hammesfahr, and A. Konovaltsev, “Suppression of Multipath and Jamming Signals by digital beamforming for GPS/Galileo applications”, *Proceedings of the European Navigation Conference*, Copenhagen, Denmark, May 2002.
- [GA205] “GA27c GPS low profile remote automobile antenna”, Tech. rep., Garmin Ltd, 2005.
- [Gag08] P. O. Gaggero, and D. Borio, “Ultra-stable oscillators: Limits of GNSS coherent integration”, *Proceedings of ION GNSS 08*, Savannah, GA, September 2008.
- [Gam95] E. Gamma, R. Helm, R. Johnson, and J. Vlissides, *Design Patterns: Elements of Reusable Object-Oriented Software*, Addison Wesley, Upper Saddle River, NJ, 1995.
- [GCC] “GCC, the GNU Compiler Collection”, Retrieved: October 21, 2010, <http://gcc.gnu.org>.
- [Ger09] C. Gernot, *Development of combined GPS L1/L2C Acquisition and Tracking methods for weak signals environments*, PhD Thesis, University of Calgary, Calgary, Alberta, October 2009.
- [Ger11] C. Gernot, K. O’Keefe, and G. Lachapelle, “Assessing three new GPS combined L1/L2C acquisition methods”, *IEEE Transactions of Aerospace and Electronic Systems*, vol. 3, no. 47, pp. 2239–2247, July 2011.
- [GFL] “Google Commandline Flags Module for C++”, Retrieved: February 1, 2012, <https://code.google.com/p/gflags/>.
- [Gil68] B. Gilbert, “A precise four-quadrant multiplier with subnanosecond response”, *IEEE Journal of Solid-State Circuits*, vol. 4, pp. 365–373, December 1968.
- [Gil03a] R. Gilmore, and L. Besser, *Practical RF Circuit Design for Modern Wireless Systems, vol. 1, Passive Circuits and Systems*, Artech House, inc, Boston, London, 1st ed., 2003.
- [Gil03b] R. Gilmore, and L. Besser, *Practical RF Circuit Design for Modern Wireless Systems, vol. 2, Active Circuits and Systems*, Artech House, inc, Boston, London, 1st ed., 2003.
- [Gim98] S. Gimore, “The Impact of Jamming on GPS”, *Symposium on GPS Interference and Mitigation Techniques*, Cambridge, Massachusetts, August 1998.
- [GIT] “GIT. The fast version control system”, Retrieved: October 21, 2010, <http://git-scm.com/>.
- [Giu05] R. Giuliano, and F. Mazzenga, “On the coexistence of power-controlled ultrawideband systems with UMTS, GPS, DCS1800, and fixed wireless systems”, *IEEE Transactions on Vehicular Technology.*, vol. 1, pp. 62–81, January 2005.
- [GLO] “Google Logging Library for C++”, Retrieved: February 1, 2012, <http://code.google.com/p/google-glog/>.
- [GLO08] “Global Navigation Satellite System GLONASS. Interface Control Document, Navigational Radiosignal in Bands L1, L2, ver 5.1”, Tech. rep., Russian Institute of space Devide Engineering, Moscow, Russia, 2008.
- [GNS] OneTalent GNSS, “SdrNav front-end family”, Accessed April, 2012, <http://www.onetalent-gnss.com>.

- [GNU06] “GNU Radio Architectural Changes”, Tech. rep., BBN Technologies Group, June 2006, <http://acert.ir.bbn.com/downloads/adroit/gnuradio-architectural-enhancements-3.pdf>.
- [Gol67] R. Gold, “Optimal binary sequences for spread spectrum multiplexing”, *IEEE Transactions on Information Theory*, vol. 13, no. 4, pp. 619–621, Oct. 1967.
- [Gol96] G. H. Golub, and C. F. van Loan, *Matrix Computations*, The John Hopkins University Press, 3rd ed., 1996.
- [Gol07] H. J. Goldberg, and F. Gruson, “Measuring GPS Sensitivity”, Tech. rep., Atmel White Paper, 2007.
- [GOO] “Google Earth”, Retrieved: February 1, 2012, <http://earth.google.com/>.
- [GRa] “GNU Radio project”, [Http://gnuradio.org/redmine/wiki/gnuradio](http://gnuradio.org/redmine/wiki/gnuradio).
- [Gre07] M. S. Grewal, L. R. Weill, and A. P. Andrews, *Global Positioning Systems, Inertial Navigation, and Integration, 2nd Ed.*, John Wiley & Sons, Inc., Hoboken, New Jersey, 2007.
- [Gur09] W. Gurtner, and L. Estey, “RINEX, The Receiver Independent Exchange Format v 3.01”, Tech. rep., Astronomical Institute, University of Bern, June 2009.
- [Häi11] C. Hättich, M. Cuntz, A. Konovaltsev, G. Kappen, and M. Meurer, “Robust Multi-Antenna Acquisition in Time, Frequency and Space for a Digital Beamforming Receiver”, *Proceedings of the ION GNSS 2011, Portland, Oregon (USA)*, September 2011.
- [Ham02] M. Hamalainen, V. Hovinen, R. Tesi, J. Iinatti, and M. Latva-aho, “On the UWB system coexistence with GSM900, UMTS/WCDMA, and GPS”, *IEEE Journal on Selected Areas*, vol. 20, pp. 1712–1721, December 2002.
- [Har01] I. Harre, “A Standardized Algorithm for the Determination of Position Errors by the Example of GPS with and without Selective Availability”, *The International Hydrographic Journal*, vol. 2, no. 1, June 2001.
- [Hay88] S. Haykin, *Digital communications*, Wiley, New York, 1988.
- [Hec06] G. W. Heckler, and J. L. Garrison, “SIMD correlator library for GNSS software receivers”, *GPS Solutions*, vol. 10, no. 4, pp. 269–276, November 2006.
- [Heg03] C. J. Hegarty, “Acquisition algorithms for the GPS L5 signal”, *Proceedings of the ION GNSS 2003*, Portland, OR, September 2003.
- [Heg06] C. J. Hegarty, “Optimal and near-optimal detectors for acquisition of the GPS L5 signal”, *ION National Technical Meeting*, Monterey, CA, January 2006.
- [Hei07] G. W. Hein, M. Irsigler, J. A. Avila-Rodriguez, S. Wallner, T. Eissfeller, and P. Hartl, “Envisioning a Future GNSS system of systems: Part3 A role for C-Band?”, *Inside GNSS*, vol. 2, no. 2, pp. 64–73, 2007.
- [Hei10] G. Hein, M. Anghileri, M. Paonni, S. Wallner, J. A. Ávila Rodríguez, and B. Eissfeller, “Ready to Navigate! A Methodology for the Estimation of the Time-to-First-Fix”, *Inside GNSS*, pp. 47–56, March–April 2010.
- [Hen06] J. L. Hennessy, and D. A. Patterson, *Computer Architecture: A Quantitative Approach*, Morgan Kaufmann, Burlington, MA, 4th ed., Sept. 2006.
- [Hin84] M. E. Hines, “The virtues of nonlinearity: Detection, frequency conversion, parametric amplification, and harmonic generation”, *IEEE Transactions on Microwave Theory and Techniques*, vol. 32, pp. 1097–1104, September 1984.
- [Hob10] T. Hobiger, T. Gotoh, J. Amagai, Y. Koyama, and T. Kondo, “A GPU based real-time GPS software receiver”, *GPS Solutions*, vol. 14, no. 2, pp. 207–216, March 2010.
- [Hor90] R. M. Hord, *Parallel supercomputing in SIMD architectures*, CRC Press, 1990.

- [HP08] M. Hernández-Pajares, J.M. Zornoza, and J. Sanz, *GPS data processing: code and phase Algorithms, Techniques and Recipes*, Research group of Astronomy and GEomatics (gAGE/UPC), 2008.
- [HP10a] M. Hernández-Pajares, J. M. Juan, J. Sanz, A. Aragon-Angel, P. Ramos-Bosch, D. Odijk, P. Teunissen, J. Samson, M. Tossaient, and M. Albertazzi, “Wide-Area RTK: High Precision Positioning on a Continental Scale”, *Inside GNSS*, pp. 35–46, March-April 2010.
- [HP10b] M. Hernández-Pajares, J. M. Juan, J. Sanz, P. Ramos-Bosch, A. Rovira-García, D. Salazar, J. Ventura-Traveset, C. López-Echazarreta, and G. Hein, “The ESA/UPC GNSS-Lab Tool (gLAB)”, *Proceedings of the 5th ESA Workshop on Satellite Navigation Technologies (NAVITEC’2010)*, ESTEC, Noordwijk, The Netherlands, December 2010.
- [HS08] U.S Department of Homeland Security, “United States Positioning, Navigation, and Timing Interference Detection and Mitigation Plan Summary”, Tech. rep., Washington, D.C, USA, April 2008.
- [Hum11] T. E. Humphreys, J. A. Bhatti, T. Pany, B. M. Ledvina, and B. W. O’Hanlon, “Exploiting multicore technology in software-defined GNSS receivers”, *Proceedings of the ION GNSS 2011, Portland, Oregon (USA)*, pp. 326–338, September 2011.
- [Hur09] H. Hurskainen, J. Raasakka, T. Ahonen, and J. Nurmi, “Multicore software-defined radio architecture for GNSS receiver signal processing”, *EURASIP Journal on Embedded Systems*, 2009.
- [HW08] B. Hofmann-Wellenhof, H. Lichtenegger, and E. Wasle, *GNSS - Global Navigation Satellite Systems: GPS, GLONASS, Galileo & more*, Springer, New York, 2008.
- [IAL08] “IALA Recommendation R-129 on GNSS Vulnerability and Mitigation Measures Edition 2”, Tech. rep., International Association of Marine Aids to Navigation and Light-house Authorities, December 2008.
- [Inc11] Xilinx Inc., “ISE foundation web page”, Sept. 2011, <http://www.xilinx.com/ise/>.
- [Irs04] M. Irsingler, G.M Hein, and A. Schmitz-Peiffer, “Use of C-Band frequencies for satellite navigation: Benefits and drawbacks”, *GPS Solutions*, vol. 8, no. 3, 2004.
- [ISO11] “Programming languages – c++, third edition,”, Tech. rep., ISO/IEC 14882:2011(E), 2011.
- [Jon04] J. Jones, P. Fenton, and B. Smith, “Theory and Performance of the Pulse Aperture Correlator”, Tech. rep., NovAtel, Calgary, Alberta, Canada, September 2004.
- [Kah74] G. Kahn, “The semantics of a simple language for parallel programming”, *Proceedings of Information Processing*, pp. 471–475, Stockholm, August 1974.
- [Kah77] G. Kahn, and D. B. MacQueen, “Coroutines and networks of parallel processes”, *Proceedings of Information Processing*, pp. 993–998, Toronto, August 1977.
- [Kap96] E.D. Kaplan, *Understanding GPS. Principles and Applications*, Artech House Publishers, 1996.
- [Kap05] E.D. Kaplan, and C. Hegarty, *Understanding GPS. Principles and Applications, Second Edition*, Artech House Publishers, Norwood, MA, 2005.
- [Kar56] S. Karlin, and H. Rubin, “Distributions possessing a monotone likelihood ratio”, *Journal of the American Statistical Association*, vol. 51, no. 276, pp. 637–643, December 1956.
- [Kar05] B. Karlsson, *Beyond the C++ Standard Library: An Introduction to Boost*, Addison Wesley Professional, Reading, MA, 2005.
- [Kay93] S. M. Kay, *Fundamentals of statistical signal processing: Estimation theory*, Prentice Hall, Upper Saddle River, New Jersey, 1993.

- [Kay98] S. M. Kay, *Fundamentals of statistical signal processing: Detection theory*, Prentice Hall, Upper Saddle River, New Jersey, 1998.
- [Kel86] E. J. Kelly, “An adaptive detection algorithm”, *IEEE Transactions on Aerospace and Electronic Systems*, vol. 22, no. 22, pp. 115–127, March 1986.
- [Ker74] B. W. Kernighan, and P. J. Plauger, *The Elements of Programming Style*, McGraw-Hill, New York, 1974.
- [Ker04] J. Kerievsky, *Refactoring to Patterns*, Addison-Wesley Professional, Reading, MA, 2004.
- [Klu03] R. Klukas, G. Lachapelle, C. Ma, and G. I. Jee, “GPS Signal Fading Model for Urban Centres”, *IEEE Proceedings on Microwaves, Antennas and Propagation*, vol. 150, pp. 245–252, 2003.
- [Klu04] R. Klukas, O. Julien, L. Dong, E. Cannon, and G. Lachapelle, “Effects of Building Materials on UHF Ranging Signals. GPS Solutions”, *GPS Solutions*, vol. 8, pp. 1–8, 2004.
- [Kna76] C Knapp, and G. Carter, “The generalized correlation method for estimation of time delay”, *IEEE Transactions on Acoustics, Speech and Signal Processing*, vol. 24, no. 4, pp. 320–327, August 1976.
- [Kon07] A. Konovaltsev, F. Antreich, and A. Hornbostel, “Performance assessment of antenna array algorithms for multipath and interference mitigation”, *Proceedings of the 2nd European Workshop on GNSS Signals and Signal Processing*, Noordwijk, The Netherlands, April 2007.
- [Kra11] T. Kraus, R. Bauernfeind, and B. Eissfeller, “Survey of In-Car Jammers-Analysis and Modeling of the RF signals and IF samples (suitable for active signal cancellation)”, *Proceedings of the ION GNSS 2011, Portland, Oregon (USA)*, September 2011.
- [Kru01] K. Krumvieda, P. Madhani, C. Cloman, E. Olson, J. Thomas, P. Axelrad, and W. Kober, “A complete IF software GPS receiver: A tutorial about the details”, *Proceedings of the 14th International Technical Meeting of the Satellite Division of the Institute of Navigation (ION GPS’01)*, pp. 789–829, 2001.
- [Kun03] W. Kunysz, “A three dimensional choke ring ground plane antenna”, *Proceedings of the 16th Int. Tech. Meeting of the Satellite Division of the U.S. Inst. of Navigation*, vol. 16, pp. 1883–1888, Portland, Oregon, September 2003.
- [Kun10] W. Kunysz, “Antenna phase center effects and measurements in gnss ranging applications”, *International Symposium on Antenna Technology and Applied Electromagnetics the American Electromagnetics Conference (ANTEM-AMEREM)*, pp. 1–4, July 2010.
- [Lan97] R. J. Landry, and A. Renard, “Analysis of potential interference sources and assessment of present solutions for GPS/GNSS receivers”, *4th Saint Petersburg International Conference on Integrated Navigation Systems*, Saint Petersburg, Russia, May 1997.
- [Led03] B. M. Ledvina, S. P. Powell, P. M. Kintner, and M. L. Psiaki, “A 12-channel real-time GPS L1 software receiver”, *Proceedings of the National Technical Meeting of the Institute of Navigation (ION NTM’03)*, pp. 767–782, Anaheim, CA,, January 2003.
- [Lei04] A. Leick, *GPS Satellite Surveying*, John Wiley & Sons, Inc., Hoboken, NJ, 3rd ed., 2004.
- [LEO] Aeroflex Gaisler, Göteborg, Sweden, *LEON3 Multiprocessing CPU Core*, <http://www.gaisler.com/cms/>.
- [Li10] X. Li, and D. Akos, “Implementation and performance of clock steering in a software GPS L1 single frequency receiver”, *Journal of The Institute of Navigation*, vol. 57, no. 1, pp. 69–85, Spring 2010.
- [Lim12] Altium Limited, “Altium Designer web page”, February 2012, <http://www.altium.com>.

- [Lin02] D. M. Lin, and J. B. Y. Tsui, “A Weak Signal Tracking Technique for a Stand-Alone Software GPS Receiver”, *Proceedings of the 15th International Technical Meeting of the Satellite Division of The Institute of Navigation (ION GPS 2002)*, pp. 2534–2538, Portland, OR, September 2002.
- [LMX07] “LMX2531 High Performance Frequency Synthesizer System with Integrated VCO datasheet”, Tech. rep., National Semiconductor Corp., January 2007.
- [LMX08] “LMX2531LQ1146E Evaluation Board Operating Instructions datasheet”, Tech. rep., National Semiconductor Corp., March 2008.
- [Lor05] D.S. De Lorenzo, J. Gautier, J. Rife, P. Enge, and D. Akos, “Adaptive array processing for GPS interference rejection”, *Proceedings of ION GPS'05*, Long Beach, CA, Sept. 2005.
- [LVD01] *Electrical Characteristics of Low Voltage Differential Signaling (LVDS) Interface Circuits*, Feb. 2001, ANSI/TIA/EIA-644-A Standard.
- [Mac02] G. MacGougan, G. Lachapelle, R. Klukas, K. Siu, L. Garin, H. Shewfelt, and G. Cox, “Degraded GPS signal measurements with a stand-alone high sensitivity receiver”, *Proceedings of National Technical Meeting*, pp. 191–204, San Diego, CA, January 2002.
- [Mar04] Marvell Semiconductor, Inc., Sunnyvale, CA, *88E1111 Datasheet. Integrated 10/100/1000 Ultra Gigabit Ethernet Transceiver*, Dec. 2004, doc. No. MV-S100649-00, Rev. F.
- [Max02] Maxim Integrated Products, Inc., Sunnyvale, CA, *MAXIM application note 957: The MAX2681 SiGe Downconverter Mixer Tuned for GPS Front Ends*, May 2002.
- [Max03a] Maxim Integrated Products, Inc., Sunnyvale, CA, *MAX2650 Datasheet. DC-to-Microwave +5V Low-Noise Amplifier*, August 2003.
- [Max03b] Maxim Integrated Products, Inc., Sunnyvale, CA, *MAX2680/MAX2681/MAX2682 Datasheet. 400 MHz to 2.5 GHz, Low-Noise, SiGe Downconverter Mixers*, August 2003.
- [Max09] Maxim Integrated Products, Inc., Sunnyvale, CA, *MAX2659 Datasheet. GPS/GNSS Low-Noise Amplifier*, September 2009.
- [McD04] K.F. McDonald, R. Raghavan, and R. Fante, “Lessons learned through the implementation of Space-Time Adaptive Processing algorithms for GPS reception in jammed environments”, *Proceedings of Position Location and Navigation Symposium (PLANS)*, pp. 418–428, April 2004.
- [Meg09] D. Megahed, C. O'Driscoll, and G. Lachapelle, “Performance evaluation of combined L1/L5 Kalman filter-based tracking versus standalone L1/L5 tracking in challenging environments”, *Proceedings of the 22nd International Meeting of the Satellite Division of The Institute of Navigation (ION GNSS)*, pp. 2591–2601, Savannah, GA, September 2009.
- [Men09] J. Mendizabal, *GPS & Galileo: Dual RF Front-end Receiver and Design, Fabrication, and Test*, Mc Graw Hill, 2009.
- [Mey96] S. Meyers, *More Effective C++: 35 New Ways to Improve Your Programs and Designs, Computing Series*, Addison-Wesley Professional, Upper Saddle River, NJ, September 1996.
- [Mey01] S. Meyers, *Effective STL: 50 Specific Ways to Improve Your Use of the Standard Template Library*, Addison-Wesley Professional, Reading, MA, 2001.
- [Mey05] S. Meyers, *Effective C++: 55 Specific Ways to Improve Your Programs and Designs, Computing Series*, Addison-Wesley Professional, Upper Saddle River, NJ, 3rd ed., May 2005.
- [Mis06] P. Misra, and P. Enge, *Global Positioning System: Signals, Measurements, and Performance, Second Edition*, Ganga-Jamuna Press, 2006.

- [Mit08] A. Mitelman, M. Reidevall, and S. Strickland, “Apples to apples: Standardized testing for high-sensitivity receivers”, *GPS World*, vol. 1, pp. 26–33, January 2008.
- [Mit09] A. Mitelman, J. Almqvist, R. Håkanson, D. Karlsson, F. Lindström, T. Renström, C. Ståhlberg, and J. Tidd, “Testing software receivers”, *GPS World*, vol. 20, no. 12, pp. 28–34, December 2009.
- [Mit11] R. H. Mitch, R. C. Dougherty, M. L. Psiaki, S. P. Powell, B. W. O’Hanlon, J. A. Bhatti, and T. E. Humphreys, “Signal Characteristics of Civil GPS Jammers”, *Proceedings of the ION GNSS 2011, Portland, Oregon (USA)*, September 2011.
- [Moe09] G. J. K. Moernaut, and D. Orban, “GNSS antennas: an introduction to bandwidth, gain pattern, polarization, and all that”, *GPS World*, February 2009.
- [Mog96] J. Mogul, and K. Ramakrishnan, “Eliminating receive livelock in an interrupt-driven kernel”, *Proceedings of the USENIX 1996 Annual Technical Conference*, San Diego, CA, January 1996.
- [Mon80] R. A. Monzingo, and T. W. Miller, *Introduction to adaptive arrays*, John Wiley & Sons, New York, 1980.
- [Mor07] D. Morgan, *Surface Acoustic Wave Filters: With Applications to Electronic Communications and Signal Processing*, Academic Press, Elsevier, Ltd, Oxford, UK, 2nd ed., 2007.
- [Mui82] R. J. Muirhead, *Aspects of Multivariate Statistical Theory*, Wiley, New York, 1982.
- [Mur07] Murata Manufacturing Co., Ltd, Nagaokakyo, Kyoto, *SAFSE1G57KA0T90 Datasheet. SAW filter for GPS*, March 2007.
- [Myr01] W. L. Myrick, J. S. Goldstein, and M. D. Zoltowski, “Low Complexity Anti-Jam Space-Time Processing for GPS”, *Proceedings of the IEEE International Conference on Acoustics, Speech and Signal Processing (ICASSP ’01)*, vol. 4, pp. 2233–2236, Salt Lake City, UT, USA, May 2001.
- [Nak10] B. Nakache, and A. Deschamps, “Now’s the time: FMCs bring I/O modularity to modern FPGA applications”, *VME and Critical Systems*, August 2010.
- [Nee94] R. D. J. Van Nee, J. Siereveld, P. C. Fenton, and B. R. Townsend, “The multipath estimating delay lock loop: approaching theoretical accuracy limits”, *Position, Location and Navigation Symposium*, vol. 251, pag. 246, April 1994.
- [Nor03] M. Norris, *Gigabit Ethernet Technology and Applications*, Artech House Publishers, Norwood, MA, 2003.
- [Nov01] NovaTel Inc., Calgary, Alberta, *NovaTel GPS-600 datasheet*, September 2001.
- [Nov03] “APN-029 GPS Position Accuracy Measures”, Tech. rep., NovAtel Inc., Calgary, Alberta, December 2003.
- [NTO08] *PF_RING User Guide V. 1.1. Linux High Speed Packet Capture*, January 2008, <http://www.ntop.org>.
- [O'B08] A. J. O’Brien, and I. J. Gupta, “Optimum Adaptive Filtering for GNSS Antenna Arrays”, *Proceedings of the 21st International Technical Meeting of the Satellite Division of The Institute of Navigation (ION GNSS 2008)*, vol. 4, pp. 2796–2805, Savannah, GA, USA, September 2008.
- [OCO] *Opencores developers community*, <http://www.opencores.org>.
- [O'D07] C. D. O’Driscoll, *Performance Analysis of the Parallel Acquisition of Weak GPS Signals*, PhD Thesis, National University of Ireland, Cork, Ireland, January 2007.
- [Opp00] A. V. Oppenheim, *et al.*, *Discrete-Time Signal Processing (2nd Edition)*, Prentice-Hall Signal Processing Series, 2000.
- [Oue02] J. Ouellette, “Silicon-germanium gives semiconductors the edge”, *The Industrial Physicist*, June–July 2002.

- [Pan10] T. Pany, E. Gohler, M. Irsigler, and J. Winkel, “On the state-of-the-art of real-time GNSS signal acquisition: a comparison of time and frequency domain methods”, *Int. Conf. Indoor Position. Indoor Navig.*, Zurich, Switzerland, September 2010.
- [Par95] T. M. Parks, *Bounded Scheduling of Process Networks*, PhD Thesis, University of California, Berkeley, California, December 1995.
- [Par96] B.W. Parkinson, and J.J. Spilker (eds.), *Global Positioning System: Theory and Applications, vol. I, II*, Progress in Astronautics and Aeronautics, American Institute of Aeronautics, Inc., Washington DC, 1996.
- [Pat08] D. A. Patterson, and J. L. Hennessy, *Computer Organization and Design: The Hardware/Software Interface*, Morgan Kaufmann, Burlington, MA, 4th ed., Nov. 2008.
- [Ped04] R. Pedone, and G. E. Corazza, “Generalized and Average Post Detection Integration Methods for Code Acquisition”, *ISSSTA 2004*, pp. 207–211, Sydney, Australia, 2004.
- [Pet09a] M. Petovello, M. Lashley, and D. Bevly, “What are vector tracking loops, and what are their benefits and drawbacks?”, *Inside GNSS*, vol. 4, no. 3, pp. 18–21, 2009.
- [Pet09b] M. G. Petovello, C. O'Driscoll, G. Lachapelle, D. Borio, and H. Murtaza, “Architecture and benefits of an advanced GNSS software receiver”, *Positioning*, vol. 1, no. 1, pp. 66–78, 2009.
- [Pia98] F. Piazza, and Q. Huang, “A 1.57 GHz RF front end for triple conversion GPS receiver”, *IEEE Journal of Solid-State Circuits*, vol. 33, pp. 202–209, February 1998.
- [Pin08] M. Pini, E. Falletti, and M. Fantino, “Evaluation of C/N0 Estimators using a Real Time GNSS Software Receiver”, *Proceedings of the IEEE 10th International Symposium on Spread Spectrum Techniques and Applications*, pp. 28–30, August 2008.
- [Poz98] D. M. Pozar, *Microwave Engineering*, John Wiley and Sons, Inc., New York, 2nd ed., 1998.
- [Poz01] D. M. Pozar, *Microwave and RF Design of Wireless Systems*, John Wiley and Sons, inc, New York, 1st ed., 2001.
- [Pre09] L. Lo Presti, Z. Xuefen, M. Fantino, and P. Mulassano, “GNSS signal acquisition in the presence of sign transition”, *IEEE Journal of Selected Topics in Signal Processing*, vol. 3, no. 4, pp. 557–570, Aug. 2009.
- [Pri11] F. Principe, G. Bacci, F. Giannetti, and M. Luise, “Software-defined radio technologies for GNSS receivers: A tutorial approach to a simple design and implementation”, *International Journal of Navigation and Observation*, vol. 1, pp. 1–27, 2011.
- [Pro00] J. G. Proakis, *Digital communications*, McGraw-Hill, 2000.
- [Psi03] M. L. Psiaki, S. P. Powell, H. Jung, and P. M. Kintner, “Design and practical implementation of multi-frequency RF front ends using direct RF sampling”, *Proceedings of the ION GNSS*, vol. 16, pp. 90–102, Portland, Oregon, September 2003.
- [Pus07] H. Puska, H. Saarnisaari, J. Iinatti, and P. Lilja, “Performance Comparison of DS/SS Code Acquisition using MMSE and MVDR Beamforming in Jamming”, *IEEE Military Communications Conference, 2007. MILCOM 2007*, pp. 1–7, October 2007.
- [Pus08] H. Puska, H. Saarnisaari, J. Iinatti, and P. Lilja, “Serial search code acquisition using smart antennas with single correlator or matched filter”, *IEEE Transactions on Communications*, vol. 56, no. 2, pp. 299–308, Feb 2008.
- [Qua12] Qualcomm Inc., *Snapdragon mobile processor family specifications*, February 2012, <http://www.qualcomm.com/snapdragon/processors>.
- [Rai06] M. Raimondi, O. Julien, C. Macabiau, and F. Bastide, “Mitigating pulsed interference using frequency domain adaptive filtering”, *19th International Technical Meeting of the satellite division of the Institute of Navigation (ION GNSS'06)*, pp. 2252–2260, Fort Worth, TX, 2006.

- [Rao12] M. Rao, and G. Falco, “How can pseudorange measurements be generated from code tracking?”, *Inside GNSS*, vol. 2, pp. 26–33, January–February 2012.
- [Rap96] T. S. Rappaport, *Wireless communications: principles and practice 2nd Edition*, Prentice-Hall, 1996.
- [RED] “Redmine”, Retrieved: October 21, 2010, <http://www.redmine.org/>.
- [Roh11] Rohde & Schwarz corp., “Rohde & Schwarz ZVA 24 Vector Network Analyzer”, May 2011, <http://www2.rohde-schwarz.com/product/ZVA.html>.
- [Rue11] A. Ruegamer, I. Suberviola, F. Foerster, G. Rohmer, A. Konovaltsev, N. Basta, M. Meurer, J. Wendel, M. Kaindl, and S. Baumann, “A Bavarian Initiative towards a Robust Galileo PRS Receiver”, *Proceedings of the ION GNSS 2011, Portland, Oregon (USA)*, September 2011.
- [Sal10] D. Salazar, M. Hernández-Pajares, J. M. Juan, and J. Sanz, “GNSS data management and processing with the GPSTk”, *GPS Solutions*, vol. 14, no. 3, pp. 293–299, June 2010.
- [Sch91] L. L. Scharf, *Statistical Signal Processing: Detection, Estimation and Time Series Analysis*, Addison-Wesley, Boston, MA, 1991.
- [Sch99] J. J. Schamus, and J. B. Y. Tsui, “Acquisition to Tracking and Coasting for Software GPS Receiver”, *Proceedings of ION GPS-99*, pp. 325–328, Nashville, TN, September 1999.
- [Sch00] D. C. Schmidt, M. Stal, H. Rohnert, and F. Buschmann, *Pattern-Oriented Software Architecture: Patterns for Concurrent and Networked Objects*, vol. 2 of *Wiley Series in Software Design Patterns*, John Wiley & Sons, Chichester, England, 2000.
- [Sch04] A. Schmid, and A. Neubauer, “Performance of differential correlation for single shot measurement positioning”, *GNSS 17th International Technical Meeting of the Satellite Division*, pp. 1998–2009, Long Beach, CA, September 2004.
- [Sch05] A. Schmid, “Combined Galileo/GPS architecture for enhanced sensitivity reception”, *International Journal on Electronics and Communications*, vol. 59, pp. 297–306, April 2005.
- [Sec00] Gonzalo Seco, *Antenna Arrays for Multipath and Interference Mitigation in GNSS Receivers*, PhD Thesis, Dept. of Signal Theory and Communications, Universitat Politècnica de Catalunya, Barcelona, Spain, July 2000.
- [Sec05] G. Seco, J. A. Fernández-Rubio, and C. Fernández-Prades, “ML estimator and Hybrid Beamformer for multipath and interference mitigation in GNSS receivers”, *IEEE Transactions on Signal Processing*, vol. 53, no. 3, pp. 1194–1208, March 2005.
- [Sha04] A. Shalloway, and J. R. Trott, *Design Patterns Explained: A New Perspective on Object-Oriented Design*, 2nd edition, Addison-Wesley Professional, Reading, MA, 2004.
- [Sha06] A. Shalyto, N. Shamgunov, and G. Korneev, “State machine design pattern”, *Proc. of the 4th International Conference on .NET Technologies*, vol. 251, pp. 51–57, Plzeň, Czech Republic, June 2006.
- [Sha07] S. K. Shanmugam, “Narrowband interference suppression performance of multi-correlation differential detection”, *Proceedings of ENC-GNSS*, Geneva, Switzerland, May 2007.
- [Sha08] S. K. Shanmugam, *New Enhanced Sensitivity Detection Techniques for GPS L1 C/A and Modernized Signal Acquisition*, PhD Thesis, University of Calgary, Calgary, Alberta, January 2008.
- [SiG09] SiGe Semiconductor, Ottawa, ON, Canada, *SE4120L GNSS receiver IC datasheet*, May 2009.

- [Sim06] Marvin K. Simon, *Probability Distributions Involving Gaussian Random Variables: A Handbook for Engineers, Scientists and Mathematicians*, Springer-Verlag New York, Inc., Secaucus, NJ, USA, 2006.
- [Sol09] M. Solé, J. Arribas, C. Fernández-Prades, D. Bernal, and J. A. Fernández-Rubio, “Correlador doble delta para GPS en tiempo real”, *Proceedings XXIV Simposium Nacional de la Unión Científica Internacional de Radio (URSI 2009)*, Santander (Spain), September 2009.
- [Sot10] F. Sottile, M. A. Spirito, P. Closas, J. Arribas, C. Fernández-Prades, M. Kieffer, M. Nájar, A. Mallat, P. Gérard, L. Vandendorpe, D. Dardari, N. Decarli, and A. Conti, “Evaluation of tracking algorithms using heterogeneous technologies”, *Demo at the IEEE Global Communications Conference, (IEEE GLOBECOM 2010)*, Miami, Florida (USA), December 2010.
- [Spa06] J. Spacek, and P. Puricer, “Front-end Module for GNSS Software Receiver”, *Proceedings of the 48th International Symposium ELMAR*, pp. 211–214, Zadar, Croatia, June 2006.
- [Spi09] Spirent Communications, Inc, *GSS6700 Multi-GNSS Simulation System*, Oct. 2009.
- [SSE] “Intel Streaming SIMD Extensions (SSE)”, Accessed February 21, 2012, <http://intel.com/>.
- [Ste04] A. Steingass, and A. Lehner, “Measuring the Navigation Multipath Channel - A Statistical Analysis”, *Proceedings of the ION GPS/GNSS 2004*, Long Beach, CA, September 2004.
- [Ste05] A. Steingass, and A. Lehner, “A channel model for land mobile satellite navigation”, *Proceedings of the European Navigation Conference, ENC-GNSS 2005*, Munich, July 2005.
- [Sto10] C. Stober, M. Anghileri, A. Sicramaz-Ayaz, D. Dötterböck, I. Kräme, V. Kroppand, J. H. Won, B. Eissfeller, D. Sanromà-Güixens, and T. Pany, “ipexSR: A real-time multi-frequency software GNSS receiver”, *Proceedings of the 52nd International Symposium ELMAR-2010*, pp. 407–416, Zadar, Croatia, September 2010.
- [Str97] G. Strang, and K. Borre, *Linear Algebra, Geodesy, and GPS*, Wellesley-Cambridge Press, 1997.
- [Str07] C. Strässle, D. Megnet, H. Mathis, and C. Bürgi, “The Squaring-Loss Paradox”, *Proceedings of ION GNSS 07*, Fort Worth, TX, September 2007.
- [Sud01] N. S. Sudhir, C. Vimala, and J. K. Ray, “Reiceiver sensitivity analysis and results”, *ION International Technical Meeting*, Salt Lake City (USA), September 2001.
- [SVN] “Apache Subversion”, Retrieved: October 21, 2010, <http://subversion.apache.org/>.
- [Tex05a] Texas Instruments, Dallas, TX, *ADS5273 Datasheet*, September 2005.
- [Tex05b] Texas Instruments, Dallas, TX, *ADS5273EVM Evaluation Module Datasheet*, September 2005.
- [Tol04] B. W. Tolman, R. B. Harris, T. Gaussiran, D. Munton, J. Little, R. Mach, S. Nelsen, B. Renfro, and D. Schlossberg, “The GPS toolkit - open source GPS software”, *Proceedings of the 17th International Technical Meeting of the Satellite Division of the Institute of Navigation (ION GNSS'04)*, pp. 2044–2053, Long Beach, CA, September 2004.
- [Tor08] D. Torrieri, and K. Bakhru, “Adaptive-Array Algorithm for Interference Suppression Prior to Acquisition of Direct-Sequence Signal”, *IEEE Transactions on Wireless Communications*, vol. 7, no. 9, pp. 3341–3346, 2008.
- [TRA] “TRAC. Integrated SCM & Project Management”, Retrieved: October 21, 2010, <http://trac.edgewall.org/>.
- [Tre02] H. L. Van Trees, *Optimum Array Processing*, John Wiley & Sons, New York, 2002.

- [Tri05] Triquint / Sawtek,. Inc, Orlando,, FL, *854669 Datasheet. 70 MHz passband SAW filter*, October 2005.
- [Tsu00] J. Bao-Yen Tsui, *Fundamentals of Global Positioning System Receivers. A Software Approach*, John Wiley & Sons, Inc., New York, 2000.
- [UML11] “OMG Unified Modeling Language (OMG UML), Superstructure Version 2.4.1”, Tech. Rep. formal/2011-08-06, 2011, version 2.4.1 is a minor revision to the UML 2.3 specification. It supersedes formal/2010-05-06.
- [Und10] Galileo Joint Undertaking, “Galileo Open Service. Signal In Space Interface Control Document (OS SIS ICD)”, Tech. rep., European Space Agency / European GNSS Supervisory Authority, September 2010.
- [Ver98] S. Verdu, *Multiuser Detection*, Cambridge University Press, 1998.
- [VME08] VMEbus International Trade Association, *ANSI/VITA 57.1, FPGA Mezzanine Card (FMC) Standard*, January 2008.
- [VOL] “GNU Radio vector-optimized library of kernels (volk)”, <Http://gnuradio.org/redmine/projects/gnuradio/wiki/Volk>.
- [VOL01] “Vulnerability assessment of the transportation infrastructure relying on the Global Positioning System”, Tech. rep., John A. Volpe National Transportation Systems Center, January 2001.
- [WAA08] “Global Positioning System Wide Area Augmentation System (WAAS) Performance Standard GPS WAAS PS v1.0”, Tech. rep., US Departament of transportation and Federal Aviation Administration, 2008.
- [Wad91] B. C. Wadell, *Transmission Line Design handbook*, Artech House Publishers, Norwood, MA, 1991.
- [Wan03] B. Wang, and H. M. Kwon, “PN code acquisition using smart antenna for spread-spectrum wireless communications part I”, *IEEE Transactions on Vehicular Technology*, vol. 52, no. 1, pp. 142–149, Jan 2003.
- [War82] P. Ward, “An Advanced Navstar GPS Multiplex Receiver/Navigator For Geophysical Exploration Applications”, *Proceedings of Society of Exploration Geophysicists annual meeting*, Dallas, Texas, October 1982.
- [War94] W. P. Ward, “GPS receiver RF interference monitoring, mitigation and anaylsis techniques”, *Journal of The Institute of Navigation*, vol. 41, no. 4, pp. 367–391, 1994.
- [War06] W. P. Ward, and W. J. Betz, *Interference, Multipath, and Scintillation, 2nd edition*, Artech House, Inc., Boston, Massachusetts, 2006.
- [Wat05] R. Watson, G. Lachapelle, R. Klukas, S. Turunen, S. Pietila, and I. Halivaara, “Investigating GPS signals indoors with extreme high-sensitivity detection techniques”, *Journal of Navigation, The Institute of Navigation*, pp. 199–213, 2005.
- [Wei94] L. Weill, “C/A Code Pseudoranging Accuracy-How Good Can it Get?”, *Proceedings of ION GPS-94, the 7th International Technical Meeting of the Satellite Division of the Institute of Navigation*, pp. 133–141, Salt Lake City, UT, 1994.
- [Wei11] L. R. Weill, and M. Petovello, “Differences between Signal Acquisition and Tracking”, *Inside GNSS*, vol. 6, pp. 22–27, January 2011.
- [WGS97] “World Geodetic System 1984, Its Definition and Relationships With Local Geodetic Systems, Third Edition”, Tech. rep., Department of Defense, National Geospatial-Intelligence Agency, USA, 1997.
- [Wid56] B. Widrow, “A study of rough amplitude quantization by means of nyquist sampling theory”, *IRE Transactions on Circuit Theory*, vol. 3, no. 4, pp. 266–276, December 1956.
- [Wid08] B. Widrow, and I. Kollar, *Quantization Noise*, Cambridge University Press, New York, 2008.

- [Wil02] J. R. Williams, "U.S. Spectrum Allocations 300 - 3000 MHz", Tech. rep., OPP/FCC, 2002.
- [Win04] L. Winternitz, M. Moreau, and G. J. Boegner, "Navigator GPS receiver for fast acquisition and weak signal space applications", *Proceedings of ION International Technical Meeting*, Long Beach, CA, September 2004.
- [Win05] Global Positioning Systems Wing, "Navstar GPS space segment / user segment L5 interfaces (IS-GPS-705). Revision IRN-705-003", Tech. rep., GPS Navstar JPO, September 2005.
- [Win08] Global Positioning Systems Wing, "Navstar GPS space segment/user segment L1C interfaces (IS-GPS-800)", Tech. rep., GPS Navstar JPO, September 2008.
- [Win10] Global Positioning Systems Wing, "Navstar GPS space segment. Navigation user interfaces (IS-GPS-200E). Revision IS-GPS-200E", Tech. rep., GPS Navstar JPO, June 2010.
- [Woo85] W. Wooden, "NAVSTAR Global Positioning System", *Proceedings of the first international symposium on precise positioning with the global positioning system, Rockville, Maryland (USA)*, April 1985.
- [Wor10] GPS World, "GPS Antenna Survey 2010", *GPS World*, pp. 36–49, February 2010.
- [Xia09] J. Xiang, L. Guo, and Q. Liu, "Study of GPS Nulling Antenna Based on Space-Time Processing Algorithm", *Proceedings of the International Conference on Wireless Communications, Networking and Mobile Computing (WiCom)*, pp. 1 –4, September 2009.
- [Xil10a] Xilinx Inc., *FMC XM105 Debug Card User Guide*, September 2010, uG537 (v1.2).
- [Xil10b] Xilinx Inc., *LogiCORE IP Fast Simplex Link (FSL) V20 Bus*, April 2010, <http://www.xilinx.com/ipcenter>.
- [Xil10c] Xilinx Inc., *Virtex-6 FPGA Embedded Tri-Mode Ethernet MAC Wrapper v1.4, DS710 Product Specification*, April 2010, <http://www.xilinx.com/ipcenter>.
- [Xil11a] Xilinx Inc., *LogiCORE IP Adder/Subtractor v11.0*, March 2011, <http://www.xilinx.com/ipcenter>.
- [Xil11b] Xilinx Inc., *LogiCORE IP Block Memory Generator v6.1*, March 2011, <http://www.xilinx.com/ipcenter>.
- [Xil11c] Xilinx Inc., *LogiCORE IP ChipScope Pro Integrated Logic Analyzer (ILA)*, March 2011, <http://www.xilinx.com/support/documentation>.
- [Xil11d] Xilinx Inc., *LogiCORE IP Complex Multiplier v3.1*, March 2011, <http://www.xilinx.com/ipcenter>.
- [Xil11e] Xilinx Inc., *LogiCORE IP DDS Compiler v4.0*, March 2011, <http://www.xilinx.com/ipcenter>.
- [Xil11f] Xilinx Inc., *MicroBlaze Soft Processor Core*, 2011, <http://www.xilinx.com/tools/microblaze.htm>.
- [Xil11g] Xilinx Inc., *ML605 Hardware User Guide*, July. 2011, uG534 v1.6.
- [Xil11h] Xilinx Inc., *Platform Cable USB II*, March 2011, <http://www.xilinx.com/support/documentation>.
- [Xil11i] Xilinx Inc., *UG660 v13.1 ISim User Guide*, March 2011, <http://www.xilinx.com/ipcenter>.
- [Xil11j] Xilinx Inc., *Virtex-6 Family Overview*, March 2011, dS150 v2.3.
- [Yak74] W. C. Yakes, *Microwave Mobile Communications*, Wiley, New York, 1974.
- [Zha03] Y. Zhang, L. Zhang, and G. Liao, "PN code acquisition and beamforming weight acquisition for DS-CDMA systems with adaptive array", *14th IEEE Proceedings on*

- Personal, Indoor and Mobile Radio Communications, 2003. PIMRC 2003.*, vol. 2, pp. 1385–1389, September 2003.
- [Zie79] A. Zielinski, “On inversion of complex matrices”, *International Journal for Numerical Methods in Engineering*, vol. 14, no. 10, pp. 1563–1566, January 1979.
- [Zol95] M. D. Zoltowski, and A. S. Gecan, “Advanced adaptive null steering concepts for GPS”, *IEEE Military Communications Conference, 1995. MILCOM 1995*, vol. 3, pp. 1214–1218, November 1995.

Index

- acquisition, 23, 31, 212
acquisition time, 86
active antenna, 121
ADC (Analog-to-Digital Converter), 116, 159, 168
array element, 105, 127
array model, 64, 103
attenuation, 18
autocovariance matrix, 171
bandwidth, 51, 119
baseband, 8
beamformer, 79
 MVDR (Minimum Variance Distortionless Response), 81
 power minimization, 81
binary hypothesis, 32
calibration, 180
CMF (Coherent Matched Filter), 56
Compass, 15
correlation, 26
covariance matrix, 65, 72, 75, 86
cross-correlation, 89, 174
deflection coefficient, 34, 35, 71
demodulation, 27
detection theory, 32
detector
 clairvoyant, 34, 36, 65
 GLRT (Generalized Likelihood Ratio Test), 37, 68
 NP (Neyman-Pearson), 33
 UMP (Uniformly Most Powerful) test, 33, 74
Doppler effect, 17
embedded processor, 175
filter, 114, 131
FPGA (Field Programmable Gate Array), 168
front-end, 102, 117
gain, 119
Galileo, 13
geodesic distance, 86
GLONASS, 15
GNSS (Global Navigation Satellite System), 7
GNU Radio, 200
GPS (Global Positioning System), 11
harmonic balance, 125
interferences, 19, 75
joint acquisition, 41
linearity, 111, 156
LNA (Low Noise Amplifier), 107, 129
LO (Local Oscillator), 114, 145
mixer, 113, 136
MLE (Maximum Likelihood Estimator), 37, 69
navigation data, 27, 218
NCMF (Non-coherent Matched Filter), 56
NF (Noise Figure), 108, 120, 156
NMEA (National Marine Electronics Association), 205
noise
 colored, 72
 phase, 158
 white, 70
observables, 221
PCB (Printed Circuit Board), 162
PCDD (Post-correlation differential detector), 58
PCND (Post-Correlation Non-coherent Detector), 57
PDD (Pre-correlation differential detector), 58
PQN (Pseudo Quantization Noise), 87
processor, embedded, 175
propagation, 17
PVT (Position, Velocity, and Time), 28, 222
quantization, 87
receiver
 architecture, 202
 software defined, 192, 199
RINEX (Receiver Independent Exchange Format), 205
S-Parameters, 125
sensitivity, 67, 74
software design pattern, 195
space-time matrix, 64

- sufficient statistics, 33
- synchronization, 89
- telemetry, 27, 218
- tracking, 25, 216
 - pull-in, 236
- transmitter, 8
- UML (Unified Modeling Language), 193, 194
- wavenumber matrix, 103
- Wiener-Khinchine theorem, 51